RECONSTRUCTING PLIOCENE CLIMATIC, OCEANIC AND TECTONIC INTERACTIONS IN THE NORTH EAST ATLANTIC, NORDIC SEAS AND ONSHORE ICELAND BY GEOCHEMICAL FINGERPRINTING OF MARINE AND TERRESTRIAL SEDIMENTS

by

JONATHAN RICHARD HALL

A thesis submitted to the University of Birmingham
for the degree of DOCTOR OF PHILOSOPHY

School of Geography, Earth and Environmental Sciences
College of Life and Environmental Sciences
University of Birmingham
December 2020

UNIVERSITY OF
BIRMINGHAM

University of Birmingham Research Archive

e-theses repository

This unpublished thesis/dissertation is copyright of the author and/or third parties. The intellectual property rights of the author or third parties in respect of this work are as defined by The Copyright Designs and Patents Act 1988 or as modified by any successor legislation.

Any use made of information contained in this thesis/dissertation must be in accordance with that legislation and must be properly acknowledged. Further distribution or reproduction in any format is prohibited without the permission of the copyright holder.

ABSTRACT

During the Pliocene (5.33−2.58 Ma), the NE Atlantic and Nordic Seas witnessed a transition from enhanced warming, whereby surface temperatures were up to 8°C warmer than present, to cooling associated with the intensification of the Northern Hemisphere Glaciation. Currently, there are few reliable multiproxy datasets to document this change, and a notable mismatch between data- and model-based temperature reconstructions. This thesis develops a new palaeoclimatic, palaeoceanographic and palaeogeographic understanding of this region during the Pliocene by geochemical fingerprinting of marine and terrestrial sediments. First, new benthic foraminifera $\delta^{13}C$ and authigenic εNd records are used to assess tectonic and climatic controls on deep-water connectivity between the NE Atlantic and Norwegian basins. Secondly, new alkenone and TEX_{86} records are used to evaluate the magnitude of warming, and to unravel whether data/model discrepancies are attributable to proxy biases. Thirdly, brown coals from the Pliocene Tjörnes Beds in northern Iceland are investigated to establish whether they preserve branched GDGTs capable of reconstructing terrestrial temperatures. Together, these results suggest climatic events are at least as important as tectonic events in driving regional oceanic circulation at this time, and reveal data/model discrepancies are influenced by warming biases, associated with the analysis of low concentration alkenones.

ACKNOWLEDGEMENTS

None of the work contained in this thesis would have been possible without the help and support of so many people. First, I would like to thank my supervisory team Steve Jones, Tom Dunkley Jones and James Bendle for their continual support, insight and guidance throughout my PhD. I am very grateful to Steve for this opportunity, his constructive feedback and for introducing me to the wonders of Icelandic geology and their culinary delights.

This research is underpinned by the efforts of several collaborators at external institutions, who have shown invaluable interest in my project and have assisted with sample selection, preparation and analysis. I would like to thank Ian Bull, Leila Behrooz and Helen Whelton at the Organic Geochemistry Unit (OGU), University of Bristol, for analysing my polar lipid fractions for isoprenoid- and branched-GDGTs. For assisting with the analysis of $\delta^{13}C$ in my benthic foraminifera, thank you Melanie Leng and Hilary Sloane at the Stable Isotope Facility, British Geological Survey. Thank you to Alex Piotrowski and Christina Larkin at the Department of Earth Sciences, University of Cambridge, for their generous hospitality and training to leach and analyse Nd isotopes from my deep-sea sediments. I would like to thank Christopher Vane at the Organic Geochemistry Facility, British Geological Survey, for facilitating the Rock Eval™ pyrolysis of my lignite samples. Thank you to Dan Barfod at the Argon Isotope Facility, Scottish Universities Environmental Research Centre (SUERC), for his hospitality and training to prepare my basalts for $^{40}Ar/^{39}Ar$ dating. For supporting my research declaration and sharing their knowledge of the Tjörnes Beds, thank you to Jón Eiríksson and Áslaug Geirsdóttir at the University of Iceland. Finally, I would like to thank Holger Kuhlmann at the IODP Bremen Core Repository, University of Bremen, for assisting with my sampling requests.

The UK Natural Environmental Research Council (NERC) and the Centre for Doctoral Training (CDT) in Oil and Gas are thanked for providing the studentship (NE/M00578X/1) which made this PhD possible. Further thanks are to NERC for additional financial awards (BRIS/115/0418, IP/1855/1118, BRIS/138/1019) to support the analyses at the OGU and SUERC. I would like

to thank Lorna Morrow and Anna Clark at the CDT in Oil and Gas, for organising and delivering an exceptional 20-week training programme throughout my PhD, providing valuable insight into the evolving energy sector and offering unparalleled access to industry-led field courses in some geologically stunning locations, of which the French Alps, Almería and County Clare were a particular highlight.

I am also very grateful to my friends and colleagues at the University of Birmingham who have supported me throughout the last four years. My deepest thanks to Jack Richardson, Gaël Lymer, Derren Cresswell and Murray Hoggett in the subsurface imaging room for their noble friendship, humour and motivation. For training and assistance in the Birmingham Molecular Climatology laboratory, thank you to Yvette Eley, Matt O'Callaghan, Kweku Yamoah and Kate Newton. I am very thankful to MSci students Matthew Allison and Max Papadopoulos for assisting with fieldwork in Iceland; it was a pleasure to supervise you and your dedication and support was invaluable. For rock preparation, thin sectioning and uplifting banter, thank you to Andy Rees. Finally, I would like to offer a big thank you to Gretchel Coldicott and Aruna Mistry for providing a warm, supportive and friendly welcome to the department, assisting me with administrative duties and their dependable knowledge of University procedures.

Finally, my greatest thanks go to my family, especially my parents Christianne and Geoff, for without their unwavering support, love and encouragement over the years none of this would have been possible. Last but not least, a very big thank you to Rhiannon for your love and support, enduring my unforeseen visits to the GC room, and forcing me to rest and explore the outdoors with you every now and then.

CONTENTS

1. INTRODUCTION 1

1.1 PLIOCENE CLIMATE IN THE NE ATLANTIC AND NORDIC SEAS 1

1.2 OPENING OF THE NE ATLANTIC AND NORDIC SEAS 6

1.3 GEOLOGY OF ICELAND 8

1.4 SCOPE AND OUTLINE 11

2. A NEW COMPOSITE SECTION AND LITHOSTRATIGRAPHY FOR THE PLIOCENE TJÖRNES BEDS, NORTHERN ICELAND 15

2.1 ABSTRACT 16

2.2 INTRODUCTION 18

2.2.1 Geological Setting 19

2.3 MATERIALS AND METHODS 22

2.4 RESULTS 28

2.4.1 Composite Section 28

2.4.1.1 Stratigraphic architecture 28

2.4.1.2 Revised lithostratigraphy 30

2.4.2 Lithofacies analysis 33

2.4.2.1 Facies Association 1 (FA1): Tidally-modulated shoreface 33

2.4.2.2 Facies Association 2 (FA2): Intertidal sand flats 37

2.4.2.3 Facies Association 3 (FA3): Intertidal mixed flats 39

2.4.2.4 Facies Association 4 (FA4): Upper-estuarine distributary channels 41

2.4.2.5 Facies Association 5 (FA5): Coastal marshlands 43

2.5. DISCUSSION 45

2.5.1 Comparison of our revised stratigraphy with previous interpretations 45

2.5.2 Depositional model 51

2.5.3 Modern analogue 56

2.5.4 Implication of sediment reworking on biostratigraphy and relative age 59

2.6 CONCLUSIONS 62

3. TECTONIC AND CLIMATIC CONTROLS ON THE DEEP-WATER CONNECTIVITY OF THE NE ATLANTIC AND NORDIC SEAS DURING THE PLIOCENE 65

3.1 ABSTRACT 66
3.2 INTRODUCTION 68
3.2.1 Modern NE Atlantic and Nordic Seas Oceanography 69
3.2.2 Northern Component Water and Dynamic Support 71
3.3 NE ATLANTIC AND NORDIC SEAS $\delta^{13}C_{BF}$ DATASETS 77
3.4 MATERIAL, AGE MODEL AND METHODS 86
3.5 RESULTS 91
3.6 DISCUSSION 95
3.6.1 Secondary influences on $\delta^{13}C_{BF}$ and εNd records 95
3.6.2 Comparison of our $\delta^{13}C_{BF}$ and authigenic εNd datasets 98
3.6.3 Late Neogene evolution of Norwegian Sea deep-waters 107
3.6.3.1 Late Miocene to mid-Pliocene (7.0−3.0 Ma) 107
3.6.3.2. Late Pliocene: intensification of the NHG (3.0−2.5 Ma) 111
3.6.4 Long-term controls on Norwegian Sea deep-water ventilation 116
3.7 CONCLUSIONS 120

4. MID-PLIOCENE WARMING: CLOSING THE GAP BETWEEN GEOLOGICAL ARCHIVES AND CLIMATE MODELS IN THE NE ATLANTIC AND NORDIC SEAS 123

4.1 ABSTRACT 124
4.2 INTRODUCTION 126
4.2.1 Alkenones and irreversible adsorption 127
4.2.2 NE Atlantic PRISM discrepancies 130
4.3 NE ATLANTIC ALKENONE DATASETS 137
4.4 MATERIAL, AGE MODEL AND METHODS 145
4.4.1 Alkenones 147
4.4.1.1 Correcting $U^{K'}_{37}$ results for irreversible adsorption effects 148
4.4.2 Isoprenoid GDGTs 151
4.5 RESULTS 154
4.5.1 $U^{K'}_{37}$-derived SST estimates 154
4.5.2 Alkenone concentrations 156
4.5.3 Corrected $U^{K'}_{37}$-derived SSTs 158
4.5.4 TEX_{86} SSTs 159

4.6 DISCUSSION 162
4.6.1 Fidelity of our PRISM-interval $U^{K'}_{37}$ and TEX_{86} datasets 162
4.6.2 Comparison with existing NE Atlantic and Nordic Sea PRISM-interval $U^{K'}_{37}$ records 169
4.6.3 Unravelling the magnitude of mid-Pliocene warming at DSDP Site 552 171
4.6.4 Implications for PRISM and GCM discrepancies in the NE Atlantic 175
4.7 CONCLUSIONS 180

5. GEOCHEMICAL ANALYSES OF BROWN COALS AND BASALTS FROM THE PLIOCENE TJÖRNES BEDS, NORTHERN ICELAND: PRELIMINARY RESULTS 183

5.1 OPENING REMARKS 184
5.2 INTRODUCTION 185
5.2.1 Geological Setting 187
5.3 BACKGROUND 190
5.3.1 Previous age models for the Tjörnes Beds 190
5.3.2 Branched GDGTs at Tjörnes: a potential onshore Pliocene palaeothermometer 196
5.3.3 Hydrocarbon-related research at Tjörnes 200
5.4 MATERIALS, AGE MODEL AND METHODS 205
5.4.1 Basaltic lavas 205
5.4.2 Lignite seams 208
5.4.3 Branched GDGTs 209
5.4.3.1 Proxy Calculation 210
5.4.4 Rock-Eval™ Pyrolysis 213
5.5 RESULTS 215
5.5.1 Tjörnes lava descriptions 215
5.5.2 Branched GDGT distributions in the Tjörnes lignites 215
5.5.3 Branched GDGT ratios and MAAT, pH and BIT trends 217
5.5.4 Rock-Eval™ Pyrolysis 219
5.6 DISCUSSION 222
5.6.1 Fidelity of br-GDGT palaeothermometry in the Tjörnes lignite deposits 222
5.6.1.1 Calibration uncertainties 224
5.6.1.2 Fossil versus extant br-GDGTs 229
5.6.1.3 Influence of diagenetic and catagenic effects 233

5.6.2 Reliability of Tjörnes br-GDGTs for Pliocene temperature reconstructions 235
5.6.3 Source rock potential of the Tjörnes lignite seams..... 237
5.7 CONCLUSIONS..... 241
6. SUMMARY 244
6.1 General conclusions..... 244
6.2 Future recommendations 249
6.2.1 Chapter 2: A new composite section and lithostratigraphy for the Pliocene Tjörnes Beds, northern Iceland. 249
6.2.2 Chapter 3: Tectonic and climatic controls on the deep-water connectivity of the NE Atlantic and Nordic Seas during the Pliocene..... 249
6.2.3 Chapter 4: Mid-Pliocene warming: closing the gap between geological archives and climate models in the NE Atlantic and Nordic Seas 250
6.2.4 Chapter 5: Geochemical analyses of brown coals and basalts from the Pliocene Tjörnes Beds, northern Iceland: preliminary results..... 251
REFERENCES 252
APPENDIX A: METHODS..... 304
A.1 Extracting and picking foraminifera from bulk sediments..... 304
A.2 Leaching authigenic coatings and neodymium column chemistry 306
A.3 Extraction of marine biomarkers from bulk sediments..... 310
A.4 Correcting alkenone SSTs for warming and cooling biases 312
A.5 Argon dating sample preparation for basalts..... 316
A.6 Extraction of terrestrial biomarkers from brown coal 317
APPENDIX B: DATA TABLES..... 319

LIST OF FIGURES

1.1. Bathymetric map of the NE Atlantic Ocean, Nordic Seas and Arctic Ocean 2
1.2. Cenozoic chronostratigraphic column showing the position of the Pliocene Epoch 5
1.3. Tectonic reconstructions showing the pre- and post-breakup of the NE Atlantic 8
1.4. Geological map of Iceland 9
1.5. Conceptual model showing the materials and methods used in this study 12
2.1. Location and geological setting of the Tjörnes Peninsula, northern Iceland 21
2.2. Geological map and sections of the Tjörnes Beds 24
2.3. Structure contouring technique used to estimate the thickness of missing strata 25
2.4. Images of faulting in the Tjörnes Beds, obtained using an UAV-mounted camera 27
2.5. Summary composite stratigraphic section 30
2.6. Photo panel of important Tjörnes localities 31
2.7. Detailed summary of sedimentological data collected from the Tjörnes Beds 39
2.8. Photo panel of characteristic Tjörnes sedimentological features 41
2.9. Comparison between the revised and existing Tjörnes stratigraphic sections 47
2.10. Summary 3D palaeodepositional history for the Tjörnes Beds 54
2.11. Annotated satellite image of the Kaldárós Lagoon in western Iceland 58
3.1. Bathymetric map of the NE Atlantic Ocean, Nordic Seas and Arctic Ocean 70
3.2. Schematic cross section across the Greenland-Scotland Ridge 72
3.3. Global summary of compiled $\delta^{13}C_{BF}$ records and associated %NCW estimates 75
3.4. Location map of NE Atlantic and Nordic Seas DSDP/ODP/IODP drilling sites 78
3.5. Compilation of NE Atlantic and Nordic Seas $\delta^{13}C_{BF}$ records for the 0−8000 kyr interval 82
3.6. Stable isotope fractionation of *C. teretis* versus *C. wuellerstorfi* 82
3.7. Deconstructed regional compilations of $\delta^{13}C_{BF}$ records for the 0−8000 kyr interval 85
3.8. Stratigraphic summary of NE Atlantic and Nordic Seas DSDP/ODP/IODP drilling sites 88
3.9. $\delta^{13}C_{BF}$ results from ODP Hole 642B and DSDP Hole 552A 93
3.10. εNd results from ODP Hole 642B and DSDP Hole 552A 93
3.11. SEM images of single foraminifera specimens analysed for $\delta^{13}C$ 97
3.12. Planktic-benthic $\delta^{13}C$ gradient ($\Delta\delta^{13}C$) at ODP Site 642 101
3.13. Compilation of existing NE Atlantic and Nordic Seas εNd records 106
3.14. Summary 3D palaeoceanographic evolution of the NE Atlantic and Nordic Seas 110
3.15. Summary palaeoceanographic sections across the Greenland-Scotland Ridge 116
4.1. Map showing the distribution of PRISM localities and associated ΔSST values 129
4.2. Chemical structures of alkenones and isoprenoid GDGTs 131

4.3. Regional summary of PRISM SSTs and the relationship with GCM simulations..... 135
4.4. Location map of NE Atlantic and Nordic Seas DSDP/ODP/IODP drilling sites 137
4.5. Compilation of NE Atlantic and Nordic Sea alkenone records from 0−8000 kyr..... 141
4.6. Compilation of NE Atlantic and Nordic Sea alkenone records from the mPWP 143
4.7. Alkenone dilution series 149
4.8. Raw and corrected alkenone-based SST results for the 0−8000 kyr interval..... 156
4.9. Raw and corrected alkenone-based SST results during the PRISM-interval 158
4.10. TEX_{86} and OPTiMAL based SST results during the PRISM-interval..... 161
4.11. Cross plots showing the relationships between the alkenone and TEX_{86} SSTs..... 164
4.12. Summary of BIT index, ΔRI and %GDGT-0 records from our TEX_{86} based SSTs 168
4.13. Comparison of our alkenone-based SST results with existing records 171
4.14. NE Atlantic mid-Pliocene SST reconstructions based on the ΔSSTs proposed here. 175
4.15. Global mid-Pliocene SST reconstructions based on the ΔSSTs proposed here 177
5.1. Location and geological setting of the Tjörnes Peninsula, northern Iceland..... 189
5.2. Comparison of existing age models for the Tjörnes Beds..... 193
5.3. Chemical structures of branched GDGTs..... 199
5.4. Maturation and source rock characterisation after Richter (2003) 204
5.5. Geological map of the Tjörnes sequence showing sampling locations 208
5.6. Petrographic features of the Tjörnes lava samples..... 217
5.7. Mineralogical abundances of the Tjörnes lavas..... 217
5.8. Summary of br-GDGTs, MAAT and pH estimates derived from the Tjörnes lignites.... 219
5.9. Comparison of Tjörnes Beds br-GDGT, pollen and mollusc temperature records 224
5.10. Comparison of br-GDGT abundances in Icelandic soils, peats and lignites..... 226
5.11. Location and geological setting of Hengifoss, eastern Iceland 232
5.12. Organic matter, maturation and source rock characterisation of the Tjörnes lignites. 239
A.1. Dilution series showing the sensitivity of SSTs to high and low C_{37} concentrations..... 314

LIST OF TABLES

2.1. Descriptions of lithofacies identified in the Tjörnes Beds 36
3.1. Sources of $\delta^{13}C_{BF}$ records used in the NE Atlantic and Nordic Seas compilation 79
3.2. Sources of εNd records used in the NE Atlantic and Nordic Seas compilation 103
4.1. Sources of alkenone records used in the NE Atlantic and Nordic Seas compilation 141
4.2. Summary of the mean raw and corrected alkenone-based SSTs and ΔSSTs 154
5.1. Lignite and basalt sampling localities 208
5.2. Rock-Eval™ pyrolysis data derived from the Tjörnes lignites 220
5.3. K-Nearest Neighbour (k-NN) analyses for the Tjörnes and Hengifoss lignite..... 228
A.1. Example alkenone SST corrections 313
A.2. Frantz Isodynamic Separator settings..... 316
B.1. $\delta^{13}C$ in benthic foraminifera from DSDP Hole 552A 319
B.2. $\delta^{13}C$ in benthic foraminifera from ODP Hole 642B 320
B.3. Authigenic Fe-Mn leachate εNd from ODP Hole 642B and DSDP Hole 552A..... 321
B.4. Alkenone-based SST reconstructions from IODP Site U1308..... 322
B.5. Alkenone-based SST reconstructions from DSDP Hole 552A..... 323
B.6. Alkenone-based SST reconstructions from ODP Hole 642B..... 325
B.7. Alkenone-based SST reconstructions from ODP Hole 907A..... 327
B.8. TEX_{86} SST reconstructions from IODP Site U1308 328
B.9. TEX_{86} SST reconstructions from DSDP Hole 552A..... 329
B.10. TEX_{86} SST reconstructions from ODP Hole 642B 331
B.11. TEX_{86} SST reconstructions from ODP Hole 907A 333
B.12. Tjörnes basalt thin section descriptions 334
B.13. Branched GDGT temperature reconstructions from the Tjörnes lignites 336

LIST OF EQUATIONS

3.1. Percentage overflow of Northern Component Water. 73
3.2. Epsilon notation used to express the isotopic composition of neodymium. 90
4.1. Alkenone unsaturation index 129
4.2. Global core-top $U^{K'}_{37}$ versus SST calibration 129
4.3. TEX_{86}^{L} index 152
4.4. TEX_{86}^{H} index 152
4.5. Global core-top TEX_{86}^{L} versus SST calibration 152
4.6. Global core-top TEX_{86}^{H} versus SST calibration 152
4.7. BIT index 153
4.8. %GDGT-0 index 166
4.9. Ring index (RI) 166
4.10. TEX_{86}−RI quadratic regression 166
4.11. ΔRI 166
5.1. MBT' index 210
5.2. MBT'_{5ME} index 211
5.3. Linear regression of MBT'_{5ME} against MAT 211
5.4. Multiple linear regression analysis (MAT_{mr}) 211
5.5. Peat-specific MAAT proxy 211
5.6. CBT' index 212
5.7. CBT' index modelled as a function of pH in mineral soil 212
5.8. CBT' index modelled as a function of pH in peat 212
5.9. CBT_{peat} index 213
5.10. Peat-specific pH calibration 213
5.11. BIT index 213
5.12. Hydrogen index (HI) 214
5.13. Oxygen index (OI) 214
5.14. Production index (PI) 214

LIST OF ABBREVIATIONS

AMOC	Atlantic Meridional Overturning Circulation
ATNTS	Astronomically-tuned Neogene Time Scale
BIT	Branched and Isoprenoid Tetraether index
Br-GDGTs	Branched Glycerol Dialkyl Glycerol Tetraethers
CAS	Central American Seaway
CBT	Cyclisation of Branched Tetraethers
DEM	Digital Elevation Model
DSDP	Deep Sea Drilling Project
DSOW	Denmark Strait Overflow Water
EGC	East Greenland Current
EIC	East Iceland Current
EVZ	Eastern Volcanic Zone
GC	Gas Chromatography
GCM	General Circulation Model
GSR	Greenland-Scotland Ridge
HC	Hydrocarbon
HI	Hydrogen Index
iNHG	Intensification of the Northern Hemisphere Glaciation
IODP	Integrated Ocean Drilling Program
IPCC	Intergovernmental Panel on Climate Change
IRD	Ice Rafted Debris
Iso-GDGTs	Isoprenoid Glycerol Dialkyl Glycerol Tetraethers
ISOW	Iceland-Scotland Overflow Water
k-NN	k-Nearest Neighbours algorithm
MAAT	Mean Annual Air Temperature
MAR	Mid Atlantic Ridge
MAT	Mean Annual Temperature
MBT	Methylation of Branched Tetraethers
MIS	Marine Isotope Stage
MLD	Mixed Layer Depth
mPWP	mid-Piacenzian Warm Period
NAC	North Atlantic Current
NADW	North Atlantic Deep Water

NCW	Northern Component Water
NSDW	Norwegian Sea Deep Water
NVZ	Northern Volcanic Zone
NWAC	Norwegian Atlantic Current
ODP	Ocean Drilling Program
OI	Oxygen Index
OPTiMAL	Optimised Palaeothermometry from Tetraethers via MAchine Learning
PI	Production Index
PRISM	Pliocene Research, Interpretation and Synoptic Mapping group
SCW	Southern Component Water
SST	Sea Surface Temperature
TEX_{86}	Tetraether index of tetraethers
TFZ	Tjörnes Fracture Zone
TLE	Total Lipid Extract
TOC	Total Organic Carbon
UAV	Unmanned Aerial Vehicle
$U^{K'}_{37}$	Alkenone unsaturation index
WVZ	Western Volcanic Zone
$\delta^{13}C_{BF}$	$^{13}C/^{12}C$ in benthic foraminifera, reported in per mil (‰)
$\delta^{13}C_{DIC}$	$^{13}C/^{12}C$ of dissolved inorganic carbon, reported in per mil (‰)
$\delta^{18}C_{BF}$	$^{18}O/^{16}O$ in benthic foraminifera, reported in per mil (‰)

1. INTRODUCTION

1.1 PLIOCENE CLIMATE IN THE NE ATLANTIC AND NORDIC SEAS

The Pliocene Epoch extends from 5.33 to 2.58 Ma and occurs between the older Miocene Epoch and the younger Pleistocene Epoch (Hilgen et al., 2012). The Pliocene is divided into the Zanclean (5.33−3.60 Ma) and Piacenzian (3.60−2.58 Ma). The base of the Zanclean corresponds to the top of polarity chron C3r, within the Gilbert reversed chron (Van Couvering et al., 2000). The base of the Piacenzian is marked by the Gilbert/Gauss magnetic reversal and marine isotope stage (MIS) MG8 (Castradori et al., 1998). The base of the overlying Pleistocene Epoch corresponds to the Gauss/Matuyama reversal and MIS 103 (Rio et al., 1998). The global benthic $\delta^{18}O$ stack (Lisiecki and Raymo, 2005), indicates the Pliocene Epoch was relatively warm and climatologically stable, with reduced ice sheet volumes.

The Zanclean contains the warmest interval (4.4−4.0 Ma) of the Pliocene, with a global average temperature c. 4°C warmer than present (Brierley and Fedorov, 2010). Zonal and meridional sea surface temperature (SST) gradients lowered at this time due to the development of tropical warm pools and warm high latitude oceans. This weakened atmospheric circulation and caused a deeper thermocline in the tropics (Brierley et al., 2009; Fedorov et al., 2013). Atmospheric CO_2 varied between 380−400 ppm (Pagani et al., 2010; Seki et al., 2010). Global ice volumes were relatively stable (Lisiecki and Raymo, 2005). However, ice-rafted debris (IRD) records indicate the occasional expansion of localised ice sheets in the Arctic region. Pulses of IRD are found in the Irminger Basin, Iceland and Norwegian Seas between 4.9 and 4.0 Ma (Fig. 1.1; St. John and Krissek, 2002; Fronval and Jansen, 1996; Bachem et al., 2017). Major changes in oceanic circulation occurred during the Zanclean: (1) shoaling of the Central American Seaway (CAS) strengthened Atlantic Meridional Overturning Circulation and poleward heat transport (Fig. 1.2; Haug and Tiedemann, 1998; Steph et al., 2010; Bell et al., 2015), initiated the development of a Pacific-

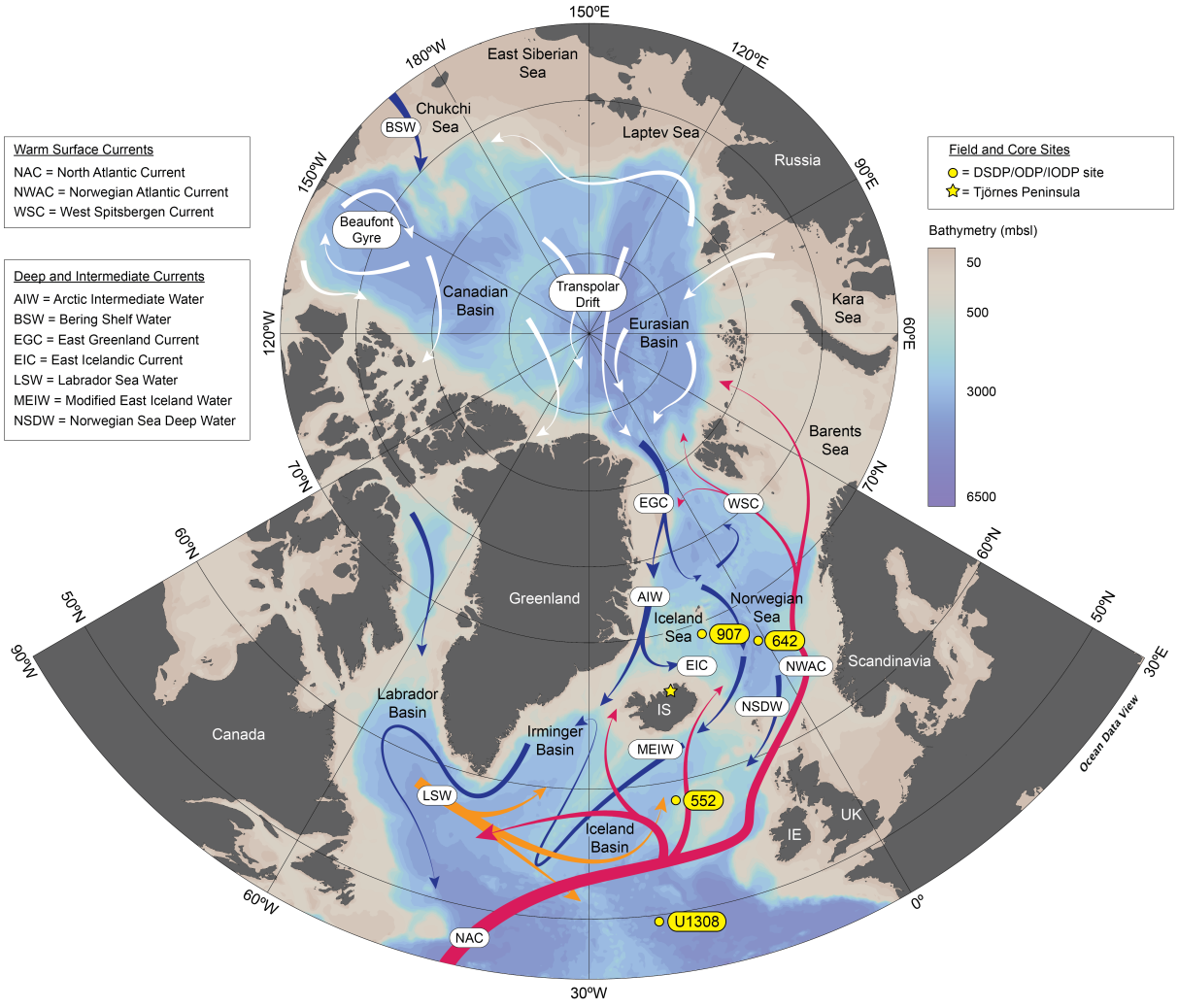


Figure 1.1. Bathymetric map of the NE Atlantic Ocean, Nordic Seas and Arctic Ocean. Red, orange and blue arrows indicate surface, intermediate and deep ocean currents respectively. Relevant DSDP/ODP/IODP drilling sites and fieldwork localities discussed in this study are highlighted yellow. Bathymetric map created in Ocean Data View v.5.1.7.

Atlantic salinity contrast and increased the steric sea level elevation of the Pacific compared to the Atlantic (Schneider and Schmittner, 2006; Sarnthein et al., 2009); and (2) opening of the Bering Strait strengthened the northward throughflow of Pacific waters into the Arctic and Nordic Seas c. 4.5 Ma (Fig. 1.2; De Schepper et al., 2015). This enhanced Arctic throughflow is supported by the arrival of North Pacific molluscs in the North Atlantic around 3.6 Ma (Fig. 1.2; Marincovich, 2000; Símonarson and Eiríksson, 2008). From c. 4.0 Ma, the Iceland Sea cooled relative to the Norwegian Sea, resulting in a sea surface temperature gradient of c.

10°C, which is attributed to the strengthened influence of a cooler East Greenland Current (EGC) (Fig. 1.1; De Schepper et al., 2015; Bachem et al., 2017; Herbert et al., 2016).

The Piacenzian contains the mid-Piacenzian Warm Period (mPWP; 3.264−3.025 Ma), during which average global surface temperatures were 2−3°C warmer than preindustrial conditions, within the range estimated by the Intergovernmental Panel on Climate Change for the end of the 21st Century (Dowsett et al., 2010a, 2012; Salzmann et al., 2011). Atmospheric CO_2 varied between 365−415 ppm (Pagani et al., 2010; Seki et al., 2010), similar to present (2019 average 409.8 ppm; NOAA, 2020). The global benthic $\delta^{18}O$ stack indicates ice volume increased slightly during the mPWP compared to the Zanclean (Lisiecki and Raymo, 2005). IRD input increased in the Iceland, Greenland and Labrador Seas (Fig. 1.1; Fronval and Jansen, 1996; Jansen et al., 2000; Sarnthein et al., 2009; Wolf and Thiede, 1991), associated with small-scale glaciations in southeast Greenland (Dolan et al., 2011; Koenig et al., 2015) and onshore Iceland (Eiríksson and Geirsdóttir, 1991). SSTs in the NE Atlantic and Nordic Seas were up to 8°C warmer than modern (Robinson et al., 2008; Robinson, 2009), reflecting enhanced poleward heat transport associated with the closure of the CAS (Fig. 1.2; Dowsett et al., 2012). Dowsett et al. (2010a) suggest the extent of Arctic sea ice during the Pliocene winter corresponds to present-day summer minimum conditions. The mPWP follows the short MIS M2 glaciation (c. 3.3 Ma), commonly interpreted to represent a failed attempt to initiate a large Northern Hemisphere Glaciation (Haug and Tiedemann, 1998). During MIS M2, North Atlantic SSTs reduced by 4°C and warm water dinoflagellates were replaced by cooler species (De Schepper et al., 2009; 2013; Lawrence et al., 2009; Naafs et al., 2010). The causal mechanism for MIS M2 is uncertain. De Schepper et al. (2013) suggest the MIS M2 was driven by a temporary weakening in poleward heat transport due to the brief re-opening of the CAS, and the inflow of cooler, less saline Pacific waters into the Caribbean, which impeded the northward flow of the warm North Atlantic Current. However, recent modelling suggests the re-opening of the CAS would only cause Northern Hemisphere ice sheets to expand slightly, and is unlikely to drive the MIS M2 glaciation alone (Tan et al., 2017).

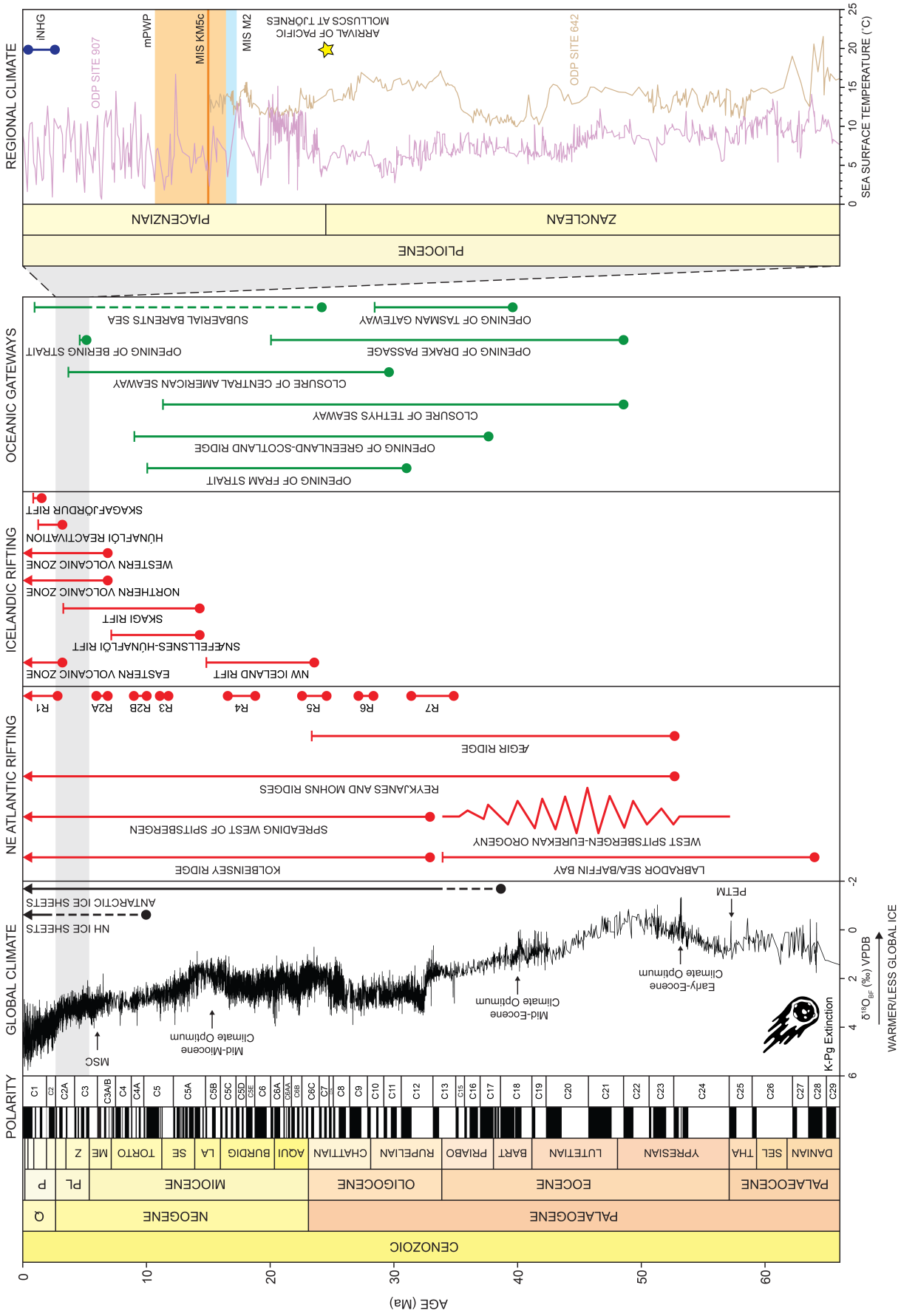

REGIONAL CLIMATE
SEA SURFACE TEMPERATURE (°C)
iNHG
ODP SITE 907
mPWP
MIS KM5c
MIS M2
ARRIVAL OF PACIFIC MOLLUSCS AT TJÖRNES
ODP SITE 642
PLIOCENE
PLACENZIAN
ZANCLEAN
OCEANIC GATEWAYS
OPENING OF TASMAN GATEWAY
SUBAERIAL BARENTS SEA
OPENING OF DRAKE PASSAGE
OPENING OF BERING STRAIT
CLOSURE OF CENTRAL AMERICAN SEAWAY
CLOSURE OF TETHYS SEAWAY
OPENING OF GREENLAND-SCOTLAND RIDGE
OPENING OF FRAM STRAIT
ICELANDIC RIFTING
SKAGAFJÖRDUR RIFT
HÚNAFLÓI REACTIVATION
WESTERN VOLCANIC ZONE
NORTHERN VOLCANIC ZONE
SKAGI RIFT
SNÆFELLSNES-HÚNAFLÓI RIFT
NW ICELAND RIFT
EASTERN VOLCANIC ZONE
NE ATLANTIC RIFTING
R1
R2A
R2B
R3
R4
R5
R6
R7
AEGIR RIDGE
REYKJANES AND MOHNS RIDGES
SPREADING WEST OF SPITSBERGEN
WEST SPITSBERGEN-EUREKAN OROGENY
KOLBEINSEY RIDGE
LABRADOR SEA/BAFFIN BAY
GLOBAL CLIMATE
ANTARCTIC ICE SHEETS
NH ICE SHEETS
PETM
MSC
Mid-Miocene Climate Optimum
Mid-Eocene Climate Optimum
Early-Eocene Climate Optimum
K-Pg Extinction
δ18OBF (‰) VPDB
WARMER/LESS GLOBAL ICE
POLARITY
CENOZOIC
PALAEOGENE
NEOGENE
Q
P
PL
MIOCENE
OLIGOCENE
EOCENE
PALAEOCENE
DANIAN
SEL
THA
YPRESIAN
LUTETIAN
BART
PRIABO
RUPELIAN
CHATTIAN
AQUI
BURDIG
LA
SE
TORTO
ME
Z
AGE (Ma)

Figure 1.2 (previous page). Cenozoic chronostratigraphic column showing the position of the Pliocene Epoch (shaded grey) after Gradstein et al. (2012). Published records of $\delta^{18}O$ in benthic foraminifera ($\delta^{18}O_{BF}$) (Zachos et al., 2001), NE Atlantic and Icelandic rifting (Doré and Lundin, 1996; Garcia et al., 2003; Walters et al., 2013), V-shaped ridge (R1 etc.) formation (Jones et al., 2002), oceanic gateway events (Straume et al., 2020) and regional sea surface temperature records (Herbert et al., 2016; Bachem et al., 2017; Clotten et al., 2018) are also shown. PETM, Palaeocene-Eocene Thermal Maximum; MSC, Messinian Salinity Crisis; MIS M2, Marine Isotope Stage M2; mPWP, mid-Piacenzian Warm Period; MIS KM5c, Marine Isotope Stage KM5c (dark orange line); iNHG, intensification of the Northern Hemisphere Glaciation; ODP, Ocean Drilling Program.

Following the mPWP, global ice volume increased rapidly with the intensification of the Northern Hemisphere Glaciation (iNHG; c. 2.7 Ma), before culminating in the intense glacial/interglacial cycles indicative of the Quaternary (Fig. 1.2; Lisiecki and Raymo, 2005). Continental ice sheets expanded across Scandinavia, Greenland and North America, with increased inputs of IRD recorded in the Barents Sea, Nordic Seas, Labrador Sea, North Atlantic and North Pacific (Knies et al., 2009, 2014; Jansen et al., 2000; Sarnthein et al., 2009; Henrich et al., 1989; Flesche Kleiven et al., 2002; Haug et al., 2005). Multiple mechanisms were proposed including variations in orbital parameters (Maslin et al., 1998), oceanic gateways (Einarsson et al., 1967) and atmospheric CO_2 (Lunt et al., 2008). One theory suggests the Greenland-Scotland Ridge (GSR) acts as a regional lock-gate in response to thermal perturbations within the Icelandic plume (Wright and Miller, 1996). A reduction in dynamic support of the GSR during the Pliocene, caused by a cooler perturbation, is believed to have enhanced regional circulation and poleward heat transport, possibly preconditioning the Nordic Seas for the iNHG (Wright and Miller, 1996; Poore et al., 2006). However, the most favoured mechanism suggests cooling and ice-sheet growth was controlled by the interaction of two main processes: long-term CO_2 drawdown modulated by orbital forcing and the emergence of the CAS, which strengthened poleward oceanic heat transport and moisture supply to the mid to high latitudes (Haug and Tiedemann, 1998; Lunt et al., 2008; De Schepper et al., 2013; Willeit et al., 2015).

1.2 OPENING OF THE NE ATLANTIC AND NORDIC SEAS

Tectonic reconstructions indicate rifting commenced in the Central Atlantic during the Jurassic (c. 180−175 Ma; Lundin, 2002), before propagating northwards into the NE Atlantic by the early Cretaceous. Rifting occurred along a chain of basins extending between the Iberia and Newfoundland margins, via the Rockall, Faroe-Shetland, Norwegian, Vøring, Lofoten, and Harstad basins into the Tromsø and Bjørnøya basins of the SW Barents Sea (Doré et al. 1999). The Rockall Trough developed its present deep-water, sediment-starved, steep-sided expression by the late Cretaceous (Hitchen et al., 2013). A separate arm of the rift system propagated up into the future Labrador Sea, where seafloor spreading initiated by the early Palaeocene separating Greenland from Canada (c. 62 Ma; Mjelde et al., 2008).

The onset of the North Atlantic Igneous Province occurred between 63 to 60 Ma during the pre-breakup phase of the NE Atlantic between Greenland and NW Europe, when the proto-Icelandic plume arrived under Central Greenland, elevating the asthenosphere temperature and driving local melting (Fig. 1.3; Tegner et al., 1998; Lundin and Doré, 2005; Saunders et al., 2007; Storey et al., 2007a, 2007b). The central NE Atlantic was covered with extensive and voluminous (c. 6.6 million km^3) plateau basalts, dyke swarms and volcanic complexes on adjacent elevated margins, including Northern Ireland (Ganerød et al., 2010), Scotland (Chambers and Pringle, 2001), Norway (Sinton et al., 1998), East and West Greenland (Larsen and Saunders, 1998) and Baffin Island (Larsen et al., 2016). In the early Eocene (c. 55 Ma), the lithosphere ruptured, marking the onset of the post-breakup phase and the initiation of seafloor spreading in the NE Atlantic. A triple junction formed between the Labrador Sea, the southern North Atlantic and the NE Atlantic (Srivastava and Roest, 1999).

Seafloor spreading to the east of Greenland occurred along three mid-ocean ridge segments: the Reykjanes, Mohns and Ægir Ridges (Fig. 1.3; Oakey and Chalmers, 2012; Ellis and Stoker, 2014). During the early Oligocene (c. 33 Ma), the newly formed Kolbeinsey Ridge propagated

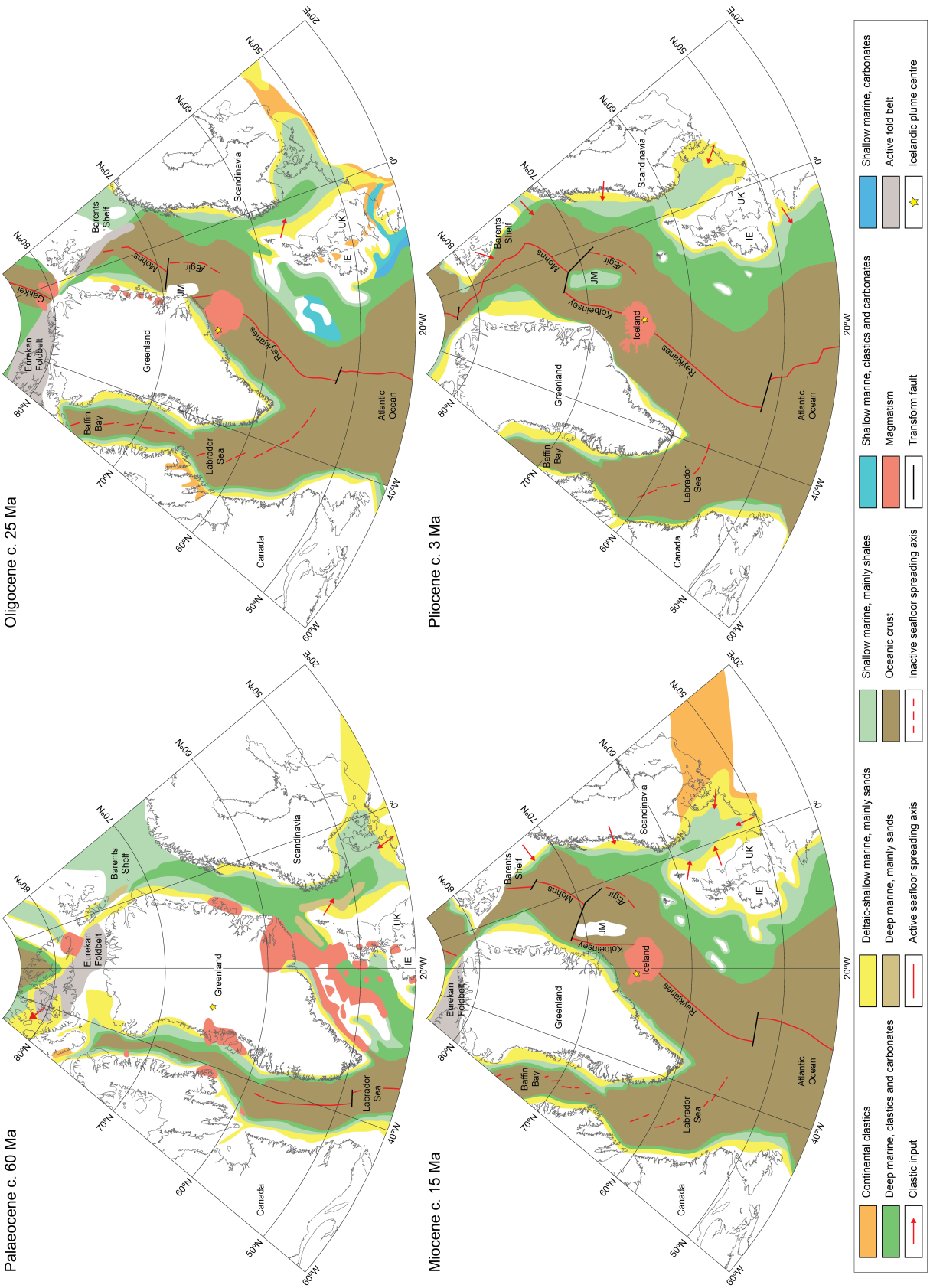

Oligocene c. 25 Ma
Pliocene c. 3 Ma
Palaeocene c. 60 Ma
Miocene c. 15 Ma
Barents Shelf
Eurekan Foldbelt
Greenland
Scandinavia
UK
IE
Baffin Bay
Labrador Sea
Canada
Atlantic Ocean
Gakkel
Mohns
Ægir
JM
Reykjanes
Kolbeinsey
Iceland
80°N
70°N
60°N
50°N
40°W
20°W
0°
20°E
Continental clastics
Deltaic-shallow marine, mainly sands
Shallow marine, mainly shales
Shallow marine, clastics and carbonates
Shallow marine, carbonates
Deep marine, clastics and carbonates
Deep marine, mainly sands
Oceanic crust
Magmatism
Active fold belt
Clastic input
Active seafloor spreading axis
Inactive seafloor spreading axis
Transform fault
Icelandic plume centre

Figure 1.3 (previous page). Tectonic reconstructions showing the pre- and post-breakup of the NE Atlantic at 60 Ma, 25 Ma, 15 Ma and 3 Ma. JM, Jan Mayan. Modified from Skogseid et al. (2000) and Torsvik et al. (2002).

north of Iceland, separating the Jan Mayen microcontinent from Greenland, and coincided with the cessation of seafloor spreading in the Labrador Sea (Fig. 1.3; Srivastava and Roest, 1999). The Ægir and Kolbeinsey Ridges formed an opposed and overlapping geometry, with the tips trying to join the Reykjanes and Mohns Ridges, respectively (Fig. 1.3). The Kolbeinsey Ridge succeeded, joining the Mohns Ridge via the Jan Mayen Fracture Zone, and caused spreading at the Ægir Ridge to terminate by the late Oligocene (Blischke et al., 2017). The proto-Icelandic plume axis crossed the East Greenland coast between 40 to 35 Ma, and reached the Mid-Atlantic Ridge (MAR) around 25 Ma (Fig. 1.3; Lawver and Müller, 1994; Gaina et al., 2009). The migration of this hotspot and its interaction with the MAR generated the GSR, a volcanic structural high which stretches across the NE Atlantic (Wright and Miller, 1996). The MAR has since undergone multiple ridge jumps to remain locked over the plume axis, where sustained magmatism and thickening of the GSR produced the Icelandic Plateau, which rises more than 3000 m above the seafloor and covers c. 350,000 km^2 (Fig. 1.3; Einarsson, 2008). The construction of Iceland, which forms the subaerial part of this plateau, is considered to have commenced around 24 Ma (Fig. 1.3; Einarsson, 2008).

1.3 GEOLOGY OF ICELAND

Iceland is divided by the central inland rift zone which represents a large subaerial section of the MAR, exposed due to the thick crustal architecture (c. 20−40 km) and increased dynamic support of the underlying plume (Fig. 1.4; Jones et al., 2002; Foulger et al., 2003). The Reykjanes Ridge connects to the Western Volcanic Zone (WVZ) on the Reykjanes Peninsula, and the Kolbeinsey Ridge connects to the Northern Volcanic Zone (NVZ) via the Tjörnes Fracture Zone (TFZ; Fig. 1.4). The full spreading rate of the MAR onshore Iceland is c. 18 mm/yr (Sigmundsson et al., 2020). The rift zones show repeated eastward relocation of the

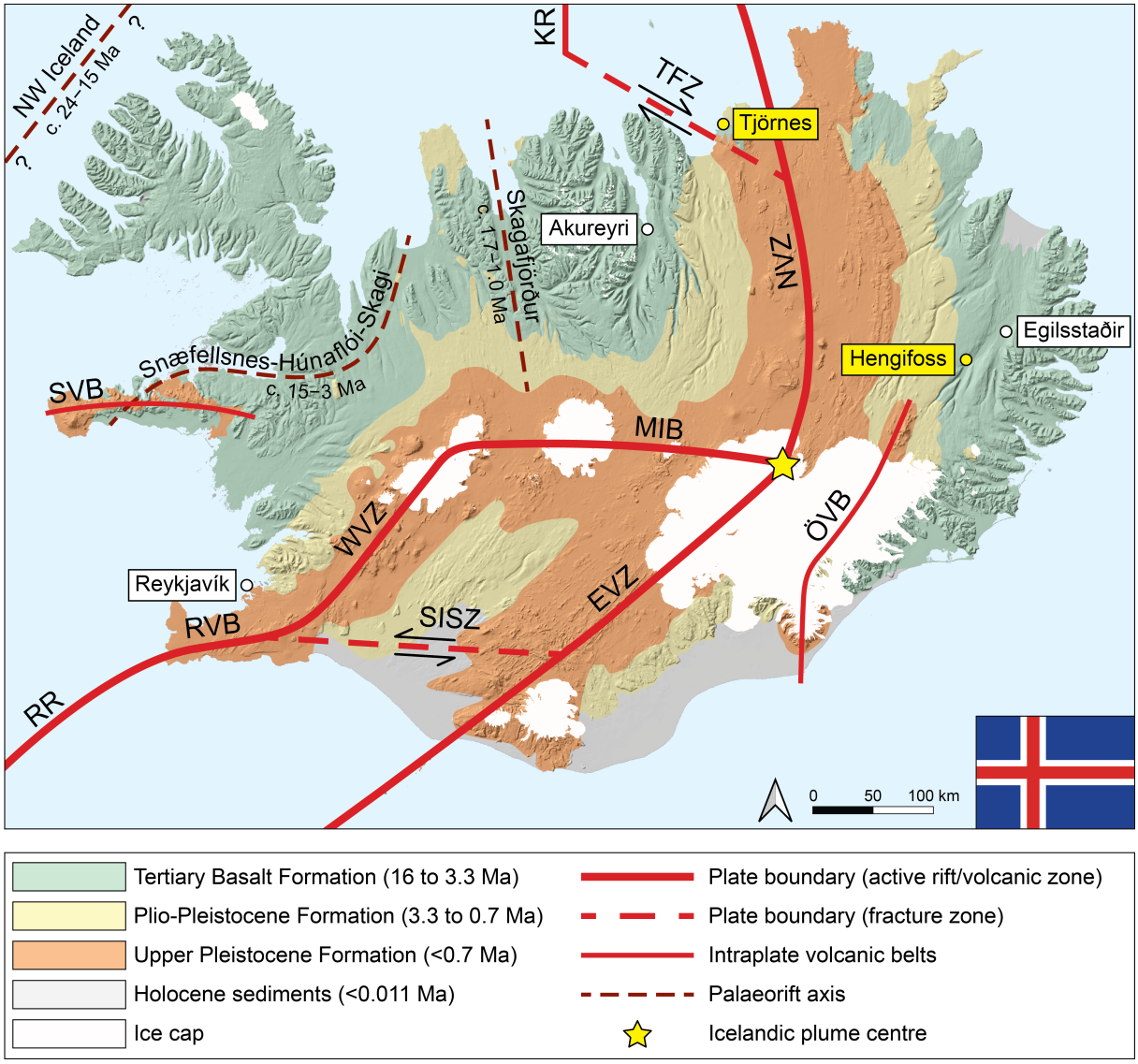


Figure 1.4. Geological map of Iceland outlining the distribution of major formations, fault structures, palaeorift axes, volcanic zones and belts. Field localities discussed herein are highlighted in yellow. RR, Reykjanes Ridge; RVB, Reykjanes Volcanic Belt; WVZ, West Volcanic Zone; MIB, Mid-Iceland Belt; SISZ, South Iceland Seismic Zone; EVZ, East Volcanic Zone; NVZ, North Volcanic Zone; TFZ, Tjörnes Fracture Zone; KR, Kolbeinsey Ridge; ÖVB, Öræfi Volcanic Belt; and SVB, Snæfellsnes Volcanic Belt. Geological map created in QGIS v.3.4 using the Landmælingum Íslands (National Land Survey of Iceland) Digital Elevation Model (available at: https://atlas.lmi.is/LmiData/index.php?id= 247152041610 [accessed 06/01/2020]). Modified from Thordarson and Höskuldsson (2008).

spreading axis due to the westward migration of the plate boundary relative to the plume, which appears to be moving slowly eastwards relative to the MAR offshore Iceland (Sigmundsson et al., 2020). Between 24 to 15 Ma rifting occurred along the NW Iceland Rift, now submarine off

the Westfjords, before extension transferred eastward to the Snæfellsnes-Húnaflói-Skagi rift zone around 15 Ma (Fig. 1.2, 1.4; Harðarson et al., 1997). Between 7 to 6 Ma, the Snæfellsnes-Húnaflói rift became extinct and extension transferred to the presently active Western and Northern Volcanic Zones (Fig. 1.2, 1.4; *S*æmundsson, 1979). Garcia et al. (2003) demonstrate the NVZ and the Skagi rift were simultaneously active for 5−5.5 myrs until the transfer of extension to the NVZ was completed around 3 Ma, at which point the Skagi rift became extinct. Walters et al. (2013) suggest melting recommenced along the Húnaflói rift between 3 to 1 Ma, when a pulse of anomalously hot asthenosphere, carried by lateral flow within the plume head, passed beneath Húnaflói. The East Volcanic Zone represents an evolving spreading system which initiated around 3−2 Ma, and reflects the preliminary transfer of extension from the WVZ (Fig. 1.2, 1.4; Sæmundsson, 1979; Scheiber-Enslin et al., 2011). The most recent rift relocation occurred in northern Iceland c. 1.7 Ma, forming the temporary Skagafjörður Rift Zone for around 1 myrs (Fig. 1.2, 1.4; Hjartarson et al., 2017).

In general, exposed rock units become younger towards the centre of Iceland (Fig. 1.4). The geological units are grouped into three stratigraphic formations: the Tertiary Basalts (16−3.3 Ma), the Plio-Pleistocene (3.3−0.7 Ma) and the Upper Pleistocene Formations (<0.7 Ma). The Tertiary Basalts cover an area of >50,000 km^2 and include the plateau basalt series typical of north-western, northern and eastern Iceland (Fig. 1.4; Harðarson et al., 2008). These extensive tholeiitic basalts were erupted from fissure systems, shield volcanoes or central volcanoes, similar to present-day volcanic activity (Harðarson et al., 2008). The Plio-Pleistocene Formation covers c. 25,000 km^2 and occupies areas between the Tertiary Basalts and Upper Pleistocene Formations (Fig. 1.4; Denk et al., 2011). The glacial/interglacial cycles indicative of the Late Pliocene and Pleistocene, influenced the type of volcanic products erupted during this interval (Eiríksson, 1994; Geirsdóttir and Eiríksson, 1994). During the interglacials, volcanism was similar to that in the Miocene and early Pliocene (Eiríksson, 1994). However, throughout the glacials magma erupted beneath expanding ice caps, producing volcanic products indicative of quenching and fragmentation, including pillow lavas, palagonite and hyaloclastites (Eiríksson and Geirsdóttir, 1991; Eiríksson, 1994). Thick and intercalated

sedimentary sequences are commonly found in the Plio-Pleistocene Formation, reflecting enhanced erosion associated with glaciations and related isostatic changes (Grímsson and Símonarson, 2008). The Tjörnes sequence forms part of the Plio-Pleistocene Formation, and is exposed along the western side of the Tjörnes Peninsula in northern Iceland (Fig. 1.1, 1.4). The Tjörnes sequence comprises marine (mudstones, sandstones and conglomerates) and terrestrial (lignite, sandstones, conglomerates and tillites) sediments deposited in estuaries, beaches, marshlands, rivers and subglacial environments (Símonarson and Eiríksson, 2008). The Upper Pleistocene Formation covers c. 30,000 km^2, with a footprint matching the active Eastern, Western and Northern Volcanic Zones (Fig. 1.4; Thordarson and Höskuldsson, 2008). The volcanic rocks are mostly interglacial basaltic lavas and subglacial pillow lavas and hyaloclastites. Following the retreat of the Weichselian glacier, Holocene volcanism has mainly been focussed in the EVZ generating large lava shields (e.g. Trölladyngja) and flood lavas (e.g. Þjórsá) (Thordarson and Höskuldsson, 2008).

1.4 SCOPE AND OUTLINE

The overarching aim of this thesis is to generate a new palaeoclimatic, palaeoceanographic and palaeogeographic understanding of the NE Atlantic and Nordic Seas during the Pliocene, using new multiproxy datasets from regional scientific boreholes and sedimentary sequences exposed onshore Iceland (Fig. 1.5). Although there has been an intense focus on the palaeoceanography of Quaternary glacial/interglacial cycles in this region (e.g. Heinrich, 1988; Howe et al., 2016; Jansen et al., 2000; Rasmussen et al., 2002; Sarnthein and Altenbach, 1995), there are few reliable proxy datasets from the warm climates of the late Neogene. Importantly, this interval contains the mPWP, the most recent period of sustained global warmth which is considered a potential analogue for the climate predicted for the late 21st Century (Dowsett et al., 2010a). Existing datasets suggest regional SSTs were up to 8°C warmer than present during the mPWP (Robinson et al., 2008; Robinson, 2009). However, there is a notable mismatch between proxy- and model-based SST reconstructions in the NE Atlantic and Nordic Seas at this time, whereby the model simulations appear to underestimate

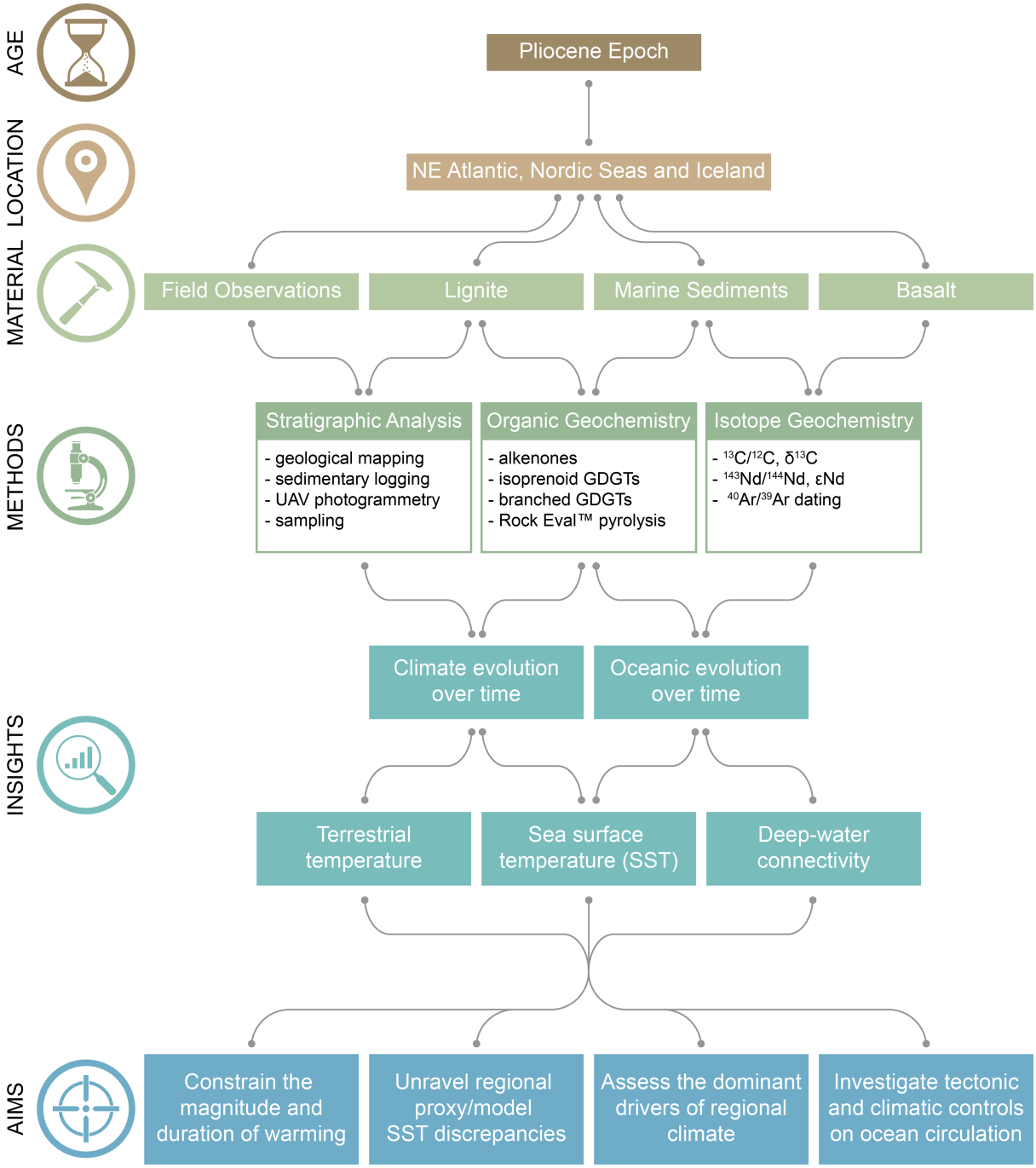


Figure 1.5. Conceptual model showing the materials and methods used in this study, the insights gained from the different data and their relationship with the project aims.

warming by up to 10°C relative to the proxy records (Dowsett et al., 2012; Dowsett et al., 2016). The new multiproxy datasets presented here will help to address the extent to which these discrepancies are influenced by proxy biases rather than model sensitivities, and to better constrain the magnitude and duration of these warming events in both marine and terrestrial

settings. These new datasets will also help to evaluate the dominant drivers of these climatic changes, and to further unravel tectonic, oceanic and climatic interactions in the NE Atlantic and Nordic Seas during the Pliocene.

The following chapters are written as standalone case studies, each in the style of a draft manuscript, in preparation for submission for publication in the near future. My contribution to this work involved conducting all parts of the research, including the field and lab work, analysing the samples and generating the data, interpreting the results, creating the figures and being the lead author on all four manuscripts. My collaborators assisted with field and lab work, provided feedback on the interpretation of data and useful comments on former versions of these manuscripts. The editorial 'we' is therefore used throughout these chapters to reflect these contributions. Inevitably, there is a small degree of repetition in certain sections due to the overlapping themes of the different chapters.

Chapter 2 focuses on reassessing the stratigraphy, sedimentology and structure of the Pliocene Tjörnes Beds in northern Iceland, using advanced fieldwork techniques including drone-based photogrammetry. This chapter aims to improve the understanding of the true thickness and structural architecture, the vertical and lateral distribution of lithofacies and disconformities, and the depositional and palaeoenvironmental evolution of the Tjörnes Beds, in order to fully exploit the palaeoclimatic signals preserved in these sediments.

Chapter 3 explores the controls on the deep-water connectivity between the NE Atlantic and Norwegian basins throughout the Pliocene using new benthic foraminifera $\delta^{13}C$ and authigenic εNd records, and assesses the extent to which varying dynamic support of the GSR modulated the ventilation of these basins and the wider rate of North Atlantic deep-water formation.

Chapter 4 investigates the magnitude and duration of mid-Piacenzian warming in the NE Atlantic and Nordic Seas, using new alkenone and TEX_{86} records. This chapter addresses on-going questions regarding discrepancies between proxy- and model-based SST

reconstructions in this region, and assesses whether these can be attributed to proxy biases associated with the chromatographic analysis of low concentration alkenones.

Chapter 5 expands on the revised stratigraphic framework proposed in Chapter 2 and outlines the preliminary geochemical work undertaken on basalts and brown coals sampled from the Tjörnes Beds. This chapter initially discusses the rationale and methods used to further constrain the Tjörnes age model, using $^{40}Ar/^{39}Ar$ radiometric dating, in order to improve the temporal framework for palaeoclimatic signals derived from these sediments. This chapter then documents the work undertaken to reconstruct the magnitude of Pliocene warming onshore Iceland, using branched glycerol dialkyl glycerol tetraethers (br-GDGTs) derived from these coals for the first time, before assessing the fidelity and compatibility of these terrestrial temperatures with existing multiproxy records of North Atlantic Pliocene climate.

Finally, Chapter 6 presents a general summary highlighting the key conclusions from each chapter, and outlines future recommendations for further work.

2. A NEW COMPOSITE SECTION AND LITHOSTRATIGRAPHY FOR THE PLIOCENE TJÖRNES BEDS, NORTHERN ICELAND

My contribution to this work involved conducting all parts of the research, including organising and leading the fieldwork in Iceland, collecting, analysing and interpreting the field data, writing the manuscript and creating the figures. M. Allison, M. Papadopoulos and S. Jones assisted with the geological mapping, sedimentary logging and UAV photogrammetry during fieldwork, and S. Jones provided feedback on the interpretations of the results. The editorial 'we' is used throughout this chapter to reflect these contributions.

2.1 ABSTRACT

The marginal-marine Tjörnes Beds form part of the thickest sedimentary sequence onshore Iceland, a landscape dominated by mid-ocean ridge volcanism. These sediments are an important archive of NE Atlantic environmental change as they record the transition from Pliocene warmth to the intensification of the Northern Hemisphere Glaciation. Previous stratigraphic and sedimentological interpretations are based on the historic, horizontal mapping of coastal outcrops. However, significant gaps exist in these records related to the exclusion of inland or inaccessible sections, which restrict our understanding of the true thickness and structural architecture of the Tjörnes Beds, the vertical and lateral distribution of lithofacies and disconformities, the depositional and palaeoenvironmental evolution and the record of palaeoclimatic signals preserved in these sediments. Here we address these issues by re-mapping the entire outcrop assisted by drone-based photogrammetry, and by undertaking a detailed lithofacies analysis of the Tjörnes Beds. Structural contour analysis indicates the total thickness is 745 m, c. 45% greater than previously reported. We demonstrate up to 230 m of sediment is unseen due to superficial cover or pervasive extensional faulting. We present a revised composite section which accommodates these unobserved intervals. We recognise 13 lithofacies within the Tjörnes Beds and group these into five facies associations. Using the vertical and lateral distribution of these lithofacies, we fully reconstruct the depositional and palaeoenvironmental evolution of the sequence. We interpret the initial environment was a tide-dominated estuary with extensive intertidal flats and coastal marshes, before a marine transgression led to a largely subtidal environment, followed by the progradation and re-establishment of intertidal flats and marshlands. We suggest the Kaldárós lagoon, western Iceland, is a modern analogue of the environment which generated the Tjörnes Beds. A measure of sediment reworking derived from our lithofacies analysis indicates the benchmark dinoflagellate biozonation in the middle of the succession may be unreliable, which also argues against a suggested significantly older age (early Pliocene) for the Tjörnes Beds. This work is a significant step toward a more complete stratigraphic and sedimentological framework for the Tjörnes Beds, by filling gaps in the stratigraphic and

palaeoenvironmental record, and revealing previously undocumented sections which may yield new palaeoclimatic records to help further unravel Pliocene climate change in the NE Atlantic.

2.2 INTRODUCTION

The Tjörnes Beds in northern Iceland (Fig. 2.1) are a significant sedimentary archive for understanding palaeoenvironmental change throughout the Pliocene in the NE Atlantic (Bárðarson, 1925; Eiríksson, 1981; Field et al., 2017; Símonarson and Eiríksson, 2008; Verhoeven et al., 2011, 2013). During the Pliocene, the NE Atlantic witnessed a transition from extreme warmth, whereby surface temperatures were up to 8°C higher than present (Dowsett et al., 2016; Haywood et al., 2016), to cooling associated with the intensification of the Northern Hemisphere Glaciation (iNHG) around 2.7 Ma (Raymo et al., 1992; Flesche Kleiven et al., 2002; Bartoli et al., 2011). The conjunction of its Pliocene age and its location on the Greenland-Scotland Ridge, whose tectonics may have driven this climatic change (Robinson et al., 2011; Parnell Turner et al., 2015), make the Tjörnes Beds an ideal site to reconstruct this palaeoclimatic variability.

However, our current understanding of the modern coastal outcrop, structure and depositional history of the Tjörnes Beds restrict its potential as a palaeoclimate archive. The most significant problem is the lack of a composite lithostratigraphic section which integrates information from both coastal and inland exposures. In particular, no published work has yet assessed the significance of inland sections or quantified how much of the Tjörnes sediment column is unexposed. These data gaps restrict our understanding of the true thickness and structural architecture of the Tjörnes Beds, the vertical and lateral distribution of facies and disconformities, the depositional and palaeoenvironmental evolution, and the palaeoclimatic signals preserved in these sediments.

The purpose of this study is to better characterise the stratigraphic completeness, the vertical and lateral distribution of lithofacies and the palaeoenvironmental evolution of the Tjörnes Beds, using advanced systematic mapping and logging techniques, including unmanned aerial vehicle (UAV) photogrammetry. These results should inform our understanding of the stratigraphic architecture, age and depositional history of the Tjörnes Beds, an essential step

to help fully exploit the palaeoclimate signals preserved within these sediments and unravel the drivers of Pliocene climate change in the NE Atlantic and Nordic Seas. We also aim to identify a modern-day analogue of the Pliocene depositional environment at Tjörnes, to investigate corresponding sedimentary processes and settings, and to further aid in the palaeoenvironmental reconstruction of the Tjörnes Beds. In the following subsection, we review the geological history of the Tjörnes sequence.

2.2.1 *Geological Setting*

The Tjörnes Beds form part of a c. 1200 m thick sequence of Pliocene to Late Pleistocene sediments, exposed on the Tjörnes Peninsula in northern Iceland (Fig. 2.1). This sequence was deposited in an extensional basin formed within the inside corner between the Tjörnes Fracture Zone and the Northern Volcanic Zone rift axis (Eiríksson, 1981, 1985). Basin uplift (500−600 m) during the Late Pleistocene produced the westward tilting horst observed today (Thoroddsen, 1902; Einarsson et al., 1967; Sæmundsson, 1974; Eiríksson, 1980). The sediments are exposed in incised river valleys and coastal cliffs for c. 10 km along the west side of the Tjörnes Peninsula. This section can be divided stratigraphically into four units: Kaldakvísl lavas, Tjörnes Beds, Höskuldsvík lavas and the Breiðavík Group (Strauch, 1963; Eiríksson, 1981). The Tjörnes Beds are separated from the underlying Kaldakvísl plateau tholeiites (dated 9.9 ± 1.8 and 8.6 ± 0.4 Ma; Aronson and Sæmundsson, 1975) by a WNW trending fault zone in the Kaldakvísl River. To the north of this river, the Tjörnes Beds rest on the erosional surface of the Kaldakvísl lavas, which includes a flow dated 4.3 ± 0.4 Ma (Albertsson, 1976).

Bárðarson (1925) undertook the original detailed stratigraphic study of the Tjörnes Beds, and estimated a thickness of 450 m for the cliff sections he logged, and a thickness of 520 m based on the whole outcrop footprint. Buchardt and Símonarson (2003) produced the most recent generalised composite section, which is commonly cited in subsequent palaeoclimate studies, and gives a logged thickness of 510 m for the Tjörnes Beds. The Tjörnes Beds dip 5−10° NW

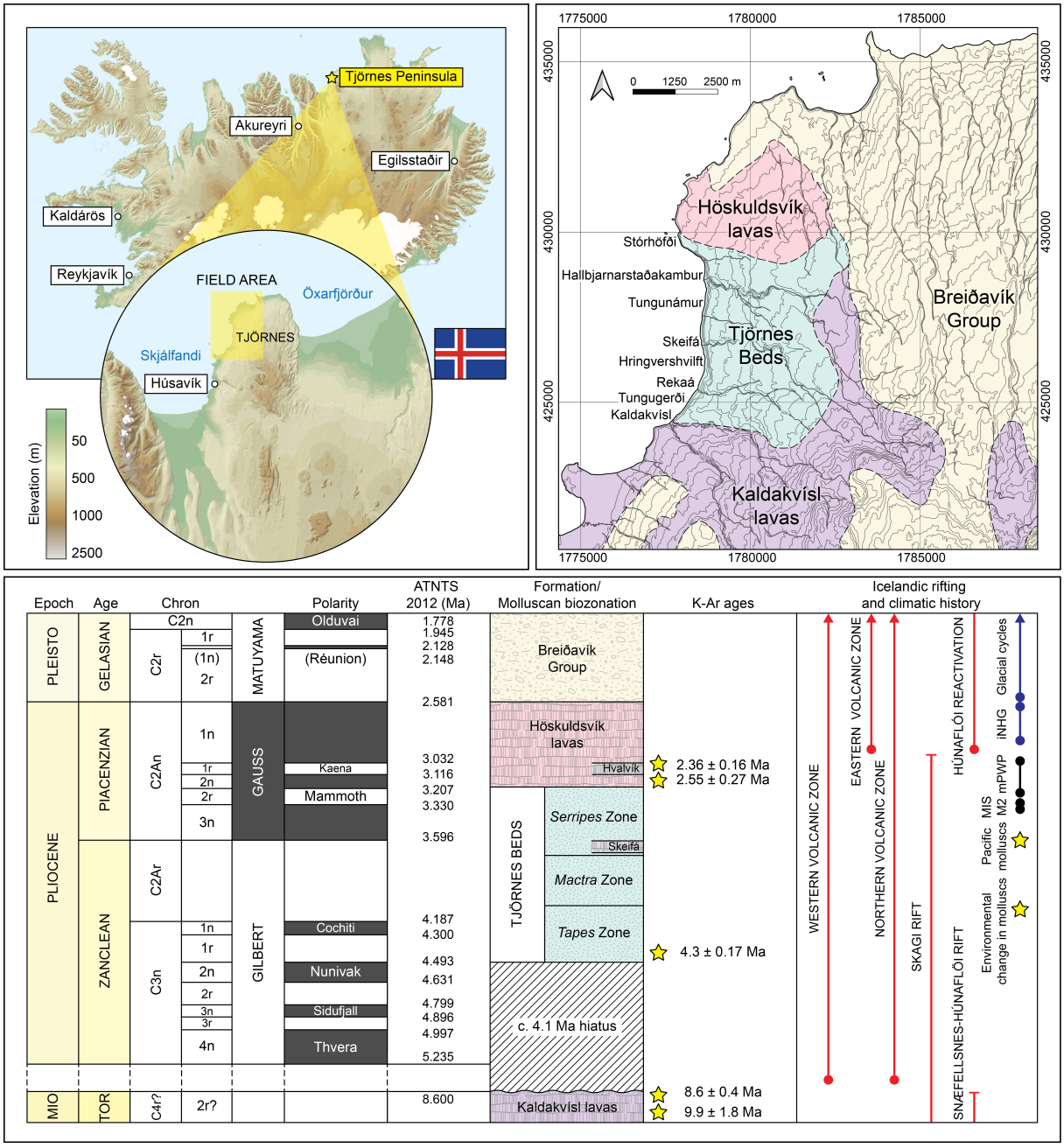

Tjörnes Peninsula
Akureyri
Egilsstaðir
Kaldárós
Reykjavík
FIELD AREA
Öxarfjörður
TJÖRNES
Skjálfandi
Húsavík
Elevation (m)
50
500
1000
2500
1775000
1780000
1785000
435000
430000
425000
0 1250 2500 m
Höskuldsvík lavas
Stórhöfði
Hallbjarnarstaðakambur
Tungunámur
Skeifá
Hringvershvilft
Rekaá
Tungugerði
Kaldakvísl
Tjörnes Beds
Breiðavík Group
Kaldakvísl lavas
Epoch
Age
Chron
Polarity
ATNTS 2012 (Ma)
Formation/ Molluscan biozonation
K-Ar ages
Icelandic rifting and climatic history
PLEISTO
PLIOCENE
MIO
GELASIAN
PIACENZIAN
ZANCLEAN
TOR
C2n
C2r
C2An
C2Ar
C3n
C4r?
MATUYAMA
GAUSS
GILBERT
Olduvai
(Réunion)
Kaena
Mammoth
Cochiti
Nunivak
Sidufjall
Thvera
1.778
1.945
2.128
2.148
2.581
3.032
3.116
3.207
3.330
3.596
4.187
4.300
4.493
4.631
4.799
4.896
4.997
5.235
8.600
Breiðavík Group
Höskuldsvík lavas
Hvalvík
TJÖRNES BEDS
Serripes Zone
Skeifá
Mactra Zone
Tapes Zone
c. 4.1 Ma hiatus
Kaldakvísl lavas
2.36 ± 0.16 Ma
2.55 ± 0.27 Ma
4.3 ± 0.17 Ma
8.6 ± 0.4 Ma
9.9 ± 1.8 Ma
WESTERN VOLCANIC ZONE
EASTERN VOLCANIC ZONE
NORTHERN VOLCANIC ZONE
SKAGI RIFT
HÚNAFLÓI REACTIVATION
SNÆFELLSNES-HÚNAFLÓI RIFT
Glacial cycles
iNHG
mPWP
MIS M2
Pacific molluscs
Environmental change in molluscs

Figure 2.1 (previous page). Location and geological setting of the Tjörnes Peninsula, northern Iceland. Place names discussed in the text are shown. Geological map modified after Eiríksson (1981), using the geocentric coordinate system for Iceland (ISN2004/Lambert 2004; EPSG:5325). The stratigraphic summary of the Tjörnes sequence is after Símonarson and Eiríksson (2008), including palaeopolarity (Eiríksson, 1985; Eiríksson et al., 1990), radiometric K-Ar ages (Aronson and Sæmundsson, 1975; Albertsson, 1976, 1978), molluscan biostratigraphy (Bárðarson, 1925) and Icelandic rifting and climate events (Garcia et al., 2003; Haywood et al., 2016; Walters et al., 2013). MIS M2, Marine Isotope Stage M2; mPWP, mid-Piacenzian Warm Period; iNHG, intensification of the Northern Hemisphere Glaciation. Topographic map created in QGIS v.3.4 using the Landmælingum Íslands (National Land Survey of Iceland) Digital Elevation Model (available at: https://atlas.lmi.is/LmiData/index.php?id=247152041610 [accessed 06/01/2020]).

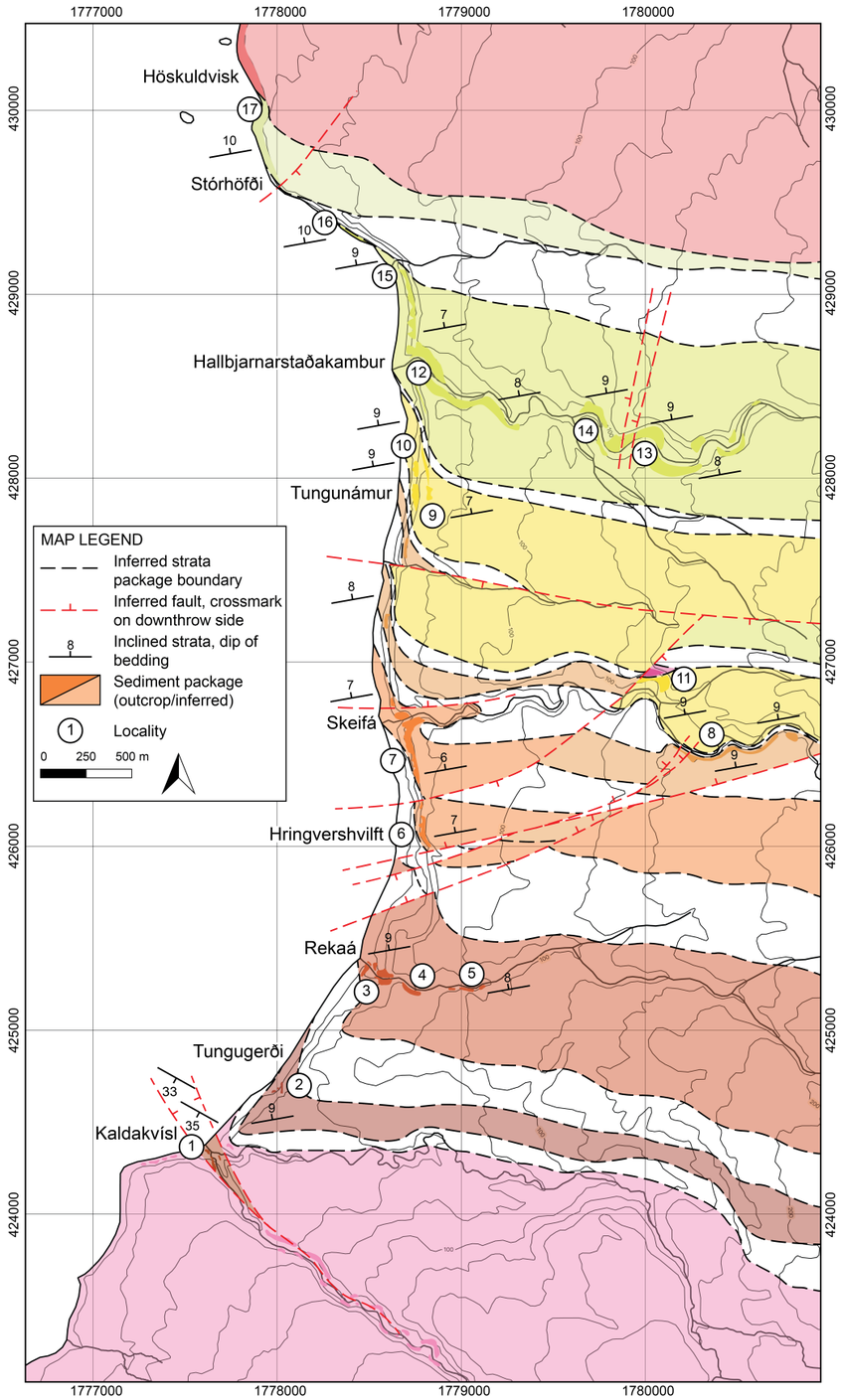
and comprise alternating marine (siltstones, sandstones and conglomerates) and terrestrial sediments (siltstones, lignites and sandstones), and basaltic lavas. Bárðarson (1925) divides the Tjörnes Beds into 25 shelly (1−25) and 10 terrestrial layers (A−J) and defines three molluscan biozones: the *Tapes* Zone (beds 1−5), the *Mactra* Zone (beds 6−12) and the *Serripes* Zone (beds 13−25). The *Tapes* and lower *Mactra* Zones consist of tidal flat and coastal swamp deposits, comprising sandstones and lignites (Símonarson and Eiríksson, 2008). The upper *Mactra* and lower *Serripes* Zones feature cross-bedded and bioclastic sandstones deposited in a subtidal environment, during increased subsidence (Símonarson and Eiríksson, 2008). The upper *Serripes* Zone is characterised by renewed estuarine and marshland deposition, associated with reduced subsidence and resumed uplift (Buchardt and Símonarson, 2003). The overlying Höskuldsvík lavas (dated 2.55 ± 0.27 and 2.36 ± 1.8 Ma; Albertsson, 1976, 1978) consist of six subaerial basaltic flows intercalated with fluvial sediments and tuffs (Eiríksson et al., 1990). 14 alternating diamictite and marine sandstone and mudstone units characterise the following Breiðavík Group, symbolising deposition during the intense glacial/interglacial cycles indicative of the Quaternary (Eiríksson, 1985, 1990, 1992; Eiríksson and Geirsdóttir, 1991; Geirsdóttir and Eiríksson, 1994).

2.3 MATERIALS AND METHODS

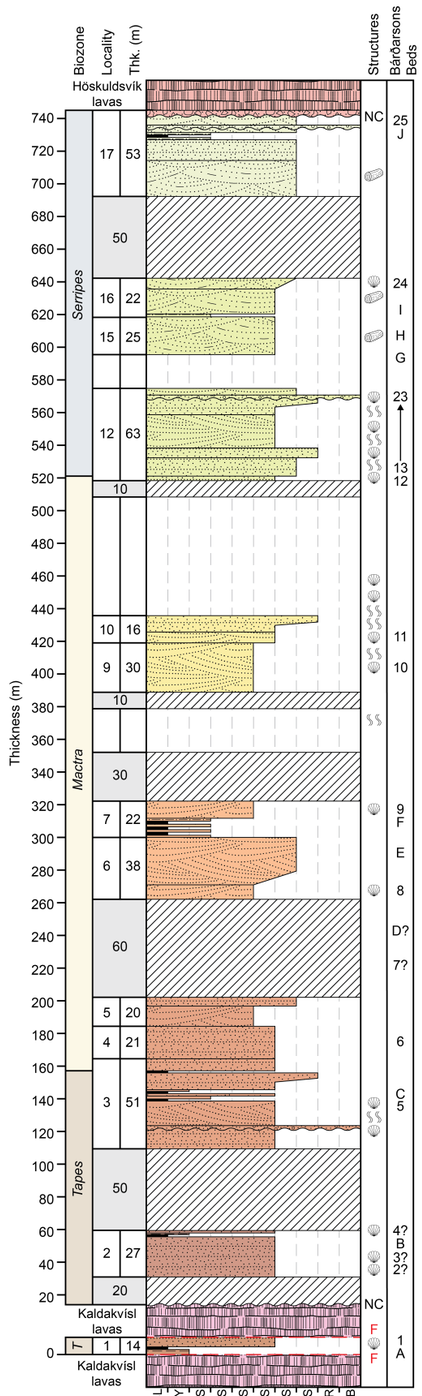
The stratigraphic and sedimentary characteristics of the Tjörnes Beds were investigated during two fieldwork seasons in summer 2018 and spring 2019. Previous stratigraphic studies focused on logging the coastal section horizontally (Bárðarson, 1925; Einarsson et al., 1967; Eiríksson, 1981). However, the lack of continuous exposure and pervasive faulting makes it challenging to measure the vertical sequence accurately using this method. Consequently, we comprehensively mapped and logged the succession upwards at 17 well-exposed coastal and inland sites (Fig. 2.2A-D). At each locality we described the lithology, grain size, sedimentary bedforms, palaeocurrent indicators, basal contacts and structural relationships between stratigraphic components, and documented these characteristics using handheld and UAV-mounted cameras. We also recorded the faunal content at each locality and correlated beds to the original mollusc zonation of Bárðarson (1925), where possible. Lithofacies were defined following the classification of Miall (1999) and Kolcon and Sachsenhofer (1999).

The distribution of exposures relative to the footprint of the entire outcrop suggests significant portions of the Tjörnes Beds may not be accessible at the surface. In this study, we use geological mapping and structural contouring to identify these missing intervals, estimate their thickness, and re-evaluate the true thickness of the Tjörnes Beds. During logging, the exposed sections were grouped into eight packages of demonstrably continuous stratigraphy, shown in different colours on Figure 2.2A-D. These packages mainly comprise sediments observed in the incised coastal valleys. The exposed thicknesses and strikes of these packages were measured directly in the field using a tape and compass-clinometer, and were verified by the UAV at inaccessible sections. The bases and tops of the logged packages were mapped using structure contours (Fig. 2.3). When constructing the structure contours, we assumed the measured thicknesses and strikes of the logged packages are constant across the entire outcrop. The thicknesses of the missing intervals were estimated using trigonometry to calculate the up-section distance between the top and basal structural contours of successive logged packages (Fig. 2.3). Based on the observed variation in bed thickness and dip across

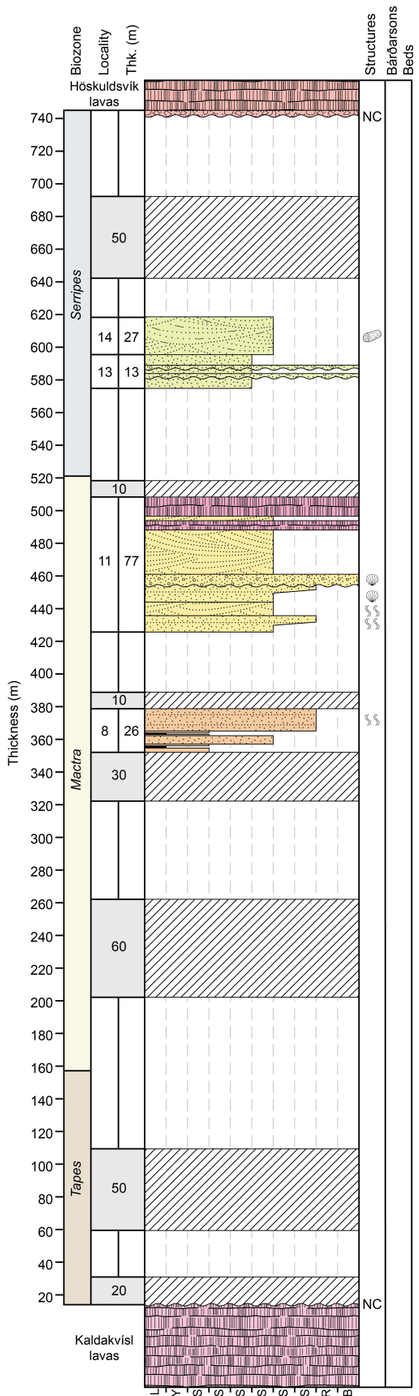
(A) TJÖRNES GEOLOGICAL MAP



(B) COASTAL STRATIGRAPHIC SECTION



(C) INLAND STRATIGRAPHIC SECTION



(D) COMPOSITE STRATIGRAPHIC SECTION

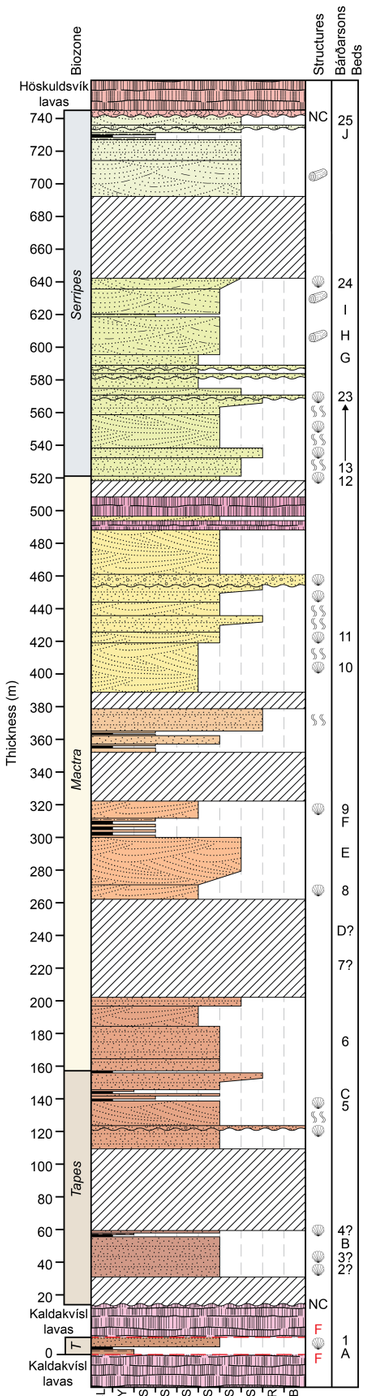


Figure 2.2 (previous page). Geological map and sections of the Tjörnes Beds produced by this study. (A) Geological map showing observed exposures and faulting. Locations of continuous logged exposures are numbered. Colours show lateral and vertical extents of the logged sediment packages, as inferred by structure contouring. (B) Coastal stratigraphic section. (C) Inland stratigraphic section. (D) Our new composite stratigraphic section, from correlating the coastal and inland exposures. The hatched areas between the coloured packages show positions where significant thicknesses of strata are not exposed at the surface. Beds and biozones defined by Bárðarson (1925) are shown. Sedimentary structures and grain size are defined in Fig. 2.7.

the outcrop, we estimate that the uncertainty in our estimate of the total missing section is in the order of 10s of metres.

Fault traces were inferred inland by measuring the orientation of each exposed fault plane and using topographic features including scarps, incised valleys and breaks in slope. Fault geometries were also measured inland at localities 8, 11 and 13, where the sediments are visibly cut by extensional basinward-dipping faults (Fig. 2.4A-D). The placement of these inferred faults is uncertain and will inevitably impact the reconstruction of missing sections by structure contouring. The thicknesses of missing intervals in extensionally faulted areas should therefore be considered to represent maximum values. To illustrate the typical scale and the pervasive nature of the faulting, a digital elevation model (DEM) of the Rekaá fault scarp (Fig. 2.4E) was generated using imagery captured by a DJI™ Mavic Pro UAV, mounted with a high-resolution (12 megapixel) and tilting (0° to −90°) camera. Three georeferenced ground control points and a scale were positioned at the site. The UAV was flown across Rekaá in several passes at multiple angles to capture images with 60−80% overlap needed to fully characterise topographic variations. Agisoft Metashape was used to compile the UAV images and create a DEM using Structure-from-Motion photogrammetry following the methods of Westoby et al. (2012).

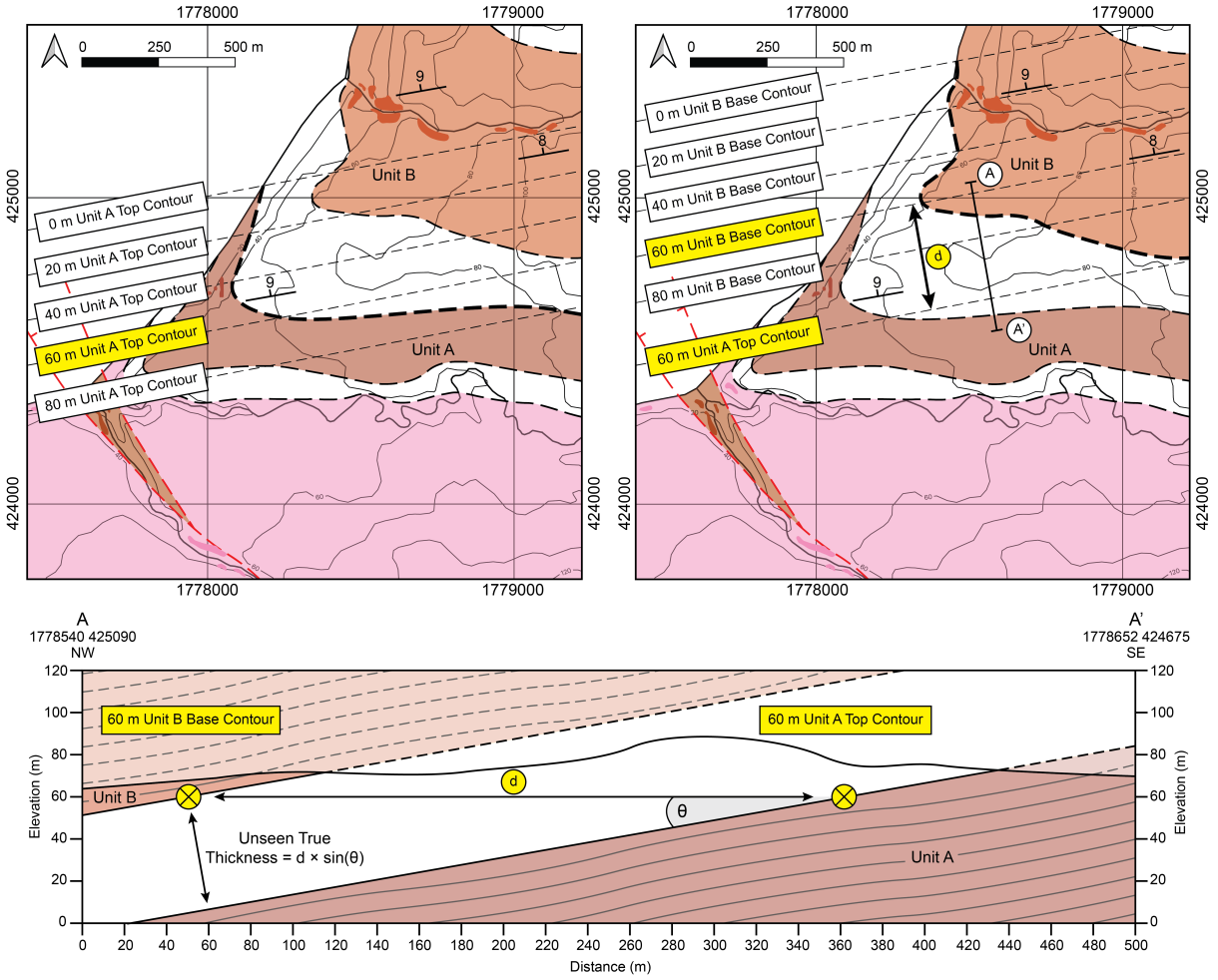


Figure 2.3. Structure contouring technique used to estimate the thickness of missing strata. This example shows the Kaldakvísl to Rekaá areas at the base of the Tjörnes Beds, and illustrates how the thickness of the unseen stratigraphic interval between logged packages A and B was estimated using trigonometry, as shown on the cross section.

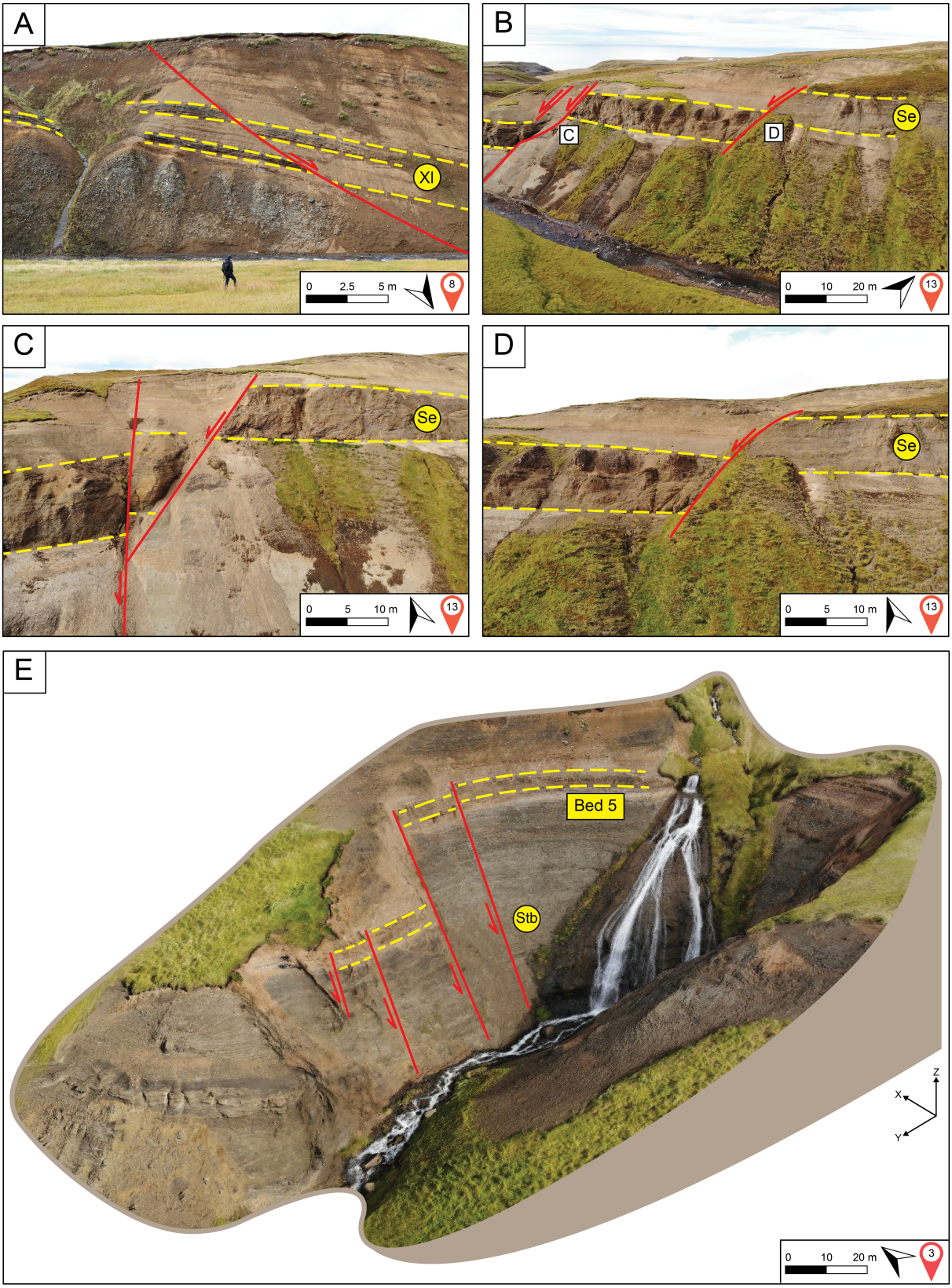

A
Xl
0 2.5 5 m
8
B
C
D
Se
0 10 20 m
13
C
Se
0 5 10 m
13
D
Se
0 5 10 m
13
E
Bed 5
Stb
Z
X
Y
0 10 20 m
3

Figure 2.4 (previous page). Images of faulting in the Tjörnes Beds, obtained using an UAV-mounted camera. (A) Normal fault cutting two xylitic lignite seams in the upper Skeifá valley, with a vertical throw of c. 2 m. (B) Three basinward dipping normal faults in the upper Hallbjarnarstaðakambur valley cutting the trough cross-laminated sandstone with intraclasts and wood debris facies. (C) Zoomed-in image of the lower two normal faults, with a maximum vertical throw of c. 8 m across both faults. (D) Zoomed-in image of the upper normal fault, with a vertical throw of c. 5 m. (E) 3D DEM of Rekaá waterfall showing the rotational slip scarp below the waterfall, extensional basinward faulting, unstable cliffs and tilted sandstone fault blocks. DEM modelled in Agisoft Metashape v.1.6.2. Location pins correspond to localities shown in Fig. 2.2A. Yellow-circled abbreviations indicate lithofacies units defined herein.

2.4 RESULTS

2.4.1 *Composite Section*

2.4.1.1 Stratigraphic architecture

In total, structure contour mapping suggests the Tjörnes Beds are approximately 745 m thick (Fig. 2.5). This is 45% thicker than previously described, meaning that c. 230 m of strata is missing from previous stratigraphic interpretations. This revised thickness is supported by measurements of average bedding dip (c. 8°) (Fig. 2.2A), and the horizontal distance from the base to top of the sequence along the dip direction of the bedding (5.4 km), which predicts a composite section c. 750 m thick. The majority of faults we identify along the coast between Rekaá and Stórhöfði match those described by Bárðarson (1925). In areas where pervasive faulting occurs, such as between Hringvershvilft and Skeifá (Fig. 2.2A), the extensional faults lengthen the distribution of missing section mapped at the surface, and therefore the thickness of missing intervals predicted using structure contouring is likely to be an overestimate at these sites.

Missing intervals are evenly distributed across the field area and generally correlate with sites located between the incised valleys (Fig. 2.2A-D). The largest missing packages (up to 60 m) are inferred between Tungugerði and Skeifá. The landscape between these sites is vegetated and agricultural, and there is little bedrock exposed. Smaller thicknesses (up to 10 m) are estimated to be absent between Skeifá and Hallbjarnarstaðakambur, again due to poor exposure. Approximately 50 m is believed to be unlogged beneath the woody sandstone along the Stórhöfði headland. Although the sequence is well exposed at this locality, it remains unlogged since the cliffs are near-vertical with evidence of recent rockfalls and access to the base of this section is tide-dependent.

COMPOSITE SECTION AND LITHOFACIES ANALYSIS

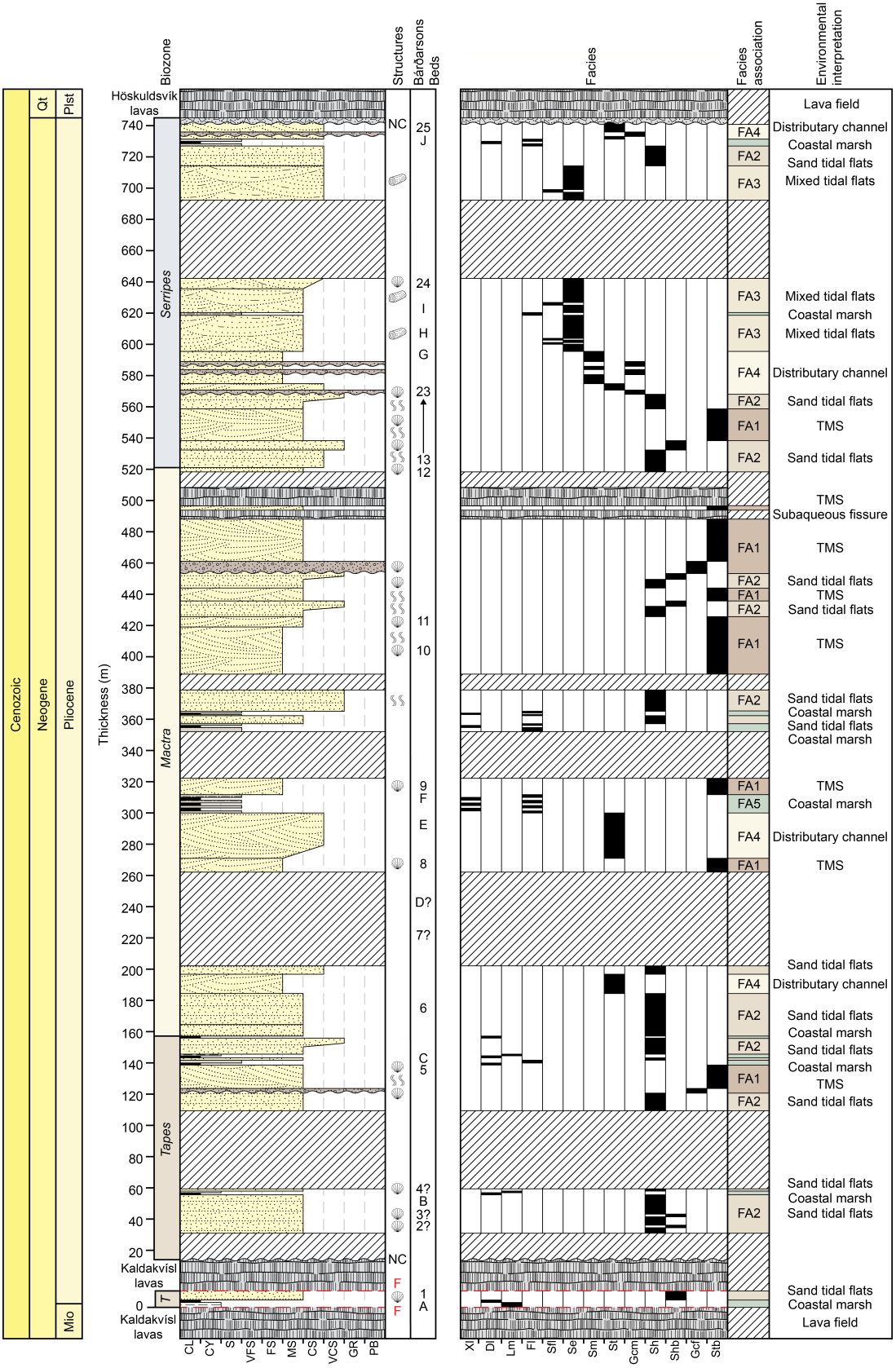


Figure 2.5 (previous page). Summary composite stratigraphic section showing the vertical distribution of lithofacies, facies associations and palaeoenvironmental interpretations. Note the dominance of terrestrial lithofacies in the *Tapes* and lower *Mactra* Zones, and the dominance of marginal-marine lithofacies in the upper *Mactra* and *Serripes* Zones. Beds and biozones defined by Bárðarson (1925) are shown. Sedimentary structures and grain size are defined in Fig. 2.7.

There are two examples where the same stratigraphic horizon is identified at both a coastal and inland locality, and where the bed thickness agrees within 2 m: the top bed at locality 10 is the same as the basal unit at locality 11; and the woody sandstone at locality 14 is identical to the sandstone at locality 15 (Fig. 2.2A-D). The strike of these beds are also identical (Fig. 2.2A). This suggests that although lateral sedimentological variations do occur in the Tjörnes Beds, they share similar bedding orientations and involve thickness changes of a few metres or less. Bárðarson's (1925) observations concur with ours in this respect. These findings support our methods used to construct structure contours, where we assumed the measured thicknesses and strikes of the logged packages are constant across the entire outcrop (Fig. 2.3).

2.4.1.2 Revised lithostratigraphy

The *Tapes* Zone extends from the Kaldakvísl river valley up the coast to Hringvershvilft, with a logged thickness of c. 85 m (Fig. 2.2A-D). The base of the *Tapes* Zone is unconformable with the underlying Kaldakvísl plateau lavas (Fig. 2.5, 2.6A). Below the nonconformity, the uppermost c. 2 m of the Kaldakvísl lavas is heavily eroded, producing an unconsolidated mudstone which is stained red and is indicative of subaerial erosion and Fe oxidation. A faulted block of *Tapes* Zone strata is found in the lower Kaldakvísl river, surrounded by the lavas. Our *Tapes* Zone consists of parallel-laminated and trough cross-bedded sandstones and five lignite seams. The lignites are relatively thin (0.2−0.6 m) and are often associated with laminated siltstones; they are challenging to identify and are commonly concealed by eroded material and soil. In the Rekaá valley, tilted blocks dominated by thick sandstones and three lignites are separated by basinward-dipping (i.e. westward dipping) rotational slip scarps, displacing the sequence towards the coastline (Fig. 2.4E).

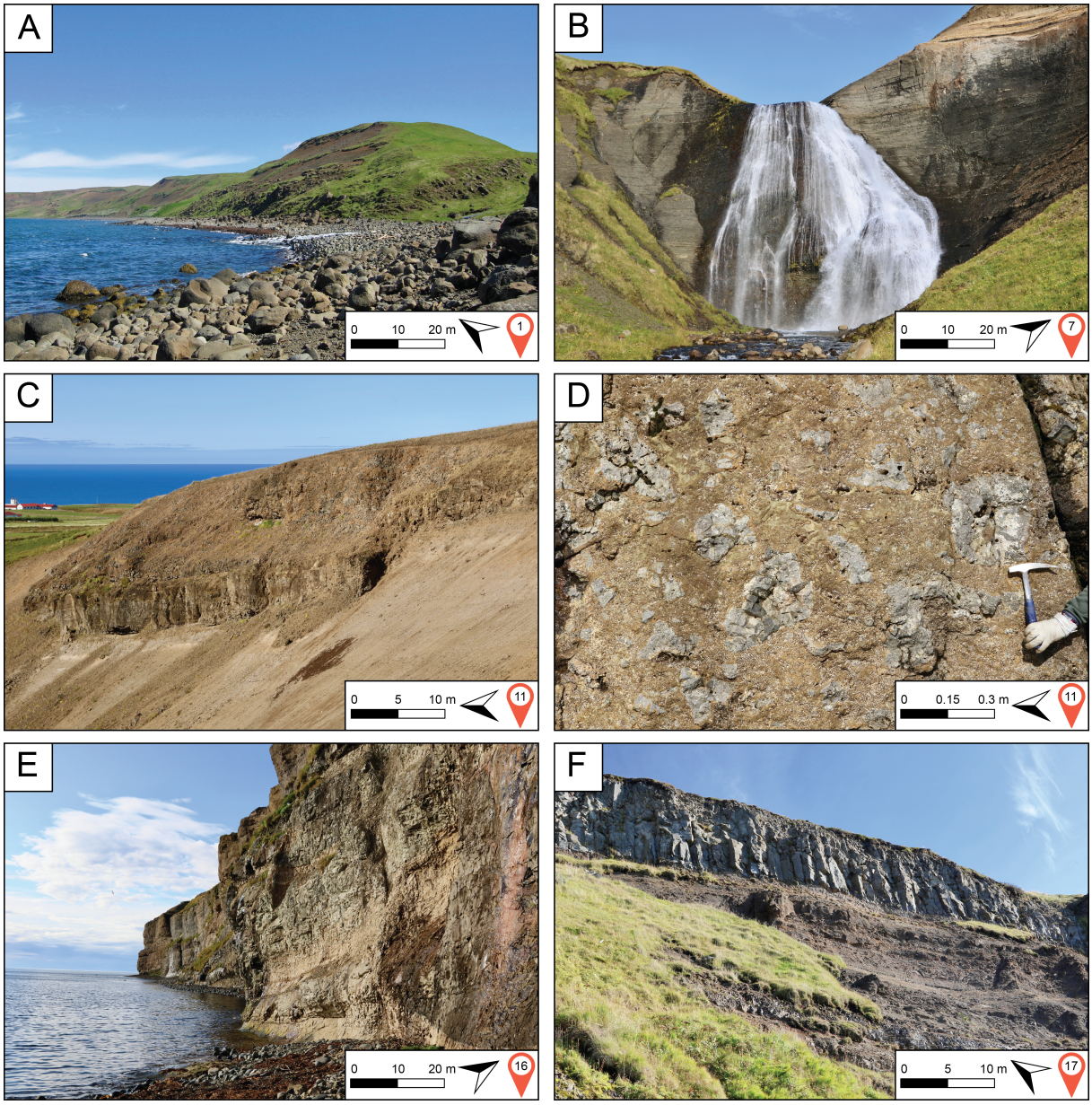


Figure 2.6. Photo panel of important Tjörnes localities. (A) The non-conformable contact between the Kaldakvísl lavas and the overlying Tjörnes Beds. (B) Skeifá waterfall comprising of c. 60 m of near-vertical, cross-stratified sandstones and three xylitic lignite seams (thin black layers observed in the top right). (C) Basaltic lavas crop out on steep slopes in the upper Skeifá valley adjacent to Route 85. (D) Bulbous pillow lavas suspended in a light-brown palagonite matrix at Skeifá. (E) Thick (>50 m), cross-stratified woody sandstone in the near-vertical and tide-dependent cliffs of the Stórhöfði headland. (F) The non-conformable contact between the Tjörnes Beds and the overlying Höskuldsvík lavas. Location pins correspond to localities shown in Fig. 2.2A.

The *Mactra* Zone represents the mid-section of the Tjörnes Beds and is classified by the occurrence of *Mytilus modiolus* and *Emarginula crassa* (Bárðarson, 1925). This zone extends from Hringvershvilft to the upper Skeifá valley, with a logged thickness of c. 255 m (Fig. 2.2A-D). The *Mactra* Zone contains several lignites interlayered between thick parallel-laminated and cross-stratified sandstone units (Fig. 2.5, 2.6B). Five seams are interbedded with laminated siltstones forming distinctive organic-rich horizons. These lignites represent the most frequent occurrence of organic sedimentation throughout the whole sequence; the seams are thicker (up to 1.5 m) compared to the other zones, and contain clear evidence of fossilised trees, including lignified bark and trunks. The top of the *Mactra Zone* is marked by a single thick (7 m), polymictic, clast-supported fossiliferous conglomerate unit overlain by thick cross-bedded sandstones and the intercalated Skeifá lavas, which are well exposed adjacent to Route 85 in the upper Skeifá valley (Fig. 2.5, 2.6C). These lavas are thick (up to 18 m), form horizontal sheets and contain a thin (~2 m) interlayered unit of cross-stratified bioclastic sandstone. Small pillow lavas suspended in a light-brown palagonite matrix are common throughout each flow, which suggest emplacement from submarine fissures or subaerial quenched flows (Fig. 2.6D).

The *Serripes* Zone represents the upper section of the Tjörnes Beds and is classified by the occurrence of *Serripes groenlandicus*, *Neptunea despecta* and *Macoma moesta* (Bárðarson, 1925). This zone extends from the upper Skeifá valley to Höskuldsvík, with a logged thickness of c. 170 m (Fig. 2.2A-D). Parallel-laminated and cross-stratified sandstone units containing channel-like structures, infilled with disarticulated molluscs, occur at the base. Lignified plant material and wood fragments are preserved within the sandstone units toward the sequence top, indicative of an increasing terrestrial influence. A single, thin (c. 0.5 m) lignite seam interbedded between laminated siltstone is present in the upper section of the *Serripes* Zone, well exposed in the Stórhöfði cliff section below the Höskuldsvík lavas (Fig. 2.5, 2.6E). The boundary between the Tjörnes Beds and the overlying lavas is nonconformable. The base of the lavas features a thick (c. 5 m) basaltic and siliciclastic breccia, which is interpreted to

represent an erosional lag which formed before extrusion of the Höskuldsvík lavas (Fig. 2.5, 2.6F).

2.4.2 *Lithofacies analysis*

13 facies are identified based on multiple criteria including lithology, sedimentary and biogenic structures, frequency of occurrence and position relative to other facies (Table 2.1; Fig. 2.5). Using this information, it is possible to ascertain estimations of water depth, flow velocity and depositional regime. These facies are categorised into five facies associations which reflect major depositional settings: tidally-modulated shoreface (FA1), intertidal sand flats (FA2), intertidal mixed flats (FA3), upper-estuarine distributary channels (FA4) and coastal marshlands (FA5) (Fig. 2.5).

2.4.2.1 Facies Association 1 (FA1): Tidally-modulated shoreface

Observations.--- FA1 comprises cross-stratified, well-sorted, bioclastic sandstone (Stb) with channel-like structures infilled with imbricated disarticulated molluscs, including epifaunal bivalves and gastropods (Fig. 2.5, 2.7, 2.8A, 2.8B). Stb also exhibits rare symmetrical wave-rippled surfaces interbedded between the trough cross-stratification (Fig. 2.8C). Stb facies are common throughout the Tjörnes Beds and are laterally continuous. Stb is intensely bioturbated with vertical burrows (including *Skolithos, Diplocraterion* and *Rhizocorallium*). In two instances, Stb is underlain by clast-supported, polymictic conglomerates (Gcf) which are also highly fossiliferous, cross-stratified and feature erosional lower contacts (Fig. 2.8D). The thicknesses of these conglomerates vary greatly over their lateral extents, and they fine-upward into the overlying bioclastic sandstones.

Facies	Lithology	Thickness (m)	Physical Structures	Biogenic Structures	Interpretation	Figure
Dl	Detritic lignite. >90% fine-grained (<187 µm) organic matter with infrequent woody xylitic fragments. Black colour.	Up to 1.5 m.	Vertical and interconnected cleat fractures, with an average cleat spacing of approximately 0.5−2 cm.	Gelification produces a vitreous, hard and brittle texture with evidence of conchoidal fractures.	Coastal, reed marshland.	8A
Xl	Xylitic lignite. Contains >90% fossilised wood particles. Light to dark brown colour.	Up to 1.5 m.	Xylites include tree trunks, fissured bark, branches, twigs and cones. Matrix is composed of fine-grained (<187 µm) detritic material.		Dry forests on elevated levees above intertidal flats.	8B
Lm	Laminated mudstone dominated by very fine (<63 µm) clay minerals. Grey colour.	Up to 5.4 m.	Parallel lamination (1−2 mm). Polygonal desiccation cracks infilled with coarser (>63 µm) silt and sand.	Moderate bioturbation with tubular root traces, *Thalassinoides* and polychaete burrows. Wood fragments. Coalified plant debris.	Tidal firmgrounds deposited from suspension during the highest flood or spring tides.	
Fl	Laminated siltstone. Pale-grey and white colour. Friable and highly weathered.	Up to 2.6 m.	Parallel lamination (1−2 mm).	Moderate bioturbation with tubular root traces, *Thalassinoides* and polychaete burrows. Wood fragments. Coalified plant debris.	Tidal firmgrounds deposited from suspension during the highest flood or spring tides.	8C
Sm	Massive sandstone. Comprises well-sorted, sub-angular, medium to coarse-grained (250−1000 µm) plagioclase, augite, quartz, lithic and volcanic clasts. Black to grey colour.	Up to 6.5 m.	Structureless, sheet-like sandstones.		Hyper-concentrated flows in upper estuarine distributary channels.	
Sh	Parallel-laminated sandstone. Comprises moderately-sorted, sub-rounded, medium to very-coarse clasts (250−1500 µm), including plagioclase, quartz and lithic fragments. Weathered orange.	Up to 25 m.	Low angle (2−10°), parallel lamination (1−10 mm).	Weak bioturbation (*Skolithos*, *Ophiomorpha,* and *Diplocraterion*).	Intertidal sand flats or beach barriers.	
Shb	Parallel-laminated sandstone. Comprises moderately-sorted, sub-rounded, medium to coarse clasts (250−500 µm), including plagioclase, quartz and lithic fragments.	Up to 5 m.	Low angle (2−10°), parallel lamination (1−10 mm).	Abundant disarticulated marine molluscs. Randomly distributed.	Intertidal sand flats or beach barriers.	
Stb	Bioclastic sandstone. Comprises well-sorted, sub-rounded, fine to coarse clasts (187−750 µm), including plagioclase, augite, quartz and volcanic fragments.	Up to 38 m.	Metre-scale trough cross-beds with tangential bottom contacts. Erosional channel structures, which are infilled with disarticulated molluscs. Rare symmetrical wave ripples, with large wavelengths (c. 20 cm) and small (c. 4 cm) amplitudes. Axial orientation of the troughs and wave ripple crests suggest a northerly palaeoflow ($\bar{x}$ = 011°; n = 8).	Intense bioturbation (*Skolithos, Diplocraterion* and *Rhizocorallium*). Abundant disarticulated marine molluscs. Valves are usually preserved convex-up and imbricated.	Subtidal channel bar in a tidally-modulated shoreface.	8D, 8E, 8F

Facies	Lithology	Thickness (m)	Physical Structures	Biogenic Structures	Interpretation	Figure
St	Trough cross-bedded sandstone. Comprises well-sorted, sub-rounded, medium to very-coarse volcanic-derived clasts (500-5000 µm), including plagioclase, quartz, augite and lithic fragments. Weathered orange.	Up to 31 m.	Metre-scale trough cross-beds with tangential bottom contacts. Axial orientation of the troughs suggest a northerly palaeoflow ($\bar{x}$ = 004°; n = 22). Thin (<5 mm) structureless mud drapes are commonly found on the sandy foresets. Gradational basal contacts, fining upwards from underlying Gcm conglomerates.	Weak bioturbation (*Palaeophycus*, *Cylindrichnus* and *Planolites*).	Migrating mid-channel sand bars in upper estuarine distributary channels.	
Se	Trough cross-laminated sandstone with intraclasts and wood debris. Comprises moderately sorted, sub-rounded, coarse volcanic-derived clasts (750−1000 µm), including plagioclase, augite, quartz and lithic fragments.	Up to 27 m.	Irregularly-shaped and randomly-orientated intraclasts of lithified sediment. Trough cross-laminations with tangential bottom contacts. Axial orientation of the troughs suggest a northerly palaeoflow ($\bar{x}$ = 349°; n = 2). Thin (<1 cm), concordant gravel layers containing rounded lithic clasts are found along the lower bounding surfaces.	Petrified branches (diameters <15 cm) and silicified wood fragments. Weak bioturbation (*Chondrites* and *Thalassinoides*).	Intertidal mixed flats influenced by tidal channels and creeks.	8G
Sfl	Trough cross-laminated sandstone with mud drapes. Comprises moderately sorted, sub-rounded, coarse volcanic-derived clasts (750−1000 µm), including plagioclase, augite, quartz and lithic fragments.	Up to 5 m.	Trough cross-laminations with tangential bottom contacts. Cross sets are generally <6 cm in height. Flaser bedding with black mud drapes (2−3 mm) preserved on some foreset laminae.	Weak bioturbation (*Chondrites* and *Thalassinoides*).	Intertidal mixed flats influenced by tidal channels and creeks.	
Gcm	Clast-supported, polymictic conglomerates. Comprises poorly sorted, large (>20 cm) sub-rounded basaltic clasts (55%). Fine-grained (<250 µm), angular matrix comprising plagioclase, quartz, augite and volcanic fragments.	Up to 6 m.	Rare and crude parallel stratification and clast imbrication. Intraclasts of lithified sediment. Erosional basal contacts.		Upper estuarine, distributary channel lags.	
Gcf	Clast-supported, fossiliferous, polymictic conglomerates. Comprises moderately sorted, large (0.2−3 cm) volcanic clasts and bioclastic debris (60%). Fine grained (187−250 µm), sub-rounded matrix comprising plagioclase, quartz, augite and volcanic fragments.	Up to 7 m.	Trough cross-bedding (0.3−0.5 m) with tangential bottom contacts. Irregularly-shaped and randomly-orientated intraclasts of lithified sediment. Erosional basal contacts.	Abundant disarticulated marine molluscs.	Subtidal channel lag in a tidally-modulated shoreface.	8H

Table 2.1 (previous page). Descriptions of lithofacies identified in the Tjörnes Beds.

Interpretations.--- The combination of sandy trough cross-beds interbedded with wave-rippled surfaces, laterally discontinuous gravel lags, *Skolithos* Ichnofacies and abundant disarticulated marine molluscs suggests deposition occurred within a tidally-modulated shoreface environment above the fair weather wave base (Dashtgard et al., 2009; Dashtgard et al., 2012). Dashtgard et al. (2009) and Pemberton et al. (2012) indicate the trough cross-bedded sandstones mark the migration of sinuous dunes produced by surf processes (onshore directed), longshore currents (shore-parallel directed) and rip currents (offshore directed). Channel-like scours, which are infilled with disarticulated mollusc valves, most likely represent the reworking and transportation of bioclastic detritus by surf processes or storms (Dashtgard et al., 2009). Wave-rippled surfaces suggest the sandy sediments were deposited in high flow velocities (40−60 cm/s), at shallow depths dominated by wave oscillations (<10 m) (Diem, 1985; Guillén et al., 2008; Guerrero and Guillén, 2020). The conglomerates are interpreted as gravel lag deposits, produced by channelised flows in subtidal channels within the seaward end of the estuary, as implied by the abundant marine fauna (Daidu et al., 2013). The accumulation of shelly detritus and gravel in these channels is caused by winnowing of finer material by longshore and tidal currents (Clifton, 1983; Flemming et al., 1992). Strong tidal or storm-driven rip currents drive bedload traction and the development of trough cross-stratification in these gravels (Dalrymple, 2010). The erosional basal contacts underlying these gravels most likely represent the local tidal-ravinement action at the base of these subtidal channels (Dalrymple et al., 2003; Willis and Gable, 2001), or may possibly represent storm events (Kidwell et al., 1986; Kidwell and Bosence, 1991; Fürsich and Oschmann, 1993). The trace-fossil assemblage in FA1 constitutes the *Skolithos* Ichnofacies, which supports deposition in a high-energy, shallow-marine environment (MacEachern et al., 2010; Plint, 2010).

2.4.2.2 Facies Association 2 (FA2): Intertidal sand flats

Observations.--- FA2 comprises weakly bioturbated (Sh) and bioclastic (Shb) parallel-laminated sandstone. Sh contains rare vertical and branching burrows (including *Skolithos, Ophiomorpha* and *Diplocraterion*), whereas Shb features abundant and randomly-distributed disarticulated molluscs, including epifaunal bivalves and gastropods (including common cockles and blue mussels) (Fig. 2.5, 2.7). Sh and Shb are interlayered facies which occur throughout the Tjörnes Beds, and represent a significant proportion of the total sediment volume (c. 30%).

Interpretations.--- The combination of parallel-laminated sandstone, *Skolithos* Ichnofacies and abundant disarticulated marine fauna suggests deposition occurred within an intertidal environment containing either sand flats or a wave-dominated beach barrier (Dalrymple et al., 2003; Dashtgard et al., 2009). Sand flats occur in the lower intertidal zone and are dominated by bedload transport of sandy sediment controlled by both tidal currents and wave action (Mángano and Buatois, 2004; Wang, 2011; Wang et al., 2019). Sand flat deposits typically consist of coarse- to medium-grained, parallel-laminated or coarse to fine-grained trough and planar cross-bedded sandstone formed in the upper flow regime (Dalrymple et al., 1990; Dalrymple and Choi, 2007; Dalrymple, 2010). The low-angle, parallel-lamination suggests the sandy sediments may have been deposited on a wave-dominated beach barrier within the intertidal zone, where swash and backwash processes flatten ripple bedforms to produce parallel laminations at high flow velocities (>80 cm/s) (Clifton, 1969; Howard and Reineck, 1981; Yokokawa and Masuda, 1991). The trace fossil assemblage in FA2 constitutes the *Skolithos* Ichnofacies, which supports deposition in a high-energy, shallow-marine environment (MacEachern et al., 2010; Plint, 2010). The weak bioturbation in Sh supports deposition on high-energy sand flats or beach barriers, where rapidly migrating bedforms often restrict intense bioturbation (Mángano and Buatois, 2004; Baucon, 2008). These assemblages may therefore reflect short-term colonisation intervals along dune reactivation surfaces

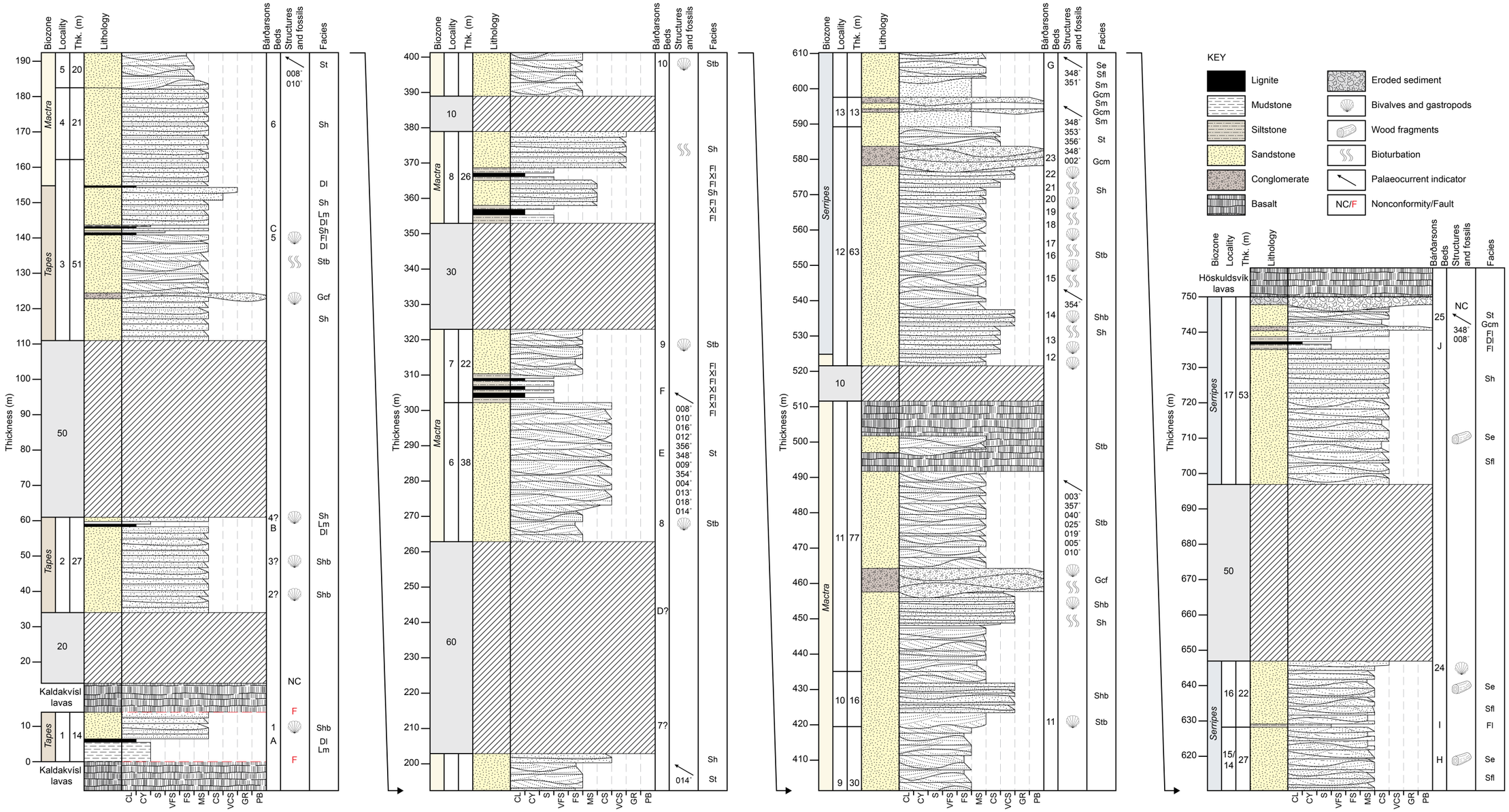

Biozone
Locality
Thk. (m)
Lithology
Bárðarsons Beds
Structures and fossils
Facies
Thickness (m)
Mactra
Tapes
Serripes
Kaldakvísl lavas
Höskuldsvík lavas
CL CY S VFS FS MS CS VCS GR PB
KEY
Lignite
Mudstone
Siltstone
Sandstone
Conglomerate
Basalt
Eroded sediment
Bivalves and gastropods
Wood fragments
Bioturbation
Palaeocurrent indicator
NC/F
Nonconformity/Fault

Figure 2.7 (previous page). Detailed summary of sedimentological data collected from the Tjörnes Beds during logging, including grain size, bedform thicknesses, nature of basal contacts, fossils and palaeocurrent indicators. Numbered localities are shown on Fig. 2.2A. CL, Coal; CY, Clay (<8 μm); S, Silt (8−63 μm); VFS, Very-fine sand (63−187 μm); FS, Fine Sand (187−250 μm); MS, Medium Sand (250−500 μm); CS, Coarse sand (500−1000 μm); VCS, Very-coarse sand (1000−1500 μm); GR, Granules (2000−4000 μm); PB, Pebbles (>4000 μm).

(Pollard et al., 1993; Mángano et al., 1996). The abundant disarticulated marine fauna preserved in the Shb facies, possibly represent the reworking, transportation and deposition of bioclastic detritus by breaking waves or storms (Dashtgard et al., 2009).

2.4.2.3 Facies Association 3 (FA3): Intertidal mixed flats

Observations.--- FA3 comprises trough cross-laminated sandstone with wood debris (Se) and mud drapes (Sfl). Se and Sfl facies occur in the upper *Serripes* Zone, are interlayered and well-exposed along the Stórhöfði headland cliffs (Fig. 2.6E). Se contains abundant petrified and silicified wood fragments (Fig. 2.8E), and features thin concordant gravel layers which occur along the bounding surfaces beneath the cross sets. Sfl exhibits distinctive tangential cross laminations which are draped by thin (2−3 mm) black mud layers, indicative of flaser bedding. Both Se and Sfl are moderately bioturbated with branching burrows, including *Chondrites* and *Thalassinoides*.

Interpretations.--- The combination of trough cross-laminated sandstone, flaser bedding, *Cruziana* Ichnofacies and petrified wood fragments suggest deposition occurred within an intertidal environment containing mixed flats. Intertidal mixed flats are found across the transition between sand flats (<5% mud) and mud flats (>95% mud), and are characterised by alternating bedload sedimentation and fallout from suspension (Dalrymple, 2010; Flemming et al., 2012). The thin gravel layers, mud intraclasts and wood fragments suggest the mixed flats were incised by tidal channels or creeks (MacEachern et al., 2012; Dalrymple et al., 2012). The cross-lamination is indicative of migrating bedforms driven by channelised flood and ebb tides, which generate current ripples under lower-energy conditions (20−60cm/s) (Dalrymple,

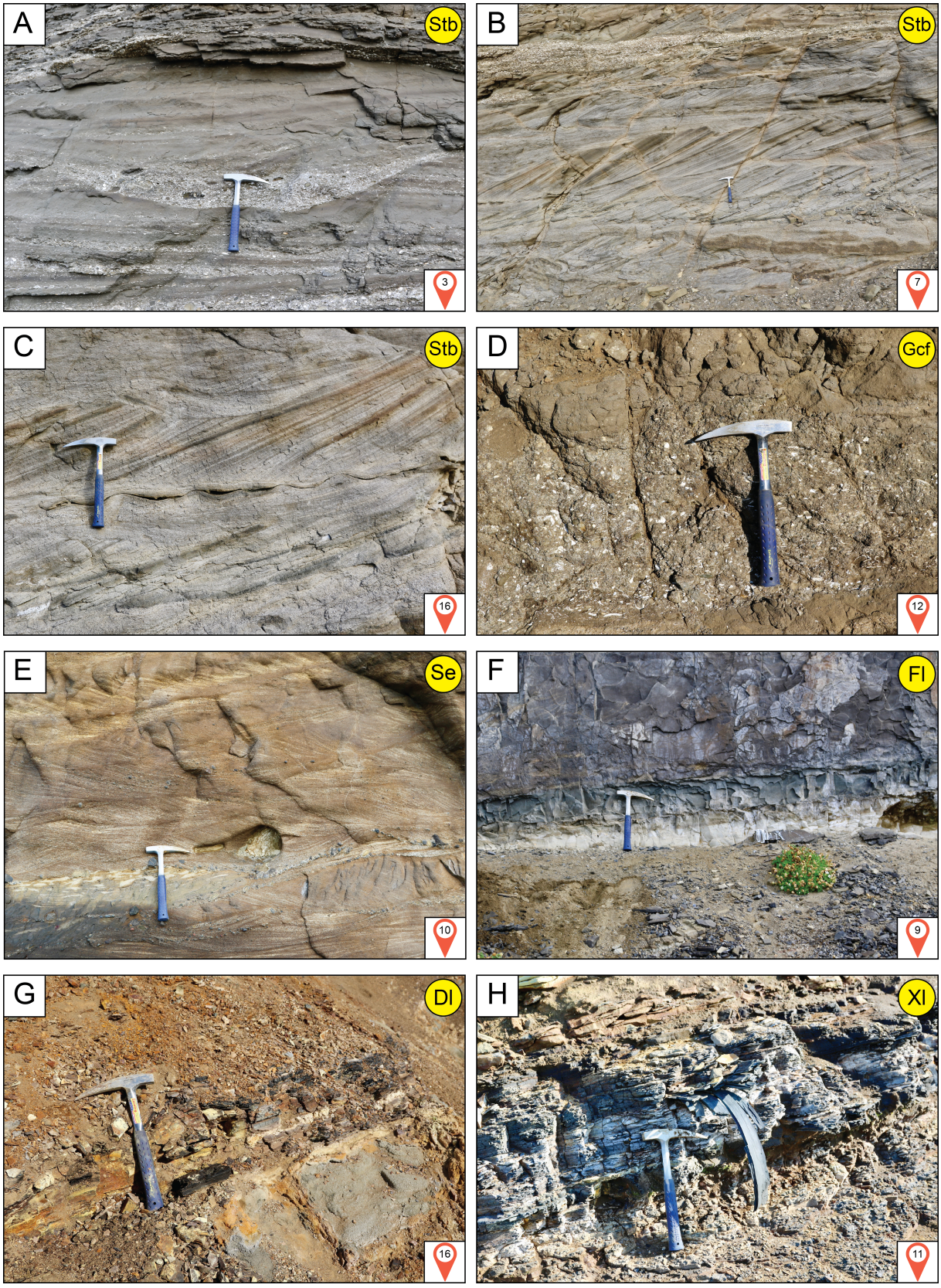

A
Stb
3
B
Stb
7
C
Stb
16
D
Gcf
12
E
Se
10
F
Fl
9
G
Dl
16
H
Xl
11

Figure 2.8 (previous page). Photo panel of characteristic Tjörnes sedimentological features. (A) Bioclastic sandstone featuring tapered channels (1−2 m width) comprising of imbricated and disarticulated molluscs. (B) Metre-scale trough cross-bedded bioclastic sandstone with tangential basal contacts. (C) Wave-rippled sandstone horizons featuring symmetrical wave ripples, with large wavelengths (c. 20 cm) and small (c. 4 cm) amplitudes. (D) Clast-supported, fossiliferous, polymictic conglomerate comprising of disarticulated, randomly-orientated mollusc fragments and grey basaltic clasts. (E) Trough cross-bedded sandstone with intraclasts and silicified wood fragments exposed in the Stórhöfði cliffs. Trough cross-beds often display black, thin (2−3 mm) mud drapes coating the tangential beds. (F) Planar laminated and friable pale-grey siltstone in the Stórhöfði cliffs. (G) Detritic lignite interbedded with fine-grained siltstones at Rekaá. (H) Xylitic lignite exposed at Hringvershvilft containing abundant fossilised wood fragments, including peeling and fissured bark. Estwing® E3-22P (0.33 m length) geological hammer for scale. Location pins correspond to localities shown in Fig. 2.2A. Yellow-circled abbreviations indicate lithofacies defined herein.

2010). During periods of slack water, the ripples are coated by thin layers of mud which settle out of suspension (Fenies et al., 1999). Tidal channels and creeks commonly contain abundant coarse detritus including shell debris, gravels, mud and wood fragments reflecting riverine inputs and local tidal-ravinement action at the base of these channels (Dalrymple et al., 1992; Dalrymple and Choi, 2007; Flemming et al., 2012). The mud intraclasts most likely represent the erosion of hardened and cemented muds from nearshore supratidal flats by flood currents at high tide. The intraclasts are then transported seaward, reworked as bedload and deposited in the mixed tidal flat channels or incorporated into the sandy ripple bedforms (Dalrymple, 2010). The trace fossil assemblage in FA3 constitutes the *Cruziana* Ichnofacies, and is commonly associated with low-energy middle and upper intertidal environments which experience short periods of subaerial exposure (Desjardins et al., 2012).

2.4.2.4 Facies Association 4 (FA4): Upper-estuarine distributary channels

Observations.--- FA4 comprises clast supported, non-fossiliferous, polymictic conglomerates (Gcm) with rare, crude parallel stratification, intraclasts, imbrication, and undulating erosional contacts. The conglomerates fine upward into thick units (up to 31 m) of trough cross-bedded (St) or massive sandstone (Sm) (Fig. 2.5, 2.7). St sandstones comprise very coarse to medium-grained clasts, which are generally well-sorted. Metre-scale trough cross-beds feature

tangential foresets and basal contacts, which often contain thin mud layers. Sm sandstones comprise coarse to medium-grained clasts, which are also well-sorted. Sm sandstones are structureless and form sheet-like units. These facies are observed in the upper *Serripes* Zone and form narrow (<25 m) channel-like structures which are laterally discontinuous and taper upwards towards the margins. St is weakly bioturbated with rare unbranched and gently curved burrows, including *Cylindrichnus, Palaeophycus* and *Planolites*.

Interpretations.--- The combination of conglomeratic lags, overlain by trough cross-bedded or massive sandstones, are interpreted to represent the erosion, subsequent infill and abandonment of individual distributary channels located landward within the upper estuary. The conglomerates are interpreted as coarse channel floor lags deposited above an erosional surface, scoured by channel avulsion and bedload traction (Bhattacharya, 2006; Li and Bhattacharya, 2014). Intraclasts were possibly formed by the scouring and reworking of underlying coastal plain deposits. The overlying trough cross-bedded sandstones represent mid-channel sand bars generated by the migration of subaqueous dunes driven by riverine currents (Bhattacharya, 2006; Kästner et al., 2017). The massive sandstones are interpreted as a result of rapid sediment dumping from high energy (>80cm/s) and hyperconcentrated flows (Martin and Turner, 1998). Horn et al. (2018) demonstrate massive sandstones are deposited as a consequence of abrupt changes in flow speed caused by deconfinement or channel avulsion. Although the trough cross-bedded sandstones reflect unidirectional flow conditions, current velocity and flow direction were most likely highly variable in the distributary channels due to the influence of tidal processes, which resulted in the deposition and preservation of thin mud drapes on the sandy foresets during low river or slack water stages (Fenies et al., 1999; Ichaso and Dalrymple, 2009). The lateral migration, bifurcation and progressive abandonment of these fluvially dominated, tidally influenced distributary channels most likely contributed to the aggradation of overbank deposits across the upper estuary and coastal plain (Bhattacharya, 2010). The assemblage of trace fossils indicate a brackish water environment, and support an upper estuarine depositional setting for these distributary channel deposits (Dalrymple et al., 1991; Corbeanu et al., 2004; MacEachern et al., 2005).

2.4.2.5 Facies Association 5 (FA5): Coastal marshlands

Observations.--- FA5 comprises Dl and Xl, commonly interbedded with Lm and Fl, which feature branching and U-shaped burrows, penetrative root traces and infilled desiccation cracks (Fig. 2.5, 2.7, 2.8F). Dl seams are composed of fine-grained organic matter, and feature pervasive cleat fractures and gelification (Fig. 2.8G). Xl seams contain abundant fossilised wood material, including trunks, fissured bark and branches (Fig. 2.8H). These facies are predominantly found in the *Tapes* and lower *Mactra* Zones (Fig. 2.5, 2.7). The lignites and argillaceous sediments are laterally discontinuous, and generally extend for a couple of hundred metres before pinching out.

Interpretations.--- The combination of detritic and xylitic lignite seams, interbedded with parallel-laminated mudstones and siltstones, are interpreted to represent deposition within coastal marshes situated within the upper estuary or the adjacent coastal plain. Kolcon and Sachsenhofer (1999) suggest detritic lignites form in treeless, reed marshlands, where sedges and grasses are the dominant parent material. Gelification is a biochemical diagenetic process which involves lignin degradation, compaction and homogenisation of humified substances by microbial activity during burial underwater (Teichmüller, 1989). Gelification commonly occurs in marine-influenced peats where bacterial activity is enhanced by the restricted flow of alkaline seawater, rich in macronutrients (Markič and Sachsenhofer, 2010). The xylitic lignites are interpreted to represent dry forests which may have formed on elevated levees or embankments above the intertidal flats (Teichmüller, 1989). The lack of gelification within the xylitic matrix indicates the decomposition and burial of organic matter occurred above the water table (Widera, 2012). The relatively thick and homogenous nature of both the detritic and xylitic lignites suggest these organic deposits were possibly isolated from clastic sources for long intervals, and may have accumulated in domed or raised marshes (Pierce et al., 1991; McCabe and Shanley, 1992; Dai et al., 2020). The interbedded, parallel-laminated mudstones and siltstones represent the deposition of fine suspended sediment transported shoreward during

the highest flood and spring tides (Eisma, 1986; Manning and Dyer, 2007). Voulgaris and Meyers (2004) demonstrate clay and silt particles settle from suspension in slow-flowing (<20 cm/s) or stagnant water during periods of slack tide at velocities as high as 1 mm/s. Polygonal cracks preserved in the parallel-laminated mudstone suggest the coastal marsh and tidal flat surfaces were subaerially exposed for long durations, during which the muddy firmgrounds were prone to desiccation (Allen, 1989; Rogers and Woodroffe, 2015). The plant root penetration structures, *Thalassinoides* and polychaete burrows constitute the *Glossifungites* Ichnofacies, which is commonly associated with low-energy firmgrounds in coastal marshlands (Pemberton and Frey, 1984; Pearson et al., 2012; Yang and Chang, 2018).

2.5. DISCUSSION

2.5.1 *Comparison of our revised stratigraphy with previous interpretations*

Overall, our stratigraphic understanding of the Tjörnes Beds differs significantly compared to the benchmark schemes proposed by Bárðarson (1925) and Buchardt and Símonarson (2003). The main differences are observed in the lower and middle sections, including the interpretation of the basal contact, the number of identifiable lignite seams and the stratigraphic position of the Skeifá lavas (Fig. 2.9). Here, we discuss these differences and outline our field evidence to support our revised interpretations.

The basal contact of the Tjörnes Beds is undescribed by Bárðarson (1925). Bárðarson (1925) suggests the rocks which overlie the Kaldakvísl lavas are a continuous succession featuring fossiliferous sandstones, a single lignite seam (Bed A), and a sequence comprising a 3−4 m thick basaltic lava (denoted Bed 2a), a poorly-consolidated conglomerate (Bed 2b) and a reddish mudstone (Bed 2c). Buchardt and Símonarson (2003) show a distinct nonconformity between the Tjörnes Beds and Kaldakvísl lavas, and a second nonconformity between a thin lava (Bed 2a) and overlying sediments, though they do not detail the evidence used to support these stratigraphic relationships (Fig. 2.9). We identify two normal faults either side of the lower Kaldakvísl river valley (Fig. 2.2A), adjacent to the modern hydroelectric plant, in agreement with Eiríksson (1981) and Símonarson and Eiríksson (2008). We interpret that these parallel faults form a graben structure containing a downthrown and rotated block of the Tjörnes Beds which has an unknown thickness. In this interpretation, the Kaldakvísl lavas form the up-thrown horst blocks either side of the Kaldakvísl valley (Fig. 2.2A), and extend northward by a few hundred metres to where the true nonconformable boundary with the Tjörnes Beds is observed, concurring with Buchardt and Símonarson (2003). We interpret that the thin lava (Bed 2a) described by Bárðarson (1925) and Buchardt and Símonarson (2003) is a continuation of the eroded and heavily-altered Kaldakvísl lavas. The c. 20 m thick missing interval overlying this non-conformable boundary (Fig. 2.2B, 2.9), represents the poorly-

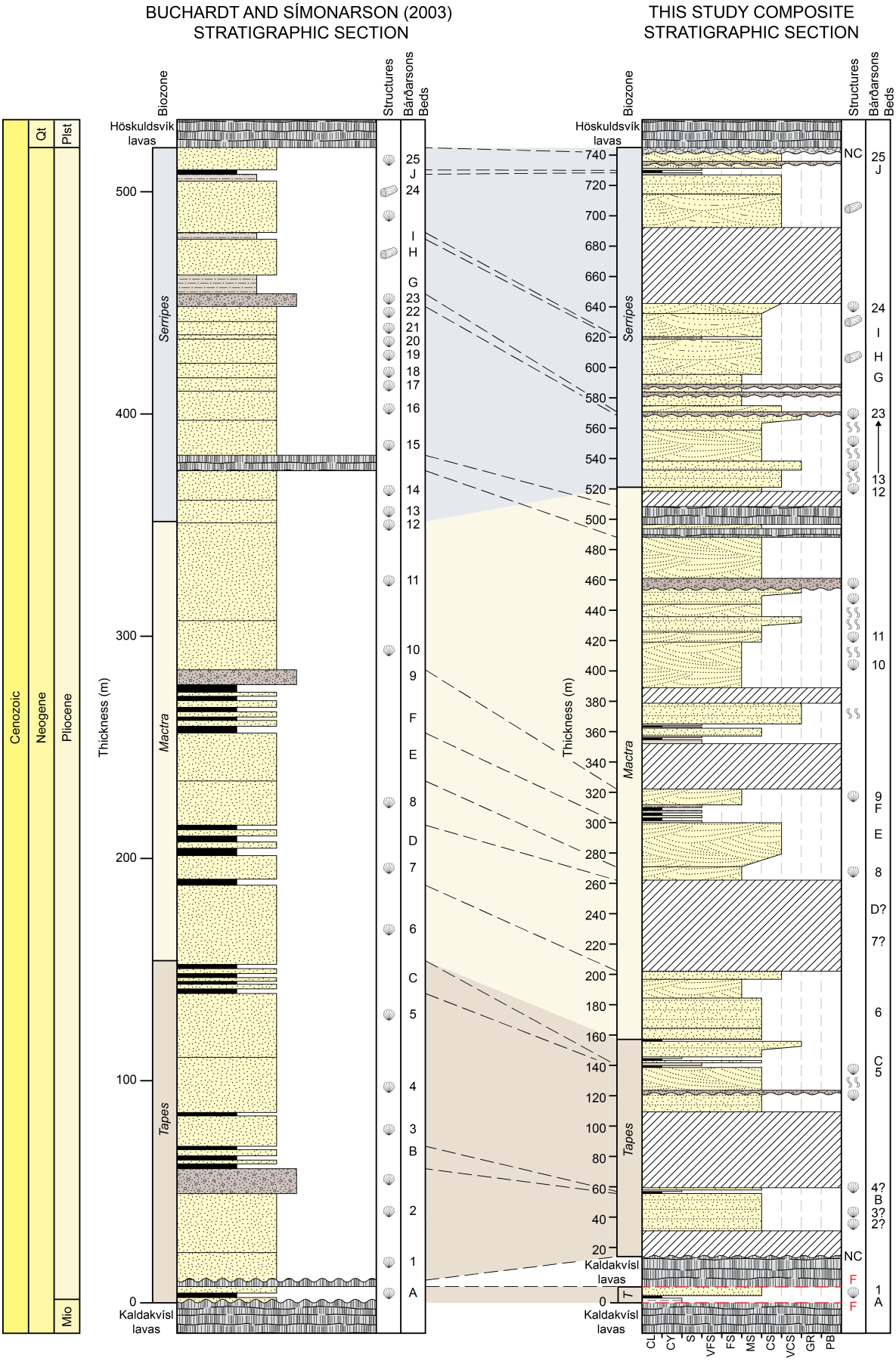

BUCHARDT AND SÍMONARSON (2003)
STRATIGRAPHIC SECTION
THIS STUDY COMPOSITE
STRATIGRAPHIC SECTION
Cenozoic
Neogene
Pliocene
Qt
Plst
Mio
Biozone
Structures
Bárðarsons Beds
Höskuldsvík lavas
Kaldakvísl lavas
Serripes
Mactra
Tapes
Thickness (m)
CL
CY
S
VFS
FS
MS
CS
VCS
GR
PB

Figure 2.9 (previous page). Comparison between the revised and existing Tjörnes stratigraphic sections (Buchardt and Símonarson, 2003). Stratigraphic horizons are correlated using dashed lines. Mollusc biozones are correlated using coloured bands.

consolidated sediments described by Bárðarson (1925) (Beds 2b to 2c), which are overgrown and concealed by scree and soil (Fig. 2.6A). The stratigraphic range of the Tjörnes Beds within the downthrown block is difficult to establish. However, the presence of disarticulated molluscs, including *Tapes aureus* and *Ligula prismatica,* suggests the *Tapes* Zone is the likely source. The lignite within the faulted block (Bed A) is underlain by laminated mudstone, a relationship which is unobserved higher in the sequence. Therefore, although Bárðarson (1925) raised the possibility that some beds at this locality duplicate those logged further north, we consider that the Bed A lignite seam is distinct and unrelated to the lignites exposed at Rekaá.

Buchardt and Símonarson (2003) show a *Tapes* Zone 150 m thick, which is significantly greater than our logged thickness of c. 85 m (Fig. 2.9), though similar in thickness to our total reconstructed section (c. 155 m; Fig. 2.2B, 2.9). Our thinner *Tapes* Zone is likely caused by recognition of a faulted base, as well as slumped, repeated and concealed strata around Rekaá which condenses this section, as acknowledged by Bárðarson (1925) (Fig. 2.4E). Buchardt and Símonarson (2003) show the *Tapes* Zone contains a further eight lignite seams interbedded between sandstone units; this is five more seams than observed in our study (Fig. 2.9). Buchardt and Símonarson (2003) suggest Bed B contains three lignites and occurs below Bed 3 of Bárðarson (1925). They identified a further seam between Beds 3 and 4. However, we found that Bed B features only one seam and occurs above Bed 3, in agreement with Bárðarson (1925). No additional seams were observed at this stratigraphic level, suggesting we may have logged a different section to Buchardt and Símonarson (2003). Buchardt and Símonarson (2003) may have also misinterpreted the position of Bed B relative to the shelly horizons of Bárðarson (1925). We found that Beds 2, 3 and 4 are difficult to distinguish with confidence, owing to the intermittent and poorly-preserved shell layers near Tungugerði. Bárðarson (1925) acknowledged these horizons are laterally discontinuous and contain decomposed shells. The individual positions of these beds on our composite section have

therefore been interpreted with help from the original descriptions in Bárðarson (1925). The single seam identified between Beds 3 and 4 on the Buchardt and Símonarson (2003) section may therefore be Bed B, as suggested by our interpretation and Bárðarson (1925). Buchardt and Símonarson (2003) show that four seams occur within Bed C (Fig. 2.9). We observe only two seams at this stratigraphic level, in agreement with Bárðarson (1925). We demonstrate the cliffs at Rekaá are unstable, based on clear evidence of a rotational slip scarp and slumped fault blocks (Fig. 2.4E), meaning these additional lignites may represent repeated strata. Bárðarson (1925) concurs and indicates some of the seams in Rekaá are slumped from higher up the cliffs where further lignites crop out.

Buchardt and Símonarson (2003) show the *Mactra* Zone is 200 m thick, significantly less than both our logged section of c. 255 m and our total reconstructed thickness of c. 370 m (Fig. 2.9). The difference in logged thickness likely reflects the different sites used to log the sequence, whereby our interpretation incorporates sediments from inland exposures which are not seen at the coast. The *Mactra* Zone in the Buchardt and Símonarson (2003) scheme comprises nine lignites. Our composite section shows five, all of which occur between a height of c. 300 and 365 m and crop out in the Skeifá valley. Three seams are exposed above the coastal waterfall (Fig. 2.6B), whereas the other two are found on a north-facing cliff inland (Fig. 2.4A). Buchardt and Símonarson (2003) show one seam below Bed 7 which is not observed by us or described by Bárðarson (1925). Buchardt and Símonarson (2003) show three lignites associated with Bed D (Fig. 2.9). Bárðarson (1925) also discusses the Bed D seams, but does not state how many exist. We did not recognise either Bed 7 or Bed D in the field; these were the only two of the original beds proposed by Bárðarson (1925) for which we could find no evidence. Bárðarson (1925) indicates these beds occur at Hringvershvilft in a depression carved by a historic landslide. We also observed mass movement at this location. Vegetation and superficial deposits make it challenging to see unambiguous solid geology, and some of the mass movement may have occurred within the past century. Therefore, we have retained Beds 7 and D on our composite section within the 60 m missing interval inferred at Hringvershvilft. Buchardt and Símonarson (2003) indicate five seams occur in Bed F (Fig. 2.9).

We logged only three seams at this horizon, in agreement with Bárðarson (1925). The five seams depicted by Buchardt and Símonarson (2003) may be the result of lateral variability, although we are not aware that any other definitive exposures of Bed F exist. We identify two previously undescribed lignites at an inland section within the upper Skeifá valley (Fig. 2.4A, locality 8). Furthermore, our structural mapping shows these newly recognised seams also crop out further north along the coast between Skeifá and Tungunámur. In contrast, Bárðarson (1925) suggests these two coastal lignites are a continuation of Bed F. However, our interpretation honours the observed 8° bedding dips, whereas that of Bárðarson (1925) requires dips considerably lower than observed (<2°). Our interpretation also recognises the displacement of these seams by E-W trending normal faults, observed in the cliffs between Rekaá and Tungunámur (Fig. 2.2A), which are also shown by Bárðarson (1925). We therefore consider that Bárðarson (1925) accidently correlated Bed F with the lignites between Skeifá and Tungunámur, and underestimated the extent of fault displacement north of Skeifá waterfall because the exposure at this locality is poor, with overgrown and scree-covered slopes.

An inland section undescribed by previous workers is found at locality 11 below the Skeifá lavas (Fig. 2.2C, 2.9). We interpret stratigraphic continuity between the packages described at localities 8 and 11. Both sequences display similar bedding orientations (Fig. 2.2A), and there are no topographic or structural evidence of faulting in the upper Skeifá valley separating these units. These sediments are well exposed and consist of trough cross-stratified bioclastic sandstones, and a thick (c. 7 m) clast-supported, fossiliferous polymictic conglomerate. The identification of *Mytilus modiolus*, marine-influenced sedimentary characteristics, and a lack of organic-rich horizons suggests this section is part of the upper *Mactra* zone sediments, which also crop out to the north along the coast between Tungunámur and Hallbjarnarstaðakambur.

A major difference between our stratigraphic interpretation and Buchardt and Símonarson (2003) is the position and thickness of the palagonitic Skeifá lavas (inland, locality 11) (Fig. 2.6C, 2.6D). Buchardt and Símonarson (2003) place the lavas between 370 and 380 m in their composite section, within the lower part of the *Serripes* Zone, and above a thick (c. 90 m)

package of uniform sandstones (Fig. 2.9). We place the lavas slightly lower, corresponding to a logged thickness of c. 320 m and a total reconstructed thickness of c. 485 m (Fig. 2.2C-D, 2.9). We record 18 m of tholeiitic lavas intercalated with cross-stratified bioclastic sandstone, considerably thicker than indicated by Buchardt and Símonarson (2003) (c. 5 m) (Fig. 2.9). Furthermore, our structural mapping indicates the lavas are situated in the upper part of the *Mactra* Zone. This is supported by the mollusca content of the underlying cross-stratified sandstones, which are indicative of the *Mactra* biozone (discussed above). We also believe the Skeifá lavas are laterally discontinuous and only crop out inland east of Route 85 around locality 11, in agreement with Bárðarson (1925). These significant differences suggest that we examined a different section compared to Buchardt and Símonarson (2003), who do not describe where they logged. Buchardt and Símonarson (2003) may have mistakenly correlated the inland lavas with an incompatible coastal section, which is stratigraphically higher than expected.

Buchardt and Símonarson (2003) show a 160 m thick *Serripes* Zone, similar to our logged thickness of c. 170 m but less than our total reconstructed thickness of c. 220 m, owing to a significant (c. 50 m) missing section toward the top of the zone (Fig. 2.9). Our log of the *Serripes* Zone comprises mainly coarse-grained siliciclastics with evidence of increasing terrigenous influence within younger stratigraphic horizons, including plant material and silicified wood fragments in trough cross-bedded sandstones near the top of the sequence (Fig. 2.8E). Buchardt and Símonarson (2003) show a similar section (Fig. 2.9). We observe only one lignite seam, bounded by parallel-laminated siltstone in a cliff section directly below the Höskuldsvík lavas, in agreement with Bárðarson (1925). Three thick (>2 m) conglomeratic units are identified in this sequence with erosional bases, crude parallel stratification and rare imbrication. These conglomerates fine-upward and are associated with overlying trough cross-bedded or structureless sandstones. A thick (c. 8 m) siltstone bed occurs at a height of approximately 450 m on the Buchardt and Símonarson (2003) composite section. We logged a comparable siltstone layer slightly higher up the sequence (Fig. 2.8F), although the thickness of this bed is significantly less (c. 1.5 m). Buchardt and Símonarson (2003) show the boundary

between the Tjörnes Beds and Höskuldsvík lavas as sharp and conformable (Fig. 2.9). We interpret that this boundary is non-conformable; a thin (c. 0.5 m) brecciated unit occurs below the lavas, containing rubbly basaltic and lithic fragments, which is interpreted to represent an erosional lag produced prior to lava extrusion (Fig. 2.6F). Dinoflagellate biostratigraphy indicates a c. 600 kyr hiatus between the deposition of the Tjörnes Beds and the extrusion of the Höskuldsvík lavas, supporting the non-conformable boundary (Verhoeven et al. 2011; Albertsson, 1976).

2.5.2 *Depositional model*

Our lithofacies analysis indicates the Tjörnes Beds reveal a dynamic and evolving depositional environment. Here, we use the vertical and lateral distribution of our lithofacies, in combination with our revised stratigraphic framework, to unravel the temporal and spatial evolution of associated sedimentary processes and depositional settings, and fully reconstruct the palaeoenvironmental history of these sediments (Fig. 2.10A-E).

Initially, a coastal estuary developed in a northerly-facing bay or fjord draining a southerly volcanic hinterland (Símonarson and Eiríksson, 2008). This coastal estuary had tidal flats, which most likely featured treeless and domed marshes, dominated by sedges and grasses (Fig. 2.10B). Pollen signals from the *Tapes* Zone lignite and sandstone deposits confirm these marshes contained *Cyperaceae* and *Poaceae* vegetation (Grímsson, 2007; Grímsson and Símonarson, 2008; Denk et al., 2005, 2011; Verhoeven et al., 2013). Fine suspended sediment was possibly transported shoreward into these marshes during the highest flood and spring tides (Manning and Dyer, 2007). Clay and silt particles settled from suspension during periods of slack water generating muddy firmgrounds. Argillaceous sediments may have also accumulated in sheltered coastal inlets or shallow embayments incised into the tidal flats, or small lakes in the adjacent coastal plain. The general scarcity of mudrock throughout the Tjörnes Beds suggests the estuary had a limited, mesotidal range similar to modern-day Iceland, in agreement with Símonarson and Eiríksson (2008). The abundance of parallel-

laminated sandstones throughout the *Tapes* Zone, suggest these early estuarine tidal flats were subjected to strong tidal or wave currents which deposited coarser, sandy sediments. The parallel-lamination indicates these sediments were possibly influenced by wave-driven swash and backwash processes (Clifton, 1969; Howard and Reineck, 1981; Yokokawa and Masuda, 1991). A thin package of cross-stratified bioclastic sandstone, underlain by a fossiliferous, clast supported, polymictic conglomerate in the *Tapes* Zone, indicates a short-lived marine incursion may have inundated the tidal flats, possibly associated with the onset of basin subsidence. The conglomerates are interpreted to be gravel lags deposited in subtidal channels, and the overlying cross-stratified sandstones possibly represent the subsequent infill and migration of dunes driven by surf processes and longshore currents (Pemberton et al., 2012). The abundance of disarticulated epifaunal molluscs and gastropods preserved in these conglomerates and sandstones, is indicative of the transportation and reworking of bioclastic material by wave action (Dashtgard et al., 2009).

The lowermost *Mactra* Zone features thick cross-stratified sandstone with metre-scale trough cross-bedding (Fig. 2.5, 2.7). These sandstones are considered to represent the progradation of distributary channels incised into the tidal flats, and the migration of mid-channel sand bars (Bhattacharya, 2006). Símonarson and Eiríksson (2008) agree and suggest the non-fossiliferous, cross-bedded sandstones in Bed E of Bárðarson (1925) are sand bars produced by current channels. The subsequent build-up of the tidal flats led to a re-establishment of coastal marshes. The preservation of xylitic lignites suggest the tidal flats featured dry forests located on either elevated embankments or levees associated with the distributary channels, or domed marshes above the tidal flat surface (Teichmüller, 1989). Pollen signals from the *Mactra* Zone lignites and siliciclastics confirm these tidal flats featured trees including black alder (*Alnus*), bayberry (*Myrica*), maple (*Acer*), walnut (*Juglans*) and willow (*Salix*) (Grímsson, 2007; Grímsson and Símonarson, 2008; Denk et al., 2005, 2011; Verhoeven et al., 2013). The upper *Mactra* Zone sediments show an increased influence of littoral processes and consist of bioclastic and parallel-laminated sandstones and a thick fossiliferous conglomerate. This littoral transition is interpreted to represent a significant transgression associated with further

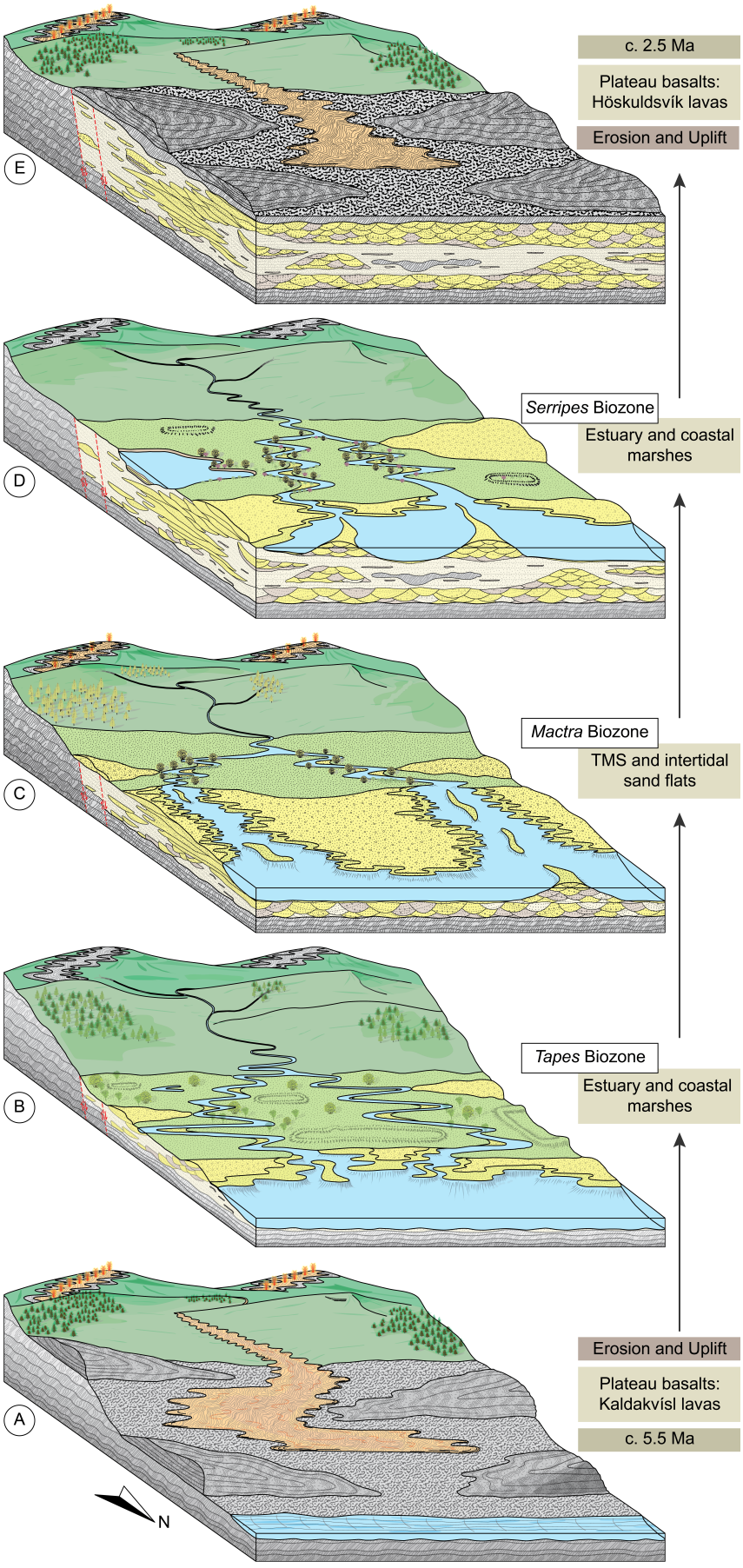

c. 2.5 Ma
Plateau basalts: Höskuldsvík lavas
Erosion and Uplift
E
Serripes Biozone
Estuary and coastal marshes
D
Mactra Biozone
TMS and intertidal sand flats
C
Tapes Biozone
Estuary and coastal marshes
B
Erosion and Uplift
Plateau basalts: Kaldakvísl lavas
c. 5.5 Ma
A
N

Figure 2.10 (previous page). Summary 3D palaeodepositional history for the Tjörnes Beds. (A) Emplacement of the Kaldakvísl lava field from nearby fissure eruptions during the late Miocene, followed by uplift and erosion. (B) Deposition of *Tapes* Zone strata in a northward-facing, marginal-marine fjord or embayment draining a southerly volcanic hinterland. Coastal marshes and intertidal sand flats dominate the estuarine environment. (C) Deepening of the Tjörnes Basin during the *Mactra* Zone results in the disappearance of coastal marshlands and the expansion of a tidally-modulated shoreface (TMS) and intertidal sand flats. Sedimentation is dominated by subtidal processes with thick accumulations of bioclastic cross-stratified and parallel-laminated sandstones. (D) Basin subsidence rates reduce during the *Serripes* Zone, leading to the progradation of intertidal flats and the re-emergence of coastal marshlands. (E) Uplift and erosion of the Tjörnes Beds during the late Pliocene precedes the eruption of the overlying Höskuldsvík lavas from nearby fissures.

basin subsidence, in agreement with Símonarson and Eiríksson (2008) (Fig. 2.10C). The cross-stratified sandstones are interpreted to represent subtidal channels infills, and were possibly deposited by migrating dunes driven by surf processes and longshore currents (Pemberton et al., 2012). These cross-stratified sandstones feature rare wave-rippled horizons indicating deposition in high flow velocities (40−60 cm/s), and shallow depths dominated by wave oscillations (<10 m) (Diem, 1985). The cross-stratified sandstones repeatedly coarsen upwards into parallel-laminated sandstones, which are synonymous with deposition on shallow, intertidal sand flats or beach barrier bars dominated by swash and backwash processes (Howard and Reineck, 1981) (Fig. 2.5, 2.7). This cyclical coarsening may represent the repeated progradation and flooding of the lower estuary, as basin subsidence continues and sediment supply exceeds accommodation space (Bhattacharya, 2010). The overlying fossiliferous conglomerate possibly represents a gravel lag deposited in seaward subtidal channels, where finer sediment was winnowed by longshore or tidal currents (Flemming et al., 1992). The erosional lower contact is most likely caused by local tidal-ravinement action at the base of these channels or may represent storm events (Dalrymple et al., 2003; Willis and Gable, 2003). During the upper *Mactra* Zone, the outpouring of a thick lava sheet produced the Skeifá lavas (Fig. 2.6C). Pillow structures (Fig. 2.6D), a palagonitic texture and the intercalation with cross-stratified bioclastic sandstones suggest the lavas were emplaced underwater either from submarine fissures or subaerial quenched flows, in agreement with Einarsson et al. (1967) and Eiríksson (1981). Similar textures are observed in the Pleistocene

Síða and Fljótshverfi volcanic groups in southern Iceland, which are interpreted to represent comparable voluminous extrusions from submarine fissures in the Eastern Volcanic Zone (Bergh and Sigvaldason, 1991; Gudmundsson, 2000; Tentler and Temperley, 2007).

Cross-stratified and parallel-laminated sandstone continue to dominate the lower *Serripes* Zone, reflecting the sustained influence of sub-tidal and intertidal sandy flat conditions (Fig. 2.10D). In the middle of the *Serripes* Zone, a thick non-fossiliferous conglomerate is overlain by cross-stratified and structureless sandstones which contain two further non-fossiliferous gravel horizons. These conglomerates are interpreted to reflect gravel lags deposited in fluvially-dominated, tidally-influenced distributary channels (Bhattacharya, 2006). The scoured bases underlying each conglomerate most likely represent the erosive action associated with either channel avulsion or bedload traction (Li and Bhattacharya, 2014). The overlying cross-stratified and structureless sandstones possibly mark the infill of these channels by subaqueous migrating sand bars and hyperconcentrated flows (Bhattacharya, 2006; Martin and Turner, 1998). These sediments denote the re-establishment and build-up of intertidal mixed flat and overbank deposits, as a consequence of reduced subsidence rates, in agreement with Símonarson and Eiríksson (2008). The overlying thick deposits of trough cross-laminated sandstones with mud drapes and abundant petrified branches and silicified wood fragments, are indicative of deposition on intertidal mixed flats incised by tidal channels or creeks (Dalrymple et al., 2012). The action of flood and ebb tides most likely powered the migration of current ripples and the development of trough cross-lamination (Dalrymple, 2010). During periods of slack tide, these bedforms were coated by thin mud layers deposited from suspension (Fenies et al., 1999). The preservation of wood fragments, indicates these tidal channels and creeks were possibly influenced by riverine inputs or nearby marshlands (Dalrymple et al., 1992; Dalrymple and Choi, 2007). A thin detritic lignite rests on this estuarine series, which indicates the renewed development of coastal marshes dominated by sedges and grasses (Kolcon and Sachsenhofer, 1999). The Tjörnes Beds terminate with a thin, non-fossiliferous conglomerate which fines-upwards into cross-stratified sandstone synonymous

with the continued influence of distributary channels across the intertidal flats (Bhattacharya, 2006).

2.5.3 *Modern analogue*

In an environment dominated by volcanic processes, the Tjörnes Beds provide a rare insight into depositional processes and environments onshore Iceland during the Pliocene, prior to a major climatic deterioration around 3 Ma during which inland ice caps expanded during cold periods, and conifers and deciduous forests vanished (Einarsson and Albertsson, 1988). We searched the modern Icelandic coast with reference to the wide range of terrestrial and marine depositional settings we have documented at Tjörnes, to assess whether similar processes and environments are observed onshore today. Using remote sensing and satellite imagery, we propose the Kaldárós Lagoon on the west coast of Iceland (Fig. 2.1) is a good modern analogue for the depositional environments and processes recorded by the Tjörnes sediments.

The Kaldárós Lagoon is a large (c. 25 km^2), shallow, river-fed, tidal embayment separated from the North Atlantic by a barrier sand bar (Fig. 2.11). Despite the differences in temperature and topography between the Pliocene and present-day Iceland, the location of the Kaldárós Lagoon on the west coast, far away from glacially-influenced sedimentation, makes this site a suitable modern analogue for the Tjörnes Beds. The Kaldárós Lagoon contains a variety of depositional environments similar to those believed to have deposited the Tjörnes sediments. Inland is an extensive, flat-lying, vegetated coastal plain which features a meandering river system feeding eroded volcaniclastics to the lagoon, from the Eldborg lava fields further east. Salt marshes mark the transition from the coastal plain to intertidal flats. These domed marshes occur along the northern margin of the lagoon, and are dominated by sedges and grasses. This environment is considered analogous to the setting in which organic matter accumulated to produce the Dl and Xl facies seen in the Tjörnes Beds (Fig. 2.8G, 2.8H). These marshlands contain small ponds and are surrounded by sheltered tidal pools, which suggest the area experiences periodic flooding by the highest flood or spring tides. During intervals of

KALDÁRÓS LAGOON



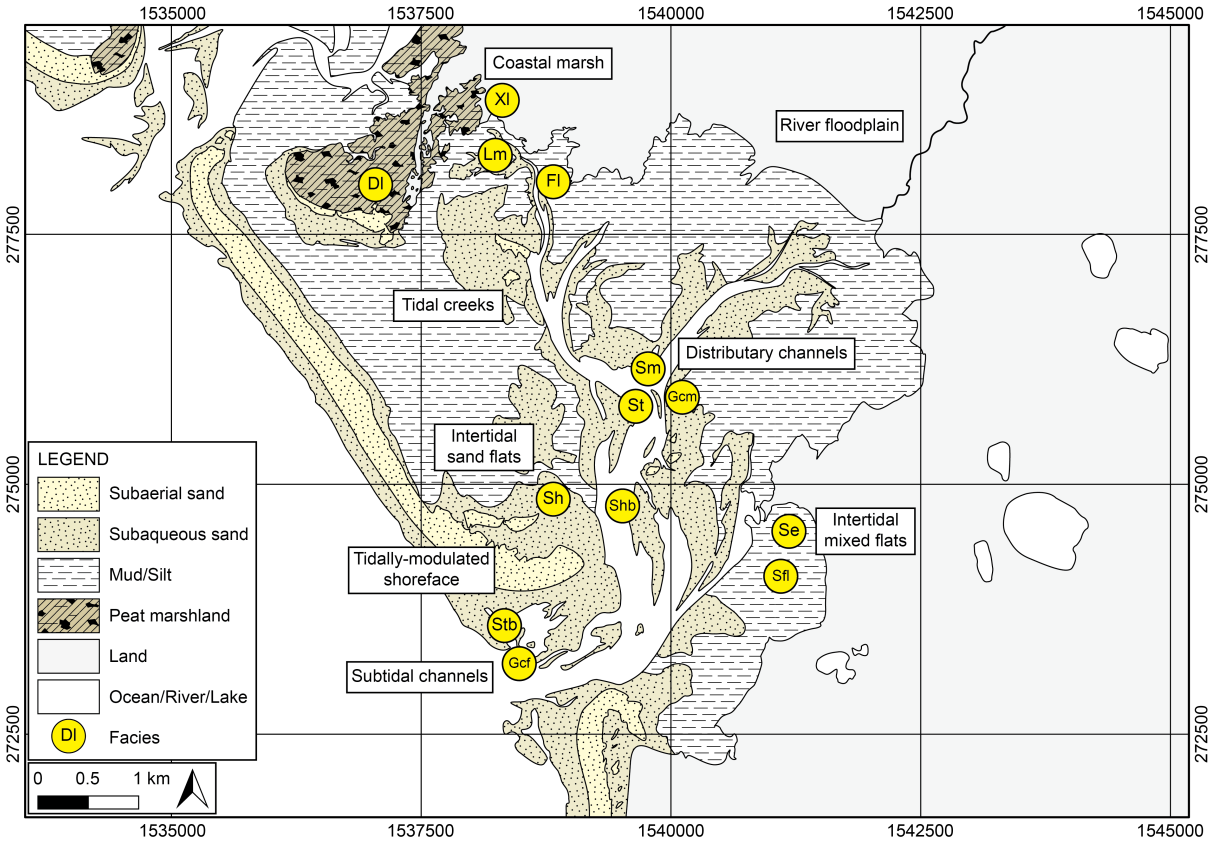


Figure 2.11 (previous page). Annotated satellite image of the Kaldárós Lagoon in western Iceland. The spatial distribution of the mappable lithologies, discussed facies and depositional environments are shown on the illustrated map. The Kaldárós Lagoon is a modern analogue for the setting in which the Tjörnes Beds were deposited, showing a similar range of sedimentary processes and environments. Location shown on Fig. 2.1. Satellite map created in QGIS v.3.4 using Esri® World Imagery (available at: https://www.arcgis.com/home/item.html?id=10df2279f9684e4a9f6a7f08febac2a9 [accessed 06/01/2020]).

slack water, fine sediment may settle from suspension to generate muddy firmgrounds, similar to the Fl and Lm facies observed at Tjörnes (Eisma, 1986; Manning and Dyer, 2007).

Intertidal mud flats occur between the landward coastal marshes and the seaward sand flats in the Kaldárós Lagoon. These mud flats comprise heterolithic sediments and feature dendritic tidal channels and creeks. This environment is interpreted to be similar to that in which the trough cross-laminated sandstone with intraclasts, wood debris and mud drapes (Se and Sfl) was deposited (Fig. 2.8E). The incised channels and creeks may deliver lithic intraclasts and vegetation scoured from landward firmgrounds or coastal marshes (Dalrymple, 2010). The tidal channels may also contain coarse gravel lags, similar to the non-fossiliferous conglomerates (Gcm) observed at Tjörnes. Mid-channel sand bars are also observed in these channels, which represent the migration of subaqueous bedforms by tidal currents (Bhattacharya, 2006). These sandbars are considered to represent the St facies, and will most likely overlie the coarser gravel lags. The lateral migration, bifurcation and abandonment of these channels may result in the rapid dumping of sandy sediments generating structureless sheet-like beds (Martin and Turner, 1998; Horn et al., 2018), similar to the Sm facies observed at Tjörnes.

A large and elongated subaerial sand barrier separates the Kaldárós Lagoon from the North Atlantic. Extensive tidal sand flats surround this barrier at the mouth of the embayment. Parallel-laminated sands (Sh and Shb) are expected in this intertidal zone, produced by the interaction of wave-driven swash and backwash processes (Clifton, 1969; Howard and Reineck, 1981; Yokokawa and Masuda, 1991). The mouth of this coastal embayment features

subtidal mid-channel sand bars, which are expected to feature trough cross-stratification (Dalrymple and Choi, 2007; Dalrymple, 2010). The migration of these subtidal sand bars may be controlled by surf processes, longshore and rip currents (Dashtgard et al., 2009; Pemberton et al., 2012). These seaward sand bars are expected to contain abundant disarticulated bioclastic material, transported and reworked by wave and tidal processes (Dashtgard et al., 2009). We interpret that similar mid-channel sand bars were present in the subtidal zone of the Pliocene estuary which deposited the Tjörnes Beds, producing similar bioclastic and trough cross-stratified sandstones (Stb) (Fig. 2.8A−C). These subtidal sand bars are expected to feature underlying gravel lags which represent local tidal-ravinement action at the base of the seaward channel (Flemming et al., 2012), similar to the Gcf facies seen at Tjörnes.

The Kaldárós Lagoon provides good insight into the range of modern sedimentary processes and environments occurring at the Icelandic shoreline, as a consequence of the local geology, hydrology, climate and ecology. All of the lithofacies recognised at Tjörnes by this study, including their primitive constituents (e.g. sedges and grasses for Dl and Xl), have equivalent depositional environments in the Kaldárós Lagoon. These lithofacies reflect a range of contemporaneous depositional settings including coastal marshes, tidal flats and channels. The good match between the Kaldárós environments and the Tjörnes lithofacies supports the application of this lagoon as a modern sedimentary analogue for the Tjörnes Beds, and strengthens the sedimentological interpretations proposed here. We suggest detailed field mapping at Kaldárós in the future will help to corroborate our aerial interpretations, improve the understanding of the Tjörnes sedimentary system, and provide further insight into the marginal-marine depositional processes most likely operating in the Pliocene.

2.5.4 *Implication of sediment reworking on biostratigraphy and relative age*

Multiple age models have been proposed for the Tjörnes Beds based on radiometric dating of intercalated lavas, magnetostratigraphy and biostratigraphy, which suggest the Tjörnes Beds were deposited throughout the early- to mid-Pliocene (Albertsson, 1976, 1978; Einarsson et

al., 1967; Buchardt and Símonarson, 2003; Símonarson and Eiríksson, 2008; Chapter 5). Recently, Verhoeven et al. (2011) proposed a revised age model based on dinoflagellate biostratigraphy. However, the suggested changes to the age model are controversial and imply the Tjörnes Beds are significantly older than previously thought. Here, we use our new lithofacies analysis to argue that this revised age model is unreliable due to sediment reworking.

Símonarson and Eiríksson (2008) place the *Mactra*/*Serripes* boundary at c. 3.6 Ma, based on the first occurrence of North Pacific molluscs linked to ocean circulation changes associated with the opening of the Bering Strait (Fig. 2.1). However, Verhoeven et al. (2011) report that a key dinoflagellate species *Reticulatosphaera actinocoronata* occurs within the *Serripes* Zone up to Bed 17 of Bárðarson (1925). This species is a key marker for the Zanclean stage and ranges no higher than c. 4.4 Ma, as indicated by correlations with Norwegian Sea marine records (Eidvin et al., 2007; Verhoeven et al., 2011). If this marker is a primary constituent of the rock, it would suggest the upper part of the Tjörnes Beds is close to 1 Ma older than previously thought. Significant implications mean the upper Tjörnes Beds do not record the mid-Piacenzian Warm Period (mPWP; 3.025−3.264 Ma), and that a large time gap exists at the top of the succession before the extrusion of the Höskuldsvík lavas (c. 2.55 Ma; Albertsson, 1976, 1978) and the deposition of the overlying Breiðavík tillites (iNHG) (Eiríksson and Geirsdóttir, 1991; Geirsdóttir and Eiríksson, 1994). The revised age model relies on the interpretation that *R. actinocoronata* has not been reworked. Verhoeven et al. (2011) address this issue, and conclude that reworking of upper *Mactra* Zone sediments is unlikely to be responsible for the incorporation of the index species higher up the succession.

In contrast, our lithofacies analysis shows significant potential for reworking of *Mactra* Zone sediments during the lower *Serripes* Zone (Fig. 2.5, 2.7). Our work demonstrates Bed 17, and the surrounding sediments, were most likely deposited in an evolving subtidal and intertidal environment, where high-energy surf, longshore and rip current processes operate (Dashtgard et al., 2009). Bed 12 to 22 are dominated by trough cross-stratified sandstones (Stb) (Fig.

2.8A-C), which coarsen upward into parallel-laminated sands (Sh and Shb). These sediments represent the infill of subtidal channels, and the build-up of intertidal sand flats prone to swash and backwash processes (Dalrymple and Choi, 2007; Dalrymple, 2010). The cross-stratified sandstones commonly feature coarse lags (Fig. 2.8D), which represent local tidal-ravinement action at the base of these channels, where tidal or storm-driven currents erode into the underlying substrate (Dalrymple et al., 2003; Fürsich and Oschmann, 1993). Both sandstone facies contain abundant disarticulated marine fauna often preserved in scoured depressions (Fig. 2.8A), which are indicative of surf and storm transportation and reworking of bioclastic detritus (Dashtgard et al., 2009). Stb is also intensely bioturbated with vertical burrows which constitute the *Skolithos* Ichnofacies, which supports deposition in a high-energy, marine environment (MacEachern et al., 2010; Plint, 2010). This evidence suggests the *Mactra* Zone sediments are very likely to have experienced erosion and reworking by wave, tidal, marine fauna and possibly storm processes during deposition of the lower *Serripes* Zone. Our lithofacies analysis and palaeoenvironmental interpretations suggest the lower *Serripes* Zone subtidal and intertidal environments had the greatest potential for sediment reworking in the entire Tjörnes Beds (Fig. 2.5, 2.10D). We therefore believe that reworking may well have been responsible for the last occurrence of *R. actinocoronata* stratigraphically higher than expected.

This assessment of sediment reworking indicates the Verhoeven et al. (2011) age model of a relatively old Tjörnes succession is unlikely, and suggests the original age models, which imply a younger age range of 3 to 4 Ma for the upper Tjörnes Beds, are more plausible. We note that there is potential to test the Tjörnes age model more directly in the future. Optical petrography confirms feldspars preserved in the Skeifá lavas are amenable to the modern $^{40}Ar/^{39}Ar$ dating technique (Chapter 5). A precise radiometric age close to the *Mactra*/*Serripes* Zone boundary would support the relative ages proposed using different biostratigraphic markers, and would therefore help resolve the proposed implications of sediment reworking on this section.

2.6 CONCLUSIONS

The Tjörnes Beds are an important sedimentary archive for understanding NE Atlantic palaeoenvironmental change because they span the transition from early Pliocene warmth to the iNHG. Our current understanding of the Tjörnes Beds stratigraphy and sedimentology is based on the historic, horizontal mapping of coastal outcrops. However, significant gaps exist in these records related to the exclusion of inland or inaccessible sections, which restrict our understanding of the true thickness and structural architecture of the Tjörnes Beds, the vertical distribution of facies and disconformities, the depositional and palaeoenvironmental evolution and the palaeoclimatic signals preserved in these sediments.

We present a revised lithostratigraphic framework which incorporates both coastal and inland exposures, quantifies the thickness of unobserved sections and accounts for pervasive faulting for the first time. We use UAV photogrammetry to efficiently and systematically map and analyse outcrops, assess inaccessible sections and verify and support our stratigraphic and structural interpretations. Structure contour analysis indicates the total thickness is 745 m, c. 45% greater than originally described. A total of c. 230 m of sediment is unobserved owing to superficial deposits or truncation by extensional faulting. Structure contouring reveals the largest missing sections (up to 60 m) occur in the lower half of the succession, within the *Tapes* and *Mactra* Zones. Our new composite section accommodates all the non-exposed intervals, and so quantifies the relative vertical positions of the various logged sections accurately for the first time.

We demonstrate important stratigraphic differences compared to existing interpretations, including the nature of the basal contact and the stratigraphic position of the intercalated Skeifá lavas. We show the lower contact comprises a fault zone containing a downthrown and rotated block of Tjörnes strata, which originate from the *Tapes* Zone. We reveal the Kaldakvísl lavas form upthrown horsts, either side of this downthrown block, and extend for a few hundred metres northwards beyond the fault zone, where the true non-conformable contact with the

overlying Tjörnes sediments is observed. We demonstrate the Skeifá lavas occur in the upper *Mactra* Zone, c. 50 m lower than originally described, and suggest previous interpretations mistakenly correlate the laterally discontinuous lavas with an incompatible coastal section, which is stratigraphically higher than expected.

We identify 13 lithofacies within the Tjörnes Beds and group these into five facies associations based on their vertical distribution. The sediments reveal a dynamic and evolving depositional environment. The Tjörnes Beds were initially deposited in a northerly-facing, tide-dominated estuary dominated by coastal marshlands and intertidal mixed flats, which featured incised tidal channels and sheltered creeks. A marine transgression during the *Mactra* Zone, led to deepening and a higher-energy subtidal environment featuring parallel- and cross-stratified and wave-rippled sandstones influenced by surf, longshore and rip current processes. Basin subsidence rates reduced during deposition of the late *Serripes* Zone, leading to the progradation and re-establishment of intertidal flats and coastal marshes. Using remote sensing, we predict that all 13 lithofacies described here are likely to occur in the present-day Kaldárós Lagoon on the west coast of Iceland. This setting provides a modern insight into onshore sedimentary processes and environments, supports our depositional interpretations inferred during the Pliocene and represents an unparalleled analogue for the Tjörnes sedimentary system.

Our lithofacies analysis also provides a quantitative measure of sediment reworking, which allows assessment of a recently proposed change to the age model for the Tjörnes Beds (Verhoeven et al., 2011). This change would mean that the uppermost part of the sequence is over 1 Ma older than previously thought, and would not therefore record enhanced warming indicative of the mPWP. The proposed new age model relies on the interpretation that specimens of the key Zanclean dinoflagellate *R. actinocoronata* within the *Serripes* biozone are not reworked from lower horizons. However, we show that the upper *Mactra* Zone and lower *Serripes* Zone sediments are the most likely to be influenced by sediment reworking, following deposition in a subtidal setting influenced by high-energy surf, longshore and rip

current processes. We therefore consider that this dinoflagellate marker species should not be used to pin an age model. The lower part of the *Serripes* Zone is likely aged around 3.6 Ma, as previously suggested by mollusc biostratigraphy.

Our revised composite section is a significant step toward a more complete stratigraphic and sedimentological framework for the Tjörnes Beds. We have shown that the exposed, logged sections across the area can be placed on a common vertical scale that formally accounts for non-exposed strata. We also show the vertical distribution of lithofacies for the first time, demonstrate the logged successions contain no major disconformities and use our lithofacies analysis to fully reconstruct the depositional history. Our interpretations increase the value of the Tjörnes Beds as a palaeoclimatic archive by filling gaps in the stratigraphic and palaeoenvironmental record, and revealing previously undocumented sections which may yield new palaeoclimatic records to help further unravel the transition from Pliocene warmth to the iNHG in the NE Atlantic.

3. TECTONIC AND CLIMATIC CONTROLS ON THE DEEP-WATER CONNECTIVITY OF THE NE ATLANTIC AND NORDIC SEAS DURING THE PLIOCENE

My contribution to this work involved conducting all parts of the research, including sample selection, laboratory preparation and analysis, interpreting the $\delta^{13}C$ and εNd data, writing the manuscript and creating the figures. H. Kuhlmann assisted with sampling requests at the IODP Bremen Core Repository, University of Bremen. M. Leng and H. Sloane helped with the analysis of $\delta^{13}C$ at the Stable Isotope Facility, British Geological Survey. A. Piotrowski and C. Larkin assisted with the leaching and analysis of neodymium at the Department of Earth Sciences, University of Cambridge. T. Dunkley Jones and S. Jones provided feedback on the interpretations of the results. As in the previous chapter, the editorial 'we' is used to reflect these contributions.

3.1 ABSTRACT

The NE Atlantic and Nordic Seas contain valuable sedimentary archives of palaeoenvironmental change throughout the late Neogene, witnessing the transition from late Miocene cooling to Pliocene warmth, followed by the intensification of the North Hemisphere Glaciation. Previous studies suggest regional deep-water ventilation and overturning circulation is controlled by the varying dynamic support of the Greenland-Scotland Ridge oceanic gateway, whose tectonics may have influenced this climatic change. However, our understanding of these tectonic and oceanic interactions are currently based on benthic $\delta^{13}C$ records compiled exclusively from five DSDP sites in the NE Atlantic south of this ridge, and consequently the influence of these lock-gate motions on the ventilation of the Nordic deep-waters, to the north of the ridge, is unknown. Here, we address these issues by compiling all available benthic $\delta^{13}C$ records from the NE Atlantic and Nordic Seas for the first time. Our regional compilation contains over 11,900 $\delta^{13}C$ data points, ten times more than previous studies. We verify our compilation by presenting new benthic $\delta^{13}C$ records, which confirm the Norwegian Sea deep-waters were significantly lighter in $\delta^{13}C$, by up to 1 ‰, compared to the NE Atlantic throughout the early to mid-Pliocene signifying poor ventilation of this deep basin for at least part of this interval. This result is somewhat unexpected since previous findings suggest the contribution of northern sourced waters to global circulation increases during this time, attributed to reduced dynamic support. We further explore patterns of deep-water connectivity between these basins by generating the first neodymium data from ODP Site 642 and DSDP Site 552, which extends the regional εNd record throughout the late Neogene. We show the Vøring Plateau deep-waters were significantly more radiogenic (up to +3.1 εNd units) during the early to mid-Pliocene (5.3−3.0 Ma) interval, compared to the Rockall Plateau. The divergence shown by our εNd results supports our $\delta^{13}C$ data, suggesting poor connectivity between the Norwegian and NE Atlantic basins at this time. We suggest the ventilation of the Norwegian Basin during the early to mid-Pliocene was weakened by the combined influence of a regional cooling event, during which sea surface temperatures reduced by 4.5°C resulting in a decline in primary productivity, and the subaerial Barents Shelf, which deflected warm

surface currents poleward to the Fram Strait, reducing the influence of dense brines in the Norwegian Sea. During the late Pliocene (3.0−2.5 Ma), our εNd record indicates the isotopic signatures of the Norwegian and NE Atlantic deep-waters converged at around c. 2.6 Ma, before showing a reversed pattern compared to the early to mid-Pliocene. This suggests greater deep-water connectivity between the Norwegian and NE Atlantic basins and improved ventilation of the Norwegian Sea at depths below 1 km during this time, relative to the early to mid-Pliocene. Ventilation of the Norwegian Sea throughout the late Pliocene, most likely reflects the interaction of regional climatic and oceanic changes associated with the closure of the Central American Seaway and the intensification of the Northern Hemisphere Glaciation. Sea-ice development and freshwater forcing is considered to have dampened deep-water production at higher latitudes, reducing the influence of the subaerial Barents Shelf on regional circulation during the late Pliocene. Sites of deep-water production most likely shifted southward into the Norwegian Sea at this time, where ventilation was driven by cooling of warm waters which continued to be transported northward by an enhanced Norwegian Atlantic Current, despite an elevated Greenland-Scotland Ridge. Norwegian Sea deep-water production most likely persisted throughout this interval, continuing to contribute to Iceland-Scotland overflow waters which influence the NE Atlantic. Consequently, we suggest benthic $\delta^{13}C$ records from the Norwegian Sea should not be used to infer fluctuations in dynamic support, since the processes governing the evolution of these deep-waters are somewhat decoupled from the wider rate of North Atlantic deep-water formation. This work is a significant step toward understanding the long-term controls on the ventilation of the Norwegian Sea throughout the late Neogene, and assessing the interactions between regional circulation and mantle-induced processes, which will help resolve the drivers of Pliocene climate and the intensification of the North Hemisphere Glaciation.

3.2 INTRODUCTION

The NE Atlantic and Nordic Seas are important sites for understanding the interactions of solid Earth processes, ocean circulation and climatic change. During the last 6 myrs this region witnessed significant palaeoenvironmental change from late Miocene cooling to Pliocene warmth, followed by the intensification of the Northern Hemisphere Glaciation (iNHG), during which large ice sheets expanded beyond Greenland and across North America and Scandinavia for the first time (Willeit et al., 2015), before culminating in the intense glacial/interglacial cycles indicative of the Quaternary. The production of North Atlantic Deep Water (NADW) in this region is vital for the global climate system, as it directly drives the Atlantic Meridional Overturning Circulation (AMOC) which is responsible for global oceanic ventilation and inter-hemispheric heat transport. The Greenland-Scotland Ridge (GSR) acts as a regional lock-gate in response to short-term (1−10 Myr) uplift and subsidence, caused by thermal perturbations within the Icelandic mantle plume (Jones et al., 2002). This lock-gate is thought to modulate the northward transport of surface waters and southward transport of deep-waters, and is believed to influence the strength of the AMOC since the middle Miocene (Poore et al., 2006). Variations in dynamic support of the GSR are deduced from V-shaped ridge records (Jones et al., 2002), which are then compared against estimates of Northern Component Water (NCW; deemed a precursor to modern NADW) inferred from global compilations of benthic foraminifera $\delta^{13}C$ ($\delta^{13}C_{BF}$) records. Several studies suggest the southward overflow of NCW rapidly increased throughout the late Neogene in response to a reduction in dynamic support of the GSR, and propose the knock-on strengthening of regional overturning circulation may have driven the iNHG (Wright and Miller, 1996; Poore et al., 2006; Robinson, et al., 2011; Parnell-Turner et al., 2015).

However, the current characterisation of NCW is exclusively based on $\delta^{13}C_{BF}$ records from south of the GSR (Wright and Miller, 1996; Poore et al., 2006), and therefore the true influence of Nordic deep-waters on the estimation of NCW is unknown. No published work has yet compiled all available benthic records from both the NE Atlantic and Nordic Seas, in order to

characterise deep-waters either side of the GSR throughout the late Neogene. The most significant problem is the lack of abundant and well-preserved benthic foraminifera from sites in the Nordic Seas, and therefore alternative tracers of bottom-water circulation are needed to support the characterisation of these regional deep-waters. Other challenges are to determine the tectonic and climatic processes which may govern the ventilation of the Nordic Seas deep-water, and the implications these have on our current understanding of variations in NCW production and the timing and influence of GSR lock-gate motions throughout the late Neogene.

The purpose of this study is to better characterise the evolution of Nordic deep-waters, in relation to the wider NE Atlantic system, during the Pliocene, using new $\delta^{13}C_{BF}$ and neodymium (Nd) isotope records. Nd isotopes are conservative tracers of bottom waters, independent of biological fractionation, which reflect the composition of differing terrigenous inputs in areas surrounding deep-water formation and are used to reconstruct simple mixing of deep-water masses (Piotrowski et al., 2005). These results should inform our understanding of the tectonic and climatic mechanisms controlling the ventilation and connectivity of the major basins to the north of the GSR, within the context of existing reconstructions of NCW. We also aim to assess the interactions between regional ocean circulation and variations in dynamic support, which may help resolve the drivers of late Neogene climate change and the iNHG. In the following subsections, we review the current understanding of NE Atlantic oceanography and NCW production.

3.2.1 *Modern NE Atlantic and Nordic Seas Oceanography*

The continental configuration and ocean circulation observed in the NE Atlantic (Fig. 3.1) during the Pliocene is considered similar to today (Risebrobakken et al. 2016). The Barents Shelf, which at present accommodates one third of poleward oceanic heat transport from the Nordic Seas into the Arctic Ocean, was subaerially exposed to its maximum extent throughout this period (Butt et al., 2002; Torsvik et al., 2002). Global sea-level estimates range from 10 to

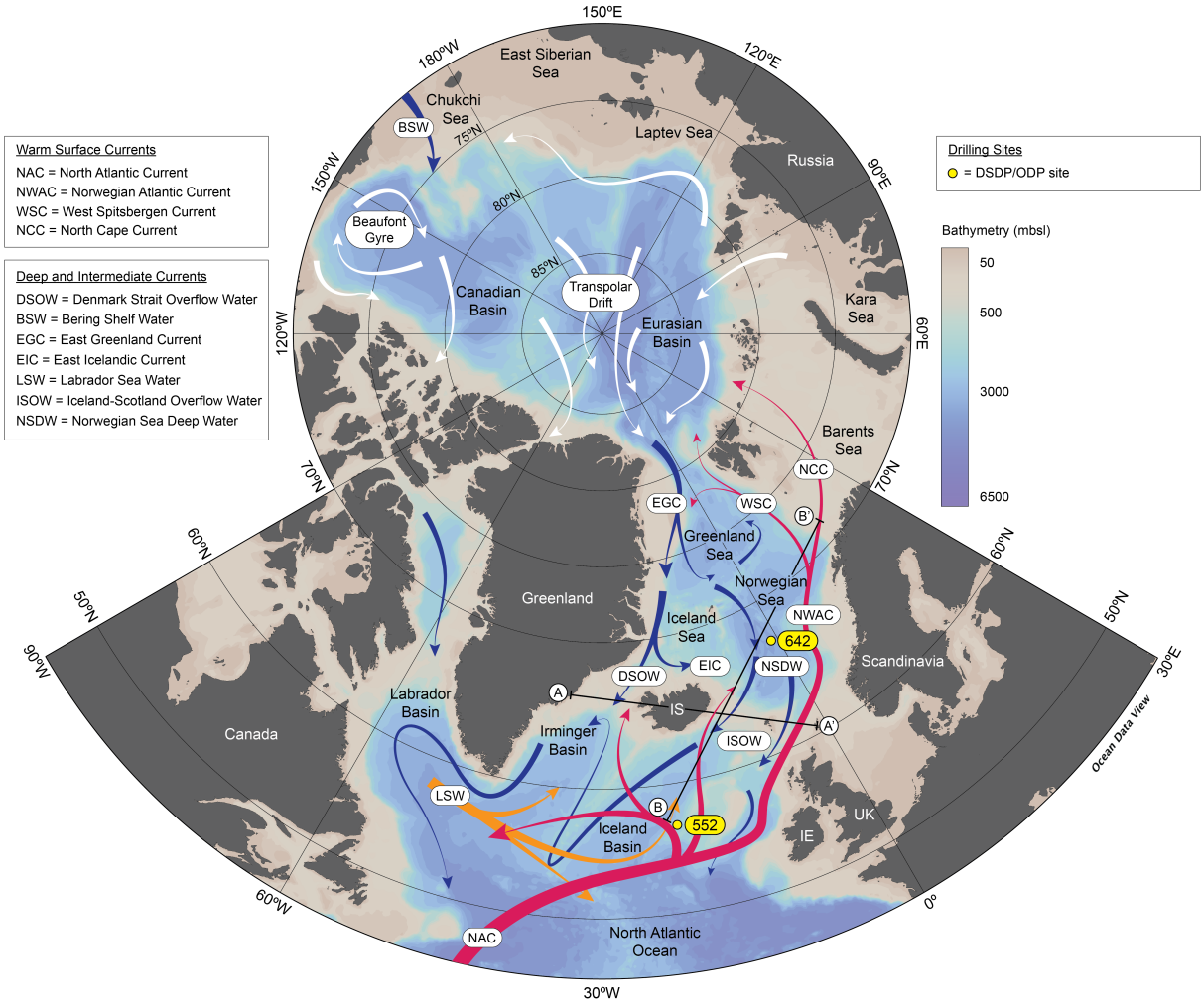


Figure 3.1. Bathymetric map of the NE Atlantic Ocean, Nordic Seas and Arctic Ocean. Red, orange and blue arrows indicate surface, intermediate and deep ocean currents respectively. Relevant DSDP and ODP drilling sites are highlighted yellow. Bathymetric map created in Ocean Data View v.5.1.7.

40 m above present due to lower ice sheet volumes on Greenland and Antarctica (Raymo et al. 2011). Modern circulation in the North Atlantic is characterised by density and wind-driven surface currents (North Atlantic Current, NAC) which flow northward into the Nordic and Labrador Seas and the northernmost Atlantic; these warm and saline currents eventually cool and sink at high latitudes due to increasing densities, producing NADW (Fig. 3.1). The main source of NADW is Norwegian Sea Deep Water (NSDW), with additional contributions from the Labrador Sea and Mediterranean Outflow Water at lower latitudes (Hansen and Østerhus, 2000). The Nordic Seas comprise three ocean basins separated by submarine ridges; the Norwegian Sea in the southeast, the Greenland Sea in the north and the Iceland Sea in the

southwest. The northerly-flowing NAC transforms into the Norwegian Atlantic Current (NWAC) before entering the Barents Sea and bifurcating further north along the Svalbard margin as the West Spitsbergen Current. The inflow of the NAC into the Nordic Seas occurs via three routes (Fig. 3.2), including the Denmark Strait with a flux of 1 Sv (10^6 m^3s^{-1}), the Iceland-Faroe Ridge (3.3 Sv) and Faroe-Shetland Channel (3.7 Sv) (Hansen and Østerhus, 2000). Surface waters continue to flow (2 Sv) poleward to the Arctic Ocean through the Barents Sea and the Fram Strait via the North Cape Current and West Spitsbergen Current, respectively (Jones, 2001). Thermohaline circulation is the main driving mechanism of this Atlantic inflow, whereby rapid cooling and brine rejection associated with the formation of sea ice, results in the sinking of the NWAC to produce NSDW. In addition, the East Iceland Current (EIC) contributes further deep-water originating from the Arctic Eurasian Basin (Moffa-Sanchez et al., 2015). The overflow leaving the Nordic Seas (Fig. 3.2) consists of near-bottom, cold and highly saline currents which flow across the Iceland-Faroe Ridge and through the Faroe-Shetland Channel (termed Iceland-Scotland Overflow Water; ISOW) (combined 3 Sv) (Hansen and Østerhus, 2000), and the East Greenland Current (EGC) which flows through the Denmark Strait (termed Denmark Strait Overflow Water; DSOW) (3 Sv).

3.2.2 *Northern Component Water and Dynamic Support*

The GSR is a volcanic structural high which stretches 1650 km across the NE Atlantic Ocean between central east Greenland and the NW European margin, and represents a hotspot track constructed by the interaction between the Mid-Atlantic Ridge (MAR) and the Iceland mantle plume (Fig. 3.2). The GSR is a significant constituent of the North Atlantic Igneous Province, and formed in the late Palaeocene and early Eocene (57−54 Ma), during the opening of the North Atlantic rift system, the formation of magma-rich margins and the onset of seafloor spreading (Hjartarson et al. 2017). The Iceland-Faroe Ridge and Denmark Strait remained subaerial prior to the middle Miocene (12 Ma), after which water depths in excess of 100 m established across the GSR either side of Iceland; an ongoing reduction in dynamic support has resulted in an overall long-term rise in the flux rate of NCW across the ridge. GSR depths

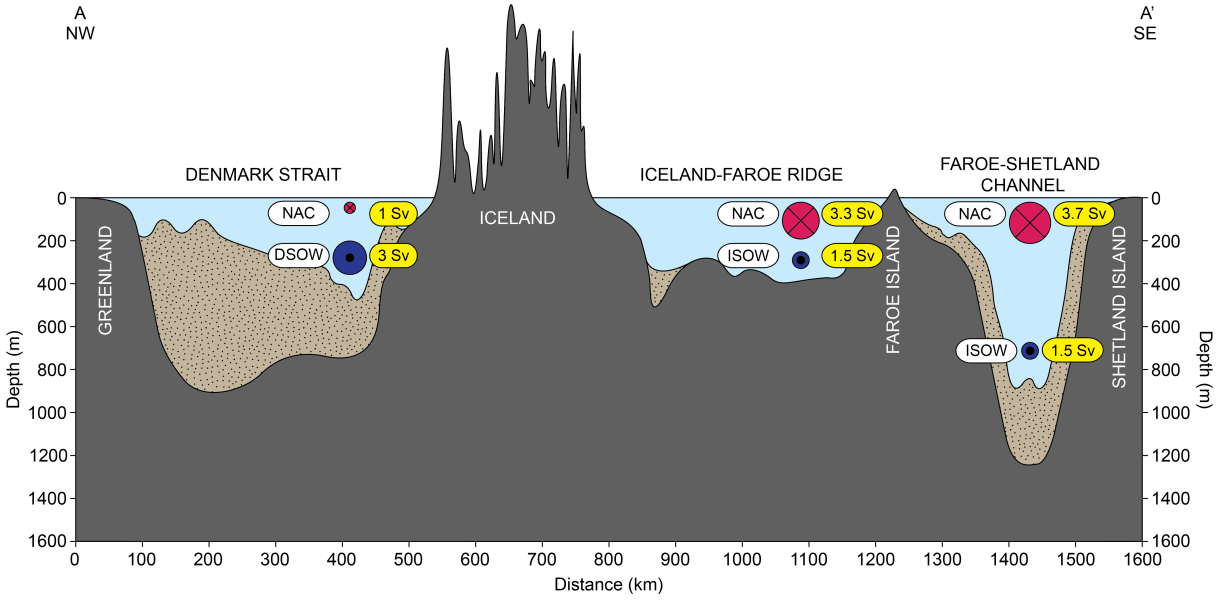


Figure 3.2. Schematic cross section across the Greenland-Scotland Ridge along line A-A' shown in Fig. 3.1. Surface (crosses; northward) and deep-water (dots; southward) oceanic currents are defined in Fig. 3.1. Surface currents continue poleward and flow into the Arctic Ocean (c. 2 Sv) through the Barents Sea and Fram Strait. Sediment highlighted by speckled unit. Fluxes are in Sverdrups (1 Sv = 1×10^6 m^3s^{-1}) beside respective oceanic currents. Modified from Wright and Miller (1996).

are generally less than 500 m, with the deepest passages being the Faroe-Shetland Channel (800−900 m) and the Denmark Strait (c. 620 m).

Several studies have focussed on the interaction between mantle-induced vertical motions of the GSR and the strength of southerly flowing NCW. Wright and Miller (1996) were the first to demonstrate a strong negative correlation between the %NCW and short-lived (1−10 Ma) vertical motions of the GSR during Neogene times by compiling $\delta^{13}C_{BF}$ records from across multiple ocean basins to define end-members for the North Atlantic ($\delta^{13}C_{NA}$), Southern ($\delta^{13}C_{SO}$) and Pacific Oceans ($\delta^{13}C_{PO}$). The $\delta^{13}C_{BF}$ records for each member were stacked, interpolated to constant 0.1 myr intervals and smoothed using a 11 point (±0.5 myr) Gaussian filter. NCW flux was estimated using Eq. 3.1 defined by Oppo and Fairbanks (1987).

Wright and Miller (1996) showed how NCW production was weak during the late Miocene (8 to 6 Ma), before the NCW flux strengthened by c. 200% during the Pliocene (5.5 to 3 Ma),

$$\%NCW = \frac{\delta^{13}C_{SO} - \delta^{13}C_{PO}}{\delta^{13}C_{NA} - \delta^{13}C_{PO}} \times 100$$

Equation 3.1. Percentage overflow of Northern Component Water.

before weakening again by c. 80% after 3 Ma. Following this decline, short high frequency (Milankovitch) variations in NCW production occur with low NCW fluxes (c. 20%) during glacial intervals and higher NCW fluxes (up to 80%) throughout interglacial intervals (Raymo et al. 1990). Wright and Miller (1996) attribute these longer-term fluctuations to variations in dynamic support of the GSR, caused by changes in Icelandic mantle plume activity; they suggest times of anomalously high melt production, associated with the formation of V-shaped ridges along the Reykjanes spreading axis, correspond well with increased dynamic support of the GSR by calculating residual depth anomalies, which represent the difference between the observed depths to oceanic basement outlined by Talwani et al. (1971) and the depths predicted by a half-space cooling model. Jones et al. (2002) produced a V-shaped ridge record based on gravity anomalies which supports and resembles a smoother version of this residual depth record. Wright and Miller (1996) suggest these changes in the elevation of the GSR may influence the flux of NCW into the Southern and Pacific Oceans; when the GSR is deeper (cooler Icelandic plume) a greater volume of water can pass over the ridge, whereas when the GSR is shallower (hotter plume) the flux of NCW is restricted. Wright and Miller (1996) acknowledge long-term climate cooling throughout the Cenozoic is controlled by factors other than NCW production. However, they do believe enhanced poleward heat transport, vigorous overturning circulation and increased %NCW during the Pliocene, preconditioned the mid to high latitudes and may have aided the development of the iNHG.

Poore et al. (2006) reassessed the influence of convective thermal perturbations on GSR vertical motions and NCW flow during the Neogene by improving the %NCW record. Poore et al. (2006) compiled new high-resolution $\delta^{13}C_{BF}$ data from sites in the North Atlantic, Southern and Pacific Oceans, tuned to the astronomical time scale (after Lourens, 2004). This record

was smoothed using a nonparametric curve-fitting technique to generate regional $\delta^{13}C_{BF}$ end members and fitted with confidence bands to account for age model, analytical and species vital effect uncertainties (Fig. 3.3A). Similar to Wright and Miller (1996), Poore et al. (2006) demonstrated a strong negative correlation between the %NCW and the vertical motion of the GSR during the Neogene (Fig. 3.3B). Poore et al. (2006) indicate a rapid increase in NCW production around 6 Ma, and attribute this rise to a reduction in dynamic support at the Denmark Strait. They suggest deepening of the GSR continued until around 2.7 Ma, after which the %NCW in the Southern Ocean steadily declined to present-day; the formation of V-shaped ridge 1 in response to a thermal perturbation in the Icelandic plume head, and the associated dynamic uplift of the GSR, is considered to have reduced the southward overflow of NCW and the strength of the AMOC during this interval. Regional contourite drift accumulation rates provide further evidence for interactions between the Icelandic plume and GSR dynamic support. Wold (1994) proposed a rapid increase in the sedimentary flux across the GSR around 6 Ma, and a slight reduction at 2 Ma, both of which correlate well with the inferred variations in %NCW suggested by Poore et al. (2006) and Wright and Miller (1996). Parnell-Turner et al. (2015) examined seismic reflection profiles through the Eirik and Björn Drifts located in the Irminger and Iceland basins respectively, either side of the Reykjanes Ridge; they reveal how the sedimentation rate of the Eirik Drift was significantly higher (160 m Ma^{-1}) between 6 and 2.5 Ma, compared to the present day rate of 60 m Ma^{-1} (Müller-Michaelis and Uenzelmann-Neben, 2014). They also show how the accumulation rates of both the Björn and Eirik Drifts reduced between 2.5 and 0.5 Ma, lowering by 66% and 50% respectively. Parnell-Turner et al. (2015) correlate these variations in contourite accumulation to transient fluctuations in dynamic support; their observations match and support the NCW flux history generated from the compiled $\delta^{13}C_{BF}$ records.

Whilst compiling $\delta^{13}C_{BF}$ data for use in the estimation of %NCW fluctuations (Fig. 3.3B), Wright and Miller (1996) and Poore et al. (2006) selected Deep Sea Drilling Project (DSDP) and Ocean Drilling Program (ODP) sites (DSDP Site 552, DSDP Site 607, DSDP Site 608, DSDP

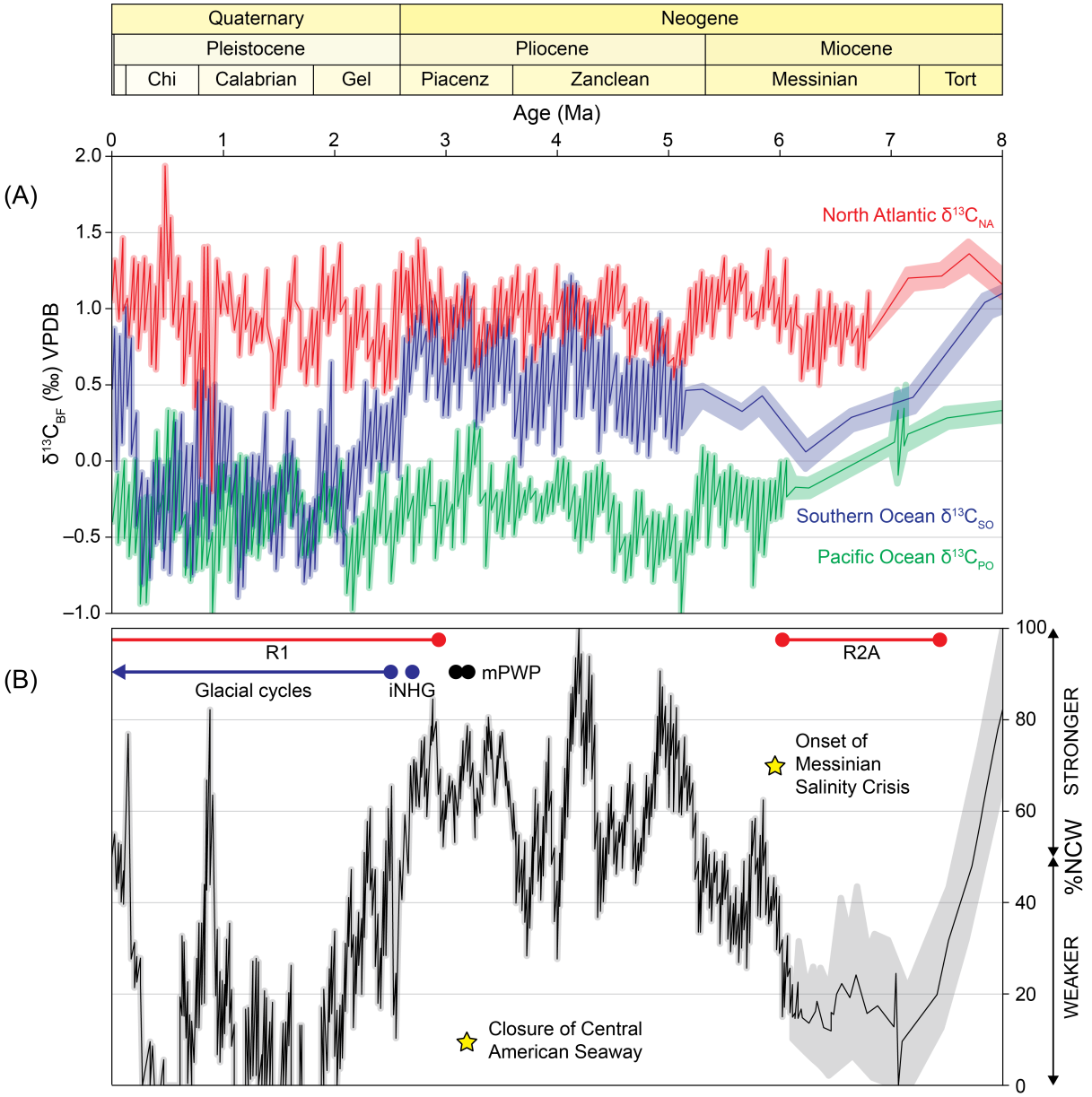


Figure 3.3. Global summary of compiled $\delta^{13}C_{BF}$ records and associated %NCW estimates for the 0−8 Ma interval. (A) Regression estimates for three sets of composite $\delta^{13}C_{BF}$ records. North Atlantic end member ($\delta^{13}C_{NA}$), red curve. Southern Ocean end member ($\delta^{13}C_{SO}$), blue curve. Pacific Ocean end member, green curve ($\delta^{13}C_{PO}$). ±2σ confidence bands for each block of data. (B) Estimated %NCW, black line. ±1σ grey confidence bands. Published records of V-shaped ridge (R1 etc.) formation (Jones et al., 2002), tectonic (Torsvik et al., 2002; Straume et al., 2020) and climatic events (Fronval and Jansen, 1996; De Schepper et al., 2013) are also shown. iNHG, intensification of the Northern Hemisphere Glaciation; mPWP, mid-Piacenzian Warm Period. Modified from Poore et al. (2006).

Site 563, ODP Site 925) in the North Atlantic which were considered sufficiently far north and at depths where benthic foraminifera are likely to be bathed by the North Atlantic end member.

However, all of these sites are located south of the GSR which is hypothesised to modulate southward deep-water migration and fluxes. This sampling strategy and characterisation of the $\delta^{13}C_{NA}$ end member is not necessarily informative of the character of deep-water masses north of the GSR, especially $\delta^{13}C$ variations in Nordic Seas deep-water, or directly representative of the extent of water mass exchange over the GSR. Rather, these NCW reconstructions reflect the contribution of North Atlantic deep-waters – characterised south of the GSR – to the global ocean. Consequently, there is significant scope to further develop our understanding of the long-term palaeoceanography of exchange over the GSR, especially the ventilation of major deep-water basins in the Nordic Seas, and their potential contributions to $\delta^{13}C$ variations in Atlantic deep-waters.

3.3 NE ATLANTIC AND NORDIC SEAS $\delta^{13}C_{BF}$ DATASETS

The $\delta^{13}C$ composition of the tests of calcifying benthic foraminifer are one of the most powerful proxies for reconstructing deep-water circulation patterns during the Neogene (Duplessy et al., 1984; Mackensen and Bickert, 1998; Mackensen, 2008). The test chemistry of epibenthic or shallow infaunal species reflects the $\delta^{13}C$ composition of the bottom water dissolved inorganic carbon ($\delta^{13}C_{DIC}$) reservoir (Duplessy et al., 1984; Mackensen, 2008). In the modern ocean, there are distinct differences in deep-water $\delta^{13}C_{DIC}$ between ocean basins, reflecting water-mass aging along deep-water flow pathways. Older deep-waters contain more regenerated, ^{13}C-depleted, organic material, with $\delta^{13}C_{DIC}$ closely following nutrient distributions in the modern deep ocean (Mackensen, 2008). In the Nordic Seas, the relatively young NADW has one of the most positive average $\delta^{13}C_{DIC}$ value of c. 1.2 ‰, whereas older North Pacific deep-water is in the region of −0.2 ‰ (Eide et al. 2017). Although $\delta^{13}C_{DIC}$ is a nonconservative tracer (susceptible to changing or being lost from the system), the short (c. ≤300 yrs) residence time of NADW (the time taken for the water to transit out of the deep Atlantic; Oppo and Curry, 2012) means it is possible to model $\delta^{13}C_{DIC}$ as a conservative tracer to quantify the mixing of deep-water masses (LeGrand and Wunsch, 1995).

Here we investigate the impact of GSR dynamic support on the strength of NCW overflow using the $\delta^{13}C_{DIC}$ signatures of regional water masses either side of the GSR since the late Miocene. These $\delta^{13}C_{DIC}$ patterns are reconstructed from a new compilation of all available $\delta^{13}C_{BF}$ records from ODP, DSDP and Integrated Ocean Drilling Program (IODP) sediment cores located in the NE Atlantic Ocean and Nordic Seas, a total of over 11,900 data points (Fig. 3.4; Table 3.1). Our compilation (Fig. 3.5) represents $\delta^{13}C_{DIC}$ trends from the late Neogene to present-day, including key intervals when %NCW is believed to have fluctuated in response to variations in GSR dynamic support (Poore et al., 2006). Age models for all sites were updated to the astronomically-tuned Neogene time scale (ATNTS) 2012 using the geomagnetic and biostratigraphic calibration points of Backman et al. (2012), Hilgen et al.

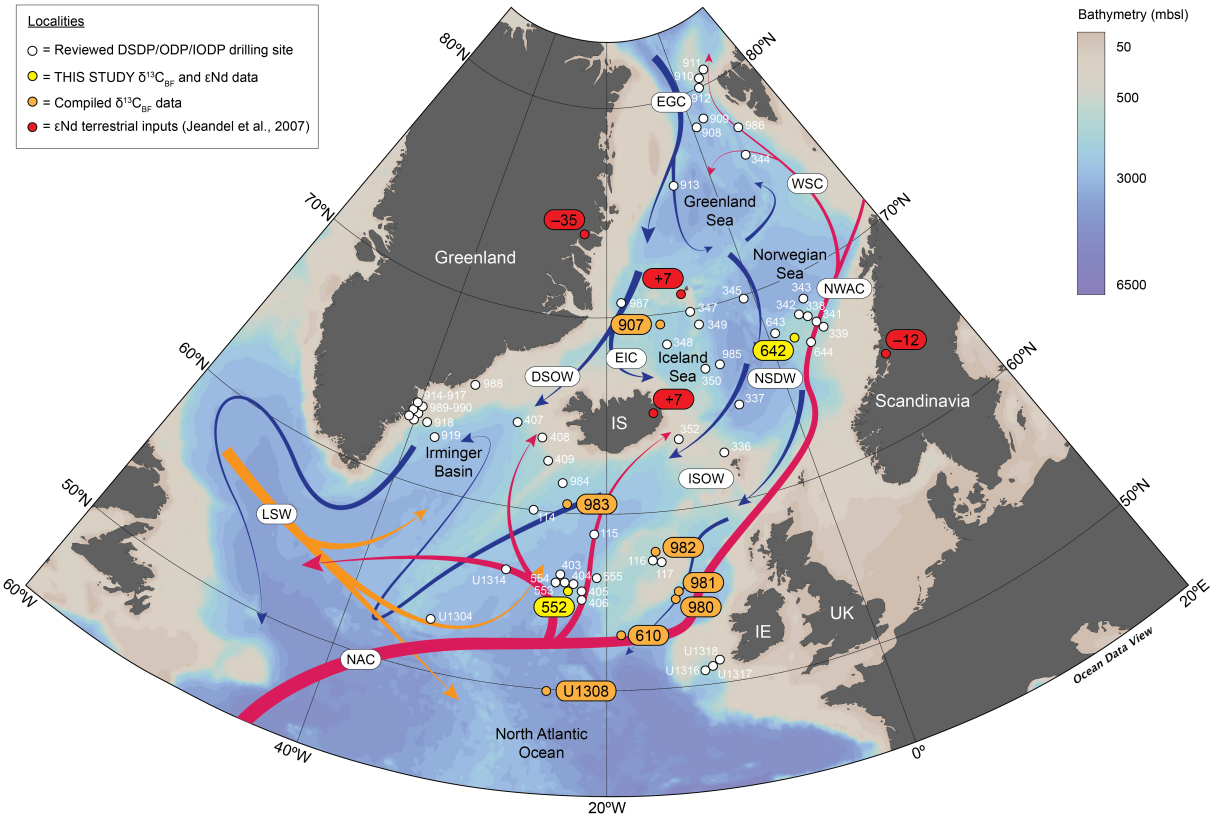


Figure 3.4. Location map of DSDP/ODP/IODP drilling sites reviewed in the NE Atlantic Ocean and Nordic Seas. Orange sites contain existing Pliocene $\delta^{13}C_{BF}$ records. Yellow sites indicate the origin of new $\delta^{13}C_{BF}$ and εNd records discussed in this study. Red markers highlight the average εNd composition of cratonic and volcanic rocks from Greenland, Iceland, Jan Mayen and Scandinavia. Oceanic currents are defined in Fig. 3.1. Bathymetric map created in Ocean Data View v.5.1.7.

(2012) and Wade et al. (2011). Poore et al. (2006) established similar age control using geomagnetic and biostratigraphic datums to correlate sites to the older ATNTS of Lourens et al. (2004).

The epibenthic species *Cibicidoides wuellerstorfi* predominates in our $\delta^{13}C_{BF}$ compilation (Fig. 3.5) and is considered a faithful recorder of deep-water $\delta^{13}C_{DIC}$ (Mackensen et al. 1993; Mackensen and Licari, 2003). Some studies (e.g. DSDP Site 610; Raymo, Hodell and Jansen, 1992) are multi-species *Cibicidoides spp.* $\delta^{13}C$ records (Table 3.1), and there is a potential that these are biased by species-specific offsets between *C. wuellerstorfi* and *C. kullenbergi*. These species $\delta^{13}C$ offsets are not necessarily constant through time and can be larger ($\Delta\delta^{13}C = -0.76 \pm 0.44$ ‰) during glacial conditions, although are likely to be less than the

primary signal caused by changing deep-water ventilation (Gottschalk et al., 2016). Records from the Nordic Seas (ODP Site 642 and ODP Site 907) are based on the infaunal species *Cassidulina teretis,* which we correct to *C. wuellerstorfi* using the $\delta^{13}C$ offset of +1.11 ‰ measured by Jansen et al. (1988), Poole (1994) and Dokken and Jansen (1999) in Holocene samples from the Norwegian Sea (Fig. 3.6).

Our compilation (Fig. 3.5) reveals a good distribution of $\delta^{13}C_{BF}$ records throughout the late Neogene to present-day in the NE Atlantic. The Holocene and Pleistocene Epochs contain approximately 78% of the available data, whereas the late Neogene has a more intermittent and lower-resolution record with data from only three sites (DSDP Site 552, ODP Site 642 and ODP Site 907). Only 6% of the $\delta^{13}C_{BF}$ data originates from sites north of the GSR (Fig. 3.7A), on the Icelandic (ODP Site 907) or Vøring Plateaus (ODP Site 642). The remaining 94% of data come from sites situated in the NE Atlantic (Fig. 3.7B), mainly on the Rockall Plateau (DSDP Site 552, ODP Site 982), Feni Drift (ODP Site 980, ODP Site 981, DSDP Site 610), Björn Drift (ODP Site 983) or on the upper-middle eastern flank of the MAR (IODP Site U1308). All of the $\delta^{13}C_{BF}$ records originate from sites which are situated well below 1 km water depth, with a maximum depth of 3871 m (IODP Site U1308). $\delta^{13}C_{BF}$ records from our seven southern sites show a relatively continuous distribution and extend from c. 7.4 Ma to present day. $\delta^{13}C_{BF}$ records from our two northern sites are more discontinuous, with large gaps present between approximately 7.4−6.2 Ma and 3.0−1.0 Ma where the cores are barren of foraminifera (Fronval and Jansen, 1996; Risebrobakken et al. 2016).

Table 3.1 (following page). Sources of $\delta^{13}C_{BF}$ records used in the NE Atlantic Ocean and Nordic Seas compilation. All primary age control points were updated to ATNTS 2012 using the calibration points of Backman et al. (2012), Hilgen et al. (2012) and Wade et al. (2011). Latitude and longitude in decimal degrees (DD).

Site	Lat (DD)	Long (DD)	Data source	Species	Age model source	Interval, Ma	No. of data points
U1308	49.885°N	24.241°W	Hodell and Channell (2016)	*Cibicidoides spp.*	Flesche Kleiven et al. (2002)	0.190–3.143	6877
610	53.299°N	18.942°W	Raymo, Hodell and Jansen (1992)	*Cibicidoides spp.*	Berggren et al. (1985)	2.227–3.480	337
			Hennissen et al. (2014)	*Cibicidoides wuellerstorfi*	De Schepper and Head (2008)	2.565–2.782	66
			Keigwin, Aubry and Kent (1987)	*Cibicidoides wuellerstorfi*	Lazarus et al. (1995)	6.604–7.975	108
980	55.507°N	14.737°W	McManus et al. (1999)	*Cibicidoides wuellerstorfi*	Channell and Lehman (1999)	0.000–0.339	326
			Flower et al. (2000)	*Cibicidoides wuellerstorfi*	Channell and Lehman (1999)	0.501–1.003	581
			Wright and Flower (2002)	*Cibicidoides wuellerstorfi*	Channell and Lehman (1999)	0.515–0.992	607
			Oppo et al. (2006)	*Cibicidoides wuellerstorfi*	Oppo et al. (2006)	0.005–0.191	368
981	55.641°N	14.664°W	McIntyre et al. (1999)	*Cibicidoides wuellerstorfi*	McIntyre et al. (1999)	1.404–1.929	220
552	56.048°N	23.241°W	Keigwin (1984)	*Cibicidoides wuellerstorfi*	Lazarus et al. (1995)	3.614–5.837	40
			Keigwin (1987)	*Cibicidoides wuellerstorfi*	Lazarus et al. (1995)	5.492–5.582	42
			Keigwin, Aubry and Kent (1987)	*Cibicidoides wuellerstorfi*	Lazarus et al. (1995)	4.718–5.951	426
			Raymo, Hodell and Jansen (1992)	*Cibicidoides spp.*	Berggren et al. (1985)	2.004–3.519	136
			Curry and Miller (1989)	*Cibicidoides spp.*	Curry and Miller (1989)	2.022–2.928	95
			Shackleton and Hall (1984)	*Cibicidoides wuellerstorfi*	Lazarus et al. (1995)	0.005–3.449	344
982	57.775°N	15.866°W	Venz et al. (1999)	*Cibicidoides spp.*	Venz and Hodell (1999)	0.000–1.002	430
983	60.455°N	23.754°W	McIntyre et al. (1999)	*Cibicidoides wuellerstorfi*	McIntyre et al. (1999)	1.390–1.965	240
907	69.508°N	12.931°W	Fronval & Jansen (1996)	*Cibicidoides wuellerstorfi*	Bleil (1989)	0.000–7.376	157
642	67.218°N	2.9186°E	Risebrobakken et al. (2016)	*Cassidulina teretis*	Bleil (1989); Risebrobakken et al. (2016)	3.129–5.044	562

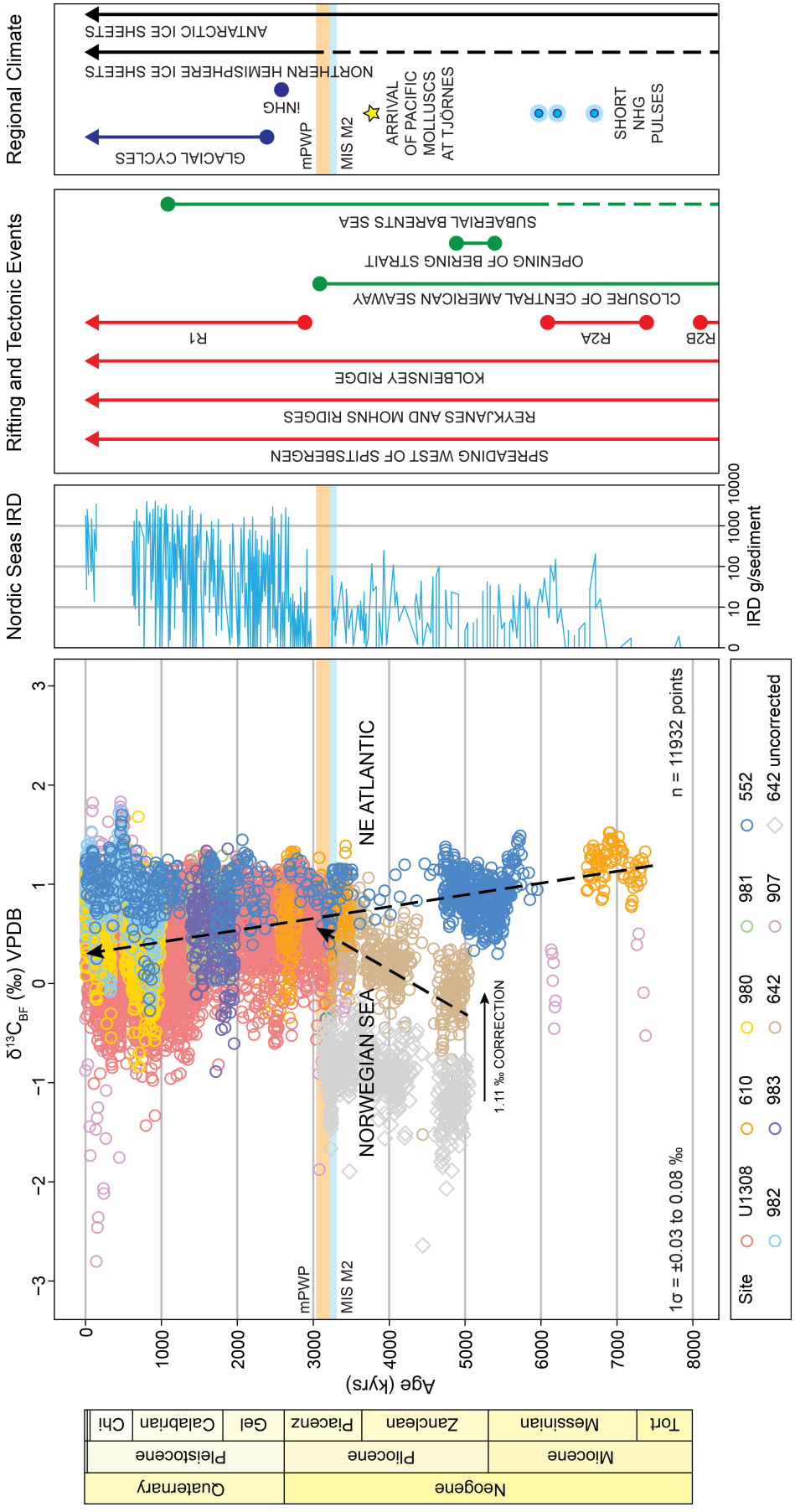

Regional Climate
ANTARCTIC ICE SHEETS
NORTHERN HEMISPHERE ICE SHEETS
iNHG
GLACIAL CYCLES
mPWP
MIS M2
ARRIVAL OF PACIFIC MOLLUSCS AT TJÖRNES
SHORT NHG PULSES
Rifting and Tectonic Events
SPREADING WEST OF SPITSBERGEN
REYKJANES AND MOHNS RIDGES
KOLBEINSEY RIDGE
R1
R2A
R2B
CLOSURE OF CENTRAL AMERICAN SEAWAY
OPENING OF BERING STRAIT
SUBAERIAL BARENTS SEA
Nordic Seas IRD
0
10
100
1000
10000
IRD g/sediment
δ13CBF (‰) VPDB
−3
−2
−1
0
1
2
3
NE ATLANTIC
NORWEGIAN SEA
1.11 ‰ CORRECTION
n = 11932 points
1σ = ±0.03 to 0.08 ‰
mPWP
MIS M2
Site
U1308
982
610
983
980
642
981
907
552
642 uncorrected
0
1000
2000
3000
4000
5000
6000
7000
8000
Age (kyrs)
Neogene
Quaternary
Miocene
Pliocene
Pleistocene
Tort
Messinian
Zanclean
Piacenz
Gel
Calabrian
Chi

Figure 3.5 (previous page). Compilation of NE Atlantic and Nordic Seas $\delta^{13}C_{BF}$ records for the 0–8000 kyr interval. Composite data are colour-coded based on DSDP/ODP/IODP site, shown in Fig. 3.4. The NSDWs are on average c. 0.6 ‰ isotopically lighter compared to the NE Atlantic during the Pliocene. Published records of ice-rafted debris (IRD; Fronval and Jansen, 1996), rifting (Doré and Lundin, 1996), V-shaped ridge (R1 etc.) formation (Jones et al., 2002), and climatic events (De Schepper et al., 2013) are also shown. Blue and orange bars denote Marine Isotope Stage (MIS) M2 and the mid-Piacenzian Warm Period (mPWP). iNHG, intensification of the Northern Hemisphere Glaciation.

$\delta^{13}C_{BF}$ values in the Holocene and Pleistocene fluctuate rapidly, from −1.37 ‰ to 1.87 ‰, reflecting circulation changes across high-amplitude glacial-interglacial cycles. Mean $\delta^{13}C_{BF}$ values are 0.59 ‰ in the late Pleistocene and Holocene (0.773–0 Ma), and 0.54 ‰ during the early Pleistocene (2.58–0.773 Ma) across all sites. In the Pliocene, a significant spatial differential develops between $\delta^{13}C_{BF}$ records from the Nordic Seas and the NE Atlantic. The

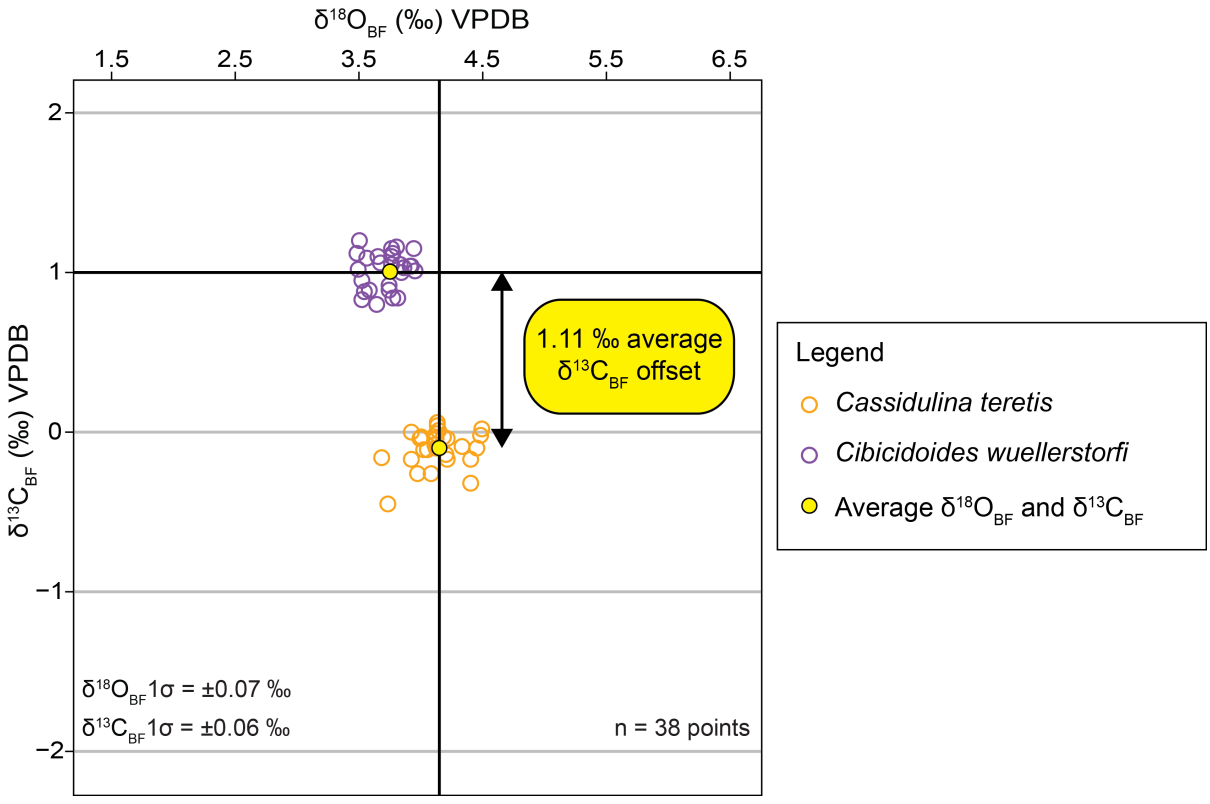


Figure 3.6. Stable isotope fractionation of *C. teretis* versus *C. wuellerstorfi*. Points are measurements from Recent samples in the Norwegian Sea, which indicate an average $\delta^{13}C_{BF}$ offset of 1.11 ‰ between these two benthic species (Jansen et al., 1988; Poole, 1994; Dokken and Jansen, 1999).

$\delta^{13}C_{BF}$ from the NE Atlantic sites (Fig. 3.7B) is relatively stable matching the $\delta^{13}C_{NA}$ end member defined by Poore et al. (2006) with an average value of 0.77 ‰, a maximum of 1.43 ‰ and a minimum of −0.74 ‰, whereas the average $\delta^{13}C$ signature in the deep-waters of the Nordic Seas is 0.55 ‰ lighter, with data ranging between −1.46 ‰ to 1.2 ‰ (corrected for vital effects; Fig. 3.6). The isotopically light Nordic Seas appear similar in composition to the $\delta^{13}C_{SO}$ and $\delta^{13}C_{PO}$ end members defined by Poore et al. (2006). The Pliocene Nordic Seas $\delta^{13}C_{BF}$ record (Fig. 3.7A) is exclusively derived from ODP Site 642 but is relatively short, only spanning c. 3.13 to 5.04 Ma (Risebrobakken et al. 2016). Towards 3 Ma the Nordic Seas $\delta^{13}C_{BF}$ trends to the more isotopically heavy values of the NE Atlantic, but the lack of records after 3 Ma, prevents the determination of whether or when convergence occurs.

Late Pleistocene $\delta^{13}C_{BF}$ records from ODP Site 907 (Table 3.1; Fig. 3.7A) match the magnitude of isotopic fluctuations observed at sites south of the GSR, suggesting the deep-water either side of the GSR had similar characteristics by c. 0.8 Ma. The oldest $\delta^{13}C_{BF}$ records are also from ODP Site 907 at around 6.2 Ma and 7.4 Ma, with an average value of 0.28 ‰ and 0.12 ‰, respectively. These values suggest that the relative isotopically light signature observed in the Nordic Seas during the Pliocene extends into the late Miocene for locations north of the GSR. At DSDP Site 610 in the NE Atlantic, $\delta^{13}C_{BF}$ records remain isotopically heavy between 6.6 and 7.3 Ma, with an average value of 1.00 ‰.

Importantly, the more negative $\delta^{13}C$ values in the NSDWs during the Pliocene (Fig. 3.5), compared to the isotopically heavier NE Atlantic, do not easily fit with our current temporal understanding of variations in GSR dynamic support and the hypothesised knock-on modulation of overflowing NCW (Fig. 3.3) (Wright and Miller, 1996; Poore et al. 2006). Instead, our compilation suggests that Nordic deep-waters were poorly ventilated and isolated from surface replenishment during the early to mid-Pliocene (5.04−3.13 Ma). These findings apparently contradict studies which suggest the GSR was up to 300 m lower during this interval (Robinson et al. 2011), resulting in greater exchange between the Nordic Seas and NE Atlantic, and a relative intensification of regional overturning circulation (Poore et al. 2006).

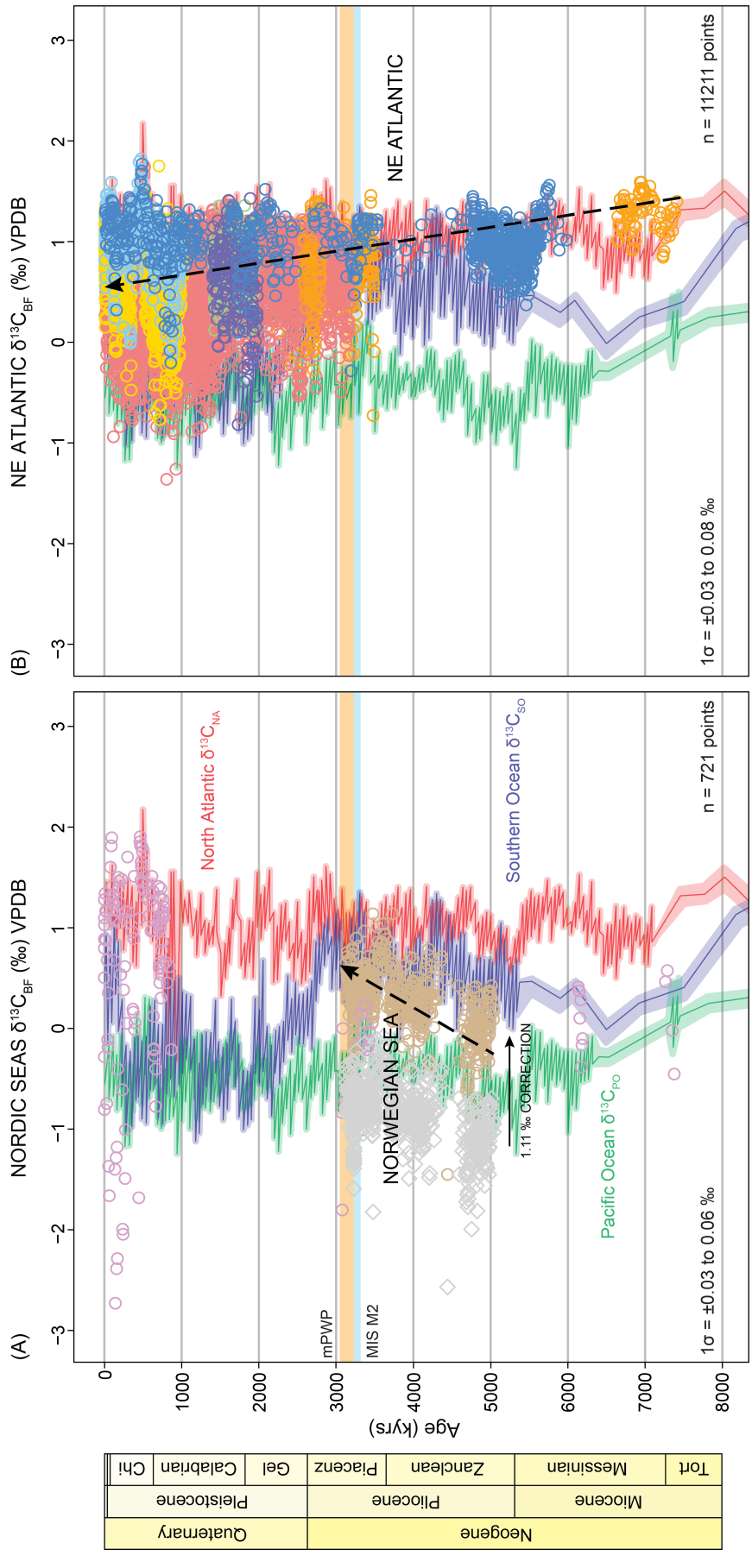

(A)
NORDIC SEAS $\delta^{13}C_{BF}$ (‰) VPDB
(B)
NE ATLANTIC $\delta^{13}C_{BF}$ (‰) VPDB
NE ATLANTIC
NORWEGIAN SEA
North Atlantic $\delta^{13}C_{NA}$
Southern Ocean $\delta^{13}C_{SO}$
Pacific Ocean $\delta^{13}C_{PO}$
1.11 ‰ CORRECTION
mPWP
MIS M2
n = 721 points
n = 11211 points
1σ = ±0.03 to 0.06 ‰
1σ = ±0.03 to 0.08 ‰
Age (kyrs)
Neogene
Quaternary
Miocene
Pliocene
Pleistocene
Tort
Messinian
Zanclean
Piacenz
Gel
Calabrian
Chi

Figure 3.7 (previous page). Deconstructed regional compilations of $\delta^{13}C_{BF}$ records for the 0−8000 kyr interval. (A) Records from the Nordic Seas. (B) Records from the NE Atlantic Ocean. Over 93% of the compiled $\delta^{13}C_{BF}$ data originates from the NE Atlantic Ocean. Colour-coded points and bars are as in Fig. 3.5. Regional end-member regression curves are described in Fig. 3.3.

Consequently, these inconsistencies in our understanding of Nordic Seas deep-water and its interactions with variations in mantle-induced dynamic support, accentuates the need to further understand the palaeoceanography of the Nordic Seas during the Pliocene. Here, new low-resolution $\delta^{13}C_{BF}$ and εNd records provide an opportunity to verify and re-examine our $\delta^{13}C_{BF}$ compilation, determine the evolution of Nordic Seas deep-water and ultimately assess the long-term controls on the ventilation of the Norwegian Sea. Using our new datasets we will test the following questions:

1. Is the observed negative $\delta^{13}C_{BF}$ signature in the Norwegian Sea during the early to mid-Pliocene caused by weakened ventilation in this region?
2. Is the observed positive $\delta^{13}C_{BF}$ shift in the Norwegian Sea during the late Pliocene, relative to the early to mid-Pliocene, associated with renewed ventilation, and does this result in deep-waters which are characteristically similar to the NE Atlantic?
3. Do variations in the dynamic support of the GSR control the ventilation of Nordic deep-waters during the late Neogene?
4. Do independent water mass tracers support interpretations of $\delta^{13}C_{BF}$? To what extent do Pliocene Nordic Seas $\delta^{13}C_{BF}$ records reflect water mass exchange, and to what extent might they be driven by regional biogeochemistry?

3.4 MATERIAL, AGE MODEL AND METHODS

65 IODP, DSDP and ODP sites across the NE Atlantic and the Nordic Seas, ranging in latitude from the Yermak Plateau northwest of Svalbard at 80.596°N to the eastern flank of the MAR at 49.855°N, were reviewed (Fig. 3.8) to determine which sites feature continuous or good recovery throughout the late Neogene and Quaternary, with argillaceous and carbonate lithologies deemed favourable for foraminifera preservation, and moderate to high (>2 cm/kyr) pelagic sedimentation rates, allowing for a high temporal resolution. It was important to identify a range of sites both north and south of the GSR at water depths below 1 km, to help spatially characterise the regional deep-waters (Fig. 3.8) and to fill key gaps in our $\delta^{13}C_{BF}$ compilation. Two sites were selected using these criteria, ODP Site 642 situated in the Nordic Seas, and DSDP Site 552 located in the NE Atlantic.

ODP Site 642 (Fig. 3.1) was drilled during ODP Leg 104, on the Vøring Plateau c. 450 km west of Norway in the Nordic Seas (67.218°N, 2.9186°E), at a water depth of 1286 m (Fig. 3.8). ODP Site 642 was selected as this is the only location where foraminifera bathe in NSDW, are well-preserved and are relatively continuous throughout the Pliocene in this region (Fig. 3.8); other Nordic Seas ODP sites (907 and 643) are barren of foraminifera during this interval due to dissolution (Fronval and Jansen, 1996), and records from ODP Site 644 only span the last 3 Ma (Eldholm et al. 1989). Here we focus on ODP Hole 642B, which extends back to the late Miocene and features high recovery (97.5%). ODP Hole 642B features a well-documented hiatus (c. 0.5 myrs) at c. 66.40 m below seafloor (mbsf), where parts of the late Pliocene Gauss polarity chron are missing (Bleil, 1989). The age model for ODP Hole 642B recognises this hiatus and is based on the magnetostratigraphy of Bleil (1989), updated to the ATNTS (Hilgen et al. 2012). DSDP Site 552 (Fig. 3.1) was drilled during DSDP Leg 81, on the western flank of the Rockall Plateau c. 860 km west of Ireland in the NE Atlantic (56.048°N, 23.241°W), at a water depth of 2301 m (Fig. 3.8). DSDP Site 552 was selected as it is believed to bathe in ISOW, is known to contain well-preserved foraminifera throughout the late Neogene and Quaternary (Keigwin, 1984; Raymo, Hodell and Jansen, 1992), and has no documented

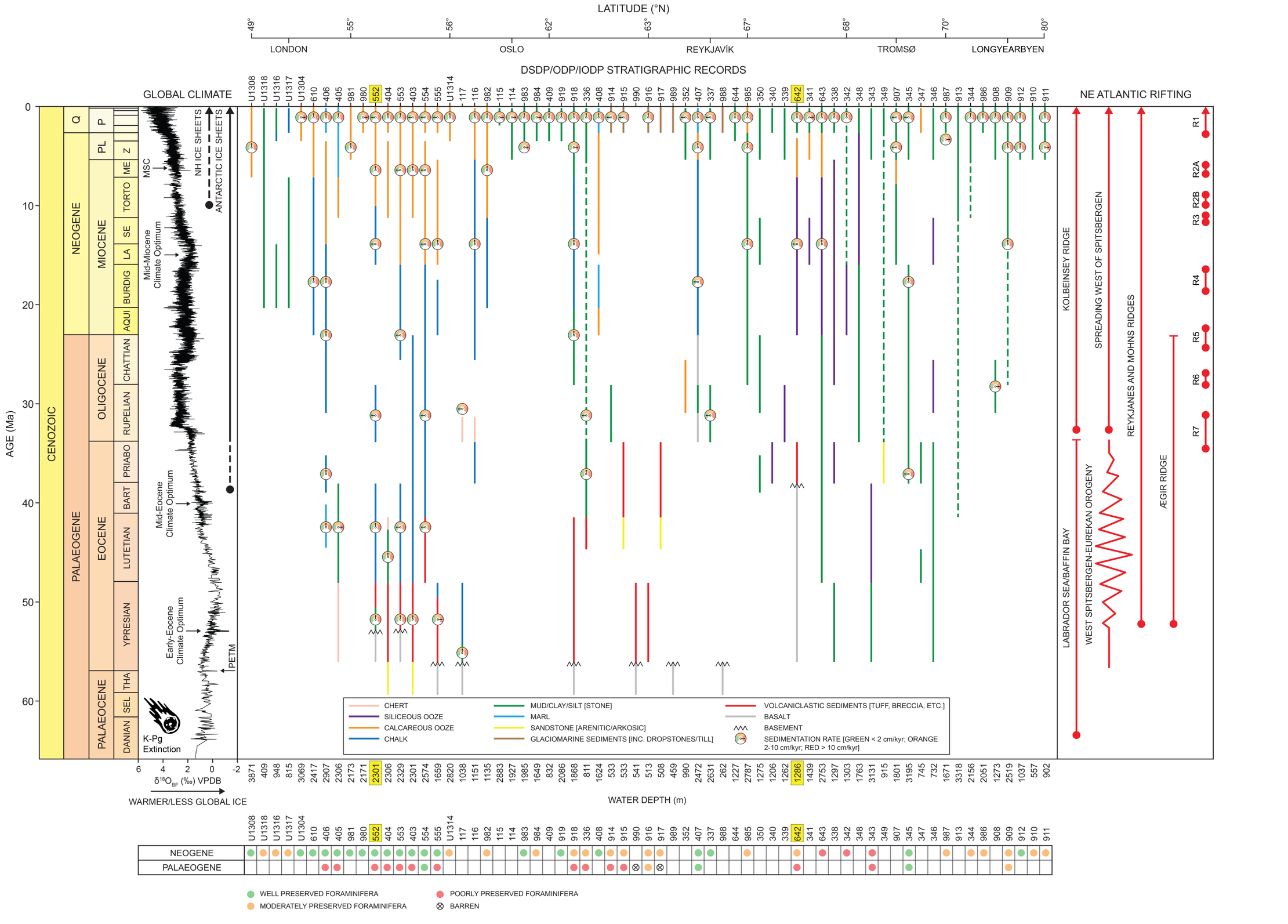

LATITUDE (°N)
49°
55°
56°
62°
63°
67°
68°
70°
80°
LONDON
OSLO
REYKJAVÍK
TROMSØ
LONGYEARBYEN
DSDP/ODP/IODP STRATIGRAPHIC RECORDS
U1308 U1318 U1316 U1317 U1304 610 406 405 981 980 552 404 553 403 554 555 U1314 117 116 982 115 114 983 984 409 919 918 336 408 914 915 990 916 917 989 352 407 337 988 644 985 350 340 339 642 341 643 338 342 348 343 349 907 345 347 346 987 913 344 986 908 909 912 910 911
GLOBAL CLIMATE
NH ICE SHEETS
ANTARCTIC ICE SHEETS
MSC
Mid-Miocene Climate Optimum
Mid-Eocene Climate Optimum
Early-Eocene Climate Optimum
PETM
K-Pg Extinction
NE ATLANTIC RIFTING
KOLBEINSEY RIDGE
SPREADING WEST OF SPITSBERGEN
REYKJANES AND MOHNS RIDGES
ÆGIR RIDGE
LABRADOR SEA/BAFFIN BAY
WEST SPITSBERGEN-EUREKAN OROGENY
R1
R2A
R2B
R3
R4
R5
R6
R7
AGE (Ma)
CENOZOIC
PALAEOGENE
NEOGENE
Q
P
PL
Z
MIOCENE
ME
TORTO
LA
SE
BURDIG
AQUI
OLIGOCENE
CHATTIAN
RUPELIAN
EOCENE
PRIABO
BART
LUTETIAN
YPRESIAN
PALAEOCENE
THA
SEL
DANIAN
0
10
20
30
40
50
60
CHERT
SILICEOUS OOZE
CALCAREOUS OOZE
CHALK
MUD/CLAY/SILT [STONE]
MARL
SANDSTONE [ARENITIC/ARKOSIC]
GLACIOMARINE SEDIMENTS [INC. DROPSTONES/TILL]
VOLCANICLASTIC SEDIMENTS [TUFF, BRECCIA, ETC.]
BASALT
BASEMENT
SEDIMENTATION RATE [GREEN < 2 cm/kyr; ORANGE 2-10 cm/kyr; RED > 10 cm/kyr]
6 4 2 0 -2
δ18OBF (‰) VPDB
WARMER/LESS GLOBAL ICE
3871 409 948 815 3069 2417 2907 2306 2173 2171 2301 2306 2329 2301 2574 1659 2820 1038 1151 1135 2883 1927 1985 1649 832 2086 1868 811 1624 533 533 541 513 508 459 990 2472 2631 262 1227 2787 1275 1206 1262 1286 1439 2753 1297 1303 1763 3131 915 1801 3195 745 732 1671 3318 2156 2051 1273 2519 1037 557 902
WATER DEPTH (m)
U1308 U1318 U1316 U1317 U1304 610 406 405 981 980 552 404 553 403 554 555 U1314 117 116 982 115 114 983 984 409 919 918 336 408 914 915 990 916 917 989 352 407 337 988 644 985 350 340 339 642 341 643 338 342 348 343 349 907 345 347 346 987 913 344 986 908 909 912 910 911
NEOGENE
PALAEOGENE
WELL PRESERVED FORAMINIFERA
MODERATELY PRESERVED FORAMINIFERA
POORLY PRESERVED FORAMINIFERA
BARREN

Figure 3.8 (previous page). Stratigraphic summary of the NE Atlantic Ocean and Nordic Seas DSDP/ODP/IODP drilling sites. Colour-coded intervals relate to stratigraphic relationships, sediment recovery and lithology at each site. Sedimentation rate is summarised by speedometers where known. Water depth and foraminifera preservation are shown for each site. Sites highlighted yellow indicate the origin of new $\delta^{13}C_{BF}$ and εNd records discussed in this study. Published chronostratigraphy (Gradstein et al., 2012), records of $\delta^{18}O$ in benthic foraminifera ($\delta^{18}O_{BF}$) (Zachos et al., 2001), NE Atlantic rifting (Doré and Lundin, 1996) and V-shaped ridge (R1 etc.) formation (Jones et al., 2002) are also shown. PETM, Palaeocene-Eocene Thermal Maximum; MSC, Messinian salinity crisis.

hiatuses during this interval (Fig. 3.8). Here we focus on DSDP Hole 552A, which extends back to the middle Eocene and features high recovery (99.7%). The age model for DSDP Hole 552A is based on the magnetostratigraphy of Lazarus et al. (1995), updated to the ATNTS (Hilgen et al. 2012).

To improve the representation of $\delta^{13}C_{BF}$ through the Pliocene, both cores were sampled at the IODP Bremen Core Repository at low-resolution (one sample per c. 150−250 kyrs) through the core sections deemed likely to yield favourable benthic foraminifera abundances and preservation. 40 samples were selected from ODP Hole 642B core sections 2H-1 through 12H-5, between 5.77 and 102.29 mbsf (c. 0.12 to 7.32 Ma). 32 samples were selected from DSDP Hole 552A core sections 1H-3 through 34H-3, between 3.93 and 162.80 mbsf (c. 0.20 and 5.85 Ma). An additional 16 bulk sediment samples were selected at an even lower resolution (one sample per c. 500 kyrs) from the same cores for the analysis of Nd isotopes. Nine samples were selected from ODP Hole 642B core sections 8H-5 through 10H-5, between 63.47 and 82.80 mbsf (c. 2.50 and 6.50 Ma). Seven samples were selected from DSDP Hole 552A core sections 9H-2 through 31H-1, between 41.87 and 144.08 mbsf (c. 2.50 and 5.50 Ma).

The 72 core samples selected for $\delta^{13}C_{BF}$ analysis, each comprising c. 20 cc of sediment, were weighed and washed-down over a >63 μm sieve with Milli-Q® deionised water until this ran clear, with the coarse foraminifera residues retained (Appendix A.1). Where samples did not fully disaggregate with water washing, the semi-disaggregated residues were boiled with the water softener Calgon® to aid sediment breakdown, before being rinsed again. The >63 μm

residues were dried overnight at 40°C and then sieved into size fractions. All specimens for isotope analysis were picked from the 250–355 μm fraction to limit the possible effects of ontogenetic change in isotope fractionation rates. *C. wuellerstorfi* and *C. teretis*, the conventional species utilised in our $\delta^{13}C_{BF}$ compilation, were dry picked under a binocular microscope and transferred into a cardboard reference slide for each sample. Six samples from ODP Hole 642B and 29 samples from DSDP Hole 552A contained benthic foraminifera; the remaining 37 samples were barren. The $\delta^{13}C$ measurements were undertaken on 1−55 specimens of *C. wuellerstorfi* and 1−12 specimens of *C. teretis*. Of the 35 measurements undertaken for this study, only three were analysed on single specimens (DSDP Hole 552A, ID: 2 and 24; ODP Hole 642B, ID: 27). The $\delta^{13}C$ measurements were carried out at the NERC Isotope Geosciences Laboratory (NIGL), British Geological Survey (Keyworth, UK) using an IsoPrime 100 dual-inlet mass spectrometer with Multiprep device. Isotope values were calculated according to the Vienna Pee Dee Belemnite (VPDB) scale in parts per thousand using a within-run internal laboratory standard (KCM), which is routinely calibrated to NBS-19 carbonate reference material. Analytical reproducibility for $\delta^{13}C$ of the calcite standard was 0.04 ‰ (1σ). Both species were also mounted on stubs and imaged using the PhenomPro X Desktop SEM at the University of Birmingham to confirm species identification; after being photographed, the same tests were removed from the stub, gently broken between two glass slides, remounted and imaged for investigation of the internal surfaces and test walls in cross section.

Neodymium isotope analyses were undertaken on dissolved authigenic ferromanganese (Fe-Mn) oxyhydroxide coatings from the 16 additional core samples (Appendix A.2). In each case, c. 2 g of bulk sediment was leached on a rotator for 15−20 minutes in 0.05 mol/L hydroxylamine hydrochloride (HH) and 2.6 mol/L acetic acid following the method of Blaser et al. (2016). This leaching method attacks the hydrogenetic Fe-Mn oxyhydroxide phase in the bulk sediments. The Fe-Mn oxyhydroxides precipitate on to sediment particles from seawater and incorporate many dissolved trace elements (e.g. Nd, Pb), whose isotopic signatures reflect the palaeo-seawater composition and oceanographic conditions at the time of accretion (Blaser et al.,

2016). These leachates were centrifuged twice, once at 5000 revolutions per minute (rpm) for at least 10 minutes, and then again at 6000 rpm for at least 20 minutes, until complete settlement of the suspended particles occurred, after which the supernatant was carefully decanted. These samples were then purified by column chromatography before isotopic measurement. The Rare Earth Element (REE) fractions were isolated from the Fe-Mn leachates using Eichron TRUspec™ resin (100−150 μm mesh). Nd was then separated from the REE fractions using Eichron LNspec™ resin (50−100 μm mesh) and volumetrically calibrated Teflon columns. Nd isotope ratios were measured using a high-sensitivity set-up in the Department of Earth Sciences, University of Cambridge, which included an Aridus II desolvating nebulizer system fed with nitrogen to minimise oxide formation, and a Thermo Fisher Neptune Plus™ multi-collector inductively coupled plasma mass spectrometer (MC-ICPMS), equipped with Jet cones (sampler Jet cone and X skimmer cone). Mass dependant fractionation effects were corrected for by normalising $^{146}Nd/^{144}Nd$ to 0.7219 and applying an exponential correction. The samples were measured across 30 separate analysis cycles, each lasting 8 seconds, to generate an average $^{143}Nd/^{144}Nd$ ratio for every sample; these samples were bracketed with analyses of the JNdi-1 Nd isotopic standard at a concentration similar to that of the sample, and corrected to a value of 0.512115 ± 7, reported by Tanaka et al. (2000). During this study, repeated measurements of JNdi-1 standards had an average $^{143}Nd/^{144}Nd$ ratio of 0.51152374 and the average reproducibility of JNdi-1 was ±0.000015 (2σ) on $^{143}Nd/^{144}Nd$, corresponding to ±0.25 (2σ) εNd external reproducibility. Nd isotope measurements are reported as Eq. 3.2, where $(^{143}Nd/^{144}Nd)_{CHUR}$ = 0.512638 denotes the 'Chondritic Uniform Reservoir' (Jacobsen and Wasserburg, 1980).

$$\varepsilon\mathrm{Nd} = \left(\left[\frac{\left(^{143}Nd/^{144}Nd_{\mathrm{Sample}}\right)}{\left(^{143}Nd/^{144}Nd_{\mathrm{CHUR}}\right)}\right] - 1\right) \times 10000$$

Equation 3.2. Epsilon notation used to express the isotopic composition of neodymium.

3.5 RESULTS

Overall, our $\delta^{13}C_{BF}$ results (Fig. 3.9A-B) reaffirm the isotopic trends observed in previous studies at both study sites, with deep-waters in the Norwegian Sea being significantly isotopically lighter than in the NE Atlantic during the Pliocene (Fig. 3.5; Table 3.1). At DSDP Site 552 (Fig. 3.1), the *C. wuellerstorfi* $\delta^{13}C_{BF}$ have an average value of 1.01 ‰ throughout the Pliocene, with a maximum value of 1.39 ‰ and a minimum value of 0.58 ‰. During the early Pleistocene, the *C. wuellerstorfi* $\delta^{13}C_{BF}$ have an average value of 0.79 ‰, with a maximum value of 1.37 ‰ and a minimum value of 0.00 ‰. The average $\delta^{13}C_{BF}$ in the late-Pleistocene and Holocene is the same as during the early Pleistocene, with a maximum value of 1.00 ‰ and a minimum value of 0.65 ‰. At ODP Site 642 (Fig. 3.1) *C. teretis* $\delta^{13}C_{BF}$, corrected for vital effects (Fig. 3.6), have an average value of −0.04 ‰ between 4.16 and 5.49 Ma, which is 1.05 ‰ lighter compared to the contemporaneous measurements from DSDP Site 552. The maximum $\delta^{13}C_{BF}$ value at ODP Site 642 is 0.11 ‰ and the minimum value is −0.26 ‰. There is a clear difference in the $\delta^{13}C$ composition of the Nordic (Norwegian Sea) and NE Atlantic deep-waters during the Pliocene, with the former up to 1.65 ‰ lighter (Fig. 3.9A).

Our authigenic Nd record (Fig. 3.10) also supports significant variations in the composition of NE Atlantic and Norwegian Sea deep-waters throughout the Pliocene; our seven Nd results from DSDP Hole 552A are relatively less radiogenic, compared to the nine measurements from ODP Hole 642B during this interval. At DSDP Site 552 (Fig. 3.1), the Nd isotopic composition of the leachate samples is relatively stable between 5.5 and 3.0 Ma, with an average value of −10.8 εNd units; the Nd signature is lowest around 5 Ma, reaching −11.3 εNd, before gradually increasing by +1.0 εNd units until 3 Ma. The largest change occurs between 3.0 and 2.5 Ma, where εNd becomes rapidly more radiogenic, increasing from −10.3 to −8.3. At ODP Site 642 (Fig. 3.1), the εNd record from our contemporaneous leachates is more varied. The εNd signal is very unradiogenic during the late Miocene (6.5 Ma), reaching −12.3, but becomes significantly more radiogenic, increasing by +4.7 εNd units, between

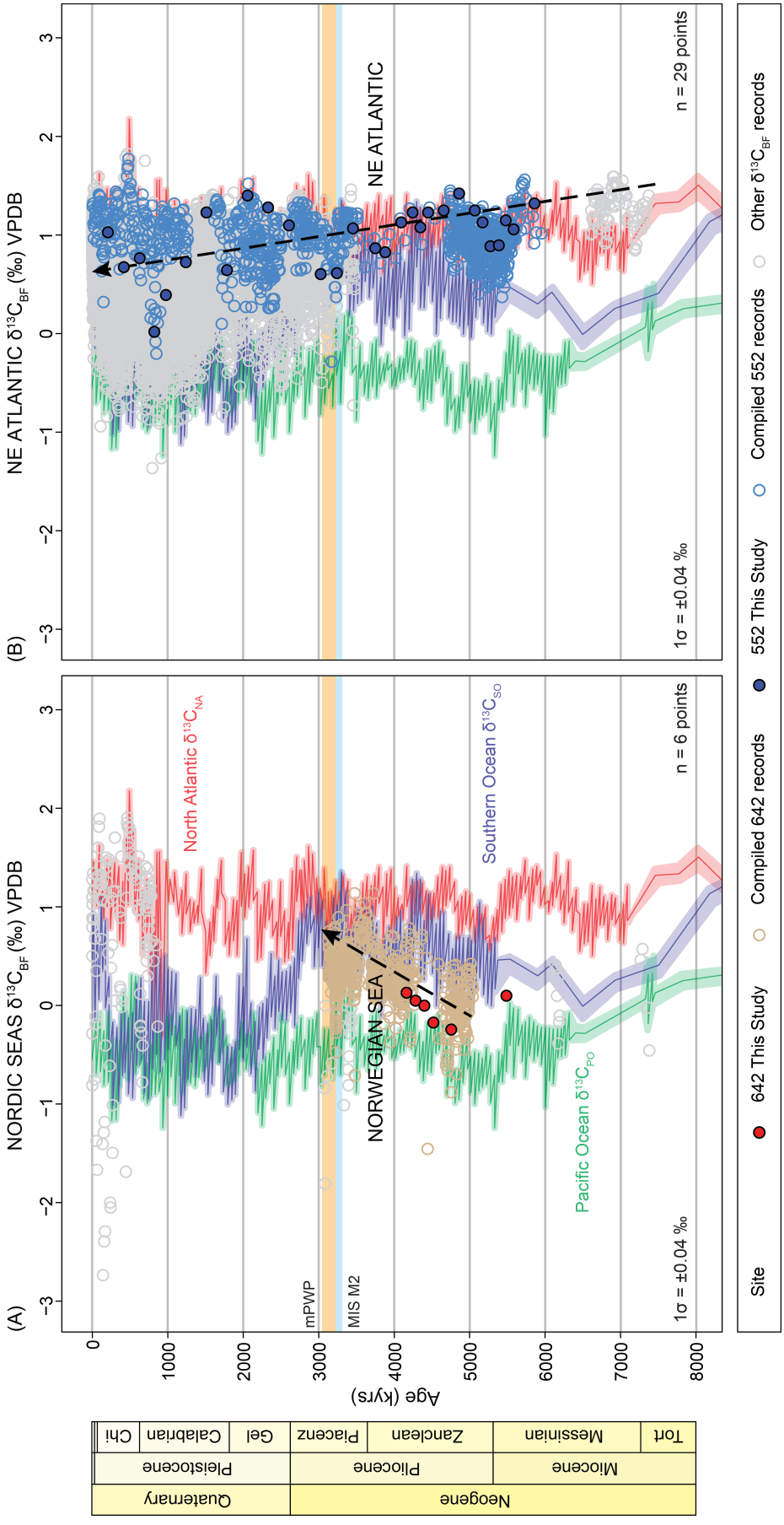
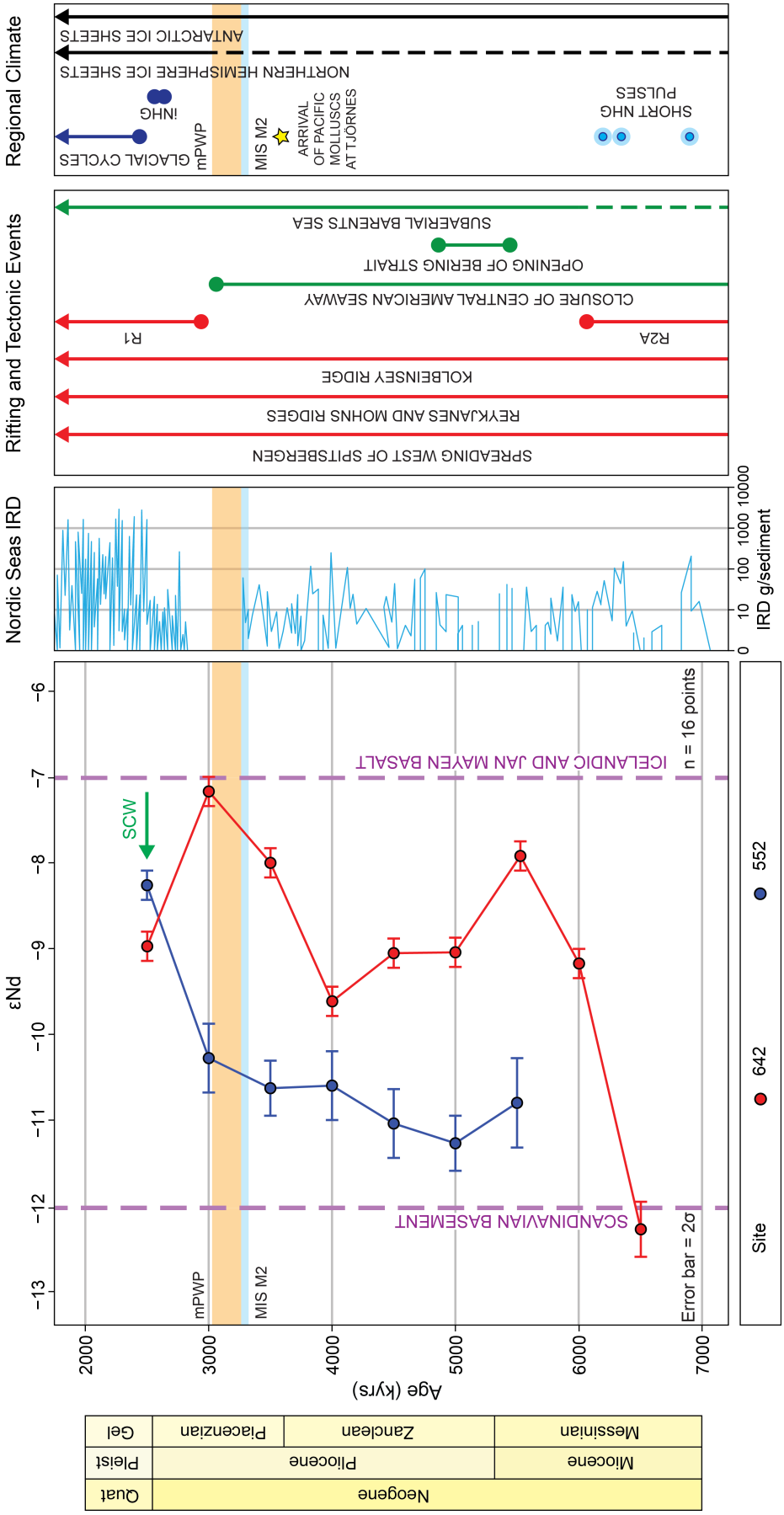

(A)
NORDIC SEAS $\delta^{13}C_{BF}$ (‰) VPDB
(B)
NE ATLANTIC $\delta^{13}C_{BF}$ (‰) VPDB
NE ATLANTIC
NORWEGIAN SEA
North Atlantic $\delta^{13}C_{NA}$
Southern Ocean $\delta^{13}C_{SO}$
Pacific Ocean $\delta^{13}C_{PO}$
mPWP
MIS M2
n = 6 points
n = 29 points
1σ = ±0.04 ‰
1σ = ±0.04 ‰
Age (kyrs)
Site
642 This Study
Compiled 642 records
552 This Study
Compiled 552 records
Other $\delta^{13}C_{BF}$ records
Neogene
Quaternary
Miocene
Pliocene
Pleistocene
Tort
Messinian
Zanclean
Piacenz
Gel
Calabrian
Chi

Figure 3.9 (previous page). $\delta^{13}C_{BF}$ results from ODP Hole 642B and DSDP Hole 552A (solid circles) plotted against compiled records from the same sites (coloured hollow circles), and the wider NE Atlantic and Nordic Seas (grey hollow circles) for the 0−8000 kyr interval (Table 3.1). (A) ODP Hole 642B results are determined from *C. teretis* and are corrected by 1.11 ‰ for vital effects. (B) DSDP Hole 552A data are determined exclusively from *C. wuellerstorfi* and require no $\delta^{13}C_{BF}$ correction. Regional end-member regression curves are described in Fig. 3.3. Colour bars are as in Fig. 3.5.

6.5 and 5.5 Ma. εNd then reduces slightly between 5.5 and 4.0 Ma, with an average value of −9.2 εNd units, before becoming gradually more radiogenic between 4.0 and 3.0 Ma, reaching −7.2 εNd. After 3 Ma, the εNd signal becomes less radiogenic and decreases from −7.2 to −9.0. Comparing the εNd records from both sites indicates that NSDWs were consistently more radiogenic throughout the early and mid-Pliocene. The maximum compositional difference between the two study localities occurs at 3 Ma, where the offset reaches up to +3.1 εNd units. Importantly, our authigenic Nd record reveals the isotopic signals from the NE Atlantic and Norwegian Sea converge during the late Pliocene at a relatively constant rate (c. 3.1 εNd per Myr); both water masses appear to exhibit an identical Nd composition of −8.6 at c. 2.6 Ma. Following this, the εNd signals switch throughout the remaining c. 90 kyrs of the Pliocene (Fig. 3.10), whereby DSDP Site 552 becomes relatively more radiogenic compared to ODP Site 642.

Figure 3.10 (following page). Nd isotopic composition of bulk sediment leaches from ODP Hole 642B (red) and DSDP Hole 552A (blue) for the 2000−7000 kyr interval. NSDWs are significantly more radiogenic than the NE Atlantic between 6 and 3 Ma. Published records of ice-rafted debris (IRD; Fronval and Jansen, 1996), rifting (Doré and Lundin, 1996), V-shaped ridge (R1 etc.) formation (Jones et al., 2002), and climatic events (De Schepper et al., 2013) are also shown. Colour bars are as in Fig. 3.5. SCW, Southern Component Water; iNHG, intensification of the Northern Hemisphere Glaciation.


Regional Climate
ANTARCTIC ICE SHEETS
NORTHERN HEMISPHERE ICE SHEETS
GLACIAL CYCLES
iNHG
mPWP
MIS M2
ARRIVAL OF PACIFIC MOLLUSCS AT TJÖRNES
SHORT NHG PULSES
Rifting and Tectonic Events
SPREADING WEST OF SPITSBERGEN
REYKJANES AND MOHNS RIDGES
KOLBEINSEY RIDGE
R1
R2A
CLOSURE OF CENTRAL AMERICAN SEAWAY
OPENING OF BERING STRAIT
SUBAERIAL BARENTS SEA
Nordic Seas IRD
0
10
100
1000
10000
IRD g/sediment
εNd
−6
−7
−8
−9
−10
−11
−12
−13
SCW
ICELANDIC AND JAN MAYEN BASALT
SCANDINAVIAN BASEMENT
n = 16 points
Error bar = 2σ
mPWP
MIS M2
2000
3000
4000
5000
6000
7000
Age (kyrs)
Site
552
642
Neogene
Quat
Pliocene
Pleist
Miocene
Messinian
Zanclean
Piacenzian
Gel

3.6 DISCUSSION

3.6.1 *Secondary influences on $\delta^{13}C_{BF}$ and εNd records*

The present water depth at NE Atlantic DSDP Site 552 (2301 m) is 1015 m deeper than Nordic Seas ODP Site 642 (1286 m). A comparison of recent $\delta^{13}C_{BF}$ records (Fig. 3.7B) from DSDP Site 552 and ODP Site 982 (1135 m; a depth similar to ODP Site 642), suggests the Rockall Plateau is bathed uniformly by ISOW across all depths, and there are no indications that this has changed substantially back through time into the Pliocene (Risebrobakken et al., 2016; Zhang et al., 2013). On this basis we interpret the differential between ODP Site 642 and DSDP Site 552 to be primarily driven by geographical variations in deep-water composition between the Norwegian Seas and the Rockall Plateau, rather than a depth-dependent differential between deep-waters.

The $\delta^{13}C_{DIC}$ porewater gradient in the uppermost seafloor sediment is associated with the flux and decomposition rates of organic matter (Mackensen, 2008). With increasing depth, more ^{12}C-enriched organic matter is re-mineralised by microbial activity (up to −1.0 ‰ cm^{-1}), resulting in porewater depletions of up to $\delta^{13}C_{DIC}$ = −4.0 ‰ (Mackensen, 2008). This porewater gradient is the main driver of vital effects in benthic foraminifera. As discussed, we corrected the $\delta^{13}C_{BF}$ records from *C. teretis* to *C. wuellerstorfi,* a faithful recorder of deep-water $\delta^{13}C_{DIC}$ (Mackensen et al. 1993), to reduce the influence of vital effects (Fig. 3.6). *C. teretis* is also a shallow infaunal species, known to dwell in the top 1 cm, and is therefore unlikely to be controlled by stronger porewater depletions found at deeper depths (Ahrens et al., 1997). In spite of these measures and assumptions, we cannot fully rule out the influence of porewaters on *C. teretis*. The $\delta^{13}C_{BF}$ records from *C. teretis* are therefore considered to represent a primary deep-water signal, which may be enhanced due to the fact that it's measured on infaunal taxa.

Recrystallisation of foraminifera occurs on the seafloor and during diagenesis, whereby the original biogenic calcite is partially dissolved in porewaters and replaced by secondary

(inorganic) calcite (Pearson and Burgess, 2008). Our SEM images (Fig. 3.11A-F) of *C. wuellerstorfi* and *C. teretis* extracted from the Pliocene carbonate-rich pelagic oozes of DSDP Site 552 and ODP Site 642 (Fig. 3.1), reveal both species are well-preserved. The wall cross sections from both *C. wuellerstorfi and C. teretis* show a microgranular texture, and the inner wall surfaces of both species are relatively smooth with visible and unfilled pores (Fig. 3.11E, 11F). *C. teretis* shows very minor overgrowth on the inner wall surface (Fig. 3.11E). There is no evidence of recrystallization, infilling, or cementation. The impact of diagenesis on our $\delta^{13}C_{BF}$ records is therefore considered minimal due to the lack of recrystallisation. In addition, both Sexton et al. (2006) and Edgar et al. (2013) argue $\delta^{13}C_{BF}$ is relatively unaffected by extensive recrystallisation, and suggest that diagenetic alteration of foraminiferal calcite predominantly occurs at shallow burial depths (<100 m) in the uppermost porewaters, which exhibit a temperature and isotopic composition similar to the overlying deep-water. They indicate the diagenetic offsets from primary $\delta^{13}C$ values are negligible, and therefore we are confident our $\delta^{13}C_{BF}$ records faithfully represent changes in regional deep-waters.

The authigenic Nd proxy is susceptible to modification by boundary exchange and diagenetic flux processes (Abbot et al., 2016; Jeandel, 2016). Boundary exchange describes the addition of Nd from ocean margin sediments, including the riverine discharge of freshly weathered particles and the submarine weathering of deposited sediments along continental margins. Diagenetic flux involves the Nd efflux from pore water to seawater caused by early diagenetic interactions between sediment and porewater on the seafloor. In the NE Atlantic, vigorous deep-water replenishment minimises these effects, and the variation in deep-water εNd is deemed representative of large-scale water mass mixing (Piotrowski et al., 2005). Diagenetic overprinting also modifies the εNd record, whereby the marine weathering of silicate minerals in the methanogenic zone releases Nd from bulk sediments into pore waters, before it is re-incorporated into preformed authigenic phases, which essentially rewrites the authigenic εNd record (Du et al., 2016). Significant uncertainty remains when assessing the magnitude of late diagenetic effects on authigenic εNd, and several studies suggest the authigenic εNd coatings are actually immune to later diagenetic alteration due to the higher Nd concentrations in the

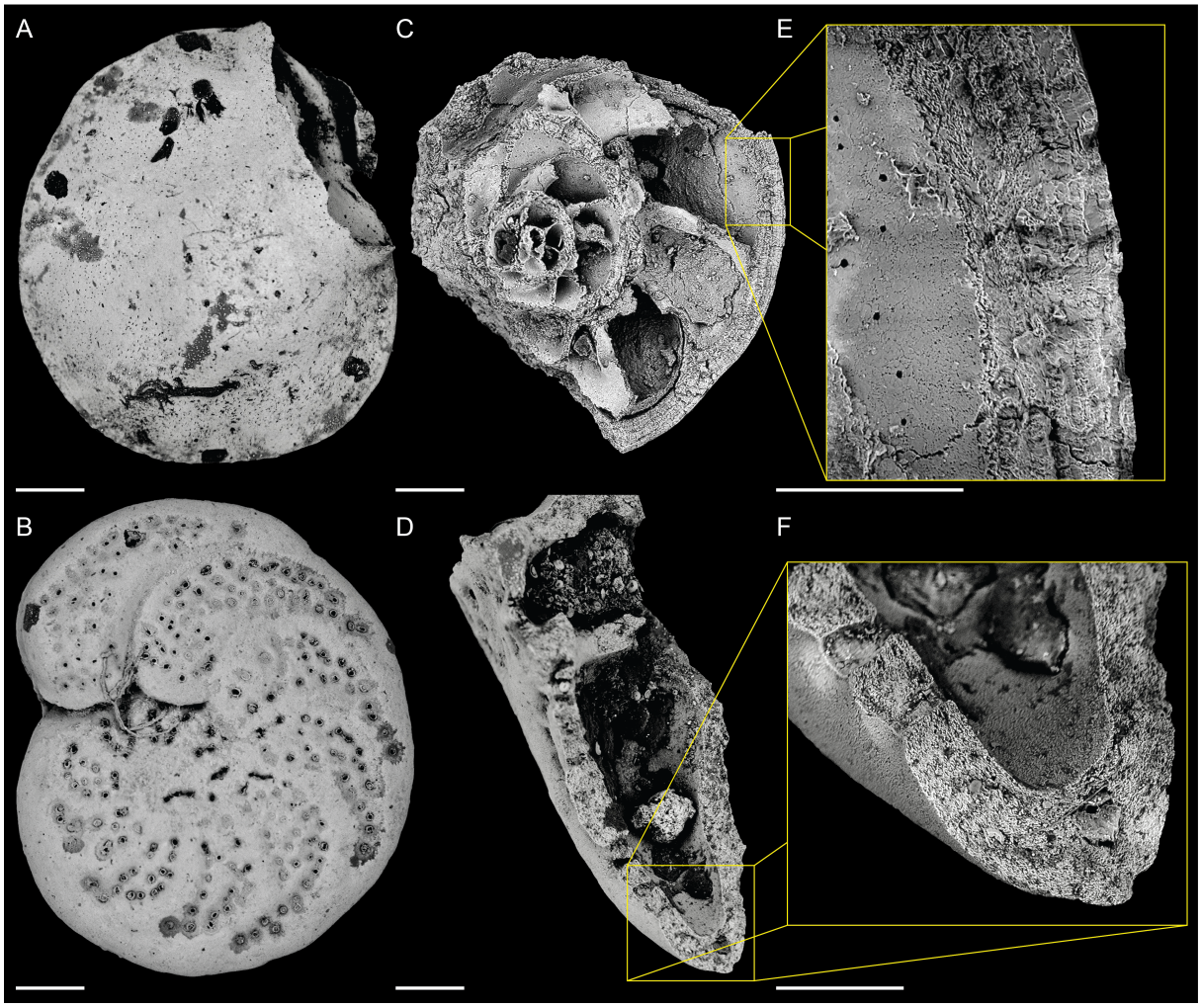


Figure 3.11. SEM images of single foraminifera specimens analysed for $\delta^{13}C$ from ODP Hole 642B (A, C, E) and DSDP Hole 552A (B, D, F) Pliocene sediment samples. (A) *Cassidulina teretis* (Tappan, 1951). (B) *Cibicidoides wuellerstorfi* (Schwager, 1866). (C and D) Cross section of whole test. (E and F) Magnified cross section of test wall. Scale bars are 100 μm (A-D) and 20 μm (E and F).

original authigenic phases relative to pore water (Du et al., 2016). The transport and dissolution of preformed authigenic coatings on aeolian sediments by sea-ice and icebergs may also contaminate water mass εNd records (Bayon et al., 2004; Chen et al., 2012). However, this effect is negligible considering the relative long-term (myr-scale) consistency in the Nd isotope distribution alongside relatively ice-free conditions, at both sites during the early to mid-Pliocene. The leaching of bulk sediments contaminated with volcanic ash can also bias the εNd signature towards radiogenic values (Elmore et al., 2011). There is no evidence of volcanic ash preserved in the Pliocene calcareous oozes at DSDP Site 552 (Fig. 3.8). The closer

proximity of ODP Site 642 to Iceland, however, inevitably results in low traces of ash within the Pliocene oozes and mudstones on the Vøring Plateau (Fig. 3.4). The lack or low abundances of alternative Nd archives – fish teeth and planktonic foraminifera – restricted the options that could avoid volcanic contamination at this locality. Consequently, the leaching method proposed by Blaser et al. (2016) was used for all samples which involves a weaker HH leaching solution and a shorter leaching duration compared to conventional acid-reductive leaches. Blaser et al. (2016) showed their method more reliably extracts authigenic Nd, lowers the risk of contamination by leaching volcanic phases, and provides excellent reproducibility with data obtained from uncleaned foraminifera, which are unaffected by volcanic ash. We are therefore confident our εNd results most likely reflect the enhanced residence times of Norwegian and NE Atlantic deep-waters.

3.6.2 *Comparison of our $\delta^{13}C_{BF}$ and authigenic εNd datasets*

Examining the trends in our NE Atlantic and Nordic Seas $\delta^{13}C_{BF}$ compilation (Fig. 3.5) alongside our new $\delta^{13}C_{BF}$ (Fig. 3.9A-B) and εNd (Fig. 3.10) results, undertaken to authenticate these patterns, reveals two main findings: (1) Norwegian and NE Atlantic deep-waters were isotopically dissimilar during the early to mid-Pliocene (5.5−3.0 Ma), with Norwegian deep-waters having a significantly lighter $\delta^{13}C$ composition and a more radiogenic εNd signature relative to NE Atlantic deep-waters; and (2) our εNd records (Fig. 3.10) indicate the isotopic signatures of the deep-waters at both sites converged during the late Pliocene at around c. 2.6 Ma, before showing a reversed pattern compared to the early to mid-Pliocene. The isotopic convergence in εNd is also supported by the $\delta^{13}C_{BF}$ records at ODP Site 642 (Fig. 3.7A), which become gradually heavier and more similar to the values observed at NE Atlantic localities throughout the last 2 myrs.

The significantly lighter $\delta^{13}C_{BF}$ records (Fig. 3.7A) at ODP Site 642 during the early-Pliocene (up to 1.05 ‰), suggest the Norwegian Basin deep-waters were poorly ventilated throughout this interval, with restricted mixing (Risebrobakken et al., 2016). This isolation would enable

these deep-waters to accumulate sinking organic matter which undergoes oxidation as it falls through the water column, producing lower $\delta^{13}C_{DIC}$ values. In comparison, the $\delta^{13}C$ composition of the deep-waters observed at sites south of the GSR, which bathe in ISOW and DSOW, show heavier $\delta^{13}C$ values throughout the Pliocene (Fig. 3.7B), as expected for a well-ventilated region supplied by deep-waters originating from higher latitudes where dense and mature surface waters, with inherently higher $\delta^{13}C_{DIC}$ values, sink and return southwards (Hansen and Østerhus, 2000). During the mid-Pliocene, the lighter $\delta^{13}C$ composition of the NSDW appears to converge towards the heavier $\delta^{13}C$ values observed in the NE Atlantic records (Fig. 3.5). However, it is impossible to say whether or when full convergence occurs, based solely using our $\delta^{13}C_{BF}$ compilation, since these lighter Norwegian Sea measurements only extend between c. 3.13 and 5.49 Ma. The observable shift in Norwegian Sea $\delta^{13}C$ towards heavier NE Atlantic values through the mid-Pliocene, however, does suggest a gradual increase in ventilation of the eastern Nordic Seas with deeper overturning circulation during this time (Risebrobakken et al., 2016).

An early-Pliocene reduction in Norwegian Sea ventilation, followed by relative strengthening in the mid-Pliocene, is also supported by the planktic-benthic foraminifera $\delta^{13}C$ gradient ($\Delta\delta^{13}C$) (Fig. 3.12) at ODP Site 642 (Risebrobakken et al., 2016). Between 5.0 and 4.5 Ma, the $\Delta\delta^{13}C$ has an average value of c. 0.60 ‰, indicating good subsurface to bottom-water ventilation. Between 4.5 and 4.0 Ma, the $\Delta\delta^{13}C$ has an average value of c. −1.00 ‰. During this interval, the average value of the planktic foraminifera $\delta^{13}C$ ($\delta^{13}C_{PF}$) (−0.78 ‰) is significantly lighter than the mean value of the $\delta^{13}C_{BF}$ (0.22 ‰), indicating the Norwegian Sea is poorly ventilated and the bottom waters are disconnected from surface processes (Risebrobakken et al., 2016). Bachem et al. (2017) suggest the isotopically light $\delta^{13}C_{PF}$ reflect a reduction in primary productivity, caused by a cooling phase. Alkenone records demonstrate sea surface temperatures (SSTs) declined by 4.5°C during this interval (Chapter 4; Bachem et al., 2017), and IRD records indicate an enhanced influence of cooler surface waters in the Norwegian Sea, possibly associated with the contemporaneous strengthening of the EGC and

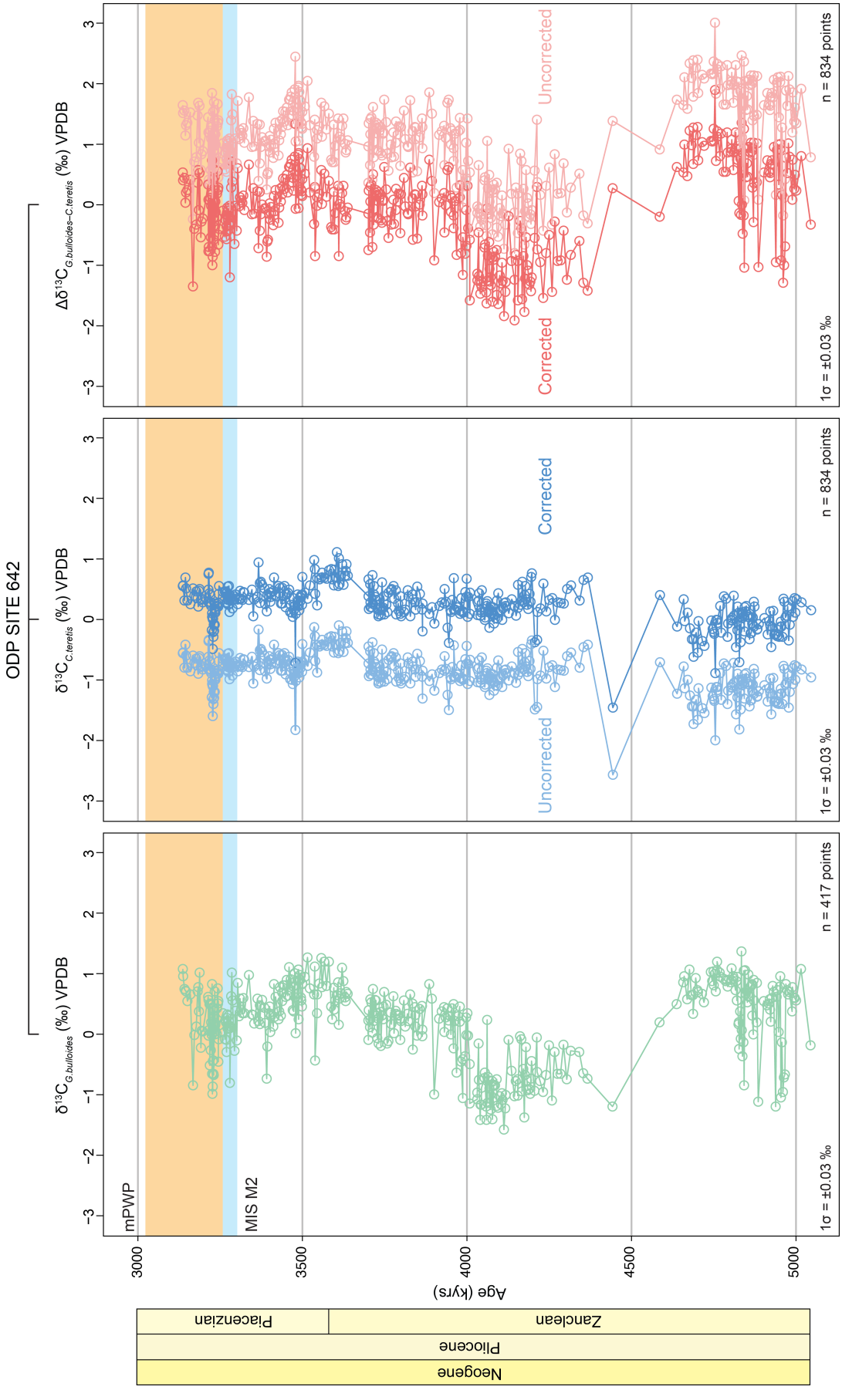

ODP SITE 642
$\delta^{13}C_{G.bulloides}$ (‰) VPDB
$\delta^{13}C_{C.teretis}$ (‰) VPDB
$\Delta\delta^{13}C_{G.bulloides-C.teretis}$ (‰) VPDB
mPWP
MIS M2
Corrected
Uncorrected
n = 417 points
n = 834 points
1σ = ±0.03 ‰
Age (kyrs)
3000
3500
4000
4500
5000
Neogene
Pliocene
Zanclean
Piacenzian

Figure 3.12 (previous page). Planktic-benthic $\delta^{13}C$ gradient ($\Delta\delta^{13}C$) at ODP Site 642 in the Norwegian Sea during the early to mid-Pliocene (5490−3130 kyr) based on high-resolution $\delta^{13}C_{BF}$ records from Risebrobakken et al. (2016). The $\Delta\delta^{13}C$ denotes the isotopic difference between the planktic (*G. bulloides*) and benthic (*C. teretis*) foraminifera, where lower numbers indicate improved subsurface to bottom water ventilation. Colour bars are as in Fig. 3.5.

the onset of northward through-flow in the Bering Strait (Marincovich and Gladenkov, 1999). Between c. 4.0 and 3.0 Ma, the $\Delta\delta^{13}C$ has an average value of c. 0.00 ‰, indicating renewed subsurface to bottom-water ventilation throughout the mid-Pliocene. Bachem et al. (2017) attribute this re-established ventilation to surface warming, indicated by their alkenone records (Chapter 4), and strengthened surface circulation driven by an enhanced NWAC associated with the shoaling of the Central American Seaway (CAS).

Several studies (Table 3.2; Fig. 3.13A-B) have focused on using Nd datasets to characterise deep-waters during the Pleistocene and Holocene at North Atlantic and Nordic Seas drilling localities (e.g. Crocket et al., 2011; Werner et al., 2013; Khélifi and Frank, 2014; Teschner et al., 2016). The average εNd compositions of modern NSDW and ISOW at the Vøring and Rockall plateaus are −10.2 and −9.8, respectively (Piepgras and Wasserburg, 1987; Lacan and Jeandel, 2004a; Dubois-Dauphin, 2017; Morrison et al., 2019). The εNd signature of modern NSDW is considered to be predominantly controlled by the westward drainage basins, hydrology and unradiogenic geology of the Norwegian Caledonian margin (εNd = −12.0 to −20.0), alongside inputs from the Norwegian Basin basaltic margins, including Iceland, Jan Mayen and the Faroe Islands (Fig. 3.4), which have a modern radiogenic εNd signature of +5.0 to +10.0 (Jeandel et al., 2007). There are no indications that the εNd signature of these basalts has changed substantially back through time into the late Neogene (Condomines et al., 1983 and Sigmarsson and Steinthórsson, 2007). The εNd composition of modern ISOW is slightly more radiogenic, compared to NSDW, reflecting a source controlled by NSDW, the erosion of Icelandic and Faroe basalts and inputs from the Greenland and Icelandic Seas (Fig. 3.4). The modern EGC and EIC share an average εNd composition of −9.5, and are influenced by the dissolution of ancient cratonic rocks on Greenland (εNd = −35.0 to −40.0) (Lacan and Jeandel, 2004b; Jeandel et al., 2007).

Site	Lat (DD)	Long (DD)	Data source	Type	Age model source	Interval, kyr	No. of data points
U1308	49.885°N	24.241°W	Blaser et al. (2019)	L	Obrochta et al., (2014)	0.07–24.54	35
911	80.596°N	8.394°E	Teschner et al. (2016)	L	Knies et al. (2009)	0.00–5198.00	78
980	55.508°N	14.737°W	Khélifi and Frank (2014)	L	Lisiecki and Raymo (2005)	1.98–3920.11	51
			Crocket et al. (2011)	L	Lisiecki and Raymo (2005)	2.11–42.16	39
610	53.299°N	18.943°W	Khélifi and Frank (2014)	L	De Schepper and Head (2008)	1.98–4010.65	35
BOFS 5K	50.687°N	21.864°W	Roberts and Piotrowski (2015)	L, F, FD, BS, L-IRD & D-IRD	Roberts et al. (2014)	2.30–27.30	22
BOFS 8K	52.503°N	22.062°W	Piotrowski et al. (2012)	L	Barker et al. (2004)	6.86–22.44	50
			Roberts and Piotrowski (2015)	L, F, FD, BS, L-IRD & D-IRD	Roberts et al. (2014)	0.60–32.40	63
BOFS 10K	54.667°N	20.654°W	Roberts and Piotrowski (2015)	L, F, FD, BS, L-IRD & D-IRD	Roberts et al. (2014)	0.90–28.10	51
BOFS 11K	55.193°N	20.346°W	Roberts and Piotrowski (2015)	L, F, FD, BS, L-IRD & D-IRD	Roberts and Piotrowski (2015)	0.60–32.80	60
BOFS 17K	58.001°N	16.501°W	Roberts and Piotrowski (2015)	L	Roberts et al. (2014)	1.40–37.70	40
MD01-2454G	55.522°N	15.652°W	Copard et al. (2010)	C	Alive	0.00	1
Pos-241-364	57.420°N	11.720°W	Copard et al. (2010)	C	Alive	0.00	1
Pos-241-362	59.359°N	10.570°W	Copard et al. (2010)	C	Alive	0.00	1
Pos-292-526	59.185°N	17.219°W	Copard et al. (2010)	C	Alive	0.00	1
PL 127-05	52.309°N	13.030°W	Copard et al. (2010)	C	Alive	0.00	1
MD01-2463G	51.429°N	11.770°W	Copard et al. (2010)	C	Copard et al. (2010)	0.26–0.85	2
Bioice 2472	63.120°N	20.630°W	Copard et al. (2010)	C	Copard et al. (2010)	0.05	1
Bioice 2424H	63.020°N	20.150°W	Copard et al. (2010)	C	Copard et al. (2010)	0.04	1
MSM5-5 712	78.916°N	6.767°E	Werner et al. (2014)	L	Müller et al. (2012)	0.00–8.53	16
MSM5-5 715	79.200°N	6.250°E	Werner et al. (2014)	L	Müller et al. (2012)	0.00	1
MSM5-5 723	79.160°N	5.340°E	Werner et al. (2014)	L	Müller et al. (2012)	0.00	1
MSM5-5 725	80.950°N	11.320°E	Werner et al. (2014)	L	Müller et al. (2012)	0.00	1
643	67.703°N	1.033°E	Blaser et al. (2016)	L	Henrich and Baumann (1994)	0.00	2
U1314	56.613°N	28.490°W	Blaser et al. (2016)	L	Zarikian et al. (2009)	0.00–10.00	3
U1304	53.061°N	33.538°W	Blaser et al. (2016)	L	Zarikian et al. (2009)	0.00	1

Table 3.2 (previous page). Sources of εNd records used in the NE Atlantic Ocean and Nordic Seas compilation. Nd isotopic compositions include: leachates (L), foraminifera (F), coral (C), fish debris (FD), bulk sediment digestion (BS), leachate of ice-rafted debris (L-IRD) and digestion of ice-rafted debris (D-IRD). All primary age control points were updated to ATNTS 2012 using the calibration points of Backman et al. (2012), Hilgen et al. (2012) and Wade et al. (2011). Latitude and longitude in decimal degrees (DD).

Our εNd measurements (Fig. 3.10) are the first Nd results generated from ODP Hole 642B and DSDP Hole 552A (Fig. 3.1), and extend the regional εNd record throughout the late Neogene (Fig. 3.13B). During the late Miocene, the εNd signal at ODP Site 642 reaches −12.3 (Fig. 3.10), coinciding with short-lived glacial intensifications in the Nordic Seas between 7 and 6 Ma (Larsen et al., 1994). Ice-rafted debris (IRD) and benthic foraminiferal $\delta^{18}O$ ($\delta^{18}O_{BF}$) records from ODP Site 642 indicate a late Miocene onset of small-scale glaciation in the Northern Hemisphere (Fronval and Jansen, 1996); $\delta^{18}O_{BF}$ exceed Holocene values for the first time around 6.5 Ma, signifying cooling of deep-waters to <0°C and periods with global ice volumes above present. Provenance studies suggest the late-Miocene pulses of IRD at ODP Site 642 reflect the drift of icebergs originating from Greenland (Fronval and Jansen, 1996), and consequently the unradiogenic peak observed during this period, may be caused by the fallout and dissolution of ancient cratonic IRD modifying the water mass chemistry.

During the early to mid-Pliocene, our εNd signals resemble the patterns observed in our $\delta^{13}C_{BF}$ compilation (Fig. 3.5), with a clear, long-term isotopic difference in the εNd composition between the Norwegian Sea and NE Atlantic deep-waters. NSDWs are significantly more radiogenic (up to +3.1 εNd units) between 6.0 and 3.0 Ma compared to the NE Atlantic (Fig. 3.10), reflecting the localised erosion and dissolution of radiogenic basaltic margins and a poor connection between the two deep-water masses. Between 5.5 and 4.0 Ma, the εNd signal at ODP Site 642 becomes temporarily less radiogenic changing from −7.9 to −9.6. The εNd record at ODP Site 911 in the Fram Strait also converges with the εNd signal in the Norwegian Sea during this interval (Fig. 3.13B) (Teschner et al., 2016). We attribute this unradiogenic shift to the culmination of a previously-discussed cooling phase (4.5−4.0 Ma), during which Norwegian SSTs reduced by 4.5°C (Chapter 4; Bachem et al., 2017). Bachem et al. (2017)

indicate pulses of IRD occur in ODP Hole 642B between 4.9−4.0 Ma, and suggest an enhanced influence of cooler surface waters in the Norwegian Sea during this interval. Jansen and Sjøholm (1991) indicate the IRD originated from Scandinavia throughout this period. This temporary shift toward less radiogenic values between 4.5−4.0 Ma, therefore most likely reflects the enhanced glacial erosion, fallout and dissolution of cratonic IRD from nearby Scandinavia. The convergence of the Fram Strait and Norwegian Sea εNd records, also suggests the Scandinavian-derived IRD or εNd signals may have been carried northward by the NWAC and West Spitsbergen Current during this cooling phase. Between 4.0 and 3.0 Ma, the εNd signal at ODP Site 642 becomes more radiogenic shifting from −9.6 to −7.2. During this period, SSTs increased by up to 7°C in the Norwegian Sea (Bachem et al., 2017), and the $\delta^{13}C_{BF}$ records indicate renewed primary productivity and strengthened surface to bottom ventilation (Risebrobakken et al., 2016). The radiogenic shift may therefore reflect enhanced boundary exchange with the basaltic margins during this interval of regional warming and better oceanic ventilation. During the early to mid-Pliocene, the deep-waters at DSDP Site 552 exhibit a relatively stable unradiogenic signal (c. −10.5 εNd units; Fig. 3.10). DSDP Site 610, also located on the Rockall Plateau (Fig. 3.4), shows a near-identical unradiogenic trend to DSDP Site 552 between 4.0 and 3.0 Ma (Khélifi and Frank, 2014; Fig. 3.13B). Khélifi and Frank (2014) suggest the stable unradiogenic εNd signal at DSDP Site 610 reflects the sustained mixing of ISOW and less radiogenic Labrador Sea Water (εNd = −14.0; Lacan and Jeandel, 2005). The proximity of both drilling localities, suggests the same processes are likely to be responsible for the stable unradiogenic signals at DSDP Site 552 throughout the early to mid-Pliocene.

During the late Pliocene (3.0−2.5 Ma), the εNd signals (Fig. 3.10) at both sites appear to converge, with DSDP Site 552 becoming slightly more radiogenic compared to ODP Site 642 around 2.6 Ma. This convergence implies the NSDWs were better ventilated during the late-Pliocene, relative to the early to mid-Pliocene. Improved deep-water connectivity is also supported by our $\delta^{13}C_{BF}$ compilation (Fig. 3.5), where the isotopically lighter Nordic Seas converge towards the heavier values of the NE Atlantic sites. At ODP Site 642, the εNd signal

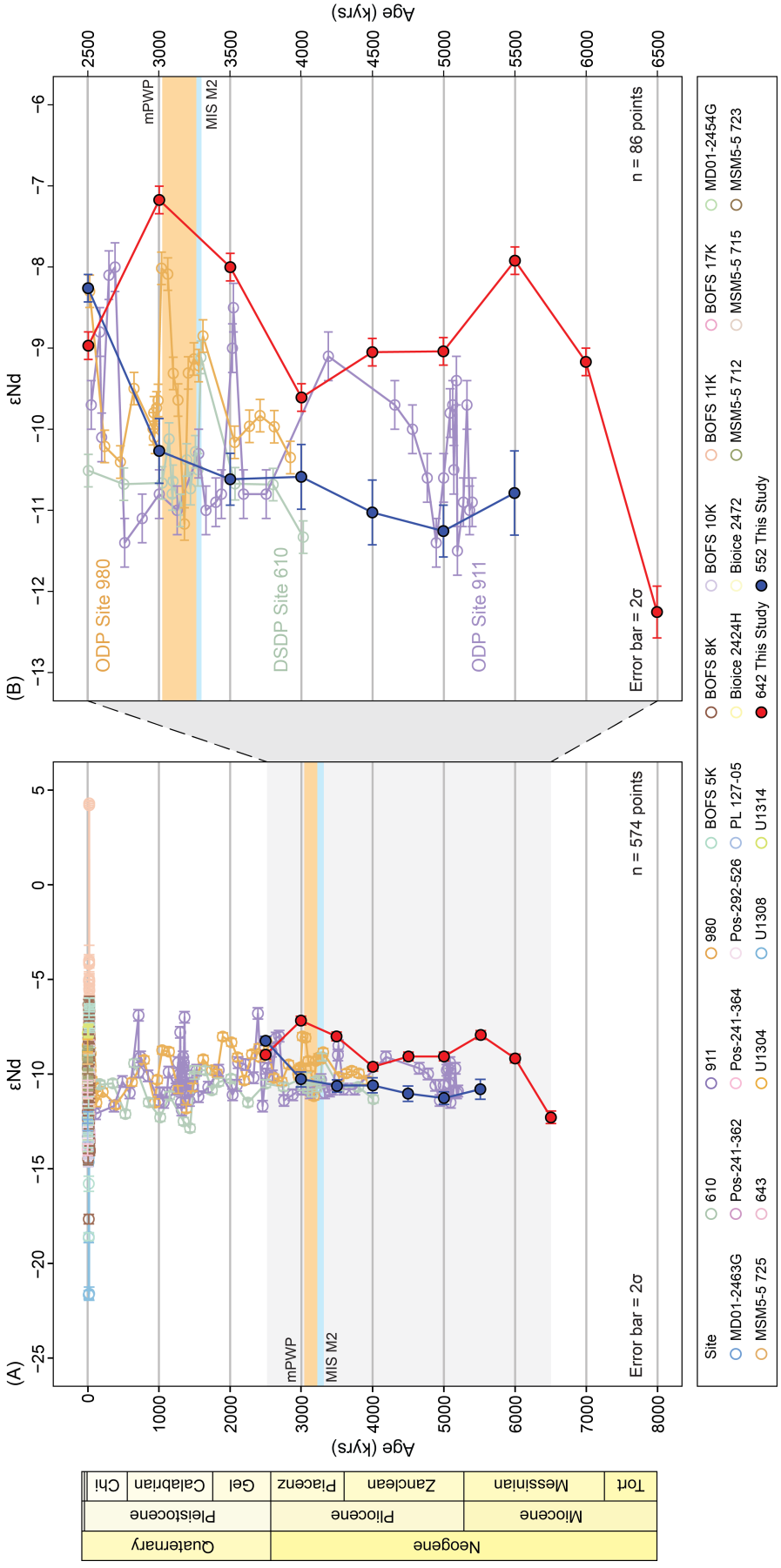

Neogene
Quaternary
Miocene
Pliocene
Pleistocene
Tort
Messinian
Zanclean
Piacenz
Gel
Calabrian
Chi
(A)
(B)
εNd
Age (kyrs)
mPWP
MIS M2
ODP Site 980
DSDP Site 610
ODP Site 911
n = 574 points
n = 86 points
Error bar = 2σ
Site
MD01-2463G
MSM5-5 725
610
Pos-241-362
643
911
Pos-241-364
U1304
980
Pos-292-526
U1308
BOFS 5K
PL 127-05
U1314
BOFS 8K
Bioice 2424H
642 This Study
BOFS 10K
Bioice 2472
552 This Study
BOFS 11K
MSM5-5 712
BOFS 17K
MSM5-5 715
MD01-2454G
MSM5-5 723

Figure 3.13 (previous page). Compilation of existing NE Atlantic and Nordic Seas εNd records (hollow circles), including the εNd data from ODP Site 642 and DSDP Site 552 presented in this study (solid circles). (A) Compilation of εNd records throughout the 0−8000 kyr interval. 73% of regional εNd records are Holocene or late Pleistocene (0−774 kyrs) in age. (B) Expanded compilation of εNd records throughout the Pliocene and late Miocene. Composite data are colour-coded based on DSDP/ODP/IODP, Biogeochemical Ocean Flux Study (BOFS) and Marion Dufresne (expedition MD 123) drilling sites. Colour bars are as in Fig. 3.5.

becomes less radiogenic, reaching −9.0 (Fig. 3.10). This is believed to represent an increased contribution of Nd derived from the fallout and dissolution of IRD, carved during the iNHG and the associated expansion of Greenland and Scandinavian ice sheets. Fronval and Jansen (1996) demonstrate an order of magnitude increase in IRD input around 2.75 Ma at ODP Site 642 (Fig. 3.10), and suggest the IRD originated from glacial erosion of the ancient Greenland and Scandinavian cratons. Regional studies in the NW Atlantic and Arctic Oceans reveal similar εNd shifts around 2.7 Ma, which are attributed to changes in the composition of eroded material from neighbouring Archean shields linked to an alteration in the dominant mode of transport (from riverine to ice-rafted), or a change in ice-flow direction accompanying the glaciation (Reynolds et al., 1999; Burton et al., 1999; Haley et al. 2008). At DSDP Site 552, the εNd signal becomes more radiogenic, reaching −8.3 (Fig. 3.10). Lang et al. (2016) identify a corresponding shift nearby at IODP Site U1313, which is suggested to have been triggered by an incursion of Southern Component Water (SCW), known to exhibit modern εNd values of c. −7.0 to −9.0. Lang et al. (2016) suggest the incursion of SCW may have been driven by the dampening of deep-water production due to cooling and sea-ice development in the high-latitude Nordic Seas associated with the iNHG. The radiogenic shift at DSDP Site 552 between 3.0−2.5 Ma is therefore believed to reflect the mixing of ISOW with SCW. ODP Site 980, also located on the Rockall Plateau (Fig. 3.4), shows a near-identical radiogenic shift between 3.0 and 2.5 Ma (Fig. 3.13B), supporting this incursion of SCW (Crocket et al. 2011; Khélifi and Frank, 2014).

3.6.3 *Late Neogene evolution of Norwegian Sea deep-waters*

3.6.3.1 Late Miocene to mid-Pliocene (7.0−3.0 Ma)

During the late Miocene (7.0−5.3 Ma), short-lived glacial intensifications are well documented in the Nordic Seas by dense pulses of IRD (up to 200 IRD per g sediment) (Larsen et al., 1994). Fronval and Jansen (1996) suggest a short-term glacial intensification occurred in the Nordic Seas around 6.5 Ma, based on the increased abundance of IRD at ODP Site 642 at this time. As discussed, the unradiogenic εNd signal at ODP Site 642 around 6.5 Ma (Fig. 3.10) is attributed to the fallout and dissolution of this IRD, which most likely originated from the glacial erosion of ancient cratonic rocks by expanding ice-sheets on Greenland and Scandinavia (Fronval and Jansen, 1996). The unradiogenic εNd signal therefore supports a short-term glacial intensification in the Nordic Seas around this time.

During the early to mid-Pliocene (5.3−3.0 Ma), Poore et al. (2006) and Wright and Miller (1996) suggest the AMOC and NCW overflow strengthened due to reduced dynamic support of the GSR, in particular the Denmark Strait, and the enhanced poleward oceanic heat transport associated with the progressive constriction of the CAS (Karas et al., 2017). Climate model simulations (Robinson et al., 2011; Hill, 2015), $\delta^{13}C_{BF}$ compilations (Otto-Bliesner et al., 2017; Poore et al., 2006; Wright and Miller, 1996; Raymo et al., 1992) and regional SST records (Dowsett et al., 2012; Naafs et al., 2010) all support the strengthening of the AMOC and poleward oceanic heat transport throughout this interval. However, the strengthened AMOC and NCW overflow disagree with the poor deep-water connectivity observed between the Norwegian and NE Atlantic basins during this time, implied by our $\delta^{13}C_{BF}$ and εNd records. This suggests the mixing of the Norwegian Sea during the early to mid-Pliocene was most likely controlled by mechanisms unrelated to the strengthening of the AMOC or NCW overflow.

As discussed, the $\Delta\delta^{13}C$ record (Fig. 3.12) shows the Norwegian Sea was relatively well ventilated during the earliest Pliocene (5.3−4.5 Ma) with good connectivity between the surface

and bottom waters. Between 4.5 and 4.0 Ma, the $\Delta\delta^{13}C$ is negative indicating a decline in primary productivity, weakened ventilation and a lack of connectivity between the Norwegian surface and bottom waters. The isolation of the NSDWs during this period is also supported by our isotopically light $\delta^{13}C_{BF}$ records from ODP Site 642 (Fig. 3.9A). Bachem et al. (2017) attribute the reduction in primary productivity to a cool period, during which SSTs reduced by 4.5°C. Bachem et al. (2017) indicate the Norwegian Sea was influenced by cool and fresh surface waters during this interval and identify pulses of IRD between 4.3 and 4.0 Ma at ODP Hole 642B. Our εNd record supports the cooling of the Norwegian Sea during the early Pliocene by temporarily shifting to slightly less radiogenic values (Fig. 3.10), reflecting the input and dissolution of IRD eroded from Scandinavia (Jansen and Sjøholm, 1991). The $\Delta\delta^{13}C$ record indicates ventilation gradually strengthened between 4.0 and 3.0 Ma (Risebrobakken et al., 2016). The shift in our $\delta^{13}C_{BF}$ record towards heavier NE Atlantic values during this interval, also supports improved ventilation of the Norwegian Sea. Bachem et al. (2017) indicate SSTs increased by up to 7°C between 4.0 and 3.0 Ma, and describe a notable reduction in IRD during this interval at ODP Hole 642B. Our εNd record shifts to more radiogenic values during this time (Fig. 3.10), possibly reflecting increased boundary exchange with the basaltic margins, which also supports strengthened ventilation.

The palaeogeography of the Nordic Seas has also changed substantially since the Pliocene; several studies modelling and reconstructing regional variations in isostatic elevation, glacial erosion rates, platform sedimentation and palaeogeography suggest the Barents Shelf (Fig. 3.14) was exposed to its maximum extent throughout the late Neogene until the early Pleistocene (c. 1.0 Ma) (Solheim et al., 1998; Torsvik et al., 2002; Rasmussen and Fjeldskaar et al., 1995; Butt et al., 2002; Knies et al., 2014). The Barents Sea currently represents one of the main pathways of warm Atlantic surface water transport towards the Arctic; heat is released here, producing dense brines which sink southward and contribute to the formation of NADW. A subaerial Barents Shelf would be expected to hamper the bifurcation of the NWAC and impede the branching of the North Cape Current, which normally extends from northern-most

Late Pliocene (3.0−2.5 Ma)

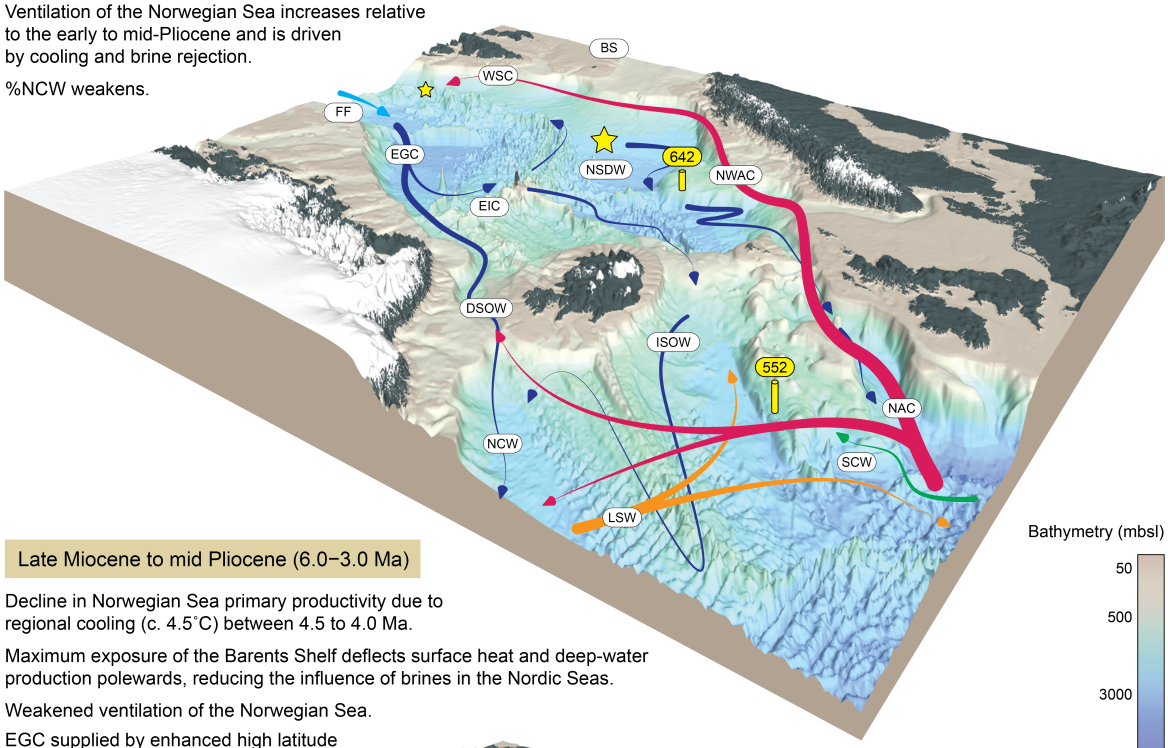
CAS closure strengthens NAC and NWAC. The northward transport of warm surface waters continues, despite an elevated GSR.

Sea ice formation and cooling associated with the iNHG dampen high latitude deep-water production, weakening the EGC.

The influence of a subaerial Barents Shelf lessens and deep-water production shifts southward into the Norwegian Sea.

Ventilation of the Norwegian Sea increases relative to the early to mid-Pliocene and is driven by cooling and brine rejection.

%NCW weakens.



Late Miocene to mid Pliocene (6.0−3.0 Ma)

Decline in Norwegian Sea primary productivity due to regional cooling (c. 4.5˚C) between 4.5 to 4.0 Ma.

Maximum exposure of the Barents Shelf deflects surface heat and deep-water production polewards, reducing the influence of brines in the Nordic Seas.

Weakened ventilation of the Norwegian Sea.

EGC supplied by enhanced high latitude deep-water production.

GSR lowered.

%NCW strengthens.

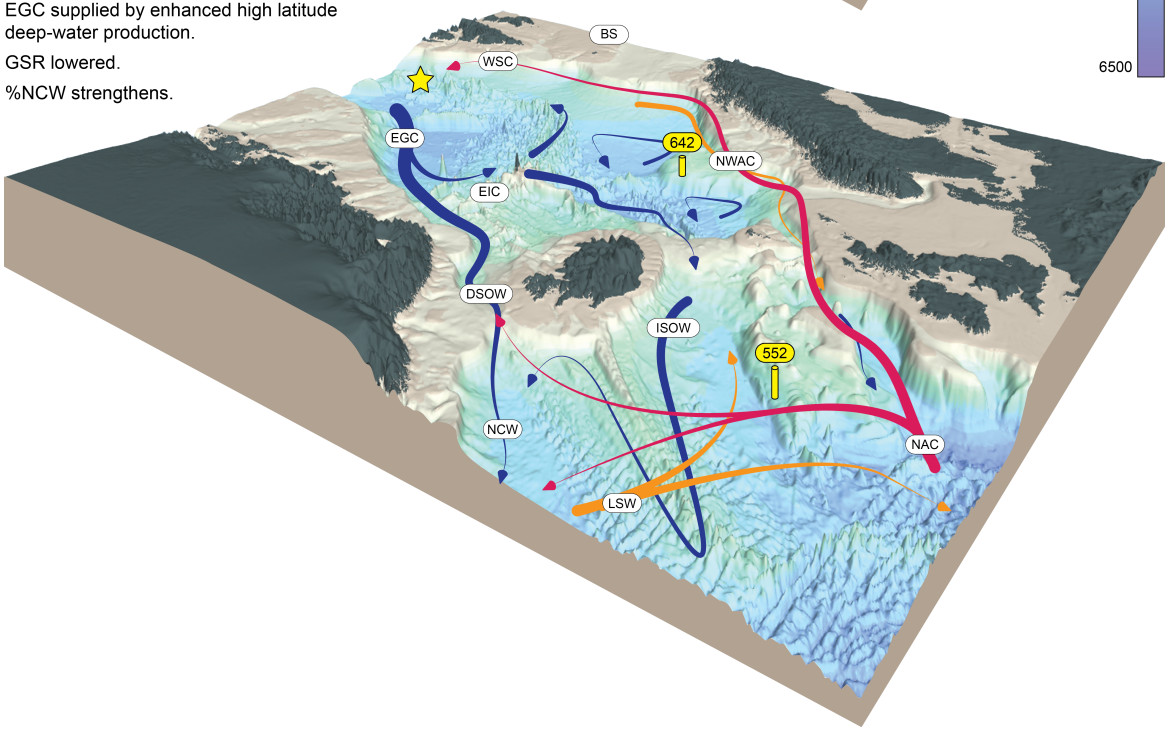


Figure 3.14 (previous page). Summary 3D palaeoceanographic evolution of the NE Atlantic Ocean and Nordic Seas from the late Miocene to the late Pliocene (6.0−2.5 Ma). The block diagram reconstructions show intensification of high latitude deep-water formation and poor ventilation of the Norwegian Sea between 6.0 and 3.0 Ma, followed by strengthening of the NWAC, renewed NSDW ventilation and freshwater forcing of high latitude deep-water production between 3.0 and 2.5 Ma. Surface and deep-water oceanic currents are defined in Fig. 3.1. Origin of new benthic $\delta^{13}C$ and εNd records highlighted by yellow DSDP and ODP sites. Bathymetric models created in Ocean Data View v.5.1.7 using GEBCO gridded bathymetry data (available at: https://www.gebco.net/data_and_products/gridded_bathymetry_data/ [accessed 01/02/2020]).

Norway into the Arctic (Fig. 3.1). It is believed the warm and saline waters of the NWAC were deflected further north during the early to mid-Pliocene (Fig. 3.14), enhancing the West Spitsbergen Current and causing the Fram Strait to significantly warm as modelled by Hill (2015); surface warming around the Fram Strait is also supported by vegetation records from the margins of NE Greenland and western Svalbard, which imply ice-free conditions onshore around this time (Funder et al., 1985, Butt et al., 2000, de Vernal and Hillaire-Marcel, 2008). This increased Arctic heat transport shifted the influence of dense brines to higher latitudes (Fig. 3.14), restricting the potential for deep-water formation and reducing ventilation within the Nordic Seas (Hill, 2015). This enhanced, high latitude deep-water formation is considered to have supplied the EGC and EIC before flowing southwards, bypassing the Norwegian Sea, into the North Atlantic via the Denmark Strait and Iceland-Faroe Ridge and significantly contributing to the strengthened NCW production proposed during this period, which is consistent with the Poore et al. (2006) model. This northerly migration of dense brines is also supported by Pb isotope and unradiogenic εNd records (ODP Site 911; Fig. 3.13B) from the Fram Strait, which indicate a strong influence of North Atlantic surface waters at high latitudes during this interval (Teschner et al., 2016).

Consequently, it is believed the interaction between regional climate change and the exposed Barents Shelf exerted the greatest control over the ventilation of the Norwegian Basin during this interval, compared to changes in the elevation of the GSR. The subaerial Barents Shelf most likely reduced the influence of brines in the Norwegian Sea throughout the Pliocene, limiting convection and mixing to sill depths but isolating water masses below c. 1 km, which

remained poorly ventilated (Jansen et al., 2000). Cooling of the Norwegian Sea between 4.5 and 4.0 Ma, associated with a short-lived glacial intensification, resulted in a decline in primary productivity and weakened deep-water ventilation further (Bachem et al., 2017). Warming followed between 4.0 and 3.0 Ma resulting in a relative strengthening of deep-water ventilation (Bachem et al., 2017; Risebrobakken et al., 2016). Importantly, our $\delta^{13}C_{BF}$ and εNd records at ODP Site 642, clearly reflect these processes and environmental changes, and support a lack of deep-water connectivity between the Norwegian Sea and NE Atlantic basins during the early to mid-Pliocene (Fig. 3.9A-B, 3.10). It is important to reiterate, the reduced dynamic support of the GSR is considered to have minimal influence over the ventilation of Norwegian Sea at this time; the overall increase in %NCW observed throughout this period most likely reflects the deflection of warm surface currents and deep-water production by the Barents Shelf to higher latitudes, which in combination with reduced dynamic support of the GSR strengthened the southward NCW overflow via the Denmark Strait and Iceland-Faroe Ridge.

3.6.3.2. Late Pliocene: intensification of the NHG (3.0−2.5 Ma)

SST palaeoclimate records (Chapter 4; Lisiecki and Raymo, 2005; Lawrence et al., 2009; Dekens et al., 2007; Medina-Elizalde et al., 2008; Herbert et al., 2010; Naafs et al., 2010; Venti et al., 2013) indicate significant global cooling between 3.0 and 2.5 Ma. This cooling is associated with an increase in IRD at several localities in the North Atlantic, Nordic Seas and the North Pacific, indicative of the expansion of major ice sheets across Scandinavia, Greenland and North America around 2.7 Ma (Fronval and Jansen, 1996; Jansen et al., 2000; John and Krissek, 2002; Flesche Kleiven et al., 2002; Haug et al., 2005).

Multiple hypotheses for the iNHG have been proposed which involve major tectonic events, and their interaction with both oceanic/atmospheric circulation and the global carbon cycle, including the uplift and erosion of the Himalaya (Ruddiman and Raymo, 1988; Raymo, 1994), deepening of the Bering Strait and the GSR (Einarsson et al., 1967; Wright and Miller, 1996), the restriction of the Indonesian Seaway (Cane and Molnar, 2001) and the closure of the

Panama Isthmus (Montes et al., 2015). Considerable uncertainty remains regards the driving mechanisms of the iNHG. However, several studies suggest cooling and ice-sheet growth was controlled by the interaction of two main processes: long-term CO_2 drawdown modulated by orbital forcing, and the emergence of the CAS (Raymo, 1994; Maslin et al., 1996; Jansen et al., 2000; Flesche Kleiven et al., 2002; Lunt et al., 2008; De Schepper et al., 2013; Willeit et al., 2015).

Haug and Tiedemann (1998) suggest the obliquity cycle (41 kyr) − influencing the distribution of solar insolation − changed from low-amplitude to high-amplitude obliquity around 3.0 Ma, which resulted in cooler summers, favourable for ice sheet growth. CO_2 drawdown is argued the most likely candidate to stimulate the growth of the Northern Hemisphere ice sheets (Lunt et al., 2008). A reduction in CO_2 could be attributed to: (1) increased North Pacific stratification, which strengthened the biological pump and removed atmospheric CO_2 (Haug et al., 1999); (2) enhanced chemical weathering of the uplifted Himalayan and Rocky Mountains (Ruddiman and Kutzbach, 1989; Raymo, 1994); and (3) stratification and sea-ice formation in the Southern Ocean, enhancing deep ocean CO_2 storage (Woodard et al., 2014; Lang et al., 2016).

The CAS is believed to have emerged by 2.7 Ma (O'Dea et al., 2016; Straume et al., 2020) due to the noted absence of further gene flow between shallow marine bivalves, gastropods and echinoderms either side of the isthmus after 3.2 Ma (Webb, 2006; O'Dea et al., 2016), the end of surface water exchange around 2.76 Ma based on coccolithophore assemblages and surface salinity contrasts (Kameo and Sato, 2000; Schneider and Schmittner, 2006), and an observed increase in the rate of dispersal of North and South American terrestrial mammals shortly before 2.7 Ma (Flynn et al., 2005; Castañeda and Miller, 2004; McDonald, 2005). The shoaling of the CAS, alongside the relative drop in global sea level (c. 40 m) associated with the iNHG (Miller et al., 2005; Willeit et al., 2015), halted the inflow of Pacific water to the North Atlantic and likely enabled the build-up of a Caribbean Warm Pool; this warm pool is believed to have invigorated the Gulf Stream and NAC, resulting in enhanced poleward ocean heat transport during the late Pliocene (Naafs et al., 2010; De Schepper et al., 2013). This northward

transport of moisture, alongside the global cooling associated with the drawdown of CO_2, preconditioned the mid to high latitudes and likely triggered the iNHG (Lunt et al., 2008). Haug and Driscoll (1998) suggest this moisture also enhanced the supply of freshwater delivery from Siberian rivers to the Kara and Laptev shelves, facilitating high latitude sea-ice formation, increasing the regional albedo and confining the high heat capacity of the Arctic Ocean from the atmosphere. Knies et al. (2008) reveal how the Scandinavian ice sheet protruded beyond the coastline and onto the Norwegian Continental Shelf around 2.7 Ma, but do not quantify the extent of this protrusion or assess whether sea-ice developed in the Nordic Seas during this interval.

Raymo et al. (1992) and Poore et al. (2006) indicate NCW overflow was strongest prior to 2.7 Ma, before gradually weakening in conjunction with the iNHG around 2.5 Ma to levels lower than present, but not as weak as during the late Pleistocene glaciations. Raymo et al. (1992) attribute this decline to reduced North Atlantic SSTs and freshwater forcing, which lowered evaporation rates and restricted density-driven overturning circulation. Sarnthein et al. (2009) suggest the increased poleward flux of atmospheric moisture associated with the closure of the Panamanian seaway, and the low-saline and cold North Pacific surface waters flowing through the newly-opened Bering Strait, caused cooling (up to 6°C) and freshening (by c. 2 psu) of the EGC, and dampened regional high latitude deep-water production during this interval (Fig. 3.14, 3.15). A freshened EGC thermally isolated Greenland from the increased poleward oceanic and atmospheric heat flux and stimulated the persistent glaciation of Greenland and the iNHG (Lunt et al., 2008). Sarnthein et al. (2009) indicate the Norwegian Sea was less sensitive to freshwater forcing compared to the other Nordic Seas during this interval, since the EGC bypasses this region, and therefore NSDW production continued, most likely to a lesser extent compared to between 3.0 and 2.7 Ma.

Wright and Miller (1996) and Poore et al. (2006) indicate this %NCW weakening also coincided with increased dynamic support of the GSR caused by the formation of V-shaped Ridge 1 around 3.1 Ma (Fig. 3.3; Jones et al., 2002), in response to a thermal perturbation in the

Icelandic plume head; the uplift of the GSR is believed to have restricted the flux of southward-flowing deep-water, contributing to a decline in NCW formation. Raymo et al. (1992) reveal South Atlantic deep-water becomes more Pacific-like (more negative, $\delta^{13}C$ = c. −0.5 ‰) after 2.7 Ma, suggesting a reduced influence of NCW at southern latitudes. However, they demonstrate the North Atlantic is less sensitive to the apparent reduction in NCW production, since DSDP Sites 552 and 607 show near-identical positive trends ($\delta^{13}C$ = 0.5 ‰ to 1.0 ‰) between 3.0 and 2.1 Ma.

Our Norwegian Sea $\delta^{13}C_{BF}$ results do not extend into the late Pliocene. However, the general positive trajectory displayed by our compilation in the prior c. 2.35 myrs and the $\Delta\delta^{13}C$ record of Risebrobakken et al. (2016) (Fig. 3.12), suggest the Norwegian Basin became gradually more ventilated at depths below 1 km during this time, relative to the early to mid-Pliocene (Fig. 3.15). Better ventilation is also supported by our εNd record (Fig. 3.10), which suggests the isotopic signatures of the Norwegian Sea and NE Atlantic deep-waters converged during the late Pliocene at around c. 2.6 Ma, before showing a reversed pattern compared to the early to mid-Pliocene. Sea-ice development and freshwater forcing is considered to have dampened deep-water production at higher latitudes (Raymo, 1992), reducing the influence of the subaerial Barents Shelf on regional circulation during the late Pliocene. Sites of deep-water production most likely shifted southward into the Norwegian Sea, which was less sensitive to freshwater forcing (Sarnthein et al., 2009). Norwegian Sea ventilation may have been cooling-driven, whereby warm surface waters transported northward by the strengthened NWAC, cooled prematurely and sank to form NSDWs. Our εNd record at ODP Site 642 (Fig. 3.10) reveal a sudden unradiogenic shift between 3.0 and 2.5 Ma, which most likely signals the expansion of the Scandinavian and Greenland ice sheets during the iNHG, and the increased fallout and dissolution of IRD eroded from these nearby ancient cratons (Smith et al., 2018). Our late Pliocene εNd signals therefore support the occurrence of sea ice in the Norwegian Sea after c. 2.6 Ma. The formation of this sea ice may have stimulated the rejection of brine, further driving the ventilation of the Norwegian Sea during this interval.

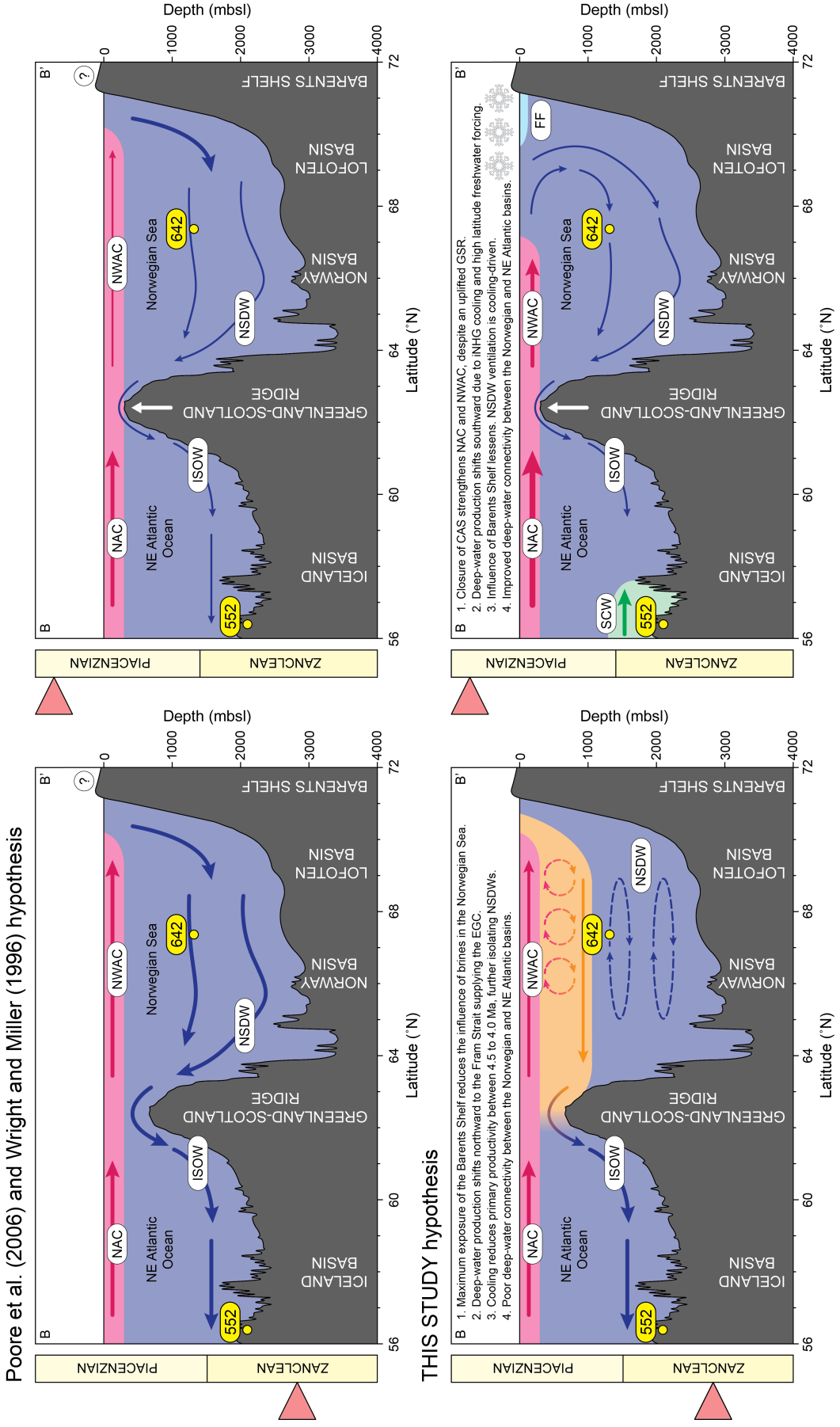

Poore et al. (2006) and Wright and Miller (1996) hypothesis
THIS STUDY hypothesis
Depth (mbsl)
Latitude (°N)
PLIOCENZIAN
ZANCLEAN
BARENTS SHELF
LOFOTEN BASIN
NORWAY BASIN
ICELAND BASIN
GREENLAND-SCOTLAND RIDGE
NE Atlantic Ocean
Norwegian Sea
NAC
NWAC
ISOW
NSDW
SCW
FF
552
642
B
B'
1. Maximum exposure of the Barents Shelf reduces the influence of brines in the Norwegian Sea.
2. Deep-water production shifts northward to the Fram Strait supplying the EGC.
3. Cooling reduces primary productivity between 4.5 to 4.0 Ma, further isolating NSDWs.
4. Poor deep-water connectivity between the Norwegian and NE Atlantic basins.
1. Closure of CAS strengthens NAC and NWAC, despite an uplifted GSR.
2. Deep-water production shifts southward due to iNHG cooling and high latitude freshwater forcing.
3. Influence of Barents Shelf lessens. NSDW ventilation is cooling-driven.
4. Improved deep-water connectivity between the Norwegian and NE Atlantic basins.

Figure 3.15 (previous page). Schematic summary palaeoceanographic sections across the Greenland-Scotland Ridge along line B-B' shown in Fig. 3.1, showing a comparison between the controls on regional deep-water ventilation suggested by Poore et al. (2006) and Wright and Miller (1996), and those advocated in this study during the early to mid-Pliocene and the late Pliocene. The main differences are the weakened ventilation of the Norwegian Sea during the early to mid-Pliocene (5.3−3.0 Ma), followed by relative strengthening in the late Pliocene (3.0−2.5 Ma) driven by the combined effects of enhanced poleward heat transport and global cooling, associated with the iNHG. Surface and deep-water oceanic currents are defined in Fig. 3.1. Origin of new $\delta^{13}C_{BF}$ and εNd records highlighted by yellow DSDP and ODP sites. FF, Freshwater Forcing; SCW, Southern Component Water.

Whilst the increased dynamic support of the GSR appears to have restricted the flux of southward-flowing deep-waters during the late Pliocene (Poore et al., 2006), it is deemed to have little effect on Norwegian Sea ventilation. Ventilation at this time was most likely controlled by the interaction between changes in ocean circulation and climate, including the strengthening of the NAC and NWAC, important conveyors of poleward heat, and global cooling associated with the iNHG. The influence of the subaerial Barents Shelf lessens during the late Pliocene, as global cooling and freshwater forcing dampened high latitude overturning circulation. It is suggested that Norwegian Sea ventilation was most likely driven by cooling during the late Pliocene, and may have been enhanced by brine rejection during periods of sea ice formation after c. 2.6 Ma (Fig. 3.14, 3.15). The reduction in %NCW during this period, most likely reflects a weakening in deep-water production caused by freshwater forcing at high latitude sites which supply the EGC. In agreement with Sarnthein et al. (2009), it is believed the Norwegian Sea was less sensitive to freshwater forcing during this interval, and that NSDW production persisted throughout this time, continuing to contribute to the ISOWs which influenced the NE Atlantic.

3.6.4 *Long-term controls on Norwegian Sea deep-water ventilation*

Vertical motions of the GSR (Fig. 3.2) appear to have minimal effect on deep-water ventilation in the Norwegian Sea. Lowering of the GSR between 5.5 and 3.0 Ma, attributed to a reduction in mantle-induced dynamic support (Wright and Miller, 1996; Poore et al., 2006), does not appear to strengthen deep-water production or overturning circulation in all of the Nordic

basins (Fig. 3.3); our $\delta^{13}C_{BF}$ and εNd records (Fig. 3.5, 3.9, 3.10) demonstrate poor deep-water connectivity between the Norwegian and NE Atlantic basins, and suggest the NSDWs were poorly ventilated for at least part of this interval. This poor ventilation is attributed to the combined influence of a short-term cooling phase (4.5–4.0 Ma), which reduced primary productivity in the Norwegian Sea (Bachem et al., 2017), and the subaerial Barents Shelf, which concentrated deep-water production at higher latitudes and reduced the influence of brines in the Norwegian Sea throughout the early to mid-Pliocene (Fig. 3.14; Jansen et al., 2000). The contemporaneous strengthening of NCW overflow (Fig. 3.3), linked to the lowering of the GSR by Poore et al. (1996), is believed to be caused by the combined effects of a deeper GSR (Robinson et al., 2011), and the intensification of deep-water formation near the Fram Strait (Hill, 2015), which supplied the EGC and EIC before flowing southwards into the North Atlantic via the Denmark Strait and Iceland-Faroe Ridge (Fig. 3.14).

Between 3.0 and 2.5 Ma, an increase in dynamic support of the GSR after 3 Ma is linked to the gradual weakening of %NCW (Fig. 3.3) (Poore et al., 2006). A rise in the elevation of the GSR would be expected to restrict the northerly flux of warm surface waters which help drive the overturning circulation and deep-water production in the Nordic Seas. However, this assumption disagrees with the improved deep-water connectivity between Norwegian and NE Atlantic basins implied by our $\delta^{13}C_{BF}$ and εNd records (Fig. 3.5, 3.10), suggesting other factors may have controlled the ventilation of the Norwegian Sea at this time. The greatest control on the ventilation of the Norwegian Sea during this interval is believed to be the combined influence of a strengthened NAC and NWAC, attributed to the emergence of the CAS, alongside global cooling associated with the iNHG (Fig. 3.14) (Lunt et al., 2008; Naafs et al., 2010; De Schepper et al., 2013). Sea ice development and freshwater forcing at higher latitudes is believed to have dampened deep-water production around the Fram Strait (Raymo, 1992), restricting the influence of the subaerial Barents Shelf on regional circulation during the late Pliocene. Sarnthein et al. (2009) suggest deep-water production shifted southward into the Norwegian Sea, which was less sensitive to freshwater forcing. Ventilation of the Norwegian Basin increased relatively compared to the early to mid-Pliocene, and was most

likely driven by cooling. The strengthened NWAC continued to transport warm water northward, despite an elevated GSR, which then cooled and sank to form NSDW. A significant unradiogenic shift in our εNd record at ODP Site 642 between 3.0 and 2.5 Ma, signals increased input of IRD and supports the occurrence of sea ice in the Norwegian Sea from c. 2.6 Ma (Fronval and Jansen, 1996). Sea ice formation may have helped to further drive ventilation during this interval via brine rejection (Fig. 3.14). The relative stability of our $\delta^{13}C_{BF}$ compilation (Fig. 3.5, 3.7) demonstrates that although %NCW weakened throughout the late Pliocene, the North Atlantic was relatively immune to this change compared to further afield (Raymo et al., 1992), which supports the continued connectivity and contribution of NSDW to ISOW during this time.

This work also highlights the need to consider spatial variability in $\delta^{13}C_{BF}$ signatures across the North Atlantic when estimating %NCW and defining the $\delta^{13}C_{NA}$ end member (Fig. 3.3) prior to 3 Ma. Our $\delta^{13}C_{BF}$ compilation (Fig. 3.5) reveals that $\delta^{13}C_{NA}$ defined by previous workers (Wright and Miller, 1996; Poore et al., 2006) is representative of North Atlantic deep-water masses during the early to mid-Pliocene, but overlooks the relatively isotopically light $\delta^{13}C$ signals observed in the Norwegian Sea. At first glance, the incorporation of these negative $\delta^{13}C_{BF}$ records in the characterisation of $\delta^{13}C_{NA}$ would inevitably strengthen %NCW even more, which further advocates reduced dynamic support of the GSR between 5.5 and 3.0 Ma. However, this study demonstrates the need to fully assess the interaction of other tectonic and climatic controls on regional oceanography before utilising $\delta^{13}C_{BF}$ records in the %NCW proxy. Our $\delta^{13}C_{BF}$ and εNd records demonstrate poor deep-water connectivity between the Norwegian and NE Atlantic basins during the early to mid-Pliocene. We demonstrate Norwegian Sea ventilation was most likely controlled by both climatic cooling and ocean circulation changes associated with an exposed Barents Shelf throughout this interval, in agreement with Jansen et al. (2000), Risebrobakken et al., (2016) and Bachem et al. (2017). Incorporating these Norwegian Sea $\delta^{13}C_{BF}$ records in the characterisation of $\delta^{13}C_{NA}$ is not advised and is unrepresentative of the regional oceanographic processes operating at this time, which are

unrelated to dynamic motions of the GSR; the original characterisation of $\delta^{13}C_{NA}$ requires no modification to account for the influence of Norwegian deep-waters during this interval.

3.7 CONCLUSIONS

The NE Atlantic and Nordic Seas are important palaeoclimate archives for understanding the interactions between tectonic, oceanic and climatic processes throughout the Pliocene, during which this region witnessed the transition from early Pliocene warmth to the iNHG. Previous work suggests fluctuations in the dynamic support of the GSR modulates the overflow of NCW, which may have preconditioned the mid to high latitudes and stimulated the onset of the iNHG. However, our temporal understanding of NCW fluctuations and GSR lock-gate motions believed to control this palaeoenvironmental change, is currently based on $\delta^{13}C_{BF}$ records compiled exclusively from drilling sites in the NE Atlantic and not the Nordic Seas.

We present a new $\delta^{13}C_{BF}$ compilation which incorporates all records from both the NE Atlantic and Nordic Seas for the first time. Our compilation contains over 11,900 $\delta^{13}C$ data points, ten times more than previous studies. We reveal NSDWs were significantly lighter, by up to 1 ‰, throughout the early to mid-Pliocene, compared to our NE Atlantic sites. This observation is inconsistent with previous findings, which suggest the Nordic and NE Atlantic basins were well connected at this time, attributed to reduced dynamic support of the GSR. We verified our $\delta^{13}C_{BF}$ deep-water trends by presenting new $\delta^{13}C_{BF}$ and εNd records from DSDP Site 552 and ODP Site 642, extending the regional εNd record throughout the late Neogene for the first time. Our εNd results support the trends observed in our $\delta^{13}C_{BF}$ compilation, and indicate a clear difference in the geochemical characteristics between the two sites; Vøring Plateau deep-waters were significantly more radiogenic (up to +3.1 εNd units) compared to the Rockall Plateau in the early to mid-Pliocene.

We suggest these $\delta^{13}C_{BF}$ and εNd differences are associated with poor deepwater connectivity between the Norwegian and NE Atlantic basins throughout the early to mid-Pliocene (5.3−3.0 Ma), most likely controlled by the combined interaction of regional climate and the subaerial Barents Shelf. Cooling between 4.5−4.0 Ma, weakened primary productivity, and isolated the NSDWs (Bachem et al., 2017). Our light $\delta^{13}C_{BF}$ records from ODP Site 642 support a reduction

in ventilation, and our εNd record becomes temporarily slightly less radiogenic during this period reflecting the increased input of IRD associated with cooling. The Barents Shelf, which was exposed to its maximum extent throughout this period (Butt et al., 2002; Torsvik et al., 2002), is considered to have deflected deep-water production to higher latitudes, contributing to the EGC, and further reducing the influence of brines in the Norwegian Sea (Jansen et al., 2000). The incorporation of Norwegian Sea $\delta^{13}C_{BF}$ records in the characterisation of $\delta^{13}C_{NA}$, used to estimate %NCW and assess variations in dynamic support, is not recommended since the processes governing NSDWs at this time are deemed unrelated to the GSR.

During the late Pliocene (3.0−2.5 Ma), our $\delta^{13}C_{BF}$ and εNd records suggest an improvement in deepwater connectivity between the Norwegian and NE Atlantic basins relative to the early to mid-Pliocene, which disagrees with the apparent weakening of %NCW attributed to increased dynamic support of the GSR during this interval (Poore et al., 2006), and suggests other factors most likely controlled the strengthened ventilation of the Norwegian Sea at this time. An enhanced NAC and NWAC, attributed to the shoaling of the CAS, alongside global cooling linked to the iNHG are thought to have exerted the greatest control on NSDWs during this time (Raymo, 1992; Lunt et al., 2008; Naafs et al., 2010). Sea-ice formation and freshwater forcing at higher latitudes most likely dampened deepwater production around the Fram Strait (Raymo, 1992), reducing the influence of the subaerial Barents Shelf on regional circulation during the late Pliocene. Sarnthein et al. (2009) suggest deep-water production shifted southward into the Norwegian Sea, which was less sensitive to freshwater forcing. Ventilation was driven by the cooling of warm waters transported northward by the enhanced NWAC, despite an elevated GSR. A significant unradiogenic shift in our εNd record at ODP Site 642 during this time, signals increased input of IRD and supports the occurrence of sea ice in the Norwegian Sea from c. 2.6 Ma (Fronval and Jansen, 1996). Sea ice formation may have helped to further drive ventilation during this interval via brine rejection. The relative stability of our $\delta^{13}C_{BF}$ compilation throughout the late Pliocene, indicates that although %NCW weakened, the North Atlantic was relatively immune to this change compared to further afield (Raymo et al.,

1992), which supports the continued connectivity and contribution of NSDW to ISOW during this time.

Our new $\delta^{13}C_{BF}$ and εNd records represent a significant step in the understanding of the long-term controls on the ventilation of the Norwegian Sea during the Pliocene. We have shown that fluctuations in the dynamic support of the GSR have minimal influence on the deep-water circulation in the Norwegian Basin during the Pliocene, which appears to be dominated by the interaction of climate and changes in ocean circulation associated with the emergence of the Barents Shelf and CAS. We also demonstrate the importance of acknowledging localised controls on oceanographic processes, and the knock-on implications these may have when compiling tracers of ocean circulation and characterising regional end members used to predict global deep-water patterns. Detailed examination of bottom-water tracers from other drilling sites in the Iceland and Greenland Seas, would provide additional spatial insights into the potential controls on regional deep-water ventilation during this interval, their influence on deep-water formation and the characterisation of $\delta^{13}C_{NA}$, and facilitate the continued assessment of the feasibility of mantle-induced dynamic support to modulate NE Atlantic circulation and climate.

4. MID-PLIOCENE WARMING: CLOSING THE GAP BETWEEN GEOLOGICAL ARCHIVES AND CLIMATE MODELS IN THE NE ATLANTIC AND NORDIC SEAS

My contribution to this work involved conducting all parts of the research, including sample selection, laboratory preparation and analysis, interpreting the $U^{K'}_{37}$ and TEX_{86} data, writing the manuscript and creating the figures. H. Kuhlmann assisted with sampling requests at the IODP Bremen Core Repository, University of Bremen. I. Bull, L. Behrooz and H. Whelton helped with the analysis of isoprenoid GDGTs at the Organic Geochemistry Unit (OGU), University of Bristol. J. Bendle and S. Jones provided feedback on the interpretations of the results. As in previous chapters, the editorial 'we' is used to reflect these contributions.

4.1 ABSTRACT

The mid-Piacenzian Warm Period (mPWP) (3.264−3.025 Ma) is an important analogue for global warming predicted for the end of the 21st Century, with similar continental configurations and atmospheric CO_2 concentrations to present day. Global mPWP sea surface temperature (SST) compilations indicate enhanced warming in the NE Atlantic and Nordic Seas, with anomalies of +6°C based on alkenone methods. However, this warming far exceeds the more conservative SST estimates (a rise of 2−3°C) predicted by the Pliocene Research, Interpretation and Synoptic Mapping (PRISM) reconstructions and leading climate models. Unfortunately, none of the published alkenone-based SSTs include information on the injection concentrations used to generate these records. Low concentrations are known to be susceptible to warming biases caused by chromatographic irreversible adsorption, and these may be responsible for the large discrepancies (up to 10°C) between proxy and model SST estimates. Here, we address these issues by compiling all available alkenone-based SSTs from the NE Atlantic and Nordic Seas for the first time. We verify these records with new $U^{K'}_{37}$ and TEX_{86} SSTs from four regional ocean-drilling localities (IODP Site U1308, DSDP Site 552, ODP Site 642 and ODP Site 907), including a high-resolution record at DSDP Site 552, a key PRISM locality. We demonstrate PRISM-interval SSTs peaked up to 21.5°C and 19.7°C in the NE Atlantic and Nordic Seas, respectively, consistent with existing studies. We reveal that 60% of our alkenone-based SSTs are derived from GC injections of relatively low total alkenone concentrations (<50 ng/µl), which bias our SST records towards warmer temperatures. The similarity in the magnitude of warming between the results presented here and published records confirms that the latter were also likely derived from low concentrations. We propose a new mathematical technique to correct for potential warming biases using a dilution series to quantify the sensitivity of a GC system to irreversible adsorption. Correcting our alkenone records results in a reduction in PRISM-interval SSTs, by up to 3.2°C, across all four sites. We suggest the existing PRISM SST anomaly (ΔSST) at DSDP Site 552 overestimates warming by c. 1.2°C. We propose a revised mean ΔSST of 4.3°C at this site, using our corrected alkenone and existing Mg/Ca palaeothermometry. This cooler ΔSST reduces local

discrepancies between proxy-based records and the PRISM3 reconstruction by one third (from 3.5°C to 2.3°C). Larger discrepancies (up to 6.5°C) remain between our revised ΔSST and the climate models. However, we attribute this difference due to model inaccuracies associated with the strength and position of the Gulf Stream and North Atlantic Current, important conveyors of poleward oceanic heat, associated with certain simulations (CCSM4 and GISS-ER). This work is a significant step toward assessing the influence of low alkenone concentrations on global multiproxy SST reconstructions, unravelling regional discrepancies between multiproxy records and climate models, and further understanding the magnitude of warming in the NE Atlantic and Nordic Seas during this important analogue for future climate change.

4.2 INTRODUCTION

The mid-Piacenzian Warm Period (mPWP) is a short time slice (3.264−3.025 Ma) during the Pliocene Epoch when global mean surface temperatures are estimated to have been approximately 2−3°C higher than preindustrial conditions, within the range estimated by the Intergovernmental Panel on Climate Change (IPCC) for the end of the 21st Century. The mPWP is an analogue for future climate, with global atmospheric CO_2 concentrations (c. 400 ppmv), continental configuration, ocean circulation patterns and the distribution of extant biota similar to present (Pagani et al., 2010). The likeness of these boundary conditions enables comparisons of environmental conditions with present-day. Understanding mPWP climate is therefore essential for our ability to predict, adapt to and mitigate the effects of future predicted climate change.

The Pliocene Research, Interpretation and Synoptic Mapping (PRISM) project is the gold standard reconstruction of sea surface temperature (SST) for the mPWP (Fig. 4.1). More than 20,000 studies and general circulation models (GCMs) rely on these large proxy datasets, which are subject to robust quality control (Dowsett et al., 2012). Nevertheless, the PRISM reconstruction does have some well-known problems. In the NE Atlantic and Nordic Seas, there are acknowledged discrepancies between GCM simulations and the PRISM proxy datasets, whereby the models appear to underestimate warming by up to 10°C (Dowsett et al., 2012; Dowsett et al., 2016). These inconsistencies are attributed to the GCMs, which are believed to inaccurately simulate the strength and position of the North Atlantic Current (NAC), leading to cooler SST estimates (Rosenbloom et al., 2013; Dowsett et al., 2012). However, this problem alone is unlikely to fully account for this model-data disagreement. Zhang et al. (2013) suggest this spatial discrepancy may be caused by uncertainties associated with both the simulated surface currents and proxy reconstructions. Regional proxy-based SST estimates are derived from planktic foraminifera, Mg/Ca and alkenone palaeothermometry at six Deep Sea Drilling Project (DSDP Sites 552, 609, 610) and Ocean Drilling Program (ODP Sites 907, 909 and 911) localities. However, no published work has yet explored whether these

discrepancies are caused by inherent warming biases associated with the alkenone records. A significant potential problem is that alkenone-derived SSTs are susceptible to warming biases at low C_{37} concentrations (Grimalt et al., 2001; Villanueva and Grimalt, 1996). Alkenone-derived SSTs at DSDP Site 552, DSDP Site 609, ODP Site 909 and ODP Site 911 are used in PRISM reconstructions to estimate standalone mean annual SSTs or to corroborate foraminifera-derived SSTs (Robinson et al., 2008; Robinson, 2009). However, none of the concentrations injected to generate the alkenone-based PRISM SST records are published, and therefore it is impossible to verify whether they possibly bias SSTs towards warmer values at these sites.

The purpose of this study is to better characterise the magnitude of mid-Pliocene warming in the NE Atlantic and Nordic Seas and determine whether existing regional SSTs are potentially biased by low alkenone concentrations, using new $U^{K'}_{37}$ and TEX_{86} SSTs from four regional ocean-drilling localities, including a high-resolution record at DSDP Site 552, a key PRISM locality in the NE Atlantic. These results should inform our understanding of the influence of low alkenone concentrations on global multiproxy SST reconstructions, enable us to shed light on regional discrepancies between proxy records and GCM simulations, and help to further comprehend the temporal and spatial patterns of mid-Pliocene warming in the NE Atlantic and Nordic Seas during this important analogue for future climate change. In the following subsections, we review the current understanding of the alkenone proxy and SST discrepancies in the NE Atlantic and Nordic Seas.

4.2.1 *Alkenones and irreversible adsorption*

Alkenones are long-chained (C_{37}), unsaturated (containing 2−4 double bonds) methyl and ethyl ketones synthesised by predominantly marine haptophyte algae, including coccolithophores, which reside in the upper photic zone (<20 m water depth) (Fig. 4.2). Alkenone-producing organisms are sensitive to changes in their environment and vary the relative degree of

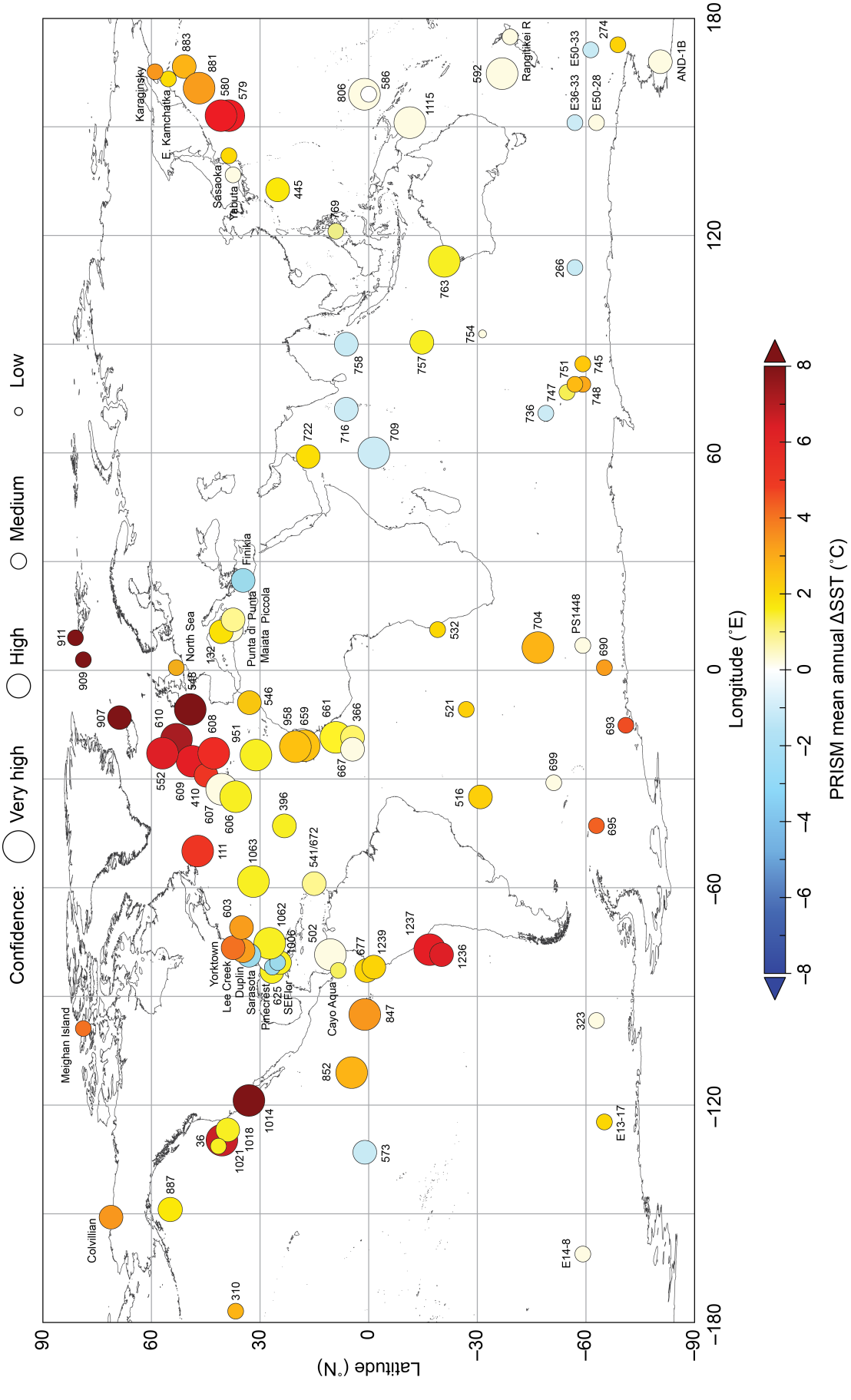

Confidence: Very high High Medium Low
Latitude (°N)
Longitude (°E)
PRISM mean annual ΔSST (°C)
Karaginsky
E. Kamchatka
Sasaoka
Yabuta
Rapgitikei R
AND-1B
E36-33
E50-33
E50-28
North Sea
Finikia
Punta di Punta Maiata Piccola
PS1448
Meighan Island
Colvillian
Yorktown
Lee Creek
Duplin
Sarasota
Pliocrest
SEFlor
Cayo Aqua
E13-17
E14-8

Figure 4.1 (previous page). Map showing the distribution of PRISM localities and sea surface temperature anomalies (ΔSST), calculated by subtracting modern from Pliocene sea surface temperatures. The reliability of each ΔSST estimate is indicated by the relative circle size (where larger circles represent greater confidence). Map created in ArcGIS® v.10.5 using the NCEI World Vector Shorelines (available at: https://www.ngdc.noaa.gov/mgg/shorelines/ [accessed 01/03/2020]). Modified from Dowsett et al. (2012).

unsaturation with growth temperature, producing greater quantities of saturated alkenones at higher temperatures (Herbert, 2006). The extent of unsaturation therefore reflects a direct estimate of near-surface temperatures. First discovered in Miocene sediments from the Walvis Ridge (Boon et al., 1978), alkenones appear recalcitrant to diagenesis compared to other membrane lipids, and are recorded in sediments dating back to the Aptian (c. 120 Ma) (Brassell et al., 2004). Originally defined by Brassell et al. (1986), the $U^{K'}_{37}$ index (Eq. 4.1) reflects the proportions of di-($C_{37:2}$) and tri-($C_{37:3}$) unsaturated ketones, and varies positively with temperature (Prahl and Wakeham, 1987). The global core-top SST calibration of Conte et al. (2006) is well established and based on the analyses of $U^{K'}_{37}$ from 592 localities (Eq. 4.2). At the time of our alkenone analyses, the Conte et al. (2006) equation was the most comprehensive calibration of $U^{K'}_{37}$ versus SST available, hence its utilisation in this study. Tierney and Tingley (2018) have since published the Bayesian B-spline regression (BAYSPLINE) global core-top calibration, which is claimed to reduce the response of $U^{K'}_{37}$ to SSTs at warm temperatures (>24°C). We intend to consider the application of BAYSPLINE in the future preparation of this chapter for publication, to determine whether BAYSPLINE SSTs are representative of the results presented here.

$$U^{K'}_{37} = \frac{C_{37:2}}{(C_{37:2} \div C_{37:3})}$$

Equation 4.1. Alkenone unsaturation index (Brassell et al., 1986)

$$SST\ (calibration\ error: \pm 1.1°C) = 29.876 \times (U^{K'}_{37}) - 1.334$$

Equation 4.2. Global core-top $U^{K'}_{37}$ versus SST calibration (Conte et al., 2006)

Irreversible adsorption is a major error source in the GC determination of palaeotemperatures from the analysis of alkenones injected at low (<10 ng/µl) concentrations (Grimalt et al. 2001). Irreversible adsorption describes the preferential adsorption of the $C_{37:3}$ species due to the accumulation of non-volatile residues on the stationary phase within the GC column. The higher adsorption of $C_{37:3}$ results in deviations of the $U^{K'}_{37}$ index towards higher temperatures, which is important the lower the proportion of this species is in the mixture (Villanueva and Grimalt, 1996). Villanueva and Grimalt (1996) demonstrated this effect by injecting triplicate $C_{37:2}$ and $C_{37:3}$ solutions which were repeatedly diluted into a new column, and showed the dispersion between the replicates increases as the quantity of ketones added to the system are reduced. The estimated temperatures are also seen to increase by up to 2°C (the so-called warming bias), as the concentrations halved from 20 ng/µl to 10 ng/µl. They also indicate the effects of irreversible adsorption are amplified when the GC column is older and has been previously used for multipurpose analyses, with a greater reduction in accuracy observed between replicate results. Grimalt et al. (2001) suggest the effects of irreversible adsorption can be observed by producing a dilution series to assess the sensitivity of an individual GC system to changes in sample concentrations, whereby the same sample is measured repeatedly at varying concentrations. Dilution series enable analysts to observe and quantify the extent of any warming bias at low concentrations.

4.2.2 *NE Atlantic PRISM discrepancies*

PRISM datasets are used to test the ability of GCMs to simulate mid-Piacenzian climate, and to provide an insight into the potential causes, mechanisms and effects of global warming. The PRISM project was originally devised to reconstruct surface conditions during the mPWP, including systematically characterising the magnitude and variability of Pliocene SSTs on a global scale. PRISM has evolved through five generations (PRISM 0−4) during the last three decades. The SST reconstruction was introduced in PRISM3, using multiproxy records from 95 globally distributed marine sites (Fig. 4.1; Dowsett et al., 2010a). The PRISM3

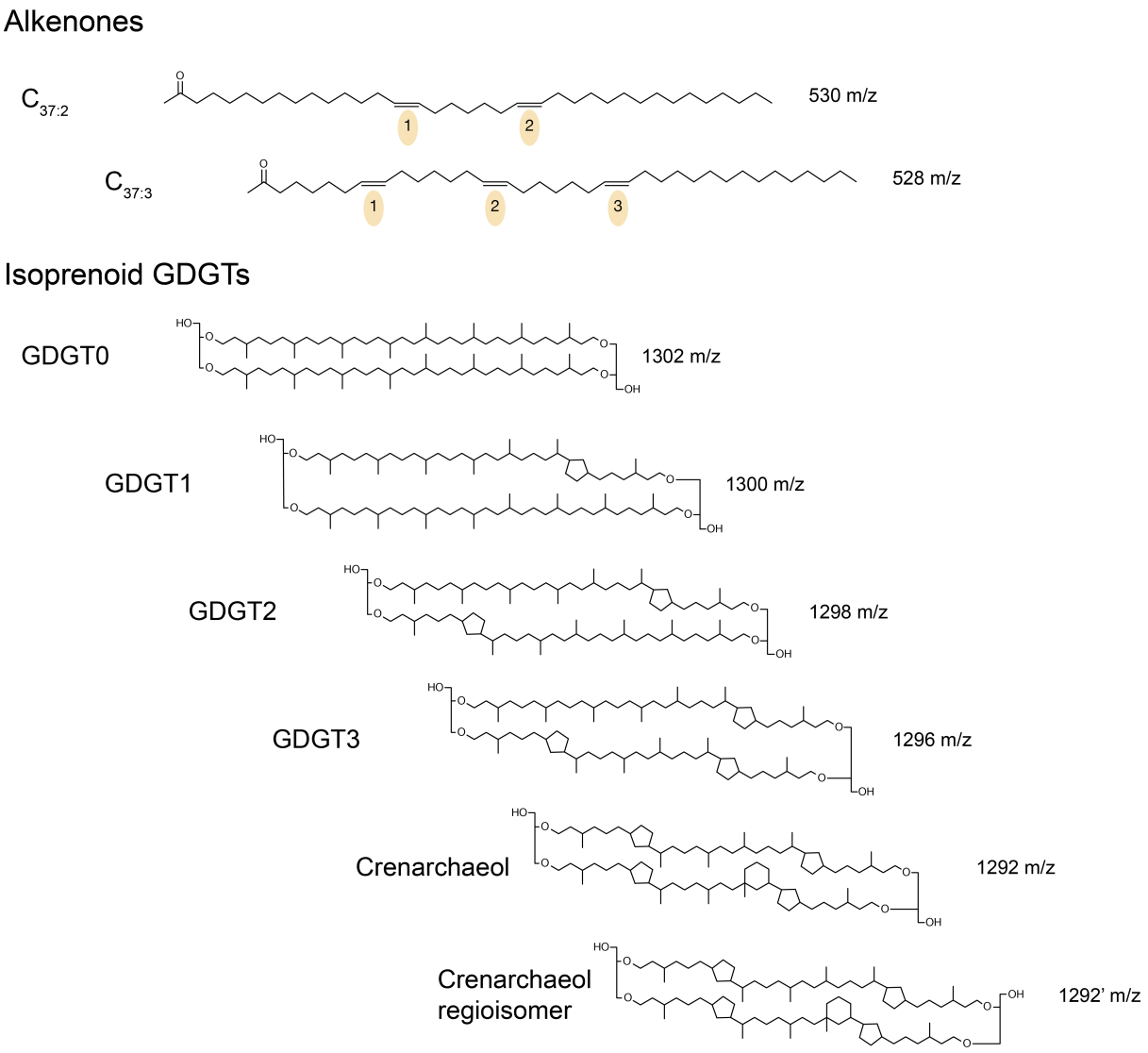


Figure 4.2. Chemical structures of alkenones and isoprenoid glycerol dialkyl glycerol tetraethers (iso-GDGTs) found in marine sediments and used in the $U^{K'}_{37}$ and TEX_{86} temperature proxies, respectively. Mass-to-charge ratios (*m*/*z*) are associated with the analysis and identification of alkenones using gas chromatography-mass spectrometry and iso-GDGTs via high performance liquid chromatography mass spectrometry. The differences in the degree of alkenone unsaturation are highlighted in yellow.

reconstruction was constructed by interpolating between SST anomalies from 86 of these localities. Nine sites were omitted as these are situated within upwelling zones (e.g. DSDP Site 532 on the Walvis ridge which is influenced by the Benguela Current), which are known to produce cooler signals than other estimates at equivalent latitudes. This SST reconstruction remains largely unchanged in the latest PRISM4 generation, which incorporates a further 18 marine localities, adds soils and lakes to the terrestrial realm, and includes new topography

and bathymetry (Dowsett et al., 2016). PRISM4 datasets are used as boundary conditions in the Pliocene Model Intercomparison Project Phase 2 (PlioMIP2) experiments, which focus on modelling climate during the Marine Isotope Stage (MIS) KM5c interglacial (c. 3.205 Ma), a narrower target analogue with near-identical orbital configurations to present day (McClymont et al., 2020).

The majority of mean PRISM ΔSSTs (Fig. 4.1) are calculated by taking the average of faunal-based cold and warm season SST estimates compared to modern (Dowsett et al., 2010a). For PRISM sites which have Mg/Ca and/or alkenone-based SST estimates that do not fall between the faunal-based cold and warm season estimates, the mean annual SST value is calculated on a case-by-case basis (Dowsett et al., 2010a). PRISM proxy data from each site are therefore generally limited to single average SST values that, while fundamental for GCM reconstructions, signify a considerable loss of palaeoenvironmental information which may result in an erroneous understanding of the spatial magnitude of mid-Piacenzian global warming (Dowsett et al., 2013a). It is therefore vital that these average proxy SST estimates are accurate and representative of surface conditions at the time in order to fully comprehend Pliocene climate conditions and fulfil the primary aim of the PRISM project.

Dowsett et al. (2012) assessed the performance of the PRISM3 reconstruction by comparing the zonally averaged mean annual SST results from four principal climate models (the National Centre for Atmospheric Research CCSM4; the Hadley Centre HadCM3; the University of Tokyo/Japan Agency for Marine-Earth Science and Technology MIROC4m and NASA Goddard Institute for Space Studies GISS-ER) to the PRISM SST data. The general shape of the pole-to-pole temperature profile of this four-model average is near-identical to the modern and zonally averaged PRISM SST reconstructions. The similarity of the PRISM reconstruction to the other models highlights the commonalties between Pliocene, present day and near-future climates, relative to ancient warmer intervals (e.g. the Palaeocene-Eocene Thermal Maximum).

Dowsett et al. (2012) show the models are in good agreement with the PRISM proxy datasets in the Southern Hemisphere and Antarctic Ocean. However, the main differences between the SST proxy data and model simulations occur in the NE Atlantic (Fig. 4.3A), where the PRISM3 reconstruction and four-model average appear to underestimate warming by up to 8°C at DSDP Site 552, DSDP Site 610 and ODP Site 907. These sites show increasing SST anomalies with increasing latitude, and the largest differences (up to 10°C) are observed at higher latitude ODP Sites 909 and 911 in the Fram Strait (Fig. 4.3B). Dowsett et al. (2012) attribute these discrepancies to differences in the strength and position of the Gulf Stream and NAC in the GCM simulations, and suggest the PRISM proxy data are accurate and record enhanced poleward oceanic heat transport caused by circulation changes associated with the shoaling of the Central American Seaway c. 3.2 Ma and a reduction in the dynamic support of the Greenland-Scotland Ridge (GSR) (Chapter 3; Robinson et al., 2011; O'Dea et al., 2016). Reduced sea-ice in the NE Atlantic and Nordic Seas and the associated positive feedbacks, whereby the darker sea surface absorbs more heat promoting additional melting and causing SSTs to rise further, are also considered to amplify these increased anomalies (Robinson, 2009).

Dowsett et al. (2012) reviewed the proxy SST records used in the PRISM reconstruction to ensure they are accurate and reliable, reinforce confidence in the proxy datasets and to help rule-out potential causes for the observed discrepancies. All of the proxy SST records were scored (out of 18 points) based on the robustness of the sample age control at each site, sample quality and density, proxy method or technique, and the performance of the proxy method used, in order to semi-quantitatively assess the confidence of the data. Dowsett et al. (2012) defined a quality threshold for alkenone-derived SST estimates, based on sediment concentrations (≥0.3 μg/g). Alkenone records which fulfil this criteria are scored the maximum for sample quality (3 out of 3 points).

In the NE Atlantic alkenone-derived PRISM SST records originate from three DSDP and ODP localities (Fig. 4.3A). Both ODP Sites 909 and 911 are classified as medium-confidence sites

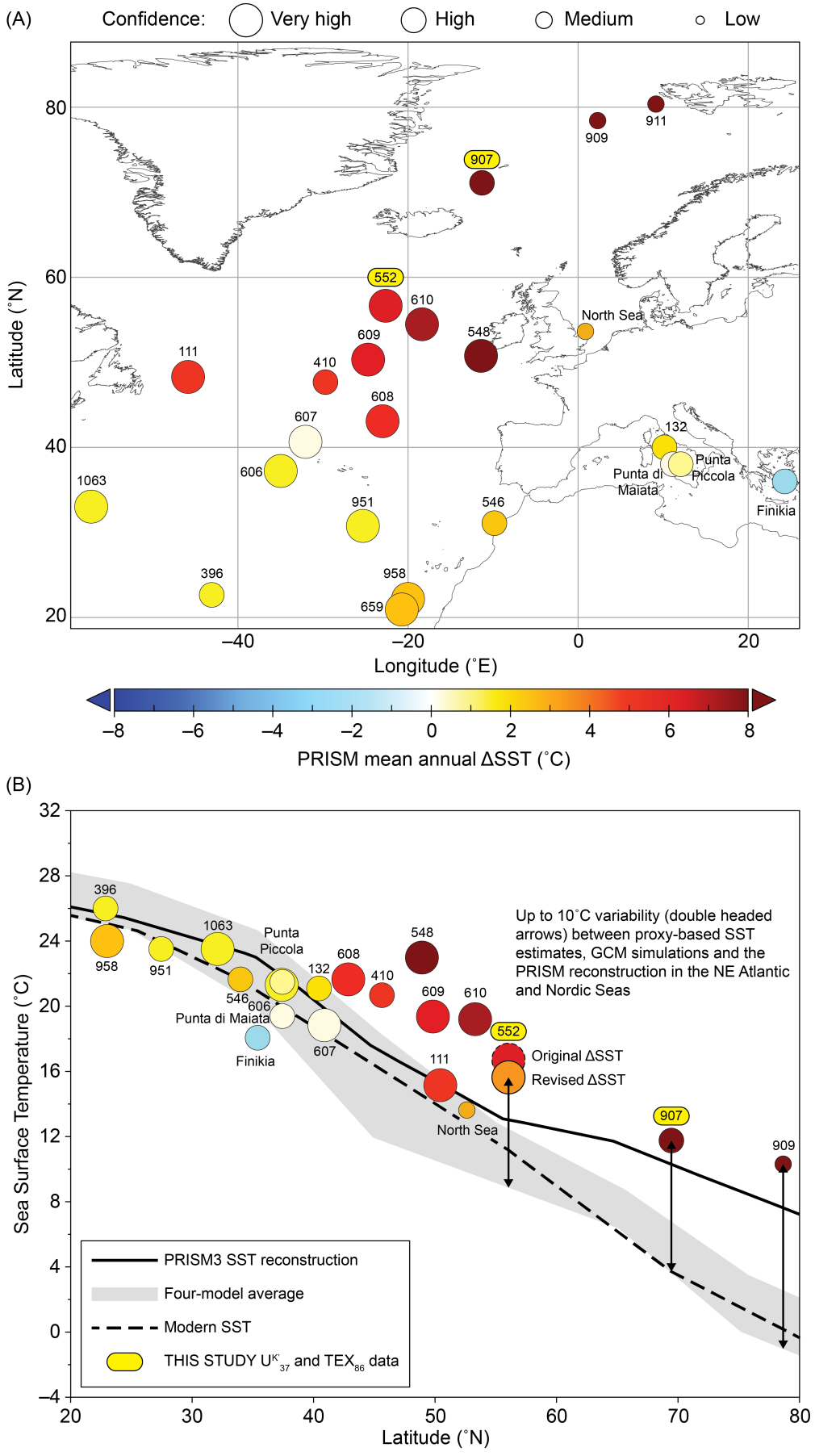

(A)
Confidence:
Very high
High
Medium
Low
Latitude (˚N)
Longitude (˚E)
PRISM mean annual ΔSST (˚C)
North Sea
Punta Piccola
Punta di Maiata
Finikia
(B)
Sea Surface Temperature (˚C)
Latitude (˚N)
Up to 10˚C variability (double headed arrows) between proxy-based SST estimates, GCM simulations and the PRISM reconstruction in the NE Atlantic and Nordic Seas
Original ΔSST
Revised ΔSST
PRISM3 SST reconstruction
Four-model average
Modern SST
THIS STUDY U^K'37 and TEX86 data

Figure 4.3 (previous page). Regional summary of PRISM SST datasets and the relationship with GCM simulations. (A) Map showing the distribution of PRISM localities, regional ΔSSTs, and the reliability of each locality estimate in the NE Atlantic and Nordic Seas. (B) PRISM dataset SST estimates superimposed on zonally averaged multimodal mean annual SSTs from four climate model simulations shown as a grey band with width equal to ±2σ. Zonally averaged modern mean annual SST shown as dashed line, PRISM3 reconstruction shown as solid line. Alkenone records originating from sites discussed in this study are highlighted yellow. Modified from Dowsett et al. (2012).

(11 and 12 points, respectively) based exclusively on alkenone records, with good geomagnetic and nannofossil datums (Myhre and Thiede, 1995; Mattingsdal et al., 2014). However, both sites feature only a handful of $U^{K'}_{37}$ samples (ODP Site 909, nine samples; ODP Site 911, four samples). DSDP Site 552 is classified as a very-high confidence site (16 points), with robust geomagnetic age control (Lazarus et al., 1995). SSTs at DSDP Site 552 are based on planktic foraminifera, verified by Mg/Ca and alkenone (13 samples) palaeothermometry. Unfortunately, the concentration of the alkenones injected during analysis remain unpublished at these localities (Robinson et al., 2008; Robinson, 2009), and are not included in the official USGS Data Release of PRISM alkenone-derived SST data (Dowsett et al., 2017). However, it is possible to infer the injected concentrations using information about the quantity of sediment extracted and the dilution at which these samples were analysed. At ODP Site 909, the average sediment C_{37} concentration is 0.10 µg/g (Robinson, 2009), well below the recommended limit for PRISM datasets (Dowsett et al., 2012). At ODP Site 911, the average sediment C_{37} concentration is 0.33 µg/g (Robinson, 2009), only slightly above the recommended limit. Robinson (2009) extracted c. 7 g of sediment from both sites and diluted the alkenones in c. 200 µl toluene prior to analysis, where the injection volume was 1 µl. This equates to an average concentration of 3.77 ng/µl for ODP Site 909 and 11.55 ng/µl for ODP Site 911, which are significantly low and most likely susceptible to the effects of irreversible adsorption (Villanueva and Grimalt, 1996).

At DSDP Site 552, the sediment C_{37} concentrations are unpublished (Robinson et al., 2008). Dowsett et al. (2012) suggest they meet the required minimum threshold set for PRISM datasets (0.3 µg/g). However, personal communication with Lawrence (2020), the original

alkenone analyst in the Robinson et al. (2008) study, reveals the sediment concentrations were actually lower (0.013−0.201 µg/g) than the threshold set by Dowsett et al. (2012). Robinson et al. (2008) extracted c. 5 g of sediment and diluted the alkenones in c. 200 µl toluene prior to analysis. Robinson et al. (2008) states the injection volume was 1 µl. However, Lawrence (2020) says the injection volume was actually raised to 5 µl, to counteract known low concentrations associated with North Atlantic sediment samples. Using this information, we can infer the injection concentrations in the Robinson et al. (2008) study were between 0.06−1.00 ng/µl for DSDP Site 552. Again, this is extremely low and demonstrates that even larger injection volumes from these localities will be susceptible to the effects of irreversible adsorption. Ultimately, the alkenone-based SSTs at all three sites are likely to be biased towards warmer temperatures due to these low C_{37} concentrations.

This highlights the significant uncertainty associated with the current characterisation of $U^{K'}_{37}$-derived SST estimates in the NE Atlantic, which are only based on a small number (n = 26) of samples with very low concentrations (<12 ng/µl). These samples are responsible for some of the highest observed SST anomalies in the global PRISM reconstruction. Consequently, it is important to verify these alkenone records to determine the true magnitude of regional warming and to assess the potential influence of low concentrations on the regional PRISM proxy/model discrepancies.

4.3 NE ATLANTIC ALKENONE DATASETS

Since the publication of the PRISM3 reconstruction (Dowsett et al., 2010a), there have been multiple studies which have produced high-resolution regional alkenone records from various DSDP/ODP/Integrated Ocean Drilling Program (IODP) sites (Fig. 4.4) throughout the late Neogene and Quaternary (De Schepper et al., 2013; Lawrence et al., 2009; Herbert et al., 2016; Bachem et al., 2017; Schreck et al., 2013; Dowsett et al., 2017; Clotten et al., 2018; Naafs et al., 2020). Here, we present a compilation (Fig. 4.5) of all available $U^{K'}_{37}$ records to gain an independent insight into the characterisation of SST estimates in this region and to

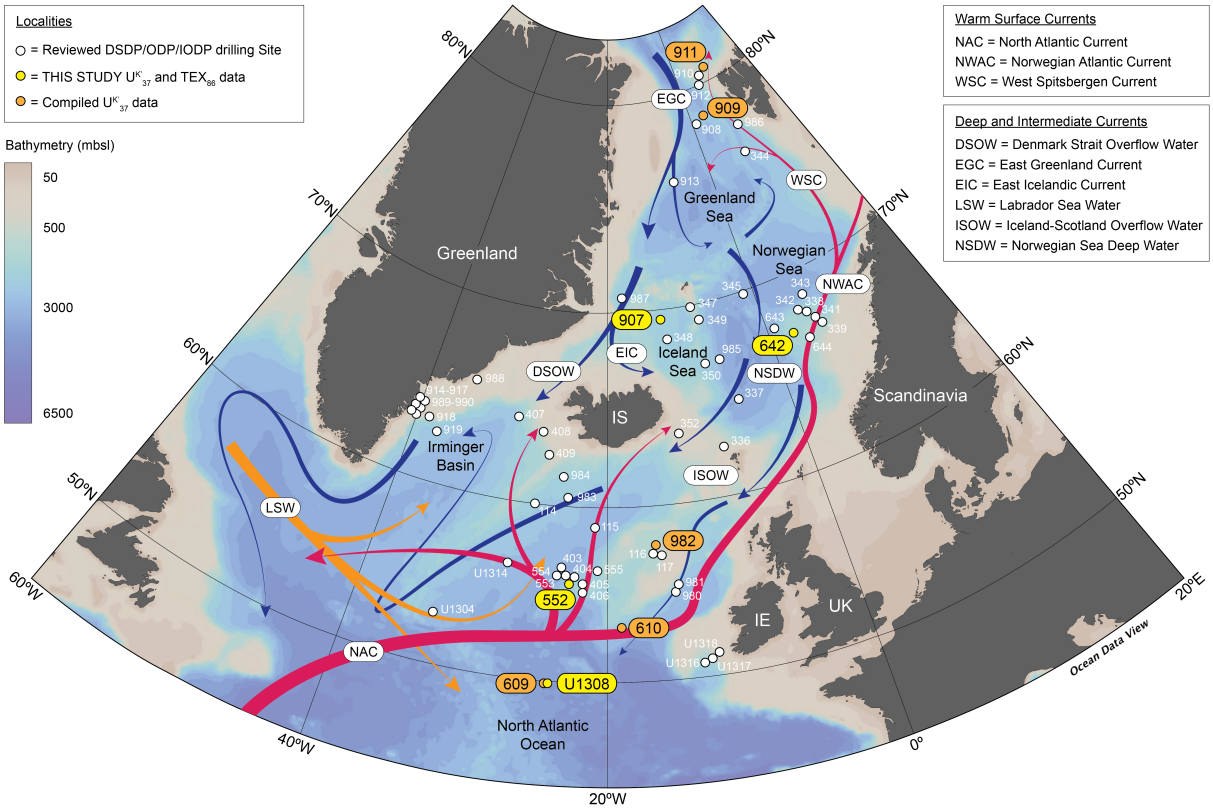
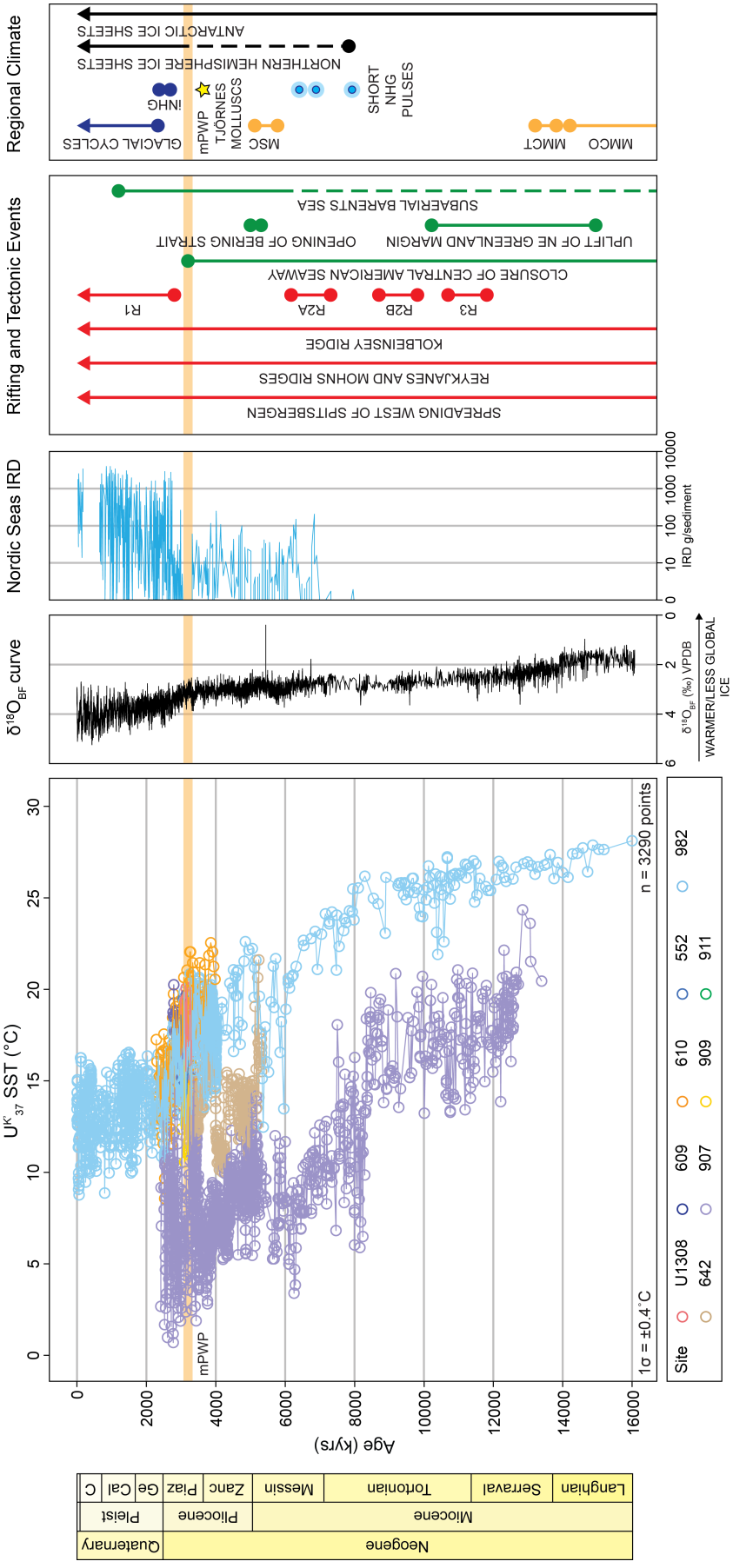


Figure 4.4. Location map of DSDP/ODP/IODP drilling sites reviewed in the NE Atlantic Ocean and Nordic Seas. Orange sites contain existing Pliocene alkenone records. Yellow sites indicate the origin of new alkenone and and TEX_{86} records discussed in this study. Red, orange and blue arrows indicate surface, intermediate and deep ocean currents respectively. Bathymetric map created in Ocean Data View v.5.1.7.

reveal the magnitude of warming shown by existing records during the PRISM-interval. The $U^{K'}_{37}$ records (Table 4.1) are sourced from published scientific literature, the PANGAEA and NCEI palaeoclimate databases and Drilling Program Scientific Reports. This compilation is the first collection of alkenone records from the NE Atlantic and comprises 3290 SST estimates (Table 4.1). Age models for all sites were updated to the astronomically-tuned Neogene time scale (ATNTS) 2012 using the geomagnetic and biostratigraphic calibration points of Backman et al. (2012), Hilgen et al. (2012) and Wade et al. (2011).

Our compilation (Fig. 4.5) reveals a good distribution of $U^{K'}_{37}$ records throughout the late Neogene to present day in the NE Atlantic. The Pliocene Epoch features the greatest quantity of available SST estimates (70%), and the Holocene and Pleistocene Epochs feature the least (14%). The oldest SST records are from the Miocene (16%), where the regional record extends back c. 16 myrs to the Langhian Stage. 47% of the SST estimates in our compilation are derived from sites in the NE Atlantic (Fig. 4.4), situated on the Feni Drift in the Rockall Trough (DSDP Site 610), the Rockall Plateau (DSDP Site 552 and ODP Site 982) and the eastern flank of the Mid-Atlantic Ridge (MAR; DSDP Site 609 and IODP Site U1308). The remaining 53% of $U^{K'}_{37}$ records are sourced from sites in the Nordic Seas (Fig. 4.4) on the eastern Icelandic (ODP Site 907) and Vøring Plateaus (ODP Site 642), and the Hovgaard Ridge (ODP Site 909) and Yermak Plateau (ODP Site 911) near the Fram Strait. All of the $U^{K'}_{37}$ records originate from sites which are situated well below 1 km water depth, with a maximum depth of 3871 m (IODP Site U1308). The longest ranging and most continuous alkenone-derived SST record is found at ODP Site 982 (37% of the total assembled data), which reveals a relatively high-resolution insight into SST patterns from the early-Miocene to present day (Herbert et al., 2016). In terms of the PRISM-interval datasets, there are 337 alkenone-derived SST estimates with 28% from the Nordic Sea and 72% from the NE Atlantic.

Overall, the average alkenone-derived SST trends in the NE Atlantic are seen to reduce by up to 10.7°C throughout the late Neogene and Quaternary (Fig. 4.5). The SST signature in the Holocene and Pleistocene rapidly fluctuates reflecting the climatic changes caused by the


Regional Climate
Rifting and Tectonic Events
Nordic Seas IRD
$\delta^{18}O_{BF}$ curve
$U^{K'}_{37}$ SST (°C)
Age (kyrs)
mPWP
n = 3290 points
1σ = ±0.4°C
Site U1308 642 609 907 610 909 552 911 982
$\delta^{18}O_{BF}$ (‰) VPDB
WARMER/LESS GLOBAL ICE
IRD g/sediment
SPREADING WEST OF SPITSBERGEN
REYKJANES AND MOHNS RIDGES
KOLBEINSEY RIDGE
CLOSURE OF CENTRAL AMERICAN SEAWAY
UPLIFT OF NE GREENLAND MARGIN
OPENING OF BERING STRAIT
SUBAERIAL BARENTS SEA
R1
R2A
R2B
R3
MMCO
MMCT
SHORT NHG PULSES
MSC
TJÖRNES MOLLUSCS
mPWP
iNHG
GLACIAL CYCLES
NORTHERN HEMISPHERE ICE SHEETS
ANTARCTIC ICE SHEETS
Neogene
Quaternary
Miocene
Pliocene
Pleist
Langhian
Serravai
Tortonian
Messin
Zanc
Piaz
Ge
Cal
C

Site	Lat (DD)	Long (DD)	Data source	Age model source	Interval, Ma	No. of data points
609	49.885°N	24.241°W	Robinson et al. (2008)	Bartoli et al. (2005)	2.975–3.282	28
			Naafs et al. (2020)		2.766–2.933	21
U1308	49.885°N	24.241°W	Dowsett et al. (2017)	Flesche Kleiven et al. (2002); De Schepper, Head and Groeneveld (2009)	3.109–3.297	116
610	53.299°N	18.942°W	De Schepper et al. (2013)	De Schepper and Head (2008); Naafs et al. (2020)	3.252–3.330	25
			Naafs et al. (2020)		2.284–3.975	115
552	56.048°N	23.241°W	Robinson et al. (2008)	Lazarus et al. (1995)	2.977–3.286	19
982	57.775°N	15.866°W	Lawrence et al. (2009)	Venz et al. (1999); Venz and Hodell (2002)	0.000–4.012	1001
			Herbert et al. (2016)		3.957–15.996	206
642	67.218°N	2.9186°E	Bachem et al. (2017)	Bleil (1989); Risebrobakken et al. (2016)	3.140–5.321	395
907	69.508°N	12.931°W	Schreck et al. (2013)	Channell et al. (1999)	3.160–13.390	9
			Herbert et al. (2016)		2.863–13.075	1173
			De Schepper et al. (2015)		3.550–6.000	22
			Clotten et al. (2018)		2.413–3.402	147
909	78.601°N	3.171°E	Robinson (2009)	Myhre et al. (1995)	3.000–3.200	9
911	80.596°N	8.394°E	Robinson (2009)	Sato and Kameo, (1996); Myhre et al. (1995)	3.300	4

Figure 4.5 (previous page). Compilation of NE Atlantic and Nordic Sea alkenone records derived from the 0−8000 kyr interval. Composite data are color-coded based on DSDP/ODP/IODP site, shown in Fig. 4.4. The average alkenone-derived SST trends in the NE Atlantic are seen to reduce by up to 10.7°C throughout the late Neogene and Quaternary. Published records of $\delta^{18}O$ in benthic foraminifera ($\delta^{18}O_{BF}$) (Zachos et al., 2001), NE Atlantic rifting (Doré and Lundin, 1996), V-shaped ridge (R1 etc.) formation (Jones et al., 2002) and climatic events (De Schepper et al., 2013) are also shown. MMCO, Middle Miocene Climatic Optimum; MMCT, Middle Miocene Climatic Transition; MSC, Messinian Salinity Crisis; iNHG, intensification of the Northern Hemisphere Glaciation. Orange bar denotes the PRISM-interval (3.025−3.264 Ma).

Table 4.1 (previous page). Sources of alkenone-based SST records used in the NE Atlantic Ocean and Nordic Seas compilation. All primary age control points were updated to ATNTS 2012 using the calibration points of Backman et al. (2012), Hilgen et al. (2012) and Wade et al. (2011). Latitude and longitude in decimal degrees (DD).

intensification of the Northern Hemisphere Glaciation (iNHG) (c. 2.7 Ma) and an increase in the amplitude of glacial-interglacial cycles. In the NE Atlantic, this signature varies between 8.7°C and 16.2°C, with an average SST of 12.7°C during the late-Pleistocene and Holocene (0.773−0 Ma). During the early-Pleistocene (2.58−0.773 Ma), the temperature varies between 8.5°C and 17.5°C, with an average SST of 13.6°C. Alkenone-derived records in the Nordic Seas do not begin until c. 2.43 Ma. The lack of younger records at these higher latitude sites is attributed to the regional cooling associated with the iNHG which culminated in the intense glacial/interglacial cycles indicative of the Quaternary (Ternois et al., 1998). The associated harsh polar conditions and sea-ice formation are known to generally restrict alkenone production to warmer summer months, and consequently the alkenone concentrations preserved at these sites are vanishingly small (Samtleben and Bickert, 1990; Thomsen et al., 1998). Throughout the Pliocene, the SST estimates in the Nordic Seas vary between 0.6°C and 21.5°C, with an average value of 9.6°C. At the lower latitude NE Atlantic sites, the SSTs are expectedly warmer and vary between 11.0°C and 22.6°C, with an average temperature which is 4.0°C warmer compared to Nordic localities. During the Miocene, we observe the highest SST estimates in the NE Atlantic which vary between 12.4°C and 28.1°C, with an average value of 24.3°C. In the Nordic Seas, the alkenone-derived SST record extends back

to 13.39 Ma in the Serravallian Stage and varies between 3.3°C and 24.3°C, with an average value which is 10.5°C cooler compared to the NE Atlantic.

Our compilation includes the original alkenone SST records (DSDP Site 552, DSDP Site 609, ODP Site 909 and ODP Site 911) from the PRISM reconstruction (Robinson et al., 2008; Robinson, 2009), and includes new SST records from IODP Site U1308, ODP Site 907, ODP Site 642, DSDP Site 610 and ODP Site 982 (Fig. 4.4, 4.5) which also span the PRISM-interval. During the PRISM-interval (Fig. 4.6), SSTs in the Nordic Seas have an average temperature of 11.5°C. Nordic Sea SSTs peak at 16.9°C around 3.02 myrs ago at ODP Site 907. The average SSTs in the NE Atlantic are 5.9°C warmer during this time slice, varying between 12.6°C and 22.0°C. The warmest NE Atlantic SSTs occur at DSDP Site 610 around 3.25 myrs ago. DSDP Site 552, one of the key PRISM dataset localities, has an average $U^{K'}_{37}$-derived SST of 16.9°C, equating to a temperature anomaly of 5.3°C compared to present-day (Robinson et al., 2008). It is important to highlight, the temperature estimates derived from these additional sites fall within range of PRISM temperature anomalies, which indicate warming of up to 6°C in the NE Atlantic and up to 8°C in the Nordic Seas during the mPWP compared to modern.

Unfortunately, none of these studies publish the concentration of alkenones injected during analysis and therefore it is challenging to assess whether these SST records are influenced by warming biases associated with chromatographic irreversible adsorption. Using the sediment concentrations published by Robinson (2009), Robinson et al. (2008) and discussed with Lawrence (2020), we have inferred that the PRISM-interval SSTs at ODP Site 909, ODP Site 911 and DSDP Site 552 are most likely derived from very low concentrations (Fig. 4.6; <12 ng/ul). Clotten et al. (2018) published their sediment concentrations for ODP Site 907, with an average concentration of 0.031 µg/g during the PRISM-interval. Clotten et al. (2018) extracted 4.58 g of sediment, on average, and diluted the alkenones in c. 200 µl hexane prior to analysis, where the injection volume was 1 µl. This equates to an average concentration of 0.66 ng/µl, which again is extremely low (Fig. 4.6). Lawrence et al. (2013) publish the sediment

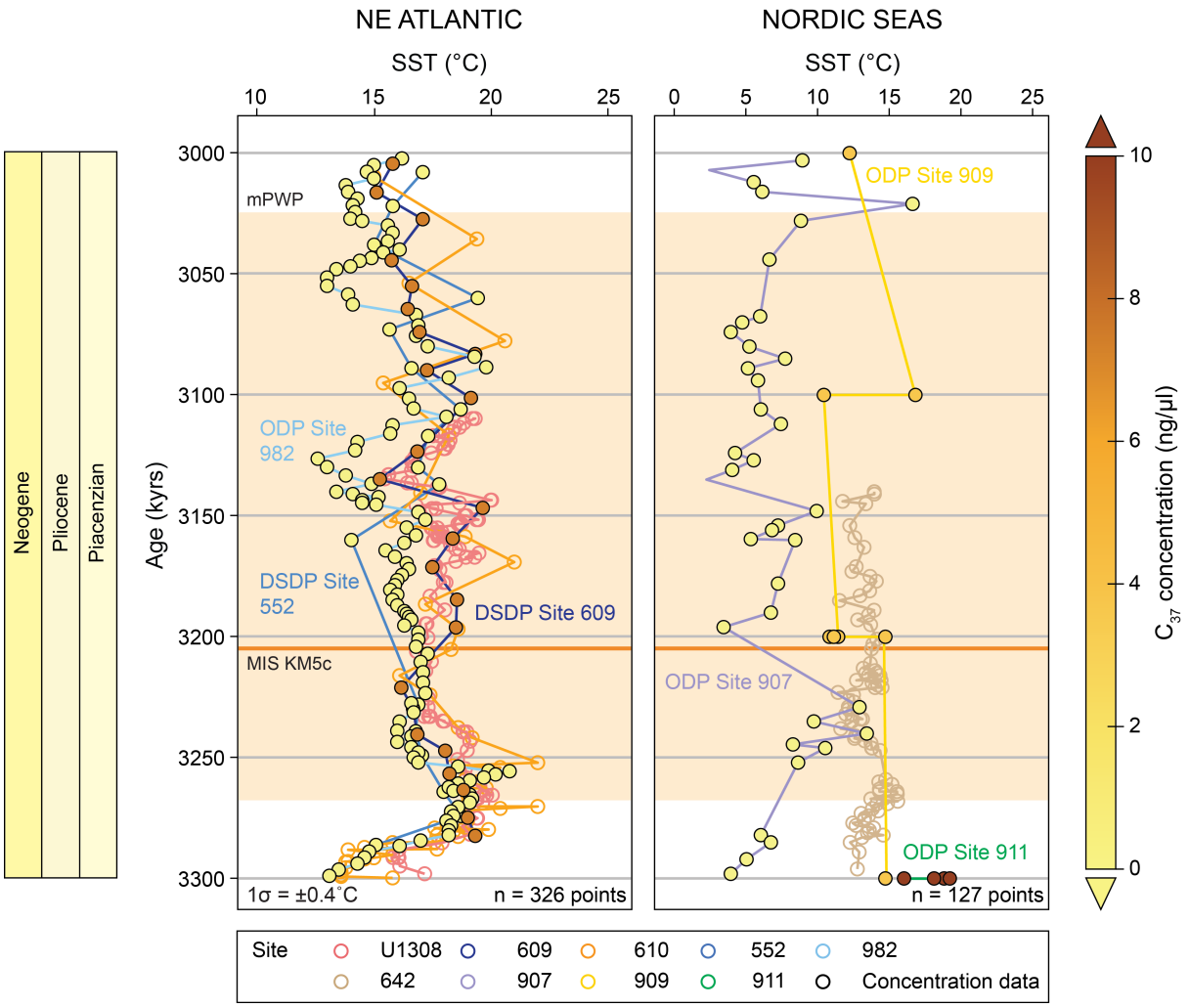


Figure 4.6. Compilation of NE Atlantic and Nordic Sea alkenone records derived from the mPWP. Composite data are color-coded based on DSDP/ODP/IODP site, shown in Fig. 4.4. SSTs in the NE Atlantic are 5.9°C warmer, on average, compared to the Nordic Seas during the PRISM-interval, highlighted in orange. MIS KM5c, Marine Isotope Stage KM5c (dark orange line). Injected C_{37} concentrations are inferred from existing studies, where information on injection volumes, dilutions and sedimentary concentrations are published. Alkenone-based SSTs are derived from very low concentrations (<12 ng/ul) at DSDP Site 552, DSDP Site 609, ODP Site 907, ODP Site 909, ODP Site 911 and ODP Site 982, as shown by the colour ramp.

concentrations for ODP Site 982, and demonstrate an average C_{37} concentration of 0.14 µg/g during the mPWP. Lawrence et al. (2009) and Herbert et al. (2016) extracted c. 5 g of sediment, and diluted the alkenones in 200 µl toluene prior to analysis, where the injection volume was 5 µl. This equates to an average injected concentration of 0.70 ng/µl, which is very low and comparable with those at the other sites. Importantly, concentrations this low are known to be

susceptible to irreversible adsorption during GC quantification, which can result in significant warming biases and overestimation of SSTs (Villanueva and Grimalt, 1996).

This highlights the need to verify alkenone-based SST records at various DSDP/ODP/IODP sites in the NE Atlantic and Nordic Seas throughout the PRISM-interval, to establish whether the enhanced magnitude of warming observed in this region is a consequence of low alkenone concentrations, as suggested by our examination of DSDP Site 552, ODP Site 907, ODP Site 909 and ODP Site 911. Importantly, this will enable us to determine the extent to which NE Atlantic warming and related discrepancies between proxy records and GCM simulations, are possibly influenced by warming biases associated with irreversible adsorption. Here, new high-resolution alkenone and TEX_{86}-derived SST estimates from four regional localities (Fig. 4.4) throughout the PRISM-interval provide an opportunity to verify and re-examine existing SST anomalies, assess whether these records are susceptible to irreversible adsorption associated with low concentrations, and determine the potential influence of proxy warming biases on existing discrepancies between PRISM SST datasets and GCM simulations. Using our new datasets we will examine the following questions:

1. What is the magnitude of alkenone-derived sea-surface warming in the NE Atlantic and Nordic Seas during the mPWP, and is this compatible with previous records?
2. What are the alkenone concentrations used to estimate regional SSTs?
3. Are the injected concentrations susceptible to irreversible adsorption during analysis, does this phenomenon result in an overestimation of SSTs and can this effect be corrected for?
4. Are the corrected alkenone-derived SST estimates compatible with the magnitude of warming predicted by existing multiproxy SSTs and GCM simulations?
5. What effect will these corrected SST estimates have on existing PRISM reconstructions and our understanding of mPWP climate in the NE Atlantic and Nordic Seas?

4.4 MATERIAL, AGE MODEL AND METHODS

Four DSDP/ODP/IODP sites across the North Atlantic and Nordic Seas (Fig. 4.4), ranging in latitude from the Icelandic Plateau at 69.508°N to the eastern flank of the MAR at 49.885°N, were selected based on continuous and good recovery throughout the late Neogene and Quaternary and moderate to high (>2 cm/kyr) pelagic sedimentation rates, which are favourable for alkenone preservation and allow for high time resolution (Herbert, 2006). Two of these sites (DSDP Site 552 and ODP Site 907) are important localities in the PRISM reconstruction. Selecting the same sites enables us to verify the magnitude of warming at these localities and determine whether existing alkenone-based SST estimates are derived from low alkenone concentrations. Two sites (IODP Site U1308 and ODP Site 642) are not included in the PRISM reconstruction. However, these sites allow us to assess the regional variation in alkenone-derived temperature change and concentrations.

IODP Site U1308 was drilled during IODP Leg 303, on the upper-middle eastern flank of the MAR approximately 1000 km southwest of Ireland in the NE Atlantic (49.885°N, 24.241°W), at a water depth of 3871 m, and constitutes a reoccupation of DSDP Site 609 (Fig. 4.4). DSDP Site 609 has intervals of poor recovery, so six holes were drilled at IODP Site U1308 and a composite splice was constructed to 262 metres composite depth (mcd). IODP Site U1308 features high recovery (95.4%) of calcareous oozes until the mid-Pliocene, and no documented hiatuses. The age model for IODP Site U1308 is based on the correlation of the Hodell and Channel (2016) high-resolution benthic $\delta^{18}O$ record to the LR04 benthic $\delta^{18}O$ stack. DSDP Site 552 was drilled during DSDP Leg 81, on the western flank of the Rockall Plateau around 860 km west of Ireland in the NE Atlantic (56.048°N, 23.241°W), at a water depth of 2301 m (Fig. 4.4). Here we focus on DSDP Hole 552A, which extends back to the middle Eocene and features high recovery of calcareous oozes (99.7%). The age model for DSDP Hole 552A is based on the magnetostratigraphy of Lazarus et al. (1995), updated to the ATNTS (Hilgen et al. 2012). ODP Site 907 was drilled during ODP Leg 151, on the eastern Icelandic Plateau (69.508°N, 12.931°W) approximately 330 km north of Iceland in the Icelandic Sea, at

a water depth of 1801 m (Fig. 4.4). Here we focus on ODP Hole 907A, which extends back to the middle Miocene, features high recovery (102.6%) of mud and claystone and contains no documented hiatuses. The age model for ODP Hole 907A is based on the magnetostratigraphy of Myhre (1989), updated to the ATNTS (Hilgen et al. 2012). ODP Site 642 was drilled during ODP Leg 104, on the Vøring Plateau approximately 450 km west of Norway in the Nordic Seas (67.218°N, 2.9186°E), at a water depth of 1286 m. Here we focus on ODP Hole 642B, which extends back to the late Miocene and features high recovery (97.5%) of mud and claystone. ODP Hole 642B features a well-documented hiatus (c. 0.5 myrs) at c. 66.40 m below seafloor (mbsf), where parts of the late Pliocene Gauss polarity chron are missing (Bleil, 1989). The age model for ODP Hole 642B recognises this hiatus and is based on the magnetostratigraphy of Bleil (1989), updated to the ATNTS (Hilgen et al. 2012).

In order to characterise the alkenone concentrations and produce new biomarker-based SST estimates, all four cores were sampled at the IODP Bremen Core Repository. All cores were sampled initially at very low resolution (one sample per 250−1000 kyrs) throughout the late-Miocene to present day (8−0 Ma), and at a slightly higher resolution (one sample per c. 100−250 kyrs) during the mPWP interval to gain a preliminary overview of alkenone concentrations and temperature estimates throughout each core. Following this pilot study, DSDP Hole 552A and ODP Hole 642B cores were later resampled at a higher resolution (one sample per c. 12 kyrs) throughout the mPWP to determine a greater temporal and spatial understanding of SST changes during this warm interval. 15 samples were selected from IODP U1308 core sections 2H-4 through 24H-4, between 17.26−242.91 mcd (0.27−3.10 Ma). 56 samples were selected from DSDP Hole 552A core sections 1H-3 through 34H-3, between 3.93−162.28 mbsf (0.20−5.85 Ma). 64 samples were selected from ODP Hole 642B core sections 2H-1 through 12H-5, between 5.77−102.29 mbsf (0.12−7.32 Ma). 40 samples were selected from ODP Hole 907A core sections 1H-3 through 12H-2, between 4.33−104.23 mbsf (0.20−7.99 Ma).

The 175 core samples selected for biomarker analysis, each comprising c. 20 g of sediment, were initially weighed and washed-down over a 63 μm sieve, until the Milli-Q® deionised water ran clear, to remove clays and extract coarse foraminifera residues. The fines were collected for biomarker analysis and dried overnight at 40°C (Appendix A.3). The fines were powdered using a solvent-cleaned agate pestle and mortar and freeze-dried, before extraction by repeated heating at 40°C for 1 hour using a dichloromethane/methanol mixture (3:1 v/v). Extractions were repeated at least three times or until the supernatant was colourless. After each extraction step, the extracts were centrifuged at 3000 revolutions per minute (rpm) for 3 minutes, before the supernatants were combined and concentrated, using a rotary evaporator, under vacuum. An aliquot of these total lipid extracts (TLE) was separated further into three sub-fractions using silica-gel column chromatography: aliphatic hydrocarbons/*n*-alkanes, aldehydes and ketones, and alcohols by elution with *n*-hexane, dichloromethane and a dichloromethane/methanol (95:5 v/v) mixture, respectively. The polar fractions were re-dissolved in 200 μl of *n*-hexane/*i*-propanol (99:1 v/v) and filtered using a 0.45 μm polytetrafluoroethylene (PTFE) syringe filter prior to analysis.

4.4.1 *Alkenones*

Alkenone samples were diluted with a small volume (10−50 μl) of *n*-hexane, before being quantified at the University of Birmingham using an Agilent® 7890B gas chromatograph (GC) system interfaced with a flame ionisation detector (FID), with hydrogen as a carrier gas (constant pressure: 277.01 kPa). Compound separation was achieved using a new Restek® Rtx-200 column (105 m; diameter: 0.25 mm; film thickness: 0.25 μm; coating: 100% crossbond trifluoropropylmethyl polysiloxane). Alkenones (Fig. 4.2) were identified using an Agilent® 5977A GC system interfaced with an Agilent® 5977A Mass Selective Detector (MSD), with helium as a carrier gas (constant pressure: 38.43 kPa). Compound separation was achieved using a Trajan® BP5MS column (60 m; diameter: 0.32 mm; film thickness: 0.25 μm; coating: 5% phenyl polysilphenylene-siloxane). Injection volumes were 1 μl. Both GC ovens were held at 70°C for 1 min, before the temperature was ramped up to 150°C at 30°C min^{-1} and then to

320°C at 3°C min^{-1}, where the temperature was held for 10 minutes. The MSD ion source and interface temperatures were 230°C and 280°C, respectively, the ionisation energy was 70 eV, and the scan width was 50−800 atomic mass units.

The alkenones were quantified by comparing their peak areas with that of heptatriacontane ($C_{37}H_{76}$) (10 $\mu g ml^{-1}$) in our laboratory external standard run prior to every sequence and after every 10 samples. One quarter of the total samples were analysed in triplicate and the mean analytical error (1σ) associated with the $U^{K'}_{37}$ index is ±0.007, which translates into an average temperature uncertainty of ±0.2°C. No alkenones were detected in one sample from IODP Site U1308, six samples from DSDP Site 552, six samples from ODP Site 642 and 15 samples from ODP Site 907. Site-specific ΔSSTs are calculated relative to modern SSTs obtained from the NOAA World Ocean Atlas (Levitus and Boyer, 1994) following the methods of Dowsett et al. (2010a).

4.4.1.1 Correcting $U^{K'}_{37}$ results for irreversible adsorption effects

In order to correct for the effects of irreversible adsorption, the sensitivity of our GC-FID system was assessed by producing a dilution series (Fig. 4.7) which involved analysing one sample repeatedly at 16 different dilutions (10−250 µl). The $C_{37:2}$ and $C_{37:3}$ peaks from each analysis were integrated, before total C_{37} concentrations were calculated and plotted against estimated SSTs using the calibration of Conte et al. (2006). A third-degree polynomial was plotted in the statistical programme R, which has the best fit to our data. A third-degree polynomial was selected on the physical basis for expecting a function with a central section where the temperature estimate is good, and the over/underestimation of SSTs at low/high concentrations.

Our dilution series (Fig. 4.7) demonstrates SST estimates from the same sample can vary by up to 5.8°C, depending on C_{37} concentration. At higher concentrations, we observe a cooling

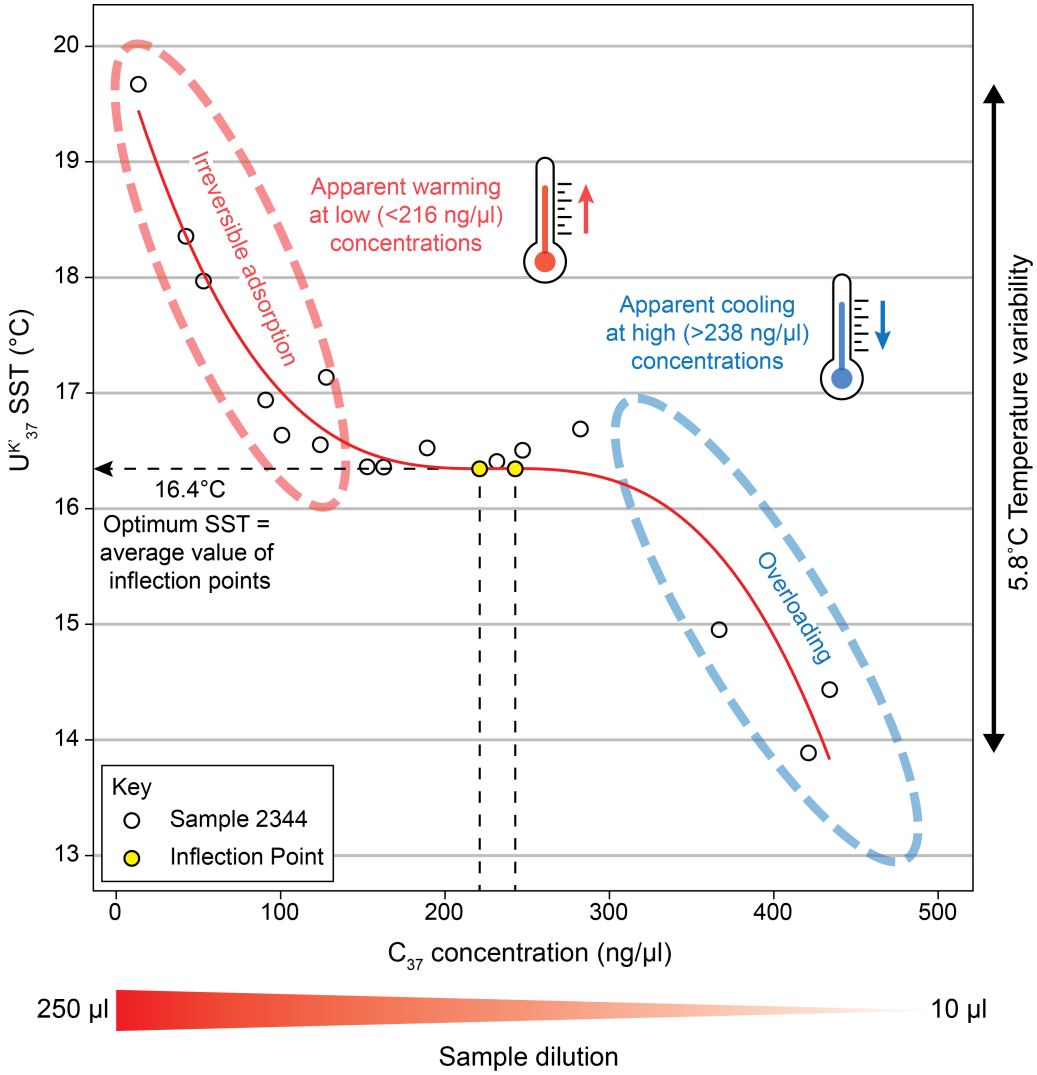


Figure 4.7. Alkenone dilution series showing changes in SSTs with decreasing concentration of total alkenones. A dilution series enables analysts to assess the sensitivity of a GC system to the effects of irreversible adsorption. Repeated analysis of the same sample (#2344) at 16 different dilutions (10−250 µl) reveals large (5.8°C) temperature variability in the SST estimates. At low concentrations (<216 ng/ul), samples are susceptible to warming biases and at higher concentrations (>238 ng/ul) samples are prone to cooling biases associated with overloading. Samples with injection concentrations between the inflection points are generally unaffected by irreversible adsorption and overloading. SST calibration derived from Conte et al. (2006) (circles; Eq. 4.2).

bias. This may be caused by a number of factors relating to interactions between the compounds and the column. Peak shape can change at higher concentrations when the sample capacity of the stationary phase is exceeded (overloading), resulting in abnormal shapes which are either asymmetric with a wider front half (peak fronting) or flat topped (clipped) (Rood, 2007). Our higher concentration samples exhibit asymmetric peaks symbolic

of peak fronting. Higher concentration injections on our GC column and system most likely resulted in a greater relative proportion of the $C_{37:3}$ species versus the $C_{37:2}$ homologue, in contrast with the lower concentration samples, generating lower $U^{K'}_{37}$ values and cooler SST estimates.

In order to correct for the effects of irreversible adsorption and overloading (Appendix A.4) we found the equation of the third-degree polynomial, and calculated the average temperature of the line at the inflection points (x = 0) by differentiation. This average temperature (16.4°C) is the most accurate and representative temperature for the sample analysed, and is believed to be least affected by irreversible adsorption and overloading. We then took our remaining C_{37} concentrations measured under the same GC-FID conditions, and using the polynomial equation, we calculated a predicted temperature for each sample, which fits the data points to our dilution series curve. We then calculated the difference between this predicted temperature, and our average temperature value derived from the inflection points. To correct for warming and cooling biases associated with irreversible adsorption and overloading, respectively, we subtracted this difference from the original raw temperatures calculated using the Conte et al. (2006) calibration for each respective sample.

Our dilution series (Fig. 4.7) can correct temperatures derived from alkenone samples which have concentrations between 0−435 ng/µl. Reducing the dilution further (<10 µl) or injecting directly would inevitably expand this range. However, we avoided this to prevent losing the whole sample. Correcting our triplicate SSTs reveals the average temperature uncertainty (1σ) is ±0.6°C for values amended using our dilution series. Importantly, our dilution series reveals that alkenone-based SST estimates derived from samples with low injection concentrations (<216 ng/µl) are susceptible to a warming bias, whereas SSTs derived from samples with a high concentration (>238 ng/µl) are biased towards cooler temperatures. Verifying our dilution series using a separate identical GC-FID set-up and the same alkenone sample, would help support the validity of our dilution series and derived corrections. This was unachievable since the whole TLE from this sample was separated into single sub-fractions to maximise our C_{37}

concentrations. In hindsight, we recommend selecting a sample with abundant TLE so multiple aliquots can be separated into sub-fractions and analysed independently to validate the dilution series.

4.4.2 *Isoprenoid GDGTs*

The polar fractions were analysed using high-performance liquid chromatography-atmospheric pressure chemical ionisation-mass spectrometry (HPLC-APCI-MS) at the University of Bristol Organic Geochemistry Unit. The analyses were conducted on a Thermo Scientific™ TSQ Quantum™ Access MAX Triple Quadrupole MS equipped with an automatic injector. Separation was achieved in normal phase on two Waters® ACQUITY UPLC® BEH HILIC columns (150 mm; diameter: 2.1 mm; particle size: 1.7 µm; pore size: 130 Å). The flow rate of the hexane/isopropanol (IPA) 99:1 (v/v) eluent was 0.2 ml min^{-1}, isocratically for the first 25 min, followed by an increase in solvent polarity to 3.5% IPA in 25 min, and then by a sharp increase to 10% IPA in 30 min (after Hopmans et al., 2016). Injection volumes were 15 µl and GDGT determinations were based on single injections. Target compounds (Fig. 4.2) were analysed with a mass range of *m*/*z* 653 to 1302. Selected ion mode (SIM) was used to monitor the abundance of the $[M+H]^+$ ion (protonated molecular ion) in order to improve the signal-to-noise ratio and increase sensitivity and reproducibility. The peak areas were integrated using Xcalibur™ software to calculate the relative abundance of each GDGT. No GDGTs were detected in two samples from ODP Site 642 and five samples from ODP Site 907. Based on daily measurements of an inhouse marine standard over an annual period, analytical precision (1σ) is ±0.01 for the TEX_{86} proxy indices defined below (Kim et al., 2010).

TEX_{86} (Tetraether index of tetraethers) is based on the relative abundance of 86-carbon membrane lipids, termed isoprenoid glycerol dialkyl glycerol tetraethers (iso-GDGTs) (Fig. 4.2), predominantly produced by mesophilic marine and lacustrine Thaumarchaeota (Tierney, 2012). The TEX_{86} ratio was derived to provide an index of cyclisation for iso-GDGTs (Schouten et al., 2002). Several calibrations exist for TEX_{86} palaeothermometry, however there are

significant concerns regarding proxy behaviour at both low (Kim et al., 2008) and high (Liu et al., 2009) temperature limits of the modern calibration. To circumvent these problems, we use the exponential calibrations (Eq. 4.3 and 4.4) proposed by Kim et al. (2010), which are recommended when SSTs are higher (TEX_{86}^{H}) or lower (TEX_{86}^{L}) than 15°C. In certain marine realms, TEX_{86}^{L} is subject to large variability unseen in TEX_{86}^{H}, which is attributed to varying GDGT2 and GDGT3 ratios linked to environmental factors (water depths >1000 m) and deep-water lipid production (Taylor et al., 2013). Kim et al. (2010) and Tierney (2012) suggest TEX_{86}^{L} is unreliable for the majority of palaeotemperature reconstructions, and its use should be limited to polar environments. Consequently, the TEX_{86}^{L} calibration is only used at ODP Sites 907 and 642, located above the Arctic Circle, when the SSTs inferred from our respective $U^{K'}_{37}$ results are <15°C. The TEX_{86} values were converted to SSTs using the linear calibrations (Eq. 4.5 and 4.6) of Kim et al. (2010), based on a global dataset of 651 core-top sediment samples.

$$TEX_{86}^{L} = log\left(\frac{GDGT2}{GDGT1 + GDGT2 + GDGT3}\right)$$

Equation 4.3. TEX_{86}^{L} index (Kim et al., 2010)

$$TEX_{86}^{H} = log\left(\frac{GDGT2 + GDGT3 + Cren'}{GDGT1 + GDGT2 + GDGT3 + Cren'}\right)$$

Equation 4.4. TEX_{86}^{H} index (Kim et al., 2010)

$$SST\ (calibration\ error: \pm 4.0°C) = 67.5 \times TEX_{86}^{L} + 46.9$$

Equation 4.5. Global core-top TEX_{86}^{L} versus SST calibration (Kim et al., 2010)

$$SST\ (calibration\ error: \pm 2.5°C) = 68.4 \times TEX_{86}^{H} + 38.6$$

Equation 4.6. Global core-top TEX_{86}^{H} versus SST calibration (Kim et al., 2010)

The Branched and Isoprenoid Tetraether (BIT) index was calculated using the equation (Eq. 4.7) proposed by Hopmans et al. (2004). Roman numerals indicate the relative abundances and structures of terrestrially derived tetraether lipids (Ia−IIIa) versus marine- and lacustrine-derived crenarchaeol. Equation 4.7 includes the 5-methyl (e.g. IIa) and 6-methyl (e.g. IIa' and IIIa') branched GDGTs (Chapter 5) which were analysed as co-eluting compounds in the original BIT study (Hopmans et al., 2004).

$$BIT = \frac{(\mathrm{Ia} + \mathrm{IIa} + \mathrm{IIa'} + \mathrm{IIIa} + \mathrm{IIIa'})}{(\mathrm{Ia} + \mathrm{IIa} + \mathrm{IIa'} + \mathrm{IIIa} + \mathrm{IIIa'} + \mathrm{Crenarchaeol})}$$

Equation 4.7. BIT index (Hopmans et al., 2004).

We have also used the Gaussian process regression model OPTiMAL (Optimised Palaeothermometry from Tetraethers via MAchine Learning) to produce an additional set of isoGDGT-derived SSTs for comparison with our $U^{K'}_{37}$ and TEX_{86} records (Dunkley Jones et al., 2020). OPTiMAL assesses the strength of the relationship between fossil GDGT distributions and a modern calibration dataset (Tierney and Tingley, 2015) to calculate maximum likelihood SST estimates, with reliable confidence intervals (Dunkley Jones et al., 2020). The uncertainty associated with these SST estimates reduces where there are strong constraints from near analogues in the modern data. Unlike the TEX_{86} proxy, OPTiMAL considers all six isoprenoid compounds (GDGT-0, -1, -2, -3, Cren and Cren') and avoids the dimensionality reduction and loss of information which occurs when calibrating single parameters (TEX_{86}) to SST. OPTiMAL outputs a nearest neighbour distance metric ($D_{nearest}$), which quantifies whether the modern GDGT assemblage provides an adequate framework to estimate ancient SSTs for each sample. When $D_{nearest}$ >0.5, samples are unlikely to generate reliable SST estimates and are considered unconstrained by the calibration data (Dunkley Jones et al., 2020).

4.5 RESULTS

4.5.1 *$U^{K'}_{37}$-derived SST estimates*

Our original raw alkenone-derived SST estimates (denoted SST_{raw}) from IODP Site U1308, DSDP Site 552, ODP Site 642 and ODP Site 907 reveal a similar latitudinal pattern to present day (Table 4.2). Lower latitude IODP Site U1308 and DSDP Site 552 exhibit the warmest conditions, whereas higher latitude ODP Sites 642 and 907 are significantly cooler (Fig. 4.8). During the PRISM-interval (Fig. 4.9), IODP Site U1308 is the warmest locality with a SST_{raw} of 21.4°C, equating to a ΔSST_{raw} of 7.2°C compared to modern (Dowsett et al., 2010a; Dowsett et al., 2013b). The average ΔSST_{raw} at DSDP Site 552 is 1.3°C cooler than observed at IODP Site U1308. Our SST_{raw} results vary between 14.8°C to 21.5°C at DSDP Site 552. In the Norwegian Sea, ODP Site 642 exhibits an average SST_{raw} (12.6°C) which is 4.9°C cooler compared to DSDP Site 552, with a maximum temperature of 19.7°C and a minimum temperature of 8.9°C. The average ΔSST_{raw} at ODP Site 642 is 1.6°C cooler compared to the Icelandic Sea during this interval. ODP Site 907 is the coolest locality during the PRISM-interval with an average SST_{raw} of 9.8°C. SST_{raw} values vary between 8.5°C to 10.7°C at ODP Site 907.

	Mean PRISM-interval SST (°C)				Mean PRISM-interval ΔSST (°C)			
DSDP/ODP/IODP Site	U1308	552	642	907	U1308	552	642	907
$U^{K'}_{37}$ (SST_{raw})	21.4*	17.5	12.6	9.8	7.2*	5.9	4.4	6.0
Corrected $U^{K'}_{37}$ (SST_{corr})	20.3*	15.4	11.6	6.8	6.0*	3.8	3.4	3.0
TEX_{86} (SST_{tx86})	10.3*	15.1	6.9	5.5	−4.0*	3.4	1.3	1.7
OPTiMAL (SST_{opt})	9.1*	8.8	1.4	6.5	−5.1*	−2.9	−6.8	2.7

Table 4.2. Summary of the mean raw and corrected alkenone-based SSTs and ΔSSTs, and the mean TEX_{86} and OPTiMAL based SSTs and ΔSSTs during the PRISM-interval. Asterisk denotes SST values derived from a single sample (IODP Site U1308).

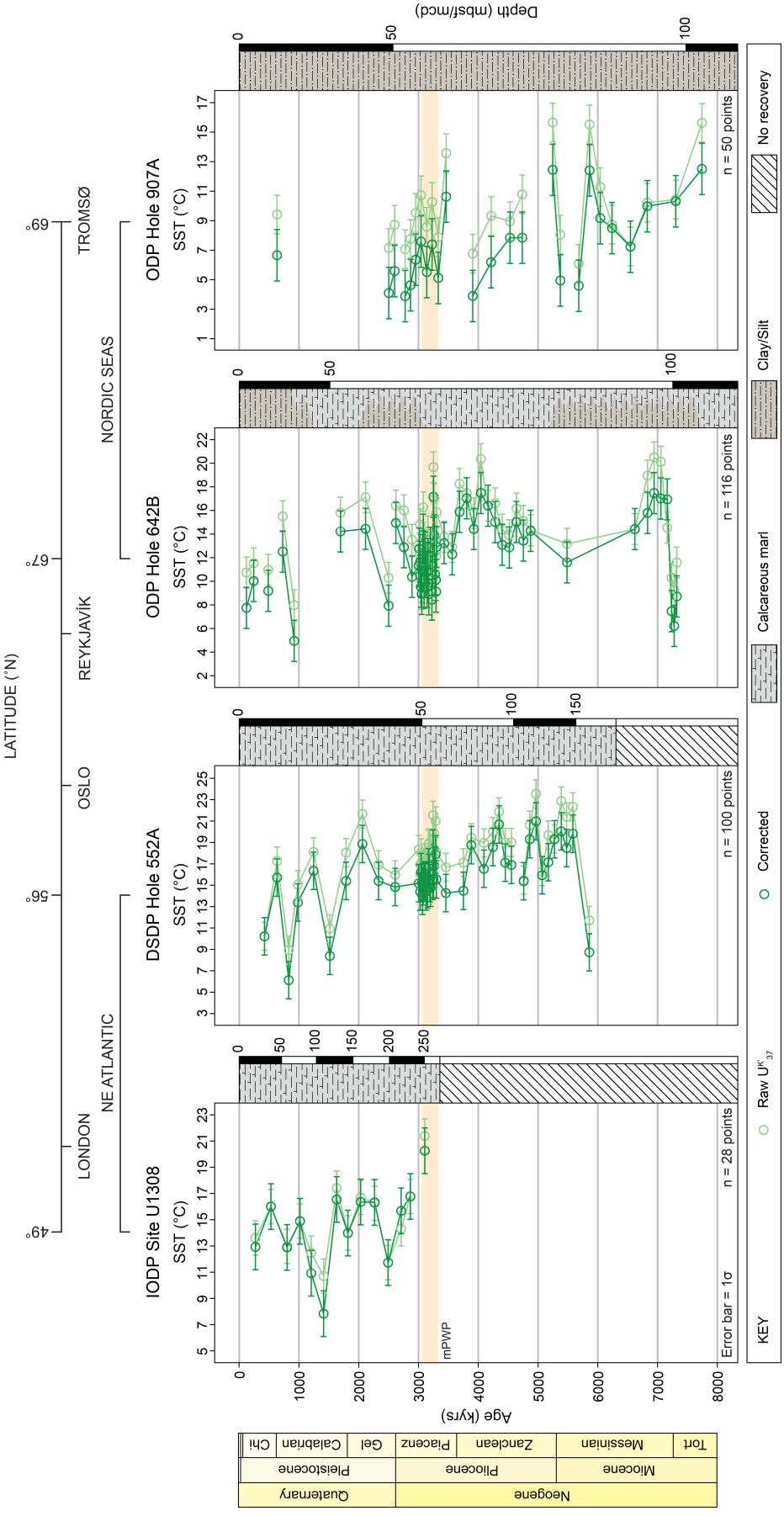

LATITUDE (°N)
49°
56°
67°
69°
LONDON
OSLO
REYKJAVÍK
TROMSØ
NE ATLANTIC
NORDIC SEAS
IODP Site U1308
DSDP Hole 552A
ODP Hole 642B
ODP Hole 907A
SST (°C)
Depth (mbsf/mcd)
n = 28 points
n = 100 points
n = 116 points
n = 50 points
mPWP
Age (kyrs)
Neogene
Quaternary
Miocene
Pliocene
Pleistocene
Tort
Messinian
Zanclean
Piacenz
Gel
Calabrian
Chi
KEY
Error bar = 1σ
Raw U^K'37
Corrected
Clay/Silt
Calcareous marl
No recovery

Figure 4.8 (previous page). Raw and corrected alkenone-based SST results from IODP Site U1308, DSDP Hole 552A, ODP Hole 642B and ODP Hole 907A for the 0−8000 kyr interval. 95% of our corrected SST measurements are cooler by 1.9°C on average, compared to the original raw SST values. Sites are ordered based on latitude and geographic region. SST records are plotted against age and depth. Stratigraphic relationships and lithology are also shown for each site. Orange bar as in Fig. 4.5. SST calibration derived from Conte et al. (2006) (circles; Eq. 4.2).

4.5.2 *Alkenone concentrations*

86% of our PRISM-interval SST estimates are derived from GC injections of relatively low total C_{37} concentrations (<216 ng/µl), which are susceptible to warming biases associated with irreversible adsorption (Fig. 4.7, 4.9). 60% of our PRISM-interval SST estimates are derived from very low concentrations (<50 ng/µl). 4% of our PRISM-interval SST estimates are derived from concentrations (216−238 ng/µl) which are considered optimum, falling between our inflection point values, and require no or very minor corrections. The remaining 10% of our SST estimates are derived from high concentrations (>238 ng/µl) susceptible to cooling biases.

All of our PRISM-interval SSTs from IODP Site U1308, DSDP Site 552 and ODP Site 907 are derived from low concentrations (31 ng/µl on average), which inherently bias these SSTs towards warmer values (Fig. 4.9). Importantly, DSDP Site 552 is one of the key NE Atlantic localities where existing alkenone records are used in the PRISM reconstruction to corroborate planktic foraminifer SSTs (Robinson et al., 2008). Our alkenone-based SSTs at this site are derived from relatively low concentrations (33 ng/µl on average). This is slightly greater than those (0.06−1.00 ng/µl) inferred from Robinson et al. (2008) and Lawrence (2020). However, these C_{37} concentrations are still considered low enough to be very susceptible to the effects of irreversible adsorption. Derived SST estimates most likely overestimate warming and require correcting. At ODP Site 642 in the Nordic Seas, 73% of the alkenone-based SSTs are derived from low concentrations (1−151 ng/µl), whereas 16% of the SST estimates are generated from higher concentrations (250−270 ng/µl). 11% of the SSTs fall within the optimum concentration range, and require either no or very small corrections.

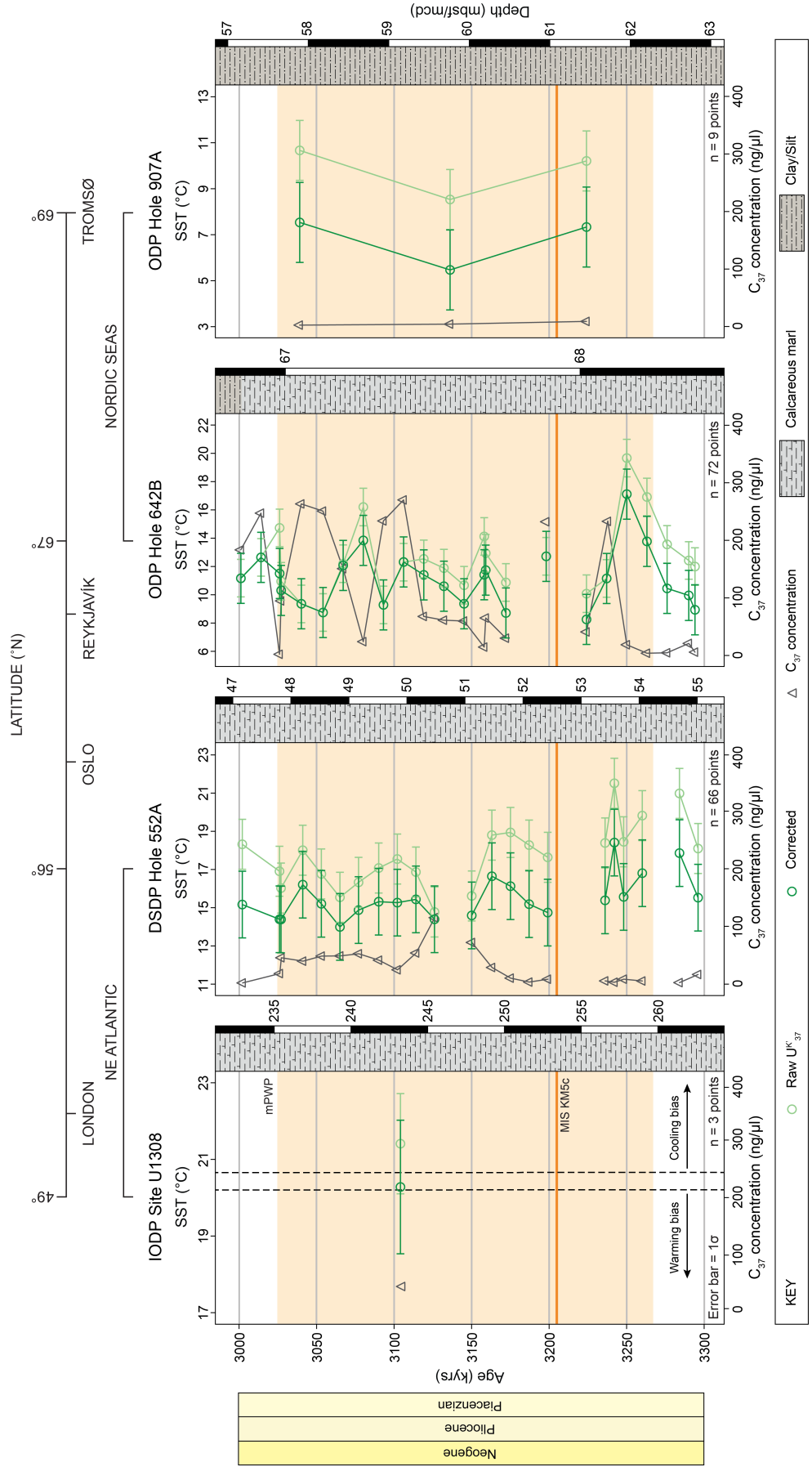

LATITUDE (°N)
49°
56°
67°
69°
LONDON
OSLO
REYKJAVÍK
TROMSØ
NE ATLANTIC
NORDIC SEAS
IODP Site U1308
DSDP Hole 552A
ODP Hole 642B
ODP Hole 907A
SST (°C)
Depth (mbsf/mcd)
Age (kyrs)
Neogene
Pliocene
Piacenzian
mPWP
MIS KM5c
Cooling bias
Warming bias
n = 3 points
n = 66 points
n = 72 points
n = 9 points
KEY
Raw U^K'37
Corrected
C37 concentration
Calcareous marl
Clay/Silt
Error bar = 1σ
C37 concentration (ng/µl)

Figure 4.9 (previous page). Raw and corrected alkenone-based SST results from IODP Site U1308, DSDP Hole 552A, ODP Hole 642B and ODP Hole 907A during the PRISM-interval, highlighted in orange. MIS KM5c, Marine Isotope Stage KM5c (dark orange line). Sites are ordered based on latitude and geographic region. The injected concentrations used to predict the alkenone-based SSTs are shown, alongside the concentration limits (dashed lines) known to drive deviations in SSTs established using our dilution series. SST and alkenone concentration records are plotted against age and depth. Stratigraphic relationships and lithology are also shown for each site. SST calibration derived from Conte et al. (2006) (circles; Eq. 4.2).

4.5.3 *Corrected $U^{K'}_{37}$-derived SSTs*

Our corrected alkenone-derived SSTs (denoted SST_{corr}) show a similar latitudinal pattern to our SST_{raw} results (Fig. 4.8, 4.9). However, the magnitude of warming inferred from our corrected records is considerably less compared to our SST_{raw} values (Table 4.2). 95% of our SST measurements are significantly cooler (by 1.9°C on average) after being corrected for irreversible adoption. The largest temperature changes are observed at ODP Sites 642 and 907, where some of the SST_{raw} estimates derived from low concentrations are reduced by up to 3.2°C following correction. The remaining 5% of our SST results are slightly warmer (by 0.6°C on average) after being corrected owing to higher concentrations.

During the PRISM-interval, all of our mean SST_{corr} values are significantly cooler (by 1.9°C on average) compared to the original raw SSTs (Fig. 4.9). IODP Site U1308 is the warmest locality with a SST_{corr} value of 20.3°C, equating to ΔSST_{corr} of 6.0°C compared to modern. This is 1.2°C cooler than our respective ΔSST_{raw} at this site. At DSDP Site 552, the SST_{corr} values vary between 14.0°C to 18.4°C, and the average SST_{corr} is 2.1°C cooler compared to our mean SST_{raw}. In the Norwegian Sea, ODP Site 642 features an average SST_{corr} of 11.6°C during this interval. The maximum and minimum SST_{corr} at ODP Site 642 are 2.5°C and 0.4°C cooler, respectively, compared to our SST_{raw} values. The average ΔSST_{corr} at ODP Site 642 is 1.0°C cooler compared to our mean ΔSST_{raw}. The mean SST_{corr} at ODP Site 907 is 6.8°C, and the SST_{corr} values vary between 5.5°C to 7.5°C. The average ΔSST_{corr} at ODP Site 907 is 3.0°C

cooler than our mean ΔSST_{raw}, which represents the largest mean temperature correction observed during the PRISM-interval.

4.5.4 *TEX_{86} SSTs*

Our TEX_{86} (denoted SST_{tx86}) and OPTiMAL SSTs (denoted SST_{opt}) generally resemble the latitudinal temperature gradient implied by our $U^{K'}_{37}$ results throughout the PRISM-interval (Table 4.2). During this timeslice, the average SST_{tx86} at all four localities is 9.5°C, which is 3.0°C warmer compared to the average SST_{opt} (Fig. 4.10). The SST_{tx86} estimates vary between −3.0°C to 23.5°C during this interval, compared to the SST_{opt} values which range from 1.6°C to 15.6°C. At DSDP Site 552, the SST_{tx86} values vary between 2.8°C to 23.5°C and the SST_{opt} estimates vary between −0.2°C to 15.6°C. Our average SST_{tx86} is 6.3°C warmer compared to the average SST_{opt}. At IODP Site U1308, the SST_{opt} value is 1.2°C cooler than our SST_{tx86} estimate. At ODP Site 642, the SST_{tx86} values vary between −2.6°C to 19.0°C and SST_{opt} estimates vary between −1.6°C to 14.6°C. Our average SST_{tx86} is 5.5°C warmer compared to our mean SST_{opt}. At ODP Site 907, SST_{tx86} values vary between −3.0°C to 21.6°C. Our average SST_{opt} at ODP Site 907 is 1.0°C warmer compared to our mean SST_{tx86}. However, ODP Site 907 also witnesses the smallest variation in SST_{opt} estimates, with values varying between 6.2°C to 6.8°C. Importantly, our ΔSST_{tx86} at IODP Site U1308 and our average ΔSST_{opt} estimates from IODP Site U1308, DSDP Site 552 and ODP Site 642 disagree with the high magnitude of warming suggested by our mean alkenone-derived ΔSSTs, and imply these localities were up to 12.3°C cooler during the PRISM-interval.

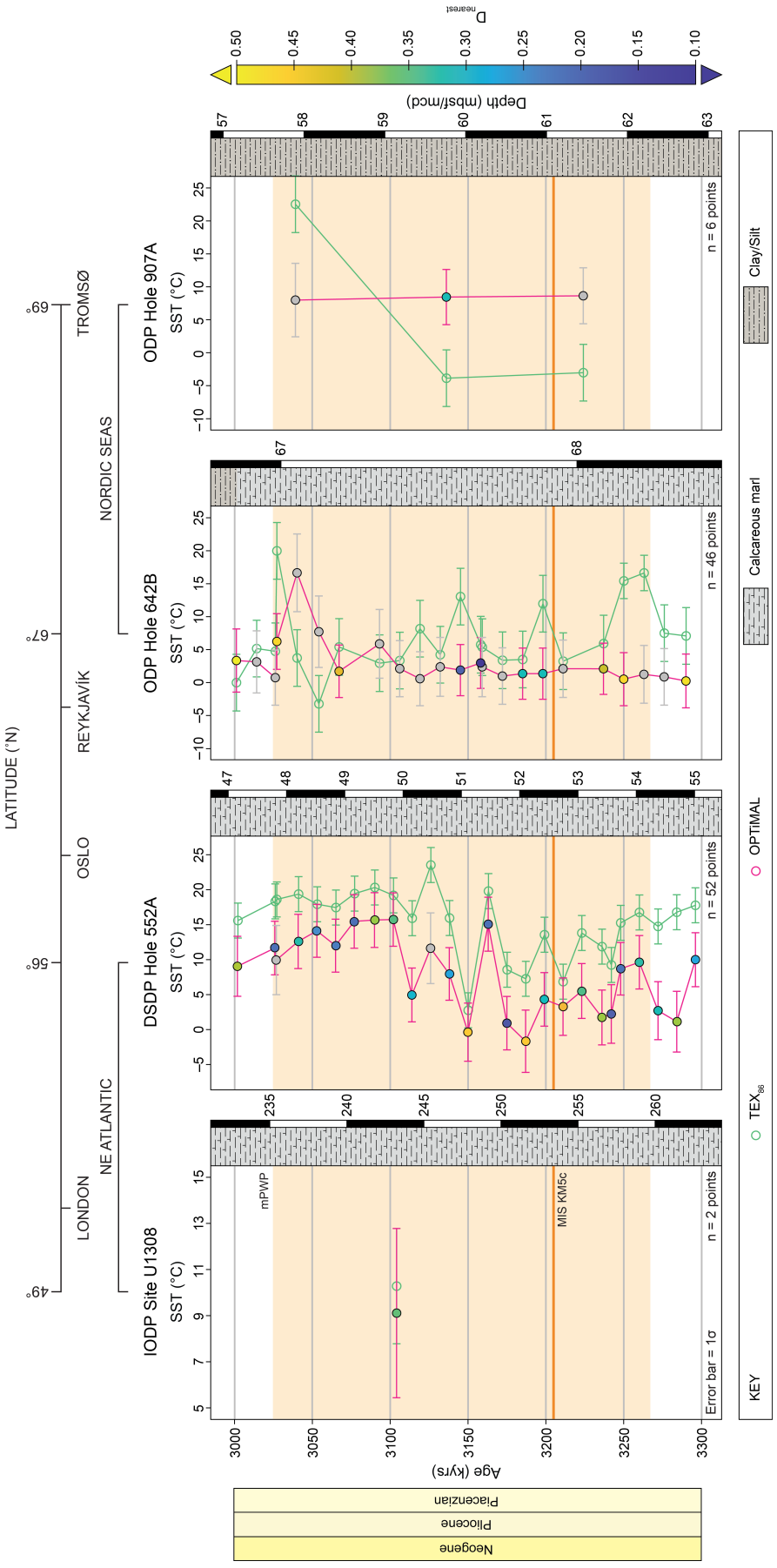

Neogene
Pliocene
Piacenzian
Age (kyrs)
3000
3050
3100
3150
3200
3250
3300
IODP Site U1308
DSDP Hole 552A
ODP Hole 642B
ODP Hole 907A
SST (°C)
mPWP
MIS KM5c
n = 2 points
n = 52 points
n = 46 points
n = 6 points
Error bar = 1σ
KEY
TEX86
OPTIMAL
Clay/Silt
Calcareous marl
Depth (mbsf/mcd)
D nearest
LATITUDE (°N)
49°
56°
67°
69°
LONDON
OSLO
REYKJAVÍK
TROMSØ
NE ATLANTIC
NORDIC SEAS

Figure 4.10 (previous page). TEX_{86} and OPTiMAL based SST results from IODP Site U1308, DSDP Hole 552A, ODP Hole 642B and ODP Hole 907A during the PRISM-interval, highlighted in orange. MIS KM5c, Marine Isotope Stage KM5c (dark orange line). Sites are ordered based on latitude and geographic region. SST records are plotted against age and depth. The colour ramp indicates the $D_{nearest}$ values for OPTiMAL SST estimates, ranging between 0.10 to 0.50. Samples which fail the $D_{nearest}$ test (>0.50) are coloured grey, indicating no relationship between the fossil GDGT distributions and the modern calibration dataset. Stratigraphic relationships and lithology are also shown for each site. SST calibrations derived from Kim et al. (2010) (hollow circles; Eq. 4.5, 4.6).

4.6 DISCUSSION

4.6.1 *Fidelity of our PRISM-interval $U^{K'}_{37}$ and TEX_{86} datasets*

In general, our NE Atlantic and Nordic Seas $U^{K'}_{37}$ records are significantly warmer by 5.9°C on average, compared to our TEX_{86} records during the PRISM-interval. Our $U^{K'}_{37}$ and TEX_{86}-derived SST trends generally show very weak correlation during the PRISM-interval (Fig. 4.11), with R^2 values varying between 0.47 (ODP Site 907) and 0.07 (DSDP Site 552). The highest R^2 values are observed between our SST_{raw} and SST_{tx86} results at each site, whereas the lowest R^2 values, which indicate virtually no correlation, occur between our corrected $U^{K'}_{37}$ and OPTiMAL TEX_{86} SSTs (Fig. 4.11). ODP Site 907 has the highest R^2 values for the strength of the relationship between our $U^{K'}_{37}$ (SST_{raw} and SST_{corr}) and TEX_{86} (SST_{tx86} and SST_{opt}) records, whereas DSDP Site 552 has the lowest values. Filtering our OPTiMAL SSTs for samples with $D_{nearest}$ values <0.5, considered reliable indicators of SSTs, indicates our filtered SST_{opt} records are also significantly cooler than our $U^{K'}_{37}$ SST records by 8.6°C on average, across all four sites (Fig. 4.9, 4.10).

This mismatch between our $U^{K'}_{37}$ and TEX_{86} SST records is most likely attributable to ecological and environmental factors. TEX_{86} records are known to be influenced by non-thermal effects, such as seasonality (Herfort et al., 2006), water depth (Rodrigo-Gámiz et al., 2015), *in situ* GDGT production (Sinninghe Damsté et al., 2012) and terrestrial organic matter contamination (Zhang et al., 2016). The water depth at which the different biomarkers are synthesised is known to influence SST records (Taylor et al., 2013; Villanueva et al., 2014). Rodrigo-Gámiz et al. (2015) and Lee et al. (2008) suggest Crenarchaeota production is higher below the mixed layer, whereas alkenone production is generally confined to the sea surface (0−20 m depth) (Herbert, 2006). The synthesis of these iso-GDGTs at deeper depths results in cooler TEX_{86}-based temperatures. At present, throughout the summer months the model mean mixed-layer depth (MLD) at our NE Atlantic and Nordic Sea sites is between 0−100 m (Tjiputra et al., 2013). Storm-driven mixing strengthens in the winter months and the model mean MLD at all sites

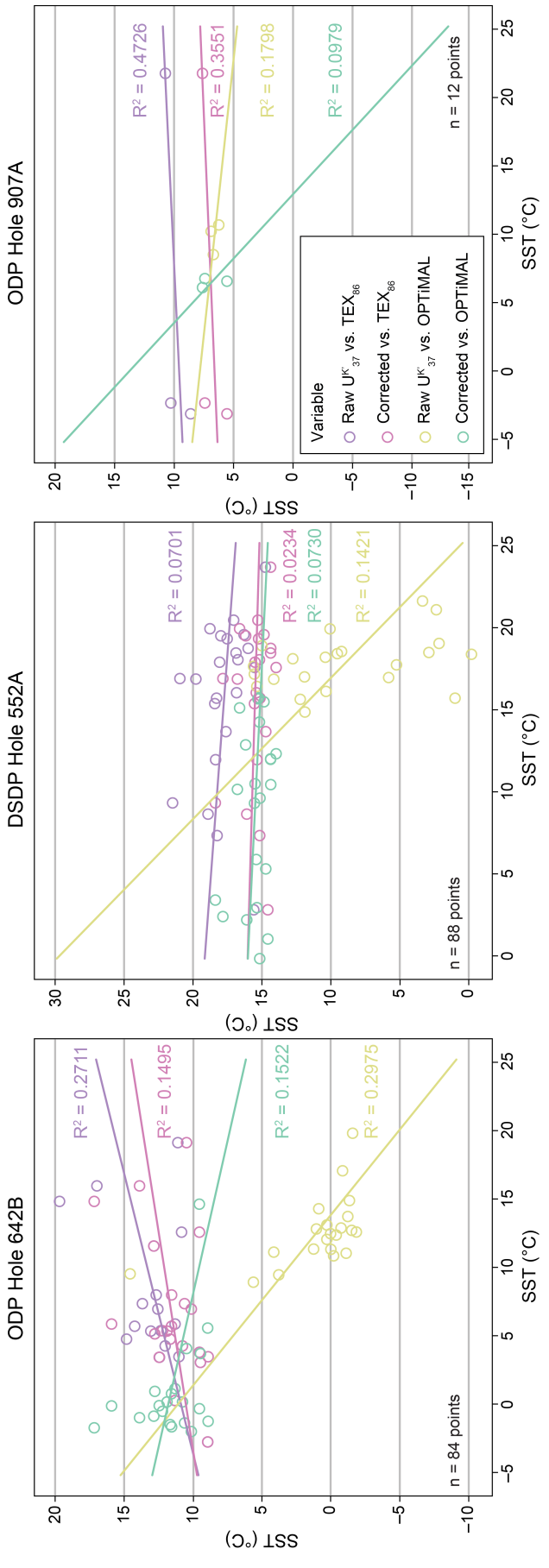

ODP Hole 907A
DSDP Hole 552A
ODP Hole 642B
SST (°C)
R² = 0.4726
R² = 0.3551
R² = 0.1798
R² = 0.0979
n = 12 points
R² = 0.0701
R² = 0.0234
R² = 0.0730
R² = 0.1421
n = 88 points
R² = 0.2711
R² = 0.1495
R² = 0.1522
R² = 0.2975
n = 84 points
Variable
Raw U^K'37 vs. TEX86
Corrected vs. TEX86
Raw U^K'37 vs. OPTiMAL
Corrected vs. OPTiMAL

Figure 4.11 (previous page). Cross plots showing the relationships between the raw and corrected alkenone-based SSTs, and the TEX_{86} and OPTiMAL based SST records at ODP Hole 642B, DSDP Hole 552A and ODP Hole 907A. R^2 values assess the degree to which the data points cluster around the linear regression line, and is a measure of the proportion of variation in the dependent variable attributed to the independent variable.

deepens to around c. 250 m (Tjiputra et al., 2013). This significant annual variation in regional MLD suggests our TEX_{86} SSTs may reflect a strong subsurface temperature bias, and is most likely responsible for our significantly cooler TEX_{86} SST records. The difference between our $U^{K'}_{37}$ and TEX_{86}-based temperatures may also be explained by seasonal changes in the production of iso-GDGTs and alkenones observed in other regions, such as the North Sea (Pitcher et al., 2011) and offshore Spain (Galand et al. 2010). However, Rodrigo-Gámiz et al. (2015), Dandonneau et al. (2004) and Chapman et al. (1996) demonstrate modern production of both iso-GDGTs and alkenones increase during the late spring and early summer in the Nordic Seas and NE Atlantic. It is still unclear how, or whether, seasonal biases in lipid production affect sedimentary $U^{K'}_{37}$ and TEX_{86} records, which are typically calibrated to mean annual temperatures. However, the regional simultaneous production of both biomarkers limits the potential for any seasonal bias in our records.

The slightly stronger correlation ($R^2 = 0.47$) between our $U^{K'}_{37}$ and TEX_{86}-based temperatures at ODP Site 907 (Fig. 4.11) may be linked to warming biases associated with the influence of terrestrially-derived organic matter on the TEX_{86} index. Thaumarchaeota and their iso-GDGTs are also abundant in terrestrial soils, albeit at lower concentrations compared to marine sediments (Weijers et al., 2006). Weijers et al. (2006) and Blaga et al. (2009) demonstrate that sediments with a BIT index of >0.4 significantly bias TEX_{86}-derived SSTs towards warmer values (by up to 2°C). Weijers et al. (2006) suggest the largest temperature deviations are likely to occur at sites with cooler deep-waters, as soils generally contain a relatively warm TEX_{86} signal. ODP Site 907 has the highest average BIT index (0.80) during the PRISM-interval (Fig. 4.12), possibly accumulating terrestrially-derived organic matter from nearby Iceland, Jan Mayen or the East Icelandic Current transporting eroded material from Greenland. This high BIT index (Fig. 4.12) may therefore be responsible for the enhanced warming

observed in our TEX_{86} records and the stronger relationship with our $U^{K'}_{37}$ SSTs at this site (Fig. 4.11).

In situ production of GDGTs by methanogenic and methanotrophic archaea can also influence the TEX_{86} index. The contribution of *in situ* GDGTs is quantified using the relative abundance of GDGT-0 to crenarchaeol (Eq. 4.8) (Sinninghe Damsté et al., 2012). The %GDGT-0 value for 91% of our TEX_{86} records is <67%, suggesting nearly all of our samples are unaffected by additional non-water column sources of GDGT-1, GDGT-2 or GDGT-3 (Fig. 4.12). Zhang et al. (2016) propose the Ring Index (RI; Eq. 4.9) for assessing non-thermal factors on TEX_{86}, which also identifies results which deviate from modern analogues. The RI represents a weighted average of the cyclopentane moieties, which is correlated with TEX_{86} in a modern global core top dataset (Eq. 4.10) (Ho et al., 2011, 2014; Kim et al., 2010). Zhang et al. (2016) suggest samples which deviate from this relationship should not be used for palaeothermometry with confidence. Zhang et al. (2016) use the difference between the RI value and the modern TEX_{86}−RI relationship (termed ΔRI; Eq. 4.11) to identify false samples (ΔRI >0.3). All of our samples from IODP Site U1308, ODP Site 642 and ODP Site 907 have ΔRI values >0.3, suggesting non-temperature factors likely affect our GDGT distributions at these localities (Fig. 4.12). At DSDP Site 552, 45% of our samples have ΔRI values <0.3 indicating these samples have similar GDGT distributions to modern analogues and are potentially reliable indicators of palaeotemperatures.

Factors which influence $U^{K'}_{37}$-derived SST records include changes in dominant alkenone producers (Volkman et al., 1995), seasonality (Chapman et al., 1996), salinity (Ono et al., 2012), diagenetic alteration (Freitas et al., 2017) and nutrient dynamics (Epstein et al. 1998). During the mid-Pliocene, *Gephyrocapsa oceanica* was the dominant alkenone producer, alongside now-extinct relatives (Zhang et al., 2013). Consequently, our temperature estimations rely on the assumption that $U^{K'}_{37}$ sensitivity to seawater temperature is the same as today (Tierney and Tingley, 2018). Similar assumptions are made for nonextant species of planktic foraminifera used for Mg/Ca and $\delta^{18}O$ palaeothermometry, so this is a common and

$$\%GDGT0 = \frac{GDGT0}{(GDGT0 + Cren)} \times 100$$

Equation 4.8. %GDGT-0 index (Sinninghe Damsté et al., 2012)

$$RI = 0 \times (GDGT0) + 1 \times (GDGT1) + 2 \times (GDGT2) + 3 \times (GDGT3) + 4 \times (Cren) + 4 \times (Cren')$$

Equation 4.9. Ring index (RI) (Zhang et al., 2016)

$$RI_{TEX} = -0.77(\pm 0.38) \times TEX_{86} + 3.32(\pm 0.34) \times (TEX_{86})^2 + 1.59(\pm 0.10)$$

Equation 4.10. TEX_{86}−RI quadratic regression (Zhang et al., 2016)

$$\Delta RI = RI_{TEX} - RI_{sample}$$

Equation 4.11. ΔRI (Zhang et al., 2016)

unavoidable problem in palaeoclimatology which is not exclusive to $U^{K'}_{37}$. Hoefs et al. (1998) demonstrate diagenesis may preferentially degrade the $C_{37:3}$ ketone due to postdepositional oxidation. The extra double bond in $C_{37:3}$ makes this species susceptible to increased reactivity. Grimalt et al. (2000) suggest the preferential degradation of $C_{37:3}$ in low concentration samples can bias $U^{K'}_{37}$-derived SSTs towards warmer values. It is difficult to fully assess the true impact of diagenetic effects on $U^{K'}_{37}$ records without prior insight into the correct SST values for ancient sediments. Hoefs et al. (1998) suggest once alkenones survive the high metabolic rates above the sediment redox boundary, the perceptible decay rates (c. 10^{-5} $year^{-1}$) should produce near monotonic trends in alkenone degradation as a function of sediment age. Importantly, our alkenone-based SSTs are derived from low concentrations (Fig. 4.9) which may exacerbate the effects caused by the preferential degradation of the $C_{37:3}$ species. Our SSTs are therefore

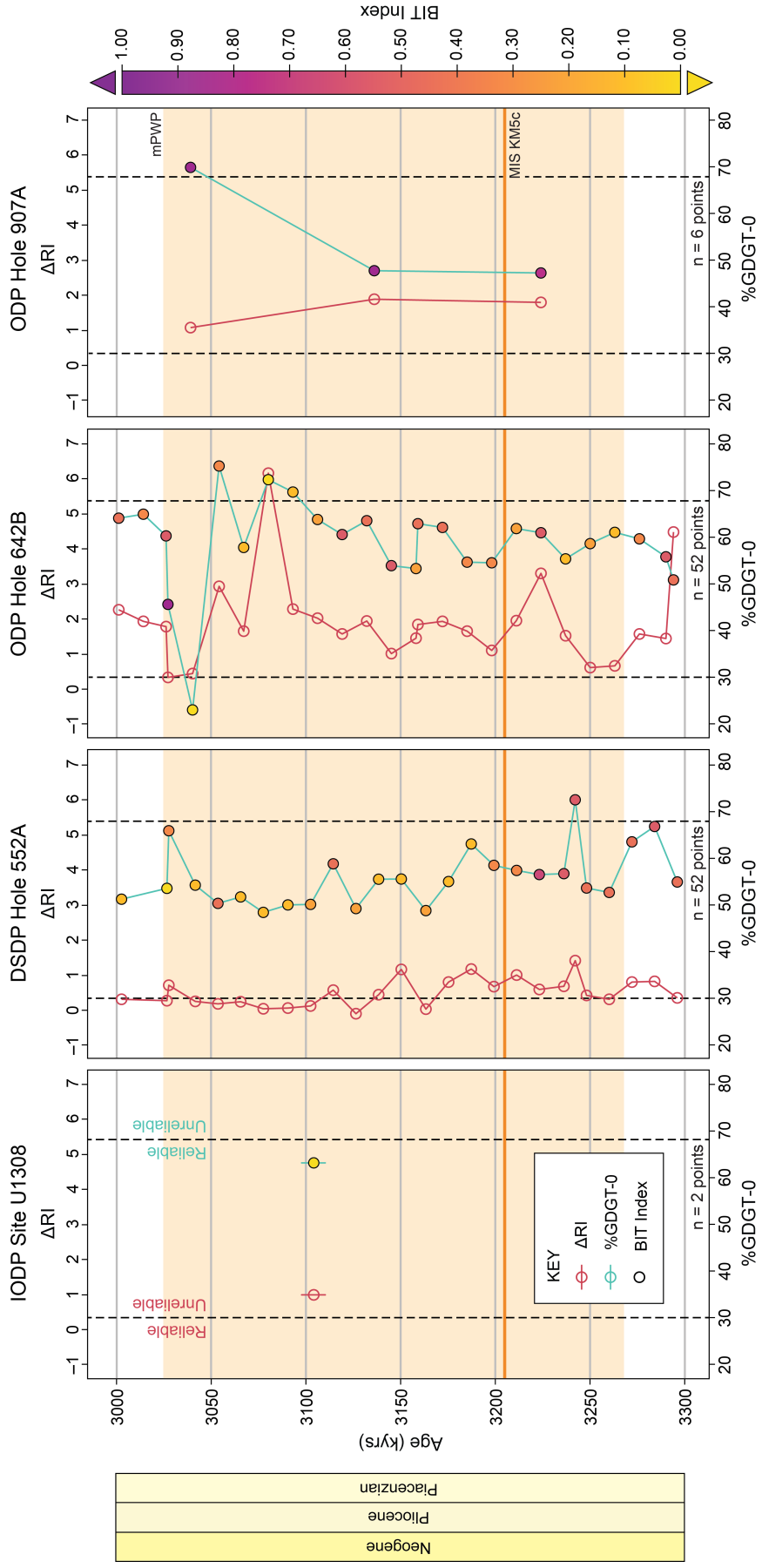

BIT Index
1.00
0.90
0.80
0.70
0.60
0.50
0.40
0.30
0.20
0.10
0.00
ODP Hole 907A
DSDP Hole 552A
ODP Hole 642B
IODP Site U1308
ΔRI
%GDGT-0
mPWP
MIS KM5c
n = 6 points
n = 52 points
n = 52 points
n = 2 points
Reliable
Unreliable
Reliable
Unreliable
KEY
ΔRI
%GDGT-0
BIT Index
Age (kyrs)
3000
3050
3100
3150
3200
3250
3300
Neogene
Pliocene
Piacenzian

Figure 4.12 (previous page). Summary of BIT index, ΔRI and %GDGT-0 records deduced from our TEX_{86} based SSTs. Higher BIT index values signify a greater influence of terrestrially derived tetraether lipids, as shown by the colour ramp. ΔRI values >0.3 (dashed black line) indicate GDGT distributions with cyclopentane moieties which fail to resemble distributions in a modern global core-top dataset. Zhang et al. (2016) suggest these samples should not be used for palaeothermometry with confidence. %GDGT-0 signifies the contribution of *in situ* GDGT production by methanogenic and methanotrophic archaea. %GDGT-0 values <67% (dashed black line) suggest GDGT distributions are unaffected by additional non-water column sources of GDGT-1, GDGT-2 or GDGT-3. BIT (filled circles; Eq. 4.7), %GDGT-0 (green lines; Eq. 4.8) and ΔRI (red circles; Eq. 4.9, 4.10, 4.11) calibrations derived from Hopmans et al. (2004), Sinninghe Damsté et al. (2012) and Zhang et al. (2016). MIS KM5c, Marine Isotope Stage KM5c (dark orange line).

potentially biased by both irreversible adsorption and diagenetic degradation. However, Freitas et al. (2017) suggest the impacts are minimal and that diagenetic SST biases are largely within the $U^{K'}_{37}$ calibration error (<1.1°C).

Nutrient dynamics can also influence alkenone producers. Epstein et al. (1998) demonstrated $U^{K'}_{37}$-derived SSTs can increase under nutrient stress. Nutrient concentrations in the North Atlantic and Nordic Seas during the Pliocene are believed to be similar to present-day, varying between 5−35 μmol/kg (NO_2 + NO_3) (Olafsson and Olsen, 2010). This is significantly higher than the cut-off point (<1 μmol/kg) for unbiased SST records advocated by Epstein et al. (1998). Whilst elevated regional nutrient concentrations may influence the offset between our TEX_{86} and $U^{K'}_{37}$ SST records, they do not appear to be the dominant controlling factor since our most recent $U^{K'}_{37}$ SSTs from our four sites (Fig. 4.8) show little deviation from modern mean annual SSTs.

Overall, we believe our TEX_{86} SST records are unreliable and underestimate the magnitude of PRISM-interval warming in the NE Atlantic and Nordic Seas compared to our $U^{K'}_{37}$ based results (Fig. 4.9). The high quantity of abnormal ΔRI values (79% of our TEX_{86} results) (Fig. 4.12) and the lack of any match between our filtered OPTiMAL and $U^{K'}_{37}$ SSTs (Fig. 4.9, 4.10, 4.11), suggest our TEX_{86} SST records should not be used in palaeothermometry and are most likely influenced by environmental factors. The offset between our warmer $U^{K'}_{37}$ and cooler

TEX_{86} results (Fig. 4.9, 4.10) implies the iso-GDGTs were synthesised at deeper and cooler depths, exacerbated by significant regional annual fluctuations in MLD. The stronger relationship between our TEX_{86} and $U^{K'}_{37}$ records at ODP Site 907 coincides with a very high BIT index (Fig. 4.12), indicating an increased influence of terrestrially-derived organic matter. This may have contributed additional soil-derived iso-GDGTs which possibly biased our TEX_{86} records at this site towards warmer temperatures. Based on the above, we interpret our $U^{K'}_{37}$ records as more reliable indicators of regional sea surface conditions, which match the magnitude of warming predicted by pre-existing records (Fig. 4.5, 4.6) (Robinson et al., 2008; Robinson, 2009). Unsurprisingly, the existing PRISM datasets (Dowsett et al., 2016) do not include any TEX_{86} records, and all SST reconstructions at our sites are based on either alkenone, planktic foraminifera or Mg/Ca palaeothermometry. Consequently, the application of TEX_{86} as a tool to investigate regional PRISM-interval warming will be discussed no further.

4.6.2 *Comparison with existing NE Atlantic and Nordic Sea PRISM-interval $U^{K'}_{37}$ records*

The magnitude of alkenone-derived warming varies latitudinally with the warmest ΔSST_{corr} (6.0°C) observed at IODP Site U1308 and the coolest ΔSST_{corr} (3.0°C) at ODP Site 907 (Table 4.2). There is good agreement at DSDP Site 552 and ODP Site 642 between the magnitude of alkenone-derived warming inferred by previous studies (Robinson et al., 2008; Bachem et al., 2017) and that proposed here (Fig. 4.13). This good agreement suggests these existing alkenone-based SSTs were also derived from low concentrations, similar to observed here (Fig. 4.9). At DSDP Site 552, our average SST_{raw} is only 0.6°C warmer and our mean SST_{corr} estimate is 1.5°C cooler than the average $U^{K'}_{37}$ SST (16.9°C) calculated by Robinson et al. (2008). At ODP Site 642, our mean SST_{raw} and SST_{corr} are 0.8°C and 1.8°C cooler, respectively, than the average $U^{K'}_{37}$ SST (13.4°C) proposed by Bachem et al. (2017).

It is challenging and unrepresentative to compare the magnitude of warming indicated by our results at IODP Site U1308 and ODP Site 907 with the patterns of warming derived from

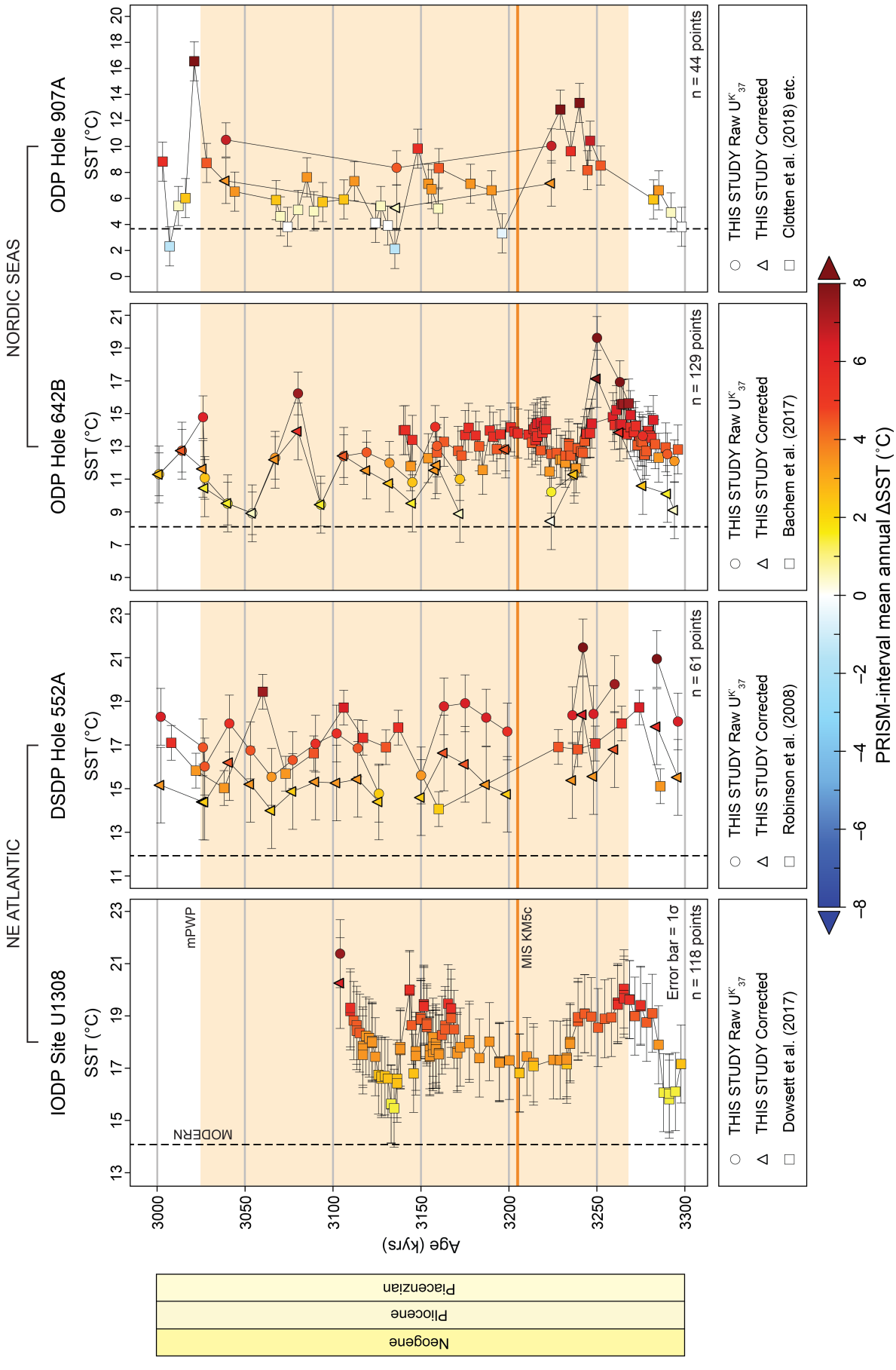

NE ATLANTIC
NORDIC SEAS
IODP Site U1308
DSDP Hole 552A
ODP Hole 642B
ODP Hole 907A
SST (°C)
Age (kyrs)
MODERN
mPWP
MIS KM5c
Error bar = 1σ
n = 118 points
n = 61 points
n = 129 points
n = 44 points
THIS STUDY Raw $U^{K'}_{37}$
THIS STUDY Corrected
Dowsett et al. (2017)
Robinson et al. (2008)
Bachem et al. (2017)
Clotten et al. (2018) etc.
PRISM-interval mean annual ΔSST (°C)
Neogene
Pliocene
Piacenzian

Figure 4.13 (previous page). Comparison of our alkenone-based SST results with existing records at IODP Site U1308, DSDP Hole 552A, ODP Hole 642B and ODP Hole 907A. Our raw alkenone-based SSTs are most similar to the magnitude of warming implied by existing records. Our corrected alkenone-based SSTs are significantly cooler (by 1.9°C on average) compared to the existing records. Points are coloured based on ΔSST, as shown by the colour ramp. Dashed black line represents modern SST at each site. MIS KM5c, Marine Isotope Stage KM5c (dark orange line).

existing alkenone records at these localities (Dowsett et al., 2017; Clotten et al., 2018). As previously stated, our PRISM-interval alkenone records at IODP Site U1308 and ODP Site 907 are based on only four data points, which are considered an insufficient sample to be indicative of average warming throughout this time slice. Our IODP Site U1308 SST_{raw} and SST_{corr} values are 3.4°C and 2.3°C warmer, respectively, compared to the average $U^{K'}_{37}$ SST (18.0°C) calculated by Dowsett et al. (2017). Our mean ODP Site 907 SST_{raw} value is 2.8°C warmer and the mean SST_{corr} is 0.2°C cooler than the average $U^{K'}_{37}$ SST (7.0°C) predicted by Schrek et al. (2013), Herbert et al. (2016) and Clotten et al. (2018). Ultimately, we discourage the use of our mean SSTs and anomalies from IODP Site U1308 and ODP Site 907 in mPWP North Atlantic reconstructions, since they are based on only four data points, which are considered an insufficient insight into the true magnitude and duration of SST changes during this interval. The large differences between our SST_{raw} results and the average SST estimates proposed by Dowsett et al. (2017), Schrek et al. (2013), Herbert et al. (2016) and Clotten et al. (2018), suggest our SST_{raw} records at IODP Site U1308 and ODP Site 907 represent higher-end temperatures (Fig. 4.13), most likely biased by very low injection concentrations (66.21 ng/µl at IODP Site U1308; 4.84 ng/µl on average at ODP Site 907). Higher-resolution $U^{K'}_{37}$ records are needed from these sites in order to create more accurate mean ΔSSTs which can be compared with existing records, and to confidently assess, and correct for, the influence of low concentrations at these localities.

4.6.3 *Unravelling the magnitude of mid-Pliocene warming at DSDP Site 552*

DSDP Site 552 is a key NE Atlantic PRISM dataset locality for mid-Piacenzian warming and is classified a very-high confidence site (Fig. 4.1, 4.3; Dowsett et al., 2012). In the PRISM

reconstruction the mean annual SST estimate at DSDP Site 552 is 16.7°C, equating to a mean PRISM ΔSST of 5.5°C based on planktic foraminifera (Dowsett and Poore, 1990; Dowsett et al., 2010b; Dowsett et al., 2012). The $U^{K'}_{37}$ and Mg/Ca records from DSDP Site 552 are merely used to corroborate the planktic foraminifera SST records (Robinson et al. 2008; Dowsett et al. 2010b).

More than a million Pliocene planktic foraminifera were identified to species level and counted to produce census data from PRISM localities. SSTs were estimated from this census data using factor analytic transfer functions, the modern-analogue technique or by a semi-quantitative comparison to modern faunas (Dowsett and Poore 1990; 1991; Dowsett 1991; Dowsett et al. 1996; Dowsett and Robinson 1998). Transfer functions are empirically derived equations used to calculate quantitative estimates of past oceanic conditions from core-top foraminiferal data. PRISM developed a set of 18 counting categories (based on environmental preferences) for modern and Pliocene taxa, which enabled a transfer function, termed GSF18, to be applied to mPWP sequences (Dowsett and Poore, 1990). GSF18 was calibrated to the SST analysis of Reynolds and Smith (1995) to transform planktic foraminifera data into February and August SST estimates. At DSDP Site 552, the February ΔSST is 3.3°C and the August ΔSST is 7.8°C, with an average planktic ΔSST of 5.5°C (Dowsett et al., 2010b).

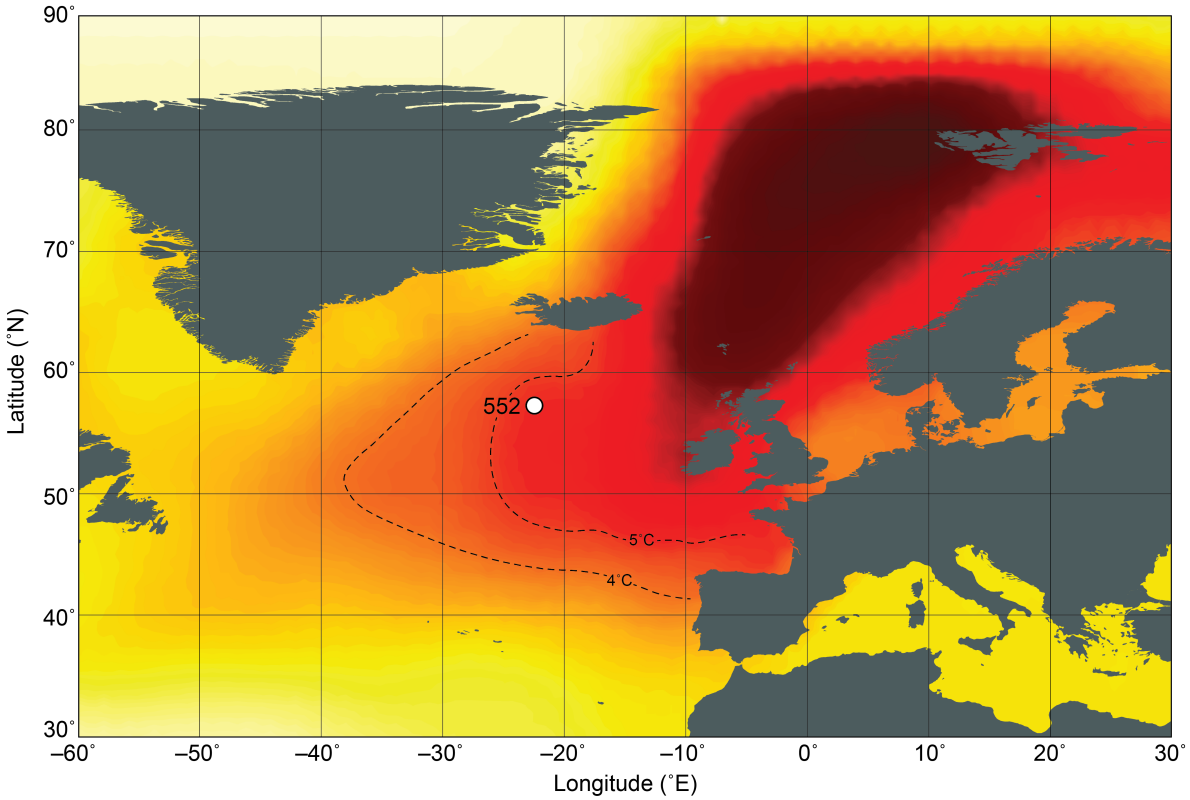
The GSF18 commonalities are high (0.869−0.994) at this site (Dowsett and Poore, 1990), suggesting the transfer function is effective at estimating mPWP SSTs from core-top assemblages. However, Robinson et al. (2008) indicate the GSF18 function may overestimate warming due to high abundances of *Globigerina puncticulata* and *Neogloboquadrina acostaensis* at this site. SST estimates from these species, which are now extinct, are based on ecological resemblances to extant taxa *G. inflata* and *N. dutertrei*, common in lower subtropical and tropical latitudes (Dowsett and Robinson, 2007). The original census data reveals that up to 45% of the total foraminifera identified in PRISM-interval samples at DSDP Site 552, between 54.44−63.61 mbsf, were *G. puncticulata* and *N. acostaensis* (Dowsett and Poore, 1990). Dowsett and Poore (1990) also admit difficulty in

differentiating between *N. acostaensis* and *N. "dupac"* (a term incorporating both *N. pachyderma* and *N. dutertrei*). Recounting and verifying potentially misidentified species could possibly increase the number of *N. acostaensis* specimens recognised in the PRISM-interval samples by 156%.

The Mg/Ca technique is based on the observed exponential increase in the ratio of magnesium to calcium in foraminiferal tests with increasing temperature, enabling an estimation of seawater temperature and water depth at the time of calcification (Jonkers et al., 2013). Robinson et al. (2008) calculated the PRISM Mg/Ca SST estimates at DSDP Site 552 by applying species-specific calibration equations to the Mg/Ca values of *Globigerina bulloides* and *Neogloboquadrina atlantica*. One Mg/Ca SST estimate was derived from *G. bulloides* using the high latitude calibration of Mashiotta et al. (1999). *N. atlantica* is extinct and no specific calibrations exist. Robinson et al. (2008) therefore used three calibrations (Mashiotta et al., 1999; Nuernberg, 1995; Anand et al., 2003), designed for *G. bulloides* and the morphologically-similar extant species *N. pachyderma* to generate Mg/Ca SSTs for *N. atlantica*. Mg/Ca estimates from *G. bulloides* are believed to be most reliable, since this species calcifies throughout the warmest months (late spring and summer) in the top 30 m of the North Atlantic Ocean (Vázquez Riveiros et al., 2016), and requires a simple species-specific calibration. In the modern ocean, the temperature at 30 m depth is c. 2.1°C cooler than at the surface (Levitus and Boyer, 1994). Consequently, the PRISM Mg/Ca ΔSST (4.9°C) used to verify the planktic foraminifer SSTs at DSDP Site 552 is based exclusively on *G. bulloides* corrected for calcification depth.

Our high-resolution $U^{K'}_{37}$ records from DSDP Site 552, demonstrate our average ΔSST_{raw} exhibits near-identical warming to the mean PRISM ΔSST derived from planktic foraminifera, supporting the high magnitude of warming proposed at this locality during this interval (Fig. 4.3, 4.14). However, we show that our alkenone-based SST estimates at this site are derived from low injection concentrations (33 ng/µl on average) which bias our SST records towards warmer values. Our ΔSST_{corr} is 1.7°C cooler than the mean PRISM ΔSST proposed by Dowsett

(A) PRISM3 SST Reconstruction (Dowsett et al., 2012)



(B) THIS STUDY PRISM-interval SST Reconstruction

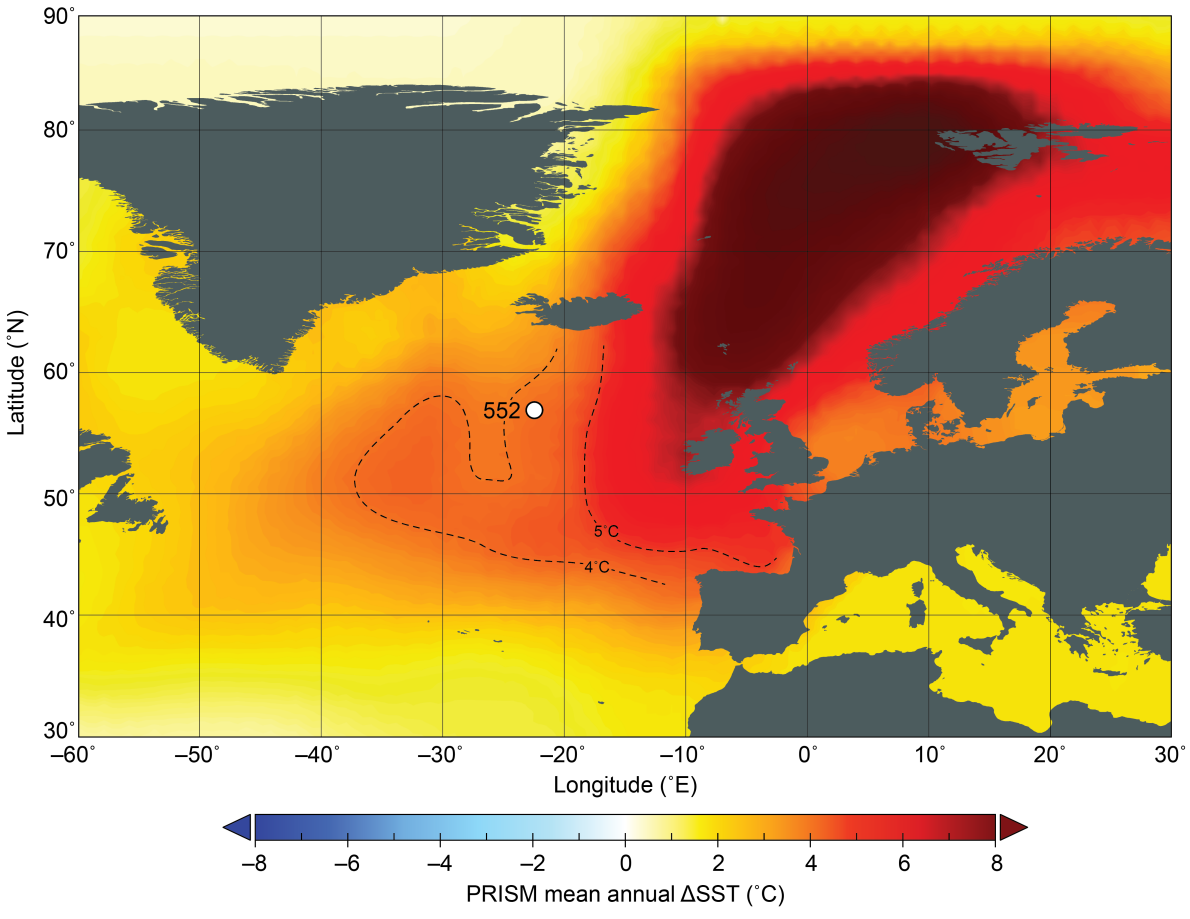


Figure 4.14 (previous page). Mid-Pliocene SST reconstructions at DSDP Site 552 based on the existing PRISM ΔSST and that proposed in this study. (A) The existing mean annual ΔSST (5.5°C) at DSDP Site 552 proposed by Dowsett et al. (2012). (B) The mean annual ΔSST at DSDP Site 552 is revised and lowered to 4.3°C to account for the influence of low total C_{37} concentrations (33 ng/µl on average), and analogous tropical and subtropical foraminifera which are believed to drive transfer functions to overestimate SSTs at this site. Our revised ΔSST represents an average of our mean corrected alkenone-based ΔSST and the depth-corrected *G. bulloides* Mg/Ca ΔSST after Robinson et al. (2008). SST reconstructions are modelled in ArcGIS® v.10.5 using the mean annual PRISM3 and modern SST data (available at: https://geology.er.usgs.gov/egpsc/prism/prism_1_23/prism_data.html [accessed 01/03/2020]).

et al. (2010b), which is more compatible with the cooler Mg/Ca and the cold-season faunal ΔSST estimates from the same site (Robinson et al. 2008). This disagrees with the magnitude of warming implied by the average and warm-season faunal ΔSSTs. However, we believe these foraminiferal transfer functions are inaccurate and overestimate SSTs, due to the influence of *G. puncticulata* and *N. acostaensis* and their warmer extant counterparts. We therefore suggest the mean PRISM ΔSST at DSDP Site 552 is lowered to 4.3°C to account for exaggerated warming, driven by low alkenone concentrations and transfer functions biased by the choice of subtropical and tropical analogues for *G. puncticulata* and *N. acostaensis* (Fig. 4.3, 4.14). This revised value represents an average of our mean $U^{K'}_{37}$ ΔSST_{corr} and the depth-corrected *G. bulloides* Mg/Ca ΔSST (Robinson et al., 2008). Until the uncertainties associated with the influence of warmer foraminifera are resolved, we recommend excluding their SST records from the calculation of the PRISM SST anomaly at this site.

4.6.4 *Implications for PRISM and GCM discrepancies in the NE Atlantic*

Our revised PRISM-interval ΔSST for DSDP Site 552 is c. 1.2°C cooler compared to the existing PRISM3 ΔSST at this site (Dowsett et al., 2010b; 2012). This cooler anomaly reduces discrepancies between proxy-based records and the PRISM3 reconstruction in the NE Atlantic by one third (Fig. 4.3, 4.14, 4.15). Larger discrepancies (up to 6.5°C) persist between our proposed ΔSST and the four GCM simulations. However, these larger differences are believed to be an artefact of uncertainties associated with the simulation of regional oceanic circulation

in the GCMs. Dowsett et al. (2012) suggest the GCMs show a high degree of fluctuation south of Iceland (up to 10°C in mean annual SSTs) and may underestimate warming due to variations in the strength and position of the Gulf Stream and NAC. Rosenbloom et al. (2013) concur and suggest an increase in northward oceanic heat transport is needed to align the CCSM4 and GISS-ER SSTs with the PRISM3 reconstruction. A strengthened NAC is also supported by alkenone records at IODP Site U1313, which indicate a stronger NAC during the PRISM-interval (Naafs et al., 2010). Robinson et al. (2011) also demonstrate a lower GSR (by up to 300 m) helped to strengthen the NAC and regional sea surface warming during the mid-Pliocene (Chapter 3). Incorporating the influence of enhanced poleward oceanic heat transport in these GCMs would inevitably align these models closer to the PRISM3 reconstruction and our proxy results, and help reduce discrepancies in regional SST estimates.

Whilst we propose a reduction in ΔSST at DSDP Site 552, higher ΔSST estimates remain at other nearby PRISM dataset localities in the NE Atlantic, such as DSDP Sites 610, 609 and 548. It is beyond the scope of this study to comprehensively assess the proxy records at these localities (Fig. 4.1, 4.3, 4.4). However, in general, the ΔSSTs at these sites are also based on planktic foraminifera known to drive the GSF18 transfer function to overestimate warming. At DSDP Site 610, the PRISM ΔSST (6.5°C) is based exclusively on planktic foraminifera (Dowsett et al., 2015). The planktic foraminifera census data from DSDP Site 610 reveals the 33 samples used in the PRISM dataset comprise up to 56% of *N. acostaensis* and *G. puncticulata* (35% on average), known to have tropical extant counterparts which bias SSTs towards warmer estimates (Robinson et al., 2008; Dowsett et al., 2015). At DSDP Site 609, the PRISM ΔSST (6.5°C) is based on the average of the planktic foraminifera, depth-corrected Mg/Ca and alkenone temperature estimates (Dowsett et al., 2010b; Dowsett et al., 2015; Bartoli et al., 2005; Robinson et al., 2008). The planktic foraminifera census data from DSDP Site 609 reveals the 34 samples used in the PRISM dataset comprise up to 67% of the two warmer foraminifera (51% on average) (Dowsett et al., 2015). The depth-corrected Mg/Ca SST at DSDP Site 609 is based on *G. bulloides*, an extant and reliable indicator of SSTs. The alkenone-records suggest lower magnitudes of warming (ΔSST 3.4°C) compared to the

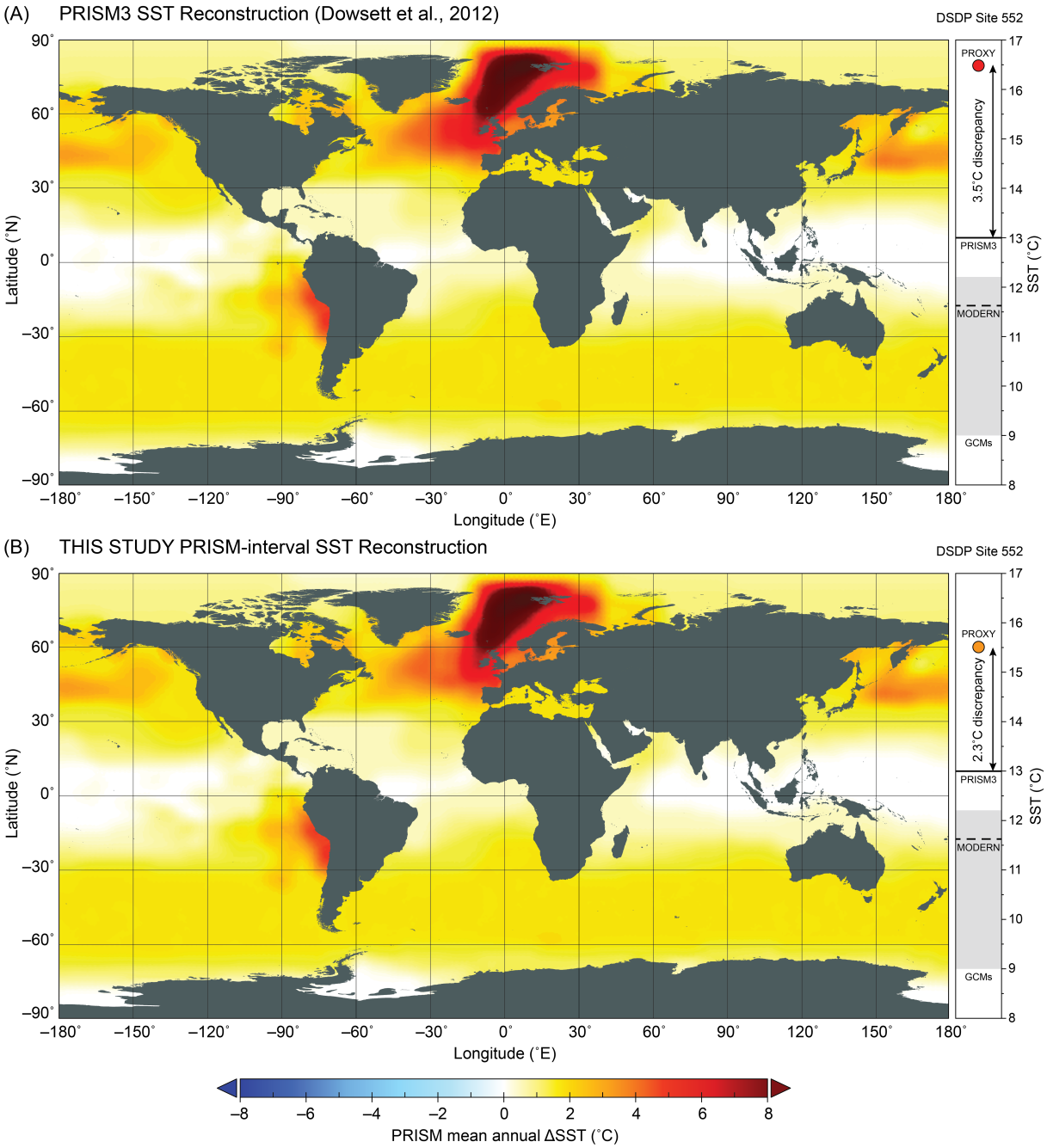


Figure 4.15. Global mid-Pliocene SST reconstructions based on existing PRISM ΔSSTs and those proposed in this study. (A) The existing mean annual ΔSST (5.5°C) at DSDP Site 552 proposed by Dowsett et al. (2012), equates to a 3.5°C discrepancy between the proxy SST data and the PRISM3 reconstruction at this site in the NE Atlantic. (B) Our revised ΔSST (4.3°C) suggests the NE Atlantic was c. 1.2°C cooler during the mid-Pliocene, and reduces the discrepancy between the proxy SST data and the PRISM3 reconstruction by one third at this site. PRISM3 reconstruction, dashed modern SST and GCM grey error band are defined in Fig. 4.3. SST reconstructions are modelled in ArcGIS® v.10.5 using the mean annual PRISM3 and modern SST data (available at: https://geology.er.usgs.gov/egpsc/prism/prism_1_ 23/ prism_data.html [accessed 01/03/2020]).

faunal-based estimates. The concentrations injected to predict SSTs from DSDP Site 609 are unpublished (Robinson et al., 2008; Dowsett et al., 2017), and therefore it is difficult to verify whether these are responsible for potential warming biases. Robinson et al. (2008) extracted c. 5 g of sediment from DSDP Site 609 and diluted the alkenones in c. 200 µl toluene prior to analysis, where the injection volume was 1 µl. Based on the minimum sediment concentration threshold proposed by Dowsett et al. (2012), it is possible to infer a concentration of at least 7.5 ng/µl (Fig. 4.6), which is very low and most likely biases the SSTs to overestimate warming at this locality (Villanueva and Grimalt, 1996). At DSDP Site 548, the PRISM ΔSST (8.7°C) is also based exclusively on planktic foraminifera (Loubere and Moss, 1986; Dowsett and Poore, 1991; Dowsett and Loubere, 1992). The planktic foraminifer census data from DSDP Site 548 reveals the 21 samples used in the PRISM dataset comprise up to 48% of *G. puncticulata* (15% on average) (Dowsett and Loubere, 1992). Dowsett and Loubere (1992) discuss the occurrence of *N. acostaensis* throughout the Pliocene samples. However, the specific abundances of this species are not described. Ultimately, the high abundances of these foraminifera are likely to drive the GSF18 function to overestimate warming at these three DSDP sites. The low alkenone concentrations inferred at DSDP Site 609 are also concerning, and suggest existing alkenone-based SSTs, used to generate the mean PRISM ΔSST at this locality, most likely overestimate warming.

This study suggests the current PRISM discrepancies in the NE Atlantic are caused by inherent problems associated with both the proxy datasets and GCM simulations, whereby the proxies overestimate and the models underestimate warming. Several sites in the NE Atlantic appear to rely heavily on transfer functions to generate SSTs. However, we demonstrate the samples used to calculate these SSTs, comprise relatively high abundances of certain foraminifer species (*G. puncticulata* and *N. acostaensis*) which have extant tropical counterparts known to drive the GSF18 function to overestimate warming (Robinson et al. 2008). We also show how the NE Atlantic alkenone SSTs used in the PRISM reconstruction, are most likely derived from low alkenone concentrations susceptible to irreversible adsorption, which biases SSTs towards warmer values (Villanueva and Grimalt, 1996; Grimalt et al., 2001). We believe the

sample quality threshold (0.3 µg/g) proposed by Dowsett et al. (2012) for PRISM alkenone-based SSTs is irrelevant. We demonstrate that the injection concentrations are a far more important factor during the analysis of alkenone-based SSTs, compared to sediment concentrations which only indicate the quantity of alkenones preserved and extracted, and not those analysed in the GC system. This study suggests injection concentrations are a far more reliable measure of sample quality, and should be utilised more transparently in future PRISM datasets. We show that low concentrations (<216 ng/µl) injected during analysis, have the potential to bias SSTs by up to 3.2°C. We believe the existing alkenone PRISM records at DSDP Sites 552 and 609 are derived from very low alkenone concentrations (<7.5 ng/µl) which most likely drive the SSTs to overestimate warming (Fig. 4.6). Certain GCM simulations (CCSM4 and GISS-ER) also appear to underestimate warming due to variations in the strength and position of the modelled Gulf Stream and NAC (Rosenbloom et al., 2013).

Our work ultimately highlights the innate sensitivity of NE Atlantic PRISM ΔSSTs to the influence of biased transfer functions, low alkenone concentrations and inaccurate model simulations. Utilising transfer functions based exclusively on extant planktic species with known ecological niches, diligently correcting alkenone-based SSTs derived from low concentrations, and improving model simulations to fully represent the strengthened poleward oceanic heat transport inferred from proxy records (Naafs et al., 2010), is inevitably needed to further reduce the PRISM temperature discrepancies observed in this region.

4.7 CONCLUSIONS

The mPWP is an important analogue for future climate, during which global mean surface temperatures are estimated to have been approximately 2−3°C warmer than preindustrial conditions, within the range estimated by the IPCC for the end of the 21st Century. Understanding the mPWP is therefore essential for our ability to predict, adapt to and mitigate the effects of future climate change. Previous work based on PRISM proxy-based datasets suggest SSTs were approximately 6°C warmer in the NE Atlantic and more than 8°C warmer in the Nordic Seas during the mPWP, compared to present-day. However, large temperature discrepancies exist between these proxy estimates and the magnitude of warming predicted by four-leading GCM simulations, which appear to underestimate regional warming by up to 10°C (Dowsett et al., 2012). This study focuses on NE Atlantic and Nordic Sea alkenone records to further unravel these discrepancies and determine whether low concentrations are responsible for potential warming biases.

We present a new alkenone compilation which incorporates all published records from both the NE Atlantic and Nordic Seas for the first time. Our compilation reveals SSTs varied up to 22.0°C and 16.9°C in the NE Atlantic and Nordic Seas, respectively, throughout the PRISM-interval. However, we believe the alkenone-based SSTs at DSDP Site 552, ODP Site 907, ODP Site 909 and ODP Site 911 (Robinson et al., 2008; Robinson, 2009; Clotten et al., 2018; Lawrence, 2020) are derived from very low (<12 ng/µl) injection concentrations, known to be susceptible to chromatographic irreversible adsorption, which drives SSTs to overestimate warming by several degrees (Grimalt et al. 2001). In order to verify the magnitude of warming and the influence of injected concentrations, we present new $U^{K'}_{37}$ and TEX_{86} records from four DSDP/ODP/IODP localities in the NE Atlantic and Nordic Seas throughout the mPWP, including a high-resolution record at the key NE Atlantic PRISM locality DSDP Site 552. We also present a new mathematical method to quantify the potential warming bias associated with irreversible adsorption, and to correct alkenone results for these effects using a dilution series.

Our average $U^{K'}_{37}$ results show very good agreement with alkenone-based PRISM-interval SSTs at DSDP Site 552 and ODP Site 642. However, our $U^{K'}_{37}$ results at IODP Site U1308 and ODP Site 907 far exceed the warming inferred from existing PRISM-interval records. Unlike DSDP Site 552 and ODP Site 642, our records at IODP Site U1308 and ODP Site 907 are based only on four data points, which are considered an insufficient sample to be representative of average warming throughout this interval. Importantly, we show that 60% of our alkenone-based SST records are derived from GC injections of relatively low total C_{37} concentrations (<50 ng/µl). These low concentrations are susceptible to irreversible adsorption, causing our SSTs to overestimate warming (Villanueva and Grimalt, 1996). The similarity in the magnitude of warming observed between our and existing alkenone-based SST records at DSDP Site 552, confirms the original results were most likely derived from low concentrations (Robinson et al., 2008). Correcting our alkenone records to eliminate any potential warming biases associated with these low concentrations, results in significantly cooler PRISM-interval SSTs by up to 3.2°C across all four sites.

Our NE Atlantic and Nordic Seas $U^{K'}_{37}$ records are significantly warmer, by 5.9°C on average, compared to our TEX_{86} records. Our filtered PRISM-interval OPTiMAL ($D_{nearest}$ <0.5) SSTs are also significantly cooler than our $U^{K'}_{37}$ SST records, by 8.6°C on average, across all four sites. 80% of our samples exhibit ΔRI values >0.3, suggesting the majority of our TEX_{86} records are unreliable palaeothermometric indicators. We attribute this mismatch to environmental factors, most notably the deeper mixed-layer depth at which iso-GDGTs are synthesised compared to alkenones (Rodrigo-Gámiz et al., 2015). Subsequently, we exclude our TEX_{86} SSTs from further discussion and discourage their utility in PRISM datasets.

Our corrected alkenone SSTs suggest the current PRISM ΔSST at DSDP Site 552 overestimates warming by c. 1.2°C. We believe the choice of subtropical analogues for extinct foraminifera in the census data drives the GSF18 transfer function to overestimate warming at this site. We demonstrate the existing ΔSST is corroborated by erroneous alkenone-based

SSTs, most likely biased by low C_{37} concentrations (0.06−1.00 ng/µl). We propose that the mean PRISM ΔSST at DSDP Site 552 is revised to 4.3°C, which represents an average of our mean corrected alkenone ΔSST and the depth-corrected *G. bulloides* Mg/Ca ΔSST after Robinson et al. (2008). Our cooler anomaly reduces discrepancies between proxy-based records and the PRISM3 reconstruction in the NE Atlantic by one third. Larger discrepancies remain between our revised ΔSST and the four GCM simulations. However, we attribute these differences due to model inaccuracies associated with the strength and position of the Gulf Stream and NAC, important conveyors of poleward oceanic heat (Rosenbloom et al., 2013).

Our new $U^{K'}_{37}$ SST records represent a significant step in the understanding of the magnitude of mid-Piacenzian warming in the NE Atlantic and Nordic Seas. We have shown the importance of low alkenone concentrations and the influence of warming biases associated with irreversible adsorption on alkenone-based SSTs. We propose the magnitude of warming in the NE Atlantic during the mPWP is c. 1.2°C cooler than originally thought at DSDP Site 552, and we attribute the regional discrepancies between proxy-based records and GCM simulations to challenges associated with the fidelity of both palaeoclimate tools. We suggest injection concentrations are a far more reliable indicator of alkenone sample quality, compared to sediment concentrations, and should be properly documented to reveal potential sources of warming bias, and also preferably used to assess the integrity of alkenone records in multiproxy SST datasets and future PRISM reconstructions.

5. GEOCHEMICAL ANALYSES OF BROWN COALS AND BASALTS FROM THE PLIOCENE TJÖRNES BEDS, NORTHERN ICELAND: PRELIMINARY RESULTS

My contribution to this work involved conducting all parts of the research, including organising and leading the fieldwork in Iceland, collecting samples, laboratory preparation and analysis, interpreting the br-GDGT and Rock Eval™ data, writing the manuscript and creating the figures. M. Allison, M. Papadopoulos and S. Jones assisted with the sampling of brown coals and basalts during fieldwork. M. Allison and M. Papadopoulos helped with the organic extractions and column chromatography. I. Bull, L. Behrooz and H. Whelton assisted with the analysis of branched GDGTs at the Organic Geochemistry Unit (OGU), University of Bristol. C. Vane facilitated the Rock Eval™ pyrolysis at the Organic Geochemistry Facility, British Geological Survey. D. Barfod assisted with the basalt preparation for radiometric dating at the Argon Isotope Facility, Scottish Universities Environmental Research Centre (SUERC). J. Bendle and S. Jones provided feedback on the interpretations of the results. As in previous chapters, the editorial 'we' is used to reflect these contributions.

5.1 OPENING REMARKS

This chapter documents the preliminary geochemical work undertaken on basalt and lignite samples collected from the Tjörnes sequence in northern Iceland, including the radiometric dating of basaltic lavas and the analysis of organic biomarkers in the lignite seams.

Basaltic lavas were sampled to help better constrain the age of this important sedimentary archive of Pliocene palaeoenvironmental change using argon dating, and to provide a reliable temporal framework for integrating our organic geochemical results derived from the lignite seams. Unfortunately, our irradiated basalt samples are yet to undergo $^{40}Ar/^{39}Ar$ analyses by our collaborators at SUERC due to lab closures associated with the COVID-19 pandemic. At the time of writing, we are yet to receive these results and we have no indication of when they will be delivered. Consequently, the rationale and methods behind improving the geochronology of the sequence are discussed here, but the results will be interpreted and published in the future, once we receive them.

Lignite seams were also sampled to determine whether they contain biomarkers which can be used to reconstruct ancient environmental conditions onshore Iceland during the Pliocene. We identify branched-GDGTs in several seams for the first time, analyse the distribution of these membrane lipids throughout the sequence and discuss their potential application as a palaeotemperature indicator. It is premature to fully interpret these results, since a reliable age model based on our radiometric dating is needed to help understand the onset, rate and duration of temperature change inferred from the br-GDGTs preserved in the lignites. We also assess the source-rock potential of all these seams using new pyrolysis data to help further our understanding of the maturation history of the Tjörnes Basin and unravel potential relationships with gas seeps in nearby Öxarfjörður.

5.2 INTRODUCTION

The Tjörnes Beds in northern Iceland are a significant sedimentary archive for understanding palaeoenvironmental change throughout the Pliocene in the NE Atlantic (Buchardt and Símonarson, 2003; Símonarson and Eiríksson, 2008; Verhoeven et al., 2013). During the Pliocene, the NE Atlantic witnessed a transition from extreme warmth, whereby surface temperatures were up to 8°C higher than present (Dowsett et al., 2016; Haywood et al., 2016), to cooling associated with the intensification of the Northern Hemisphere Glaciation (iNHG) around 2.7 Ma (Raymo et al., 1992; Flesche Kleiven et al., 2002; Bartoli et al., 2011). The conjunction of its Pliocene age and its location on the Greenland-Scotland Ridge, whose tectonics may have driven this climatic change, make the Tjörnes Beds a valuable site to reconstruct this palaeoclimatic variability. Previous studies have focused on investigating past climatic change at this locality using dinoflagellates (Verhoeven and Louwye, 2013), molluscs (Bárðarson, 1925; Strauch, 1972; Norton, 1975, 1977; Gladenkov et al., 1980; Símonarson and Eiríksson, 2008), ostracods (Cronin, 1991), pollen (Schwarzbach, 1955; Schwarzbach and Pflug, 1957; Willard, 1994; Verhoeven et al., 2013), vegetation (Windisch, 1886; Akhmetiev et al., 1975, 1978; Denk et al., 2005, 2011) and marine vertebrates (Field et al., 2017).

The age of the Tjörnes Beds is poorly constrained and is based on historic K-Ar dating, magneto- and bio-stratigraphic interpretations. Existing age models place the Tjörnes Beds within the Pliocene Epoch floating between c. 4.9 and 2.58 Ma (Einarsson et al., 1967, Albertsson, 1978; Buchardt and Símonarson, 2003; Símonarson and Eiríksson, 2008; Verhoeven et al., 2011). However, the specific age of the base and top varies significantly between each model and no previous studies have yet dated the Skeifá lavas, which occur mid-succession. Dating the Skeifá lavas and revising the old K-Ar ages would reveal whether the Tjörnes Beds were deposited exclusively throughout the Zanclean or whether deposition extended into the Piacenzian. This has significant implications for determining whether the Tjörnes Beds are likely to contain valuable palaeoenvironmental signals of the mid-Piacenzian

Warm Period (mPWP) (3.025−3.264 Ma) and the onset of global cooling associated with the iNHG.

Multiple brown coal (lignite) seams also occur throughout this marginal-marine succession (Bárðarson, 1925; Strauch, 1963; Eiríksson, 1980, 1981; Buchardt and Símonarson, 2003; Chapter 2). However, in a region dominated by elevated geothermal gradients associated with the Tjörnes Fracture Zone (TFZ) and Northern Volcanic Zone (NVZ), previous studies have mainly focussed on assessing their hydrocarbon (HC) potential (Richter 2001, 2002, 2003), rather than the palaeoclimate signals they may record. No published work has yet determined whether these seams contain organic biomarkers which have the potential to unlock Pliocene terrestrial temperatures in the NE Atlantic. Other challenges are to determine whether potential biomarker assemblages are influenced by thermal maturation, and to further unravel the implications of catagenesis in these organic-rich deposits.

The purpose of this study is two-fold. Firstly, we present a literature review summarising the existing age models at Tjörnes, before documenting our methods and rationale to help constrain the age of the intercalated lavas using modern $^{40}Ar/^{39}Ar$ dating. Secondly, we aim to better characterise and understand the palaeoclimate signals preserved within the lignites, and to further assess the role of these coals in regional petroleum systems, using new branched glycerol dialkyl glycerol tetraethers (br-GDGTs) and Rock Eval™ pyrolysis data. These results should inform our understanding of the geochemical characteristics and maturation history of the Tjörnes lignites, and enable us to assess the reliability and value of temperature signals recorded by biomarkers preserved within these seams. In the following subsection, we review the geological history of the Tjörnes sequence.

5.2.1 *Geological Setting*

The Tjörnes Beds form part of a c. 1200 m thick sequence of Pliocene to Late Pleistocene sediments, exposed on the Tjörnes Peninsula in northern Iceland (Fig. 5.1). This succession was deposited in an extensional basin formed within the inside corner between the TFZ and the NVZ rift axis (Eiríksson, 1981, 1985). Basin uplift (500−600 m) during the Late Pleistocene produced the westward tilting horst observed today (Thoroddsen, 1902; Einarsson et al., 1967; Sæmundsson, 1974). The sedimentary sequence is exposed in incised river valleys and coastal cliffs for c. 10 km along the west side of the Tjörnes Peninsula. This section can be divided stratigraphically into four units: Kaldakvísl lavas, Tjörnes Beds, Höskuldsvík lavas and the Breiðavík Group (Strauch, 1963; Eiríksson, 1981). The Tjörnes Beds are separated from the underlying Kaldakvísl plateau tholeiites (dated 9.9 ± 1.8 and 8.6 ± 0.4 Ma; Aronson and Sæmundsson, 1975) by a WNW trending fault zone in the Kaldakvísl River. To the north of this river, the Tjörnes Beds rest on the erosional surface of the Kaldakvísl lavas (Chapter 2), which includes a flow dated 4.3 ± 0.4 Ma (Albertsson, 1976). The Tjörnes Beds comprise alternating marine (siltstones, sandstones and conglomerates) and terrestrial sediments (siltstones, lignites and sandstones), and basaltic lavas. The sediments dip 5−10° NW and have an exposed thickness of c. 510 m (Chapter 2; Buchardt and Símonarson, 2003). Bárðarson (1925) divides the Tjörnes Beds into 25 shelly (1−25) and 10 terrestrial layers (A−J). Molluscan biostratigraphy splits these sediments into three biozones: the *Tapes* Zone (beds 1−5), the *Mactra* Zone (beds 6−12) and the *Serripes* Zone (beds 13−25) (Bárðarson, 1925). The *Tapes* and lower *Mactra* Zones consist of tidal flat and coastal swamp deposits, comprising sandstones and lignites (Símonarson and Eiríksson, 2008). The upper *Mactra* and lower *Serripes* Zones feature cross-bedded and bioclastic sandstones deposited in a sublittoral environment, during increased subsidence (Símonarson and Eiríksson, 2008). The upper *Serripes* Zone is characterised by renewed estuarine and paludal deposition, associated with reduced subsidence and resumed uplift (Buchardt and Símonarson, 2003). The overlying Höskuldsvík lavas (dated 2.55 ± 0.27 and 2.36 ± 1.8 Ma; Albertsson, 1976, 1978) consist of six subaerial basaltic flows intercalated with fluvial sediments and tuffs (Eiríksson et al., 1990).

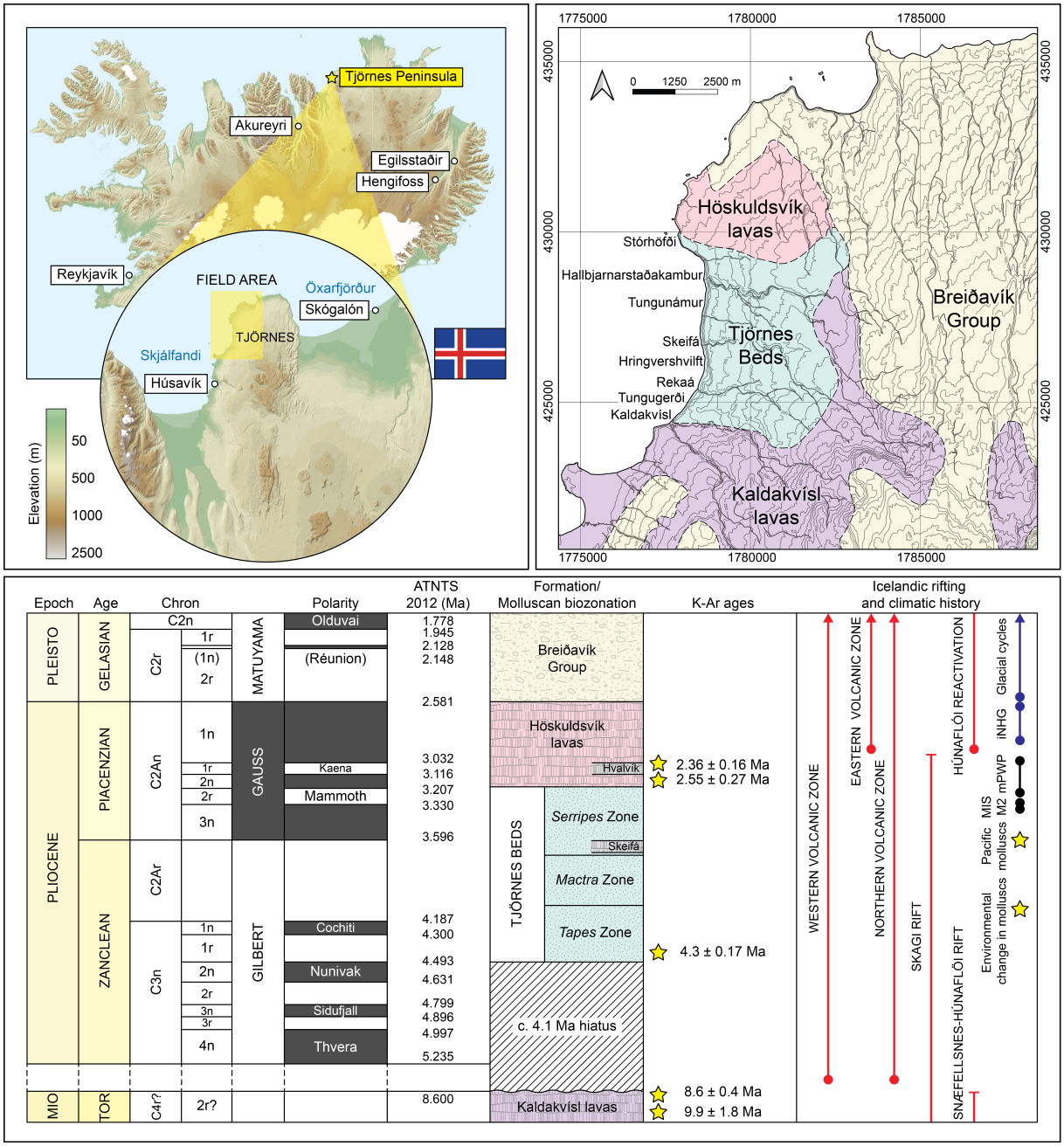

Tjörnes Peninsula
Akureyri
Egilsstaðir
Hengifoss
Reykjavík
FIELD AREA
Öxarfjörður
Skógalón
TJÖRNES
Skjálfandi
Húsavík
Elevation (m)
50
500
1000
2500
1775000
1780000
1785000
435000
430000
425000
0 1250 2500 m
Höskuldsvík lavas
Stórhöfði
Hallbjarnarstaðakambur
Tungunámur
Skeifá
Hringvershvilft
Rekaá
Tungugerði
Kaldakvísl
Tjörnes Beds
Breiðavík Group
Kaldakvísl lavas
Epoch
Age
Chron
Polarity
ATNTS 2012 (Ma)
Formation/ Molluscan biozonation
K-Ar ages
Icelandic rifting and climatic history
PLEISTO
PLIOCENE
MIO
GELASIAN
PIACENZIAN
ZANCLEAN
TOR
C2n
C2r
C2An
C2Ar
C3n
C4r?
MATUYAMA
GAUSS
GILBERT
Olduvai
(Réunion)
Kaena
Mammoth
Cochiti
Nunivak
Sidufjall
Thvera
1.778
1.945
2.128
2.148
2.581
3.032
3.116
3.207
3.330
3.596
4.187
4.300
4.493
4.631
4.799
4.896
4.997
5.235
8.600
Breiðavík Group
Höskuldsvík lavas
Hvalvík
TJÖRNES BEDS
Serripes Zone
Skeifá
Mactra Zone
Tapes Zone
c. 4.1 Ma hiatus
Kaldakvísl lavas
2.36 ± 0.16 Ma
2.55 ± 0.27 Ma
4.3 ± 0.17 Ma
8.6 ± 0.4 Ma
9.9 ± 1.8 Ma
WESTERN VOLCANIC ZONE
EASTERN VOLCANIC ZONE
NORTHERN VOLCANIC ZONE
SKAGI RIFT
HÚNAFLÓI REACTIVATION
SNÆFELLSNES-HÚNAFLÓI RIFT
Glacial cycles
iNHG
mPWP
MIS M2
Pacific molluscs
Environmental change in molluscs

Figure 5.1 (previous page). Location and geological setting of the Tjörnes Peninsula, northern Iceland. Place names discussed in the text are shown. Geological map modified after Eiríksson (1981), using the geocentric coordinate system for Iceland (ISN2004/Lambert 2004; EPSG:5325). The stratigraphic summary of the Tjörnes sequence is after Símonarson and Eiríksson (2008), including palaeopolarity (Eiríksson, 1985; Eiríksson et al., 1990), radiometric K-Ar ages (Aronson and Sæmundsson, 1975; Albertsson, 1976, 1978), molluscan biostratigraphy (Bárðarson, 1925) and Icelandic rifting and climate events (Garcia et al., 2003; Haywood et al., 2016; Walters et al., 2013). MIS M2, Marine Isotope Stage M2; mPWP, mid-Piacenzian Warm Period; iNHG, intensification of the Northern Hemisphere Glaciation. Topographic map created in QGIS v.3.4 using the Landmælingum Íslands (National Land Survey of Iceland) Digital Elevation Model (available at: https://atlas.lmi.is/LmiData/index.php?id=247152041610 [accessed 06/01/2020]).

14 alternating diamictite and marine sandstone and mudstone units characterise the following Breiðavík Group, symbolising deposition during the intense glacial/interglacial cycles indicative of the Quaternary (Eiríksson, 1985, 1990, 1992; Eiríksson and Geirsdóttir, 1991; Geirsdóttir and Eiríksson, 1994).

5.3 BACKGROUND

5.3.1 *Previous age models for the Tjörnes Beds*

Multiple age models (Fig. 5.2) have been proposed for the Tjörnes Beds based on magnetostratigraphy (Einarsson et al., 1967; Buchardt and Símonarson, 2003; Símonarson and Eiríksson, 2008), radiometric dating (Aronson and Sæmundsson, 1975; Albertsson, 1976, 1978) and dinoflagellate biostratigraphy (Verhoeven et al., 2011) during the past seven decades. All of these age models place the Tjörnes Beds within the Pliocene Epoch floating between c. 4.9 and 2.58 Ma. However, the specific age of the base and top of the sequence is unconstrained and varies significantly between each model (Fig. 5.2). The existing age models for the Tjörnes Beds assume continuous sedimentation (c. 0.024 cm/yr) without any major hiatuses (Símonarson and Eiríksson, 2008).

The first palaeomagnetic studies of the intercalated lavas collected from the Tjörnes Beds were undertaken by Hospers (1953). Hospers (1953) measured the thermoremanent magnetism using a portable magnetometer on orientated hand specimens. Hospers (1953) suggests the lowermost 160 m of the Tjörnes Beds are reversely magnetised, whereas the upper 350 m are normally magnetised. Einarsson et al. (1967) re-examined the magnetostratigraphy and proposed the first age model for the Tjörnes section by correlating polarity data with the geomagnetic polarity time scale. The lack of many intercalated lava flows within the sequence limits the number of tie-points and therefore Einarsson et al. (1967) propose two interpretations (Fig. 5.2). The first interpretation correlates the Skeifá pillow lavas with the Mammoth reversed subchron which occurred between 3.207−3.33 Ma. The second interpretation correlates the Mammoth subchron with three reversed flows which occur in the overlying Höskuldsvík lavas at Hvalvík. The Skeifá lavas are correlated with the Gilbert reversed chron, occurring slightly earlier between 3.596−4.187 Ma. Both models suggest the Tjörnes Beds were deposited before 3 Ma, with the first suggesting the majority of deposition occurred throughout the

Zanclean and Piacenzian stages, whereas the second model indicates deposition may have been limited to the Zanclean.

Potassium-argon (K/Ar) dates generated by Aronson and Sæmundsson (1975) and Albertsson (1976, 1978) provide important tie points to constrain the palaeomagnetic interpretations. K/Ar dating of the underlying Kaldakvísl lavas indicates a Tortonian age of 9.9 ± 1.8 and 8.6 ± 0.4 Ma (Aronson and Sæmundsson, 1975). Importantly, these ages are based on the analysis of bulk rock samples with low K_2O compositions (0.267−0.447%), which is considered less reliable than dating individual K-feldspars (Aronson and Sæmundsson, 1975). Albertsson (1976) discovered a significant time gap (c. 4.5 myrs) between the Kaldakvísl lavas and a second lava layer (4.3 ± 0.4 Ma) found at the base of the Tjörnes Beds (Bed 2a of Bárðarson, 1925), exposed at Tungugerði north of the modern hydroelectric plant. The Skeifá lavas are undated using the K/Ar method (Albertsson, 1976). It is suggested the Skeifá lavas may be heavily altered by weathering or hydrothermal activity (Verhoeven et al. 2011). In the Höskuldsvík lavas, the three reversed flows at Hvalvík have an age of 2.36 ± 1.8 Ma, and the normally magnetised basalt at Höskuldsvík, directly above the Tjörnes Beds, has an age of 2.55 ± 0.27 Ma (Albertsson, 1976, 1978). The age model proposed by Albertsson (1978) places the Matuyama/Gauss boundary (2.581 Ma) between these reversed and normal lavas, and the Skeifá pillows are correlated with either the Kaena or Mammoth subchrons (Fig. 5.2).

Glandenkov and Gurari (1976) discovered two reversed polarity events within the *Serripes* Zone, separated by a normal polarity interval. Eiríksson et al. (1990) suggest the three reversed lavas of the Höskuldsvík group at Hvalvík correspond with the Kaena subchron, rather than the lowermost Matuyama as implied by Albertsson (1978). Based on this work Buchardt and Símonarson (2003) propose two alternative age models (Fig. 5.2). The first model suggests the reversed lavas at Hvalvík correspond with the Kaena subchron as suggested by Eiríksson et al. (1990), and the Skeifá pillows correlate with the uppermost Gilbert chron, 0.266 myrs before the Mammoth subchron. The second model correlates the three lavas at Hvalvík to the Matuyama reversal, 451 kyrs younger than the first interpretation,

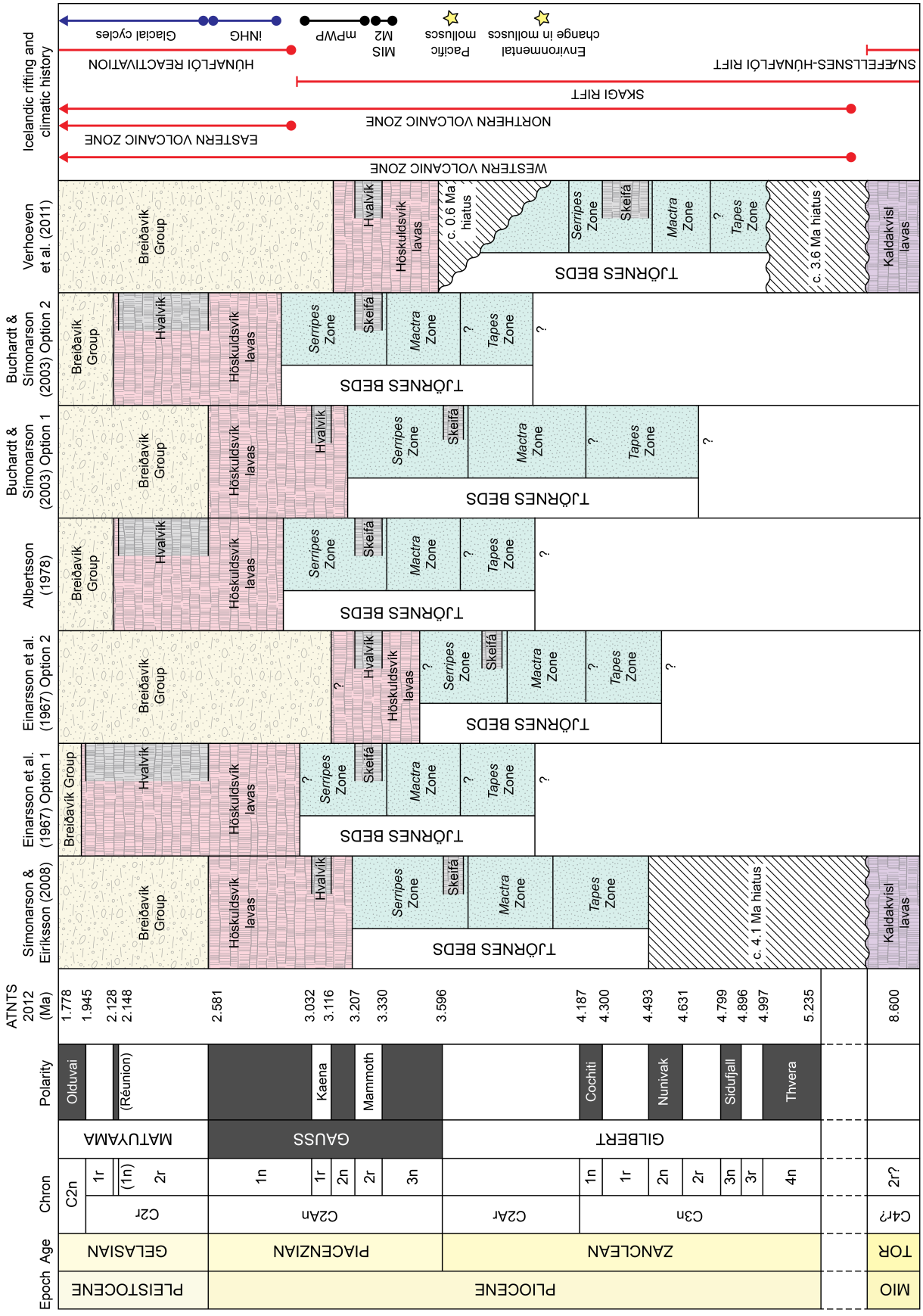

Epoch
Age
Chron
Polarity
ATNTS 2012 (Ma)
Simonarson & Eiriksson (2008)
Einarsson et al. (1967) Option 1
Einarsson et al. (1967) Option 2
Albertsson (1978)
Buchardt & Simonarson (2003) Option 1
Buchardt & Simonarson (2003) Option 2
Verhoeven et al. (2011)
Icelandic rifting and climatic history
MIO
PLIOCENE
PLEISTOCENE
TOR
ZANCLEAN
PIACENZIAN
GELASIAN
C4r?
C3n
C2Ar
C2An
C2r
2r?
4n
3r
3n
2n
2r
1n
1r
(1n)
GILBERT
GAUSS
MATUYAMA
Olduvai
(Réunion)
Cochiti
Nunivak
Sidufjall
Thvera
Kaena
Mammoth
1.778
1.945
2.128
2.148
2.581
3.032
3.116
3.207
3.330
3.596
4.187
4.300
4.493
4.631
4.799
4.896
4.997
5.235
8.600
Breiðavík Group
Hvalvík
Höskuldsvík lavas
Tjörnes beds
Serripes Zone
Skeifá
Mactra Zone
Tapes Zone
c. 4.1 Ma hiatus
Kaldakvísl lavas
c. 0.6 Ma hiatus
c. 3.6 Ma hiatus
WESTERN VOLCANIC ZONE
EASTERN VOLCANIC ZONE
NORTHERN VOLCANIC ZONE
SKAGI RIFT
SNÆFELLSNES-HÚNAFLÓI RIFT
HÚNAFLÓI REACTIVATION
Glacial cycles
iNHG
mPWP
MIS M2
Pacific molluscs
Environmental change in molluscs

Figure 5.2 (previous page). Comparison of existing age models for the Tjörnes Beds. The units are correlated with the Astronomically Tuned Neogene Time Scale (ATNTS 2012; Hilgen et al., 2012) based on the palaeomagnetic polarity correlations of each author. Icelandic rifting and regional climatic events are also shown (Garcia et al., 2013; Haywood et al., 2016; Walters et al., 2013). MIS M2, Marine Isotope Stage M2; mPWP, mid-Piacenzian Warm Period; iNHG, intensification of the Northern Hemisphere Glaciation. Modified from Verhoeven et al. (2011).

and links the Skeifá lavas to the Mammoth subchron, as suggested by Albertsson (1978) and Einarsson et al. (1967). Kristjánsson (2004) does not propose an age model, but suggests the *Serripes* Zone is normally magnetised up to Bed I, before reversing for Beds 24−25. Kristjánsson (2004) confirm the Skeifá pillows exhibit reversed magnetism and suggest they correspond to the uppermost Gilbert chron, supporting the interpretations of Glandenkov and Gurari (1976) and the first model of Buchardt and Símonarson (2003). Símonarson and Eiríksson (2008) propose the most recent palaeomagnetic age model using the magnetostratigraphy of Kristjánsson (2004), and suggest Beds 24−25 correlate with the Mammoth subchron (Fig. 5.2). Símonarson and Eiríksson (2008) suggest the Skeifá lavas correlate to the uppermost Gilbert chron, and indicate the *Mactra*/*Serripes* boundary corresponds with the Gilbert/Gauss boundary at 3.6 Ma. Símonarson and Eiríksson (2008) also note an invasion of cold-water molluscs of North Pacific origin at the *Mactra*/*Serripes* boundary, which supports their magnetostratigraphic interpretation. Símonarson and Eiríksson (2008) suggest the closure of the Central American Seaway induced a flow of surface water from the North Pacific through the Bering Strait and Arctic Ocean, which transported Pacific molluscs to the Nordic Seas and northern Iceland around 3.6 Ma (Backman, 1979; Marinovich, 2000). This age is further constrained by the appearance of North Pacific molluscs at other Pliocene sequences in the North Atlantic, including the Coralline Crag Formation of eastern England, where the cooccurrence of the foraminifers *Globorotalia puncticulata* and *Neogloboquadrina atlantica* and the calcareous nannofossil *Sphenolithus* constrain the minimum age of the invasion to precisely 3.6 Ma (Jenkins and Houghton, 1987; Jenkins et al., 1988; Berggren et al., 1995).

Verhoeven et al. (2011) present the most recent age model for the Tjörnes Beds based on dinoflagellate biostratigraphy (Fig. 5.2), correlated with biostratigraphical ranges of marker species from NE Atlantic and Nordic Sea ocean drilling studies, including six regional Deep Sea Drilling Project (607, 610, 611) and Ocean Drilling Program (642, 909, 987) sites. Verhoeven et al. (2011) demonstrate the Tjörnes Beds mainly consist of Pliocene taxa. However, they suggest the sediments are older than c. 3.8 Ma based on the discovery of *Operculodinium tegillatum* and *Batiacasphaera minuta*, key Zanclean marker species which both have highest occurrences (HO) of c. 3.8 Ma, between Beds 21 and 22 in the middle *Serripes* Zone. Verhoeven et al. (2011) also discovered *Reticulatosphaera actinocoronata*, another key Zanclean marker species with a HO of 4.4 Ma, up to Bed 17. Verhoeven et al. (2011) suggest the whole of the *Serripes* Zone was likely deposited between c. 4.0−4.5 Ma, and correlate the normal polarities above and below the Skeifá pillows to the Cochiti and Nunivak subchrons, respectively. The reversed polarity signal at the top of the *Serripes* Zone, above Bed I, is correlated to the Gilbert chron with an age between 3.596−4.187 Ma. However, Verhoeven et al. (2011) suggest the top of the *Serripes* Zone most likely has an age of c. 4.0 Ma, based on the assumption of continuous sedimentation and an observed sediment thickness of c. 40 m above Bed I. Verhoeven et al. (2011) correlate the overlying Höskuldsvík lavas with the lowermost Gauss chron and link the three reversed flows at Hvalvík with the Mammoth subchron in agreement with the second interpretation of Einarsson et al. (1967). This implies that a large hiatus of c. 600 kyrs occurs between the Tjörnes Beds (>4.187 Ma) and the Höskuldsvík lavas (<3.596 Ma) (Fig. 5.2). However, this hiatus may have been slightly shorter due to lower sedimentation rates associated with the increasing terrestrial input and basin uplift, as implied by the sedimentology (Símonarson and Eiríksson, 2008).

One of the main problems of the Verhoeven et al. (2011) age model is the reconciliation with existing radiometric dating. The K-Ar age (c. 4.3 Ma) of the basalt layer found near the base of the Tjörnes Beds (Bed 2a of Bárðarson, 1925) supports the maximum age implied by the dinoflagellate biostratigraphy. However, when combined with the palaeomagnetic data this age appears to be a few hundred thousand years too young. Verhoeven et al. (2011) also correlate

the reversed three flows at Hvalvík with the Mammoth subchron (3.207−3.330 Ma), which is c. 700 kyrs older than the K-Ar ages of the underlying normal polarity Höskuldsvík lavas (Albertsson, 1976, 1978). Verhoeven et al. (2011) attribute this age difference to post-emplacement radiogenic argon loss associated with weathering, which can bias K-Ar ages towards younger values, and the analytical limitations involved with measuring both potassium and argon on separate aliquots using different methods, including flame photometry for potassium and mass spectrometry for argon. Another problem with the Verhoeven et al. (2011) age model is the influence of reworking on the distribution of dinoflagellates throughout the Tjörnes Beds. Beds 13−17 of the *Serripes* Zone document the HO of *R. actinocoronata*. These sediments were deposited in a shallow sublittoral environment (Símonarson and Eiríksson, 2008). Verhoeven et al. (2011) doubt wave currents alone could cause the reworking of the underlying *Mactra* Zone sediments. However, this author and Símonarson and Eiríksson (2008) indicate these upper *Mactra* Zone and lower *Serripes* Zone sediments are characterised by layers of disarticulated and broken valves, indicating energetic crushing and transportation by wave and tidal currents. Consequently, reworking of *Mactra* sediments by wave and tidal processes cannot be ruled out and may be responsible for the HO of *R. actinocoronata* (Chapter 2). Verhoeven et al. (2011) also indicate that layer J and Bed 25 of Bárðarson (1925) were not sampled, and suggest the intervals between Bed 21 and layer J were barren of dinoflagellates. It is therefore impossible to demonstrate a Zanclean age for the top of the Tjörnes Beds based exclusively on this dinoflagellate biostratigraphy.

This summary of the existing age models clearly indicates a lack of agreement between existing age models and the problems associated with correlating between different chronological techniques, when there is a limited number of outdated radiometric tie-points. It is apparent in all models that successfully dating the Skeifá lavas would significantly improve our understanding of the age of the Tjörnes sequence and would help link the correct reversely magnetised subchron. At present, the implied age of the Skeifá lavas varies by over 1 myrs between the Mammoth and C3n.1r subchrons, depending on age model. Successfully dating these pillows would reveal whether the Tjörnes Beds were deposited exclusively throughout

the Zanclean, as suggested by Verhoeven et al. (2011), or whether deposition extended into the Piacenzian as implied by Einarsson et al. (1967), Buchardt and Símonarson (2003) and Símonarson and Eiríksson (2008). If this is the case, the Tjörnes Beds may contain valuable palaeoclimatic and palaeoenvironmental evidence of the mPWP and the onset of global cooling associated with the iNHG. It is also apparent that existing K-Ar ages, generated more than four decades ago, are now considered unreliable due to problems associated with argon loss, analytical limitations and compatibility with palaeomagnetic data (Símonarson and Eiríksson, 2008; Verhoeven et al., 2011).

These challenges accentuate the need to revise and further constrain the radiometric age model for the Tjörnes Beds using modern techniques to develop a more reliable temporal framework to corroborate biostratigraphic and magnetostratigraphic schemes, and integrate palaeoclimatic results to accurately reveal the onset, rate and duration of palaeoenvironmental changes onshore Iceland during the Pliocene. In this chapter, our progress to revise existing K-Ar ages is documented, including determining the first radiometric age for the Skeifá lavas, using modern argon dating.

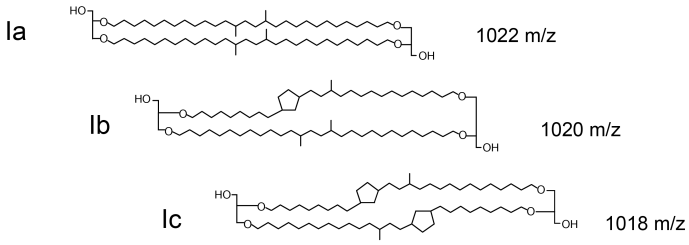
5.3.2 *Branched GDGTs at Tjörnes: a potential onshore Pliocene palaeothermometer*

The NE Atlantic witnessed significant climate change throughout the Pliocene, including enhanced warming during the mPWP followed by global cooling associated with the iNHG. Some of the current age models (Einarsson et al. 1967; Albertsson, 1978; Buchardt and Símonarson, 2003) suggest the Tjörnes Beds span the early to mid-Pliocene (Fig. 5.2), and are comparable to the Coralline Crag Formation in the UK (Balson et al., 1993) and the Kap København Formation in Greenland (Funder et al., 2001). Buchardt and Símonarson (2003) were the first to quantify the palaeotemperature signals preserved in the Tjörnes Beds. Buchardt and Símonarson (2003) analysed the $\delta^{18}O$ signature of bivalve shells sampled from 18 of the 25 beds defined by Bárðarson (1925). They discovered a gradual change from warm-water conditions (10−15°C) during the deposition of the lower part of the Tjörnes Beds (*Tapes*

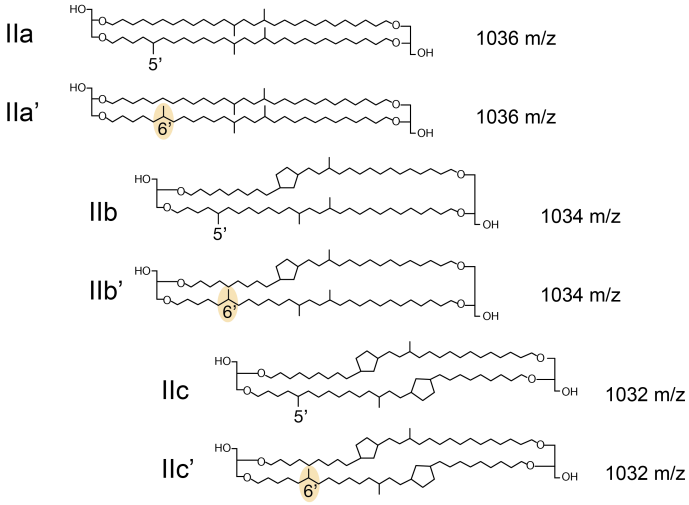
Zone to lower *Mactra* Zone sediments) to colder-water conditions (5−10°C) at the top of the succession (upper *Mactra* Zone to *Serripes* Zone sediments). Buchardt and Símonarson (2003) suggest the coldest (5−8°C) interval occurs in the middle part of the *Serripes* Zone (around Bed 17), and they demonstrate cooling of the Icelandic Sea predated the arrival of cold-water molluscs of North Pacific origin around 3.6 Ma (Backman, 1979; Marinovich, 2000). Dinoflagellate cysts and pollen derived from the Tjörnes Beds are also used to reconstruct palaeotemperature changes throughout the Pliocene (Verhoeven et al. 2013; Verhoeven and Louwye, 2013).

During the last decade, ancient deposits of peat – and by extension lignite – have been used to reconstruct past terrestrial temperatures using br-GDGTs (Ballantyne et al., 2010; Liu et al., 2010; Huguet et al., 2010; Weijers et al., 2011; Naafs et al., 2017; Inglis et al., 2017; Naafs et al., 2018). Br-GDGTs are a group of membrane-spanning lipids produced by heterotrophic bacteria in soils, lakes, peats and marginal-marine environments (Fig. 5.3) (Schouten et al., 2013). The distribution of br-GDGTs is expressed as the MBT'/CBT proxy (methylation of branched tetraethers/cyclisation of branched tetraethers), which strongly correlates with soil temperature (approximated by mean air temperature, MAT or mean annual air temperature, MAAT) and soil pH (Weijers et al., 2007; Peterse et al., 2012). Recent studies have demonstrated additional methyl group(s) can occur in penta- and hexa-methylated br-GDGTs in either the α and/or ω-5 position (5-methyl br-GDGTs) or the α and/or ω-6 position (6-methyl br-GDGTs) (Fig. 5.3) (De Jonge et al., 2013; 2014). De Jonge et al. (2014) discovered 6-methyl br-GDGTs are strongly dependent on pH, and consequently the CBT index was revised to CBT' to incorporate all of the 6-methyl br-GDGTs. Due to this strong correlation with pH, 6-methyl br-GDGTs are now excluded from the MBT' index (now denoted as MBT'_{5ME}) which results in more accurate MAAT calibrations (De Jonge et al., 2014). Recently, Naafs et al. (2017) proposed the first peat-specific br-GDGT based MAAT and pH calibrations based on the analysis of br-GDGTs in 470 samples from 96 global peatlands. Naafs et al. (2017) suggest this calibration is well-suited to reconstruct large amplitude, long-term (>10 kyr) shifts in climate and reveal a good match between absolute temperatures derived from the $MAAT_{peat}$ calibration

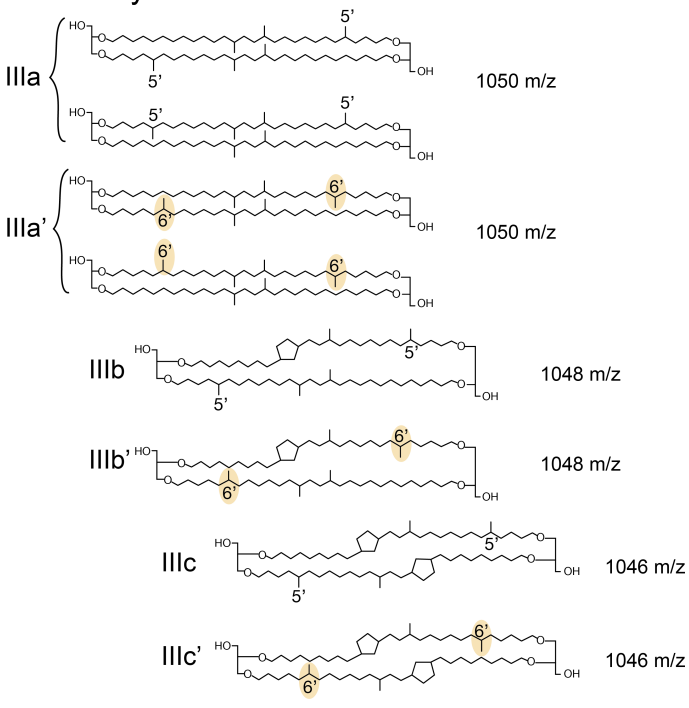
Tetramethylated br-GDGTs



Pentamethylated br-GDGTs



Hexamethylated br-GDGTs



Crenarchaeol

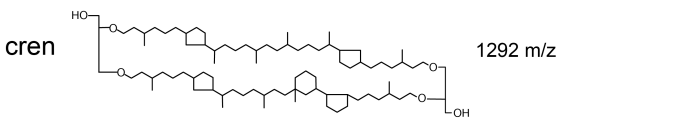


Figure 5.3 (previous page). Chemical structures of branched GDGTs with numbering alongside the isoprenoid GDGT crenarchaeol (cren) following De Jonge et al. (2014). Roman numerals denote tetra- (I), penta- (II) and hexamethylated (III) br-GDGTs. Letters denote the absence (a), presence of one (b) or two (c) cyclopentane rings. 6-methyl br-GDGTs are highlighted with prime symbols, whereby additional methyl groups of the penta- or hexamethylated br-GDGTs occur at the α and/or ω-6 position instead of the α and/or ω-5 position of 5-methyl br-GDGTs. Mass-to-charge ratios (*m*/*z*) are associated with the analysis and identification of br-GDGTs and crenarchaeol using high performance liquid chromatography mass spectrometry.

and those from other proxies. However, it is important to note that the calibration error is large (4.7°C) and major scatter is observed within the mid to high latitude population of samples.

Br-GDGTs are abundant in soils and peats. However, they are susceptible to transport by rivers and readily accumulate in continental shelf sediments (Zell et al., 2014). Consequently, many marginal-marine sediments have been used to reconstruct terrestrial temperature records, including throughout the Pliocene (Crampton-Flood et al., 2018). Recent studies have highlighted uncertainties associated with br-GDGT provenance, with potential sources including *in situ* production in marine (Weijers et al., 2014), fluvial (Zell et al., 2014) and lacustrine environments (Weber et al., 2015), and the wider catchment (Bendle et al., 2010). Changes in organic matter sources associated with catchment scale sediment dynamics, driven by climatic change or other processes, can introduce complications in interpreting the br-GDGT signal (Bendle et al., 2010). Fortunately, peat and lignite are largely unaffected by these processes, recording *in situ* environmental conditions and may provide a unique archive into environmental change (Inglis et al., 2017). The application of the br-GDGT palaeothermometer may be complicated by additional effects on br-GDGT distributions. Schouten et al. (2004; 2013), Weijers et al. (2011) and Zheng et al. (2015) demonstrate that factors such as pore water temperatures and thermal degradation appear to influence GDGTs in modern settings. However, these investigations predate the modern analytical methods which facilitate the separation of 5-methyl and 6-methyl br-GDGTs and do not utilise the most recent calibrations (De Jonge et al., 2014; Naafs et al., 2017).

These studies demonstrate the scope of br-GDGTs preserved within ancient lignite deposits to unlock an understanding of terrestrial temperatures during the time of peat accumulation. Here, we present the first organic geochemical investigation of the Tjörnes lignite seams. We examine br-GDGTs within these ancient peatlands, compare our distributions with modern Icelandic peat deposits and assess the controlling factors which may influence these fossil biomarkers. We propose the first lignite-based MAAT estimates from the Tjörnes Beds, and evaluate whether these results are representative of climatic conditions onshore Iceland during the Pliocene via comparisons with existing palaeoclimate records (Buchardt and Símonarson, 2003; Verhoeven et al. 2013; Verhoeven and Louwye, 2013). Finally, we determine whether our MAAT estimates are reliable indicators of NE Atlantic climate during the mid-Pliocene.

5.3.3 *Hydrocarbon-related research at Tjörnes*

During 1989, thermogenic gas was discovered by the Icelandic Geosurvey (ÍSOR) seeping from geothermal boreholes drilled near Skógalón in Öxarfjörður, situated approximately 15 km east of the Tjörnes Peninsula (Fig. 5.1). Thermogenic gases are generated from the cracking of complex organic molecules as they are cleaved and saturated to produce the alkanes (CH_4 though C_6H_{14}) of natural gas. The Tjörnes Beds extend eastward towards the Öxarfjörður rift zone, where they are buried at more than 1000−1500 m depth (Ármannsson et al. 1998). The geothermal gradient at Öxarfjörður exceeds 200°C/km (Richter and Gunnarsson, 2010). The geothermal gradient is also very high in the adjacent Tjörnes Basin, varying between 40°C/km to 110°C/km (Fridleifsson et al. 1994). These conditions suggest the base of the Tjörnes Beds in Öxarfjörður will be well within the oil window, and possibly within the top of the gas window, as expected from the observed seeps.

Ólafsson et al. (1993) demonstrate natural gas is also seeping, with high concentrations (6% CH_4), from surface sediments at Öxarfjörður. Ólafsson et al. (1993) show the total organic content (TOC) of these sediments is very low (<0.05%), and therefore the gases are believed to be thermogenic, originating from an ancient and deep source. ^{14}C dating of the gases at

Skógalón suggest an age exceeding 20 kyrs (Ólafsson et al., 1993). Analysis of the $\delta^{13}C$ in the CH_4 confirms these gases are derived from the thermal maturation of lignite and coal, rather than a magmatic source (Richter, 2003). Richter (2001) and ÍSOR suggest the origin of these gases is related to the maturation of organic-rich lignite, similar to those observed in the *Tapes* and *Mactra* Zones of the Tjörnes Beds.

In 2001, Richter (2001, 2002) drilled three wells above Skeifá waterfall to collect lignite samples to ascertain whether these coals could generate similar gases to those witnessed at Öxarfjörður. Richter (2001) drilled approximately one tenth (c. 53.50 m) of the total thickness of the Tjörnes Beds above Skeifá waterfall. Based on the stratigraphy proposed in Chapter 2 and by Símonarson and Eiríksson (2008), it is believed Richter (2001) would have only encountered two terrestrial horizons in these cores, Beds E and F of Bárðarson (1925). The 15 lignite samples were analysed at Aarhus University in Denmark. Richter (2003) undertook vitrinite reflectance (R_o) analysis of the lignites. R_o is a measurement of maturity of organic matter based on the percentage of incident light reflected from the surface of vitrinite particles. Richter (2003) concluded that all samples have R_o values <0.40%, which suggests the sampled seams are thermally immature having experienced a maximum temperature of c. <50°C. The lignites have variable TOC contents ranging from 0.05−41.80% (Richter, 2003).

Richter (2003) also undertook Rock-Eval™ pyrolysis to determine the richness and maturity of organic matter in these lignites. During Rock-Eval™ pyrolysis, a sample is progressively heated under an inert atmosphere to 650°C. For 3 min, the oven is kept isothermally at 300°C during which the HCs already present in the sample are volatised (measured as the S_1 peak). As the temperature is raised further (300°C to 650°C; 25°C/min), the insoluble organic matter (kerogen) present in the sample is volatised generating HCs, which are recorded as the S_2 peak. The CO_2 produced from kerogen cracking is then released during the cooling of the pyrolysis oven and is measured as the S_3 peak. T_{max} represents the temperature at the top of the S_2 peak, which symbolises the maximum release of HCs generated from the cracking of kerogen. T_{max} indicates the stage of maturation of organic matter. However, it is important to

note that T_{max} does not relate directly to the maximum temperature that the sediment sample has experienced *in situ*, since lab heating rates are orders faster than geological heating rates. The hydrogen (HI) and oxygen (OI) indexes help to quantify the amount of hydrogen and oxygen present in the kerogen, define the kerogen type and whether the source rock will be oil- or gas-prone. The amount of hydrogen and oxygen in a sample are determined from the S_2 and S_3 peaks, following Behar et al. (2001).

Richter (2003) demonstrate the Tjörnes lignites have T_{max} values varying between 418−429°C, indicating the seams are thermally immature for oil and gas generation, and supporting the R_o analyses (Fig. 5.4A). S_2 measurements vary between 0.00−92.87 mgHC/g rock (Fig. 5.4B), which results in HI values of 0−248 mgHC/gTOC. The Rock-Eval™ pyrolysis results suggest the kerogen is gas-prone Type III, containing higher plant organic matter dominated by vitrinite macerals (Behar et al., 2001). Type III kerogen exhibits enough hydrogen to be gas generative but not enough hydrogen to be oil prone, and is associated with brackish and paralic depositional environments (Jasper et al., 2009). Richter (2003) conclude the Tjörnes Beds on the Tjörnes Peninsula are thermally immature and below the pyrolysis oil and gas generation zones. Richter (2003) suggests the same sediments are very likely to be significantly more mature in other areas, especially when the local geothermal gradient is so high (Fridleifsson et al. 1994; Richter and Gunnarsson, 2010). The potential of the Tjörnes lignites to generate wet and dry gasses and even oil, is therefore very high given the right conditions (Fig. 5.4B). This led Richter (2003) to conclude that lignite seams, similar to those observed at Tjörnes, are most likely the source of the gas escaping at Öxarfjörður. It is also implied these seams may be lateral equivalents of those seen in the Tjörnes Beds.

Importantly, this assessment of source-rock potential for the whole Tjörnes succession is most likely based on chemical analyses from only two lignite-bearing horizons. This study, alongside Símonarson and Eiríksson (2008) and Bárðarson (1925), demonstrate the Tjörnes Beds feature at least six lignite-bearing horizons distributed throughout the sequence, but mainly

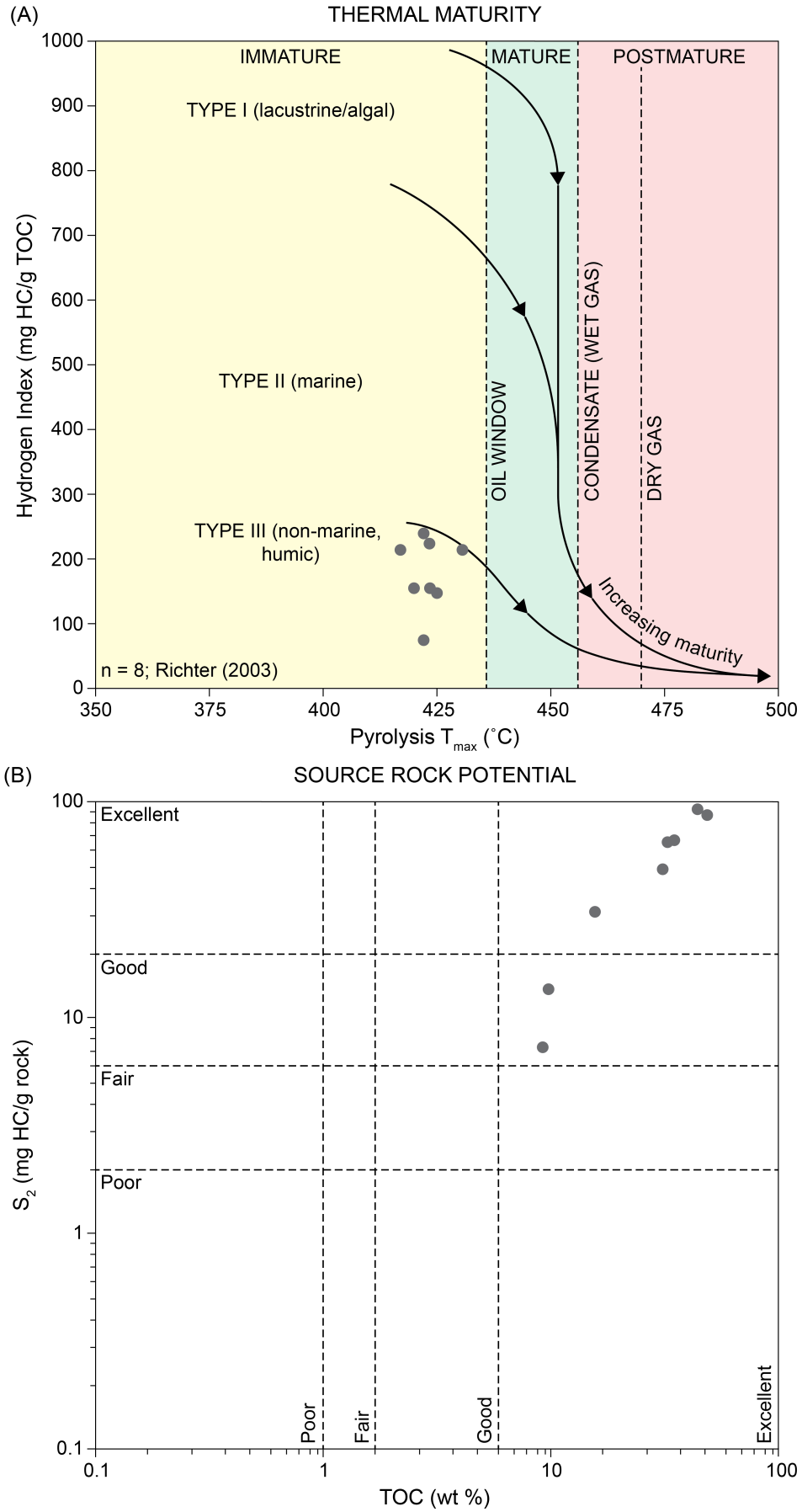

(A)
THERMAL MATURITY
IMMATURE
MATURE
POSTMATURE
TYPE I (lacustrine/algal)
TYPE II (marine)
TYPE III (non-marine, humic)
OIL WINDOW
CONDENSATE (WET GAS)
DRY GAS
Increasing maturity
n = 8; Richter (2003)
Hydrogen Index (mg HC/g TOC)
Pyrolysis T max (˚C)
(B)
SOURCE ROCK POTENTIAL
Excellent
Good
Fair
Poor
S2 (mg HC/g rock)
TOC (wt %)

Figure 5.4 (previous page). Maturation and source rock characterisation after Richter (2003) and Richter and Gunnarsson (2010). (A) Plot of Rock-Eval™ Hydrogen Index (HI) verses pyrolysis T_{max} for the analysed Tjörnes lignite samples (n=8), showing present-day kerogen quality and thermal maturity. All of the samples are thermally immature and below the pyrolysis oil and gas generation zones. (B) Plot of Rock-Eval™ S_2 versus Total Organic Carbon (TOC) (following Dembicki, 2009), indicating the lignites' good to excellent source rock potential.

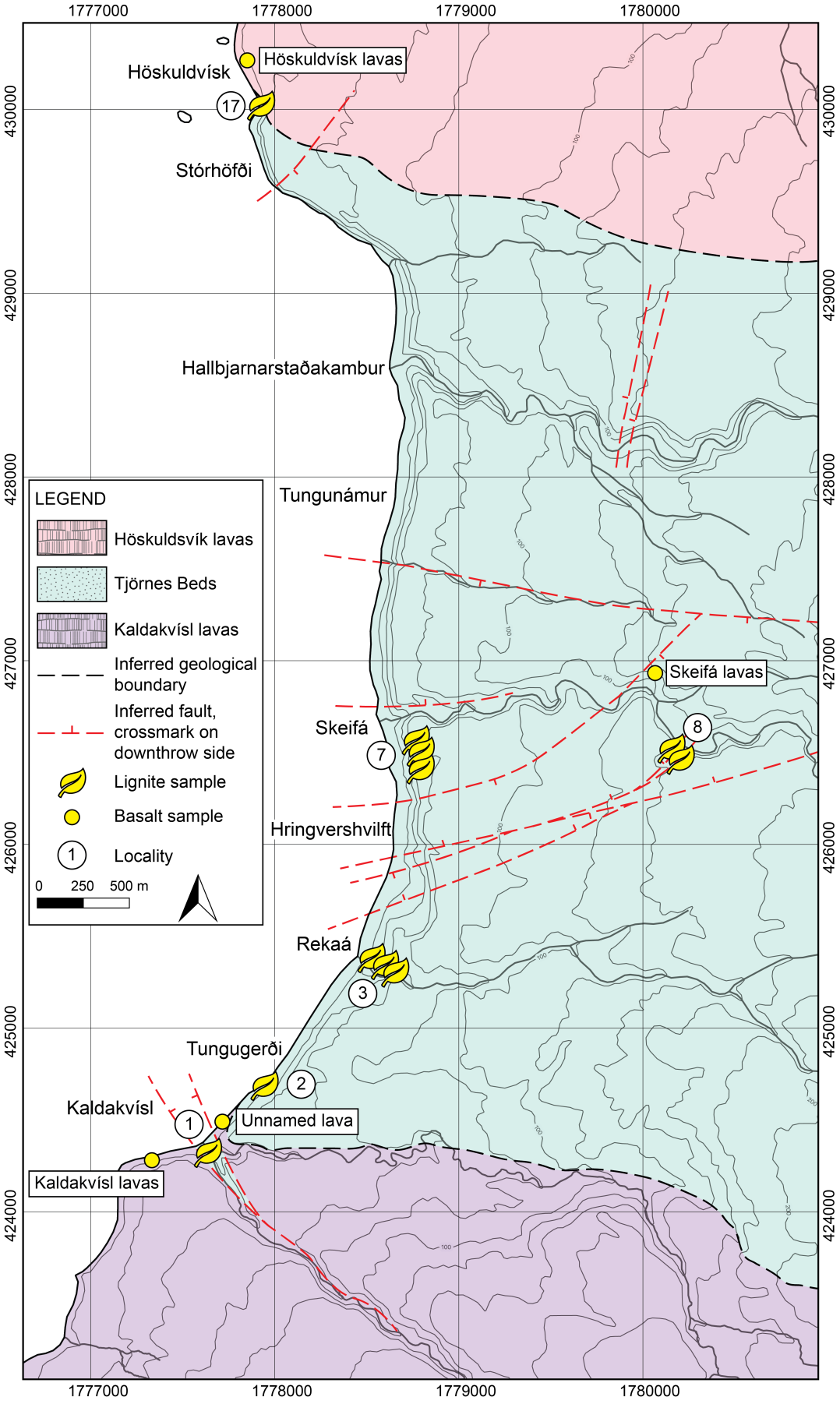
concentrated in the lower *Tapes* and *Mactra* Zones. It is therefore important to assess whether these other seams display a similar degree of maturation to those of Richter (2001, 2003), in order to get a representative insight into the HC-generating potential of the whole sequence and to determine if each seam could potentially produce gas similar to that observed at Öxarfjörður. Here, new Rock-Eval™ pyrolysis measurements derived from outcrop samples provide an opportunity to verify and re-examine existing records of HC maturation, determine whether the degree of maturation varies with depth or proximity to intercalated lavas, and assess the maturation history and HC-generating potential of the entire sequence for the first time.

5.4 MATERIALS, AGE MODEL AND METHODS

5.4.1 *Basaltic lavas*

The volcanic deposits bounding or intercalated within the Tjörnes Beds comprise the following major units, which are arranged stratigraphically from oldest to youngest based on published K-Ar ages: (1) Kaldakvísl lavas (c. 9.9 to c. 8.6 Ma), (2) Unnamed basalts north of the Kaldakvísl river (Bed 2a of Bárðarson, 1925; c. 4.3 Ma), (3) Skeifá lavas (unknown age), and (4) Höskuldsvík lavas (c. 2.55 Ma) (Fig. 5.5; Table 5.1). At Kaldakvísl and Höskuldsvík, the lava flows immediately underlying and overlying the Tjörnes Beds were sampled to constrain a basal and uppermost age, respectively. At the unnamed basalts and the Skeifá pillows, the basal flows immediately overlying the Tjörnes sediments were targeted to give an indication of the timing of renewed volcanic activity. The lavas flows were excavated using a 1.8 kg long-handled lump hammer and cold chisels, to remove weathered surfaces and to expose fresh basalt at the centre of each flow. One basalt sample (c. 1 kg) was obtained from each unit. Loose surficial material was removed with a scrubbing brush, before the samples were wrapped in packing paper and stored in labelled cloth bags.

The basalt samples were thin sectioned for optical petrography at the University of Birmingham, and prepared for triplicate $^{40}Ar/^{39}Ar$ dating of the groundmass at the NERC Argon Isotope Facility at the Scottish Universities Environmental Research Centre (SUERC) in East Kilbride (Appendix A.5). Visibly altered areas were removed using a slow rotating saw. The samples were crushed to c. 2000 μm using a club hammer, before being ground in a disc mill to 200−500 μm and rinsed in Milli-Q® deionised water. The sieved samples were leached in 3N HNO_3 in an ultrasonic bath at 50°C for 60 minutes to remove alteration, before being thoroughly ultrasonicated again in Milli-Q® for another hour. Following drying (T <150°C), the samples were passed through a Frantz isodynamic magnetic separator to remove phenocrysts, xenocrysts and alteration products from the groundmass. The samples were


1777000
1778000
1779000
1780000
430000
429000
428000
427000
426000
425000
424000
Höskuldvísk
Höskuldvísk lavas
17
Stórhöfði
Hallbjarnarstaðakambur
Tungunámur
Skeifá lavas
Skeifá
7
8
Hringvershvilft
Rekaá
3
Tungugerði
2
Kaldakvísl
1
Unnamed lava
Kaldakvísl lavas
LEGEND
Höskuldsvík lavas
Tjörnes Beds
Kaldakvísl lavas
Inferred geological boundary
Inferred fault, crossmark on downthrow side
Lignite sample
Basalt sample
Locality
0 250 500 m

Sample	Material	Location	Stratigraphic height (m)	Bárðarson's Beds	ISN2004/Lambert 2004 Latitude	ISN2004/Lambert 2004 Longitude	Latitude (DD)	Longitude (DD)
Seam 1	Lignite	Kaldakvísl river valley	5.4	A	424324	1777613	66.109°N	17.283°W
Seam 2	Lignite	Tungugerði	59.7	B	424687	1777989	66.108°N	17.275°W
Seam 3	Lignite	Rekaá river valley	140.1	C	425331	1778539	66.114°N	17.262°W
Seam 4	Lignite	Rekaá river valley	143.3	C	425318	1778590	66.114°N	17.261°W
Seam 5	Lignite	Rekaá	154.5	?	425310	1778612	66.114°N	17.261°W
Seam 6	Lignite	Skeifá waterfall	303.6	F	426531	1778718	66.122°N	17.257°W
Seam 7	Lignite	Skeifá waterfall	306.1	F	426537	1778725	66.125°N	17.258°W
Seam 8	Lignite	Skeifá waterfall	309.1	F	426535	1778730	66.125°N	17.257°W
Seam 9	Lignite	Upper Skeifá valley	356.2	?	426653	1780125	66.126°N	17.227°W
Seam 10	Lignite	Upper Skeifá valley	363.5	?	426644	1780122	66.126°N	17.227°W
Seam 11	Lignite	Höskuldsvík	729.1	J	430069	1777919	66.157°N	17.273°W
Kaldakvísl lavas	Basalt	Kaldakvísl headland	0.0	N/A	424296	1777340	66.105°N	17.290°W
Unnamed lava	Basalt	Kaldakvísl river valley	13.9	2a	424443	1777682	66.107°N	17.282°W
Skeifá lavas	Basalt	Upper Skeifá valley	486.1	N/A	426958	1780034	66.129°N	17.228°W
Höskuldsvík lavas	Basalt	Höskuldsvík	745.6	N/A	430328	1777818	66.159°N	17.275°W
Hengifoss pilot	Lignite	Litlanesfoss waterfall	N/A	N/A	315334	1893440	65.081°N	14.884°W

Figure 5.5 (previous page). Geological map of the Tjörnes sequence showing the basalt and lignite sampling locations. Bedrock geology after Eiríksson (1981) and Chapter 2. Locality numbers correspond to sites where lignite seams are preserved within the logged sections, as defined in Fig. 2.2. Place names discussed in the text are shown.

Table 5.1 (previous page). Lignite and basalt sampling localities. Sampled units are described in terms of composite stratigraphic height (Chapter 2), and are correlated with the terrestrial horizons of Bárðarson (1925), where appropriate. Latitude and longitude in ISN2004/Lambert 2004 (EPSG:5325) and decimal degrees (DD), measured using a Garmin® eTrex Vista® HCx (accuracy ±10 m).

handpicked under a binocular microscope to harvest a homogenous groundmass separate (360−500 mg; 120 mg for each replicate). These separates were then irradiated in the CLICIT Facility at the Oregon State University TRIGA reactor.

The irradiated samples are yet to undergo $^{40}Ar/^{39}Ar$ analyses at SUERC due to lab closures associated with the COVID-19 pandemic. At the time of writing, we have yet to receive these results which were originally due by March 2020. As yet we have no indication of when the results will be delivered. Consequently, we are unable to reveal or interpret our new $^{40}Ar/^{39}Ar$ ages for the Tjörnes lavas. We intend to publish our $^{40}Ar/^{39}Ar$ results in the future and revise the age model for the Tjörnes Beds upon receipt of this data.

5.4.2 *Lignite seams*

Lignite samples were collected from 11 terrestrial horizons in the Tjörnes Beds identified in Chapter 2 (Fig. 5.5; Table 5.1). Several of these horizons correspond with the terrestrial beds (A, B, C, F and J) identified by Bárðarson (1925). As discussed in Chapter 2, Bed D was unidentified in the field due to slumping observed at Hringvershvilft and Beds G, H and I are lignite-free and correspond with argillaceous sediments. Two previously undescribed lignite seams at an inland section in the upper Skeifá valley were also sampled. 5 samples per seam (n = 55) were collected randomly along the lateral extent of each exposure. The seams were excavated, where possible, to remove weathered surfaces and expose fresh lignite. Each

lignite sample (c. 100 g) was collected using a solvent-cleaned geological hammer and the samples were stored in furnaced aluminium envelopes packed in labelled sterile Whirl-Pak® bags. Details of the different terrestrial horizons, including facies descriptions, field images and lithological logs are provided in Chapter 2. Based on the most recent magneto- and bio-stratigraphic age models of Buchardt and Símonarson (2003), Símonarson and Eiríksson (2008) and Verhoeven et al. (2011) the age of these seams span nearly the entirety of the Pliocene Epoch, with a maximum age of c. 5.00 Ma and a minimum age of c. 2.58 Ma.

The lignite samples were initially weighed, freeze-dried and homogenised using a solvent-cleaned disc mill (Appendix A.6). C. 20 g of powdered sediment were extracted by repeated heating at 40°C for 1 hour using a dichloromethane/methanol mixture (3:1 v/v). Extractions were repeated at least three times or until the supernatant was colourless. After each extraction step, the extracts were centrifuged at 3000 revolutions per minute (rpm) for 3 minutes, before the supernatants were combined and concentrated, using a rotary evaporator, under vacuum. An aliquot of these total lipid extracts (TLE) was separated further into two sub-fractions using silica-gel column chromatography: apolar and polar fractions by elution with *n*-hexane and a dichloromethane/methanol (95:5 v/v) mixture, respectively. The polar fractions, containing the br-GDGTs, were re-dissolved in 200 µl of *n*-hexane/*i*-propanol (99:1 v/v) and filtered using a 0.45 µm polytetrafluoroethylene (PTFE) syringe filter prior to analysis.

5.4.3 *Branched GDGTs*

The polar fractions were analysed using high-performance liquid chromatography-atmospheric pressure chemical ionisation-mass spectrometry (HPLC-APCI-MS) at the University of Bristol Organic Geochemistry Unit. The analyses were conducted on a Thermo Scientific™ TSQ Quantum™ Access MAX Triple Quadrupole MS equipped with an automatic injector. Separation was achieved in normal phase on two Waters® ACQUITY UPLC® BEH HILIC columns (150 mm; diameter: 2.1 mm; particle size: 1.7 µm; pore size: 130 Å). The flow rate of the hexane/isopropanol (IPA) 99:1 (v/v) eluent was 0.2 ml min^{-1}, isocratically for the first 25

min, followed by an increase in solvent polarity to 3.5% IPA in 25 min, and then by a sharp increase to 10% IPA in 30 min (after Hopmans et al., 2016). Injection volumes were 15 µl and GDGT determinations were based on single injections. Target compounds were analysed with a mass range of *m*/*z* 653 to 1302. Selected ion mode (SIM) was used to monitor the abundance of the $[M+H]^+$ ion (protonated molecular ion) in order to improve the signal-to-noise ratio and increase sensitivity and reproducibility. The peak areas were integrated using Xcalibur™ software to calculate the relative abundance of each membrane lipid. Based on daily measurements of an inhouse peat standard over an annual period, analytical precision (1σ) is ±0.01 for the MBT'_{5ME} proxy index defined below (De Jonge et al., 2014).

5.4.3.1 Proxy Calculation

Informed by previous studies, we employ a range of proxies to express ratios of different br-GDGTs following the classification of De Jonge et al. (2014). The MBT' index (Eq. 5.1) compares the relative abundance of tetramethylated (Ia−Ic) to that of pentamethylated (IIa−IIc') and hexamethylated (IIIa−IIIa') br-GDGTs, which exhibit one or two extra methyl groups (Weijers et al. 2007; Peterse et al., 2012).

$$MBT' = \frac{(Ia + Ib + Ic)}{(Ia + Ib + Ic + IIa + IIa' + IIb + IIb' + IIc + IIc' + IIIa + IIIa')}$$

Equation 5.1. MBT' index (De Jonge et al. 2014).

As discussed, De Jonge et al. (2013) discovered additional methyl groups in the pentamethylated and hexamethylated br-GDGTs which occur in the α and/or ω-6 position (6-methyl br-GDGTs). Excluding 6-methyl br-GDGTs from the MBT' index creates the MBT'_{5ME} index (Eq. 5.2) (De Jonge et al., 2014). De Jonge et al. (2014) propose a linear regression of the MBT'_{5ME} index against MAT (Eq. 5.3), using a global soil dataset composed of 239 soils, which resulted in an improved correlation with temperature compared to the MBT'-based calibration of Peterse et al. (2012). De Jonge et al. (2014) also advocate multiple linear

regression analysis, which results in the strongest correlation with MAT and low residual errors (Eq. 5.4). Recently, Naafs et al. (2017) proposed a peat-specific calibration (Eq. 5.5) using only 5-methyl br-GDGTs featured in the MBT'$_{5ME}$ index. Naafs et al. (2017) show strong correlations between MBT'$_{5ME}$ and MAAT, which are significantly higher than those found in the global soil dataset of De Jonge et al. (2014).

$$MBT'_{5ME} = \frac{(Ia + Ib + Ic)}{(Ia + Ib + Ic + IIa + IIb + IIc + IIIa)}$$

Equation 5.2. MBT'$_{5ME}$ index (De Jonge et al., 2014).

$$MAT = -8.57 + (31.54 \times MBT'_{5ME})$$
$$(r^2 = 0.66, n = 222, RMSE = 4.8°C)$$

Equation 5.3. Linear regression of MBT'$_{5ME}$ against MAT (De Jonge et al., 2014).

$$MAT_{mr} = 7.17 + (17.1 \times [Ia]) + (25.9 \times [Ib]) + (34.4 \times [Ic]) - (28.6 \times [IIa])$$
$$(r^2 = 0.68, n = 222, RMSE = 4.6°C)$$

Equation 5.4. Multiple linear regression analysis (MAT$_{mr}$) (De Jonge et al., 2014).

$$MAAT_{peat} = 52.18 \times MBT'_{5ME} - 23.05$$
$$(r^2 = 0.76, n = 96, RMSE = 4.7°C)$$

Equation 5.5. Peat-specific MAAT proxy (Naafs et al., 2017).

In addition to a varying number of methyl groups, br-GDGTs can also exhibit up to two cyclopentane moieties. CBT' is a revised version of the original CBT index proposed by Weijers et al. (2007) incorporating both 5- and 6-methyl br-GDGTs (Eq. 5.6), and in mineral soils CBT' has a strong correlation with pH (Eq. 5.7) (De Jonge et al., 2014). Naafs et al. (2017)

demonstrate CBT' in peat can be modelled as a function of pH (Eq. 5.8). However, they find the coefficient of determination is lower and the root mean square error (RMSE) is higher compared to the mineral soil calibration (De Jonge et al., 2014). Consequently, Naafs et al. (2017) revise the CBT' index by selecting compounds which are strongly correlated to pH in the numerator (Eq. 5.9). Naafs et al. (2017) propose a peat-specific pH calibration incorporating the new CBT_{peat} index (Eq. 5.10). They acknowledge the coefficient of determination is higher and the RMSE is lower for their peat-specific pH calibration compared to using CBT'. However, the calibration uncertainties remain greater than those suggested for mineral soils (De Jonge et al., 2014). Naafs et al. (2017) attribute this difference due to variations in water content between soil and peat which influences br-GDGTs, especially 6-methyl br-GDGTs (Menges et al., 2014). Dang et al. (2016) demonstrate CBT_{5ME} is higher in dry soils compared to wet soils. Peats are usually water saturated and therefore this may explain the weaker relationship between CBT' and pH in peat compared to mineral soils (Naafs et al., 2017).

$$CBT' = log\left(\frac{Ic + IIa' + IIb' + IIc' + IIIa' + IIIb' + IIIc'}{Ia + IIa + IIIa}\right)$$

Equation 5.6. CBT' index (De Jonge et al., 2014).

$$pH = 7.15 + (1.59 \times CBT')$$
$$(r^2 = 0.85, n = 221, RMSE = 0.52)$$

Equation 5.7. CBT' index modelled as a function of pH in mineral soil (De Jonge et al., 2014).

$$pH = 9.19 + (2.69 \times CBT')$$
$$(r^2 = 0.44, n = 50, RMSE = 1.0)$$

Equation 5.8. CBT' index modelled as a function of pH in peat (Naafs et al., 2017).

$$CBT_{peat} = log\left(\frac{Ib + IIa' + IIb + IIb' + IIIa'}{Ia + IIa + IIIa}\right)$$

Equation 5.9. CBT_{peat} index (Naafs et al., 2017).

$$pH = 8.07 + (2.49 \times CBT_{peat})$$
$$(r^2 = 0.58, n = 51, RMSE = 0.8)$$

Equation 5.10. Peat-specific pH calibration (Naafs et al., 2017).

The Branched and Isoprenoid Tetraether (BIT) index was calculated using the equation (Eq. 5.11) proposed by Hopmans et al. (2004). Roman numerals indicate the relative abundances and structures of terrestrially derived tetraether lipids (Ia−IIIa) versus marine- and lacustrine-derived crenarchaeol. Equation 5.11 includes the 5-methyl (e.g. IIa) and 6 methyl (e.g. IIa' and IIIa') br-GDGTs which were analysed as co-eluting compounds in the original BIT study (Hopmans et al., 2004).

$$BIT = \frac{(Ia + IIa + IIa' + IIIa + IIIa')}{(Ia + IIa + IIa' + IIIa + IIIa' + Crenarchaeol)}$$

Equation 5.11. BIT index (Hopmans et al., 2004).

5.4.4 *Rock-Eval™ Pyrolysis*

Pyrolysis was performed on 33 samples (3 per seam) using a Rock-Eval™ 6 analyser (Vinci Technologies Ltd), in standard configuration (pyrolysis followed by oxidation), at the British Geological Survey Organic Geochemistry Laboratory (Keyworth, UK). C. 60 mg (dry weight) of powdered sediment was heated at 300°C for 3 min, and then from 300°C to 650°C at 25°C per min in an inert nitrogen atmosphere. HCs released during the two-stage pyrolysis were measured using a flame ionisation detector (FID). The CO and CO_2 released during the thermal cracking of bound organic matter were measured using an infrared cell. Rock-Eval™

parameters were calculated by integrating the amounts of HC, including S_1 and S_2 (in mg HC/g rock). The HI, OI and production index (PI) were calculated (Eq. 5.12, 5.13, 5.14) following the methods of Behar et al. (2001). PI is another indicator of thermal maturation, whereby values <0.1 and 0.1−0.4, indicate immature and mature source rocks, respectively (Behar et al., 2001). Thermal maxima values were calculated using the highest yield of bound HCs (top of the S_2 peak). Instrument performance was verified every 10 samples against the accepted values of the Institut Français du Pétrole (IFP) standard (IFP 160000, S/N1 5-081840). Instrument error (1σ) was S_1: ±0.01 mg HC/g rock, S_2: ±0.46 mg HC/g rock, TOC: ±0.51% weight and T_{max} ±0.75°C.

$$HI = \frac{S2\ (mg\ HC/g\ rock)}{\%TOC} \times 100$$

Equation 5.12. Hydrogen index (Behar et al., 2001).

$$OI = \frac{S3\ (mg\ HC/g\ rock)}{\%TOC} \times 100$$

Equation 5.13. Oxygen index (Behar et al., 2001).

$$PI = \frac{S1\ (mg\ HC/g\ rock)}{S1\ (mg\ HC/g\ rock) + S2\ (mg\ HC/g\ rock)}$$

Equation 5.14. Production index (Behar et al., 2001).

5.5 RESULTS

5.5.1 *Tjörnes lava descriptions*

The Kaldakvísl lavas and the unnamed flow north of the Kaldakvísl river (Bed 2a of Bárðarson, 1925) have near-identical very-fine grained (<0.5 mm), holocrystalline and porphyritic textures (Fig. 5.6). Both tholeiite basalts exhibit extensive evidence of hydrothermal alteration, including sericitic alteration of plagioclase and pervasive oxidation of groundmass minerals. The similar petrographic characteristics suggest the lavas are related. This supports our stratigraphic interpretation proposed in Chapter 2, where we suggest the Kaldakvísl lavas form up-thrown horst blocks either side of the Kaldakvísl valley in agreement with Buchardt and Símonarson (2003). The associated faulting is believed to have facilitated fluid flow, causing the localised sericitic alteration and oxidation.

The Skeifá lavas are hypocrystalline and porphyritic tholeiite basalts dominated by plagioclase and clinopyroxene phenocrysts and a glassy groundmass (Fig. 5.7). Dissolved rims are common, with some phenocrysts becoming so dissolved they are almost skeletal in form. The Höskuldsvík lavas are sparsely porphyritic and equigranular holocrystalline tholeiite basalts comprising a fine-grained (<1 mm) groundmass of plagioclase, pyroxene and rare olivine. Detailed thin-section descriptions for each unit are outlined in Appendix B.

5.5.2 *Branched GDGT distributions in the Tjörnes lignites*

Br-GDGTs occur in all seams, apart from the lowermost lignite (Bed A of Bárðarson, 1925) found in the tilted fault block near the Kaldakvísl river. The distributions are dominated by pentamethylated br-GDGTs which comprise 43% of the total br-GDGT assemblage (Fig. 5.8). The most abundant br-GDGT is IIa which make up 37% of the total br-GDGT assemblage. Seam 2 contains the lowest quantity of br-GDGTs (Ia, Ib, Ic), whereas Seam 8 exhibits the maximum number of br-GDGTs (Ia, Ib, Ic, IIa, IIa’, IIb, IIb’, IIc, IIIa, IIIa’). Detritic facies contain

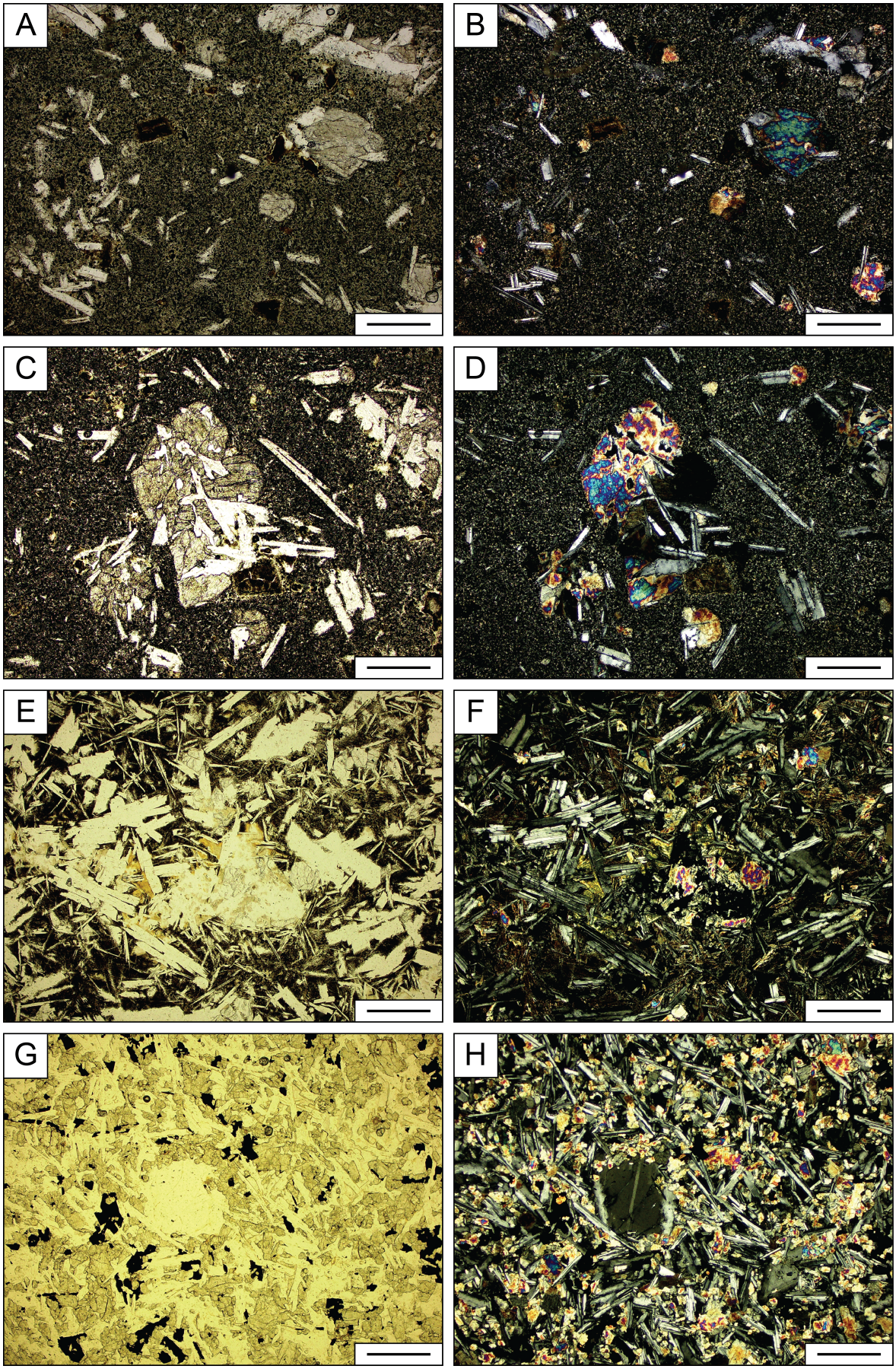

A
B
C
D
E
F
G
H

Figure 5.6 (previous page). Petrographic features of the Kaldakvísl (A, B), Unnamed (C, D), Skeifá (E, F) and Höskuldsvík (G, H) lava samples under plane-polarised (A, C, E, G) and cross-polarised light (B, D, F, H). Detailed petrographic descriptions are outlined in Appendix B. Scale bars represent 100 µm.

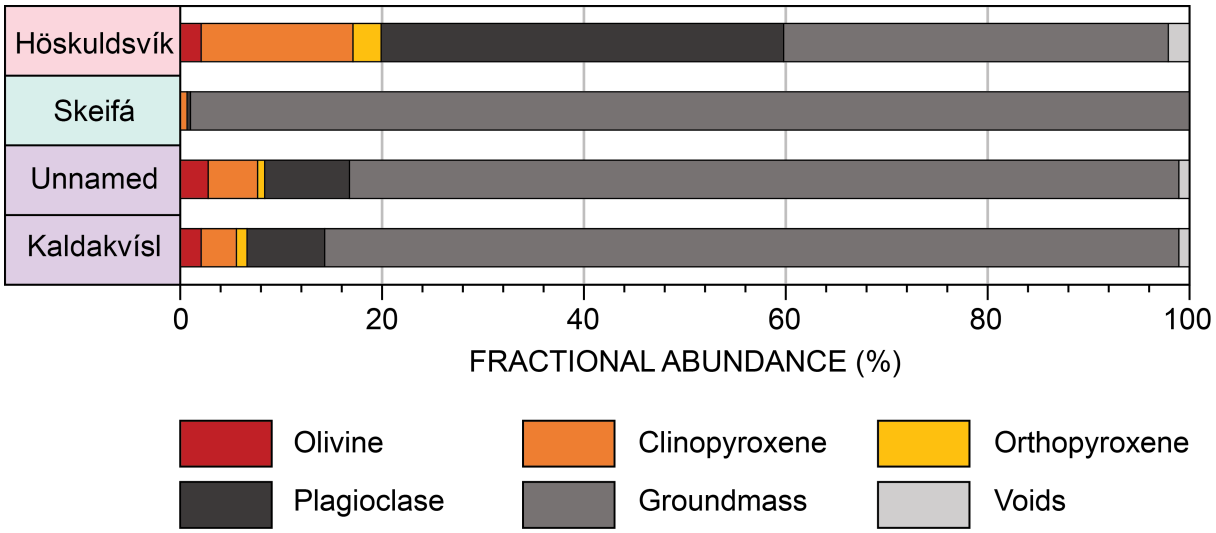


Figure 5.7. Mineralogical abundances of the Kaldakvísl, Unnamed, Skeifá and Höskuldsvík lavas. Samples are arranged stratigraphically from oldest to youngest (bottom to top).

more IIa, IIa', IIIa and IIIa' br-GDGTs, whereas xylitic seams feature more Ia and Ib br-GDGTs. 6-methyl br-GDGTs comprise only 6% of the total br-GDGT assemblage, where the hexamethylated br-GDGT IIIa' is the most abundant (4%). Br-GDGTs IIb', IIc', IIIb' and IIIc' are usually absent. The lack of 6-methyl br-GDGTs is attributed to the dominance of the tetra- and pentamethylated br-GDGTs, which do not feature a methyl group in the α and/or ω-6 position, and the relatively acidic and water saturated depositional settings which are linked to low abundances of 6-methyl br-GDGTs in the global soil dataset (De Jonge et al., 2014).

5.5.3 *Branched GDGT ratios and MAAT, pH and BIT trends*

We limit the following analysis to the most recent indices and calibrations which feature the greatest correlation with modern MAAT and pH (De Jonge et al., 2014; Naafs et al., 2017). Both MAT_{mr} and $MAAT_{peat}$ values are highly variable, ranging between −5.1°C to 10.4°C and −12.0°C to 6.0°C, respectively (Fig. 5.8). The $MAAT_{peat}$ results are 6.8°C cooler, on average, compared to the MAT_{mr} temperature estimates. Seam 3 exhibits the warmest MAT_{mr} and

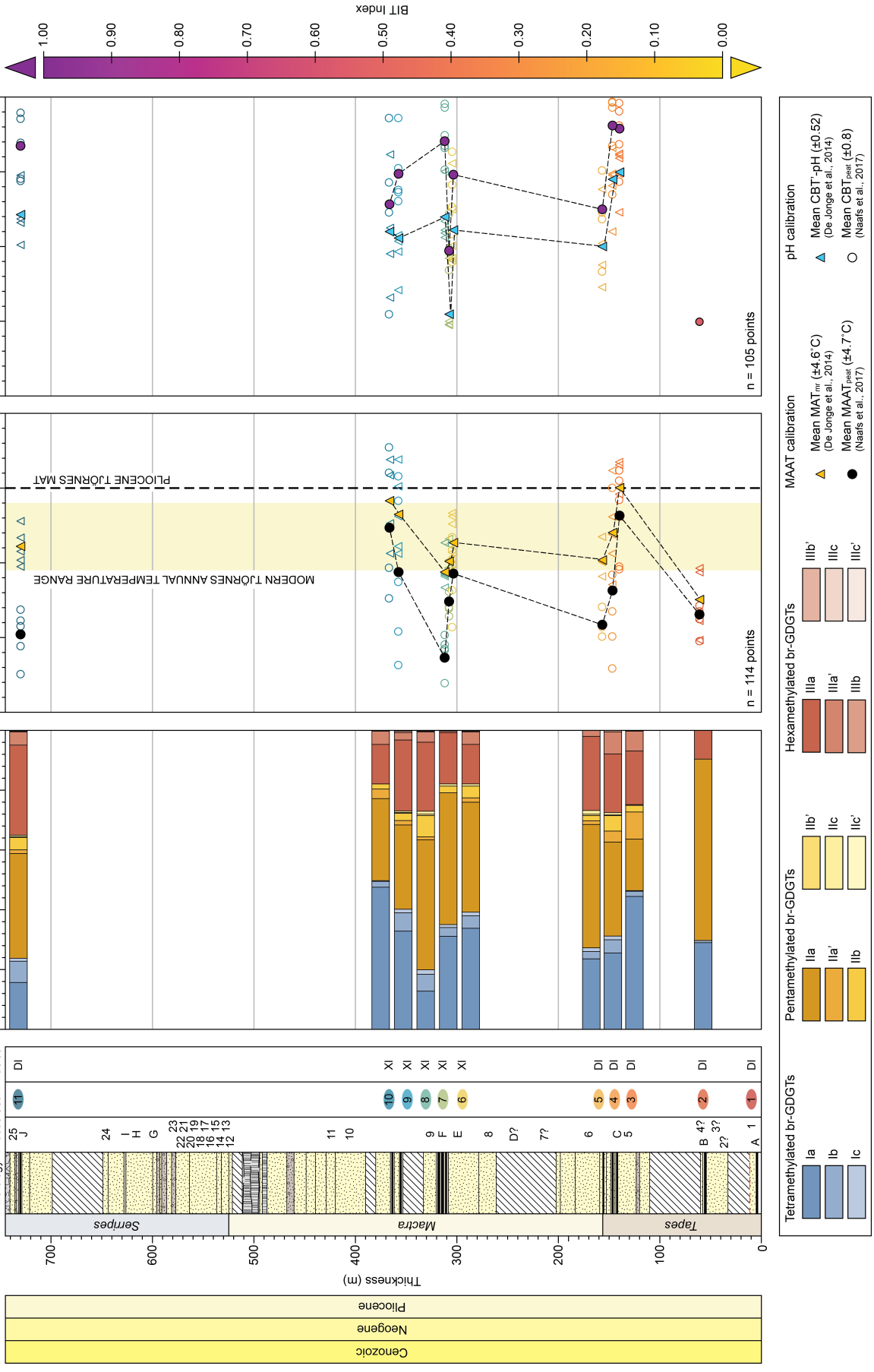

TJÖRNES STRATIGRAPHY
Lithology
B' beds
Seam
Facies
Thickness (m)
Tapes
Macta
Serripes
Cenozoic
Neogene
Pliocene
br-GDGT FRACTIONAL ABUNDANCE (%)
MAAT (˚C)
MODERN TJÖRNES ANNUAL TEMPERATURE RANGE
PLIOCENE TJÖRNES MAT
n = 114 points
pH
n = 105 points
BIT Index
Tetramethylated br-GDGTs
Pentamethylated br-GDGTs
Hexamethylated br-GDGTs
MAAT calibration
Mean MATmr (±4.6˚C)
(De Jonge et al., 2014)
Mean MAATpeat (±4.7˚C)
(Naafs et al., 2017)
pH calibration
Mean CBT'-pH (±0.52)
(De Jonge et al., 2014)
Mean CBTpeat (±0.8)
(Naafs et al., 2017)

Figure 5.8 (previous page). Summary of br-GDGTs, MAAT and pH estimates derived from the Tjörnes lignite seams. Br-GDGT fractional abundances show the relative percent proportions of the different tetra-, penta- and hexamethylated br-GDGTs within each seam. Raw MAAT and pH estimates are plotted as hollow symbols from which the mean values (solid triangles and circles) are calculated. Calibrations derived from De Jonge et al. (2014) (triangles; Eq. 5.4, 5.6 and 5.7) and Naafs et al. (2017) (circles; Eq. 5.2, 5.5, 5.9 and 5.10). Symbols are colour-coded based on the numbered seams. Estimated Pliocene MAT shown by dashed line (Verhoeven et al., 2013). Modern annual temperature range highlighted by yellow bar (Icelandic Meteorological Office, 2020). Mean CBT_{peat} symbols are coloured based on the average BIT index derived from each seam (Hopmans et al., 2004; Eq. 5.11). High BIT index values (>0.5) signify a greater influence of terrestrially derived tetraether lipids, as shown by the colour ramp. Lithostratigraphic section, mollusc biozonation (B' beds; Bárðarson's beds) and sedimentary facies are outlined in Chapter 2. Dl, Detritic lignite; Xl, Xylitic lignite.

$MAAT_{peat}$ estimates (10.4°C and 6.0°C, respectively). Seam 2 exhibits the coolest MAT_{mr} value of −5.1°C, whereas seam 8 has the coolest $MAAT_{peat}$ estimate of −12.0°C.

Both CBT'-pH and CBT_{peat}-pH estimates are relatively stable and range from 4.1 to 6.0 and 4.0 to 6.6, respectively (Fig. 5.8). The CBT_{peat}-pH results are more alkaline, by 0.52 units on average, compared to the CBT'-pH estimates. The average CBT'-pH in detritic seams is 4.5 and in xylitic lignites is 5.0. The average CBT_{peat}-pH (5.78) is the same in both detritic and xylitic facies. Seams 3 to 11 exhibit BIT indices ranging from 0.94 to 1.00, indicating the majority of GDGTs are terrestrially derived (Fig. 5.8). Seam 2 has the lowest BIT index value of 0.62. However, this is a consequence of a reduction in br-GDGT concentrations rather than an increase in marine-derived crenarchaeol. Xylitic seams have a higher average BIT value (1.00), compared to the detritic lignites (0.90).

5.5.4 *Rock-Eval™ Pyrolysis*

TOC content of the 33 pyrolysates vary between 6.33−68.03% (Table 5.2). Seam 10 features the highest average TOC (57.35%) and Seam 5 exhibits the lowest (15.74%). TOC content in the xylitic seams is approximately 37% higher, on average, compared to the detritic facies. S_1 values vary between 0.13−7.24 mg HC/g rock and S_2 values vary between 0.90−79.57 mg

Tjörnes seam	S_1 (mg HC/g rock)	S_2 (mg HC/g rock)	HI (mgHC/gTOC)	OI ($mgCO_2$/gTOC)	PI	T_{max} (°C)	TOC (%)
1	1.12	79.57	185	30	0.01	419	43.10
	0.91	59.96	162	31	0.02	420	36.91
	0.75	45.82	92	34	0.02	418	50.05
2	0.45	18.36	97	164	0.02	426	18.99
	0.13	9.05	63	151	0.01	424	14.35
	0.20	10.33	67	186	0.02	429	15.38
3	0.80	14.69	31	115	0.05	362	47.37
	0.92	13.06	25	116	0.07	363	51.38
	0.85	13.70	25	98	0.06	371	53.92
4	0.27	5.25	19	103	0.05	376	27.61
	0.21	6.62	31	82	0.03	383	21.20
	0.70	10.28	75	73	0.06	421	13.68
5	0.25	11.49	104	154	0.02	431	11.07
	0.20	10.21	87	176	0.02	431	11.78
	0.46	27.30	112	169	0.02	427	24.36
6	5.08	50.41	139	71	0.09	406	36.23
	2.43	22.05	45	75	0.10	367	48.50
	0.14	0.90	14	130	0.14	378	6.33
7	7.24	62.27	160	70	0.10	409	38.98
	5.25	37.51	149	62	0.12	412	25.16
	6.65	52.50	133	68	0.11	407	39.44
8	2.08	16.08	55	102	0.11	392	29.02
	1.60	14.55	50	108	0.10	390	28.89
	2.67	21.48	58	94	0.11	395	37.25
9	0.22	3.48	22	90	0.06	378	16.04
	4.00	35.89	56	79	0.10	369	63.63
	0.55	6.93	37	96	0.07	380	18.96
10	3.40	19.13	34	90	0.15	355	56.72
	0.93	38.08	81	45	0.02	366	47.29
	2.32	43.78	64	56	0.05	365	68.03
11	0.55	10.33	66	99	0.05	413	15.71
	0.59	11.72	69	108	0.05	413	17.02
	0.52	10.28	62	109	0.05	414	16.62

Table 5.2. Rock-Eval™ pyrolysis data derived from the Tjörnes lignites, including S_1, S_2, Hydrogen Index (HI), Oxygen Index (OI), Production Index (PI), T_{max} and Total Organic Carbon (TOC). Numbered seams correspond to those colour-coded in Fig. 5.8 and listed in Table 5.1.

HC/g rock. The xylitic seams exhibit average S_1 and S_2 values which are 2.42 mg HC/g rock and 7.89 mg HC/g rock higher, respectively, compared to the detritic facies. HI values vary between 14−185 mgHC/gTOC, and OI measurements vary between 17−62 mgCO_2/gTOC. The low HI values (<200 mgHC/gTOC) indicate the seams are characteristic of gas-prone Type III kerogen. The seams exhibit an average PI value of 0.06. The T_{max} values vary between 355−431°C. The T_{max} values for the detritic seams is 23°C warmer, on average, compared to the xylitic facies. Seams 1, 2, 5 and 11 show the highest average T_{max} values (413−429°C). The low T_{max}, HI, PI and S_1 indices indicate all of the seams, as seen on the Tjörnes Peninsula, are thermally immature and below the pyrolysis oil and gas generation zones.

5.6 DISCUSSION

5.6.1 *Fidelity of br-GDGT palaeothermometry in the Tjörnes lignite deposits*

Existing pollen and mollusc palaeotemperature records derived from the Tjörnes Beds suggest northern Iceland was significantly warmer during the Pliocene compared to today (Fig. 5.9) (Verhoeven et al., 2013; Buchardt and Símonarson, 2003). Palynological reconstructions indicate winter and summer temperatures were at least 1.3°C and 8°C warmer than present (Verhoeven et al., 2013). Denk et al. (2011) and Verhoeven et al. (2013) show the dominant plant types represented by spores throughout the Tjörnes Beds are warmth-loving *Ilex aquifolium* (common holly), *Castaneae* (chestnut), *Carya* (hickory) and *Hedera* (ivy), which demand winter and summer temperatures greater than 0°C and 12°C respectively. Verhoeven et al. (2013) indicate this vegetation displays similarities to modern temperate, western European vegetation, and corresponds to a Cfb climate of the Köppen-Geiger classification system. These pollen air temperature estimates are also supported by localised sea surface temperature (SST) reconstructions based on the $\delta^{18}O$ composition of bivalves preserved in the Tjörnes Beds (Fig. 5.9), which indicate warm (5−15°C) surface water conditions during deposition (Buchardt and Símonarson, 2003). Regional multiproxy SST reconstructions also suggest the Nordic Seas were considerably warmer (+6°C) during the early to mid-Pliocene compared to present (Fig. 5.9) (Dowsett et al., 2016; Haywood et al., 2016; Chapter 4).

Our MAT_{mr} and $MAAT_{peat}$ estimates are significantly cooler (by up to 28°C) than the multiproxy temperature reconstructions predicted for northern Iceland and the Nordic Seas during the Pliocene (Fig. 5.9). This mismatch suggests the lignite br-GDGTs are either controlled by factors which are unrelated to the climate conditions at the time of deposition, such as thermal degradation, or are misrepresented by the calibrations which are based on non-transferable linear correlations between br-GDGTs and surface temperature in modern peats and soils. The fairly recent application of br-GDGTs as palaeothermometers in ancient lignite deposits

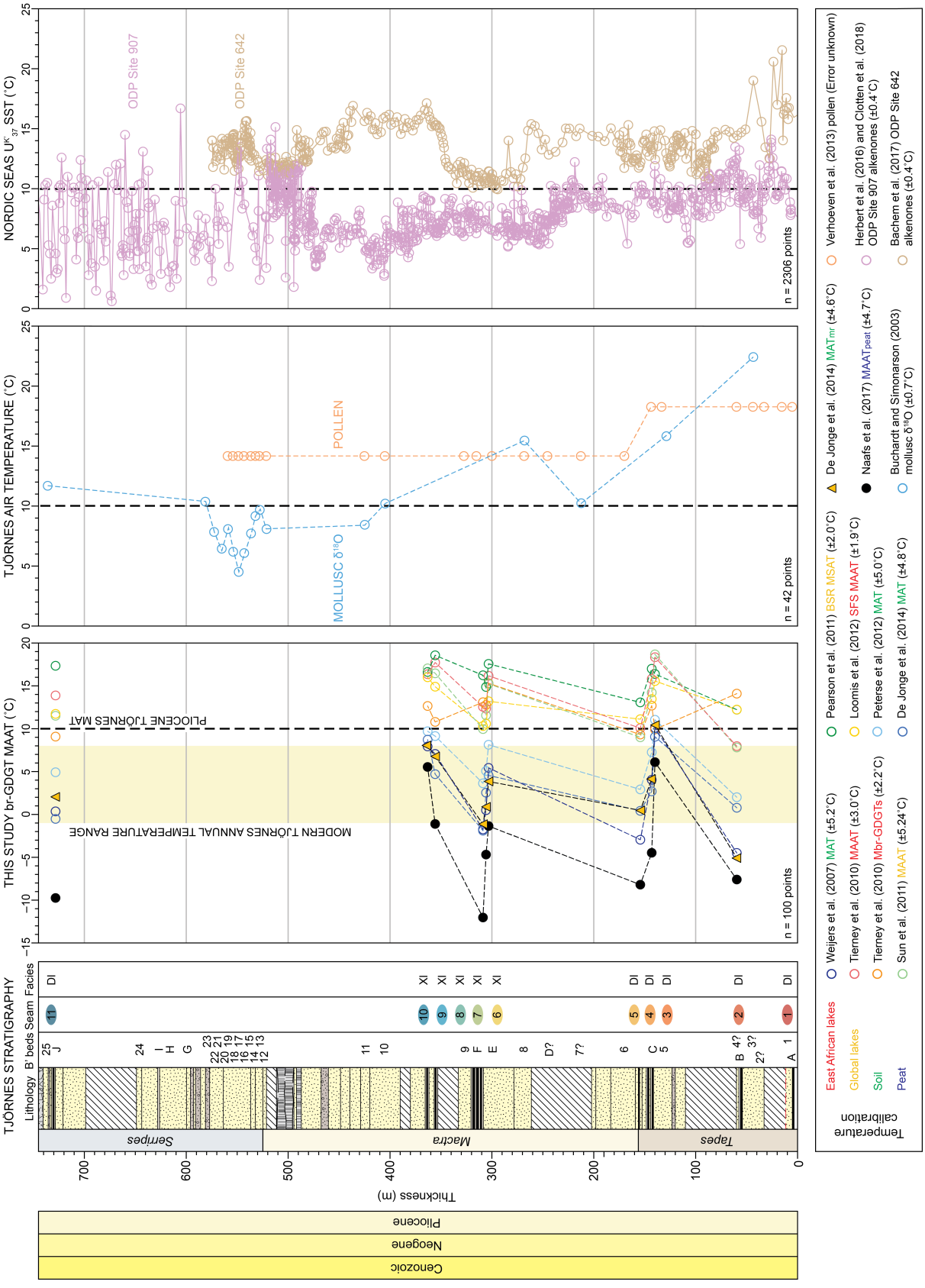

NORDIC SEAS $U^{K'}_{37}$ SST (°C)
ODP Site 907
ODP Site 642
n = 2306 points
TJÖRNES AIR TEMPERATURE (°C)
POLLEN
MOLLUSC $\delta^{18}O$
n = 42 points
THIS STUDY br-GDGT MAAT (°C)
MODERN TJÖRNES ANNUAL TEMPERATURE RANGE
PLIOCENE TJÖRNES MAT
n = 100 points
TJÖRNES STRATIGRAPHY
Lithology B' beds Seam Facies
Tapes
Macta
Serripes
Thickness (m)
Cenozoic
Neogene
Pliocene
Temperature calibration
East African lakes
Global lakes
Soil
Peat
Weijers et al. (2007) MAT (±5.2°C)
Tierney et al. (2010) MAAT (±3.0°C)
Tierney et al. (2010) Mbr-GDGTs (±2.2°C)
Sun et al. (2011) MAAT (±5.24°C)
Pearson et al. (2011) BSR MSAT (±2.0°C)
Loomis et al. (2012) SFS MAAT (±1.9°C)
Peterse et al. (2012) MAT (±5.0°C)
De Jonge et al. (2014) MAT (±4.8°C)
De Jonge et al. (2014) MAT_{mr} (±4.6°C)
Naafs et al. (2017) $MAAT_{peat}$ (±4.7°C)
Buchardt and Simonarson (2003) mollusc $\delta^{18}O$ (±0.7°C)
Verhoeven et al. (2013) pollen (Error unknown)
Herbert et al. (2016) and Clotten et al. (2018) ODP Site 907 alkenones (±0.4°C)
Bachem et al. (2017) ODP Site 642 alkenones (±0.4°C)

Figure 5.9 (previous page). Comparison of br-GDGT, pollen (Verhoeven et al., 2013) and mollusc (Buchardt and Símonarson, 2003) temperature records derived from the Tjörnes Beds, and alkenone SSTs from Ocean Drilling Program (ODP) sites in the Nordic Seas (Bachem et al., 2017; Clotten et al., 2018 and Herbert et al., 2016). Br-GDGT MAATs represent mean values for each seam and are calculated using several colour-coded soil, peat and lacustrine calibrations, including De Jonge et al. (2014) (triangles; Eq. 5.4) and Naafs et al. (2017) (circles; Eq. 5.2 and 5.5) as in Fig. 5.8. Mbr-GDGTs, major, non-cyclised br-GDGTs (Tierney et al., 2010); BSR MSAT, Best subsets regression mean summer air temperature (Pearson et al., 2011); SFS, Stepwise forward selection (Loomis et al., 2012). Estimated Pliocene MAT shown by dashed line (Verhoeven et al., 2013). Modern annual temperature range highlighted by yellow bar (Icelandic Meteorological Office, 2020). Lithostratigraphic section, mollusc biozonation (B' beds; Bárðarson's beds) and sedimentary facies are outlined in Chapter 2. Dl, Detritic lignite; Xl, Xylitic lignite.

means the number of existing studies is very limited (Weijers et al., 2011; Stock et al., 2016; Inglis et al., 2017; Naafs et al; 2017; Naafs et al; 2018). These studies mainly focus on reconstructing early Palaeogene climate using lignite deposits (Schöningen, Cobham, Otaio River and Beulah Zap) from low to mid palaeolatitudes. To our knowledge, only one other study (Ballantyne et al., 2010) has focused on reconstructing terrestrial temperatures using a high latitude Pliocene lignite. Ballantyne et al. (2010) analysed br-GDGTs in a lignite from Beaver Pond on Ellesmere Island (Canada), and suggest Arctic temperatures were c. 19°C warmer during the Pliocene compared to present. However, Ballantyne et al. (2010) do not discuss the fidelity of their records or publish their distributions used to infer this warming. It is therefore challenging to interpret our results and explain the observed trends with certainty, when there is so little evidence to compare our records against. However, observations from modern peat-forming environments (Weijers et al., 2011; Zheng et al., 2015), suggest there are a number of factors which may influence br-GDGTs in lignified deposits.

5.6.1.1 Calibration uncertainties

The temperature calibrations of Naafs et al. (2017) and De Jonge et al. (2014) are based on the analysis of br-GDGTs in modern-day peat and soil samples collected from 318 global sites. The calibrations work on the basic assumption that heterotrophic bacteria in peats and soils

produce varying proportions of br-GDGTs at different surface temperatures. As discussed, Naafs et al. (2017) demonstrate strong correlations between 5-methyl br-GDGTs lacking cyclopentane moieties (Ia, IIa and IIIa) and MAAT. The degree of methylation of 5-methyl br-GDGTs is captured in the MBT'_{5ME} index (Eq. 5.2), which is used in their temperature calibration (Eq. 5.5). De Jonge et al. (2014) propose a multiple linear regression calibration which results in a robust correlation with MAT, and incorporates br-GDGTs Ia, Ib, Ic and IIa (Eq. 5.4).

Both Naafs et al. (2017) and De Jonge et al. (2014) analysed br-GDGTs in modern Icelandic peat and soil samples which are used to calibrate their temperature equations (Fig. 5.10). Naafs et al. (2017) show Icelandic peats are dominated by br-GDGTs Ia, IIa' and IIIa', whereas De Jonge et al. (2014) reveal Icelandic soils contain high proportions of br-GDGTs Ia, IIa and IIIa. The Tjörnes br-GDGTs do not resemble the distributions observed in modern Icelandic peats (Fig. 5.10; Table 5.3A). The lignites lack the high abundances of br-GDGTs IIa', IIb' and IIIa' observed in the modern peats. The proportions of br-GDGTs at Tjörnes are more similar to those in modern Icelandic soils (De Jonge et al., 2014). This comparison is also supported by the k-Nearest Neighbours (k-NN) algorithm (Table 5.3A) which indicates the distribution of br-GDGTs at Tjörnes are most similar to those preserved in the moderns soils of De Jonge et al. (2014). Both the soils and lignites contain similar abundances of Ia, IIa, IIIa and IIIa'. However, the Tjörnes seams lack the greater abundances of IIa', IIb' and IIc observed in the soils.

In terms of the peat calibration, the key br-GDGTs (Ia, IIa and IIIa) used to formulate the $MAAT_{peat}$ equation have relatively low abundances (8−17%, 7−14% and 4−9%, respectively) in the Icelandic peats compared to the ancient lignites (30%, 37% and 19%, respectively) (Fig. 5.10). Using this calibration, it is possible to 'reverse engineer' and calculate a hypothetical br-GDGT distribution, needed to generate MAAT estimates similar to those predicted for northern Iceland during the Pliocene by the pollen and mollusc records (c. 10°C) (Verhoeven et al., 2013; Buchardt and Símonarson, 2003). Naafs et al. (2017) indicate a hypothetical br-GDGT

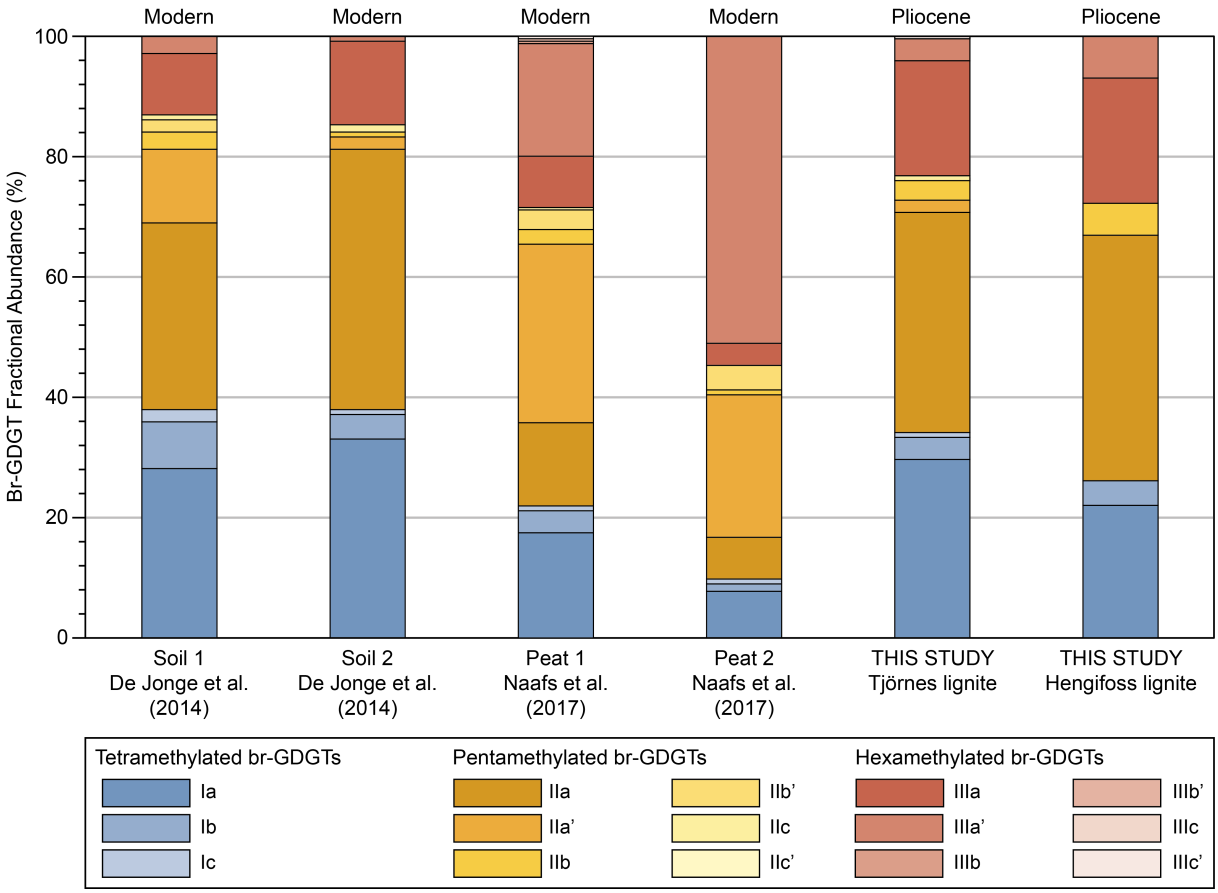


Figure 5.10. Comparison of Icelandic br-GDGT fractional abundances in modern soil (De Jonge et al., 2014), modern peat (Naafs et al., 2017) and Pliocene lignite (Tjörnes and Hengifoss; this study). br-GDGT fractional abundances show the relative percent proportions of the different tetra-, penta- and hexamethylated br-GDGTs within each material. The fractional abundance at Tjörnes is an average of the distributions shown in Fig. 5.8.

distribution of Ia (58%), IIa (29%) and IIIa (4%) is needed to generate $MAAT_{peat}$ estimates of c. 10°C, based on modern peats (Table 5.3A). In the soil calibration, the key br-GDGTs (Ia, Ib, Ic and IIa) used to calibrate the MAT_{mr} equation have similar abundances (28−33%, 4−8%, 1−2%, 31−43%, respectively) to the Pliocene lignites (30%, 4%, 1%, 37%, respectively). De Jonge et al. (2014) suggest a hypothetical br-GDGT distribution of Ia (44%), Ib (7%), Ic (1%) and IIa (24%) is required to obtain MAT_{mr} values of c. 10°C, based on modern soils (Table 5.3A). Importantly, both of these hypothetical distributions, which yield temperature estimates expected for the Pliocene, are incompatible with the proportions of br-GDGTs preserved in the Tjörnes lignites (Fig. 5.10; Table 5.3A). This suggests the ancient relationships between surface temperature and br-GDGT production at the time of peat accumulation, were possibly

(A)

Sample	Branched GDGT fractional abundance															Euclidean distance	Rank
	Ia	Ib	Ic	IIa	IIa'	IIb	IIb'	IIc	IIc'	IIIa	IIIa'	IIIb	IIIb'	IIIc	IIIc'		
Tjörnes lignite THIS STUDY	0.30	0.04	0.01	0.37	0.02	0.03	0.00	0.01	0.00	0.19	0.04	0.00	0.00	0.00	0.00		
Soil 1 (De Jonge et al., 2014)	0.28	0.08	0.02	0.31	0.12	0.03	0.02	0.01	0.00	0.10	0.03	0.00	0.00	0.00	0.00	0.15	2
Soil 2 (De Jonge et al., 2014)	0.33	0.04	0.01	0.43	0.02	0.01	0.00	0.01	0.00	0.14	0.01	0.00	0.00	0.00	0.00	0.09	1
Hypothetical soil (De Jonge et al., 2014)	0.44	0.07	0.01	0.24	0.06	0.04	0.01	0.02	0.00	0.06	0.05	0.00	0.00	0.00	0.00	0.24	3
Peat 1 (Naafs et al., 2017)	0.17	0.04	0.01	0.14	0.30	0.03	0.03	0.00	0.00	0.09	0.19	0.00	0.00	0.00	0.00	0.42	5
Peat 2 (Naafs et al., 2017)	0.08	0.01	0.01	0.07	0.24	0.01	0.04	0.00	0.00	0.04	0.51	0.00	0.00	0.00	0.00	0.66	6
Hypothetical peat (Naafs et al., 2017)	0.58	0.02	0.01	0.29	0.01	0.02	0.01	0.01	0.00	0.04	0.01	0.00	0.00	0.00	0.00	0.33	4

(B)

Sample	Branched GDGT fractional abundance															Euclidean distance	Rank
	Ia	Ib	Ic	IIa	IIa'	IIb	IIb'	IIc	IIc'	IIIa	IIIa'	IIIb	IIIb'	IIIc	IIIc'		
Hengifoss lignite THIS STUDY	0.22	0.04	0.00	0.41	0.00	0.05	0.00	0.00	0.00	0.21	0.07	0.00	0.00	0.00	0.00		
Tjörnes lignite THIS STUDY	0.30	0.04	0.01	0.37	0.02	0.03	0.00	0.01	0.00	0.19	0.04	0.00	0.00	0.00	0.00	0.10	1
Soil 1 (De Jonge et al., 2014)	0.28	0.08	0.02	0.31	0.12	0.03	0.02	0.01	0.00	0.10	0.03	0.00	0.00	0.00	0.00	0.21	3
Soil 2 (De Jonge et al., 2014)	0.33	0.04	0.01	0.43	0.02	0.01	0.00	0.01	0.00	0.14	0.01	0.00	0.00	0.00	0.00	0.15	2
Hypothetical soil (De Jonge et al., 2014)	0.44	0.07	0.01	0.24	0.06	0.04	0.01	0.02	0.00	0.06	0.05	0.00	0.00	0.00	0.00	0.24	4
Peat 1 (Naafs et al., 2017)	0.17	0.04	0.01	0.14	0.30	0.03	0.03	0.00	0.00	0.09	0.19	0.00	0.00	0.00	0.00	0.44	7
Peat 2 (Naafs et al., 2017)	0.08	0.01	0.01	0.07	0.24	0.01	0.04	0.00	0.00	0.04	0.51	0.00	0.00	0.00	0.00	0.65	6
Hypothetical peat (Naafs et al., 2017)	0.58	0.02	0.01	0.29	0.01	0.02	0.01	0.01	0.00	0.04	0.01	0.00	0.00	0.00	0.00	0.33	5

Table 5.3 (previous page). K-Nearest Neighbour (k-NN) analyses for the Tjörnes and Hengifoss lignite samples which classifies br-GDGT fractional abundances based on a similarity measure (the Euclidean distance function). The smallest Euclidean distance value is ranked the lowest and considered the nearest neighbour. (A) Comparison of the average Tjörnes br-GDGT fractional abundances (highlighted orange) with the modern Icelandic soil and peat br-GDGT distributions of De Jonge et al. (2014) and Naafs et al. (2017), and the hypothetical distributions needed to generate $MAAT_{peat}$ and MAT_{mr} estimates similar to those predicted for northern Iceland during the Pliocene (c. 10°C; Verhoeven et al., 2013). The Tjörnes br-GDGTs are most similar to those preserved in soil 2 of De Jonge et al. (2014), with the lowest Euclidean distance (0.09). (B) Comparison of the Hengifoss br-GDGT fractional abundances (highlighted orange) with the modern Icelandic soil and peat br-GDGT distributions of De Jonge et al. (2014) and Naafs et al. (2017), the average br-GDGT distributions in the Tjörnes lignites and the hypothetical distributions needed to generate $MAAT_{peat}$ and MAT_{mr} estimates similar to those predicted for northern Iceland during the Pliocene (c. 10°C; Verhoeven et al., 2013). The Hengifoss br-GDGTs are most similar to those preserved in the Tjörnes lignites, with the lowest Euclidean distance (0.10).

different to the linear correlations utilised in the modern peat and soil calibrations. In simple terms, there were significantly different bacterial communities at Tjörnes during the Pliocene, compared to the microbial systems in Icelandic peat and soil at present. Consequently, the peat and soil calibrations cannot be used with confidence to reconstruct MAATs at Tjörnes, since they are based on modern linear MAAT correlations which may not represent those operating at the time of br-GDGT production in the ancient peat deposits. This potentially explains why our $MAAT_{peat}$ and MAT_{mr} estimates are significantly cooler compared to the climate conditions inferred by other proxies for northern Iceland during the Pliocene (Fig. 5.9).

Other calibrations (Tierney et al., 2010; Pearson et al., 2011; Sun et al., 2011; Loomis et al., 2012) based on modern lacustrine sediments yield warmer temperatures, similar to those inferred for northern Iceland during the Pliocene (Fig. 5.9). Pearson et al. (2011) analysed br-GDGTs from core-top samples in 90 global lakes, and proposed the best-subsets regression which incorporates br-GDGTs Ib, IIa and IIIa. This calibration generates the warmest temperature estimates for Tjörnes with MAATs peaking at 18.7°C (Fig. 5.9), more than 12°C warmer than the peat calibration of Naafs et al. (2017). However, it is uncertain how reliable these estimates are since the origin and history of br-GDGTs in lacustrine sediments differs significantly to peat and lignite deposits. Weber et al. (2015) demonstrate the composition of

lacustrine br-GDGTs not only reflects the catchment soils, but is also influenced by aquatic *in situ* production. In contrast, peat and lignite deposits record *in situ* environmental conditions (Weijers et al., 2011; Inglis et al., 2017; Naafs et al., 2017), and are largely unaffected by other sources of br-GDGTs. Another problem is whether the temperature sensitivity captured by the lacustrine calibrations is comparable to the behaviour of br-GDGTs in peat and lignite deposits. The global datasets (Pearson et al., 2011; Sun et al., 2011) used to formulate the lacustrine calibrations generally underrepresent high latitude localities, compared to the relatively well-studied tropical lakes (Tierney et al., 2010; Loomis et al., 2012). As a result, these calibrations may not faithfully represent the responsiveness of br-GDGTs to surface temperatures in high latitude lakes, where environmental conditions and seasonality differs significantly to the tropics (Peterse et al., 2014). The ability of these calibrations to accurately reconstruct MAATs in high latitude lakes, let alone ancient lignites, is therefore highly uncertain. Consequently, the temperature estimates derived using the lacustrine calibrations are also considered unreliable, since so little is known regarding the behaviour of br-GDGTs from lake deposits at high latitudes, their deep-time application and whether their origin and temperature sensitivity is comparable with those preserved in peat deposits. This comparison highlights the importance of carefully selecting a calibration which best suits the source of the br-GDGTs and their susceptibility to surface temperatures at the time of production.

5.6.1.2 Fossil versus extant br-GDGTs

Since our lignite br-GDGTs are similar to the distributions observed in modern Icelandic soils (Fig. 5.10) (De Jonge et al., 2014), it is important to assess whether our distributions are possibly influenced by extant signals or whether they are truly representative of Pliocene environmental conditions. Climate records (1962−2016) from the Mánárbakki weather station demonstrate the Tjörnes Peninsula currently experiences polar tundra conditions, with average winter and summer temperatures of −1°C and 8°C, respectively (Icelandic Meteorological Office, 2020). The majority of our MAT_{mr} and $MAAT_{peat}$ results fall within this temperature range (Fig. 5.9), suggesting our br-GDGTs may reflect modern climate. However,

Inagaki et al. (2015) demonstrate the microbial concentration in ancient lignites (10^4 cells cm^3) is several orders of magnitude lower than in the superficial regolith (>10^8 cells cm^3), suggesting the potential influence of extant signals in lignite is far less than in surface soils. Contamination of our lignite with soil during sampling may have also contributed extant br-GDGT signals, which reflect modern climate conditions. However, the influence of contamination is considered to be minimal, since considerable care was taken to ensure only lignite was collected, including deeply excavating the seams to remove surface sediments, thus sampling freshly exposed lignite. Comparing our br-GDGTs with those from another Pliocene lignite onshore Iceland, would help to resolve whether the br-GDGTs preserved at Tjörnes are representative of the Pliocene or modern-day. The Fljótsdalur valley in eastern Iceland features a continuous section (c. 1500 m) of basaltic lava flows which alternate with thick marine and terrestrial sediments, including sandstones, mudstones, conglomerates and lignites (Fig. 5.11). These sediments comprise more than 500 m of the total section and were deposited over c. 5.5 myrs between the late Miocene and early Pleistocene (Geirsdóttir and Eiríksson, 1994). Hengifoss (Fig. 5.1), the third highest waterfall in Iceland, is located in an incised valley which transects part of this thick sequence (Fig. 5.11). Hengifoss is surrounded by basaltic lavas which are interbedded with thin, oxidised, red layers of clay, sandstone and lignite (Fig. 5.11). Historic K-Ar dating of basalts sampled from the base of the Hengifoss section indicate a late Miocene age of 5.69 ± 0.07 Ma and 6.05 ± 0.14 Ma, suggesting the overlying intercalated sediments and lavas extend into the Pliocene (McDougall et al., 1976). Pflug (1959) examined spores and pollen from the lignite horizons in the Hengifoss section and reported a flora indicative of a temperate climate, comparable to the pollen records at Tjörnes.

Following fieldwork in northern Iceland, we collected additional material from a single seam at Hengifoss (Table 5.1) and analysed the br-GDGTs to reveal whether they show any similarities to Tjörnes. The Hengifoss lignite is dominated by Ia (22%), Ib (4%), IIa (41%), IIb (5%), IIIa (21%) and IIIa' (7%) (Fig. 5.10; Table 5.3B). This distribution is very similar to the fractional abundances of br-GDGTs observed in the lignites at Tjörnes, and is supported by the k-NN

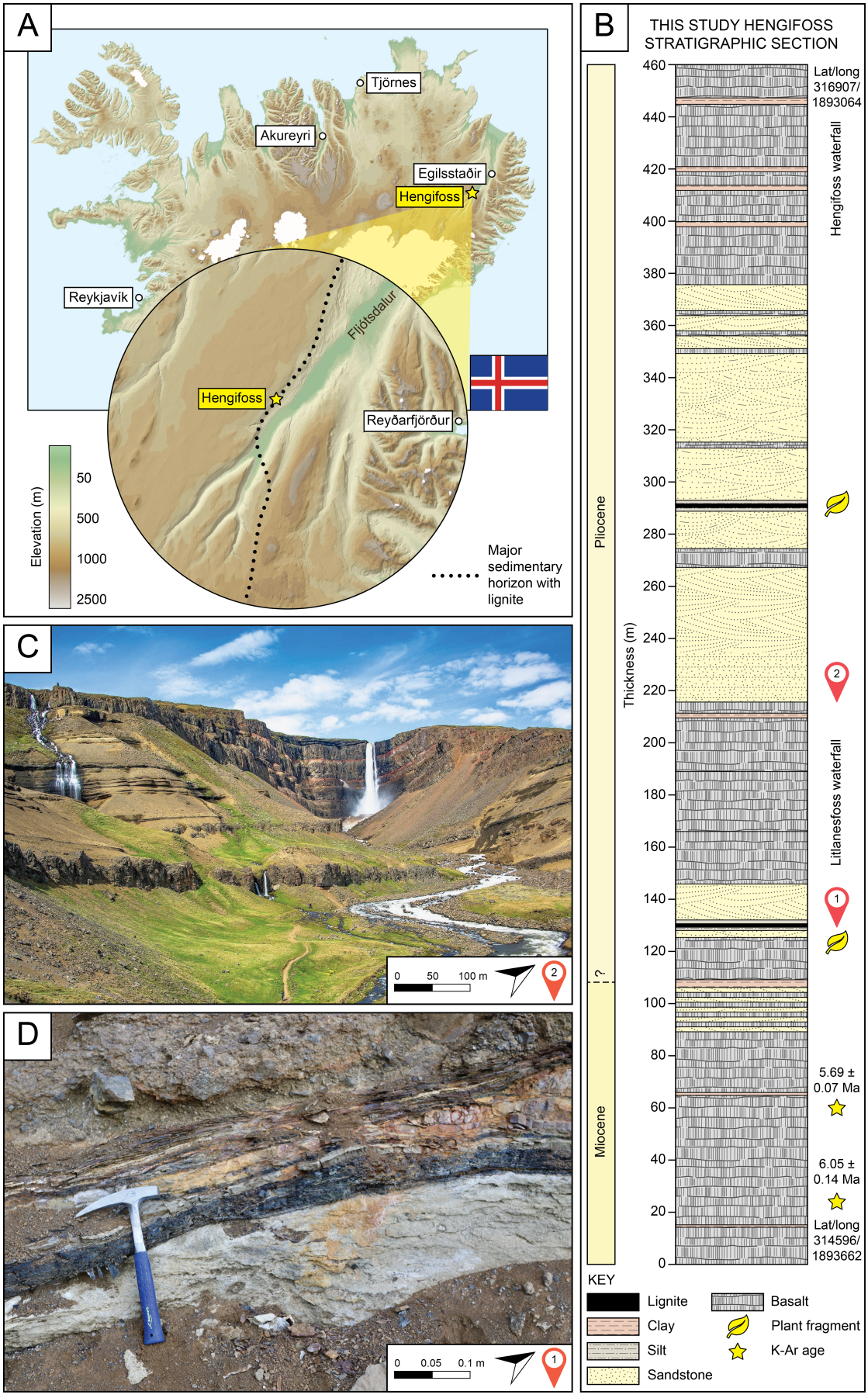

A
Tjörnes
Akureyri
Egilsstaðir
Hengifoss
Reykjavík
Fljótsdalur
Hengifoss
Reyðarfjörður
Elevation (m)
50
500
1000
2500
Major sedimentary horizon with lignite
B
THIS STUDY HENGIFOSS STRATIGRAPHIC SECTION
Lat/long 316907/ 1893064
Hengifoss waterfall
Litlanesfoss waterfall
Lat/long 314596/ 1893662
5.69 ± 0.07 Ma
6.05 ± 0.14 Ma
Pliocene
Miocene
?
Thickness (m)
460
440
420
400
380
360
340
320
300
280
260
240
220
200
180
160
140
120
100
80
60
40
20
0
KEY
Lignite
Clay
Silt
Sandstone
Basalt
Plant fragment
K-Ar age
C
0 50 100 m
2
D
0 0.05 0.1 m
1

Figure 5.11 (previous page). Location and geological setting of Hengifoss, eastern Iceland. (A) Map showing the location of Hengifoss in the Fljótsdalur valley and the extent of the lignite-bearing sedimentary sequence after Hjartarson and Sæmundsson (2014). Topographic map created in QGIS v.3.4 using the Landmælingum Íslands (National Land Survey of Iceland) Digital Elevation Model (available at: https://atlas.lmi.is/LmiData/index.php?id=247152041610 [accessed 06/01/2020]). (B) Hengifoss stratigraphic section showing the lithological variations, position of the lignite seams and the radiometric K-Ar ages after McDougall et al. (1976). Grid references mark the base and top of the logged section, using the geocentric coordinate system for Iceland (ISN2004/Lambert 2004; EPSG:5325). Location pins correspond to the following images. (C) Hengifoss waterfall comprises thick basaltic lavas (c. 25 m) intercalated with red clay, cross-stratified sandstone and lignite. (D) Xylitic lignite seam containing fossilised wood and plant fragments, including peeling and fissured bark. Estwing® E3-22P (0.33 m length) geological hammer for scale.

algorithm which indicates the distribution of br-GDGTs at Hengifoss are most similar to those preserved at Tjörnes (Table 5.3B). Like Tjörnes, the br-GDGTs at Hengifoss show no resemblance to the distributions which occur in modern Icelandic peatlands (Naafs et al., 2017; Table 5.3B). The br-GDGTs at Hengifoss are more comparable to the distributions observed in modern Icelandic soils (De Jonge et al., 2014; Table 5.3B). However, they lack the greater abundances of IIa', IIb' and IIc observed in the soils, similar to Tjörnes (Fig. 5.10; Table 5.3B). The similarity between the distributions at Hengifoss and Tjörnes, together with the accepted minor microbial concentrations in ancient lignites (Inagaki et al., 2015), supports the assumption that the Tjörnes br-GDGTs are most likely fossilised signals, and implies the distributions are unlikely to be affected by extant *in situ* GDGT production associated with modern microbial communities. However, it is important to note the Hengifoss seam is located only c. 15 m below a thick (c. 70 m) basaltic lava unit at Litlanesfoss, and therefore it is possible the br-GDGTs may be influenced by thermal degradation (Schouten et al., 2013). Additional work is needed to assess the maturity of the Hengifoss seam to provide greater insight into the preservation of the br-GDGTs, and to further inform comparisons with the Tjörnes distributions.

5.6.1.3 Influence of diagenetic and catagenic effects

The influence of diagenetic effects on br-GDGTs are not very well constrained due to the novelty of the proxy. Existing studies have briefly assessed the influence of diagenesis in lacustrine sediments. Tierney et al. (2012) discovered greater abundances of the IIIa, IIIb and IIIc species in recently deposited anoxic lake sediments, compared to deeper sediments deposited in a pre-anthropogenic oxic environment. However, no studies have yet examined whether peat deposits are susceptible to similar diagenetic effects upon burial and coalification.

The influence of diagenetic effects on marine-derived isoprenoid GDGTs (iso-GDGTs; Chapter 4) is slightly better understood, compared to br-GDGTs. Huguet et al. (2008) indicate iso-GDGTs degrade approximately two times faster than br-GDGTs during post-depositional oxidation, and suggest the physicochemical packaging of br-GDGTs within the sedimentary matrix of terrestrial organic matter provides greater protection compared to iso-GDGTs in marine organic matter. Schouten et al. (2004) show iso-GDGTs are also susceptible to thermal degradation between 240−300°C. Schouten et al. (2004) heated immature sediment samples in the lab isothermally at different temperatures (160−330°C) for 72 hours and noticed a gradual reduction in TEX_{86} with increasing temperature, despite other biomarker parameters indicating relatively low thermal maturity (17α,21β-22*S*/(22*S*+22*R*) hopane ratio >0.1 or ββ/(ββ+αβ]βα) hopane ratio <0.5; Mackenzie et al., 1980 and Inglis et al., 2018). This reduction in TEX_{86} produced cooler SST estimates, and is attributed to the preferential destruction of the more cyclic compounds (GDGT2, GDGT3 and crenarchaeol; Fig. 4.2) relative to less cyclic compounds (GDGT0 and GDGT1; Fig. 4.2) (Schouten et al., 2004). Schouten et al. (2013) revisited the artificial maturation experiments of Schouten et al. (2004) to investigate the impacts of maturity on the br-GDGT distributions. Schouten et al. (2013) show the MBT index decreases slightly with maturation, while the CBT index increases with maturity especially >240°C. Schouten et al. (2013) suggest these changes may be caused by the preferential degradation of cyclopentane moieties, as observed for iso-GDGTs. Schouten et al. (2013)

demonstrate the rise in CBT index can change reconstructed soil pH by one unit, whereas reconstructed MATs increased by up to 4°C with maturity. Importantly, no studies have yet translated the experimental temperature range reported by Schouten et al. (2013) into geological conditions, where the same degradation reactions may occur at lower temperatures (possibly below 100°C) due to the slower and sustained heating associated with burial. It is well known that other maturation reactions occur at much lower temperatures in geological settings, compared to in the lab. For example, Type III kerogen produces gas at high temperatures >465°C during Rock Eval™ pyrolysis (Tissot et al., 1987), but produces gas at lower temperatures (c. 150−200°C) when heating is by burial (Tissot et al., 1987). Although our low T_{max}, HI and S_1 indexes suggest the Tjörnes seams are thermally immature for gas generation (Table 5.2), we cannot rule out the possibility that the br-GDGTs are thermally altered since they are governed by different kinetic reactions which may operate at lower temperatures compared to those which control gas generation in Type III kerogen. Ultimately, the position regarding the thermal degradation of br-GDGTs is equivocal at present and further work is needed to assess the relative thermal stability of the 17 br-GDGTs (Weijers et al., 2011; Schouten et al., 2013).

The lack of br-GDGTs in the lowermost lignite (Bed A of Bárðarson, 1925) may be attributed to the proximity of the seam to localised faulting in the Kaldakvísl river and associated fluid flow (Eiríksson et al., 1990; Gudmundsson et al., 2001). The adjacent sediments are stained red and appear more altered compared to the overlying bulk of the Tjörnes Beds (Chapter 2). The destruction of br-GDGTs by hydrothermal fluids in this faulted horizon appears the most plausible explanation. Lupi et al. (2010) model hydrothermal convection in the Tjörnes Basin, and demonstrate fluid temperatures can reach up to 200°C in the Húsavík region at shallow depth (<2 km). We cannot therefore discount the possibility that the br-GDGTs in the lowermost seam were thermally altered by these hot fluids. Residual conductive heat from the underlying Kaldakvísl lavas is considered unlikely to influence the absence of br-GDGTs in the lowermost seam, since existing age models indicate a c. 4.5 myr hiatus between lava emplacement and

the deposition of the Tjörnes sediments, allowing sufficient time for the plateau lavas to cool (Albertsson, 1976, 1978).

5.6.2 *Reliability of Tjörnes br-GDGTs for Pliocene temperature reconstructions*

The majority of our new $MAAT_{peat}$ and MAT_{mr} estimates fall within the range of modern polar climate conditions observed in northern Iceland, and are significantly cooler (by up to 28°C) than regional Pliocene temperature reconstructions inferred from pollen, mollusc and alkenone-based SST records (Fig. 5.9) (Verhoeven et al., 2013; Buchardt and Símonarson, 2003; Bachem et al., 2017; Clotten et al., 2018 and Herbert et al., 2016). This suggests the br-GDGTs are possibly extant signals reflecting recent climate conditions. However, comparisons with br-GDGTs discovered in an equivalent seam of Pliocene age from the Hengifoss section (Fig. 5.11), reveal a very similar distribution to Tjörnes, dominated by comparable proportions of Ia, Ib, IIa, IIb, IIIa and IIIa' (Fig. 5.10; Table 5.3B). This reproducibility, together with the accepted negligible microbial concentrations in ancient lignites (Inagaki et al., 2015), suggests the Tjörnes br-GDGTs are most likely fossilised signals. This reduces the uncertainties associated with modern *in situ* production and contributions of extant signals linked to sampling contamination.

We prove the Tjörnes br-GDGTs are derived from seams which are thermally immature for gas generation (Table 5.2; Fig. 5.12A-C). However, we cannot discount the possibility that the br-GDGTs are thermally altered since they are most likely governed by different kinetic reactions which may operate at lower temperatures compared to those which control gas generation in the Type III kerogen preserved in the Tjörnes seams. As discussed, the thermal degradation of br-GDGTs is equivocal at present (Schouten et al., 2013; Weijers et al., 2011), and further work on the thermal stability of br-GDGTs in ancient lignite deposits is needed before we are able to fully assess whether the br-GDGTs at both Tjörnes and Hengifoss are influenced by heating associated with burial.

In addition to the potential influence of thermal degradation, the discrepancies between our cooler $MAAT_{peat}$ and MAT_{mr} estimates and the temperatures predicted by the other proxies, are further attributed to uncertainties associated with the temperature calibrations (Fig. 5.9). These calibrations are formulated using linear relationships between br-GDGTs and surface temperatures in modern peats and soils, which are believed to be different to those which operated at the time of br-GDGT production in the ancient peat deposits. We demonstrate the br-GDGTs at both Tjörnes and Hengifoss look nothing like the hypothetical distributions needed to formulate temperature values indicative of the Pliocene, using the modern soil and peat calibrations (Fig. 5.10; Table 5.3B). The bacterial communities at Tjörnes are thought to have responded differently to surface temperatures in the Pliocene, compared to the microbial systems in Icelandic peat and soil at present. We also apply lacustrine calibrations to the Tjörnes br-GDGTs, which produce much warmer temperatures (up to 12°C higher) comparable with the pollen and mollusc reconstructions (Fig. 5.9). However, it is uncertain how reliable these estimates are since the origin and history of br-GDGTs in lacustrine settings is very different to peatlands. The temperature sensitivity captured by these calibrations is also based on global br-GDGT datasets dominated by tropical lakes, which are unlikely to represent the behaviour of distributions in high latitude lakes, let alone ancient lignites.

We suggest all of the MAT_{mr} and $MAAT_{peat}$ estimates presented here are unlikely to faithfully represent Pliocene surface temperatures, due to the combined influence of possible thermal degradation associated with burial, and potential differences between the temperature sensitivity of modern br-GDGTs, utilised in the calibrations, and the ancient br-GDGTs preserved at Tjörnes. Consequently, it is advised that our MAT_{mr} and $MAAT_{peat}$ estimates should not be included within NE Atlantic reconstructions of Pliocene climate until further work on other high latitude, Pliocene lignites corroborates our findings. Our br-GDGT records may yield useful palaeotemperature estimates in the future, provided a new calibration appropriate for use with ancient datasets is established.

5.6.3 *Source rock potential of the Tjörnes lignite seams*

Our Rock Eval™ data supports the work of Richter (2003), and suggests that all of the lignite seams exposed in the Tjörnes Beds are thermally immature for gas generation. Our S_2 and HI measurements are nearly identical to those proposed by Richter (2003), which indicate the seams are characteristic of gas-prone Type III kerogen, as shown on the van Krevelen diagram (Fig. 5.12A). Gas-prone Type III kerogen is typically derived from higher plant organic matter deposited in paralic environments. This supports our depositional reconstructions outlined in Chapter 2, and similar interpretations proposed by Bárðarson (1925), Eiríksson et al. (1990) and Símonarson and Eiríksson (2008). Our range of T_{max} values (362−429°C) is slightly greater than that described by Richter (2003) (418−429°C). However, both datasets share the same maximum T_{max} value indicating that all of the analysed samples are below the pyrolysis oil and gas generation window and are thermally immature for gas generation (Fig. 5.12B). The average T_{max} values for the detritic seams are c. 23°C warmer, on average, than the xylitic seams, indicating the organic carbon in the detritic facies (fine grained with rare xylites) is slightly more resistant to generating HCs through thermal cracking (Singh et al., 2016). The average PI value (0.06) also confirms low maturity (Table 5.2). The S_1 and S_2 values are higher in xylitic facies, compared to the detritic seams, and are seen to positively correlate with TOC content (Table 5.2). This indicates the organic carbon preserved in the xylitic seams (>90% xylites) is more favourable for the generation of HCs through thermal cracking (Singh et al., 2016). The inherent elevated richness of organic carbon in these xylitic seams also results in higher S_1, S_2 and TOC values (Singh et al., 2016). The quantity of fixed hydrocarbons (S_2) are c. 22 mgHC/g rock greater, on average, than the free hydrocarbons (S_1), indicating the Tjörnes lignites will make good to excellent source rocks (Fig. 5.12C).

Maturation in the Tjörnes seams is believed to be mainly controlled by the localised elevated geothermal gradient, as reported by Flóvenz and Sæmundsson (1993) and Fridleifsson et al. (1994). Residual heat from the underlying Kaldakvísl lavas is deemed unlikely to have accelerated the degree of maturation in the lowermost seams, since a large hiatus (c. 4.5 myrs)

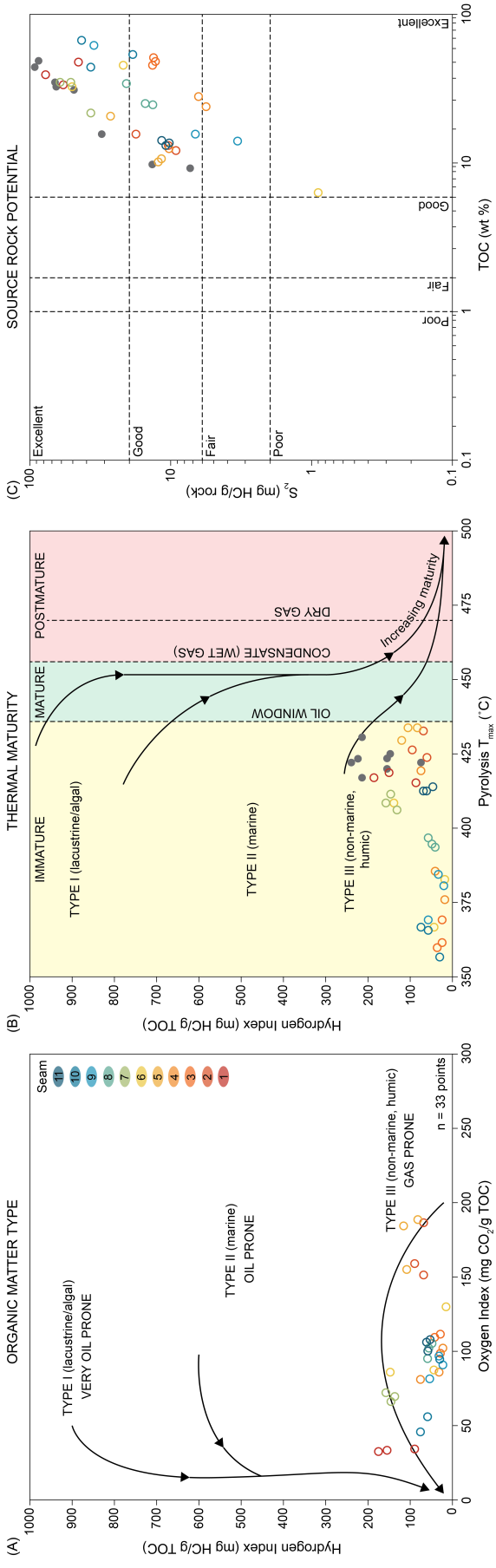

(A)
ORGANIC MATTER TYPE
Hydrogen Index (mg HC/g TOC)
Oxygen Index (mg CO2/g TOC)
Seam
11
10
9
8
7
6
5
4
3
2
1
n = 33 points
TYPE I (lacustrine/algal)
VERY OIL PRONE
TYPE II (marine)
OIL PRONE
TYPE III (non-marine, humic)
GAS PRONE
(B)
THERMAL MATURITY
Hydrogen Index (mg HC/g TOC)
Pyrolysis Tmax (°C)
IMMATURE
MATURE
POSTMATURE
OIL WINDOW
CONDENSATE (WET GAS)
DRY GAS
Increasing maturity
TYPE I (lacustrine/algal)
TYPE II (marine)
TYPE III (non-marine, humic)
(C)
SOURCE ROCK POTENTIAL
S2 (mg HC/g rock)
TOC (wt %)
Excellent
Good
Fair
Poor

Figure 5.12 (previous page). Organic matter, maturation and source rock characterisation of the Tjörnes lignites compared with the results of Richter (2003), highlighted in grey. Symbols are colour-coded based on the numbered seams, as in Fig. 5.8 and 5.9. (A) Van Krevelen plot of Rock-Eval™ Hydrogen Index (HI) versus Oxygen Index (OI) for the Tjörnes lignite samples (n=33), showing the lignites are characteristic of gas-prone Type III kerogen, and comprise higher plant matter associated with paralic environments. (B) Plot of Rock-Eval™ HI versus pyrolysis T_{max}, showing present-day kerogen quality and thermal maturity. All of the samples are thermally immature for gas generation. (C) Plot of Rock-Eval™ S_2 versus Total Organic Carbon (TOC) (following Dembicki, 2009), indicating the lignites' good to excellent source rock potential.

exists between lava emplacement and the deposition of the Tjörnes Beds (Albertsson, 1976, 1978). Residual heat from the overlying Höskuldsvík lavas is also considered unlikely to have driven the extent of maturation in the uppermost seam (Bed J of Bárðarson, 1925), since our Rock Eval™ results suggest this horizon is thermally immature for gas generation with low HI, S_2 and T_{max} values (Table 5.2).

Our Rock Eval™ records confirm all of the Tjörnes lignite seams, as seen on the Tjörnes Peninsula, are thermally immature for gas generation and make good to excellent source rocks with high average TOC contents (32%) and S_2 values (24 mg HC/g rock) (Fig. 5.12C). Our results support previous interpretations which suggest the Tjörnes lignites are thermally immature for gas generation (Richter, 2001, 2002, 2003). Based on the geological history of the Tjörnes Beds, the degree of maturation exhibited by these samples most likely indicates a minimum level. It is very likely that maturation increases subsurface in other areas of the Tjörnes Basin, especially where the geothermal gradient is elevated (Flóvenz and Sæmundsson, 1993; Fridleifsson et al., 1994). Our results confirm the Tjörnes lignites comprise gas-prone Type III organic matter, which has the potential to produce dry and wet gasses, given the optimal conditions. As suggested by Richter (2002, 2003), these sediments extend eastward and are buried at a shallow depth (1−1.5 km) in the Öxarfjörður rift zone, where the geothermal gradient reaches up to 200°C/km (Ármannsson et al., 1998). In agreement with Richter and Gunnarsson (2010), it is believed these favourable conditions drive the localised maturation of laterally equivalent brown coals, which most likely generates

the thermogenic gases detected in the petroleum seeps at Skógalón (Fig. 5.1) (Ólafsson et al., 1993).

5.7 CONCLUSIONS

The Tjörnes Beds in northern Iceland are an important sedimentary archive for understanding faunal and palaeoenvironmental change throughout the Pliocene in the NE Atlantic and Nordic Seas. Multiple lignite seams occur throughout this dominantly shallow-marine succession. However, in a region dominated by elevated geothermal gradients associated with the TFZ and NVZ, previous geochemical studies have mainly focussed on assessing their hydrocarbon-generating potential, rather than the possible palaeoclimate signals they may record.

We present a new geochemical characterisation of the 11 lignite seams which crop out in the Tjörnes Beds on the Tjörnes Peninsula. We identify br-GDGTs in 10 of these seams for the first time. The total br-GDGT assemblage is dominated by pentamethylated br-GDGTs (43%). The most abundant br-GDGT is IIa which make up 37% of the total br-GDGT assemblage. Detritic facies contain more IIa, IIa', IIIa and IIIa' species, whereas xylitic seams feature more Ia and Ib species. 6-methyl br-GDGTs comprise only 6% of the total br-GDGT assemblage, where the hexamethylated br-GDGT IIIa' is the most abundant (4%). Br-GDGTs IIb', IIc', IIIb' and IIIc' are usually absent.

We present new MAT_{mr} and $MAAT_{peat}$ estimates which are significantly cooler (by up to 28°C) than existing pollen, mollusc and alkenone-based SST records derived from the Tjörnes Beds and Nordic Seas (Bachem et al., 2017; Buchardt and Símonarson, 2003; Clotten et al., 2018; Herbert et al., 2016 and Verhoeven et al., 2013). We show the majority of our $MAAT_{peat}$ and MAT_{mr} estimates fall within the range of modern polar conditions observed in northern Iceland. However, by employing the k-NN algorithm we show the distribution of br-GDGTs at Tjörnes are most similar to those in a Pliocene seam from the Hengifoss section in eastern Iceland, with distributions dominated by comparable proportions of Ia, Ib, IIa, IIb, IIIa and IIIa'. This reproducibility, together with the accepted negligible microbial concentrations in ancient lignite deposits (Inagaki et al., 2015), suggests the Tjörnes br-GDGTs are most likely fossilised

signals. This reduces the uncertainties associated with modern *in situ* production and contributions of extant signals from sampling contamination. We also believe the Tjörnes br-GDGTs may be influenced by thermal degradation. Although our Rock Eval™ pyrolysis measurements suggest the seams are thermally immature for gas generation, we cannot rule out the possibility that the br-GDGTs are thermally altered since they are most likely governed by different kinetic reactions which may operate at lower temperatures compared to those which control gas generation in Type III kerogen. Ultimately, the position regarding thermal degradation of br-GDGTs is equivocal at present and further work is needed to assess the relative thermal stability of the 17 br-GDGTs (Schouten et al., 2013).

In addition to the potential influence of thermal degradation, the discrepancies between our cooler $MAAT_{peat}$ and MAT_{mr} estimates and the temperatures predicted by the other proxies, are further attributed to uncertainties associated with the temperature calibrations. These calibrations are formulated using linear relationships between br-GDGTs and surface temperatures in modern peats and soils, which are believed to be different to those which operated at the time of br-GDGT production in the ancient Icelandic peatlands. Using the k-NN algorithm, we demonstrate the br-GDGTs at both Tjörnes and Hengifoss look nothing like the hypothetical distributions needed to formulate temperatures indicative of the Pliocene, using the modern soil and peat calibrations. The bacterial communities at Tjörnes are considered to have responded differently to surface temperatures in the Pliocene, compared to the microbial systems in Icelandic peat and soil at present. Consequently it is believed our MAT_{mr} and $MAAT_{peat}$ records are unlikely to record Pliocene surface temperatures, due to the combined influence of possible thermal degradation linked to burial, and potential differences between the temperature sensitivity of modern br-GDGTs, utilised in the calibrations, and the ancient br-GDGTs preserved at Tjörnes. It is advised that our MAT_{mr} and $MAAT_{peat}$ estimates should not be included within NE Atlantic reconstructions of Pliocene climate until further work on other high latitude, Pliocene lignites corroborates our findings. Our br-GDGT records may yield useful palaeotemperature estimates in the future, provided a new calibration appropriate for use with ancient datasets is established.

New Rock Eval™ pyrolysis measurements reveal all 11 lignite seams at Tjörnes are thermally immature for gas generation with low S_2 (0.90−79.57 mg HC/g rock), HI (14−185 mgHC/gTOC) and T_{max} (355−431°C) values, supporting previous analyses undertaken by Richter (2001, 2002, 2003). Our S_2 and HI measurements indicate the seams are characteristic of gas-prone, Type III kerogen associated with higher plant organic matter deposited in paralic environments. The S_1 and S_2 values are 2.42 mg HC/g rock and 7.89 mg HC/g rock higher, respectively, in the xylitic facies compared to the detritic seams, and positively correlate with TOC content (6.33−68.03%). This indicates the organic carbon preserved in the xylitic seams is more favourable for HC generation through thermal cracking. The quantity of fixed hydrocarbons (S_2) are c. 22 mgHC/g rock greater, on average, than the free hydrocarbons (S_1) indicating the Tjörnes lignites will make good to excellent source rocks. The Tjörnes Beds extend eastward and are buried at a shallow depth (1−1.5 km) in the Öxarfjörður rift zone, where the geothermal gradient reaches up to 200°C/km (Ármannsson et al., 1998). In agreement with Richter and Gunnarsson (2010), it is believed these conditions drive the localised maturation of laterally equivalent brown coals, which most likely generates the thermogenic gases detected in the petroleum seeps at Skógalón (Ólafsson et al., 1993).

Our new br-GDGT and Rock Eval™ records represent an important step in the understanding of the geochemical characterisation and thermal evolution of the Tjörnes lignite seams. We show our MAT_{mr} and $MAAT_{peat}$ records are most likely derived from fossilised signals, which are potentially misrepresented by calibrations based on non-transferable linear relationships between br-GDGTs and surface temperature in modern peats and soils. Further work is needed on the composition of br-GDGTs in other Icelandic and high latitude Pliocene lignites, such as the Borgarfjörður seams in western Iceland (Geirsdóttir and Eiríksson, 1994), to determine whether these distributions respond to environmental conditions in a similar way to those at Tjörnes, and to provide further evidence which may dispute the ability of these calibrations to accurately reconstruct ancient surface temperatures.

6. SUMMARY

This thesis focuses on reconstructing tectonic, oceanic and climatic interactions in the NE Atlantic and onshore Iceland during the Pliocene by geochemical fingerprinting of marine and terrestrial sediments. The NE Atlantic witnessed a significant transition throughout this interval from enhanced warmth during the early to mid-Pliocene, where sea surface temperatures (SST) were up to 8°C warmer than present, to cooling associated with the intensification of the Northern Hemisphere Glaciation (iNHG) during the late Pliocene. This thesis employs a variety of organic and isotopic geochemical techniques on sediments from regional ocean drilling sites and the Tjörnes Beds in northern Iceland, to unravel the patterns and drivers of this climate change. This section revisits and summarises the main conclusions outlined in each of the four chapters, and highlights areas for future work.

6.1 General conclusions

Chapter 2 is based on fieldwork to re-evaluate the stratigraphy, sedimentology and structure of the Tjörnes Beds onshore northern Iceland. Significant gaps exist in historic stratigraphic interpretations of the Tjörnes Beds due to the exclusion of inland or inaccessible sections (Bárðarson, 1925; Einarsson, 1967; Buchardt and Símonarson, 2003), which limit understanding of the true thickness and structural architecture, the vertical and lateral distribution of lithofacies and disconformities, the depositional and palaeoenvironmental evolution, and the record of palaeoclimatic signals preserved in these sediments. These issues are addressed by re-mapping the entire outcrop using advanced and systematic techniques (drone-based photogrammetry), and undertaking a detailed lithofacies analysis. The total thickness is found to be c. 745 m, 45% greater than previously reported (Eiríksson, 1981; Buchardt and Símonarson, 2003), and up to 230 m of sediment is unseen due to superficial cover or pervasive extensional faulting. A revised composite section is presented which accommodates these unobserved intervals. 13 lithofacies are recognised, which are grouped

into five facies associations. Using the vertical and lateral distribution of these lithofacies, the initial depositional environment is interpreted to be a tide-dominated estuary with extensive intertidal flats and coastal marshes, before a marine transgression led to a largely subtidal environment, followed by the progradation and re-establishment of intertidal flats and marshlands, in agreement with Símonarson and Eiríksson (2008). This work helps to fill gaps in the stratigraphic and palaeoenvironmental record, and reveals previously undocumented sections which may yield new palaeoclimatic records to help further unravel Pliocene climate in the NE Atlantic. This revised stratigraphic framework is fundamental for the sampling of basaltic lavas and brown coals in Chapter 5.

Chapter 3 focuses on the controls of deep-water connectivity between the NE Atlantic and Norwegian basins throughout the Pliocene. Existing studies suggest varying dynamic support of the Greenland-Scotland Ridge (GSR) controlled the southward overflow of Northern Component Water (NCW) (Wright and Miller, 1996; Poore et al., 2006; Robinson et al., 2011). However, estimates of NCW are currently based on global compilations of benthic foraminifera $\delta^{13}C$ ($\delta^{13}C_{BF}$) records, which exclude data from north of the GSR, and therefore the influence of Nordic deep-waters on the estimation of NCW is unknown. In Chapter 3, over 11,900 $\delta^{13}C_{BF}$ data points from the NE Atlantic and Nordic Seas are compiled for the first time, which show Norwegian Sea deep-waters (NSDWs) were significantly lighter, by up to 1 ‰, compared to the NE Atlantic throughout the early to mid-Pliocene (5.3−3.0 Ma), signifying poor ventilation. This result is somewhat unexpected since previous studies suggest the contribution of northern sourced waters to global circulation increases during this time, attributed to reduced dynamic support (Poore et al., 2006). New εNd records from ODP Site 642 and DSDP Site 552 show the NSDWs were significantly more radiogenic (up to +3.1 εNd units), compared to the Rockall Plateau, supporting poor connectivity between the Norwegian and NE Atlantic basins during the early to mid-Pliocene. Weakened ventilation in the Norwegian Basin was possibly controlled by the combined influence of a short cooling event (4.5−4.0 Ma), which lowered primary productivity (Bachem et al., 2017), and the maximum emergence of the Barents Shelf (Butt et al., 2002; Torsvik et al., 2002), which deflected deep-water production poleward and

reduced the influence of brines in the Norwegian Sea (Jansen et al., 2000; Hill, 2015). During the late Pliocene (3.0−2.5 Ma), the εNd records converge c. 2.6 Ma, before showing a reversed pattern compared to the early to mid-Pliocene. Norwegian Sea ventilation was most likely controlled at this time by climatic and oceanic changes associated with the closure of the Central American Seaway and the iNHG (Raymo, 1992; Lunt et al., 2008; Naafs et al., 2010). Sea-ice development and freshwater forcing possibly dampened high latitude deep-water production, lessening the influence of the subaerial Barents Shelf (Raymo, 1992). Sites of deep-water production most likely shifted southward into the Norwegian Sea at this time (Sarnthein et al., 2009), where ventilation was driven by cooling of warm waters which continued to be transported northward by an enhanced Norwegian Atlantic Current, despite an elevated GSR. This work suggests fluctuations in dynamic support of the GSR had minimal influence on the ventilation of NSDWs during the Pliocene. It is suggested that Norwegian Sea $\delta^{13}C_{BF}$ records should not be incorporated in global compilations used to estimate NCW or infer fluctuations in dynamic support, since the processes governing the evolution of these deep-waters are somewhat decoupled from the wider rate of North Atlantic deep-water formation.

Chapter 4 focuses on assessing the magnitude of mid-Pliocene warming in the NE Atlantic and unravelling discrepancies between proxy- and model-based SST estimates. Previous work suggest that this region was up to 6°C warmer than present, based on alkenone methods (Robinson et al., 2008; Robinson, 2009; Dowsett et al., 2012). However, this warming far exceeds the more conservative SST estimates (a rise of 2−3°C) predicted by the Pliocene Research, Interpretation and Synoptic Mapping (PRISM) reconstructions and leading climate models (including HadCM3) (Dowsett et al., 2012, 2016). This proxy-model mismatch is addressed by generating new alkenone SST records from IODP Site U1308, DSDP Site 552, ODP Site 642 and ODP Site 907. The new records show SSTs peaked up to 21.5°C and 19.7°C in the NE Atlantic and Nordic Seas, respectively, consistent with existing studies (Robinson et al., 2008; Bachem et al., 2017; Clotten et al., 2018). However, it is revealed that 60% of the SST estimates are derived from relatively low total alkenone concentrations (<50

ng/µl), which are susceptible to warming biases caused by chromatographic irreversible adsorption (Villanueva and Grimalt, 1996). The similarity in the magnitude of warming between the records presented here and published records confirms that the latter were also likely derived from low concentrations (Robinson et al., 2008). A new mathematical technique is proposed, involving a dilution series curve, to correct for these warming biases. It results in a reduction in PRISM-interval SSTs, by up to 3.2°C, across all four sites. Subsequently, the existing PRISM SST anomaly (ΔSST) at DSDP Site 552 is revised from 5.5°C to 4.3°C, using the corrected alkenone and existing Mg/Ca palaeothermometry (Robinson et al., 2008). This revision reduces local discrepancies between proxy-based records and the PRISM3 reconstruction by one third (from 3.5°C to 2.3°C). Larger discrepancies (up to 6.5°C) remain between the revised ΔSST and climate models (Dowsett et al., 2012). These differences are currently attributed to model inaccuracies associated with the strength and position of the Gulf Stream and North Atlantic Current in certain simulations (CCSM4 and GISS-ER) (Naafs et al., 2010; Rosenbloom et al., 2013). This study therefore attributes proxy-model discrepancies in the NE Atlantic to challenges associated with the fidelity of both palaeoclimate tools. It is advocated that injection concentrations should be properly documented to reveal potential sources of warming bias, and also preferably used to assess the integrity of alkenone records in multiproxy datasets and future PRISM reconstructions.

Chapter 5 builds on the work of Chapter 2 by outlining the preliminary geochemical work undertaken on basalts and brown coals (lignites) sampled from the Tjörnes Beds, including the radiometric dating of basaltic lavas and the analysis of organic biomarkers in the lignite seams. Existing K-Ar, magneto- and bio-stratigraphic age models suggest the Tjörnes Beds were deposited sometime between c. 4.9 and 2.58 Ma (Einarsson et al., 1967, Albertsson, 1978; Buchardt and Símonarson, 2003; Símonarson and Eiríksson, 2008; Verhoeven et al., 2011). In Chapter 5, the rationale and methods to better constrain these age models, using modern $^{40}Ar/^{39}Ar$ dating on the intercalated lavas, are outlined to provide a reliable temporal framework for the lignite biomarker records and to determine whether deposition occurred exclusively throughout the Zanclean or into the Piacenzian. Unfortunately, the irradiated basalt

samples are yet to undergo $^{40}Ar/^{39}Ar$ analyses at SUERC due to lab closures associated with COVID-19. A revised age model for the Tjörnes Beds based on these new $^{40}Ar/^{39}Ar$ results will be published in the near future upon receipt of this data. The biomarker analyses reveal for the first time that branched glycerol dialkyl glycerol tetraethers (br-GDGTs) are preserved in 10 of the Tjörnes seams, with an assemblage dominated by pentamethylated br-GDGTs (43%). Temperature calibrations of De Jonge et al. (2014) and Naafs et al. (2017) are applied to these distributions in order to assess palaeotemperature variability onshore Iceland during the Pliocene. However, the MAT_{mr} and $MAAT_{peat}$ estimates are shown to be significantly cooler (by up to 28°C) than existing palaeotemperature records derived from the Tjörnes Beds and Nordic Seas (Buchardt and Símonarson, 2003; Clotten et al., 2018). Using the k-Nearest Neighbours algorithm, the distribution of br-GDGTs at Tjörnes are proven to be very similar to those preserved in another Pliocene seam from Hengifoss in eastern Iceland. This reproducibility, together with the accepted negligible microbial concentrations in ancient lignite deposits (Inagaki et al., 2015), suggests the br-GDGTs at Tjörnes are most likely fossilised, rather than extant, signals. The mismatch between the MAT_{mr} and $MAAT_{peat}$ estimates and existing palaeoclimate records suggests the br-GDGT distributions are either controlled by factors which are unrelated to climate at the time of deposition, such as thermal degradation, or are misrepresented by the calibrations which are based on non-transferable linear correlations between br-GDGTs and surface temperature in modern peats and soils (De Jonge et al., 2014; Naafs et al., 2017; Schouten et al., 2004, 2013). New Rock Eval™ pyrolysis measurements also reveal all of the lignites exposed on the Tjörnes Peninsula are thermally immature for gas generation, supporting previous analyses undertaken by Richter (2001, 2002, 2003). These new pyrolysis data support the hydrocarbon-generating potential and local maturation of laterally equivalent brown coals, driven by deeper burial in nearby Öxarfjörður, in agreement with Richter and Gunnarsson (2010). It is premature to fully interpret these biomarker and Rock Eval™ results, since a reliable age model based on the $^{40}Ar/^{39}Ar$ data will provide greater insight into the onset, rate and duration of maturation and palaeoenvironmental conditions inferred from these geochemical records.

6.2 Future recommendations

6.2.1 *Chapter 2: A new composite section and lithostratigraphy for the Pliocene Tjörnes Beds, northern Iceland.*

Beds 7 and D of Bárðarson (1925) were not recognised in the field and are believed to occur in a depression carved by a historic landside at Hringvershvilft. The absence of Beds 7 and D is attributed to recent mass movement concealing these horizons. It is recommended the cliffs between Rekaá and Skeifá are resurveyed to determine whether these horizons are exposed elsewhere. Locating these horizons will help to fill a gap in the new composite section and the depositional evolution of the lower *Mactra* Zone. Buchardt and Símonarson (2003) also indicate Bed D contains three lignite seams, which may yield further br-GDGT data to help reconstruct terrestrial temperatures onshore Iceland during the Pliocene.

The Kaldárós Lagoon in western Iceland is recognised as a modern sedimentary analogue for the Tjörnes Beds. Remote sensing shows the Kaldárós Lagoon contains depositional environments, including coastal marshes, tidal flats and channels, which are synonymous with the deposition of the 11 lithofacies recognised at Tjörnes. Field mapping of the Kaldárós Lagoon will help to corroborate the aerial interpretations presented here, strengthen the understanding of the Tjörnes sedimentary system, and provide further insight into the depositional processes which most likely operated during the Pliocene.

6.2.2 *Chapter 3: Tectonic and climatic controls on the deep-water connectivity of the NE Atlantic and Nordic Seas during the Pliocene.*

Generating new εNd records from ocean drilling sites either side of the Denmark Strait (e.g. DSDP Site 407, ODP Site 907 and ODP Site 913) is recommended to determine whether deep-water connectivity between the Greenland and Irminger basins was stronger compared to the Norwegian and NE Atlantic basins during the Pliocene. This may reveal whether the

dynamic support of the Denmark Strait had greater control on the southward overflow and production of Northern Component Water at this time, compared to the Iceland-Faroe Ridge and Faroe-Shetland Channel. New εNd records from these sites could also confirm whether the East Greenland Current strengthened during the early to mid-Pliocene, as a result of a northward shift in deep-water production driven by the deflection of warm surface waters by the Barents Shelf (Jansen et al., 2000; Torsvik et al., 2002). This would further support the argument for poor deep-water connectivity between the Norwegian and NE Atlantic basins at this time.

6.2.3 *Chapter 4: Mid-Pliocene warming: closing the gap between geological archives and climate models in the NE Atlantic and Nordic Seas.*

The dilution series used to correct the alkenone-based SST estimates for warming and cooling biases associated with irreversible adsorption and overloading, was produced by analysing one sample repeatedly at 16 different dilutions on the Agilent® 7890B GC-FID system at the University of Birmingham. The reproducibility of the dilution series was unverifiable because the whole total lipid extract (TLE) from the analysed sample was separated into single sub-fractions to maximise the alkenone concentrations. In hindsight, it is recommended that future studies select a sample with abundant TLE, so multiple aliquots can be split into sub-fractions and analysed on two identical GC-FID set-ups. This procedure will provide a robust assessment of the sensitivity of the GC-FID system to irreversible adsorption and overloading, and will ensure the validity of the dilution series used to correct the alkenone-based SSTs.

Alkenone records from ODP Sites 909 and 911 in the Fram Strait are responsible for the greatest temperature anomalies (+8°C) in the PRISM reconstruction (Dowsett et al., 2012). However, using the methods outlined in Robinson (2009), the anomalies at both sites are shown to be derived from very low average concentrations (3.77 ng/µl for ODP Site 909; 11.55 ng/µl for ODP Site 911), which are undoubtably influenced by warming biases associated with irreversible adsorption. It is recommended that new mid-Pliocene $U^{K'}_{37}$ records are generated

from ODP Sites 909 and 911, in order to verify whether the existing anomalies overestimate regional warming due to the effects of irreversible adsorption and low injection concentrations.

6.2.4 *Chapter 5: Geochemical analyses of brown coals and basalts from the Pliocene Tjörnes Beds, northern Iceland: preliminary results.*

The thermal degradation of br-GDGTs is equivocal at present due to the novelty of this palaeotemperature proxy (Weijers et al., 2011). Further work is needed to establish whether br-GDGTs respond similarly to isoprenoid GDGTs when heated (Schouten et al., 2004, 2013), assess the possible effects of thermal degradation on the MBT'_{5ME} index and determine how the rate of experimental heating translates into geological conditions, where the same degradation reactions may occur at lower temperatures due to the slower and sustained heating associated with burial. A robust assessment of the thermal stability of the 17 br-GDGTs may reveal whether thermal degradation is possibly responsible for the mismatch between the MAT_{mr} and $MAAT_{peat}$ estimates and existing palaeotemperature records derived from the Tjörnes Beds (Buchardt and Símonarson, 2003; Verhoeven et al., 2013).

Sampling other Icelandic Pliocene lignites, such as the Borgarfjörður seams in western Iceland (Geirsdóttir and Eiríksson, 1994), is recommended to determine whether these seams contain br-GDGT distributions comparable to those at Tjörnes. This will help to further characterise the composition of br-GDGTs preserved in these seams, and whether they are representative of the palaeotemperatures expected for Iceland during the Pliocene. This could provide additional evidence which disputes the ability of the modern soil and peat calibrations (De Jonge et al., 2014 and Naafs et al., 2017) to accurately reconstruct ancient high latitude surface temperatures using fossilised br-GDGTs.

REFERENCES

Abbott, A.N., Haley, B.A., and McManus, J., 2016, The impact of sedimentary coatings on the diagenetic Nd flux: Earth and Planetary Science Letters, v. 449, p. 217−227.

Ahrens, M.J., Graf, G., and Altenbach, A.V., 1997, Spatial and temporal distribution patterns of benthic foraminifera in the Northeast Water Polynya, Greenland: Journal of Marine Systems, v. 10 (1−4), p. 445−465.

Akhmetiev, M.A., Bratzeva, G.M., Giterman, R.E., Golubeva, L.V., and Moiseyeva, A.I., 1978, Late Cenozoic stratigraphy and flora of Iceland: Transactions of the Academy of Sciences of the USSR Soviet Geophysical Committee, v. 316, p. 1−188.

Akhmetiev, M.A., Golubeva, L.V., and Skiba, L.A., 1975, Palaeobotanical characteristics of the main section of the Plio-Pleistocene deposits on Tjörnes peninsula, North Iceland: Proceedings of the USSR Academy of Sciences, Geological Series, v. 7, p. 100−107.

Albertsson, K.J., 1976, K/Ar Ages of Pliocene-Pleistocene Glaciations in Iceland with Special Reference to the Tjörnes Sequence, Northern Iceland: Doctoral dissertation, University of Cambridge, 268 p.

Albertsson, K.J., 1978, Um aldur jarðlaga á Tjörnesi (in Icelandic): Náttúrufræðingurinn, v. 48, p. 1−8.

Allen, J.R.L., 1990, Salt-marsh growth and stratification: a numerical model with special reference to the Severn Estuary, southwest Britain: Marine Geology, v. 95 (2), p. 77−96.

Anand, P., Elderfield, H., and Conte, M.H., 2003, Calibration of Mg/Ca thermometry in planktonic foraminifera from a sediment trap time series: Paleoceanography and Paleoclimatology, v. 18 (2), 15 p.

Ármannsson, H., Ófafsson, M., Fridleifsson, G.Ó., Darling, W.G., and Laier, T., 1998, Organic gas in Öxarfjörður, NE Iceland: Proceedings of the 9th International Symposium on Water-Rock Interactions - Taupo, New Zealand, 30 March to 3 April 1998, p. 609−612.

Aronson, J.L., and Sæmundsson, K., 1975, Relatively old basalts from structurally high areas in central Iceland: Earth and Planetary Science Letters, v. 28 (1), p. 83−97.

Bachem, P.E., Risebrobakken, B., De Schepper, S., and McClymont, E.L., 2017, Highly variable Pliocene sea surface conditions in the Norwegian Sea: Climate of the Past, v. 13 (9), p. 1153−1168.

Backman, J., 1979, Pliocene biostratigraphy of DSDP Sites 111 and 116 from the North Atlantic Ocean and the age of Northern Hemisphere glaciation: Stockholm Contributions in Geology, v. 32, p. 115−137.

Backman, J., Raffi, I., Rio, D., Fornaciari, E., and Pälike, H., 2012, Biozonation and biochronology of Miocene through Pleistocene calcareous nannofossils from low and middle latitudes: Newsletters on Stratigraphy, v. 45 (3), p. 221−244.

Ballantyne, A.P., Greenwood, D.R., Sinninghe Damsté, J.S., Csank, A.Z., Eberle, J.J., and Rybczynski, N., 2010, Significantly warmer Arctic surface temperatures during the Pliocene indicated by multiple independent proxies: Geology, v. 38 (7), p. 603−606.

Balson, P.S., Mathers, S.J., and Zalasiewicz, J.A., 1993, The lithostratigraphy of the Coralline Crag (Pliocene) of Suffolk: Proceedings of the Geologists' Association, v. 104 (1), p. 59−70.

Bárðarson, G.G., 1925, A stratigraphical survey of the Pliocene deposits at Tjörnes in northern Iceland: Det Kongelige Danske Videnskabernes Selskab, Biologiske Meddelelser, v. 4 (5), 118 p.

Barker, S., Kiefer, T., and Elderfield, H., 2004, Temporal changes in North Atlantic circulation constrained by planktonic foraminiferal shell weights: Paleoceanography, v. 19 (3), p. 1−15.

Bartoli, G., Hönisch, B., and Zeebe, R.E., 2011, Atmospheric CO_2 decline during the Pliocene intensification of Northern Hemisphere glaciations: Paleoceanography, v. 26 (4), p. 1−14.

Bartoli, G., Sarnthein, M., Weinelt, M., Erlenkeuser, H., Garbe-Schönberg, D., and Lea, D.W., 2005, Final closure of Panama and the onset of northern hemisphere glaciation: Earth and Planetary Science Letters, v. 237 (1−2), p. 33−44.

Baucon, A., 2008, Neoichnology of a microbial mat in a temperate, siliciclastic environment: Spiaggia al Bosco (Grado, Northern, Adriatic, Italy), *in:* Avanzini, M., and Petti, F., (eds.), Italian Ichnology: Studi trentini di scienze naturali: Acta geologica, v. 83, p. 183−203.

Bayon, G., German, C.R., Burton, K.W., Nesbitt, R.W., and Rogers, N., 2004, Sedimentary Fe-Mn oxyhydroxides as paleoceanographic archives and the role of aeolian flux in regulating oceanic dissolved REE: Earth and Planetary Science Letters, v. 224 (3−4), p. 477−492.

Behar, F., Beaumont, V., and Penteado, H.D.B., 2001, Rock-Eval 6 technology: performances and developments: Oil and Gas Science and Technology, v. 56 (2), p. 111−134.

Bell, D.B., Jung, S.J., and Kroon, D., 2015, The Plio-Pleistocene development of Atlantic deep-water circulation and its influence on climate trends: Quaternary Science Reviews, v. 123, p. 265−282.

Bendle, J.A., Weijers, J.W., Maslin, M.A., Sinninghe Damsté, J.S., Schouten, S., Hopmans, E.C., Boot, C.S., and Pancost, R.D., 2010, Major changes in glacial and Holocene terrestrial temperatures and sources of organic carbon recorded in the Amazon fan by tetraether lipids: Geochemistry, Geophysics, Geosystems, v. 11 (12), p. 1−13.

Berggren, W.A., Hilgen, F.J., Langereis, C.G., Kent, D.V., Obradovich, J.D., Raffi, R., Raymo, M.W., and Shackleton, N.J., 1995, Late Neogene chronology: New perspectives in high-resolution stratigraphy: Geological Society of America Bulletin, v. 107, p. 1272−1287.

Berggren, W.A., Kent, D.V., Flynn, J.J., Van Couvering, J.A., 1985, Cenozoic geochronology: Geological Society of America Bulletin, v. 96, p. 1407−1418.

Berggren, W.A., Kent, D.V., Swisher III, C.C., and Aubry, M.P., 1995, A revised Cenozoic geochronology and chronostratigraphy, *in:* Berggren, W.A., (ed.), Geochronology, Time Scales and Global Stratigraphic Correlation, Special Publications Society for Sedimentary Geology, v. 54, p. 129−212.

Bergh, S.G., and Sigvaldason, G.E., 1991, Pleistocene mass-flow deposits of basaltic hyaloclastite on a shallow submarine shelf, South Iceland: Bulletin of Volcanology, v. 53 (8), p. 597−611.

Bhattacharya, J.P., 2006, Deltas, *in:* Walker, R.G., and Posamentier, H., (eds.), Facies Models Revisited: Society for Sedimentary Geology, Special Publication, v. 84, p. 237−292.

Bhattacharya, J.P., 2010, Deltas, *in:* James, N.P., and Dalrymple, R.W., (eds.), Facies Models 4: Geological Association of Canada, p. 233−264.

Blaga, C.I., Reichart, G.J., Heiri, O., and Sinninghe Damsté, J.S., 2009, Tetraether membrane lipid distributions in water-column particulate matter and sediments: a study of 47 European lakes along a north-south transect: Journal of Paleolimnology, v. 41 (3), p. 523−540.

Blaser, P., Lippold, J., Gutjahr, M., Frank, N., Link, J.M., and Frank, M., 2016, Extracting foraminiferal seawater Nd isotope signatures from bulk deep sea sediment by chemical leaching: Chemical Geology, v. 439, p. 189−204.

Blaser, P., Pöppelmeier, F., Schulz, H., Gutjahr, M., Frank, M., Lippold, J., Heinrich, H., Link, J.M., Hoffmann, J., Szidat, S., and Frank, N., 2019, The resilience and sensitivity of Northeast Atlantic deep water εNd to overprinting by detrital fluxes over the past 30,000 years: Geochimica et cosmochimica acta, v. 245, p. 79−97.

Bleil, U, 1989, Magnetostratigraphy of Neogene and Quaternary sediment series from the Norwegian Sea: Ocean Drilling Program, *in:* Eldholm, O., Thiede, J., Taylor, E., et al., (eds.), Proceedings of the Ocean Drilling Program, Scientific Results, College Station, TX (Ocean Drilling Program), v. 104, p. 829−902.

Blischke, A., Gaina, C., Hopper, J.R., Péron-Pinvidic, G., Brandsdóttir, B., Guarnieri, P., Erlendsson, Ö., and Gunnarsson, K., 2017, The Jan Mayen microcontinent: an update of its architecture, structural development and role during the transition from the Ægir Ridge to the mid-oceanic Kolbeinsey Ridge: Geological Society, London, Special Publications, v. 447 (1), p. 299−337.

Boon, J.J., v.d. Meer, F.W., Schuyl, P.J.W., De Leeuw, J.W., Schenck, P.A., and Burlingame, A.C., 1978, Organic geochemical analyses of core samples from Site 362, Walvis Ridge, DSDP Leg 40, *in:* Natland, J.H., (ed.), Initial Reports DSDP US Government Print Office, v. 40, p. 627−637.

Brassell, S.C., and Dumitrescu, M., 2004, Recognition of alkenones in a lower Aptian porcellanite from the west-central Pacific: Organic Geochemistry, v. 35 (2), p. 181−188.

Brassell, S.C., Eglinton, G., Marlowe, I.T., Pflaumann, U., and Sarnthein, M., 1986, Molecular stratigraphy: a new tool for climatic assessment: Nature, v. 320 (6058), p. 129−133.

Brierley, C.M., and Fedorov, A.V., 2010, Relative importance of meridional and zonal sea surface temperature gradients for the onset of the ice ages and Pliocene-Pleistocene climate evolution: Paleoceanography, v. 25 (2), p. 1−16.

Brierley, C.M., Fedorov, A.V., Liu, Z., Herbert, T.D., Lawrence, K.T., and LaRiviere, J.P., 2009, Greatly expanded tropical warm pool and weakened Hadley circulation in the early Pliocene: Science, v. 323 (5922), p. 1714−1718.

Buchardt, B., and Símonarson, L.A., 2003, Isotope palaeotemperatures from the Tjörnes Beds in Iceland: evidence of Pliocene cooling: Palaeogeography, Palaeoclimatology, Palaeoecology, v. 189 (1-2), p. 71−95.

Burton, K.W., Lee, D.C., Christensen, J.N., Halliday, A.N., and Hein, J.R., 1999, Actual timing of neodymium isotopic variations recorded by Fe-Mn crusts in the western North Atlantic: Earth and Planetary Science Letters, v. 171 (1), p. 149−156.

Butt, F.A., Drange, H., Elverhøi, A., Otterå, O.H., and Solheim, A., 2002, Modelling Late Cenozoic isostatic elevation changes in the Barents Sea and their implications for oceanic and climatic regimes: preliminary results: Quaternary Science Reviews, v. 21 (14−15), p. 1643−1660.

Butt, F.A., Elverhøi, A., Solheim, A., and Forsberg, C.F., 2000, Deciphering Late Cenozoic development of the western Svalbard Margin from ODP Site 986 results: Marine Geology, v. 169 (3−4), p. 373−390.

Cane, M.A., and Molnar, P., 2001, Closing of the Indonesian seaway as a precursor to east African aridification around 3−4 million years ago: Nature, v. 411 (6834), p.157−162.

Castañeda, O.C., and Miller, W.E., 2004, Late Tertiary terrestrial mammals from Central Mexico and their relationship to South American immigrants: Revista Brasileira de Paleontologia, v. 7 (2), p. 249−261.

Castradori, D., Rio, D., Hilgen, F.J., and Lourens, L.J., 1998, The global standard stratotype-section and point (GSSP) of the Piacenzian Stage (Middle Pliocene): Episodes, v. 21, p. 88−93.

Chambers, L.M., and Pringle, M.S., 2001, Age and duration of activity at the Isle of Mull Tertiary igneous centre, Scotland, and confirmation of the existence of subchrons during Anomaly 26r: Earth and Planetary Science Letters, v. 193 (3−4), p. 333−345.

Channell, J.E.T., Amigo, A.E., Fronval, T., Rack, F., Lehman, B., 1999, Magnetic stratigraphy at Sites 907 and 985 in the Norwegian-Greenland Sea and a revision of the Site 907 composite section, *in:* Raymo, M.E., Jansen, E., Blum, P., Herbert, T.D., (eds.), Proceedings of the Ocean Drilling Program, Scientific Results, v. 16: Ocean Drilling Program, Texas A & M University, College Station, Texas, p. 131−148.

Chapman, M.R., Shackleton, N.J., Zhao, M., and Eglinton, G., 1996, Faunal and alkenone reconstructions of subtropical North Atlantic surface hydrography and paleotemperature over the last 28 kyr: Paleoceanography, v. 11 (3), p. 343−357.

Chen, T.Y., Frank, M., Haley, B.A., Gutjahr, M., and Spielhagen, R.F., 2012, Variations of North Atlantic inflow to the central Arctic Ocean over the last 14 million years inferred from hafnium and neodymium isotopes: Earth and Planetary Science Letters, v. 353, p. 82−92.

Clifton, H.E., 1969, Beach lamination: nature and origin: Marine geology, v. 7 (6), p. 553−559.

Clifton, H.E., 1983, Discrimination between subtidal and intertidal facies in Pleistocene deposits, Willapa Bay, Washington: Journal of Sedimentary Research, v. 53 (2), p. 353−369.

Clotten, C., Stein, R., Fahl, K., and De Schepper, S., 2018, Seasonal sea ice cover during the warm Pliocene: Evidence from the Iceland Sea (ODP Site 907): Earth and Planetary Science Letters, v. 481, p. 61−72.

Condomines, M., Grönvold, K., Hooker, P.J., Muehlenbachs, K., o'Nions, R.K., Oskarsson, N., and Oxburgh, E.R., 1983, Helium, oxygen, strontium and neodymium isotopic relationships in Icelandic volcanics: Earth and Planetary Science Letters: v. 66, p.125−136.

Conte, M.H., Sicre, M.A., Rühlemann, C., Weber, J.C., Schulte, S., Schulz-Bull, D., and Blanz, T., 2006, Global temperature calibration of the alkenone unsaturation index ($U^{K'}_{37}$) in surface waters and comparison with surface sediments: Geochemistry, Geophysics, Geosystems, v. 7 (2), 22 p.

Copard, K., Colin, C., Douville, E., Freiwald, A., Gudmundsson, G., De Mol, B., and Frank, N., 2010, Nd isotopes in deep-sea corals in the North-eastern Atlantic: Quaternary Science Reviews, v. 29 (19−20), p. 2499−2508.

Corbeanu, R.M., Wizevich, M.C., Bhattacharya, J.P., Zeng, X., McMechan, G.A., Chidsey, T.C., and Adams, R.D., 2004, Three-dimensional architecture of ancient lower delta-plain point bars using ground-penetrating radar, Cretaceous Ferron Sandstone, Utah. The Fluvial-deltaic Ferron Sandstone: Regional to Wellbore Scale Outcrop Analog Studies and Applications to Reservoir Modelling (Chidsey, TC), p. 427−449.

Crampton-Flood, E.D., Peterse, F., Munsterman, D., and Sinninghe Damsté, J.S., 2018, Using tetraether lipids archived in North Sea Basin sediments to extract North Western European Pliocene continental air temperatures: Earth and Planetary Science Letters, v. 490, p. 193−205.

Crocket, K.C., Vance, D., Gutjahr, M., Foster, G.L., and Richards, D.A., 2011, Persistent Nordic deep-water overflow to the glacial North Atlantic: Geology, v. 39 (6), p. 515−518.

Cronin, T.M., 1991, Late Neogene marine Ostracoda from Tjörnes, Iceland: Journal of Paleontology, v. 65 (5), p. 767−794.

Curry, W.B, Miller, K.G, 1989, Oxygen and carbon isotopic variation in Pliocene benthic foraminifers of the equatorial Atlantic, *in:* Rudimann, W; Sarnthein, M; et al. (eds.), Proceedings of the Ocean Drilling Program, Scientific Results, College Station, TX (Ocean Drilling Program), v. 108, p. 157−166.

Dai, S., Bechtel, A., Eble, C.F., Flores, R.M., French, D., Graham, I.T., Hood, M.M., Hower, J.C., Korasidis, V.A., Moore, T.A., and Püttmann, W., 2020, Recognition of peat depositional environments in coal: A review: International Journal of Coal Geology, v. 219, p.103−383.

Daidu, F., Yuan, W., and Min, L., 2013, Classifications, sedimentary features and facies associations of tidal flats: Journal of Palaeogeography, v. 2 (1), p. 66−80.

Dalrymple, R.W., Makino, Y., and Zaitlin, B.A., 1991, Temporal and spatial patterns of rhythmite deposition on mud flats in the macrotidal Cobequid Bay-Salmon River estuary, Bay of Fundy, Canada; *in:* Clastic Tidal Sedimentology, Smith, D.G., Reinson, G.E., Zaitlin, B.A., and Rahmani, R.A., (eds.), Canadian Society of Petroleum Geologists, v. 16, p. 137−160.

Dalrymple, R.W., 2010, Tidal depositional systems, *in:* James, N.P., and Dalrymple, R.W., (eds.), Facies Models 4: Geological Association of Canada, p. 201−232.

Dalrymple, R.W., and Choi, K., 2007, Morphologic and facies trends through the fluvial-marine transition in tide-dominated depositional systems: a schematic framework for environmental and sequence-stratigraphic interpretation: Earth-Science Reviews, v. 81 (3−4), p. 135−174.

Dalrymple, R.W., Baker, E.K., Harris, P.T., and Hughes, M.G., 2003, Sedimentology and stratigraphy of a tide-dominated, foreland-basin delta (Fly River, Papua New Guinea): SEPM Special Publication, v. 76, p. 147−173.

Dalrymple, R.W., Knight, R.J., Zaitlin, B.A., and Middleton, G.V., 1990, Dynamics and facies model of a macrotidal sand-bar complex, Cobequid Bay-Salmon River Estuary (Bay of Fundy): Sedimentology, v. 37 (4), p. 577−612.

Dalrymple, R.W., Mackay, D.A., Ichaso, A.A., and Choi, K.S., 2012, Processes, morphodynamics, and facies of tide-dominated estuaries, *in:* Davis, R.A. and Dalrymple, R.W. (eds.), Principles of Tidal Sedimentology: Springer Science and Business Media, p. 79−107.

Dalrymple, R.W., Zaitlin, B.A., Boyd, R., 1992, Estuarine facies models: conceptual basis and stratigraphic implications: Journal of Sedimentary Petrology, v. 62, p. 1130−1146.

Dandonneau, Y., Deschamps, P.Y., Nicolas, J.M., Loisel, H., Blanchot, J., Montel, Y., Thieuleux, F., and Bécu, G., 2004, Seasonal and interannual variability of ocean colour and composition of phytoplankton communities in the North Atlantic, equatorial Pacific and South Pacific: Deep Sea Research Part II: Topical Studies in Oceanography, v. 51 (1−3), p. 303−318.

Dang, X., Yang, H., Naafs, B.D.A., Pancost, R.D., and Xie, S., 2016, Evidence of moisture control on the methylation of branched glycerol dialkyl glycerol tetraethers in semi-arid and arid soils: Geochimica et Cosmochimica Acta, v. 189, p. 24−36.

Dashtgard, S.E., Gingras, M.K., and MacEachern, J.A., 2009, Tidally modulated shorefaces: Journal of Sedimentary Research, v. 79 (11), p. 793−807.

Dashtgard, S.E., MacEachern, J.A., Frey, S.E., and Gingras, M.K., 2012, Tidal effects on the shoreface: towards a conceptual framework: Sedimentary Geology, v. 279, p. 42−61.

De Jonge, C., Hopmans, E.C., Stadnitskaia, A., Rijpstra, W.I.C., Hofland, R., Tegelaar, E., and Sinninghe Damsté, J.S., 2013, Identification of novel penta- and hexamethylated-branched glycerol dialkyl glycerol tetraethers in peat using HPLC-MS2, GC-MS and GC-SMB-MS: Organic geochemistry, v. 54, p. 78−82.

De Jonge, C., Hopmans, E.C., Zell, C.I., Kim, J.H., Schouten, S., and Sinninghe Damsté, J.S., 2014, Occurrence and abundance of 6-methyl branched glycerol dialkyl glycerol tetraethers in soils: Implications for palaeoclimate reconstruction: Geochimica et Cosmochimica Acta, v. 141, p. 97−112.

De Schepper, S., and Head, M.J., 2008, Age calibration of dinoflagellate cyst and acritarch events in the Pliocene-Pleistocene of the eastern North Atlantic (DSDP Hole 610A): Stratigraphy, v. 5 (2), p. 137−161.

De Schepper, S., Gibbard, P.L., Salzmann, U., and Ehlers, J., 2014, A global synthesis of the marine and terrestrial evidence for glaciation during the Pliocene Epoch: Earth-Science Reviews, v. 135, p. 83−102.

De Schepper, S., Groeneveld, J., Naafs, B.D.A., Van Renterghem, C., Hennissen, J., Head, M.J., Louwye, S., and Fabian, K., 2013, Northern hemisphere glaciation during the globally warm early late Pliocene: PloS one, v. 8 (12), p. e81508.

De Schepper, S., Head, M.J., and Groeneveld, J., 2009, North Atlantic Current variability through marine isotope stage M2 (c. 3.3 Ma) during the mid-Pliocene: Paleoceanography, v. 24 (4), p. 1−17.

De Schepper, S., Schreck, M., Beck, K.M., Matthiessen, J., Fahl, K., and Mangerud, G., 2015, Early Pliocene onset of modern Nordic Seas circulation related to ocean gateway changes: Nature communications, v. 6 (1), p. 1−8.

de Vernal, A., and Hillaire-Marcel, C., 2008, Natural variability of Greenland climate, vegetation, and ice volume during the past million years: Science, v. 320 (5883), p. 1622−1625.

Dekens, P.S., Ravelo, A.C., and McCarthy, M.D., 2007, Warm upwelling regions in the Pliocene warm period: Paleoceanography, v. 22 (3), p. 1−12.

Dembicki, H., 2009, Three common source rock evaluation errors made by geologists during prospect or play appraisals: AAPG bulletin, v. 93 (3), p. 341−356.

Denk, T., Grímsson, F., and Kvaček, Z., 2005, The Miocene floras of Iceland and their significance for late Cainozoic North Atlantic biogeography: Botanical Journal of the Linnean Society, v. 149 (4), p. 369−417.

Denk, T., Grimsson, F., Zetter, R., and Símonarson, L.A., 2011, Late Cainozoic floras of Iceland: 15 million years of vegetation and climate history in the northern North Atlantic: Springer Science and Business Media, v. 35, 854 p.

Desjardins, P.R., Buatois, L.A., and Mángano, M.G., 2012, Tidal flats and subtidal sand bodies: Developments in Sedimentology, v. 64, p. 529−561.

Diem, B., 1985, Analytical method for estimating palaeowave climate and water depth from wave ripple marks: Sedimentology, v. 32 (5), p. 705−720.

Dokken, T., and Jansen, E., 1999, Rapid changes in the mechanism of ocean convection during the last glacial period: Nature, v. 401 (6752), p. 458−461.

Dolan, A.M., Haywood, A.M., Hill, D.J., Dowsett, H.J., Hunter, S.J., Lunt, D.J., and Pickering, S.J., 2011, Sensitivity of Pliocene ice sheets to orbital forcing: Palaeogeography, Palaeoclimatology, Palaeoecology, v. 309 (1−2), p. 98−110.

Doré, A.G., and Lundin, E.R., 1996, Cenozoic compressional structures on the NE Atlantic margin; nature, origin and potential significance for hydrocarbon exploration: Petroleum Geoscience, v. 2 (4), p. 299−311.

Doré, A.G., Lundin, E.R., Jensen, L.N., Birkeland, Ø., Eliassen, P.E., and Fichler, C., 1999, Principal tectonic events in the evolution of the northwest European Atlantic margin, *in:* Fleet, A.J. and Boldy, S.A.R., (eds.), Petroleum geology of the Northwest Europe: Geological Society of London, v. 5 (1), p. 41−61.

Dowsett, H., Barron, J., and Poore, R., 1996, Middle Pliocene sea surface temperatures: a global reconstruction: Marine Micropaleontology, v. 27 (1−4), p. 13−25.

Dowsett, H., Dolan, A., Rowley, D., Pound, M., Salzmann, U., Robinson, M., Chandler, M., Foley, K., and Haywood, A., 2016, The PRISM4 (mid-Piacenzian) palaeoenvironmental reconstruction: Climate of the Past Discussions, v. 12, p. 1519−1538.

Dowsett, H.J., 1991, The development of a long-range foraminifer transfer function and application to late Pleistocene North Atlantic climatic extremes: Paleoceanography, v. 6 (2), p. 259−273.

Dowsett, H.J., and Loubere, P., 1992, High resolution late Pliocene sea-surface temperature record from the Northeast Atlantic Ocean: Marine Micropaleontology, v. 20 (2), p. 91−105.

Dowsett, H.J., and Poore, R.Z., 1990, A new planktic foraminifer transfer function for estimating Pliocene-Holocene paleoceanographic conditions in the North Atlantic: Marine Micropaleontology, v. 16 (1−2), p. 1−23.

Dowsett, H.J., and Poore, R.Z., 1991, Pliocene sea surface temperatures of the North Atlantic Ocean at 3.0 Ma: Quaternary Science Reviews, v. 10 (2−3), p. 189−204.

Dowsett, H.J., and Robinson, M.M., 1998, Application of the modern analog technique (MAT) of sea surface temperature estimation to middle Pliocene North Pacific planktonic foraminifer assemblages: Palaeontologia Electronica, v. 1 (1), 22 p.

Dowsett, H.J., and Robinson, M.M., 2007, Mid-Pliocene planktic foraminifer assemblage of the North Atlantic Ocean: Micropaleontology, v. 53 (1-2), p. 105−126.

Dowsett, H.J., Foley, K.M., Robinson, M.M., and Herbert, T.D., 2017, PRISM late Pliocene (Piacenzian) alkenone-derived SST data: U.S. Geological Survey data release, viewed 01 March 2020, <https://doi.org/10.5066/F7959G1S>.

Dowsett, H.J., Foley, K.M., Stoll, D.K., Chandler, M.A., Sohl, L.E., Bentsen, M., Otto-Bliesner, B.L., Bragg, F.J., Chan, W.L., Contoux, C., and Dolan, A.M., 2013b. Sea surface temperature of the mid-Piacenzian ocean: a data-model comparison: Nature Scientific reports, v. 3, 8 p.

Dowsett, H.J., Robinson, M., Haywood, A.M., Salzmann, U., Hill, D., Sohl, L.E., Chandler, M., Williams, M., Foley, K., and Stoll, D.K., 2010a, The PRISM3D paleoenvironmental reconstruction: Stratigraphy, v. 7 (2−3), p. 123−139.

Dowsett, H.J., Robinson, M.M., and Foley, K.M., 2009, Pliocene three-dimensional global ocean temperature reconstruction: Climate of the past, v. 5 (4), p. 769−783.

Dowsett, H.J., Robinson, M.M., and Foley, K.M, 2015, A global planktic foraminifer census data set for the Pliocene ocean: Nature Scientific Data, v. 2, p. 150076.

Dowsett, H.J., Robinson, M.M., Haywood, A.M., Hill, D.J., Dolan, A.M., Stoll, D.K., Chan, W.L., Abe-Ouchi, A., Chandler, M.A., Rosenbloom, N.A., and Otto-Bliesner, B.L., 2012, Assessing confidence in Pliocene sea surface temperatures to evaluate predictive models: Nature Climate Change, v. 2 (5), p. 365−371.

Dowsett, H.J., Robinson, M.M., Stoll, D., and Foley, K., 2010b, Mid-Piacenzian mean annual sea surface temperature analysis for data-model comparisons: Stratigraphy, v. 7 (2−3), p.189−198.

Dowsett, H.J., Robinson, M.M., Stoll, D.K., Foley, K.M., Johnson, A.L., Williams, M., and Riesselman, C.R., 2013a, The PRISM (Pliocene palaeoclimate) reconstruction: time for a paradigm shift: Philosophical Transactions of the Royal Society A: Mathematical, Physical and Engineering Sciences, v. 371 (2001), p. 20120524.

Driscoll, N.W., and Haug, G.H., 1998, A short circuit in thermohaline circulation: A cause for northern hemisphere glaciation?: Science, v. 282 (5388), p. 436−438.

Du, J., Haley, B.A., and Mix, A.C., 2016, Neodymium isotopes in authigenic phases, bottom waters and detrital sediments in the Gulf of Alaska and their implications for paleo-circulation reconstruction: Geochimica et Cosmochimica Acta, v. 193, p. 14−35.

Dubois-Dauphin, Q., Colin, C., Bonneau, L., Montagna, P., Wu, Q., Van Rooij, D., Reverdin, G., Douville, É., Thil, F., Waldner, A., and Frank, N., 2017, Fingerprinting Northeast Atlantic water masses using Neodymium isotopes: Geochimica et Cosmochimica Acta, v. 210, p. 267−288.

Dunkley Jones, T., Eley, Y.L., Thompson, W., Greene, S.E., Mandel, I., Edgar, K., and Bendle, J.A., 2020, OPTiMAL: A new machine learning approach for GDGT-based palaeothermometry: Climate of the Past, v. 16 (6), p. 2599−2617.

Duplessy, J.C., Shackleton, N.J., Matthews, R.K., Prell, W., Ruddiman, W.F., Caralp, M., and Hendy, C.H., 1984, $\delta^{13}C$ record of benthic foraminifera in the last interglacial ocean: implications for the carbon cycle and the global deep water circulation: Quaternary Research, v. 21 (2), p. 225−243.

Edgar, K.M., Pälike, H., and Wilson, P.A., 2013, Testing the impact of diagenesis on the $\delta^{18}O$ and $\delta^{13}C$ of benthic foraminiferal calcite from a sediment burial depth transect in the equatorial Pacific: Paleoceanography, v. 28 (3), p. 468−480.

Eide, M., Olsen, A., Ninnemann, U.S., and Johannessen, T., 2017, A global ocean climatology of preindustrial and modern ocean $\delta^{13}C$: Global Biogeochemical Cycles, v. 31 (3), p. 515−534.

Eidvin, T., Bugge, T., and Smelror, M., 2007, The Molo Formation, deposited by coastal progradation on the inner Mid-Norwegian continental shelf, coeval with the Kai Formation to the west and the Utsira Formation in the North Sea: Norwegian Journal of Geology, v. 87, p. 75−142.

Einarsson, P., 2008, Plate boundaries, rifts and transforms in Iceland: Jökull, v. 58 (12), p. 35−58.

Einarsson, T., and Albertsson, K.J., 1988, The glacial history of Iceland during the past three million years: Philosophical Transactions of the Royal Society of London, Series B, Biological Sciences, v. 318 (1191), p. 637−644.

Einarsson, T., Hopkins, D.M., and Doell, R.R., 1967, The stratigraphy of Tjörnes, northern Iceland, and the history of the Bering Land Bridge, *in*: Hopkins, D.M., (ed.), The Bering Land Bridge, Stanford University Press, Stanford, p. 312−325.

Eiríksson, J., and Geirsdóttir, Á., 1991, A record of Pliocene and Pleistocene glaciations and climatic changes in the North Atlantic based on variations in volcanic and sedimentary facies in Iceland: Marine Geology, v. 101 (1−4), p. 147−159.

Eiríksson, J., 1980, Tjörnes, North Iceland: A Bibliographical Review of the Geological Research History: Jökull, v. 30, p. 1−20.

Eiríksson, J., 1981, Lithostratigraphy of the upper Tjörnes sequence, North Iceland: the Breiðavík Group: Icelandic museum of natural history, Acta Naturalia Islandica, v. 29, p. 1−37.

Eiríksson, J., 1985, Facies analysis of the Breiðavík Group sediments on Tjörnes, North Iceland: Acta Naturalia Islandica, v. 31, p. 1−56.

Eiríksson, J., Gudmundsson, A.I., Kristjánsson, L., and Gunnarsson, K., 1990, Palaeomagnetism of the Pliocene-Pleistocene sediments and lava flows on Tjörnes and Flatley, North Iceland: Boreas, v. 19, p. 39−55.

Eiríksson, J., Knudsen, K.L., and Viljálmsson, M., 1992, An early Pleistocene glacial-interglacial cycle in the Breiðavík Group on Tjörnes, Iceland: sedimentary facies, foraminifera, and molluscs: Quaternary Science Reviews, v. 11, p. 733−757.

Eiríksson, J., 1994, Growth of an intermittent ice sheet in Iceland during the late Pliocene and early Pleistocene: Quaternary research, v. 42 (2), p. 115−130.

Eisma, D., 1986, Flocculation and de-flocculation of suspended matter in estuaries: Netherlands Journal of Sea Research, v. 20 (2−3), p. 183−199.

Eldholm, O., Thiede, J., and Taylor, E., 1989, The Norwegian continental margin: tectonic, volcanic, and paleoenvironmental framework, *in:* Proceedings of the Ocean Drilling Program: Scientific Results, v. 104, p. 5−25.

Ellis, D., and Stoker, M.S., 2014, The Faroe-Shetland Basin: a regional perspective from the Paleocene to the present day and its relationship to the opening of the North Atlantic Ocean: Geological Society, London, Special Publications, v. 397 (1), p. 11−31.

Elmore, A.C., Piotrowski, A.M., Wright, J.D., and Scrivner, A.E., 2011, Testing the extraction of past seawater Nd isotopic composition from North Atlantic deep sea sediments and foraminifera: Geochemistry, Geophysics, Geosystems, v. 12 (9), p. 1−13.

Epstein, B.L., D'Hondt, S., Quinn, J.G., Zhang, J., and Hargraves, P.E., 1998, An effect of dissolved nutrient concentrations on alkenone-based temperature estimates: Paleoceanography, v. 13 (2), p. 122−126.

Fedorov, A.V., Brierley, C.M., Lawrence, K.T., Liu, Z., Dekens, P.S., and Ravelo, A.C., 2013, Patterns and mechanisms of early Pliocene warmth: Nature, v. 496 (7443), p. 43−49.

Fenies, H., Resseguier, A.D., and Tastet, J.P., 1999, Intertidal clay-drape couplets (Gironde estuary, France): Sedimentology, v. 46 (1), p. 1−15.

Field, D.J., Boessenecker, R., Racicot, R.A., Ásbjörnsdóttir, L., Jónasson, K., Hsiang, A.Y., Behlke, A.D., and Vinther, J., 2017, The oldest marine vertebrate fossil from the volcanic island of Iceland: a partial right whale skull from the high latitude Pliocene Tjörnes Formation: Palaeontology, v. 60 (2), p. 141−148.

Flemming, B.W., Schubert, H., Hertweck, G., and Müller, K., 1992, Bioclastic tidal-channel lag deposits: a genetic model: Senckenbergiana marit, v. 22 (3−6), p. 109−129.

Flesche Kleiven, H., Jansen, E., Fronval, T., and Smith, T.M., 2002, Intensification of Northern Hemisphere glaciations in the circum Atlantic region (3.5−2.4 Ma) ice-rafted detritus evidence: Palaeogeography, Palaeoclimatology, Palaeoecology, v. 184 (3−4), p. 213−223.

Flóvenz, Ó.G., and Sæmundsson, K., 1993, Heat flow and geothermal processes in Iceland: Tectonophysics, v. 225 (1−2), p. 123−138.

Flower, B.P., Oppo, D.W., McManus, J.F., Venz, K.A., Hodell, D.A., and Cullen, J.L., 2000, North Atlantic intermediate to deep water circulation and chemical stratification during the past 1 Myr: Paleoceanography, v. 15 (4), p. 388−403.

Flynn, J.J., Kowallis, B.J., Nuñez, C., Carranza-Castañeda, Ó., Miller, W.E., Swisher III, C.C., and Lindsay, E., 2005, Geochronology of Hemphillian-Blancan aged strata, Guanajuato, Mexico, and implications for timing of the Great American Biotic Interchange: The Journal of Geology, v. 113 (3), p. 287−307.

Foulger, G.R., Du, Z., and Julian, B.R., 2003, Icelandic-type crust: Geophysical Journal International, v. 155 (2), p. 567−590.

Freitas, F.S., Pancost, R.D., and Arndt, S., 2017, The impact of alkenone degradation on paleothermometry: A model-derived assessment: Paleoceanography, v. 32 (6), p. 648−672.

Fridleifsson, G.Ó., Eiríksson, J., Hafliðason, H., Gunnarsson, K., Ólafsson, G., Thors, K., Larsen, B., Thórhallsson, S., and Sveinbjörnsdóttir, Á.E., 1994, ODP proposal for drill sites within the Tjörnes fracture zone sedimentary basin: Late Cenozoic paleoceanography and sedimentation history at the Arctic boundary. Report 28/06/1994.

Fronval, T., and Jansen, E., 1996, Late Neogene paleoclimates and paleoceanography in the Iceland-Norwegian Sea: evidence from the Iceland and Vøring Plateaus, *in:* Thiede, J., Myhre, A.M., Firth, J.V., Johnson, G.L., and Ruddiman, W.F., (eds.), Proceedings of the Ocean Drilling Program, Scientific Results, v. 151, p. 455−468.

Funder, S., Abrahamsen, N., Bennike, O., and Feyling-Hanssen, R.W., 1985, Forested arctic: evidence from North Greenland: Geology, v. 13 (8), p. 542−546.

Funder, S., Bennike, O., Böcher, J., Israelson, C., Petersen, K.S., and Símonarson, L.A., 2001, Late Pliocene Greenland - The Kap København Formation in North Greenland: Bulletin of the Geological Society of Denmark, v. 48, p. 117-134.

Fürsich F.T., and Oschmann W., 1993, Shell beds as tools in basin analysis: the Jurassic Kachchh, western India: Journal of the Geological Society London, v. 150, p. 169−185.

Gaina, C., Gernigon, L., and Ball, P., 2009, Palaeocene-Recent plate boundaries in the NE Atlantic and the formation of the Jan Mayen microcontinent: Journal of the Geological Society, v. 166 (4), p. 601−616.

Galand, P.E., Gutiérrez-Provecho, C., Massana, R., Gasol, J.M., and Casamayor, E.O., 2010, Inter-annual recurrence of archaeal assemblages in the coastal NW Mediterranean Sea (Blanes Bay Microbial Observatory): Limnology and Oceanography, v. 55 (5), p. 2117−2125.

Ganerød, M., Smethurst, M.A., Torsvik, T.H., Prestvik, T., Rousse, S., McKenna, C., Van Hinsbergen, D.J.J., and Hendriks, B.W.H., 2010, The North Atlantic Igneous Province reconstructed and its relation to the plume generation zone: the Antrim Lava Group revisited: Geophysical Journal International, v. 182 (1), p. 183−202.

Garcia, S., Arnaud, N.O., Angelier, J., Bergerat, F., and Homberg, C., 2003, Rift jump process in Northern Iceland since 10 Ma from $^{40}Ar/^{39}Ar$ geochronology: Earth and Planetary Science Letters, v. 214 (3−4), p. 529−544.

Geirsdóttir, Á., and Eiríksson, J., 1994, Growth of an Intermittent Ice Sheet in Iceland during the Late Pliocene and Early Pleistocene: Quaternary research, v. 42, p. 115−130.

Gladenkov, Y.B., and Gurari, G.Z., 1976, Paleomagnetic characteristics of the Pliocene-Pleistocene in Iceland (Tjörnes Peninsula): Doklady Academic Nauk, v. 230, p. 1173−1175.

Gladenkov, Y.B., Norton, P.E.P., and Spaink, G., 1980, Upper Cenozoic of Iceland (in Russian): Trudy Geologicheskogo Instituta, Akademii Nauk SSSR, v. 345, p. 1−116.

Gottschalk, J., Vázquez Riveiros, N., Waelbroeck, C., Skinner, L.C., Michel, E., Duplessy, J.C., Hodell, D., and Mackensen, A., 2016, Carbon isotope offsets between benthic foraminifer species of the genus *Cibicidoides* in the glacial sub-Antarctic Atlantic: Paleoceanography, v. 31 (12), p.1583−1602.

Gradstein, F.M., Ogg, J.G., Schmitz, M.B., and Ogg, G.M., (eds.), 2012, The geologic time scale 2012: Elsevier, 1129 p.

Grimalt, J.O., Calvo, E., and Pelejero, C., 2001, Sea surface paleotemperature errors in $U^{K'}_{37}$ estimation due to alkenone measurements near the limit of detection: Paleoceanography, v. 16 (2), p. 226−232.

Grimalt, J.O., Rullkötter, J., Sicre, M.A., Summons, R., Farrington, J., Harvey, H.R., Goñi, M., and Sawada, K., 2000, Modifications of the C_{37} alkenone and alkenoate composition in the water column and sediment: Possible implications for sea surface temperature estimates in paleoceanography: Geochemistry, Geophysics, Geosystems, v. 1 (11), p. 2000GC00053.

Grímsson, F., 2007, The Miocene Floras of Iceland, Origin and Evolution of Fossil Floras from the North-West and Western Iceland, 15 to 6 Ma: PhD Dissertation, University of Iceland, Reykjavik, 273 p.

Grímsson, F., and Símonarson, L.A., 2008, Upper Tertiary non-marine environments and climatic changes in Iceland: Jökull, v. 58, p. 303−314.

Gudmundsson, A., 2000, Dynamics of volcanic systems in Iceland: example of tectonism and volcanism at juxtaposed hot spot and mid-ocean ridge systems: Annual Review of Earth and Planetary Sciences, v. 28 (1), p. 107−140.

Gudmundsson, A., Berg, S.S., Lyslo, K.B., and Skurtveit, E., 2001, Fracture networks and fluid transport in active fault zones: Journal of Structural Geology, v. 23 (2−3), p. 343−353.

Guerrero, Q., and Guillén, J., 2020, Dynamics of ripples superimposed on a sand ridge on a tideless shoreface: Estuarine, Coastal and Shelf Science, p.106826.

Guillén, J., Soriano, S., Demestre, M., Falqués, A., Palanques, A., and Puig, P., 2008, Alteration of bottom roughness by benthic organisms in a sandy coastal environment: Continental Shelf Research, v. 28 (17), p. 2382−2392.

Haley, B.A., Frank, M., Spielhagen, R.F., and Eisenhauer, A., 2008, Influence of brine formation on Arctic Ocean circulation over the past 15 million years: Nature Geoscience, v. 1 (1), p. 68−72.

Hansen, B., and Østerhus, S., 2000, North Atlantic-Nordic seas exchanges: Progress in oceanography, v. 45 (2), p. 109−208.

Harðarson, B.S., Fitton, J.G., and Hjartarson, A., 2008, Tertiary volcanism in Iceland: Jökull, v. 58, p. 161−178.

Harðarson, B.S., Fitton, J.G., Ellam, R.M., and Pringle, M.S., 1997, Rift relocation - a geochemical and geochronological investigation of a palaeo-rift in northwest Iceland: Earth and Planetary Science Letters, v. 153 (3−4), p. 181−196.

Haug, G.H., and Tiedemann, R., 1998, Effect of the formation of the Isthmus of Panama on Atlantic Ocean thermohaline circulation: Nature, v. 393 (6686), p. 673−676.

Haug, G.H., Ganopolski, A., Sigman, D.M., Rosell-Mele, A., Swann, G.E., Tiedemann, R., Jaccard, S.L., Bollmann, J., Maslin, M.A., Leng, M.J., and Eglinton, G., 2005, North Pacific seasonality and the glaciation of North America 2.7 million years ago: Nature, v. 433 (7028), p. 821−825.

Haug, G.H., Sigman, D.M., Tiedemann, R., Pedersen, T.F., and Sarnthein, M., 1999, Onset of permanent stratification in the subarctic Pacific Ocean: Nature, v. 401 (6755), p. 779−782.

Haywood, A.M., and Valdes, P.J., 2004, Modelling Pliocene warmth: contribution of atmosphere, oceans and cryosphere: Earth and Planetary Science Letters, v. 218 (3−4), p. 363−377.

Haywood, A.M., Dowsett, H.J., and Dolan, A.M., 2016, Integrating geological archives and climate models for the mid-Pliocene warm period: Nature communications, v. 7 (1), p. 1−14.

Heinrich, H., 1988, Origin and consequences of cyclic ice rafting in the northeast Atlantic Ocean during the past 130,000 years: Quaternary research, v. 29 (2), p. 142−152.

Hennissen, J.A., Head, M.J., De Schepper, S., and Groeneveld, J., 2014, Palynological evidence for a southward shift of the North Atlantic Current at ~2.6 Ma during the intensification of late Cenozoic Northern Hemisphere glaciation: Paleoceanography, v. 29 (6), p. 564−580.

Henrich, R., and Baumann, K.H., 1994, Evolution of the Norwegian Current and the Scandinavian Ice Sheets during the past 2.6 my: evidence from ODP Leg 104 biogenic carbonate and terrigenous records: Palaeogeography, Palaeoclimatology, Palaeoecology, v. 108 (1−2), p. 75−94.

Herbert, T.D., 2006, Alkenone Paleotemperature Determinations, *in:* Elderfield, H., (ed.), The Oceans and Marine Geochemistry, v. 6, p. 391−426.

Herbert, T.D., Lawrence, K.T., Tzanova, A., Peterson, L.C., Caballero-Gill, R., and Kelly, C.S., 2016, Late Miocene global cooling and the rise of modern ecosystems: Nature Geoscience, v. 9 (11), p. 843−847.

Herbert, T.D., Peterson, L.C., Lawrence, K.T., and Liu, Z., 2010, Tropical ocean temperatures over the past 3.5 million years: Science, v. 328 (5985), p.1530−1534.

Herfort, L., Schouten, S., Boon, J.P., and Sinninghe Damsté, J.S., 2006, Application of the TEX_{86} temperature proxy to the southern North Sea: Organic Geochemistry, v. 37 (12), p. 1715−1726.

Hilgen, F.J., Lourens, L.J., and van Dam, J.A., 2012, The Neogene Period, *in:* Gradstein, F.M., Ogg, J.G., Schmitz, M., and Ogg, G., (eds.), The Geologic Time Scale 2012, 2-Volume Set, Elsevier, Boston, v. 2, p. 923−978.

Hill, D.J., 2015, The non-analogue nature of Pliocene temperature gradients: Earth and Planetary Science Letters, v. 425, p. 232−241.

Hitchen, K., Johnson, H., and Gatliff, R.W., 2013, Geology of the Rockall Basin and adjacent areas: British Geological Survey, 192 p.

Hjartarson, Á., and Sæmundsson, K., 2014, Geological Map of Iceland, 1:600000, Bedrock: ÍSOR, Icelandic Geosurvey, Reykjavík.

Hjartarson, Á., Erlendsson, Ö., and Blischke, A., 2017, The Greenland-Iceland-Faroe Ridge Complex: Geological Society, London, Special Publications, v. 447 (1), p. 127−148.

Ho, S.L., Mollenhauer, G., Fietz, S., Martínez-Garcia, A., Lamy, F., Rueda, G., Schipper, K., Méheust, M., Rosell-Melé, A., Stein, R., and Tiedemann, R., 2014, Appraisal of TEX_{86} and TEX_{86}^{L} thermometries in subpolar and polar regions: Geochimica et Cosmochimica Acta, v. 131, p. 213−226.

Ho, S.L., Yamamoto, M., Mollenhauer, G., and Minagawa, M., 2011, Core top TEX_{86} values in the south and equatorial Pacific: Organic geochemistry, v. 42 (1), p. 94−99.

Hodell, D.A., and Channell, J.E., 2016, Mode transitions in Northern Hemisphere glaciation: co-evolution of millennial and orbital variability in Quaternary climate: Climates of the Past, v. 12 (9), p. 1805−1828.

Hoefs, M.J., Versteegh, G.J., Rijpstra, W.I.C., de Leeuw, J.W., and Sinninghe Damsté, J.S., 1998, Postdepositional oxic degradation of alkenones: Implications for the measurement of palaeo sea surface temperatures: Paleoceanography, v. 13 (1), p. 42−49.

Hopmans, E.C., Schouten, S., and Sinninghe Damsté, J.S., 2016, The effect of improved chromatography on GDGT-based palaeoproxies: Organic Geochemistry, v. 93, p. 1−6.

Hopmans, E.C., Weijers, J.W., Schefuß, E., Herfort, L., Sinninghe Damsté, J.S., and Schouten, S., 2004, A novel proxy for terrestrial organic matter in sediments based on branched and isoprenoid tetraether lipids: Earth and Planetary Science Letters, v. 224 (1−2), p. 107−116.

Horn, B.L.D., Goldberg, K., and Schultz, C.L., 2018, Interpretation of massive sandstones in ephemeral fluvial settings: A case study from the Upper Candelária Sequence (Upper Triassic, Paraná Basin, Brazil): Journal of South American Earth Sciences, v. 81, p.108−121.

Hospers, J., 1953, Palaeomagnetic studies of Icelandic rocks: Doctoral dissertation, University of Cambridge, 172 p.

Howard, J.D., and Reineck, H.E., 1981, Depositional facies of high-energy beach-to-offshore sequence: comparison with low-energy sequence: AAPG Bulletin, v. 65 (5), p. 807−830.

Howe, J.N., Piotrowski, A.M., Noble, T.L., Mulitza, S., Chiessi, C.M., and Bayon, G., 2016, North Atlantic deep water production during the Last Glacial Maximum: Nature communications, v. 7 (1), p. 1−8.

Huguet, A., Fosse, C., Laggoun-Défarge, F., Toussaint, M.L., and Derenne, S., 2010, Occurrence and distribution of glycerol dialkyl glycerol tetraethers in a French peat bog: Organic Geochemistry, v. 41 (6), p. 559−572.

Huguet, C., de Lange, G.J., Gustafsson, Ö., Middelburg, J.J., Sinninghe Damsté, J.S., and Schouten, S., 2008, Selective preservation of soil organic matter in oxidized marine sediments (Madeira Abyssal Plain): Geochimica et Cosmochimica Acta, v. 72 (24), p. 6061−6068.

Icelandic Meteorological Office., 2020, Mánárbakki monthly averages 1962−2016, viewed 01 May 2020, <https://en.vedur.is/climatology/data/>.

Ichaso, A.A., and Dalrymple, R.W., 2009, Tide-and wave-generated fluid mud deposits in the Tilje Formation (Jurassic), offshore Norway: Geology, v. 37 (6), p. 539−542.

Inagaki, F., Hinrichs, K.U., Kubo, Y., Bowles, M.W., Heuer, V.B., Hong, W.L., Hoshino, T., Ijiri, A., Imachi, H., Ito, M., and Kaneko, M., 2015, Exploring deep microbial life in coal-bearing sediment down to ~2.5 km below the ocean floor: Science, v. 349 (6246), p. 420−424.

Inglis, G.N., Collinson, M.E., Riegel, W., Wilde, V., Farnsworth, A., Lunt, D.J., Valdes, P., Robson, B.E., Scott, A.C., Lenz, O.K., and Naafs, B.D.A., 2017, Mid-latitude continental temperatures through the early Eocene in western Europe: Earth and Planetary Science Letters, v. 460, p. 86−96.

Inglis, G.N., Naafs, B.D.A., Zheng, Y., McClymont, E.L., Evershed, R.P., and Pancost, R.D., 2018, Distributions of geohopanoids in peat: Implications for the use of hopanoid-based proxies in natural archives: Geochimica et Cosmochimica Acta, v. 224, p. 249−261.

Jacobsen, S.B., and Wasserburg, G.J., 1980, Sm-Nd isotopic evolution of chondrites: Earth and Planetary Science Letters, v. 50 (1), p. 139−155.

Jansen, E., and Sjøholm, J., 1991, Reconstruction of glaciation over the past 6 Myr from ice-borne deposits in the Norwegian Sea: Nature, v. 349 (6310), p. 600−603.

Jansen, E., Fronval, T., Rack, F., and Channell, J.E., 2000, Pliocene-Pleistocene ice rafting history and cyclicity in the Nordic Seas during the last 3.5 Myr: Paleoceanography, v. 15 (6), p. 709−721.

Jansen, E., Bleil, U., Henrich, R., Kringstad, L., and Slettemark, B., 1988, Paleoenvironmental changes in the Norwegian Sea and the northeast Atlantic during the last 2.8 m.y: Deep Sea Drilling Project/Ocean Drilling Program Sites 610, 642, 643 and 644: Paleoceanography, v. 3, p. 563−581.

Jasper, K., Krooss, B.M., Flajs, G., Hartkopf-Fröder, C., and Littke, R., 2009, Characteristics of type III kerogen in coal-bearing strata from the Pennsylvanian (Upper Carboniferous) in the Ruhr Basin, Western Germany: Comparison of coals, dispersed organic matter, kerogen concentrates and coal-mineral mixtures: International Journal of Coal Geology, v. 80 (1), p. 1−19.

Jeandel, C., 2016, Overview of the mechanisms that could explain the 'Boundary Exchange' at the land-ocean contact: Philosophical Transactions of the Royal Society A: Mathematical, Physical and Engineering Sciences, v. 374 (2081): 20150287.

Jeandel, C., Arsouze, T., Lacan, F., Techine, P., and Dutay, J.C., 2007, Isotopic Nd compositions and concentrations of the lithogenic inputs into the ocean: A compilation, with an emphasis on the margins: Chemical Geology, v. 239 (1−2), p.156−164.

Jenkins, D.G., and Houghton, S.D., 1987, Age, correlation and paleoecology of the St. Erth Beds and the Coralline Crag of England: Mededelingen van de Werkgroep voor Tertiaire en Kwartaire Geologie, v. 24, p. 147−156.

Jenkins, D.G., Curry, D., Funnell, B.M., and Whittaker, J.E., 1988, Planktonic foraminifera from the Pliocene Coralline Crag of Suffolk, eastern England: Journal of Micropaleontology, v. 7, p. 1−10.

John, K.E.S., and Krissek, L.A., 2002, The late Miocene to Pleistocene ice-rafting history of southeast Greenland: Boreas, v. 31 (1), p. 28−35.

Jones, E.P., 2001, Circulation in the arctic ocean: Polar Research, v. 20 (2), p. 139−146.

Jones, S.M., White, N., and Maclennan, J., 2002, V-shaped ridges around Iceland: Implications for spatial and temporal patterns of mantle convection: Geochemistry, Geophysics, Geosystems, v. 3 (10), p. 1−23.

Jonkers, L., Jiménez-Amat, P., Mortyn, P.G., and Brummer, G.J.A., 2013, Seasonal Mg/Ca variability of N. pachyderma(s) and G. bulloides: Implications for seawater temperature reconstruction: Earth and Planetary Science Letters, v. 376, p. 137−144.

Kameo, K., and Sato, T., 2000, Biogeography of Neogene calcareous nannofossils in the Caribbean and the eastern equatorial Pacific - floral response to the emergence of the Isthmus of Panama: Marine Micropaleontology, v. 39 (1−4), p. 201−218.

Karas, C., Nürnberg, D., Bahr, A., Groeneveld, J., Herrle, J.O., Tiedemann, R., and Demenocal, P.B., 2017, Pliocene oceanic seaways and global climate: Scientific reports, v. 7 (1), p. 1−8.

Kästner, K., Hoitink, A.J.F., Vermeulen, B., Geertsema, T.J., and Ningsih, N.S., 2017, Distributary channels in the fluvial to tidal transition zone: Journal of Geophysical Research: Earth Surface, v. 122 (3), p. 696−710.

Keigwin, L.D., 1984, Stable isotopic results on upper Miocene and lower Pliocene foraminifers from Hole 552A, *in:* Roberts, D.G, Schnittker, D., et al. (eds.), Initial Reports of the Deep Sea Drilling Project, Washington (U.S. Govt. Printing Office), v. 81, p. 595−597.

Keigwin, L.D., 1987, Toward a high-resolution chronology for latest Miocene paleoceanographic events: Paleoceanography, v. 2 (6), p. 639−660.

Keigwin, L.D., Aubry, M.P., and Kent, D.V., 1987, North Atlantic late Miocene stable-isotope stratigraphy, biostratigraphy, and magnetostratigraphy, *in:* Ruddiman, W.F., Kidd, R.B., Thomas, E., et al. (eds.), Initial Reports of the Deep Sea Drilling Project, Washington (U.S. Govt. Printing Office), v. 94, p. 935−963.

Khélifi, N., and Frank, M., 2014, A major change in North Atlantic deep water circulation 1.6 million years ago: Climate of the Past, v. 10, p. 1441–1451.

Kidwell S.M., and Bosence D.W.J., 1991, Taphonomy and time-averaging of marine shelly faunas, *in:* Allison P.A., Briggs D.E.G., (eds.), Taphonomy: Releasing the Data Locked in the Fossil Record: Plenum Press, Berlin, p. 115−209.

Kidwell, S.M., Fürsich, F.T., and Aigner, T., 1986, Conceptual Framework for the Analysis and Classification of Fossil Concentrations: Palaios, v. 3, p. 228−238.

Kim, J.H., Schouten, S., Hopmans, E.C., Donner, B., and Sinninghe Damsté, J.S., 2008, Global sediment core-top calibration of the TEX_{86} paleothermometer in the ocean: Geochimica et Cosmochimica Acta, v. 72 (4), p. 1154−1173.

Kim, J.H., Van der Meer, J., Schouten, S., Helmke, P., Willmott, V., Sangiorgi, F., Koç, N., Hopmans, E.C., and Sinninghe Damsté, J.S., 2010, New indices and calibrations derived from the distribution of crenarchaeal isoprenoid tetraether lipids: Implications for past sea surface temperature reconstructions: Geochimica et Cosmochimica Acta, v. 74 (16), p. 4639−4654.

Knies, J., Matthiessen, J., Vogt, C., Laberg, J.S., Hjelstuen, B.O., Smelror, M., Larsen, E., Andreassen, K., Eidvin, T., and Vorren, T.O., 2009, The Plio-Pleistocene glaciation of the Barents Sea-Svalbard region: a new model based on revised Chronostratigraphy: Quaternary Science Reviews, v. 28 (9−10), p. 812−829.

Knies, J., Mattingsdal, R., Fabian, K., Grøsfjeld, K., Baranwal, S., Husum, K., De Schepper, S., Vogt, C., Andersen, N., Matthiessen, J., and Andreassen, K., 2014, Effect of early Pliocene uplift on late Pliocene cooling in the Arctic-Atlantic gateway: Earth and Planetary Science Letters, v. 387, p.132–144.

Koenig, S.J., Dolan, A.M., De Boer, B., Stone, E.J., Hill, D.J., DeConto, R.M., Abe-Ouchi, A., Lunt, D.J., Pollard, D., Quiquet, A., and Saito, F., 2015, Ice sheet model dependency of the simulated Greenland Ice Sheet in the mid-Pliocene: Climate of the Past, v. 11 (3), p. 369−381.

Kolcon, I., and Sachsenhofer, R.F., 1999, Petrography, palynology and depositional environments of the early Miocene Oberdorf lignite seam: International Journal of Coal Geology, v. 41 (3), p. 275−308.

Kristjiinsson, L., 2004, A reconnaissance study of paleomagnetic directions in the Tjörnes Beds, Northern Iceland: Jökull, v. 54, p. 57−63.

Lacan, F., and Jeandel, C., 2004a, Neodymium isotopic composition and rare earth element concentrations in the deep and intermediate Nordic Seas: Constraints on the Iceland Scotland Overflow Water signature: Geochemistry, Geophysics, Geosystems, v. 5 (11), p. 1–10.

Lacan, F., and Jeandel, C., 2004b, Denmark Strait water circulation traced by heterogeneity in neodymium isotopic compositions: Deep Sea Research Part I: Oceanographic Research Papers, v. 51 (1), p. 71−82.

Lacan, F., and Jeandel, C., 2005, Acquisition of the neodymium isotopic composition of the North Atlantic Deep Water: Geochemistry, Geophysics, Geosystems, v. 6 (12), p. 1−20.

Lang, D.C., Bailey, I., Wilson, P.A., Chalk, T.B., Foster, G.L., and Gutjahr, M., 2016, Incursions of southern-sourced water into the deep North Atlantic during late Pliocene glacial intensification: Nature Geoscience, v. 9 (5), p. 375−379.

Larsen, H.C., and Saunders, A.D., 1998, Tectonism and volcanism at the Southeast Greenland rifted margin: a record of plume impact and later continental rupture: Proceedings of the Ocean Drilling Program, Scientific Results, v. 152, p. 503−533.

Larsen, H.C., Saunders, A.D., Clift, P.D., Beget, J., Wei, W., and Spezzaferri, S., 1994, Seven million years of glaciation in Greenland: Science, v. 264 (5161), p. 952−955.

Larsen, L.M., Pedersen, A.K., Tegner, C., Duncan, R.A., Hald, N., and Larsen, J.G., 2016, Age of Tertiary volcanic rocks on the West Greenland continental margin: volcanic evolution and event correlation to other parts of the North Atlantic Igneous Province: Geological Magazine, v. 153 (3), p. 487−511.

Lawrence, K.T., 2020, Email to Jonathan Hall, 22 May.

Lawrence, K.T., Herbert, T.D., Brown, C.M., Raymo, M.E., and Haywood, A.M., 2009, High-amplitude variations in North Atlantic sea surface temperature during the early Pliocene warm period: Paleoceanography, v. 24 (2), p. 1−15.

Lawrence, K.T., Sigman, D.M., Herbert, T.D., Riihimaki, C.A., Bolton, C.T., Martinez-Garcia, A., Rosell-Mele, A., and Haug, G.H., 2013, Time-transgressive North Atlantic productivity changes upon Northern Hemisphere glaciation: Paleoceanography, v. 28 (4), p. 740−751.

Lawver, L.A., and Müller, R.D., 1994, Iceland hotspot track: Geology, v. 22 (4), p. 311−314.

Lazarus, D.B., Spencer-Cervato, C., Pika-Biolzi, M., Beckmann, J.P., von Salis, K.H., Hilbrecht, H., and Thierstein, H.R., 1995, Revised chronology of Neogene DSDP holes from the world ocean: Ocean Drilling Program, Texas A&M University, Technical Note, v. 24, 301 p.

Lee, K.E., Kim, J.H., Wilke, I., Helmke, P., and Schouten, S., 2008, A study of the alkenone, TEX_{86}, and planktonic foraminifera in the Benguela Upwelling System: Implications for past sea surface temperature estimates: Geochemistry, Geophysics, Geosystems, v. 9 (10), 19 p.

LeGrand, P., and Wunsch, C., 1995, Constraints from paleotracer data on the North Atlantic circulation during the last glacial maximum: Paleoceanography, v. 10 (6), p. 1011−1045.

Levitus, S., and Boyer, T.P., 1994, World Ocean atlas 1994, Temperature: NOAA Atlas, NESDIS, U.S. Department of Commerce, Washington D.C., U.S.A., v. 4, p. 1−117.

Li, Y., and Bhattacharya, J.P., 2014, Facies architectural study of a lower-delta-plain distributary channel system in the Ferron Notom Delta, Southern Utah: Sedimentology, v. 61, p. 1452−1483.

Lisiecki, L.E., and Raymo, M.E., 2005, A Plio-Pleistocene stack of 57 globally distributed benthic $\delta^{18}O$ records: Paleoceanography, v. 20, p. 1−17.

Liu, X.L., Leider, A., Gillespie, A., Gröger, J., Versteegh, G.J., and Hinrichs, K.U., 2010, Identification of polar lipid precursors of the ubiquitous branched GDGT orphan lipids in a peat bog in Northern Germany: Organic Geochemistry, v. 41 (7), p. 653−660.

Liu, Z., Pagani, M., Zinniker, D., DeConto, R., Huber, M., Brinkhuis, H., Shah, S.R., Leckie, R.M., and Pearson, A., 2009, Global cooling during the Eocene-Oligocene climate transition: Science, v. 323 (5918), p. 1187−1190.

Loomis, S.E., Russell, J.M., Ladd, B., Street-Perrott, F.A., and Sinninghe Damsté, J.S., 2012, Calibration and application of the branched GDGT temperature proxy on East African lake sediments: Earth and Planetary Science Letters, v. 357, p. 277−288.

Loubere, P., and Moss, K., 1986, Late Pliocene climatic change and the onset of Northern Hemisphere glaciation as recorded in the northeast Atlantic Ocean: Geological Society of America Bulletin, v. 97 (7), p. 818−828.

Lourens, L., 2004, The Neogene Period: A geologic time scale 2004, Cambridge University Press, p. 409−440.

Lundin, E.R., 2002, North Atlantic-Arctic: Overview of sea-floor spreading and rifting history: BATLAS-Mid Norway plate reconstruction atlas with global and Atlantic perspectives, Geological Survey of Norway, Trondheim, Norway, p. 40−47.

Lundin, E.R., and Doré, A.G., 2005, NE Atlantic break-up: a re-examination of the Iceland mantle plume model and the Atlantic-Arctic linkage, *in:* Doré, A.G., and Vining, B.A., (eds.), Petroleum geology of the Northwest Europe, Geological Society of London, v. 6 (1), p. 739−754.

Lunt, D.J., Foster, G.L., Haywood, A.M., and Stone, E.J., 2008, Late Pliocene Greenland glaciation controlled by a decline in atmospheric CO_2 levels: Nature, v. 454 (7208), p. 1102−1105.

Lupi, M., Geiger, S., and Graham, C.M., 2010, Hydrothermal fluid flow within a tectonically active rift-ridge transform junction: Tjörnes Fracture Zone, Iceland: Journal of Geophysical Research: Solid Earth, v. 115, p. 1−17.

MacEachern, J.A., Bann, K.L., Bhattacharya, J.P., Howell, C.D., 2005, Ichnology of deltas: organism responses to the dynamic interplay of rivers, waves, storms and tides: Special Publication - Society of Sedimentary Geology, v. 83, 49 p.

MacEachern, J.A., Bann, K.L., Gingras, M.K., Pemberton, S.G., Dashtgard, S.E., Hansen, C.D., Dafoe, L.T., Lerette, J., and Pearson, N.J., 2010, Ichnofabrics vs. Ichnofacies: A field-based test of spatial recurrence in shallow-marine successions: AAPC Search and Discovery Article, p. 90172.

MacEachern, J.A., Bann, K.L., Gingras, M.K., Zonneveld, J.P., Dashtgard, S.E., and Pemberton, S.G., 2012, The ichnofacies paradigm: Developments in sedimentology, v. 64, p. 103−138.

Mackensen, A. and Licari, L., 2003, Carbon isotopes of live benthic foraminifera from the South Atlantic: sensitivity to bottom water carbonate saturation state and organic matter rain rates, *in:* Wefer G., Mulitza S., Ratmeyer V., (eds.), The South Atlantic in the Late Quaternary: Springer, Berlin, Heidelberg, p. 623−644.

Mackensen, A., 2008, On the use of benthic foraminiferal $\delta^{13}C$ in palaeoceanography: constraints from primary proxy relationships, *in:* Austin, W., and James, R.H., (eds.), Biogeochemical Controls on Palaeoceanographic Environmental Proxies: Geological Society, London, Special Publications, v. 303, p. 121–133.

Mackensen, A., and Bickert, T., 1999, Stable carbon isotopes in benthic foraminifera: proxies for deep and bottom water circulation and new production, *in:* Fischer, G., and Wefer, G., (eds.), Use of proxies in paleoceanography, Springer, Berlin, Heidelberg, p. 229−254.

Mackensen, A., Hubberten, H.W., Bickert, T., Fischer, G., and Fütterer, D.K., 1993, The $\delta^{13}C$ in benthic foraminiferal tests of Fontbotia wuellerstorfi (Schwager) relative to the $\delta^{13}C$ of dissolved inorganic carbon in southern ocean deep water: implications for glacial ocean circulation models: Paleoceanography, v. 8 (5), p. 587−610.

Mackenzie, A.S., Patience, R.L., Maxwell, J.R., Vandenbroucke, M., and Durand, B., 1980, Molecular parameters of maturation in the Toarcian shales, Paris Basin, France. Changes in the configurations of acyclic isoprenoid alkanes, steranes and triterpanes: Geochimica et Cosmochimica Acta, v. 44 (11), p. 1709−1721.

Mángano, M.G., and Buatois, L.A., 2004, Reconstructing early Phanerozoic intertidal ecosystems: Ichnology of the Cambrian Campanario Formation in northwest Argentina: Fossils and Strata, v. 51, p. 17−38.

Mángano, M.G., Buatois, L.A., and Aceñolaza, G.F., 1996, Trace fossils and sedimentary facies from a Late Cambrian-Early Ordovician tide-dominated shelf (Santa Rosita Formation, northwest Argentina): Implications for ichnofacies models of shallow marine successions: Ichnos: An International Journal of Plant and Animal, v. 5 (1), p. 53−88.

Manning, A.J., and Dyer, K.R., 2007, Mass settling flux of fine sediments in Northern European estuaries: measurements and predictions: Marine Geology, v. 245 (1−4), p. 107−122.

Marincovich, L., 2000, Central American paleogeography controlled Pliocene Arctic Ocean molluscan migrations: Geology, v. 28 (6), p. 551−554.

Markič, M., and Sachsenhofer, R.F., 2010, The Velenje lignite - its petrology and genesis: Geološki zavod Slovenije, 218 p.

Martin, C.A., and Turner, B.R., 1998, Origins of massive-type sandstones in braided river systems: Earth Science Reviews, v. 44 (1−2), p. 15−38.

Mashiotta, T.A., Lea, D.W., and Spero, H.J., 1999, Glacial-interglacial changes in Subantarctic sea surface temperature and $\delta^{18}O$-water using foraminiferal Mg: Earth and Planetary Science Letters, v. 170 (4), p. 417−432.

Maslin, M.A., Haug, G.H., Sarnthein, M., and Tiedemann, R., 1996, The progressive intensification of northern hemisphere glaciation as seen from the North Pacific: Geologische Rundschau, v. 85 (3), p. 452−465.

Maslin, M.A., Li, X.S., Loutre, M.F., and Berger, A., 1998, The contribution of orbital forcing to the progressive intensification of Northern Hemisphere glaciation: Quaternary Science Reviews, v. 17 (4), p. 411−426.

Mathews, R.P., Singh, B.D., Singh, H., Singh, V.P., and Singh, A., 2018, Characterization of panandhro lignite deposits (Kachchh Basin), western India: Results from the bulk geochemical and palynofloral compositions: Journal of the Geological Society of India, v. 91 (3), p. 281−289.

Mattingsdal, R., Knies, J., Andreassen, K., Fabian, K., Husum, K., Grøsfjeld, K., and De Schepper, S., 2014, A new 6 Myr stratigraphic framework for the Atlantic-Arctic Gateway: Quaternary Science Reviews, v. 92, p. 170−178.

McCabe, P.J., and Shanley, K.W., 1992, Organic control on shoreface stacking patterns: Bogged down in the mire: Geology, v. 20 (8), p. 741−744.

McClymont, E.L., Ford, H.L., Ho, S., Tindall, J.C., Haywood, A.M., Alonso-Garcia, M., Bailey, I., Berke, M.A., Littler, K., Patterson, M.O., Petrick, B., Peterse, F., Ravelo, A.C., Risebrobakken, B., De Schepper, S., Swann, G.E.A., Thirumalai, K., Tierney, J.E., van der Weijst, C., White, S., Abe-Ouchi, A., Baatsen, M.L.J., Brady, E.C., Chan, W., Chandan, D., Feng, R., Guo, C., von der Heydt, A.S., Hunter, S., Li, X., Lohmann, G., Nisancioglu, K.H., Otto-Bliesner, B.L., Peltier, W.R., Stepanek, C., and Zhang, Z., 2020, Lessons from a high-CO_2 world: an ocean view from ∼3 million years ago: Climate of the Past, v. 16 (4), p. 1599−1615.

McDonald, H.G., 2005, Paleoecology of extinct xenarthrans and the Great American Biotic Interchange: Bulletin of the Florida Museum of Natural History, v. 45 (4), p. 313−333.

McDougall, I., Watkins, N.D., and Kristjánsson, L., 1976, Geochronology and paleomagnetism of a Miocene-Pliocene lava sequences at Bessastaðaá, Eastern Iceland: American Journal of Science, v. 276, p. 1078−1095.

McIntyre, K., Ravelo, A.C., and Delaney, M.L., 1999, North Atlantic intermediate waters in the late Pliocene to early Pleistocene: Paleoceanography, v. 14 (3), p. 324−335.

McManus, J.F., Oppo, D.W., and Cullen, J.L., 1999, A 0.5-million-year record of millennial-scale climate variability in the North Atlantic: Science, v. 283 (5404), p. 971−975.

Medina-Elizalde, M., Lea, D.W., and Fantle, M.S., 2008, Implications of seawater Mg/Ca variability for Plio-Pleistocene tropical climate reconstruction: Earth and Planetary Science Letters, v. 269 (3-4), p. 585−595.

Menges, J., Huguet, C., Alcaniz, J.M., Fietz, S., Sachse, D., and Rosell-Melé, A., 2014, Influence of water availability in the distributions of branched glycerol dialkyl glycerol tetraether in soils of the Iberian Peninsula: Biogeosciences, v. 11 (10), p. 2571−2581.

Miall, A.D., 1999, Perspectives: In defence of facies classifications and models: Journal of Sedimentary Research, v. 69 (1), p. 2−5.

Miller, K.G., Kominz, M.A., Browning, J.V., Wright, J.D., Mountain, G.S., Katz, M.E., Sugarman, P.J., Cramer, B.S., Christie-Blick, N., and Pekar, S.F., 2005, The Phanerozoic record of global sea-level change: Science, v. 310 (5752), p. 1293−1298.

Mjelde, R., Breivik, A.J., Raum, T., Mittelstaedt, E., Ito, G., and Faleide, J.I., 2008, Magmatic and tectonic evolution of the North Atlantic: Journal of the Geological Society, v. 165 (1), p. 31−42.

Moffa-Sanchez, P., Hall, I.R., Thornalley, D.J., Barker, S., and Stewart, C., 2015, Changes in the strength of the Nordic Seas Overflows over the past 3000 years: Quaternary Science Reviews, v. 123, p. 134−143.

Montes, C., Cardona, A., Jaramillo, C., Pardo, A., Silva, J.C., Valencia, V., Ayala, C., Pérez-Angel, L.C., Rodriguez-Parra, L.A., Ramirez, V., and Niño, H., 2015, Middle Miocene closure of the Central American seaway: Science, v. 348 (6231), p. 226−229.

Morrison, R., Waldner, A., Hathorne, E.C., Rahlf, P., Zieringer, M., Montagna, P., Colin, C., Frank, N., and Frank, M., 2019, Limited influence of basalt weathering inputs on the seawater neodymium isotope composition of the northern Iceland Basin: Chemical Geology, v. 511, p. 358−370.

Müller-Michaelis, A., and Uenzelmann-Neben, G., 2014, Development of the Western Boundary Undercurrent at Eirik Drift related to changing climate since the early Miocene: Deep Sea Research Part I: Oceanographic Research Papers, v. 93, p. 21−34.

Müller, J., Werner, K., Stein, R., Fahl, K., Moros, M., and Jansen, E., 2012, Holocene cooling culminates in sea ice oscillations in Fram Strait: Quaternary Science Reviews, v. 47, p. 1−14.

Myhre, A.M., and Thiede, J., 1995, North Atlantic-Arctic gateways, *in:* Myhre, A.M., Thiede, J., Firth, J.V., et al. (eds.), Proceedings Ocean Drilling Program Initial Reports, v. 151, College Station, Texas (Ocean Drilling Program), p. 5−26.

Naafs, B.D.A., Inglis, G.N., Zheng, Y., Amesbury, M.J., Biester, H., Bindler, R., Blewett, J., Burrows, M.A., Del Castillo Torres, D., Chambers, F.M., and Cohen, A.D., 2017, Introducing global peat-specific temperature and pH calibrations based on brGDGT bacterial lipids: Geochimica et Cosmochimica Acta, v. 208, p. 285−301.

Naafs, B.D.A., Rohrssen, M., Inglis, G.N., Lähteenoja, O., Feakins, S.J., Collinson, M.E., Kennedy, E.M., Singh, P.K., Singh, M.P., Lunt, D.J., and Pancost, R.D., 2018, High temperatures in the terrestrial mid-latitudes during the early Palaeogene: Nature Geoscience, v. 11 (10), p. 766−771.

Naafs, B.D.A., Stein, R., Hefter, J., Khélifi, N., De Schepper, S., and Haug, G.H., 2010, Late Pliocene changes in the North Atlantic current: Earth and Planetary Science Letters, v. 298 (3−4), p. 434−442.

Naafs, B.D.A., Voelker, A.H.L., Karas, C., Andersen, N., and Sierro, F.J., 2020, Repeated near-collapse of the Pliocene sea surface temperature gradient in the North Atlantic: Paleoceanography and Paleoclimatology, p. e2020PA003905.

Norton, P.E.P, 1975, Paleoecology of the Mollusca of the Tjörnes sequence, Iceland: Boreas, v. 4 (2), p. 97−110.

Norton, P.E.P, 1977, Neogene mollusca of the Tjörnes sequence, Iceland: paleoecology, zonation, correlation: Malacologia, v. 16 (1), p. 211−220.

Nuernberg, D., 1995, Magnesium in tests of Neogloboquadrina pachyderma sinistral from high northern and southern latitudes: The Journal of Foraminiferal Research, v. 25 (4), p. 350−368.

O'Dea, A., Lessios, H.A., Coates, A.G., Eytan, R.I., Restrepo-Moreno, S.A., Cione, A.L., Collins, L.S., De Queiroz, A., Farris, D.W., Norris, R.D., and Stallard, R.F., 2016, Formation of the Isthmus of Panama: Science advances, v. 2 (8), p. e1600883.

Oakey, G.N., and Chalmers, J.A., 2012, A new model for the Paleogene motion of Greenland relative to North America: Plate reconstructions of the Davis Strait and Nares Strait regions between Canada and Greenland: Journal of Geophysical Research: Solid Earth, v. 117, 28 p.

Obrochta, S.P., Crowley, T.J., Channell, J.E., Hodell, D.A., Baker, P.A., Seki, A., and Yokoyama, Y., 2014, Climate variability and ice-sheet dynamics during the last three glaciations: Earth and Planetary Science Letters, v. 406, p. 198−212.

Olafsson, J., and Olsen, A., 2010, Nordic Seas nutrients data in CARINA: Earth System Science Data, v. 2 (2), p. 205−213.

Ólafsson, M., Fridleifsson, G.Ó., Eiríksson, J., Sigvaldason, H., and Ármannsson, H., 1993, On the origin of organic gases in Öxarfjörður, NE Iceland: Orkustofnun, OS-93015/JHD-05, 76 p.

Ono, M., Sawada, K., Shiraiwa, Y., and Kubota, M., 2012, Changes in alkenone and alkenoate distributions during acclimatization to salinity change in Isochrysis galbana: Implication for alkenone-based paleosalinity and paleothermometry: Geochemical Journal, v. 46 (3), p. 235−247.

Oppo, D.W., and Curry, W.B., 2012, Deep Atlantic circulation during the Last Glacial Maximum and deglaciation: Nature Education Knowledge, v. 3 (10), p.1.

Oppo, D.W., and Fairbanks, R.G., 1987, Variability in the deep and intermediate water circulation of the Atlantic Ocean during the past 25,000 years: Northern Hemisphere modulation of the Southern Ocean: Earth and Planetary Science Letters, v. 86 (1), p.1−15.

Oppo, D.W., McManus, J.F., and Cullen, J.L., 2006, Evolution and demise of the Last Interglacial warmth in the subpolar North Atlantic: Quaternary Science Reviews, v. 25 (23−24), p. 3268−3277.

Otto-Bliesner, B.L., Jahn, A., Feng, R., Brady, E.C., Hu, A., and Löfverström, M., 2017, Amplified North Atlantic warming in the late Pliocene by changes in Arctic gateways: Geophysical Research Letters, v. 44 (2), p. 957−964.

Pagani, M., Liu, Z., LaRiviere, J., and Ravelo, A.C., 2010, High Earth-system climate sensitivity determined from Pliocene carbon dioxide concentrations: Nature Geoscience, v. 3 (1), p. 27−30.

Parnell-Turner, R., White, N.J., McCave, I.N., Henstock, T.J., Murton, B., and Jones, S.M., 2015, Architecture of North Atlantic contourite drifts modified by transient circulation of the Icelandic mantle plume: Geochemistry, Geophysics, Geosystems, v. 16 (10), p. 3414−3435.

Pearson, E.J., Juggins, S., Talbot, H.M., Weckström, J., Rosén, P., Ryves, D.B., Roberts, S.J., and Schmidt, R., 2011, A lacustrine GDGT-temperature calibration from the Scandinavian Arctic to Antarctic: Renewed potential for the application of GDGT-paleothermometry in lakes: Geochimica et Cosmochimica Acta, v. 75 (20), p. 6225−6238.

Pearson, N.J., Mángano, M.G., Buatois, L.A., Casadío, S., and Raising, M.R., 2012, Ichnology, sedimentology, and sequence stratigraphy of outer-estuarine and coastal-plain deposits: Implications for the distinction between allogenic and autogenic expressions of the Glossifungites Ichnofacies: Palaeogeography, Palaeoclimatology, Palaeoecology, v. 333, p.192−217.

Pearson, P.N., and Burgess, C.E., 2008, Foraminifer test preservation and diagenesis: comparison of high latitude Eocene sites: Geological Society, London, Special Publications, v. 303 (1), p. 59−72.

Pemberton, S.G., and Frey, R.W., 1985, The Glossifungites ichnofacies: modern examples from the Georgia coast, U.S.A., *in:* Curran, H.A., (ed.), Biogenic Structures: Their Use in Interpreting Depositional Environments: Society of Economic Paleontologists and Mineralogists Special Publication, v. 35, p. 237−259.

Pemberton, S.G., MacEachern, J.A., Dashtgard, S.E., Bann, K.L., Gingras, M.K., and Zonneveld, J.P., 2012, Shorefaces: Developments in sedimentology, v. 64, p. 563−603.

Peterse, F., van der Meer, J., Schouten, S., Weijers, J.W., Fierer, N., Jackson, R.B., Kim, J.H., and Sinninghe Damsté, J.S., 2012, Revised calibration of the MBT-CBT paleotemperature proxy based on branched tetraether membrane lipids in surface soils: Geochimica et Cosmochimica Acta, v. 96, p. 215−229.

Peterse, F., Vonk, J.E., Holmes, R.M., Giosan, L., Zimov, N., and Eglinton, T.I., 2014, Branched glycerol dialkyl glycerol tetraethers in Arctic lake sediments: Sources and implications for paleothermometry at high latitudes: Journal of Geophysical Research: Biogeosciences, v. 119 (8), p. 1738−1754.

Pflug, H.D., 1959, Sporenbilder aus Island und ihre stratigraphische Deutung (in German): Neues Jahrbuch für Geologie und Paläontologie, v. 107 (2), p. 141−172.

Piepgras, D.J. and Wasserburg, G.J., 1987, Rare earth element transport in the western North Atlantic inferred from Nd isotopic observations: Geochimica et Cosmochimica Acta, v. 51 (5), p. 1257−1271.

Pierce, B.S., Stanton, R.W., and Eble, C.F., 1991, Facies development in the Lower Freeport coal bed, west-central Pennsylvania, USA: International journal of coal geology, v. 18 (1−2), p. 17−43.

Piotrowski, A.M., Galy, A., Nicholl, J.A.L., Roberts, N., Wilson, D.J., Clegg, J.A., and Yu, J., 2012, Reconstructing deglacial North and South Atlantic deep water sourcing using foraminiferal Nd isotopes: Earth and Planetary Science Letters, v. 357, p. 289−297.

Piotrowski, A.M., Goldstein, S.L., Hemming, S.R., and Fairbanks, R.G., 2005, Temporal relationships of carbon cycling and ocean circulation at glacial boundaries: Science, v. 307, p. 1933–1938.

Pitcher, A., Wuchter, C., Siedenberg, K., Schouten, S., and Sinninghe Damsté, J.S., 2011, Crenarchaeol tracks winter blooms of ammonia-oxidizing Thaumarchaeota in the coastal North Sea: Limnology and Oceanography, v. 56 (6), p. 2308−2318.

Plint, A.G., 2010, Wave- and storm-dominated shoreline and shallow-marine systems, *in:* James, N.P., Dalrymple, R.W., (eds.), Facies Models 4: Geological Association of Canada, p. 167−200.

Pollard, J.E., Goldring, R., and Buck, S.G., 1993, Ichnofabrics containing Ophiomorpha: significance in shallow-water facies interpretation: Journal of the Geological Society, London, v. 150, p. 149−164.

Poole, D.A.R., 1994, Neogene and Quaternary paleoenvironments on the northern Norwegian shelf: Unpublished Ph.D. Thesis, University of Tromsø, 141 p.

Poore, H.R., Samworth, R., White, N.J., Jones, S.M., and McCave, I.N., 2006, Neogene overflow of northern component water at the Greenland-Scotland Ridge: Geochemistry, Geophysics, Geosystems, v. 7 (6), 24 p.

Prahl, F.G., and Wakeham, S.G., 1987, Calibration of unsaturation patterns in long-chain ketone compositions for palaeotemperature assessment: Nature, v. 330 (6146), p. 367−369.

Rasmussen, E., and Fjeldskaar, W., 1996, Quantification of the Pliocene-Pleistocene erosion of the Barents Sea from present-day bathymetry: Global and Planetary Change, v. 12 (1−4), p. 119–133.

Rasmussen, T.L., Bäckström, D., Heinemeier, J., Klitgaard-Kristensen, D., Knutz, P.C., Kuijpers, A., Lassen, S., Thomsen, E., Troelstra, S.R., and Van Weering, T.C.E., 2002, The Faroe-Shetland Gateway: Late Quaternary water mass exchange between the Nordic seas and the northeastern Atlantic: Marine Geology, v. 188 (1−2), p. 165−192.

Raymo M.E., Mitrovica J.X., O'Leary M.J., DeConto R.M., and Hearty P.J., 2011, Departures from eustasy in Pliocene sea-level records: Nature Geoscience, v. 4 (5), p. 328−332.

Raymo, M.E., 1994, The initiation of Northern Hemisphere glaciation: Annual Review of Earth and Planetary Sciences, v. 22 (1), p. 353−383.

Raymo, M.E., Hodell, D., and Jansen, E., 1992, Response of deep ocean circulation to initiation of Northern Hemisphere glaciation (3–2 Ma): Paleoceanography, v. 7 (5), p. 645−672.

Reynolds, B.C., Frank, M., and O'nions, R.K., 1999, Nd- and Pb-isotope time series from Atlantic ferromanganese crusts: implications for changes in provenance and paleocirculation over the last 8 Myr: Earth and Planetary Science Letters, v. 173 (4), p. 381−396.

Reynolds, R.W., and Smith, T.M., 1995, A high-resolution global sea surface temperature climatology: Journal of Climate, v. 8 (6), p. 1571−1583.

Richter, B., 2001, Kjarnaborun í Tjörnessetlögin til að meta þroska lifrænna efna. Áfangaskýrsla (in Icelandic). OST OS-2001/051, 29 p.

Richter, B., 2002, Dýpkun holu TG-02, Tjörnesi (in Icelandic): Orkustofnun, Short report, OS-BR-01/02, 3 p.

Richter, B., 2003, Söfnun gassýna úr söndum Öxarfjörður til samsætugreininga og greining kolefnissamsæta í surtarbrandslögum Tjörnessetlaga (in Icelandic): Orkustofnun. Short report, OS-BR-03/02, 6 p.

Richter, B., and Gunnarsson, K., 2010, Overview of hydrocarbon related research in Tjörnes: Report Iceland GeoSurvey, ÍSOR-2010/007, Prepared for National Energy Authority.

Rio, D., Sprovieri, R., Castradori, D., and Di Stefano, E., 1998, The Gelasian Stage (Upper Pliocene): A new unit of the global standard chronostratigraphic scale: Episodes, v. 21, p. 82−87.

Risebrobakken, B., Andersson, C., De Schepper, S., and McClymont, E.L., 2016, Low-frequency Pliocene climate variability in the eastern Nordic Seas: Paleoceanography, v. 31 (9), p. 1154−1175.

Roberts, N.L., and Piotrowski, A.M., 2015, Radiogenic Nd isotope labelling of the northern NE Atlantic during MIS 2: Earth and Planetary Science Letters, v. 423, p. 125−133.

Roberts, N.L., McManus, J.F., Piotrowski, A.M., and McCave, I.N., 2014, Advection and scavenging controls of Pa/Th in the northern NE Atlantic: Paleoceanography, v. 29 (6), p. 668−679.

Robinson, M.M., 2009, New quantitative evidence of extreme warmth in the Pliocene Arctic: Stratigraphy, v. 6 (4), p. 265−275.

Robinson, M.M., Dowsett, H.J., Dwyer, G.S., and Lawrence, K.T., 2008, Re-evaluation of mid-Pliocene North Atlantic sea surface temperatures: Paleoceanography, v. 23 (3), p. 1−9.

Robinson, M.M., Valdes, P.J., Haywood, A.M., Dowsett, H.J., Hill, D.J., and Jones, S.M., 2011, Bathymetric controls on Pliocene North Atlantic and Arctic sea surface temperature and deepwater production: Palaeogeography, Palaeoclimatology, Palaeoecology, v. 309 (1−2), p. 92−97.

Rodrigo-Gámiz, M., Rampen, W., Haas, H.D., Baas, M., Schouten, S., and Sinninghe Damsté, J.S., 2015, Constraints on the applicability of the organic temperature proxies $U^{K'}_{37}$, TEX_{86} and LDI in the subpolar region around Iceland: Biogeosciences, v. 12 (22), p. 6573−6590.

Rogers, K., and Woodroffe, C.D., 2015, Tidal flats and salt marshes, *in:* Masselink, G., and Gehrels, R., (eds.), Coastal Environments and Global Change: John Wiley and Sons, p. 227−250.

Rood, D., 2007, The troubleshooting and maintenance guide for gas chromatographers (Fourth Edition): John Wiley and Sons, 344 p.

Rosenbloom, N.A., Otto-Bliesner, B.L., Brady, E.C., and Lawrence, P.J., 2013, Simulating the mid-Pliocene Warm Period with the CCSM4 model: Geoscientific Model Development, v. 6 (2), p. 549−561.

Ruddiman, W.F., and Kutzbach, J.E., 1989, Forcing of late Cenozoic northern hemisphere climate by plateau uplift in southern Asia and the American West: Journal of Geophysical Research: Atmospheres, v. 94 (D15), p. 18409−18427.

Ruddiman, W.F., and Raymo, M.E., 1988, Northern Hemisphere climate regimes during the past 3 Ma: possible tectonic connections: Philosophical Transactions of the Royal Society of London B, Biological Sciences, v. 318 (1191), p. 411−430.

Sæmundsson, K., 1974., Evolution of the axial rifting zone in northern Iceland and the Tjörnes fracture zone: Geological Society of America Bulletin, v. 85 (4), p. 495−504.

Sæmundsson, K., 1979, Outline of the geology of Iceland: Jokull, v. 29, p. 7−28.

Salzmann, U., Williams, M., Haywood, A.M., Johnson, A.L., Kender, S., and Zalasiewicz, J., 2011, Climate and environment of a Pliocene warm world: Palaeogeography, Palaeoclimatology, Palaeoecology, v. 309 (1−2), p. 1−8.

Samtleben, C., and Bickert, T., 1990, Coccoliths in sediment traps from the Norwegian Sea: Marine Micropaleontology, v. 16 (1−2), p. 39−64.

Sarnthein, M., and Altenbach, A.V., 1995, Late Quaternary changes in surface water and deep water masses of the Nordic Seas and north-eastern North Atlantic: a review: Geologische Rundschau, v. 84 (1), p. 89−107.

Sarnthein, M., Bartoli, G., Prange, M., Schmittner, A., Schneider, B., Weinelt, M., Andersen, N., and Garbe-Schönberg, D., 2009, Mid-Pliocene shifts in ocean overturning circulation and the onset of Quaternary-style climates: Climate of the Past, v. 5 (2), p. 269−283.

Sato, T., and Kameo, K., 1996, Pliocene to Quaternary calcareous nannofossil biostratigraphy of the Arctic Ocean, with reference to Late Pliocene glaciation, *in:* Thiede, J., Myhre, A.M., Firth, J.V., Johnson, G.L., and Ruddiman, W.F., (eds.), Proceedings of the Ocean Drilling Program, Scientific Results, College Station, TX: Ocean Drilling Program, v. 151, p. 39−59.

Saunders, A.D., Jones, S.M., Morgan, L.A., Pierce, K., Widdowson, M., and Xu, Y.G., 2007, Regional uplift associated with continental large igneous provinces: The roles of mantle plumes and the lithosphere: Chemical Geology, v. 241 (3−4), p. 282−318.

Scheiber-Enslin, S.E., LaFemina, P.C., Sturkell, E., Hooper, A.J., and Webb, S.J., 2011, Geodetic investigation of plate spreading along a propagating ridge: the Eastern Volcanic Zone, Iceland: Geophysical Journal International, v. 187 (3), p. 1175−1194.

Schneider, B., and Schmittner, A., 2006, Simulating the impact of the Panamanian seaway closure on ocean circulation, marine productivity and nutrient cycling: Earth and Planetary Science Letters, v. 246 (3−4), p. 367−380.

Schouten, S., Hopmans, E.C., and Sinninghe Damsté, J.S., 2004, The effect of maturity and depositional redox conditions on archaeal tetraether lipid palaeothermometry: Organic Geochemistry, v. 35 (5), p. 567−571.

Schouten, S., Hopmans, E.C., and Sinninghe Damsté, J.S., 2013, The organic geochemistry of glycerol dialkyl glycerol tetraether lipids: a review: Organic geochemistry, v. 54, p. 19−61.

Schouten, S., Hopmans, E.C., Schefuß, E., and Sinninghe Damsté, J.S., 2002, Distributional variations in marine crenarchaeotal membrane lipids: a new tool for reconstructing ancient sea water temperatures?: Earth and Planetary Science Letters, v. 204 (1−2), p. 265−274.

Schreck, M., Meheust, M., Stein, R., and Matthiessen, J., 2013, Response of marine palynomorphs to Neogene climate cooling in the Iceland Sea (ODP Hole 907A): Marine Micropaleontology, v. 101, p. 49−67.

Schwager, C., 1866, Fossile Foraminiferen von Kar Nikobar (in German): KK Hof-und Staatsdruckerei, v. 2 (2), p. 187−268.

Schwarzbach, M., 1955, Beiträge zur Klimageschichte Islands 1. Allgemeiner Überblick der Klimageschichte Islands (in German): Neues Jahrbuch für Geologie und Paläontologie Monatsheft, v. 3, p. 97−130.

Schwarzbach, M., and Pflug, H.D., 1957, Beiträge zur Klimageschichte Islands 6 Das Klima des jüngeren Tertiärs in Island (in German): Neues Jahrbuch für Geologie und Paläontologie Abhandlungen, v. 104, p. 279−298.

Seki, O., Foster, G.L., Schmidt, D.N., Mackensen, A., Kawamura, K., and Pancost, R.D., 2010, Alkenone and boron-based Pliocene pCO_2 records: Earth and Planetary Science Letters, v. 292 (1−2), p. 201−211.

Sexton, P.F., Wilson, P.A., and Pearson, P.N., 2006, Microstructural and geochemical perspectives on planktic foraminiferal preservation: “Glassy” versus “Frosty”: Geochemistry, Geophysics, Geosystems, v. 7 (12), p. 1−29.

Shackleton, N.J., and Hall, M.A., 1984, Oxygen and carbon isotope stratigraphy of Deep Sea Drilling Project Hole 552A: Plio-Pleistocene glacial history, *in:* Roberts, D.G., Schnittker, D., et al. (eds.), Initial Reports of the Deep Sea Drilling Project, Washington (U.S. Govt. Printing Office), v. 81, p. 599−609.

Sigmarsson, O., and Steinthórsson, S., 2007, Origin of Icelandic basalts: A review of their petrology and geochemistry: Journal of Geodynamics, v. 43 (1), p. 87−100.

Sigmundsson, F., Einarsson, P., Hjartardóttir, Á.R., Drouin, V., Jónsdóttir, K., Árnadóttir, T., Geirsson, H., Hreinsdóttir, S., Li, S., and Ófeigsson, B.G., 2020, Geodynamics of Iceland and the signatures of plate spreading: Journal of Volcanology and Geothermal Research, v. 391, 14 p.

Símonarson, L.A., and Eiríksson, J., 2008, Tjörnes - Pliocene and Pleistocene sediments and faunas: Jökull, v. 58, p. 331−342.

Singh, P.K., Singh, V.K., Rajak, P.K., Singh, M.P., Naik, A.S., Raju, S.V., and Mohanty, D., 2016, Eocene lignites from Cambay basin, Western India: An excellent source of hydrocarbon: Geoscience frontiers, v. 7 (5), p. 811−819.

Sinninghe Damsté, J.S., Ossebaar, J., Schouten, S., and Verschuren, D., 2012, Distribution of tetraether lipids in the 25-ka sedimentary record of Lake Challa: extracting reliable TEX_{86} and MBT/CBT palaeotemperatures from an equatorial African lake: Quaternary Science Reviews, v. 50, p. 43−54.

Sinton, C.W., Hitchen, K., and Duncan, R.A., 1998, $^{40}Ar/^{39}Ar$ geochronology of silicic and basic volcanic rocks on the margins of the North Atlantic: Geological Magazine, v. 135 (2), p. 161−170.

Skogseid, J., Planke, S., Faleide, J.I., Pedersen, T., Eldholm, O., and Neverdal, F., 2000, NE Atlantic continental rifting and volcanic margin formation: Geological Society, London, Special Publications, v. 167 (1), p. 295−326.

Smith, Y.M., Hill, D.J., Dolan, A.M., Haywood, A.M., Dowsett, H.J., and Risebrobakken, B., 2018, Icebergs in the Nordic seas throughout the Late Pliocene: Paleoceanography and paleoclimatology, v. 33 (3), p. 318−335.

Solheim, A., Faleide, J.I., Andersen, E.S., Elverhøi, A., Forsberg, C.F., Vanneste, K., Uenzelmann-Neben, G., and Channell, J.E., 1998, Late Cenozoic seismic stratigraphy and glacial geological development of the East Greenland and Svalbard-Barents Sea continental margins: Quaternary Science Reviews, v. 17 (1−3), p. 155−184.

Srivastava, S.P., and Roest, W.R., 1999, Extent of oceanic crust in the Labrador Sea: Marine and Petroleum Geology, v. 16 (1), p. 65−84.

Srivastava, V.K., and Singh, B.P., 2017, Shoreface to estuarine sedimentation in the late Paleocene Matanomadh Formation, Kachchh, western India: Journal of Asian Earth Sciences, v. 136, p. 1−15.

Steph, S., Tiedemann, R., Prange, M., Groeneveld, J., Schulz, M., Timmermann, A., Nürnberg, D., Rühlemann, C., Saukel, C., and Haug, G.H., 2010, Early Pliocene increase in thermohaline overturning: A precondition for the development of the modern equatorial Pacific cold tongue: Paleoceanography, v. 25 (2), p. 1−17.

Stock, A.T., Littke, R., Lücke, A., Zieger, L., and Thielemann, T., 2016, Miocene depositional environment and climate in western Europe: the lignite deposits of the Lower Rhine Basin, Germany: International Journal of Coal Geology, v. 157, p. 2−18.

Storey, M., Duncan, R.A., and Tegner, C., 2007a, Timing and duration of volcanism in the North Atlantic Igneous Province: Implications for geodynamics and links to the Iceland hotspot: Chemical Geology, v. 241 (3−4), p. 264−281.

Storey, M., Duncan, R.A., and Swisher, C.C., 2007b, Paleocene-Eocene thermal maximum and the opening of the northeast Atlantic: Science, v. 316 (5824), p. 587−589.

Strauch, F., 1963, Zur Geologie von Tjörnes (Nordisland) (in German): Sonderveröffentlichungen des Geologischen Instituts der Universität Köln, v. 7, p. 1−129.

Strauch, F., 1972, Zum Klima des nordatlantisch-skandischen Raumes im jüngeren Känozoikum (in German): Zeitschrift der Deutschen Geologischen Gesellschaft, p. 163−177.

Straume, E.O., Gaina, C., Medvedev, S., and Nisancioglu, K.H., 2020, Global Cenozoic Paleobathymetry with a focus on the Northern Hemisphere Oceanic Gateways: Gondwana Research, v. 86, p. 126−143.

Sun, Q., Chu, G., Liu, M., Xie, M., Li, S., Ling, Y., Wang, X., Shi, L., Jia, G., and Lue, H., 2011, Distributions and temperature dependence of branched glycerol dialkyl glycerol tetraethers in recent lacustrine sediments from China and Nepal: Journal of Geophysical Research: Biogeosciences, v. 116 (G01008), p. 1−12.

Talwani, M., Windisch, C.C., and Langseth Jr, M.G., 1971, Reykjanes ridge crest: A detailed geophysical study: Journal of Geophysical Research, v. 76 (2), p. 473−517.

Tan, N., Ramstein, G., Dumas, C., Contoux, C., Ladant, J.B., Sepulchre, P., Zhang, Z., and De Schepper, S., 2017, Exploring the MIS M2 glaciation occurring during a warm and high atmospheric CO_2 Pliocene background climate: Earth and Planetary Science Letters, v. 472, p. 266−276.

Tanaka, T., Togashi, S., Kamioka, H., Amakawa, H., Kagami, H., Hamamoto, T., Yuhara, M., Orihashi, Y., Yoneda, S., Shimizu, H., and Kunimaru, T., 2000, JNdi-1: A neodymium isotopic reference in consistency with LaJolla neodymium: Chemical Geology, v. 168 (3−4), p. 279−281.

Tappan, H., 1951, Northern Alaska index foraminifera: Contributions from the Cushman Foundation for Foraminiferal Research, v. 2, p. 1−8.

Taylor, K.W., Huber, M., Hollis, C.J., Hernandez-Sanchez, M.T., and Pancost, R.D., 2013, Re-evaluating modern and Palaeogene GDGT distributions: Implications for SST reconstructions: Global and Planetary Change, v. 108, p. 158−174.

Tegner, C., Lesher, C.E., Larsen, L.M., and Watt, W.S., 1998, Evidence from the rare-earth-element record of mantle melting for cooling of the Tertiary Iceland plume: Nature, v. 395 (6702), p. 591−594.

Teichmüller, M., 1989, The genesis of coal from the view-point of coal petrology: International Journal of Coal Geology, v. 12, p. 1−87.

Tentler, T., and Temperley, S., 2007, Magmatic fissures and their systems in Iceland: A tectonomagmatic model: Tectonics, v. 26 (5), 17 p.

Teschner, C., Frank, M., Haley, B.A., and Knies, J., 2016, Plio-Pleistocene evolution of water mass exchange and erosional input at the Atlantic-Arctic gateway: Paleoceanography, v. 31 (5), p. 582−599.

Thomsen, C., Schulz-Bull, D.E., Petrick, G., and Duinker, J.C., 1998, Seasonal variability of the long-chain alkenone flux and the effect on the $U^{K'}_{37}$ index in the Norwegian Sea: Organic Geochemistry, v. 28 (5), p. 311−323.

Thordarson, T., and Höskuldsson, Á., 2008, Postglacial volcanism in Iceland: Jökull, v. 58 (198), p. 197−228.

Thoroddsen, T., 1902, Islandske Fjorde og Bugter (in Danish): Geografisk Tidsskrift, v. 16, p. 58−82.

Tierney, J.E., 2012, GDGT Thermometry: Lipid Tools for Reconstructing Paleotemperatures: The Paleontological Society Papers, v. 18, p. 115-132.

Tierney, J.E., and Tingley, M.P., 2015, A TEX_{86} surface sediment database and extended Bayesian calibration: Scientific data, v. 2 (1), p. 1−10.

Tierney, J.E., and Tingley, M.P., 2018, BAYSPLINE: A new calibration for the alkenone paleothermometer: Paleoceanography and Paleoclimatology, v. 33 (3), p. 281−301.

Tierney, J.E., Russell, J.M., Eggermont, H., Hopmans, E.C., Verschuren, D., and Sinninghe Damsté, J.S., 2010, Environmental controls on branched tetraether lipid distributions in tropical East African lake sediments: Geochimica et Cosmochimica Acta, v. 74 (17), p. 4902−4918.

Tierney, J.E., Schouten, S., Pitcher, A., Hopmans, E.C., and Sinninghe Damsté, J.S., 2012, Core and intact polar glycerol dialkyl glycerol tetraethers (GDGTs) in Sand Pond, Warwick, Rhode Island (USA): Insights into the origin of lacustrine GDGTs: Geochimica et Cosmochimica Acta, v. 77, p. 561−581.

Tissot, B.P., Pelet, R., and Ungerer, P.H., 1987, Thermal history of sedimentary basins, maturation indices, and kinetics of oil and gas generation: AAPG bulletin, v. 71 (12), p. 1445−1466.

Tjiputra, J.F., Roelandt, C., Bentsen, M., Lawrence, D.M., Lorentzen, T., Schwinger, J., Seland, Ø., and Heinze, C., 2013, Evaluation of the carbon cycle components in the Norwegian Earth System Model (NorESM): Geoscientific Model Development, v. 6 (2), p. 301−325.

Torsvik, T.H., Carlos, D., Mosar, J., Cocks, L.R.M., and Malme, T., 2002, Global reconstructions and North Atlantic paleogeography 440 Ma to recent: BATLAS-Mid Norway plate reconstruction atlas with global and Atlantic perspectives, Geological Survey of Norway, Trondheim, v. 18, 39 p.

Van Couvering, J.A., Castradori, D., Cita, M.B., Hilgen, F.J., and Rio, D., 2000, The base of the Zanclean Stage and of the Pliocene Series: Episodes, v. 23 (3), p. 179−187.

Vázquez Riveiros, N., Govin, A., Waelbroeck, C., Mackensen, A., Michel, E., Moreira, S., Bouinot, T., Caillon, N., Orgun, A., and Brandon, M., 2016, Mg/Ca thermometry in planktic foraminifera: Improving paleotemperature estimations for *G. bulloides* and *N. pachyderma* left: Geochemistry, Geophysics, Geosystems, v. 17, p. 1249−1264.

Venti, N.L., Billups, K., and Herbert, T.D., 2013, Increased sensitivity of the Plio-Pleistocene northwest Pacific to obliquity forcing: Earth and Planetary Science Letters, v. 384, p.121−131.

Venz, K.A., and Hodell, D.A., 2002, New evidence for changes in Plio-Pleistocene deep water circulation from Southern Ocean ODP Leg 177 Site 1090: Palaeogeography, Palaeoclimatology, Palaeoecology, v. 182 (3−4), p. 197−220.

Venz, K.A., Hodell, D.A., Stanton, C., and Warnke, D.A., 1999, A 1.0 Myr record of Glacial North Atlantic Intermediate Water variability from ODP site 982 in the northeast Atlantic: Paleoceanography, v. 14 (1), p. 42−52.

Verhoeven, K., and Louwye, S., 2013, Palaeoenvironmental reconstruction and biostratigraphy with marine palynomorphs of the Plio-Pleistocene in Tjörnes, Northern Iceland: Palaeogeography, Palaeoclimatology, Palaeoecology, v. 376, p. 224−243.

Verhoeven, K., Louwye, S. and Eiríksson, J., 2013, Plio-Pleistocene landscape and vegetation reconstruction of the coastal area of the Tjörnes Peninsula, Northern Iceland: Boreas, v. 42 (1), p.108−122.

Verhoeven, K., Louwye, S., Eiríksson, J., and De Schepper, S., 2011, A new age model for the Pliocene-Pleistocene Tjörnes section on Iceland: its implication for the timing of North Atlantic-Pacific palaeoceanographic pathways: Palaeogeography, Palaeoclimatology, Palaeoecology, v. 309 (1−2), p. 33−52.

Villanueva, J., and Grimalt, J.O., 1996, Pitfalls in the chromatographic determination of the alkenone $U^{K'}_{37}$ index for paleotemperature estimation: Journal of chromatography A, v. 723 (2), p. 285−291.

Villanueva, L., Sinninghe Damsté, J.S., and Schouten, S., 2014, A re-evaluation of the archaeal membrane lipid biosynthetic pathway: Nature Reviews Microbiology, v. 12 (6), p. 438−448.

Volkman, J.K., Barrerr, S.M., Blackburn, S.I., and Sikes, E.L., 1995, Alkenones in Gephyrocapsa oceanica: Implications for studies of paleoclimate: Geochimica et Cosmochimica Acta, v. 59 (3), p. 513−520.

Voulgaris, G., and Meyers, S.T., 2004, Temporal variability of hydrodynamics, sediment concentration and sediment settling velocity in a tidal creek: Continental Shelf Research, v. 24 (15), p. 1659−1683.

Wade, B.S., Pearson, P.N., Berggren, W.A., and Pälike, H., 2011, Review and revision of Cenozoic tropical planktonic foraminiferal biostratigraphy and calibration to the geomagnetic polarity and astronomical time scale: Earth Science Reviews, v. 104 (1−3), p. 111−142.

Walters, R.L., Jones, S.M., and Maclennan, J., 2013, Renewed melting at the abandoned Húnafloí Rift, northern Iceland, caused by plume pulsing: Earth and Planetary Science Letters, v. 377, p. 227−238.

Wang, Y., Wang, Y.P., Yu, Q., Du, Z., Wang, Z.B., and Gao, S., 2019, Sand-mud tidal flat morphodynamics influenced by alongshore tidal currents: Journal of Geophysical Research: Oceans, v. 124 (6), p. 3818−3836.

Wang, P., 2011, Principles of sediment transport applicable in tidal environments, *in:* Davis, R.A., and Dalrymple, R.W., (eds.), Principles of Tidal Sedimentology: Springer Science and Business Media, p. 19−34.

Webb, S.D., 2006, The great American biotic interchange: patterns and processes: Annals of the Missouri Botanical Garden, v. 93 (2), p. 245−257.

Weber, Y., De Jonge, C., Rijpstra, W.I.C., Hopmans, E.C., Stadnitskaia, A., Schubert, C.J., Lehmann, M.F., Sinninghe Damste, J.S., and Niemann, H., 2015, Identification and carbon isotope composition of a novel branched GDGT isomer in lake sediments: Evidence for lacustrine branched GDGT production: Geochimica et Cosmochimica Acta, v. 154, p. 118−129.

Weijers, J.W., Schefuß, E., Kim, J.H., Sinninghe Damsté, J.S., and Schouten, S., 2014, Constraints on the sources of branched tetraether membrane lipids in distal marine sediments: Organic Geochemistry, v. 72, p. 14−22.

Weijers, J.W., Schouten, S., Spaargaren, O.C., and Sinninghe Damsté, J.S., 2006, Occurrence and distribution of tetraether membrane lipids in soils: Implications for the use of the TEX_{86} proxy and the BIT index: Organic Geochemistry, v. 37 (12), p. 1680−1693.

Weijers, J.W., Schouten, S., van den Donker, J.C., Hopmans, E.C., and Sinninghe Damsté, J.S., 2007, Environmental controls on bacterial tetraether membrane lipid distribution in soils: Geochimica et Cosmochimica Acta, v. 71 (3), p. 703−713.

Weijers, J.W., Steinmann, P., Hopmans, E.C., Schouten, S., and Sinninghe Damsté, J.S., 2011, Bacterial tetraether membrane lipids in peat and coal: Testing the MBT-CBT temperature proxy for climate reconstruction: Organic Geochemistry, v. 42 (5), p. 477−486.

Werner, K., Frank, M., Teschner, C., Müller, J., and Spielhagen, R.F., 2014, Neoglacial change in deep water exchange and increase of sea-ice transport through eastern Fram Strait: evidence from radiogenic isotopes: Quaternary Science Reviews, v. 92, p. 190−207.

Westoby, M.J., Brasington, J., Glasser, N.F., Hambrey, M.J., and Reynolds, J.M., 2012, 'Structure-from-Motion' photogrammetry: A low-cost, effective tool for geoscience applications: Geomorphology, v. 179, p. 300−314.

Widera, M., 2012, Macroscopic lithotype characterisation of the 1st Middle-Polish (1st Lusatian) Lignite Seam in the Miocene of central Poland: Geologos, v. 18 (1), p. 1−11.

Willard, D.A., 1994, Palynological record from the North Atlantic region at 3 Ma: vegetational distribution during a period of global warmth: Review of Palaeobotany and Palynology, v. 83 (4), p. 275−297.

Willeit, M., Ganopolski, A., Calov, R., Robinson, A., and Maslin, M., 2015, The role of CO_2 decline for the onset of Northern Hemisphere glaciation: Quaternary Science Reviews, v. 119, p. 22−34.

Willis, B.J., and Gabel, S., 2001, Sharp-based, tide-dominated deltas of the Sego Sandstone, Book Cliffs, Utah, U.S.A: Sedimentology, v. 48, p. 479−506.

Windisch, P., 1886, Beiträge zur Kenntniss der Tertiärflora von Island (in German): Zeitschrift für Naturwissenschaften, v. 4 (5), p. 215−262.

Wold, C.N., 1994, Cenozoic sediment accumulation on drifts in the northern North Atlantic: Paleoceanography, v. 9 (6), p. 917−941.

Wolf, T.C., and Thiede, J., 1991, History of terrigenous sedimentation during the past 10 my in the North Atlantic (ODP Legs 104 and 105 and DSDP Leg 81): Marine Geology, v. 101 (1−4), p. 83−102.

Woodard, S.C., Rosenthal, Y., Miller, K.G., Wright, J.D., Chiu, B.K., and Lawrence, K.T., 2014, Antarctic role in Northern Hemisphere glaciation: Science, v. 346 (6211), p. 847−851.

Wright, A.K., and Flower, B.P., 2002, Surface and deep ocean circulation in the subpolar North Atlantic during the mid-Pleistocene revolution: Paleoceanography, v. 17 (4), p. 20−31.

Wright, J.D., and Miller, K.G., 1996, Control of North Atlantic deep water circulation by the Greenland-Scotland Ridge: Paleoceanography, v. 11 (2), p. 157−170.

Yang, B.C., and Chang, T.S., 2018, Integrated sedimentological and ichnological characteristics of a wave-dominated, macrotidal coast: a case study from the intertidal shoreface of the Dongho coast, southwest Korea: Geo-Marine Letters, v. 38 (2), p. 139−151.

Yokokawa, M., and Masuda, F., 1991, Tidal influence on foreshore deposits, Pacific coast of Japan: Clastic Tidal Sedimentology, v. 16, p. 315−320.

Zachos, J., Pagani, M., Sloan, L., Thomas, E., and Billups, K., 2001, Trends, rhythms, and aberrations in global climate 65 Ma to present: Science, v. 292 (5517), p. 686−693.

Zell, C., Kim, J.H., Hollander, D., Lorenzoni, L., Baker, P., Silva, C.G., Nittrouer, C., and Sinninghe Damsté, J.S., 2014, Sources and distributions of branched and isoprenoid tetraether lipids on the Amazon shelf and fan: Implications for the use of GDGT-based proxies in marine sediments: Geochimica et Cosmochimica Acta, v. 139, p. 293−312.

Zhang, Y.G., Pagani, M., and Wang, Z., 2016, Ring Index: A new strategy to evaluate the integrity of TEX_{86} paleothermometry: Paleoceanography, v. 31 (2), p. 220−232.

Zhang, Y.G., Pagani, M., Liu, Z., Bohaty, S.M., and DeConto, R., 2013, A 40-million-year history of atmospheric CO_2: Philosophical Transactions of the Royal Society A: Mathematical, Physical and Engineering Sciences, v. 371 (2001), p. 20130096.

Zhang, Z., Nisancioglu, K.H., and Ninnemann, U.S., 2013, Increased ventilation of Antarctic deep water during the warm mid-Pliocene: Nature communications, v. 4 (1), p. 1−6.

Zhang, Z.S., Nisancioglu, K., Bentsen, M., Tjiputra, J., Bethke, I., Yan, Q., Risebrobakken, B., Andersson, C., and Jansen, E., 2012, Pre-industrial and mid-Pliocene simulations with NorESM-L: Geoscientific Model Development, v. 5 (2), p. 523−533.

Zheng, Y., Li, Q., Wang, Z., Naafs, B.D.A., Yu, X., and Pancost, R.D., 2015, Peatland GDGT records of Holocene climatic and biogeochemical responses to the Asian Monsoon: Organic geochemistry, v. 87, p. 86−95

APPENDIX A: METHODS

The methods described on the following pages are supplementary to Chapters 3, 4 and 5.

A.1 Extracting and picking foraminifera from bulk sediments

Sample preparation

1. First clean all glassware and implements thoroughly in Decon® disinfectant overnight. Rinse glassware and implements in Milli-Q® deionized water before allowing to dry naturally.
2. Wearing protective gloves, line a labelled weighing tray with furnaced foil (450°C, 8 hours) and weigh and record the weight of the tray.
3. Unpack the sediment core sample into the lined tray. Check the core sample for drilling mud and remove using a clean scalpel where necessary. Cut the sediment into small pieces (1 cm^3) to accelerate drying. Reweigh the tray containing the sediment and record the weight. Calculate the wet sediment weight by subtracting the empty foil-lined tray from the total weight.
4. Transfer the sample into the drying oven and dry at 40°C for up to one week, until no further significant weight loss is observed. Record the dry bulk sediment weight by subtracting the dry sediment weight from the wet sediment weight.
5. Transfer the sample into a 250 ml labelled glass beaker and add 100 ml of Milli-Q® water. Swirl the beaker to disaggregate the sediment and leave for 30 minutes to breakdown.

Washing down bulk sediment to collect fines for organic geochemistry

7. Collect three one litre glass beakers pre-cleaned in Decon® disinfectant overnight. Fill and pressurise a spray-cylinder with Milli-Q® water.
8. Wash down the sediment sample over a clean 63 µm sieve into the beaker by pouring the disaggregated sediment into the sieve. Wash down the sample gently using the spray cylinder, taking care not to splash or spill the sample. The sieve collects the coarse fraction (>63 µm) and the beaker collects the fine fraction (<63 µm). Once the beaker is full, place on the side for the fines to settle from suspension and collect another beaker to continue washing down.
9. Continue to wash the sediment sample until all of the fine fraction is removed from the sieve. The Milli-Q® water running through the sieve should eventually run clear. Transfer the coarse fraction from the sieve into the original labelled weighing tray, after removing the furnaced foil liner. Transfer the tray into a drying oven at 40°C overnight.

10. Clean the sieve thoroughly using tap water, followed by ultrasonication (5 minutes, 40 kHz) and a final rinse in Milli-Q® water.
11. Cover the beaker with furnaced foil and allow the fines to settle from suspension for up to one week. Once settled, carefully siphon off the clear water above the sample and dry overnight at 40°C to evaporate the residual water.
12. Transfer the dried fines into a furnaced foil envelope and seal in a labelled Whirl-Pak™ sample bag ready for organic geochemical analysis.

Secondary wash-down with Calgon®

13. If the coarse fraction still contains visible argillaceous or carbonate sediment after the first wash down, transfer the dry residue into another 250 ml glass beaker, top-up with Milli-Q® and add 15 g of Calgon® water softener to promote disaggregation. Boil for 5 minutes on a heating plate and decant the solution over a 63 µm sieve into a waste bucket in the fume hood.
14. Wash down the sample again over a clean 63 µm sieve following steps 7−9.
15. Once the coarse fraction is dry, record the dry weight and transfer the sample into a labelled vial, using a paper funnel and brush. Ensure the brush is cleaned and the paper is replaced between samples to prevent contamination. Store vials in a labelled box ready for picking.

Dry sieving and picking foraminifera

16. Clean the nest of sieves (500, 355 and 250 µm) thoroughly using a coarse paintbrush or ultrasonicate if necessary. Assemble the stack and attach a clean receiver pan at the base.
17. Transfer the dry coarse fraction into the top sieve and gently shake the sediment, so it passes through the nest. Collect the 355−250 µm residue for picking and transfer into a labelled vial using a clean paper funnel for each sample.
18. Transfer a small amount of the 355−250 µm residue onto a clean picking tray, and place the tray under a stereomicroscope. Power the microscope, adjust the magnification and dioptre accordingly.
19. Pick specific species using a fine paintbrush, dampened with Milli-Q®, and transfer more than >10 mg into a labelled Eppendorf™ conical tube ready for stable isotope analysis.
20. Once picking is complete, carefully transfer the coarse residue back into the original labelled vial and store in a labelled box.

A.2 Leaching authigenic coatings and neodymium column chemistry

Leaching of authigenic ferromanganese oxyhydroxide (Fe-Mn) coatings

1. Leach c. 2 g of bulk sediment on a rotator for 15−20 minutes in 0.05 mol/L hydroxylamine hydrochloride and 2.6 mol/L acetic acid following the methods of Blaser et al. (2016).
2. Centrifuge the leachates twice: once at 5000 rpm for at least 10 minutes, and then again at 6000 rpm for at least 20 minutes until the suspended particles completely settle. Decant the supernatant into 15 ml Teflon vials and dry on a hot plate overnight at 45°C.

TRUspec™ column chemistry for Rare Earth Element (REE) extraction

3. Re-dissolve the samples in 200 µl 3M QD HNO_3 which aims to produce the Nd in a nitrate salt form, which helps the Nd stick to the TRUspec™ resin. Return the 15 ml Teflon vials to the hot plate and dry down at 45°C.
4. Prepare the columns:
- Clean column stand with Milli-Q® deionized water, and place clean waste cups underneath.
- Rinse the storage acid off the columns with Milli-Q®.
- Ensure the fret (white plastic disc) is in the right position (around one-third of way down). Clean column thoroughly with Milli-Q® using a wash bottle and place the rinsed column into clean column stand.
- Inject Milli-Q® into the stem, and the reservoir above it, from the bottom up using the wash bottle so that all the air is removed from the stem above the fret. Continue to fill the column up with Milli-Q® from the top using the wash bottle.
- Use 1000 µl pipette (set to around 230 µl) to inject Eichron TRUspec™ resin into the reservoir while there is still water in it.
- Place the column back into the column stand and let the resin settle onto the fret in the stem, as the water drains through into the waste cup below.
- Once the water has drained through the columns and the resin has settled there should be resin above the fret up to the basal rim of the reservoir with no air bubbles.
- If there are air bubbles in the resin, inject Milli-Q® into the stem, and the reservoir above it, from the bottom up using the wash bottle to re-suspend the resin and remove the air bubbles, place the column back in the stand, and let the resin re-settle.
- If there is not enough resin in the stem, inject Milli-Q® into the stem, and the reservoir above it, from the bottom up using the wash bottle to re-suspend the resin, add some resin to the

column reservoir while there is still water in the 200 µl pipette and place the column back into the stand to let the resin re-settle.

- If there is too much resin in the column, add some water carefully from the top to the reservoir to resuspend some of the resin, remove the excess resin from the reservoir using the pipette and return it to the resin vial.

- Place TRUspec™ resin, column stands with columns and waste cups into the clean cabinet.

5. Add 1 ml 1M QD HCl to each column and let it drain into the waist cups. Repeat three times. This removes potential contamination.

6. Re-dissolve the samples in 1 ml 1M QD HNO_3 and transfer the samples from the 15 ml Teflon vials into acid-cleaned, labelled 1.5 ml microcentrifuge tubes stored in a rack (lids open) using a 1000 µl pipette (set to 600 µl). Use a new tip each time for different samples.

7. Centrifuge samples in a minicentrifuge for at least 20 minutes at 10,000 rpm. Clean 15 ml Teflon vials while samples are in the minicentrifuge by rinsing in Milli-Q®, scrubbing with clean tissue paper and rinsing again in Milli-Q®. Add a drop of 6M QD HCL to the vials, close the lids and fume on a hotplate in a fume cupboard at 85°C for at least 1 hour.

8. Once the 1M QD HCl has trickled through the resin, tap columns gently, flick acid from columns over sink and return to stand.

9. Add 1 ml 1M QD HNO_3 to each column and let it drain to waste. HNO_3 primes the column and helps Nd stick to the TRUspec™ resin. Once the 1M QD HNO_3 has trickled through the resin, tap columns gently, flick acid from columns over the sink and return to stand.

10. Prepare and label a set of acid-cleaned microcentrifuge tubes to collect the non-REE portion. Empty waste cups and stand the appropriately labelled 1.5 ml microcentrifuge tubes inside them to collect the sample.

11. Stop the minicentrifuge and transfer the supernatant from the microcentrifuge tubes into the corresponding columns using a 1000 µl pipette (set to 800 µl). Draw 700 µl of supernatant, avoiding precipitate, from the microcentrifuge tube into the tip and add the supernatant to the corresponding column. Repeat for all of the samples, using a clean pipette tip for each sample.

12. Add 0.5 ml 1M QD HNO_3 to each column. Repeat twice. All elements apart from REEs are flushed from the TRUspec™ resin and collected in the 1.5 ml microcentrifuge tubes. Once all of the HNO_3 has drained, flick the acid from the column as before.

13. Remove the 15 ml Teflon vials from the fume hood, empty 6M QD HCL, rinse with Milli-Q® and replace caps. Place the respective Teflon vials under each column.

14. Add 1 ml 1M QD HCl to each column. Repeat three times. All REEs are flushed from the TRUspec™ resin and collected in the 15 ml Teflon vials. Remove the 15 ml Teflon vials from the columns and place on a hot plate overnight at 45°C.

15. Clean columns after separating REEs:
- Fill the column storage container halfway with Milli-Q®.
- Inject Milli-Q® into the stem of each column, and the reservoir above it, from the bottom up using the wash bottle to remove all the resin from the column. Repeat and shake out.
- While there is still some water in the reservoir and no air bubbles in the stem, fill the column up with Milli-Q® from the top using the wash bottle until the reservoir is full.
- Before all the Milli-Q® is gone from the reservoir drop the column into the container.
- Add some 15M QD HNO_3 (c. 5 ml) to the water in the container to make a dilute acid. Replace the lid on the container and place it on the hot plate.

LNspec™ column chemistry for REE separation and isolation of Nd

16. Remove the 15 ml Teflon vials containing the REEs from the hot plate. Clean the column stand, add the Eichron LNspec™ columns and waste cups underneath the columns.
17. Add 4 ml 6M QD HCl to each column. This flushes any contaminants from the columns and can take >1 hour to trickle through the LNspec™ resin.
18. Add 100 µl 0.3M QD HCl to dissolve each sample in the Teflon vials using a 1000 µl pipette. Leave the sample to dissolve for one hour.
19. Add 1 ml 0.3M QD HCl to the LNspec™ columns. This re-equilibrates (changes the molarity from 6M to 0.3M) the columns after earlier washing them with 6M QD HCl. 1 ml of acid takes approximately 15 minutes to trickle through the resin. Repeat twice.
20. Dissolve the samples in the Teflon vials in 100 µl 0.3M QD HCl using a 200 µl pipette (set to 120 µl). Transfer and load the sample onto the column, drop by drop on to the LNspec™ resin. Allow the 100 µl 0.3M QD HCl to trickle through the resin.
21. Clean the 15 ml Teflon vials. Rinse the vials in Milli-Q®, scrub with tissue paper and rinse again. Wash the vials in 6M QD HCl. Add 1 ml of acid to the vials, recap and place on the hotplate in the fume hood for at least 1 hour.
22. Add 800 µl 0.3M QD HCl to the columns in three steps. This step washes samples onto the resin, and removes unwanted cations into the waste cup:
- Add 100 µl 0.3M QD HCl to the columns and allow to trickle through.
- Add 200 µl 0.3M QD HCl to the columns and allow to trickle through.
- Add 500 µl 0.3M QD HCl to the columns.
- Once all of the 0.3M QD HCl has trickled through the LNspec™ resin, gently tap the columns to remove the last drops of acid into the waste cups.
- Remove the waste cups from underneath the columns, dispose of the acid, rinse the waste cups with Milli-Q® and place back underneath the columns.

23. Add 5 ml 0.3M QD HCl to the columns. This washes samples through the resin and removes unwanted cations into the waste cups (takes c. 1.25 hours to trickle through the resin).
24. Add 1.5 ml of 0.3M QD HCl to the columns using a 1000 µl pipette. This is the stage when Nd may start unsticking from the resin if there is a calibration error. Collect the acid in the waste beakers or elute to a microcentrifuge tube to check for calibration errors (not necessary provided the acid is correct, i.e. titrated and the columns are calibrated).
25. Remove the 15 ml Teflon vials from the fume hood, empty 6M QD HCL, rinse with Milli-Q® and replace caps. Remove the waste cups and place the respective Teflon vials under the columns.
26. Add 4 ml 0.3M QD HCl to the columns and elute to the Teflon vials. This flushes the Nd from the columns (takes c. 1 hour to trickle through the resin). Once all of the acid has trickled through the resin gently tap the columns to remove the last droplets. Seal each vial and place onto the hotplate at 60°C.
27. Return the waste cups and add 3 ml 6M QD HCl to each column (takes c. 45 minutes to trickle through the LNspec™ resin). This flushes the remaining Nd from the columns.
28. Add 2 ml 0.3M QD HCl to the columns. This re-equilibrates the columns at a concentration of 0.3M after having flushed them with 6M QD HCL. Pour acid from waste beakers and clean with Milli-Q® and leave upside down on clean tissue paper to dry.
29. Before the 0.3M QD HCl totally disappears from the column reservoirs, pull caps tight on the columns, remove the columns from the stand and place in the test tubes with 0.3M QD HCl. Wrap parafilm around the top of the test tubes and the base of the column reservoirs so that it holds them firmly together, and place columns back into the test tube stand.

<u>Remove organics prior to analysis by MC-ICPMS</u>

30. Remove organics by adding 45 µl of 30% H_2O_2 to the sample and dry down at 45°C.
31. To conduct a concentration run prior to the full analysis, dissolve the sample in 1 ml of 0.1M HNO_3 for 2 hours on a hotplate (60°C). Once cool, collect all of the droplets before opening the vial. Remove 10 µl for analysis of Nd concentrations (dilute with 390 µl of 0.1M HNO_3). Dry down at 45°C.
32. For full isotope analysis, dissolve the remaining sample in 400 µl 2% HNO_3 for 24 hours on the hotplate. Transfer the sample into a 0.5 ml acid-cleaned centrifuge tube, before centrifuging at 5000 rpm for at least 5 minutes.

A.3 Extraction of marine biomarkers from bulk sediments

Homogenising sediment sample

1. Homogenise the freeze-dried lithified sediment with a solvent-cleaned agate mortar and pestle. Clean tools with solvent between samples to avoid cross-contamination.
2. Place homogenised, powdered sediment into pre-weighed, labelled 30 ml test tubes. Record the dry sediment mass. Transfer around 20 g of sediment into each test tube.

Sediment extractions

3. Extract samples in batches of 12 (maximum capacity for block heater and evaporator).
4. Ensure all solvents are high-performance liquid chromatography (HPLC) grade.
5. Add 20 ml of dichloromethane:methanol (DCM:MeOH) (3:1 v/v) to the test tubes and cap.
6. Homogenise solvent and sediment using a Fisherbrand™ Whirlimixer™ vortex mixer.
7. Warm the samples using a Techne Dri-Block® heater at 40°C for 1 hour.
8. Centrifuge the samples at 3000 rpm for 3 minutes using an Eppendorf™ 5810 to separate Total Lipid Extract (TLE) from the sediment.
9. Pipette the TLE supernatant into labelled Syncore® Polyvap test tubes.
10. Add 10 ml of DCM:MeOH (3:1 v/v) to the remaining sediment, before mixing and reheating.
11. Repeat steps 6−10 at least 3 times until the supernatant is clear.
12. Dry the TLE using a BUCHI Syncore® Polyvap rotary evaporator under vacuum. Set the speed at 200 rpm and the pressure at 850 mbar for DCM.
13. Once all the solvent is dry (usually after c. 8 hours), transfer the TLE from the Syncore® Polyvap test tubes using 0.75 ml DCM and 0.75 ml MeOH into labelled, pre-weighed GC vials. Gently dry down under nitrogen.
14. Split the TLE into two aliquots to prevent overloading the column if there is >10 mg. One aliquot is archived in a GC vial and the other is put through separations.
15. Split the TLE by adding DCM:MeOH (95:5 v/v) to fully dissolve the TLE and split with a Hamilton syringe.

Column chromatography

16. Collect and label four 8 ml vials (N1, N3, N4, waste) and place into a wooden vial holder, and add one of the TLE GC vials to the holder.
17. Create a column by adding a small compressed ball of glass wool to an empty pipette followed by 2.5 cm of furnaced silicon powder and 0.5 cm of furnaced sand.
18. Add the column to the column holder and place the waste vial beneath the column.

19. Add 1 ml of *n*-Hexane to the column and allow the solvent to move through the stationary phase and collect in the waste vial.
20. Add 1 ml of *n*-Hexane to the GC vial containing the TLE and transfer the eluent using a pipette to the column. Once the column is loaded, add a further 3 ml of *n*-Hexane to the column and collect the eluate in the N1 vial (aliphatic hydrocarbons/*n*-alkanes).
21. Add 1 ml of DCM to the GC vial containing the TLE and transfer the eluent using a pipette to the column. Once the column is loaded, add a further 3 ml of DCM to the column and collect the eluate in the N3 vial (aldehydes and ketones).
22. Add 1 ml of DCM:MeOH (95:5 v/v) to the GC vial containing the TLE and transfer the eluent using a pipette to the column. Once the column is loaded, add a further 3 ml of DCM:MeOH (95:5 v/v) to the column and collect the eluate in the N4 vial (alcohols).
23. Gently dry down the eluates under nitrogen and transfer the lipid extracts from the 8 ml vials, using around 1 ml of the retrospective solvents, into labelled GC vials, before gently drying down under nitrogen again.

Transferring lipid extracts into micro-inserts (inc. filtration of N4 fractions for GDGTs)

24. Label 12 GC vials, and add a metal spring and a furnaced glass insert into each vial.
25. Clean the outside and inside of a 100 µl Hamilton syringe using both *n*-Hexane and DCM.
26. Add 200 µl of *n*-Hexane into the N1 vials, draw back and fill the syringe with the sample.
27. Transfer the 200 µl lipid extract into the associated glass insert and clean the outside and inside of the syringe again following step 23.
28. Repeat steps 24−27 for N3 vials using DCM.
29. For N4 vials (alcohols), add 200 µl of *n*-hexane/*i*-propanol (99:1 v/v) to re-dissolve the N4 fraction, draw back and fill the syringe with the sample. Carefully remove the needle above the N4 GC vial to catch any sample. Add a 0.45 µm PFTE syringe filter, replace the needle and filter the sample into the associated glass insert. Remove the filter and clean the outside and inside of the syringe again following step 25.
30. Gently dry down the micro-inserts under nitrogen before adding a septa screw cap.

Prepare the N3 inserts for GC analysis of alkenones

31. Clean the outside and inside of a 100 µl Hamilton syringe using both *n*-Hexane and DCM.
32. Remove the septa screw cap and dilute the lipid extract with between 10−50 µl of *n*-Hexane before replacing the cap. Repeat and add 10−50 µl of *n*-Hexane to the other samples.

A.4 Correcting alkenone SSTs for warming and cooling biases

Generate the dilution series

1. Produce a dilution series by repeatedly analysing the same sample (#2344 in this example) at multiple different dilutions (10−250 µl). Plot the C_{37} concentration against sea surface temperature (SST) and find the equation of the polynomial using graphical software:

$$y = (-2.79021204754886 \times 10^{-7})x^3 + (0.000189778515909963)x^2 - (0.0429288369891799) + 19.5769780420336$$

Where: y = SST (°C) and x = concentration (ng/µl)

NB: If using Microsoft® Excel, ensure the values within the equation are quoted to maximum decimal places to prevent rounding error, which can result in erroneous SST corrections by up to 0.5°C.

Calculate the concentration at the inflection points

2. Differentiating the equation of this polynomial gives us a second equation which links the gradient of the curve with its corresponding x value.

$$\frac{dy}{dx} = (-8.37063614264658 \times 10^{-7})x^2 + (0.000379557031819926)x - 0.0429288369891799$$

At the inflection points, the gradient = 0.

$$0 = (-8.37063614264658 \times 10^{-7})x^2 + (0.000379557031819926)x - 0.0429288369891799$$

This is a standard quadratic equation.

$$0 = ax^2 + bx + c$$

Where: a = $(-8.37063614264658 \times 10^{-7})$, b = 0.000379557031819926 and c = -0.0429288369891799

Solving using the quadratic equation below produces two concentrations. At these two x values, the gradient of the polynomial is 0.

$$x = \frac{-b \pm \sqrt{b^2 - 4ac}}{2a}$$

x = 215.919 or x = 237.518

Calculate the average SST value where the gradient is zero

3. Insert the above x values back into the original equation in Step 1 and solve for y.

y = 16.346°C or y = 16.348°C

Taking the average SST of the inflection points (16.347°C) gives us the optimum SST for this sample (Fig. A.1A), which is considered least affected by irreversible adsorption and overloading.

Calculate predicted temperatures for the remaining samples

4. Calculate predicted SSTs for the remaining samples measured under the same GC-FID conditions, by inserting their concentrations into the polynomial equation (Table A.1). These predicted SSTs will fit on the dilution series curve. Calculate the difference between these predicted SSTs and the optimum SST value derived from the inflection points for each sample (Table A.1; Fig. A.1B).

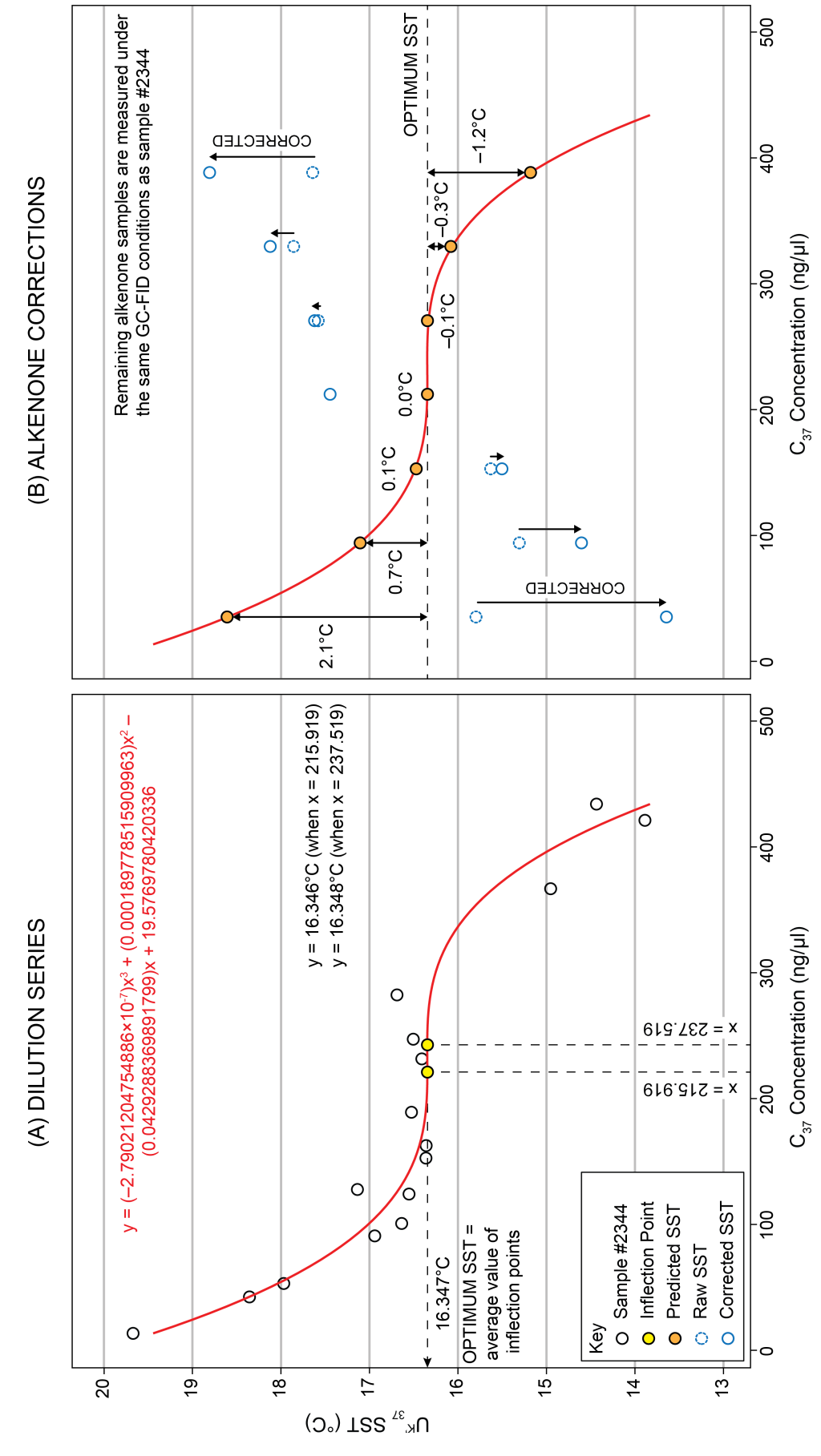
Correcting for temperature biases

5. Subtract this difference from the original raw SSTs calculated using the Conte et al. (2006) calibration for each respective sample (Table A.1; Fig. A.1B).

Sample	C_{37} concentration (ng/µl)	Predicted SST (°C)	Predicted SST minus optimum SST (°C)	Raw SST (°C)	Corrected SST (°C)
1	30	18.5	2.1	15.9	13.8
2	90	17.1	0.7	15.3	14.6
3	150	16.5	0.1	15.7	15.6
4	210	16.4	0.0	17.4	17.4
5	270	16.3	−0.1	17.6	17.7
6	330	16.1	−0.3	17.9	18.2
7	390	15.2	−1.2	17.7	18.9

Table A.1. Example alkenone SST corrections.

Figure A.1 (following page). (A) Dilution series showing the sensitivity of alkenone-derived SSTs to high and low C_{37} concentrations. One sample (#2344) is repeatedly analysed at multiple dilutions, which reveals large variability (5.8°C) in SST depending on C_{37} concentration. The optimum SST for this sample is calculated using the average value of the inflection points. (B) C_{37} concentrations from remaining samples (Table A.1), measured under the same GC-FID conditions, are used to calculate predicted temperatures, which fit on the polynomial curve. The difference between these predicted SSTs and the optimum SST value is subtracted from the original raw SSTs to correct for warming or cooling biases associated with irreversible adsorption and overloading, respectively.


(A) DILUTION SERIES
(B) ALKENONE CORRECTIONS
$U^{K'}_{37}$ SST (°C)
C_{37} Concentration (ng/µl)
y = (−2.790212047548866×10⁻⁷)x³ + (0.00018977851590996 3)x² − (0.042928836989179 9)x + 19.576978042033 6
y = 16.346°C (when x = 215.919)
y = 16.348°C (when x = 237.519)
16.347°C
OPTIMUM SST = average value of inflection points
x = 215.919
x = 237.519
Key
Sample #2344
Inflection Point
Predicted SST
Raw SST
Corrected SST
Remaining alkenone samples are measured under the same GC-FID conditions as sample #2344
CORRECTED
CORRECTED
OPTIMUM SST
2.1°C
0.7°C
0.1°C
0.0°C
−0.1°C
−0.3°C
−1.2°C

A.5 Argon dating sample preparation for basalts

1. Clean away loose surficial material using a scrubbing brush.
2. Saw samples into thin blocks and remove any weathered or altered zones using a lapidary trim saw (Lortone 8 inch FS8-C Trim Saw).
3. Crush samples to c. 2000 µm grain size using a club hammer.
4. Grind samples using a disc mill (Retsch® Disc Mill 200) to ≤500 µm.
5. Sieve sample to 250−500 µm aliquot. Retain the ≥500 µm aliquot for contingency and discard the ≤250 µm aliquot. Rinse samples in Milli-Q® deionized water to remove dust.
6. Ultrasonicate samples in Milli-Q® for 60 minutes.
7. Leach samples in 3N HNO_3 for 60 minutes in an ultrasonic bath at c. 50°C to remove alteration (carbonates, iron oxides, iron hydroxides etc.).
8. Ultrasonicate samples in Milli-Q® for 60 minutes to wash away the acid. Repeat washing until the Milli-Q® remains clear. Dry samples at T≤150°C.
10. Visually inspect samples using a binocular microscope to assess whether alteration phases have been largely removed. If necessary repeat the leaching stages using 3N HCL for 60 minutes in an ultrasonic bath, followed by 3N HNO_3 for another 60 minutes in an ultrasonic bath. Repeat Milli-Q® washing steps and dry samples at T≤150°C.
11. Pass a strong hand magnet (wrapped in paper) over the dried sample to remove metal particles introduced by the crushing process.
12. Magnetically separate samples (using a Frantz Isodynamic Separator; Table A.2) to remove phenocrysts and alteration products from the groundmass.
12. Hand-pick under a binocular microscope. Remove all phenocrysts and altered grains remaining, to produce a homogeneous groundmass separate.
15. Aim for 360−500 mg of separate (120 mg for each replicate).

Sample	Sample ID	Tilt (°)	Inclination (°)	Current (ampere)
Kaldakvísl	Kd	5	10	0.05
Unnamed lava	Un	5	10	0.05
Skeifá	Sk	5	10	0.1
Höskuldsvík	Hö	5	10	0.1

Table A.2. Frantz Isodynamic Separator settings.

A.6 Extraction of terrestrial biomarkers from brown coal

Homogenising lignite samples

1. Homogenise the freeze-dried lignite with a solvent-cleaned TEMA disc mill. Clean the grinding chamber with solvent between samples to avoid cross-contamination.
2. Place homogenised, powdered lignite into pre-weighed, labelled 30 ml test tubes. Record the dry lignite mass. Transfer around 20 g of lignite into each test tube.

Lignite extractions

3. Extract samples in batches of 12 (maximum capacity for block heater and evaporator).
4. Ensure all solvents are high-performance liquid chromatography (HPLC) grade.
5. Add 20 ml of dichloromethane:methanol (DCM:MeOH) (3:1 v/v) to the test tubes and cap.
6. Homogenise solvent and lignite using a Fisherbrand™ Whirlimixer™ vortex mixer.
7. Warm the samples using a Techne Dri-Block® heater at 40°C for 1 hour.
8. Centrifuge the samples at 3000 rpm for 3 minutes using an Eppendorf™ 5810 to separate Total Lipid Extract (TLE) from the lignite.
9. Pipette the TLE supernatant into labelled Syncore® Polyvap test tubes.
10. Add 10 ml of DCM:MeOH (3:1 v/v) to the remaining lignite, before mixing and reheating.
11. Repeat steps 6−10 at least 3 times until the supernatant is clear.
12. Dry the TLE using a BUCHI Syncore® Polyvap rotary evaporator under vacuum. Set the speed at 200 rpm and the pressure at 850 mbar for DCM.
13. Once all the solvent is dry (usually after c. 8 hours), transfer the TLE from the Syncore® Polyvap test tubes using 0.75 ml DCM and 0.75 ml MeOH into labelled, pre-weighed GC vials. Gently dry down under nitrogen.
14. Split the TLE into two aliquots to prevent overloading the column if there is >10 mg. One aliquot is archived in a GC vial and the other is put through separations.
15. Split the TLE by adding DCM:MeOH (95:5 v/v) to fully dissolve the TLE and split with a Hamilton syringe.

Column chromatography

16. Collect and label three 8 ml vials (N1, N4, waste) and place into a wooden vial holder, and add one of the TLE GC vials to the holder.
17. Create a column by adding a small compressed ball of glass wool to an empty pipette followed by 2.5 cm of furnaced silicon powder and 0.5 cm of furnaced sand.
18. Add the column to the column holder and place the waste vial beneath the column.

19. Add 1 ml of *n*-Hexane to the column and allow the solvent to move through the stationary phase and collect in the waste vial.
20. Add 1 ml of *n*-Hexane to the GC vial containing the TLE and transfer the eluent using a pipette to the column. Once the column is loaded, add a further 3 ml of *n*-Hexane to the column and collect the eluate in the N1 vial (aliphatic hydrocarbons/*n*-alkanes).
21. Add 1 ml of DCM:MeOH (95:5 v/v) to the GC vial containing the TLE and transfer the eluent using a pipette to the column. Once the column is loaded, add a further 3 ml of DCM:MeOH to the column and collect the eluate in the N4 vial (alcohols).
22. Gently dry down the eluates under nitrogen and transfer the lipid extracts from the 8 ml vials, using around 1 ml of the retrospective solvents, into labelled GC vials, before gently drying down under nitrogen again.

Transferring lipid extracts into micro-inserts (inc. filtration of N4 fractions for GDGTs)

23. Label 12 GC vials, and add a metal spring and a furnaced glass insert into each vial.
24. Clean the outside and inside of a 100 µl Hamilton syringe using both *n*-Hexane and DCM.
25. Add 200 µl of *n*-Hexane into the N1 vials, draw back and fill the syringe with the sample.
26. Transfer the 200 µl lipid extract into the associated glass insert and clean the outside and inside of the syringe again following step 24.
27. For N4 vials (alcohols), add 200 µl of *n*-hexane/*i*-propanol (99:1 v/v) to re-dissolve the N4 fraction, draw back and fill the syringe with the sample. Carefully remove the needle above the N4 GC vial to catch any sample. Add a 0.45 µm PFTE syringe filter, replace the needle and filter the sample into the associated glass insert. Remove the filter and clean the outside and inside of the syringe again following step 24.
28. Gently dry down the micro-inserts under nitrogen before adding a septa screw cap.

APPENDIX B: DATA TABLES

The data tabulated on the following pages are supplementary to Chapters 3, 4 and 5.

Site/Core/Section	Sample ID	Depth (mbsf)	Age (Ma)	Species	Specimens picked	Weight (µg)	$\delta^{13}C_{BF}$ (‰) VPDB
552A 1H 3W 93-95	1	3.93	0.21	C. wuellerstorfi	13	145.6	1
552A 2H 3W 88-90	2	7.88	0.42	C. wuellerstorfi	1	11.2	0.65
552A 3H 2W 132-134	3	11.82	0.63	C. wuellerstorfi	2	22.4	0.74
552A 4H 2W 27-29	4	15.77	0.82	C. wuellerstorfi	11	123.2	0
552A 5H 1W 71-73	5	19.71	0.98	C. wuellerstorfi	15	168	0.37
552A 5H 4W 15-17	6	23.65	1.24	C. wuellerstorfi	3	33.6	0.7
552A 6H 3W 59-61	7	27.59	1.51	C. wuellerstorfi	16	179.2	1.2
552A 7H 2W 103-105	8	31.53	1.79	C. wuellerstorfi	4	44.8	0.62
552A 8H 1W 148-150	9	35.48	2.06	C. wuellerstorfi	7	78.4	1.37
552A 9H 1W 41-45	10	39.41	2.33	C. wuellerstorfi	2	22.4	1.25
552A 9H 3W 136-139	11	43.36	2.61	C. wuellerstorfi	4	44.8	1.07
552A 10H 4W 10-12	12	48.6	3.03	C. wuellerstorfi	6	67.2	0.58
552A 11H 4W 35-37	13	53.85	3.24	C. wuellerstorfi	9	100.8	0.59
552A 13H 1W 9-14	14	59.09	3.45	C. wuellerstorfi	8	89.6	1.04
552A 14H 2W 87-89	15	66.37	3.75	C. wuellerstorfi	9	100.8	0.84
552A 15H 2W 112-114	16	69.62	3.88	C. wuellerstorfi	5	56	0.8
552A 16H 2W 133-135	17	74.83	4.09	C. wuellerstorfi	14	156.8	1.1
552A 17H 3W 8-10	18	80.08	4.24	C. wuellerstorfi	6	67.2	1.2
552A 18H 3W 32-34	19	85.32	4.35	C. wuellerstorfi	5	56	1.05
552A 19H 3W 57-59	20	90.57	4.45	C. wuellerstorfi	5	56	1.2
552A 21H 1W 82-84	21	95.82	4.55	Barren	0	0	N/A
552A 22H 2W 56-58	22	101.06	4.66	C. wuellerstorfi	3	12.6	1.22
552A 23H 2W 81-83	23	106.31	4.76	Barren	0	0	N/A
552A 24H 3W 5-7	24	111.46	4.86	C. wuellerstorfi	1	11.2	1.39
552A 25H 3W 30-32	25	116.8	4.96	Barren	0	0	N/A
552A 26H 5W 55-57	26	122.05	5.07	C. wuellerstorfi	3	33.6	1.22
552A 27H 3W 79-81	27	127.29	5.17	C. wuellerstorfi	7	78.4	1.1
552A 28H 3W 104-106	28	132.54	5.27	C. wuellerstorfi	10	112	0.86
552A 29H 4W 29-31	29	138.29	5.39	C. wuellerstorfi	6	67.2	0.87
552A 30H 4W 3-5	30	142.93	5.48	C. wuellerstorfi	3	33.6	1.12
552A 31H 5W 8-10	31	148.26	5.58	C. wuellerstorfi	7	78.4	1.03
552A 34H 3W 78-80	32	162.28	5.86	C. wuellerstorfi	23	257.6	1.29

Table B.1. $\delta^{13}C$ in benthic foraminifera from DSDP Hole 552A. Analytical reproducibility for $\delta^{13}C$ of the calcite standard was 0.04 ‰ (1σ).

Site/Core/Section	Sample ID	Depth (mbsf)	Age (Ma)	Species	Specimens picked	Weight (µg)	$\delta^{13}C_{BF}$ (‰) VPDB
642B 2H 1W 97-99	1	5.77	0.12	Barren	0	0	N/A
642B 2H 5W 72-74	2	11.52	0.24	Barren	0	0	N/A
642B 3H 3W 0-2	3	17.3	0.36	Barren	0	0	N/A
642B 4H 2W 81-89	4	23.07	0.49	Barren	0	0	N/A
642B 4H 6W 64-66	5	28.84	0.61	Barren	0	0	N/A
642B 5H 4W 70-72	6	34.6	0.73	Barren	0	0	N/A
642B 6H 1W 147-149	7	40.37	0.92	Barren	0	0	N/A
642B 6H 5W 124-126	8	46.14	1.13	Barren	0	0	N/A
642B 7H 4W 0-2	9	51.9	1.69	Barren	0	0	N/A
642B 8H 1W 77-79	10	57.67	2.11	Barren	0	0	N/A
642B 8H 5W 54-56	11	63.44	2.50	Barren	0	0	N/A
642B 8H 5W 127-129	12	64.15	2.55	Barren	0	0	N/A
642B 8H 6W 46-48	13	64.86	2.62	Barren	0	0	N/A
642B 8H 6W 117-119	14	65.57	2.76	Barren	0	0	N/A
642B 8H 7W 38-40	15	66.28	2.89	Barren	0	0	N/A
642B 9H 1W 59-61	16	66.99	3.03	Barren	0	0	N/A
642B 9H 1W 129-131	17	67.69	3.16	Barren	0	0	N/A
642B 9H 2W 50-52	18	68.4	3.29	Barren	0	0	N/A
642B 9H 2W 121-123	19	69.11	3.43	Barren	0	0	N/A
642B 9H 3W 42-44	20	69.82	3.56	Barren	0	0	N/A
642B 9H 3W 113-115	21	70.53	3.69	Barren	0	0	N/A
642B 9H 4W 34-36	22	71.24	3.81	Barren	0	0	N/A
642B 9H 4W 105-107	23	71.95	3.92	Barren	0	0	N/A
642B 9H 5W 26-28	24	72.66	4.04	Barren	0	0	N/A
642B 9H 5W 97-99	25	73.37	4.16	C. teretis	5	53	0.11
642B 9H 6W 18-20	26	74.08	4.28	C. teretis	2	16.8	0.03
642B 9H 6W 88-90	27	74.78	4.40	C. teretis	1	10.6	-0.02
642B 9H 7W 9-11	28	75.49	4.52	C. teretis	3	31.8	-0.19
642B 10H 1W 30-32	29	76.2	4.64	Barren	0	0	N/A
642B 10H 1W 100-102	30	76.9	4.76	C. teretis	2	21.2	-0.26
642B 10H 2W 22-24	31	77.62	4.88	Barren	0	0	N/A
642B 10H 3W 146-148	32	80.36	5.49	C. teretis	6	50.4	0.08
642B 10H 5W 118-120	33	83.08	6.62	Barren	0	0	N/A
642B 11H 1W 44-46	34	85.84	6.83	Barren	0	0	N/A
642B 11H 3W 18-20	35	88.58	6.94	Barren	0	0	N/A
642B 11H 5W 0-2	36	91.4	7.05	Barren	0	0	N/A
642B 11H 6W 117-119	37	94.07	7.16	Barren	0	0	N/A
642B 12H 2W 41-43	38	96.81	7.24	Barren	0	0	N/A
642B 12H 4W 15-17	39	99.55	7.28	Barren	0	0	N/A
642B 12H 5W 139-142	40	102.29	7.32	Barren	0	0	N/A

Table B.2. $\delta^{13}C$ in benthic foraminifera from ODP Hole 642B. Analytical reproducibility for $\delta^{13}C$ of the calcite standard was 0.04 ‰ (1σ).

Site/Core/Section	Sample ID	Depth (mbsf)	Age (Ma)	εNd	Error (2σ)
642B 1H 1W 22-24	1	0.23	0.00	-11.08	0.17
642B 1H 1W 100-102	2	1.01	0.02	-12.39	0.17
642B 8H 5W 56-58	3	63.47	2.50	-8.96	0.17
642B 9H 1W 45-47	4	66.86	3.00	-7.16	0.17
642B 9H 3W 8-10	5	69.49	3.50	-7.99	0.17
642B 9H 5W 0-2	6	72.41	4.00	-9.60	0.17
642B 9H 6W 147-149	7	75.38	4.50	-9.04	0.17
642B 10H 2W 95-97	8	78.36	5.00	-9.03	0.17
642B 10H 4W 5-8	9	80.46	5.53	-7.91	0.17
642B 10H 4W 119-121	10	81.60	6.00	-9.16	0.17
642B 10H 5W 89-91	11	82.80	6.50	-12.25	0.32
552A 1H 1W 13-15	12	0.14	0.01	-7.54	0.17
552A 1H 1W 39-41	13	0.40	0.02	-6.49	0.17
552A 9H 2W 136-138	14	41.87	2.50	-8.25	0.17
552A 10H 3W 126-128	15	48.27	3.00	-10.26	0.40
552A 13H 1W 120-122	16	60.21	3.50	-10.61	0.32
552A 16H 1W 53-55	17	72.54	4.00	-10.58	0.40
552A 20H 1W 110-112	18	93.11	4.50	-11.02	0.40
552A 26H 1W 8-10	19	118.59	5.00	-11.25	0.32
552A 31H 1W 57-59	20	144.08	5.50	-10.78	0.52

Table B.3. Authigenic Fe-Mn leachate εNd from ODP Hole 642B and DSDP Hole 552A.

Site/Core/Section	Sample ID	Depth (mcd)	Age (Ma)	C_{37} (ng/µl)	$U^{K'}_{37}$	Raw SST (°C)	Corrected SST (°C)
U1308E 2H 4W 108-114	2302	17.26	0.27	91.25	0.50	13.6	12.9
U1308A 4H 3A 0-2	2303	34.54	0.53	571.23	0.58	16.0	16.0
U1308C 6H 2W 125-129	2304	51.8	0.80	157.57	0.48	13.0	12.9
U1308F 7H 3W 31-35	2350	69.04	1.02	186.11	0.54	14.9	14.9
U1308E 9H 2W 38-43	2305	86.35	1.20	49.08	0.46	12.5	10.9
U1308B 11H 2W 80-85	2306	103.64	1.41	8.66	0.40	10.7	7.8
U1308A 12H 5W 136-142	2307	120.87	1.63	80.06	0.63	17.4	16.6
U1308B 14H 4W 40-44	2351	138.19	1.82	228.74	0.51	14.0	14.0
U1308F 15H 5W 10-14	2308	155.44	2.03	118.62	0.60	16.7	16.4
U1308B 17H 5W 28-31	2309	172.71	2.26	291.86	0.59	16.3	16.3
U1308A 19H 5W 25-29	2310	189.98	2.49	201.83	0.44	11.7	11.7
U1308C 20H 5W 6-9	2352	202.08	2.71	397.21	0.52	14.3	15.7
U1308E 21H 4W 37-40	2311	215.79	2.86	186.61	0.61	16.8	16.8
U1308C 23H 2W 66-68	2312	229.35	2.97	0.00	N/A	N/A	N/A
U1308C 24H 4W 90-92	2313	242.91	3.10	66.22	0.76	21.4	20.3

Table B.4. Alkenone-based SST reconstructions from IODP Site U1308, calculated using the Conte et al. (2006) calibration. Analytical reproducibility (1σ) for the $U^{K'}_{37}$ index is ±0.007, which translates into an average temperature uncertainty of ±0.2°C.

Site/Core/Section	Sample ID	Depth (mbsf)	Age (Ma)	C_{37} (ng/µl)	$U^{K'}_{37}$	Raw SST (°C)	Corrected SST (°C)
552A 1H 3W 93-95	2314	3.93	0.21	0.00	N/A	N/A	N/A
552A 2H 3W 88-90	2353	7.88	0.42	186.92	0.39	10.2	10.2
552A 3H 2W 132-134	2354	11.82	0.63	49.22	0.62	17.2	15.7
552A 4H 2W 27-29	2315	15.77	0.82	10.38	0.34	8.9	6.1
552A 5H 1W 71-73	2355	19.71	0.98	44.85	0.55	15.0	13.4
552A 5H 4W 15-17	2356	23.65	1.24	40.84	0.65	18.1	16.3
552A 6H 3W 51-61	2316	27.59	1.51	17.33	0.41	10.9	8.4
552A 7H 2W 103-105	2357	31.53	1.79	14.64	0.65	18.0	15.4
552A 8H 1W 148-150	2358	35.48	2.06	10.49	0.77	21.6	18.8
552A 9H 1W 41-45	2317	39.41	2.33	50.19	0.61	16.9	15.4
552A 9H 3W 136-139	2359	43.36	2.61	66.15	0.58	15.9	14.8
552A 10H 3W 137-139	2586	48.37	3.00	1.90	0.66	18.3	15.1
552A 10H 4W 12-14	2587	48.6	3.03	18.17	0.61	16.9	14.4
552A 10H 4W 10-12	2360	48.62	3.03	45.60	0.58	16.0	14.4
552A 10H 4W 36-38	2588	48.86	3.04	39.73	0.65	18.0	16.2
552A 11H 1W 17-19	2589	49.17	3.05	48.53	0.60	16.7	15.2
552A 11H 1W 49-51	2590	49.49	3.07	48.85	0.56	15.5	14.0
552A 11H 1W 77-79	2591	49.77	3.08	52.54	0.59	16.3	14.8
552A 11H 1W 107-109	2592	50.07	3.09	41.36	0.62	17.0	15.3
552A 11H 1W 137-139	2593	50.37	3.10	24.68	0.63	17.5	15.2
552A 11H 2W 17-19	2594	50.67	3.11	53.87	0.61	16.8	15.4
552A 11H 2W 46-48	2595	50.96	3.13	115.28	0.54	14.7	14.4
552A 11H 2W 77-79	2596	51.27	3.14	0.00	N/A	N/A	N/A
552A 11H 2W 107-109	2597	51.57	3.15	72.13	0.57	15.6	14.6
552A 11H 2W 137-139	2598	51.87	3.16	28.73	0.67	18.8	16.6
552A 11H 3W 17-19	2599	52.17	3.17	10.22	0.68	18.9	16.1
552A 11H 3W 50-52	2600	52.5	3.19	3.37	0.66	18.3	15.2
552A 11H 3W 77-79	2601	52.77	3.20	8.39	0.63	17.6	14.7
552A 11H 3W 107-109	2602	53.07	3.21	0.00	N/A	N/A	N/A
552A 11H 3W 137-139	2603	53.37	3.22	0.00	N/A	N/A	N/A
552A 11H 4W 17-19	2604	53.67	3.24	5.42	0.66	18.4	15.4
552A 11H 4W 35-37	2318	53.85	3.24	3.10	0.76	21.5	18.4
552A 11H 5W 6-8	2605	53.99	3.25	8.41	0.66	18.4	15.5
552A 12H 1W 27-29	2606	54.27	3.26	5.29	0.71	19.8	16.8
552A 12H 1W 57-59	2607	54.57	3.27	0.00	N/A	N/A	N/A
552A 12H 1W 86-88	2608	54.86	3.28	2.46	0.75	21.0	17.8
552A 12H 1W 117-119	2609	55.17	3.30	16.60	0.65	18.1	15.5
552A 13H 1W 9-14	2361	59.09	3.45	21.05	0.60	16.6	14.2
552A 14H 2W 87-89	2362	66.37	3.75	15.43	0.62	17.1	14.4
552A 15H 2W 112-114	2319	69.62	3.88	90.31	0.69	19.4	18.7

Table B.5. Alkenone-based SST reconstructions from DSDP Hole 552A, calculated using the Conte et al. (2006) calibration. Analytical reproducibility (1σ) for the $U^{K'}_{37}$ index is ±0.007, which translates into an average temperature uncertainty of ±0.2°C.

Site/Core/Section	Sample ID	Depth (mbsf)	Age (Ma)	C_{37} (ng/µl)	$U^{K'}_{37}$	Raw SST (°C)	Corrected SST (°C)
552A 16H 2W 133-135	2363	74.83	4.09	20.44	0.68	18.9	16.5
552A 17H 3W 8-10	2364	80.08	4.24	53.43	0.71	20.0	18.5
552A 18H 3W 32-34	2320	85.32	4.35	64.04	0.77	21.8	20.6
552A 19H 3W 57-59	2365	90.57	4.45	36.85	0.68	19.0	17.1
552A 21H 1W 82-84	2366	95.82	4.55	30.04	0.68	19.0	16.8
552A 22H 2W 56-58	2321	101.06	4.66	0.00	N/A	N/A	N/A
552A 23H 2W 81-83	2367	106.31	4.76	151.91	0.56	15.4	15.3
552A 24H 3W 5-7	2368	111.46	4.86	58.45	0.73	20.6	19.3
552A 25H 3W 30-32	2322	116.8	4.96	16.95	0.83	23.5	20.9
552A 26H 5W 55-57	2369	122.05	5.07	118.77	0.59	16.2	15.9
552A 27H 3W 79-81	2370	127.29	5.17	17.33	0.70	19.6	17.1
552A 28H 3W 104-106	2323	132.54	5.27	169.91	0.69	19.3	19.2
552A 29H 4W 29-31	2371	138.29	5.39	9.55	0.81	22.8	20.0
552A 30H 4W 3-5	2372	142.93	5.48	7.74	0.76	21.3	18.4
552A 31H 5W 8-10	2324	148.26	5.58	18.40	0.79	22.3	19.8
552A 34H 3W 78-80	2325	162.28	5.86	6.30	0.44	11.7	8.7

Table B.5 continued. Alkenone-based SST reconstructions from DSDP Hole 552A, calculated using the Conte et al. (2006) calibration. Analytical reproducibility (1σ) for the $U^{K'}_{37}$ index is ±0.007, which translates into an average temperature uncertainty of ±0.2°C.

Site/Core/Section	Sample ID	Depth (mbsf)	Age (Ma)	C_{37} (ng/µl)	$U^{K'}_{37}$	Raw SST (°C)	Corrected SST (°C)
642B 2H 1W 97-99	2338	5.77	0.12	5.26	0.40	10.8	7.7
642B 2H 5W 72-74	2401	11.52	0.24	50.81	0.43	11.5	10.0
642B 3H 3W 0-2	2402	17.3	0.36	0.00	N/A	N/A	N/A
642B 4H 2W 81-89	2403	23.07	0.49	40.06	0.41	11.0	9.2
642B 4H 6W 64-66	2339	28.84	0.61	0.00	N/A	N/A	N/A
642B 5H 4W 70-72	2404	34.6	0.73	5.71	0.56	15.5	12.5
642B 6H 1W 147-149	2405	40.37	0.92	4.68	0.31	8.0	4.9
642B 6H 5W 124-126	2406	46.14	1.13	0.00	N/A	N/A	N/A
642B 7H 4W 0-2	2340	51.9	1.69	47.63	0.57	15.8	14.2
642B 8H 1W 77-79	2407	57.67	2.11	13.37	0.62	17.1	14.4
642B 8H 5W 54-56	2408	63.44	2.50	22.10	0.39	10.3	7.9
642B 8H 5W 125-127	2409	64.15	2.55	0.00	N/A	N/A	N/A
642B 8H 6W 46-48	2341	64.86	2.62	52.37	0.59	16.4	15.0
642B 8H 6W 117-119	2410	65.57	2.76	2.43	0.58	16.0	12.9
642B 8H 7W 38-40	2411	66.28	2.89	2.06	0.50	13.5	10.4
642B 9H 1W 42-45	2562	66.82	3.00	183.31	0.42	11.3	11.3
642B 9H 1W 50-53	2563	66.9	3.01	247.30	0.47	12.8	12.8
642B 9H 1W 59-61	2412	66.99	3.03	1.39	0.54	14.8	11.7
642B 9H 1W 59-62	2564	66.99	3.03	94.39	0.42	11.1	10.5
642B 9H 1W 66-68	2565	67.06	3.04	263.41	0.36	9.5	9.5
642B 9H 1W 73-75	2566	67.13	3.05	250.88	0.34	8.9	8.9
642B 9H 1W 80-82	2567	67.2	3.07	150.57	0.46	12.3	12.2
642B 9H 1W 86-88	2568	67.26	3.08	23.40	0.59	16.3	13.9
642B 9H 1W 93-95	2569	67.33	3.09	233.75	0.36	9.5	9.5
642B 9H 1W 100-102	2570	67.4	3.11	270.34	0.46	12.4	12.5
642B 9H 1W 107-109	2571	67.47	3.12	67.31	0.47	12.7	11.6
642B 9H 1W 114-116	2572	67.54	3.13	60.77	0.45	12.0	10.8
642B 9H 1W 121-123	2573	67.61	3.15	59.30	0.41	10.8	9.5
642B 9H 1W 128-130	2574	67.68	3.16	13.95	0.52	14.2	11.6
642B 9H 1W 129-131	2342	67.69	3.16	64.59	0.48	13.1	11.9
642B 9H 1W 137-139	2575	67.77	3.17	29.44	0.41	11.0	8.9
642B 9H 1W 142-144	2576	67.82	3.18	0.00	N/A	N/A	N/A
642B 9H 2W 0-2	2577	67.9	3.20	232.29	0.47	12.8	12.8
642B 9H 2W 5-7	2578	67.95	3.21	0.00	N/A	N/A	N/A
642B 9H 2W 12-14	2579	68.02	3.22	40.31	0.39	10.2	8.5
642B 9H 2W 19-21	2580	68.09	3.24	240.89	0.42	11.3	11.3
642B 9H 2W 26-28	2581	68.16	3.25	18.01	0.70	19.7	17.2
642B 9H 2W 33-35	2582	68.23	3.26	3.22	0.61	17.0	13.9
642B 9H 2W 40-42	2583	68.3	3.28	3.97	0.50	13.7	10.6
642B 9H 2W 47-49	2584	68.37	3.29	20.31	0.46	12.6	10.1

Table B.6. Alkenone-based SST reconstructions from ODP Hole 642B, calculated using the Conte et al. (2006) calibration. Analytical reproducibility (1σ) for the $U^{K'}_{37}$ index is ±0.007, which translates into an average temperature uncertainty of ±0.2°C.

Site/Core/Section	Sample ID	Depth (mbsf)	Age (Ma)	C_{37} (ng/µl)	$U^{K'}_{37}$	Raw SST (°C)	Corrected SST (°C)
642B 9H 2W 50-52	2413	68.4	3.29	5.11	0.45	12.1	9.1
642B 9H 2W 53-55	2585	68.43	3.30	7.45	0.58	15.8	12.9
642B 9H 2W 121-123	2414	69.11	3.43	101.44	0.51	13.8	13.2
642B 9H 3W 42-44	2415	69.82	3.56	94.99	0.48	12.9	12.3
642B 9H 3W 113-115	2343	70.53	3.69	21.89	0.66	18.3	15.9
642B 9H 4W 34-36	2416	71.24	3.81	109.92	0.63	17.5	17.0
642B 9H 4W 105-107	2417	71.95	3.92	57.55	0.57	15.8	14.4
642B 9H 5W 26-28	2418	72.66	4.04	8.27	0.73	20.4	17.5
642B 9H 5W 97-99	2344	73.37	4.16	227.32	0.59	16.4	16.4
642B 9H 6W 18-20	2419	74.08	4.28	46.91	0.60	16.6	15.0
642B 9H 6W 88-90	2420	74.78	4.40	59.61	0.53	14.4	13.1
642B 9H 7W 9-11	2421	75.49	4.52	70.60	0.51	13.9	12.9
642B 10H 1W 30-32	2345	76.2	4.64	66.21	0.59	16.2	15.0
642B 10H 1W 100-102	2422	76.9	4.76	43.67	0.55	15.1	13.5
642B 10H 2W 22-24	2423	77.62	4.88	168.51	0.52	14.3	14.3
642B 10H 3W 146-148	2424	80.36	5.49	48.15	0.49	13.2	11.6
642B 10H 5W 118-120	2346	83.08	6.62	520.53	0.53	14.4	14.4
642B 11H 1W 44-46	2425	85.84	6.83	1.50	0.68	19.0	15.8
642B 11H 3W 18-20	2426	88.58	6.94	4.57	0.73	20.5	17.5
642B 11H 5W 0-2	2427	91.4	7.05	2.54	0.72	20.1	17.0
642B 11H 6W 117-119	2347	94.07	7.16	432.58	0.53	14.5	17.0
642B 12H 2W 41-43	2428	96.81	7.24	9.60	0.39	10.3	7.5
642B 12H 4W 15-17	2348	99.55	7.28	4.19	0.36	9.3	6.2
642B 12H 5W 139-142	2349	102.29	7.32	8.57	0.43	11.6	8.7

Table B.6 continued. Alkenone-based SST reconstructions from ODP Hole 642B, calculated using the Conte et al. (2006) calibration. Analytical reproducibility (1σ) for the $U^{K'}_{37}$ index is ±0.007, which translates into an average temperature uncertainty of ±0.2°C.

Site/Core/Section	Sample ID	Depth (mbsf)	Age (Ma)	C_{37} (ng/µl)	$U^{K'}_{37}$	Raw SST (°C)	Corrected SST (°C)
907A 1H 3W 133-135	2326	4.33	0.21	0.00	N/A	N/A	N/A
907A 2H 2W 137-139	2373	10.17	0.49	0.00	N/A	N/A	N/A
907A 2H 4W 120-122	2374	13	0.63	11.61	0.36	9.4	6.6
907A 3H 1W 53-55	2375	17.33	1.00	0.00	N/A	N/A	N/A
907A 3H 4W 36-38	2327	21.66	1.19	0.00	N/A	N/A	N/A
907A 3H 7W 20-22	2376	26	1.40	0.00	N/A	N/A	N/A
907A 4H 3W 103-105	2377	30.33	1.61	0.00	N/A	N/A	N/A
907A 4H 6W 86-88	2378	34.66	1.81	0.00	N/A	N/A	N/A
907A 5H 3W 19-21	2328	38.99	1.99	0.00	N/A	N/A	N/A
907A 5H 6W 3-5	2379	43.33	2.25	0.00	N/A	N/A	N/A
907A 6H 2W 87-91	2380	47.67	2.50	4.31	0.28	7.1	4.0
907A 6H 3W 109-111	2381	49.39	2.60	2.39	0.33	8.7	5.5
907A 6H 4W 138-140	2329	51.18	2.69	0.00	N/A	N/A	N/A
907A 6H 6W 6-8	2382	52.86	2.77	1.08	0.28	7.0	3.8
907A 6H 7W 34-36	2383	54.64	2.86	2.07	0.30	7.7	4.6
907A 7H 2W 5-7	2384	56.35	2.95	1.28	0.36	9.5	6.3
907A 7H 3W 26-31	2330	58.06	3.04	2.12	0.40	10.7	7.5
907A 7H 4W 47-49	2385	59.77	3.14	3.83	0.33	8.5	5.5
907A 7H 5W 70-79	2386	61.52	3.22	8.57	0.39	10.2	7.3
907A 7H 6W 92-95	2387	63.22	3.33	11.59	0.31	7.8	5.1
907A 8H 1W 72-74	2331	65.02	3.46	6.80	0.50	13.5	10.6
907A 8H 2W 92-95	2388	66.72	3.59	0.00	N/A	N/A	N/A
907A 8H 3W 117-119	2389	68.47	3.90	8.71	0.27	6.7	3.8
907A 8H 4W 143-149	2390	70.23	4.21	2.12	0.36	9.3	6.1
907A 8H 6W 14-16	2332	71.94	4.53	67.31	0.34	8.9	7.8
907A 8H 7W 37-39	2391	73.67	4.73	6.79	0.40	10.7	7.8
907A 9H 2W 10-12	2392	75.4	4.90	0.00	N/A	N/A	N/A
907A 9H 3W 34-36	2393	77.14	5.09	0.00	N/A	N/A	N/A
907A 9H 4W 57-59	2333	78.87	5.24	0.59	0.57	15.6	12.4
907A 9H 5W 81-83	2394	80.61	5.37	3.12	0.31	8.0	4.9
907A 9H 6W 103-106	2395	82.33	5.50	0.00	N/A	N/A	N/A
907A 10H 1W 147-149	2396	84.77	5.68	51.40	0.25	6.0	4.5
907A 10H 3W 92-94	2334	87.22	5.86	2.51	0.56	15.5	12.3
907A 10H 5W 34-36	2397	89.64	6.04	29.72	0.42	11.2	9.1
907A 10H 6W 127-129	2398	92.07	6.24	131.50	0.33	8.7	8.4
907A 11H 2W 20-22	2399	94.5	6.55	185.48	0.29	7.2	7.2
907A 11H 3W 113-115	2335	96.93	6.83	130.73	0.38	10.2	9.9
907A 11H 5W 56-58	2400	99.36	7.30	151.50	0.39	10.4	10.3
907A 11H 7W 0-2	2336	101.8	7.74	2.60	0.57	15.6	12.4
907A 12H 2W 43-45	2337	104.23	8.00	0.00	N/A	N/A	N/A

Table B.7. Alkenone-based SST reconstructions from ODP Hole 907A, calculated using the Conte et al. (2006) calibration. Analytical reproducibility (1σ) for the $U^{K'}_{37}$ index is ±0.007, which translates into an average temperature uncertainty of ±0.2°C.

Site/Core/Section	Sample ID	Depth (mcd)	Age (Ma)	BIT	ΔRI	%GDGT-0	TEX_{86}	SST (°C)	OPTiMAL SST (°C)
U1308E 2H 4W 108-114	2302	17.26	0.27	0.24	0.59	57.29	-0.36	13.8	7.7
U1308A 4H 3A 0-2	2303	34.54	0.53	0.05	1.17	67.23	-0.42	9.8	8.8
U1308C 6H 2W 125-129	2304	51.8	0.80	0.26	0.85	62.79	-0.38	12.7	3.7
U1308F 7H 3W 31-35	2350	69.04	1.02	0.56	0.43	60.89	-0.26	20.7	18.0
U1308E 9H 2W 38-43	2305	86.35	1.20	0.74	0.58	58.79	-0.34	15.4	8.8
U1308B 11H 2W 80-85	2306	103.64	1.41	0.21	0.57	59.37	-0.33	15.8	11.0
U1308A 12H 5W 136-142	2307	120.87	1.63	0.10	0.03	46.50	-0.30	17.9	16.0
U1308B 14H 4W 40-44	2351	138.19	1.82	0.09	0.34	53.91	-0.32	16.6	12.3
U1308F 15H 5W 10-14	2308	155.44	2.03	0.31	1.04	65.54	-0.40	11.0	4.5
U1308B 17H 5W 28-31	2309	172.71	2.26	0.08	0.39	55.90	-0.31	17.1	12.2
U1308A 19H 5W 25-29	2310	189.98	2.49	0.05	0.55	58.41	-0.34	15.6	13.2
U1308C 20H 5W 6-9	2352	202.08	2.71	0.04	0.45	57.51	-0.31	17.2	15.2
U1308E 21H 4W 37-40	2311	215.79	2.86	0.11	0.84	63.78	-0.37	13.5	11.4
U1308C 23H 2W 66-68	2312	229.35	2.97	0.12	0.74	59.57	-0.38	12.5	8.5
U1308C 24H 4W 90-92	2313	242.91	3.10	0.09	0.99	63.22	-0.41	10.3	9.1

Table B.8. TEX_{86} SST reconstructions from IODP Site U1308, calculated using the Kim et al. (2010) TEX_{86}^{H} calibration. Analytical reproducibility (1σ) for the TEX_{86} proxy is ±0.01. Branched and Isoprenoid Tetraether (BIT) index after Hopmans et al. (2004). Ring index (ΔRI) after Zhang et al. (2016). %GDGT-0 index after Sinninghe Damsté et al. (2012). Optimised Palaeothermometry from Tetraethers via MAchine Learning (OPTiMAL) after Dunkley Jones et al. (2020).

Site/Core/Section	Sample ID	Depth (mbsf)	Age (Ma)	BIT	ΔRI	%GDGT-0	TEX_{86}	SST (°C)	OPTiMAL SST (°C)
552A 1H 3W 93-95	2314	3.93	0.21	0.46	1.05	65.75	-0.41	10.9	4.0
552A 2H 3W 88-90	2353	7.88	0.42	0.72	0.97	64.75	-0.39	11.7	4.4
552A 3H 2W 132-134	2354	11.82	0.63	0.67	2.23	76.58	-0.59	-1.9	6.7
552A 4H 2W 27-29	2315	15.77	0.82	0.50	0.56	57.53	-0.35	14.6	6.0
552A 5H 1W 71-73	2355	19.71	0.98	0.45	0.48	57.92	-0.32	16.8	12.2
552A 5H 4W 15-17	2356	23.65	1.24	0.09	0.65	62.90	-0.32	17.0	14.6
552A 6H 3W 51-61	2316	27.59	1.51	0.18	0.24	54.11	-0.29	19.0	12.7
552A 7H 2W 103-105	2357	31.53	1.79	0.18	0.23	53.96	-0.28	19.2	13.5
552A 8H 1W 148-150	2358	35.48	2.06	0.45	0.84	65.63	-0.34	15.2	3.1
552A 9H 1W 41-45	2317	39.41	2.33	0.13	0.25	54.93	-0.28	19.5	13.5
552A 9H 3W 136-139	2359	43.36	2.61	0.52	0.57	68.61	-0.21	24.0	12.2
552A 10H 3W 137-139	2586	48.37	3.00	0.26	0.28	50.91	-0.34	15.6	9.5
552A 10H 4W 12-14	2587	48.6	3.03	0.15	0.24	53.22	-0.30	18.3	11.9
552A 10H 4W 10-12	2360	48.62	3.03	0.42	0.68	65.50	-0.29	18.6	10.3
552A 10H 4W 36-38	2588	48.86	3.04	0.22	0.22	53.90	-0.28	19.4	12.8
552A 11H 1W 17-19	2589	49.17	3.05	0.48	0.15	50.02	-0.30	17.9	14.1
552A 11H 1W 49-51	2590	49.49	3.07	0.16	0.21	51.39	-0.31	17.4	12.2
552A 11H 1W 77-79	2591	49.77	3.08	0.18	0.01	48.10	-0.28	19.4	15.4
552A 11H 1W 107-109	2592	50.07	3.09	0.14	0.03	49.69	-0.27	20.3	15.5
552A 11H 1W 137-139	2593	50.37	3.10	0.23	0.09	49.80	-0.28	19.2	15.6
552A 11H 2W 17-19	2594	50.67	3.11	0.41	0.54	58.45	-0.33	15.9	5.8
552A 11H 2W 46-48	2595	50.96	3.13	0.34	-0.13	48.91	-0.22	23.5	11.9
552A 11H 2W 77-79	2596	51.27	3.14	0.14	0.41	55.17	-0.33	16.0	8.5
552A 11H 2W 107-109	2597	51.57	3.15	0.16	1.13	55.21	-0.52	2.8	1.0
552A 11H 2W 137-139	2598	51.87	3.16	0.24	0.00	48.48	-0.27	19.8	15.0
552A 11H 3W 17-19	2599	52.17	3.17	0.15	0.77	54.67	-0.44	8.6	2.2
552A 11H 3W 50-52	2600	52.5	3.19	0.20	1.14	62.68	-0.46	7.3	-0.2
552A 11H 3W 77-79	2601	52.77	3.20	0.38	0.64	58.12	-0.37	13.6	5.2
552A 11H 3W 107-109	2602	53.07	3.21	0.38	0.97	57.04	-0.46	6.8	4.3
552A 11H 3W 137-139	2603	53.37	3.22	0.62	0.56	56.16	-0.36	13.8	6.3
552A 11H 4W 17-19	2604	53.67	3.24	0.57	0.65	56.35	-0.39	11.9	2.9
552A 11H 4W 35-37	2318	53.85	3.24	0.51	1.38	72.09	-0.43	9.2	3.3
552A 11H 5W 6-8	2605	53.99	3.25	0.48	0.39	53.29	-0.34	15.3	9.2
552A 12H 1W 27-29	2606	54.27	3.26	0.42	0.28	52.35	-0.32	16.8	10.1
552A 12H 1W 57-59	2607	54.57	3.27	0.52	0.77	63.13	-0.35	14.8	3.8
552A 12H 1W 86-88	2608	54.86	3.28	0.65	0.79	66.41	-0.32	16.8	2.3
552A 12H 1W 117-119	2609	55.17	3.30	0.49	0.32	54.58	-0.30	17.8	10.4
552A 13H 1W 9-14	2361	59.09	3.45	0.54	1.18	68.50	-0.41	10.6	2.5
552A 14H 2W 87-89	2362	66.37	3.75	0.71	1.42	71.43	-0.45	8.1	3.5
552A 15H 2W 112-114	2319	69.62	3.88	0.88	2.00	78.10	-0.54	1.9	10.2

Table B.9. TEX_{86} SST reconstructions from DSDP Hole 552A, calculated using the Kim et al. (2010) TEX_{86}^{H} calibration. Analytical reproducibility (1σ) for the TEX_{86} proxy is ±0.01. BIT, ΔRI, %GDGT-0 and OPTiMAL as in Table B.8.

Site/Core/Section	Sample ID	Depth (mbsf)	Age (Ma)	BIT	ΔRI	%GDGT-0	TEX_{86}	SST (°C)	OPTiMAL SST (°C)
552A 16H 2W 133-135	2363	74.83	4.09	0.91	1.89	75.09	-0.53	2.0	8.3
552A 17H 3W 8-10	2364	80.08	4.24	0.80	2.27	77.92	-0.60	-2.4	15.1
552A 18H 3W 32-34	2320	85.32	4.35	0.65	0.69	60.37	-0.36	14.1	7.1
552A 19H 3W 57-59	2365	90.57	4.45	0.15	0.42	57.03	-0.31	17.2	12.6
552A 21H 1W 82-84	2366	95.82	4.55	0.30	0.57	59.33	-0.33	16.0	9.2
552A 22H 2W 56-58	2321	101.06	4.66	0.46	0.75	68.50	-0.28	19.5	8.7
552A 23H 2W 81-83	2367	106.31	4.76	0.40	0.76	70.09	-0.26	20.6	7.9
552A 24H 3W 5-7	2368	111.46	4.86	0.12	0.31	56.50	-0.28	19.3	14.1
552A 25H 3W 30-32	2322	116.8	4.96	0.20	0.35	55.84	-0.30	18.1	13.5
552A 26H 5W 55-57	2369	122.05	5.07	0.19	0.29	55.23	-0.29	19.0	15.3
552A 27H 3W 79-81	2370	127.29	5.17	0.14	0.56	58.42	-0.34	15.5	11.3
552A 28H 3W 104-106	2323	132.54	5.27	0.07	0.33	54.41	-0.31	17.3	13.5
552A 29H 4W 29-31	2371	138.29	5.39	0.06	0.54	59.38	-0.32	16.6	14.1
552A 30H 4W 3-5	2372	142.93	5.48	0.21	0.36	58.29	-0.27	19.8	15.9
552A 31H 5W 8-10	2324	148.26	5.58	0.65	0.79	68.16	-0.30	18.3	5.3
552A 34H 3W 78-80	2325	162.28	5.86	0.65	0.76	66.47	-0.31	17.6	8.9

Table B.9 continued. TEX_{86} SST reconstructions from DSDP Hole 552A, calculated using the Kim et al. (2010) TEX_{86}^{H} calibration. Analytical reproducibility (1σ) for the TEX_{86} proxy is ±0.01. BIT, ΔRI, %GDGT-0 and OPTiMAL as in Table B.8.

Site/Core/Section	Sample ID	Depth (mbsf)	Age (Ma)	BIT	ΔRI	%GDGT-0	TEX_{86}	SST (°C)	OPTiMAL SST (°C)
642B 2H 1W 97-99	2338	5.77	0.12	0.43	1.57	63.57	-0.55	9.6	1.4
642B 2H 5W 72-74	2401	11.52	0.24	0.45	0.45	55.49	-0.34	23.7	-1.3
642B 3H 3W 0-2	2402	17.3	0.36	0.39	2.16	64.56	-0.67	1.8	2.0
642B 4H 2W 81-89	2403	23.07	0.49	0.58	1.75	59.39	-0.63	4.6	-0.4
642B 4H 6W 64-66	2339	28.84	0.61	0.57	0.74	49.65	-0.48	14.3	6.2
642B 5H 4W 70-72	2404	34.6	0.73	0.70	0.73	60.32	-0.37	13.3*	-0.4
642B 6H 1W 147-149	2405	40.37	0.92	0.85	1.12	62.98	-0.46	16.2	16.4
642B 6H 5W 124-126	2406	46.14	1.13	0.30	1.06	53.45	-0.53	11.3	-0.8
642B 7H 4W 0-2	2340	51.9	1.69	0.34	1.25	65.16	-0.46	7.1*	1.5
642B 8H 1W 77-79	2407	57.67	2.11	0.47	1.18	56.74	-0.53	11.3	-1.0
642B 8H 5W 54-56	2408	63.44	2.50	0.37	1.59	63.27	-0.56	8.9	1.4
642B 8H 5W 125-127	2409	64.15	2.55	0.76	1.42	65.33	-0.50	12.9	2.6
642B 8H 6W 46-48	2341	64.86	2.62	0.34	1.20	66.34	-0.44	8.8*	3.2
642B 8H 6W 117-119	2410	65.57	2.76	0.95	1.50	77.01	-0.41	10.9*	8.4
642B 8H 7W 38-40	2411	66.28	2.89	0.68	1.92	71.02	-0.57	8.7	6.2
642B 9H 1W 42-45	2562	66.82	3.00	0.49	2.24	63.95	-0.69	0.4	1.2
642B 9H 1W 50-53	2563	66.9	3.01	0.33	1.91	64.80	-0.62	5.2	1.0
642B 9H 1W 59-61	2412	66.99	3.03	0.52	1.76	60.16	-0.62	4.8	-1.3
642B 9H 1W 59-62	2564	66.99	3.03	0.83	0.31	45.52	-0.41	19.0	4.1
642B 9H 1W 66-68	2565	67.06	3.04	0.07	0.42	22.96	-0.64	3.9	14.6
642B 9H 1W 73-75	2566	67.13	3.05	0.31	2.91	75.10	-0.73	-2.6	5.6
642B 9H 1W 80-82	2567	67.2	3.07	0.12	1.63	57.69	-0.61	5.4	-0.4
642B 9H 1W 86-88	2568	67.26	3.08	0.00	6.14	72.18	N/A	N/A	N/A
642B 9H 1W 93-95	2569	67.33	3.09	0.13	2.26	69.54	-0.65	3.1	3.8
642B 9H 1W 100-102	2570	67.4	3.11	0.21	2.00	63.67	-0.64	3.5	0.0
642B 9H 1W 107-109	2571	67.47	3.12	0.51	1.55	60.45	-0.58	8.0	-1.5
642B 9H 1W 114-116	2572	67.54	3.13	0.42	1.92	63.41	-0.63	4.3	0.3
642B 9H 1W 121-123	2573	67.61	3.15	0.58	0.99	53.80	-0.51	12.5	-0.2
642B 9H 1W 128-130	2574	67.68	3.16	0.28	1.43	53.18	-0.61	5.8	0.9
642B 9H 1W 129-131	2342	67.69	3.16	0.41	1.82	62.77	-0.61	5.4	0.3
642B 9H 1W 137-139	2575	67.77	3.17	0.43	1.91	61.97	-0.64	3.5	-1.1
642B 9H 1W 142-144	2576	67.82	3.18	0.30	1.63	54.55	-0.64	3.7	-0.7
642B 9H 2W 0-2	2577	67.9	3.20	0.38	1.08	54.41	-0.52	11.5	-0.7
642B 9H 2W 5-7	2578	67.95	3.21	0.28	1.93	61.73	-0.64	3.4	0.0
642B 9H 2W 12-14	2579	68.02	3.22	0.52	3.28	60.84	N/A	N/A	N/A
642B 9H 2W 19-21	2580	68.09	3.24	0.15	1.50	55.25	-0.61	5.9	0.0

Table B.10. TEX_{86} SST reconstructions from ODP Hole 642B, calculated using the TEX_{86}^{L} calibration recommended for high latitude sites (Kim et al., 2010). SSTs marked (*) are calculated using the TEX_{86}^{H} calibration when conditions were warm (>15°C), as inferred from our respective $U^{K'}_{37}$ records (Kim et al., 2010). Analytical reproducibility (1σ) for the TEX_{86} proxy is ±0.01. BIT, ΔRI, %GDGT-0 and OPTiMAL as in Table B.8.

Site/Core/Section	Sample ID	Depth (mbsf)	Age (Ma)	BIT	ΔRI	%GDGT-0	TEX_{86}	SST (°C)	OPTiMAL SST (°C)
642B 9H 2W 26-28	2581	68.16	3.25	0.21	0.59	58.51	-0.35	14.8*	-1.6
642B 9H 2W 33-35	2582	68.23	3.26	0.19	0.64	60.92	-0.33	15.9*	-0.8
642B 9H 2W 40-42	2583	68.3	3.28	0.37	1.55	59.53	-0.59	7.4	-1.2
642B 9H 2W 47-49	2584	68.37	3.29	0.51	1.42	55.69	-0.59	7.0	-1.8
642B 9H 2W 50-52	2413	68.4	3.29	0.43	4.46	50.75	-1.10	-27.1	-1.1
642B 9H 2W 53-55	2585	68.43	3.30	0.41	1.73	55.62	-0.65	2.9	-1.9
642B 9H 2W 121-123	2414	69.11	3.43	0.08	3.64	56.60	N/A	N/A	N/A
642B 9H 3W 42-44	2415	69.82	3.56	0.08	3.73	65.14	N/A	N/A	N/A
642B 9H 3W 113-115	2343	70.53	3.69	0.65	0.89	65.84	-0.35	14.3*	0.6
642B 9H 4W 34-36	2416	71.24	3.81	0.25	0.91	61.02	-0.41	10.3*	-1.3
642B 9H 4W 105-107	2417	71.95	3.92	0.21	1.07	64.96	-0.42	10.0*	0.0
642B 9H 5W 26-28	2418	72.66	4.04	0.12	0.80	62.40	-0.37	13.6*	0.9
642B 9H 5W 97-99	2344	73.37	4.16	0.21	1.02	64.51	-0.41	10.9*	1.0
642B 9H 6W 18-20	2419	74.08	4.28	0.22	1.64	80.13	-0.41	10.3*	8.5
642B 9H 6W 88-90	2420	74.78	4.40	0.15	2.89	49.32	N/A	N/A	N/A
642B 9H 7W 9-11	2421	75.49	4.52	0.10	2.86	54.32	N/A	N/A	N/A
642B 10H 1W 30-32	2345	76.2	4.64	0.15	1.18	66.49	-0.43	9.3*	3.2
642B 10H 1W 100-102	2422	76.9	4.76	0.35	1.17	66.42	-0.43	9.5*	2.0
642B 10H 2W 22-24	2423	77.62	4.88	0.38	2.53	75.22	-0.66	2.4	6.6
642B 10H 3W 146-148	2424	80.36	5.49	0.19	1.86	65.47	-0.60	6.3	3.2
642B 10H 5W 118-120	2346	83.08	6.62	0.21	2.27	70.83	-0.64	3.4	2.6
642B 11H 1W 44-46	2425	85.84	6.83	0.47	0.31	42.64	-0.44	8.8*	13.3
642B 11H 3W 18-20	2426	88.58	6.94	0.17	0.97	73.68	-0.28	19.6*	6.9
642B 11H 5W 0-2	2427	91.4	7.05	0.17	0.51	62.00	-0.27	20.3*	0.0
642B 11H 6W 117-119	2347	94.07	7.16	0.16	1.15	67.43	-0.41	10.4	2.0
642B 12H 2W 41-43	2428	96.81	7.24	0.89	2.88	76.06	-0.72	-1.5	7.0
642B 12H 4W 15-17	2348	99.55	7.28	0.11	2.05	65.86	-0.64	3.9	2.6
642B 12H 5W 139-142	2349	102.29	7.32	0.19	1.79	64.95	-0.59	6.9	0.4

Table B.10 continued. TEX_{86} SST reconstructions from ODP Hole 642B, calculated using the TEX_{86}^{L} calibration recommended for high latitude sites (Kim et al., 2010). SSTs marked (*) are calculated using the TEX_{86}^{H} calibration when conditions were warm (>15°C), as inferred from our respective $U^{K'}_{37}$ records (Kim et al., 2010). Analytical reproducibility (1σ) for the TEX_{86} proxy is ±0.01. BIT, ΔRI, %GDGT-0 and OPTiMAL as in Table B.8.

Site/Core/Section	Sample ID	Depth (mbsf)	Age (Ma)	BIT	ΔRI	%GDGT-0	TEX_{86}	SST (°C)	OPTiMAL SST (°C)
907A 1H 3W 133-135	2326	4.33	0.21	0.30	2.89	71.67	-0.75	-3.8	5.0
907A 2H 2W 137-139	2373	10.17	0.49	0.66	1.26	59.92	-0.52	12.0	2.9
907A 2H 4W 120-122	2374	13	0.63	0.73	2.56	86.45	N/A	N/A	N/A
907A 3H 1W 53-55	2375	17.33	1.00	0.94	3.17	90.09	N/A	N/A	N/A
907A 3H 4W 36-38	2327	21.66	1.19	0.85	1.64	73.88	-0.65	3.0	6.1
907A 3H 7W 20-22	2376	26	1.40	0.83	-0.36	44.49	N/A	N/A	N/A
907A 4H 3W 103-105	2377	30.33	1.61	0.30	-0.09	32.81	-0.44	16.9	6.7
907A 4H 6W 86-88	2378	34.66	1.81	0.55	1.22	76.67	-0.32	25.2	8.6
907A 5H 3W 19-21	2328	38.99	1.99	0.69	0.97	57.00	-0.47	15.0	-0.1
907A 5H 6W 3-5	2379	43.33	2.25	0.00	1.67	68.88	-0.53	11.4	7.1
907A 6H 2W 87-91	2380	47.67	2.50	0.94	1.21	77.70	-0.30	26.6	8.9
907A 6H 3W 109-111	2381	49.39	2.60	0.70	1.04	71.82	-0.32	25.0	8.2
907A 6H 4W 138-140	2329	51.18	2.69	0.88	0.57	74.53	N/A	N/A	N/A
907A 6H 6W 6-8	2382	52.86	2.77	0.74	1.02	70.99	-0.33	24.8	8.2
907A 6H 7W 34-36	2383	54.64	2.86	0.75	1.93	66.65	-0.61	5.9	3.8
907A 7H 2W 5-7	2384	56.35	2.95	0.87	1.96	75.15	-0.54	10.5	6.6
907A 7H 3W 26-31	2330	58.06	3.04	0.86	1.13	70.28	-0.37	21.6	6.2
907A 7H 4W 47-49	2385	59.77	3.14	0.83	1.94	48.16	-0.74	-3.0	6.6
907A 7H 5W 70-79	2386	61.52	3.22	0.71	1.85	47.68	-0.73	-2.2	6.8
907A 7H 6W 92-95	2387	63.22	3.33	0.96	1.49	88.03	-0.30	26.5	12.2
907A 8H 1W 72-74	2331	65.02	3.46	0.76	1.14	70.42	-0.38	21.5	6.2
907A 8H 2W 92-95	2388	66.72	3.59	1.00	1.07	87.02	N/A	N/A	N/A
907A 8H 3W 117-119	2389	68.47	3.90	0.96	1.01	85.58	N/A	N/A	N/A
907A 8H 4W 143-149	2390	70.23	4.21	0.95	1.85	80.58	-0.47	15.4	9.8
907A 8H 6W 14-16	2332	71.94	4.53	0.00	1.04	25.50	-0.73	-2.1	13.0
907A 8H 7W 37-39	2391	73.67	4.73	0.28	4.16	83.62	N/A	N/A	N/A
907A 9H 2W 10-12	2392	75.4	4.90	0.21	2.45	73.41	-0.66	2.6	7.8
907A 9H 3W 34-36	2393	77.14	5.09	0.11	3.02	72.70	-0.76	-4.7	6.8
907A 9H 4W 57-59	2333	78.87	5.24	0.70	1.21	68.80	-0.41	10.4*	4.4
907A 9H 5W 81-83	2394	80.61	5.37	0.85	1.98	69.89	-0.59	6.9	2.4
907A 9H 6W 103-106	2395	82.33	5.50	0.47	2.24	69.07	-0.65	2.8	3.9
907A 10H 1W 147-149	2396	84.77	5.68	0.68	1.77	70.34	-0.54	10.3	2.5
907A 10H 3W 92-94	2334	87.22	5.86	0.51	1.15	66.75	-0.42	10.1	3.2
907A 10H 5W 34-36	2397	89.64	6.04	0.92	3.06	91.18	-0.65	3.4	12.1
907A 10H 6W 127-129	2398	92.07	6.24	0.50	1.86	62.04	-0.63	4.3	-1.1
907A 11H 2W 20-22	2399	94.5	6.55	0.31	2.13	65.25	-0.66	2.4	0.0

Table B.11. TEX_{86} SST reconstructions from ODP Hole 907A, calculated using the TEX_{86}^{L} calibration recommended for high latitude sites (Kim et al., 2010). SSTs marked (*) are calculated using the TEX_{86}^{H} calibration when conditions were warm (>15°C), as inferred from our respective $U^{K'}_{37}$ records (Kim et al., 2010). Analytical reproducibility (1σ) for the TEX_{86} proxy is ±0.01. BIT, ΔRI, %GDGT-0 and OPTiMAL as in Table B.8.

Site/Core/Section	Sample ID	Depth (mbsf)	Age (Ma)	BIT	ΔRI	%GDGT-0	TEX_{86}	SST (°C)	OPTiMAL SST (°C)
907A 11H 3W 113-115	2335	96.93	6.83	0.88	1.14	72.62	-0.35	22.9	6.8
907A 11H 5W 56-58	2400	99.36	7.30	0.91	1.92	78.82	-0.50	13.0	7.4
907A 11H 7W 0-2	2336	101.8	7.74	0.91	1.70	87.23	-0.41	10.4*	15.7
907A 12H 2W 43-45	2337	104.23	8.00	0.16	2.30	70.16	-0.65	2.8	3.8

Table B.11 continued. TEX_{86} SST reconstructions from ODP Hole 907A, calculated using the TEX_{86}^{L} calibration recommended for high latitude sites (Kim et al., 2010). SSTs marked (*) are calculated using the TEX_{86}^{H} calibration when conditions were warm (>15°C), as inferred from our respective $U^{K'}_{37}$ records (Kim et al., 2010). Analytical reproducibility (1σ) for the TEX_{86} proxy is ±0.01. BIT, ΔRI, %GDGT-0 and OPTiMAL as in Table B.8.

Table B.12 (following page). Tjörnes basalt thin section descriptions.

Lava Unit	Thin Section Description
Kaldakvísl and Unnamed lavas (Bed 2a of Bárðarson, 1925)	Porphyritic texture, with a very-fine cryptocrystalline groundmass. Phenocrysts comprise 15% of the section, including plagioclase (8%), clinopyroxene (4%), orthopyroxene (1%), and olivine (2%). Plagioclase phenocrysts occur as ≤0.5 mm laths displaying simple and albite twinning, or more rarely as larger 2−3 mm subhedral/euhedral crystals which are often zoned, and heavily altered to (sericite/other clay minerals?). Pyroxene phenocrysts are mostly rounded and ≤0.3 mm, and occur both as solo phenocrysts and as glomerocrysts with other clinopyroxene or plagioclase phenocrysts. Rare olivine phenocrysts are <0.3 mm, rounded and often heavily fractured. The very-fine groundmass comprises granular clinopyroxene and plagioclase, with significant evidence of pervasive oxidation of the groundmass minerals.
Skeifá lavas	Porphyritic texture, with a very-fine cryptocrystalline to glassy groundmass. Phenocrysts make up 60% of the section, including plagioclase (40%) and less commonly clinopyroxene (15%), orthopyroxene (3%) and olivine (2%). Plagioclase phenocrysts are present as larger ≤1.5 mm lath shaped crystals which frequently form intergrown clots with other phenocrysts, or as much smaller ≤0.2 mm acicular needles. Simple and albite twinning are common throughout. Pyroxene and olivine occur as ≤0.3 mm rounded to irregular shaped crystals, which are often fractured and occur either individually or as clots with other clinopyroxene/plagioclase phenocrysts. Dissolved rims are common, with some phenocrysts becoming so dissolved they are almost skeletal in form. The groundmass is glassy to aphinitic, and the coarsest patches appear to be formed of very fine acicular crystals of plagioclase.
Höskuldsvík lavas	Fine-grained, sparsely porphyritic, equigranular holocrystalline rock comprising mainly of a fine-grained groundmass of plagioclase, pyroxene and rare olivine. Lath shaped <0.15 mm plagioclase crystals, commonly displaying simple or albite twinning, make up 45% of the section. Rounded granular clinopyroxene crystals 0.01−0.1 mm form the majority of the rest of the section. The remainder of the groundmass is formed of small olivine crystals, and small 0.05 mm opaques (likely Fe-Ti oxides). Very rare large (up to 3 mm) subhedral/euhedral plagioclase phenocrysts are observed, commonly displaying disequilibria textures such as dissolved rims and pitted cores.

Tjörnes seam	Latitude (DD)	Longitude (DD)	Sample ID	MBT'_{5ME}	MAT_{mr} (°C)	CBT'	pH_{soil}	$MAAT_{peat}$ (°C)	CBT_{peat}	pH_{peat}	BIT
			2464	N/A	N/A	N/A	N/A	N/A	N/A	N/A	N/A
			2465	N/A	N/A	N/A	N/A	N/A	N/A	N/A	N/A
1	66.109°N	17.283°W	2466	N/A	N/A	N/A	N/A	N/A	N/A	N/A	N/A
			2467	N/A	N/A	N/A	N/A	N/A	N/A	N/A	N/A
			2468	N/A	N/A	N/A	N/A	N/A	N/A	N/A	N/A
			2469	0.33	-1.3	N/A	N/A	-5.8	N/A	N/A	0.59
			2470	0.24	-10.5	N/A	N/A	-10.5	N/A	N/A	0.37
2	66.108°N	17.275°W	2471	0.30	-7.9	N/A	N/A	-7.6	N/A	N/A	0.61
			2472	0.32	-0.8	N/A	N/A	-6.5	-1.63	4.0	0.90
			2473	N/A	N/A	N/A	N/A	N/A	N/A	N/A	N/A
			2474	0.68	13.5	-0.58	6.2	12.4	-0.50	6.8	1.00
			2475	0.60	10.1	-0.60	6.2	8.4	-0.57	6.6	0.95
3	66.114°N	17.262°W	2476	0.43	6.2	-1.06	5.5	-0.5	-0.87	5.9	1.00
			2477	0.42	9.2	-0.57	6.2	-0.9	-0.46	6.9	1.00
			2478	0.65	13.1	-0.74	6.0	11.0	-0.67	6.4	1.00
			2479	0.17	-3.0	-1.22	5.2	-14.2	-0.94	5.7	1.00
			2480	0.41	6.2	-0.75	6.0	-1.6	-0.44	7.0	0.99
4	66.114°N	17.261°W	2481	0.63	12.4	-0.74	6.0	10.1	-0.48	6.9	1.00
			2482	0.25	1.2	-0.84	5.8	-9.9	-0.68	6.4	0.99
			2483	0.32	3.8	-0.51	6.3	-6.5	-0.40	7.1	0.99
			2484	0.25	-1.9	-1.70	4.5	-9.9	-1.36	4.7	0.97
			2485	0.28	0.1	-1.33	5.0	-8.6	-1.07	5.4	0.93
5	66.114°N	17.261°W	2486	0.28	0.2	-1.51	4.8	-8.3	-1.04	5.5	0.96
			2487	N/A	N/A	N/A	N/A	N/A	N/A	N/A	N/A
			2488	0.33	3.5	-0.87	5.8	-5.9	-0.82	6.0	0.92
			2489	0.47	5.2	-1.47	4.8	1.7	-1.16	5.2	1.00
			2490	0.37	1.3	-1.45	4.8	-3.7	-0.89	5.8	0.99
6	66.122°N	17.257°W	2491	0.28	-0.2	-1.04	5.5	-8.7	-0.72	6.3	0.96
			2492	0.51	6.7	-1.34	5.0	3.4	-1.01	5.6	1.00
			2493	0.45	6.2	-0.65	6.1	0.4	-0.46	6.9	1.00
			2499	0.30	-0.8	-1.45	4.8	-7.2	-1.05	5.5	0.99
			2500	0.37	2.4	-2.01	3.9	-3.9	-1.23	5.0	0.99
7	66.125°N	17.258°W	2501	0.33	-0.8	-2.02	3.9	-6.0	-1.30	4.8	1.00
			2502	0.32	0.3	-1.99	4.0	-6.1	-1.25	4.9	1.00
			2503	0.44	3.2	-2.02	3.9	-0.3	-1.35	4.7	1.00

Table B.13. Terrestrial temperature reconstructions derived from branched GDGTs preserved in the Tjörnes lignite seams, northern Iceland. Latitude and longitude in decimal degrees (DD). MBT'_{5ME}, MAT_{mr}, CBT' and pH_{soil} indexes after De Jonge et al. (2014). $MAAT_{peat}$, CBT_{peat} and pH_{peat} indexes after Naafs et al. (2017). Branched and Isoprenoid Tetraether (BIT) index after Hopmans et al. (2004). Analytical reproducibility (1σ) for the MBT'_{5ME} proxy is ±0.01.

Tjörnes seam	Latitude (DD)	Longitude (DD)	Sample ID	MBT'_{5ME}	MAT_{mr} (°C)	CBT'	pH_{soil}	$MAAT_{peat}$ (°C)	CBT_{peat}	pH_{peat}	BIT
8	66.125°N	17.257°W	2464	0.13	-3.4	-1.14	5.3	-16.2	-0.81	6.0	1.00
			2465	0.22	-1.7	-1.24	5.2	-11.5	-0.68	6.4	1.00
			2466	0.23	-1.5	-1.28	5.1	-11.0	-0.63	6.5	1.00
			2467	0.22	-1.8	-1.21	5.2	-11.7	-0.69	6.3	1.00
			2468	0.26	2.7	-0.71	6.0	-9.7	-0.48	6.9	1.00
9	66.126°N	17.227°W	2469	0.66	13.9	-1.73	4.4	11.6	-0.98	5.6	1.00
			2470	0.60	10.3	-1.40	4.9	8.3	-0.93	5.8	1.00
			2471	0.26	1.2	-1.26	5.2	-9.2	-0.80	6.1	1.00
			2472	0.18	2.2	-1.31	5.1	-13.8	-0.92	5.8	1.00
			2473	0.39	6.2	-0.74	6.0	-2.6	-0.54	6.7	1.00
10	66.126°N	17.227°W	2474	0.74	13.9	-0.57	6.2	15.5	-0.53	6.7	1.00
			2475	0.43	5.3	-1.20	5.2	-0.7	-0.88	5.9	1.00
			2476	0.67	11.8	-1.78	4.3	12.1	-1.59	4.1	1.00
			2477	0.35	1.2	-1.41	4.9	-4.8	-1.04	5.5	1.00
			2478	N/A	N/A	N/A	N/A	N/A	N/A	N/A	N/A
11	66.157°N	17.273°W	2479	0.29	-0.6	-1.34	5.0	-7.8	-0.87	5.9	1.00
			2480	0.15	0.3	-1.15	5.3	-15.0	-0.86	5.9	1.00
			2481	0.32	5.6	-1.12	5.4	-6.3	-0.54	6.7	1.00
			2482	0.23	1.5	-1.15	5.3	-11.2	-0.67	6.4	0.88
			2483	0.28	3.3	-0.75	6.0	-8.5	-0.51	6.8	1.00

Table B.13 continued. Terrestrial temperature reconstructions derived from branched GDGTs preserved in the Tjörnes lignite seams, northern Iceland. Latitude and longitude in decimal degrees (DD). MBT'_{5ME}, MAT_{mr}, CBT', pH_{soil}, $MAAT_{peat}$, CBT_{peat}, pH_{peat} and BIT indexes as in Table B.13. Analytical reproducibility (1σ) for the MBT'_{5ME} proxy is ±0.01.